Formation and Growth of Fibrous Mineral Veins in Mudrocks during Burial and Uplift

by

Qingfeng Meng

St Peter's College



A thesis submitted for the degree of

Doctor of Philosophy

at

the University of Oxford

Hilary 2017

Abstract

Formation and Growth of Fibrous Mineral Veins in Mudrocks during Burial and Uplift

Qingfeng Meng

St Peter's College, University of Oxford

A thesis submitted for the Degree of Doctor of Philosophy

Fibrous mineral veins are extremely important structures in mudrocks because they represent phases of geological activity that occurred after the deposition of the host rocks. They are, therefore, crucial for unravelling the geological history, especially for analyzing post-depositional tectonism, diagenesis, and associated physical and chemical conditions. This research focuses on the investigation of fibrous mineral (gypsum and calcite) veins in mudrocks, using integrated field, petrographic, and geochemical methods. The aim is to obtain a better understanding of mineral vein systems in fine-grained rocks over spatial scales ranging from reservoir to microns, regarding the timing, formation mechanism, vein growth, fluid and stress conditions, fluid-rock interaction, and their expressions in vein texture. The results reveal that fibrous mineral veins are produced during different stages of basin evolution.

Fibrous calcite veins in Lower Jurassic shales in the Wessex Basin have a diagenetic growth history during early burial of the sediments. In contrast, the formation of satin spar veins in the Triassic marls of the Bristol Channel Basin is closely associated with tectonic compression during basin uplift. However, both the gypsum veins and calcite veins owe their origin to overpressure and incremental fibre growth in closed systems, with their textures exhibiting similar antitaxial characteristics. Host rock lithology, defined by mineral components, fabrics

and mechanical properties, mainly controls the development of the veins. The research highlights the kinematic implications of fibre orientations for host rock deformation and the EBSD measurement of crystallographic orientations of fibres for the analysis of paleo-stress state during fibre growth. Evidence for the force of crystallization exerted by mineral fibres, which has largely been ignored in previous studies, are revealed based on field and petrographic observations. The vein systems presented in this research provide an analogue for future studies on sub-seismic scale fracture/vein characterization and prediction in mudrocks either as caprock or source rocks for hydrocarbons.

Extended abstract

Fibrous mineral veins are extremely important structures in mudrocks because they represent the phases of geological activity that occurred after the deposition of the hosts, and are therefore crucial for unravelling the geological history, especially for analyzing the tectonism, diagenesis and the associated physical and chemical conditions. Fibrous mineral veins commonly occur in mudrocks either as caprocks or source rocks for hydrocarbons. Hence, understanding the spatial distribution, geometry and also the formation and growth process and mechanism is important for the development of oil and gas resource, especially shale gas.

In Chapter 1 I outline some of the current issues with our understanding of the development of sub-surface fractures in fine-grained rocks. I show how outcrop studies of veined fractures may help our understanding and develop the the methodology that I apply later in the thesis.

Chapter 2 reports the field and geochemical study of satin spar (fibrous gypsum) veins in the Triassic Mercia Mudstone Group in the Bristol Channel Basin. The spatial distribution of satin spar veins exhibits a high heterogeneity. Based on fracture stratigraphy, five distinct units were identified in the Keuper Marl Formation, and three in the Blue Anchor Formation. Satin spar veins are widespread in Unit 1, 2 and 4 in the Keuper Marl, exhibiting three preferred orientations, including a NW-SE striking, north dipping set, an E-W striking, south dipping set and a sub-horizontal set. Coalescence rather than cross-cutting between differently oriented veins occurs when they intersect. As the only unit that contains veins in the Blue Anchor Formation, Unit 2 includes a bedding parallel set of white veins and an E-W striking, steeply dipping set of red veins. The red veins cross-cut the white veins. Three faults with a reverse displacement, which contain fault-parallel slickenfibres in the median zones and also on vein surfaces, cross-

cut sub-horizontal veins in the bulk rock, indicating multiple phases of fault reactivation. Sub-horizontal veins in the intense folds in the hangingwall of the Helwell Bay Fault cross-cut the folded layers, suggesting that vein formation postdate strata folding. The cross-cutting relationships between gypsum veins and the other structures indicate that the formation timing is Miocene. The veins are interpreted to form as natural hydraulic fractures during basin inversion. Overpressure triggered by tectonic compression, strata buckling and sediment unloading together gave rise to the generation of sub-horizontal fractures. Inclined veins that are filled with gently dipping fibres are possibly newly formed tension gashes or wing-cracks during the propagation of sub-horizontal fractures. The other inclined veins presumably formed as fault-controlled fractures. The vein network in the Keuper Marl exhibits a high connectivity, which is largely enhanced by vein branching and coalescence. Gypsum veins and nodules contain similar chemical compositions. The red veins have a higher content of Fe^{3+} and Na^{+}, which possibly indicates a drier environment and pore waters with a higher salinity. Vein aperture follows a log-normal distribution. This is possibly caused by a random vein generation and a subsequent vein growth that was mainly localized to the largest veins due to mechanical interaction.

Chapter 3 continues the study of gypsum veins in the Mercia Mudstone with detailed petrographic characterizations. Secondary gypsum occurs in the form of nodules, laths and diffusely disseminated gypsum in the red marls. Unit 1, 2 and 4 show coexistence of gypsum veins and secondary gypsum in the rock matrix, whilst veins and secondary gypsum are both absent in Unit 5 and the evaporite-free layers in Unit 3. Given the homogeneous chemical compositions of single veins, it is interpreted that the gypsum veins mainly derived gypsum from secondary gypsum in the adjacent host rocks by diffusion. The excess gypsum derived from nodules during anhydrite-gypsum transition were transported to the nodule-rooted veins. In

contrast, the veins in the Blue Anchor Formation are mainly sourced by the nodules in multiple evaporite horizons, whilst gypsum is absent in the rock matrix. Fibrous gypsum veins contain a median zone that exhibits a blocky texture and contains multiple wall-parallel host inclusion bands, indicating the primary site of vein nucleation and a crack-seal formation mechanism. The fibres on different sides of the median zone exhibit smooth crystal boundaries and constant widths, indicating little growth competition. The growth process of fibres is interpreted to be incremental without fracturing. The fibres keep pace with vein opening and hence track the opening direction with little influence from vein-wall asperities. Precipitation of gypsum on vein surfaces and vein growth would continue if the pore fluids remain supersaturated with respect to gypsum. The crystallization pressure exerted on the surrounding rocks by gypsum precipitation could possibly produce fractures and be responsible for vein extension.

Chaper 4 characterizes the field and geochemical features of sub-horizontal fibrous calcite veins (cone-in-cone structures and beef veins) in the Lower Jurassic Shales-with-Beef Member, the Wessex Basin, UK. The beef veins, containing sub-vertical fibres and a dark median zone, exhibit varied sizes and geometries. Vein aperture does not show clear correlation to the length. The beef veins commonly exhibit tapering tips when they are isolated, and blunt tips when the veins are closely spaced. Interestingly, the short beef veins contain fossil skeletons with well-preserved morphology on vein surfaces. The skeletons on the upper and lower surfaces are separated by fibres. Cone-in-cone structures consist of nested conical bundles of calcite fibres and abundant host rock inclusions. These structures occur either along the outer rims of carbonate concretions or as bedding parallel structures. Cone-in-cone structures are persistent laterally with an aperture several up to 8 cm. The veins exhibit moderate carbon isotope values, ranging from -1.515‰ to 2.732‰. The source of carbonate is presumably mainly derived from

seawater inorganic carbon and bioclasts. The oxygen isotope compositions of the calcite veins are all negative, ranging from -8.872‰ to -4.521‰, which are too negative to reflect the primary pore water oxygen isotope signatures. The veins are interpreted to form as closed-system hydraulic fractures when the sediments entered the methanogenic zone and experienced degassing. Overpressuring may also be contributed to by rapid deposition of the overlying sediments. The shale beds with a high TOC could have generated abundant CO_2 either for overpressure buildup or cementing pores in the shale matrix. The fossil skeletons may serve as nucleus for calcite precipitation and therefore control vein distribution.

Chapter 5 continues the study of the fibrous calcite veins in the Shales-with-Beef Member with a thorough petrographic (optical, SEM and EBSD) examination. The median zones of beef veins contain equant calcite crystals, scattered organic matter, pyrite, fossil skeletons and clays and reflect the nucleation sites of primary fractures. The equant calcite crystals exhibit near-random c-axis orientations, whilst the fibres exhibit a preferred c-axis orientation normal to the median zones. The calcite fibres grew displacively, which are evident from the fibre-separated fossils, displaced and deformed clays at vein tips and fibre fronts. The force may be attributed to the crystallization pressure of calcite, which potentially modified the very local stress field and favors the growth of calcite fibres with their c-axes normal to the median zones. The blocky zones that contain small sized, equant calcite crystals and pyrite are interpreted as fossil remains that were incorporated into beef veins during fibre growth. Cone-in-cone structures are likely to predate beef veins. The apical angles of single cones, which increase towards the median zone, are possibly controlled by the degree of compaction of the host rock. Cone-in-cone structures are interpreted as closely stacked crystal bundles in overpressured horizons rather than shear fractures that were subsequently filled with calcite crystals. Organic matter patches that are

spread in the median zones of beef veins and along cone boundaries of cone-in-cone structures may not provide nutrient for the calcite fibres, but potentially show evidence for methane-triggered overpressuring in the sediments during relative early burial into the methanogenic zone.

Chapter 6 compares the similarities and differences between the gypsum veins in the Mercia Mudstone and the fibrous calcite veins in the Lower Charmouth Mudstone. Both the veins exhibit similar crystal habits, internal textures, kinetics of growth and mode of nutrient transport. Their differences in vein and crystal orientation, vein interaction, purity of composition and deformation in the hosts are the results of different stages of basin evolution, paleostress state, and mechanical properties of the host rocks. Both the two types of veins were generated as closed system hydraulic fractures and derived nutrient from the host sediments. The fibrous veins show features of displacive growth, which is possibly given rise to by the force of crystallization when given a supersaturated pore fluids and non-hydrostatic pressure.

Chapter 7 concludes the major findings in this research and offers suggestions for future studies on fibrous mineral veins.

Overall, this study presents the mineral vein networks from reservoir to micro scale in mudrocks, which can serve as an analogue for future studies on sub-seismic scale fracture characterization and prediction in mudrocks either as seals or source rocks for hydrocarbons.

Acknowledgement

First of all, I would like to express my sincere appreciation to my principal supervisor Professor Joe Cartwright. Joe has been a tremendous mentor for me during my DPhil studies. Joe's constant guidance and encouragement has been priceless, which allows me to grow as a competent researcher. What I have learned from Joe will always be a treasure for my future career.

I thank Professor Steve Hesselbo and Professor Bruce Levell for serving as my advisors and providing fruitful comments and suggestions. I would like to thank Dr. John Hooker for beneficial discussions, skill training, and thesis and paper revisions.

Many thanks go to the Shell-Oxford project members, including Dr. Claudia Bertoni, Dr. Alex Dickson, Dr. Linhao Fang, Dr. Martino Foschi, Dr. Ben Manton, Dr. Micha Ruhl, Dr. Olga Gorbanenko, Mr Matteo Paganoni and Ms Weimu Xu. Professor Lars Hansen and Dr. David Wallis are gratefully acknowledged for their generous help. Professor Conall Mac Niocaill and Dr. Jonathan Imber are acknowledged for their helpful comments.

I thank Jonathan Wells, Stephen Wyatt and Owen Green for technical support. I also thank Maria Petrunova and Elaine Sherrott for helping with daily issues.

Without the financial support from Shell, this work would not have been possible. I would like to express my appreciation to the visitors from Shell and other institutes to the Shell Geoscience Lab that have provided insightful suggestions for my projects.

Finally, I would like to thank my family. Words cannot express how grateful I am to my mother-in law, father-in-law, my mother and father. Most importantly, I had the wonderful four years at Oxford with the company of my beloved wife Lansi Wang!

Contents

Chapter 1 Introduction 1

1.1 Research background 1

1.2 Research methods 5

1.3 Aims 7

1.4 Outline 8

Chapter 2 Satin spar veins in the Mercia Mudstone, the Bristol Channel Basin 10

2.1 Introduction 10

2.2 Geological setting 13

2.2.1 Location 13

2.2.2 Basin evolution 15

2.2.3 Local geology 19

2.3 Vein characterization 34

2.3.1 Fracture stratigraphy 34

2.3.2 Orientation 36

2.3.3 Geometry 40

2.3.4 Interaction 59

2.3.5 Connectivity 66
2.3.6 Aperture 70
2.3.7 Median zone and host rock inclusions 73
2.4 Gypsum fibres 75
2.4.1 Observations 75
2.4.2 Apparent angle between gypsum fibre and vein wall 82
2.4.3 Fibre orientation 83
2.5 Element concentrations 84
2.6 Discussion 90
2.6.1 Timing of vein generation 90
2.6.2 Mechanics of fracturing 93
2.6.3 Reactivation of pre-existing faults/fractures 96
2.6.4 Vein interaction 97
2.6.5 Hydraulic fracturing in closed systems 99
2.6.6 Implication of vein-aperture distribution 101
2.7 Conclusions 105
Chapter 3 Petrographic characterization of satin spar veins in the Triassic Mercia Mudstone, the Bristol Channel Basin 106
3.1 Introduction 106

3.2 Method 108

3.3 Diagenetic gypsum 109

3.3.1 Nodular gypsum 109

3.3.2 Gypsum laths 110

3.3.3 Diffusely disseminated gypsum (DDG) 112

3.4 Gypsum veins 122

3.4.1 Geometry 122

3.4.2 En echelon veins 122

3.4.3 Vein branching 124

3.4.4 Vein coalescence 128

3.5 Microtexture of gypsum veins 136

3.5.1 Blocky veins 137

3.5.2 Elongate-fibrous veins 138

3.5.3 Fibrous veins 139

3.6 Rock segmentation and associated fibres 143

3.7 Mineral composition of the host rock 152

3.8 Discussion 157

3.8.1 Microtextural expressions of hydraulic fracturing 157

3.8.2 Growth of fibres 161

3.8.3 Kinematic implications of fibres 165

3.8.4 Force of crystallization 174

3.8.5 Lithological control on vein development 177

3.9 Conclusions 180

Chapter 4 Fibrous calcite veins in the Lower Jurassic shales of the Charmouth Mudstone Formation, the Wessex Basin 181

4.1 Introduction 181

4.2 Geological setting 183

4.2.1 Location 183

4.2.2 Basin setting 185

4.2.3 The black shale 187

4.3 Methodology 190

4.4 Vein characterization 193

4.4.1 Occurrence 193

4.4.2 Vein pattern 198

4.4.3 Host rock deformation 212

4.5 Geochemistry 218

4.5.1 Carbonate concentration 218

4.5.2 Total organic carbon 218

4.5.3 Carbon isotope data 218

4.5.4 Oxygen isotope data 225

4.6 Discussion 225

4.5.1 Source of carbonates 226

4.5.2 Diagenetic conditions 228

4.5.3 Vein formation 231

4.5.4 Controls on vein development 234

4.8 Conclusions 236

Chapter 5 Petrographic characterization of the fibrous calcite veins in the Lower Jurassic Charmouth Mudstone, the Wessex Basin 238

5.1 Introduction 238

5.2 Methods 240

5.3 Textural characteristics 241

5.3.1 Beef veins 241

5.3.2 Cone-in-cone structure 256

5.4 Composition 261

5.4.1 Skeletal fossil fragments 261

5.4.2 Amorphous organic matter (AOM) 264

5.4.3 Pyrite 268

5.5 Microtexture of clay inclusions 271
5.6 EBSD analysis 274
5.6.1 Beef veins 275
5.6.2 Cone-in-cone structures 284
5.7 Non-clay mineral composition of the black shales 290
5.8 Discussion 296
5.8.1 Diagenetic growth 296
5.8.2 Role of organic matter 297
5.8.3 Implications of C-axis orientations 299
5.8.4 Displacive growth 301
5.8.5 Formation mechanism 304
5.9 Conclusions 307
Chapter 6 Summary and discussion 309
6.1 Satin spar veins and calcite beef veins: a comparison 309
6.2 Mechanisms of mineral vein generation during basin extension and compression 311
6.3 Controls on mineral vein distribution in a chemically closed system 313
6.4 Conditions for displacive crystallization by force of crystallization 314
Chapter 7 Conclusions and suggested future work 317
Appendix 320

Bibliography 323

Chapter 1 Introduction

1.1 Research background

Shale gas is a type of unconventional gas resource that is stored in shales as free gas in natural fractures, as gas sorbed onto kerogen and clay-mineral surfaces, or as gas dissolved in kerogen and bitumen (Bowker, 2007; Curtis, 2002; Jarvie et al., 2007). Shale gas has contributed to a substantial proportion of natural gas supply and become one of the most important gas sources worldwide during the past few years (Jacoby et al., 2011). However, the extraction of shale gas largely relies on hydraulic fracture stimulation due to the extremely low bulk rock permeability in shales (Bello and Wattenbarger, 2010; Gale et al., 2007; Vengosh et al., 2014). Natural fractures in shale gas plays may reactivate during stimulation and enhance recovery efficiency (Gale and Holder, 2010; Gale et al., 2007; Montgomery et al., 2005; Olson et al., 2012). Stimulated hydraulic fractures utilize the pre-existing natural fractures of weak planes and may possibly propagate parallel to the local maximum principle stress, producing a complex fracture network as gas migration pathways (Gale et al., 2007; Maxwell et al., 2002).

If the natural fractures in shales have been sealed by minerals, the fractures may still be reopened at vein-wall interfaces due to the low tensile strength of the contact (Gale and Holder, 2008, 2010). The low strength is caused by the crystallographic discontinuity between mineral grains in fractures and grains in the wall rock, where little crystal bonding exists. Hence, the analysis of the distribution and geometry of natural fractures and mineral veins in shale gas reservoirs, prior to well planning, hydraulic stimulation and petroleum system modeling, has become a fertile field of investigation (Baihly et al., 2010; Gale et al., 2007; Rutledge and Phillips, 2003).

For similar reasons, natural fractures in low-permeability mudrock, especially tensile fractures (mode I), have become a critical factor in site evaluations for carbon dioxide sequestration, nuclear waste disposal, seal integrity analysis and geothermal resource extraction (Aydin, 2000; Chiaramonte et al., 2008; Ingram and Urai, 1999; Mazumder et al., 2006; Polak et al., 2003).

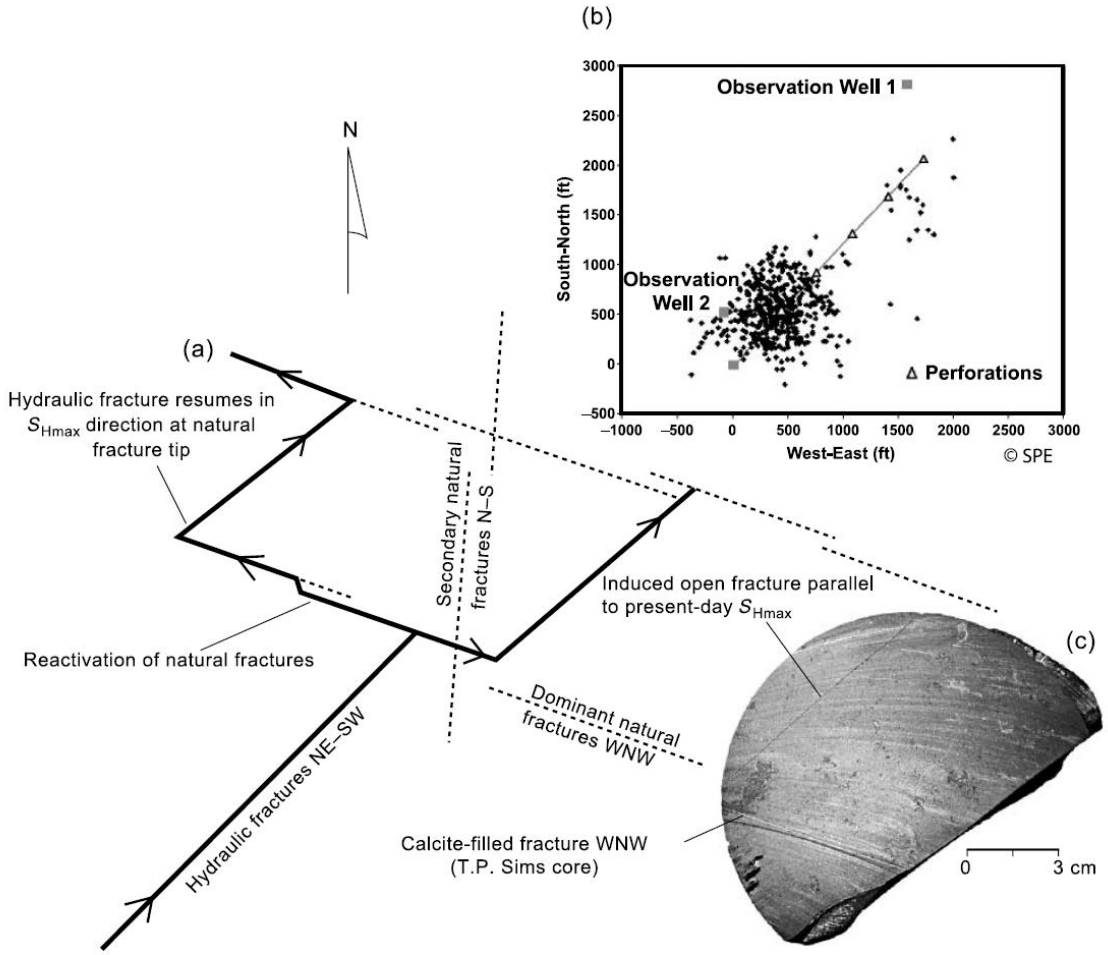


Figure 1.1 Diagram illustrating the network of pre-existing natural fractures and hydraulic stimulated fractures. (a) Propagation of Hydraulic fractures (solid lines) in the NE-SW direction and reactivation of pre-existing fractures (dashed lines). (b) Microseismic data of hydraulic fractures. Data from Warpinski et al. (2005) (c) A sealed veins and the associated stimulated fracture that is parallel to S_{Hmax}. Adopted from Gale and Holder (2008).

Because analysis of the geometry and distribution of subsurface fractures is difficult, outcrop fractures have been studied intensively as analogues for subsurface fracture evaluation and prediction (Antonellini, 2000; Gale et al., 2004; Lavenu et al., 2013; Odling et al., 1999; Strijker et al., 2012). However, outcrop fractures may have multiple origins, e.g. weathering, stress-release and cooling during uplift (Engelder, 1985; Gale and Holder, 2010; Lorenz and Finley, 1991), and do not necessarily represent subsurface reservoir fractures. Moreover, the fractures, especially early formed fractures, may experience significant modifications after their formation. Those fractures may heal, propagate, or link with other fractures, which makes it difficult to study fracture timing, depth, phases, paleo-environment and genetic mechanisms (Cosgrove, 2001; Hood et al., 2003; Ortega et al., 2006). In contrast to open fractures, fractures filled with minerals, namely veins, preserve information regarding fracture geometry and size. Hence, mineral veins in mudrocks provide a unique opportunity for studying fracture properties (Gillespie et al., 2001; Oliver and Bons, 2001).

Mineral veins are defined as natural fractures filled with mineral crystals that are precipitated from solution (Passchier and Trouw, 1996). Multiple processes give rise to fractures in mudrocks including:

(1) Regional or local tectonic stresses at different times of the basin history (Gudmundsson, 1987; Volland and Kruhl, 2004);
(2) Fault/fold related fractures (Caine et al., 1996; Cosgrove, 1999; Smart et al., 2009);
(3) Disequilibrium compaction caused by local stress perturbations (Jolly and Lonergan, 2002; Osborne and Swarbrick, 1997);

(4) Overpressuring caused by fluid/gas expulsion during diagenetic processes, such as the smectite to illite transition, and primary oil migration (Bruce, 1984; Freed and Peacor, 1989; Katahara, 2006);

(5) Stress release and cooling during uplift (Gale and Holder, 2010; Gough and Bell, 1982; Lorenz and Finley, 1991).

Regardless of fracture origins, veins, as former fluid conduits, record signals of fluid movement (Sibson, 1996; Worden et al., 2015). Vein mineralogy, texture and geochemistry may yield insights into local to basin-scale fluid flow, P-T conditions, and material flux (Oliver and Bons, 2001; Pommer, 2013). An understanding of interactions of fractures and fluids, and the associated diagenesis in a chemically reactive environment is crucial for determining how and when fractures open and close (Laubach, 2003; Marrett and Laubach, 1997; Olson et al., 2007, 2009). However, the post-depositional alternations in clays have largely focused on chemical processes by sedimentary geologists, without reference to structure or mechanics (Laubach et al., 2010). Likewise, diagenetic processes in structural geology are also curiously neglected. Hence, the mutual awareness of a cross-disciplinary study of the mechanical and chemical processes in structures in sediments, i.e. structural diagenesis, has been increasingly appreciated recently (Ábalos and Elorza, 2012; Laubach et al., 2010; Pommer, 2013). Looking at fractures from the perspective of structural diagenesis is central to an understanding of fluid flow, coupled mechanical and chemical processes, which help eliminate blind spots (Laubach et al., 2010). However, little work on structural diagenesis in mudrocks at different depth sequences of diagenetic zones has been done.

Fibrous mineral veins are considered as useful tools to unravel deformation histories in the host rocks (Cox, 1987; Ramsay, 1980). The crystal morphology and vein microtextures help refine

the tectonic analysis of the veins and paleostress fields (Bons et al., 2012; Hilgers and Urai, 2002b; Urai et al., 1991). So far, most of the literature on fibrous veins deals with syntaxial veins (Hilgers et al., 2004; Hilgers and Urai, 2002a; Nüchter and Stöckhert, 2007). Antitaxial veins have received much less attention and remain the least understood among all vein types (Bons et al., 2012). The questions mainly lie in the following aspects:

(1) timing and mechanism of vein generation;

(2) driving forces of vein propagation and volumetric expansion;

(3) mechanisms of growth of fibrous crystals;

(4) material source and the mass transport mode in the host rock;

(5) structural implications of vein microtexture.

In general, fibrous veins need to be better understood regarding (1) when and how do they form and grow; (2) why they exhibit the distinct textures.

1.2 Research methods

This research uses combined field, petrographic and geochemical methods. Field work covers a comprehensive study of the regional and local geological settings, mainly including tectonic and sedimentary structures, stratigraphy and vein system characterization. The detailed work is listed in figure 1.2.

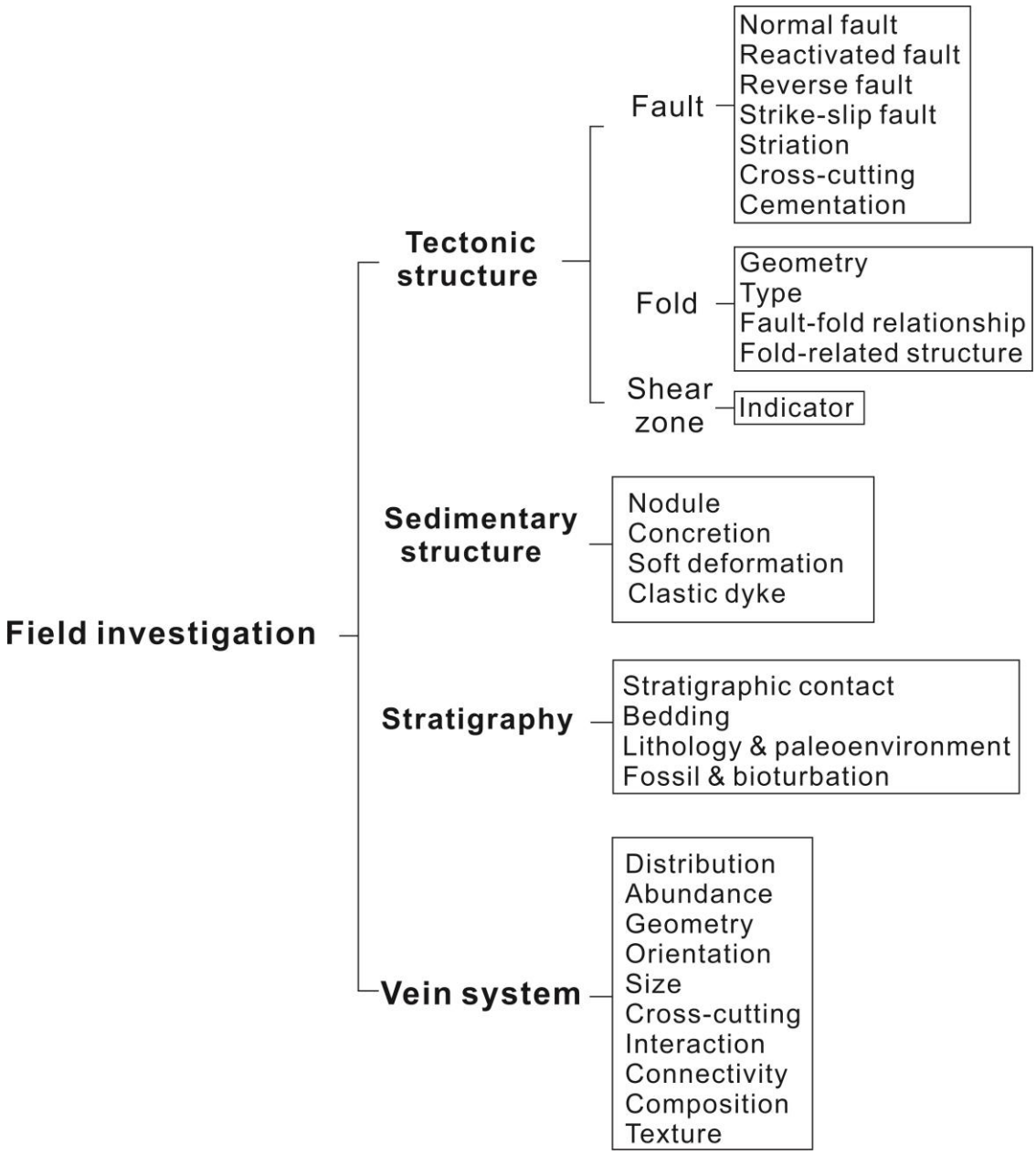


Figure 1.2 Workflow showing the contents of field investigations covered in this study.

Rock samples of mineral veins and the host rocks were collected systematically from the lower to upper parts of the outcrops for thin section preparation and geochemical measurement. The

thin sections were examined using both optical microscopes and a scanning electron microscope. The petrographic characterization mainly covers aspects in figure 1.3.

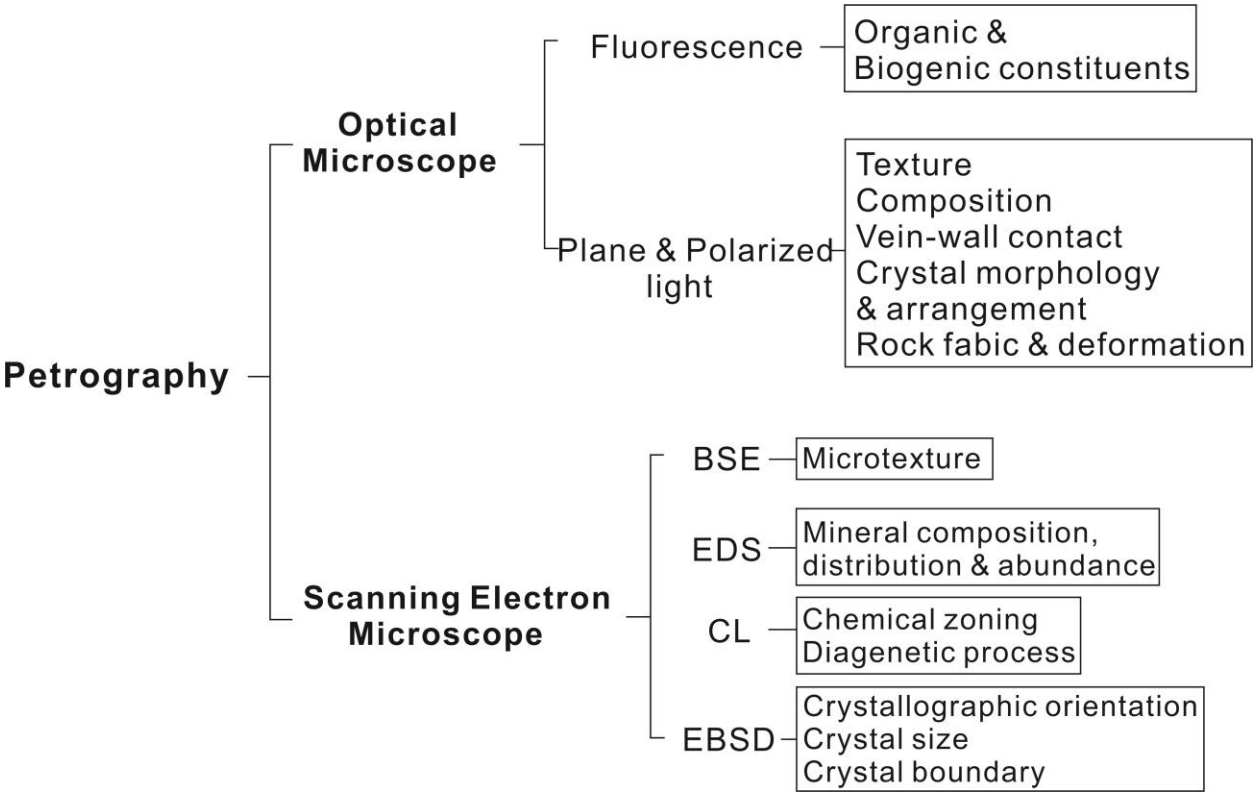


Figure 1.3 Workflow showing the contents of petrographic investigations covered in this study.

Geochemical methods used in this study include (1) using inductively coupled plasma mass spectrometry (ICP-MS) to measure elemental concentrations of rock samples; (2) using mass spectrometers to measure stable isotope ($\delta^{13}C$ and $\delta^{18}O$) compositions of samples; (3) using total organic carbon analyzer to measure TOC of host rock samples.

The combined methods used in this research provides both structural and diagenetic information of mineral veins, and insights into the structural diagenesis of the mudrocks.

1.3 Aims

In general, this research aims to investigate the timing, formation and evolution of fibrous mineral veins in mudrocks. Specifically, the research aims to address the following questions:

(1) geological controls of spatial distribution and abundance;
(2) the timing, paleo-stress, and fluid conditions of vein formation;
(3) vein network evolution;
(4) vein composition, texture and crystallographic fabric, and their kinematic and geodynamic implications;
(5) fluid conditions, nutrient sources and transport mode;
(6) the dynamic processes of vein opening, cementation and propagation;
(7) mechanics of vein extension and its relation to the bulk strain.

Ultimately, this research tries to get a better understanding of the processes of structural diagenesis of mineral veins in mudrocks and fluid-rock interactions at different stages of burial and lithification of the sediments.

1.4 Outline

Chapter 1 introduces the research background, methods and objectives of this study.

Chapter 2 reports the study of satin spar veins in Triassic Marls in the Bristol Channel Basin as a case study of late-formed veins during basin uplift. The study includes field investigations of local geology, vein spatial distribution, and patterns, in both the Keuper Marl Formation and the Blue Anchor Formation, as well as the elemental concentrations of the veins in nodules, the bulk rock and faults.

Chapter 3 covers a comprehensive petrographic study of the stain spar veins and their host rocks reported in chapter 2. The study focuses on the characteristics of vein microtexture, host rock mineralogy and also fibre orientations in satin spar veins, providing insights into the formation mechanism and kinematics of vein growth.

Chapter 4 presents the study of horizontal calcite veins, as early-formed fibrous mineral veins, in the Lower Jurassic Charmouth Mudstone in the Wessex Basin. The chapter mainly presents the field characteristics and stable isotope compositions of the calcite veins.

Chapter 5 consists of an integrated petrographic and SEM study of the fibrous calcite veins described in chapter 4. Vein texture, composition and c-axis fabrics are presented, which yield insights into the multiple questions regarding the mechanical and chemical conditions during vein generation and subsequent accretion.

Chapter 6 compares the similarities and differences of the satin spar veins and the calcite beef veins and the controls on vein development, especially the influence of basin environment. This chapter also addresses the geological significance and prerequisite of crystallization pressure exerted by veins that have been largely ignored in previous studies.

Chapter 7 summarizes the key findings in this research and makes suggestions for the future work.

Chapter 2 Satin spar veins in the Mercia Mudstone, the Bristol Channel Basin

2.1 Introduction

Evaporites, dominantly calcium sulphate and halite, are chemical sediments that have been precipitated from an aqueous solution by evaporative concentration of dissolved salts (Jackson, 2005). They are economically important due to their mineralogy, in-situ physical properties, and their behaviour within the subsurface (Tucker, 2009). Evaporites are also significant for paleoclimatological studies because evaporites are restricted to an arid environment with a high temperature. Calcium sulphate occurs in nature in a variety of polycrystalline forms (Machel, 1985). Satin spar is a distinct fibrous form of calcium sulphate, which is commonly present in outcrops and in the subsurface in evaporite basins (Gustavson et al., 1994; Kendall, 1975). They commonly occur as aggregates of fibrous gypsum crystals of vein fills.

Satin spar veins have been reported in over 30 localities worldwide (Cobbold et al., 2013; Tucker, 2009) (Figure 2.1). They frequently occur in Triassic and Neogene strata, which are times of vast evaporite production under a warm and dry climate (Cobbold et al., 2013). Satin spar veins are rarely observed in early Paleozoic, Jurassic or Cretaceous rocks. The host rocks of satin spar veins are mostly mudrocks and evaporites, less commonly carbonates (Cobbold et al., 2013; Nichols, 2009).

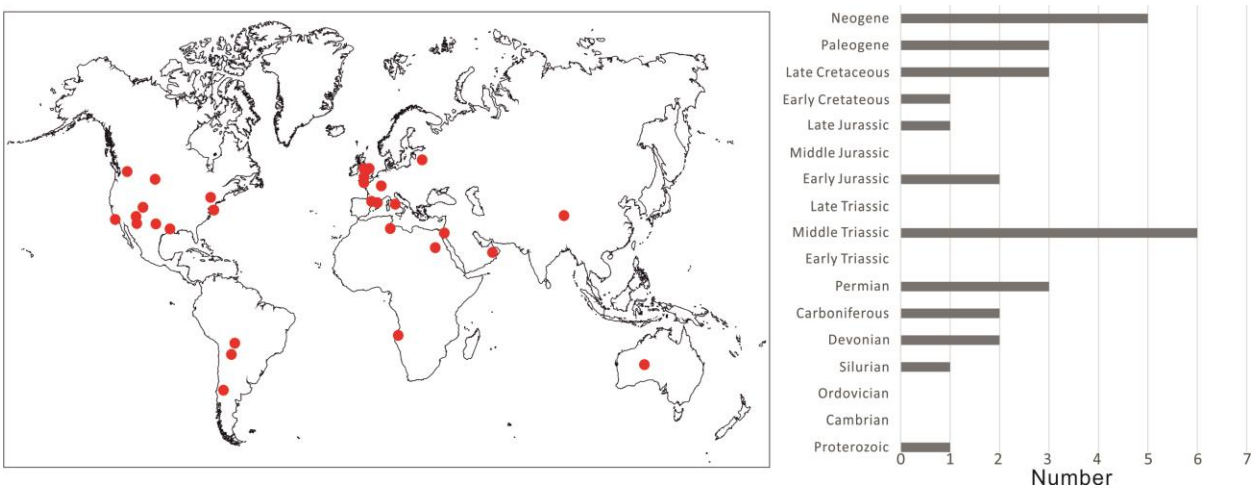


Figure 2.1 Worldwide distribution of reported satin spar veins (left) and the stratigraphic ages of the host rocks. Locations are approximate. Modified from Cobbold et al. (2013).

The similarities of satin spar veins in many evaporite basins may indicate a common origin (Gustavson et al., 1994). Although it is generally acknowledged that the formation of satin spar veins is related to fracture mechanics, no consensus exists for their genesis. Shearman et al. (1972) suggested that the satin spar veins are results of hydraulic fracturing due to anhydrite hydration that is accompanied with a volume increase of 63%. Gypsum replaces anhydrite on a volume-for-volume basis, while the excess gypsum appears in hydraulic fractures as fracture-filling cement. Machel (1985) proposed that the dilation of satin spar veins may possibly result from strata buckling by lateral tectonic compression, or hydraulic overpressure, or a combination of the two factors. Mohamed and Warren (1998) suggested a passive mode of vein formation where the opening and dilation of satin spar veins appears to be initiated by sediment unloading during basin uplift. Gustavson et al. (1994) argued that the satin spar veins are the result of mineral precipitation in pre-existing fractures or brecciated strata that are associated with evaporite beds. However, uncertainties remain in these explanations because they do not fully take into consideration the

complete process of vein formation and growth, and the origin of the fibrous habit of gypsum crystals.

This chapter documents the study of satin spar veins that occur in the Mercia Mudstone in the Bristol Channel Basin. This project provides an ideal case study of satin spar veins and also provides insights into the formation and evolution of satin spar vein network in fine-grained rocks. Cosgrove (2001) and Philipp (2008) have reported the studies on the gypsum vein networks in the Watchet area. Cosgrove (2001) interpreted the gypsum veins as natural hydraulic fractures that have formed during N-S compression of the basin in Early Cenozoic. Fibres are vertical in all veins regardless of vein orientations, which indicate that the fractures were opened by fluid injection against a vertical σ_3. Only the hydraulic fractures in evaporite-rich horizons have been preserved by gypsum filling, whilst the others have been healed subsequent to their formation. Philipp (2008) reported that the gypsum veins in the Mercia Mudstone have a random orientation by field measurement. Fluids have been transported along faults, which are evident from the fault veins, although the source of fluid is unclear. The gypsum veins are mainly sourced from the local nodules. The horizontal veins are mainly induced by high tensile stress at nodule front. The heterogeneity of vein distributions is associated with contrasting mechanical properties at layer boundaries that prevent the propagation of gypsum veins into adjacent layers. However, the previous work remains incomplete. Firstly, the spatial distribution and internal texture of fibrous gypsum veins have not been documented in detail. Secondly, detailed petrographic observations and geochemical measurements of the gypsum veins are needed to investigate for vein formation and growth. Moreover, the investigation of gypsum veins in the Blue Anchor Formation that overlies the homogeneous Keuper Marl is necessary for studying the geological controls on vein development.

This chapter starts with an introduction to the regional and local setting, then characterizes geometrical, textural and geochemical features of gypsum veins and fibres, and discusses the timing, formation and evolution of the gypsum veins.

The aims of this chapter are as follows:

(1) to present the complex geometry and anisotropic distribution of gypsum veins;
(2) to derive constraints on the timing and relative timing of gypsum veins;
(3) to examine the tectonic significance of gypsum fibres;
(4) to discuss the formation mechanism of tension fractures;
(5) to quantify fracture attributes and investigate their implications for vein network evolution.

2.2 Geological setting

2.2.1 Location

The study area is located on the southern margin of the Bristol Channel Basin (BCB) (Figure 2.2). The BCB extends from Wales to Somerset, 155 km E-W and 30 km N-S (Nemčok et al., 1995). The BCB is an early Mesozoic intracratonic extensional basin bordered by Variscan structures in the outcrop to its north (Chadwick, 1986; Dart et al., 1995; Kamerling, 1979; Keary and Vine, 1990). The northern boundary of the BCB is the folded Palaeozoic metasediment of the Pembrokeshire Ridge and Welsh Spur. To the south, the BCB is bounded by Cornubian Platform, consisting of low-grade metamorphic Palaeozoic rocks and local intruding Hercynian granites (Van Hoorn, 1987).

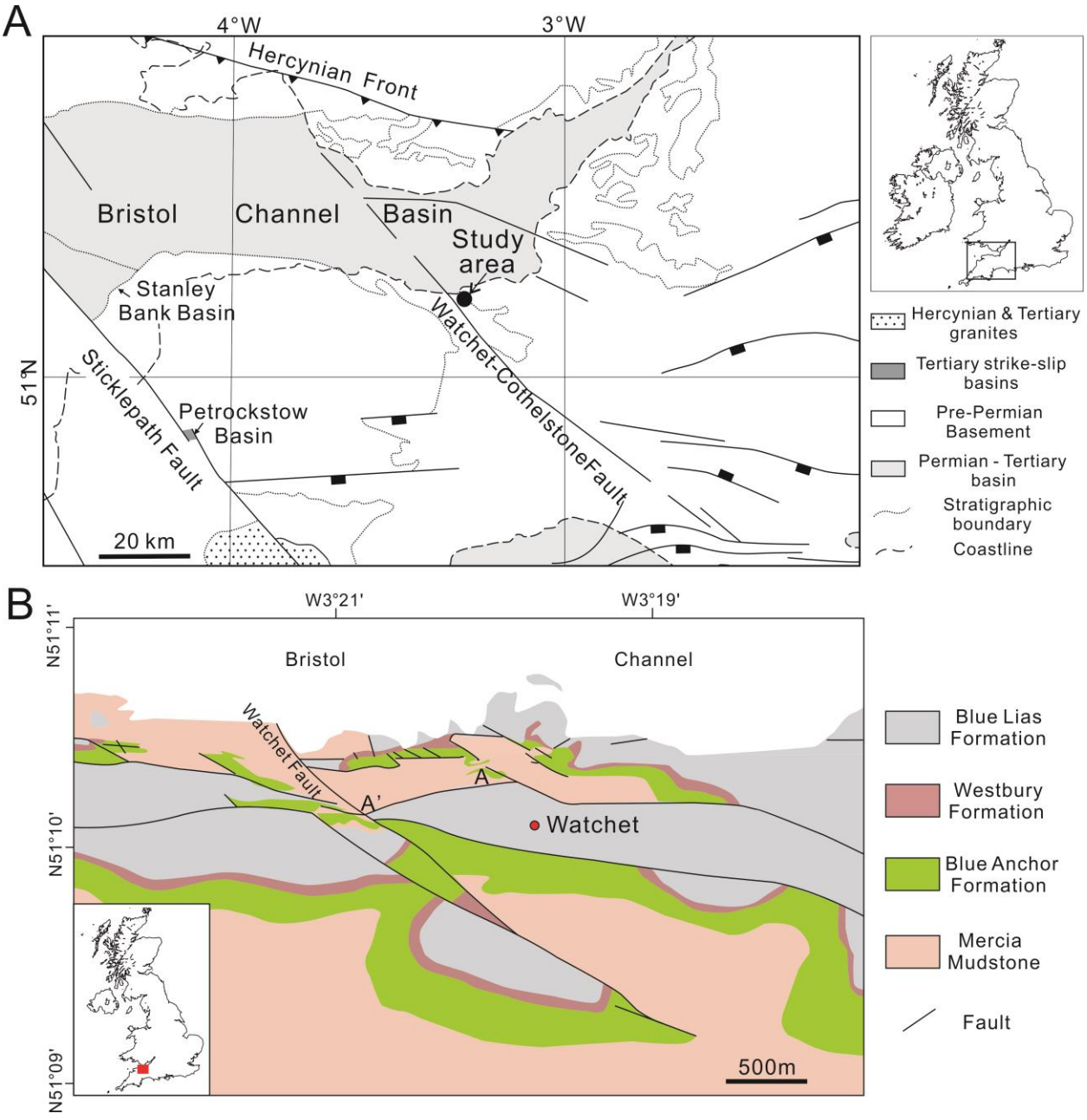


Figure 2.2 Structural framework of the Bristol Channel Basin and the adjacent areas (A) and geological map of the study area of northern Somerset, UK (B). Modified from Jackson (2008) and Dart et al. (1995).

2.2.2 Basin evolution

2.2.2.1 Tectonic evolution

The BCB was initiated in the early Permian to Triassic as one of the extensional basins developed through and around the south of England due to the breakup of the Pangaea (Brooks et al., 1988; Coward, 1995; Kamerling, 1979; Roberts, 1989; Van Hoorn, 1987). The BCB experienced continued extension and subsidence through the Triassic and Jurassic (Miliorizos and Ruffell, 1998), which led to the development of approximately E-W trending and southward dipping normal faults (Donato, 1988; Peacock and Sanderson, 1999). These basin controlling normal faults significantly influenced sedimentation in the BCB and were attached to a major Variscan thrust fault at depth that was reactivated and controlled the location and orientation of the normal faults (Donato, 1988; Peacock and Sanderson, 1991; Peacock and Sanderson, 1994; Ruffell and Coward, 1992).

The main basin developed as a half graben bounded by the Bristol Channel Fault Zone (Brooks et al., 1988; Glen et al., 2005; Kamerling, 1979). During the period of Late Cretaceous to the Early Cenozoic, inversion occurred in the BCB as the result of N-S contraction caused by the Alpine orogeny (Peacock and Sanderson, 1992; Van Hoorn, 1987) (Figure 2.3). The evidence for this phase of contraction comes from seismic profiles, field exposures of selective reverse-reactivated normal faults and strike-slip faults conjugate about a N-S orientation (Peacock and Sanderson, 1992; Peacock and Sanderson, 1999). Most reverse-reactivated normal faults retain finite normal displacements; however, some faults have passed into reverse faults (Dart et al., 1995; Peacock and Sanderson, 1992).

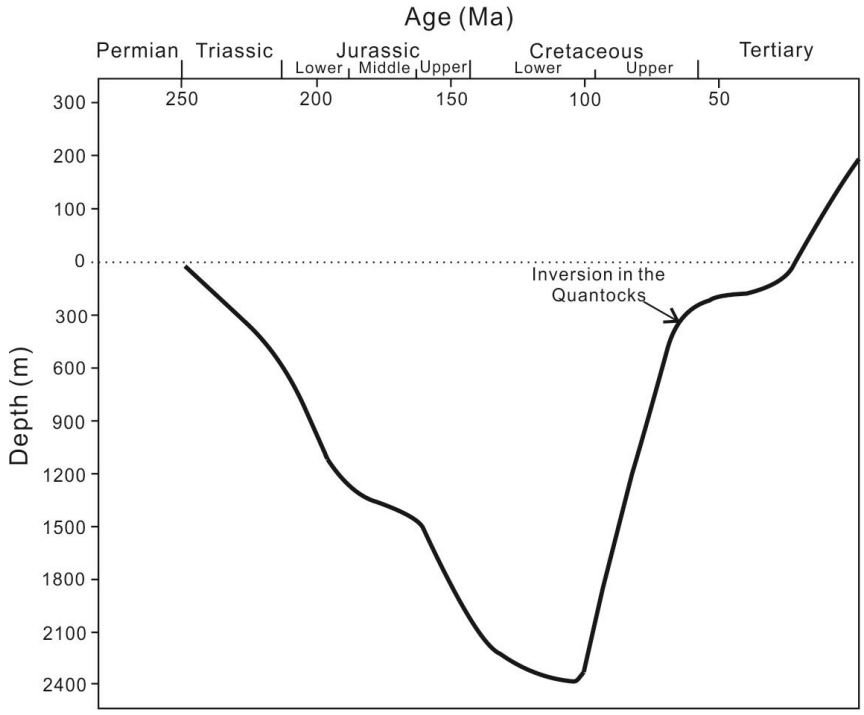


Figure 2.3 Burial curve of the Mercia Mudstone in the Bristol Channel Basin. Modified from Cosgrove (2001).

The BCB is transected by two major NW-SE striking strike-slip faults, the Sticklepath-Lustleigh Fault in the west and the Cothelstone-Watchet Fault in the east, and several other minor NW-SE striking strike-slip faults (Brooks et al., 1988; Kamerling, 1979; Whittaker and Green, 1983) (Figure 2.2).These dextral strike slip faults, which were originally formed during the Variscan orogeny, were reactivated during the Mesozoic and Tertiary. As a result, several pull-apart basins with Oligocene sediment fills preserved were developed along the Sticklepath-Lustleigh Fault (Whittaker and Green, 1983).

The basin underwent exhumation mainly in the early Cretaceous and the Cenozoic (Hillis, 1992; Kamerling, 1979; Tappin et al., 1995). The BCB experienced up to 3 km of exhumation in the Early Cretaceous, as suggested by fission track data (Holford et al., 2005b). The basin experienced

approximately 1 km of exhumation during the Cenozoic indicated by vitrinite reflectance and fission track data (Menpes and Hillis, 1995).

2.2.2.2 Depositional history and stratigraphy

The BCB overlies a basement of Carboniferous limestones and Devonian sandstones and slates and comprises sedimentary rocks from Permian to Oligocene in age (Dart et al., 1995; Kamerling, 1979; Van Hoorn, 1987). The preserved Mesozoic sediments reach up to 2250 m in thickness (Van Hoorn, 1987). During the Permian and Triassic, the interplay of sea level change, extension-driven subsidence and fluctuations of climate significantly affected the sedimentation of the BCB (Ruffell and Shelton, 1999). Sediments deposited during this period are typical of an arid environment and include lacustrine red sedimentary rocks when the BCB was located in northern desert latitude (Cosgrove, 2001). The rock types mainly include conglomerate, sandstone, siltstone and mudstone (Whittaker and Green, 1983). In the early Triassic, thick sequences of pebbly sands were deposited as the lower Sherwood Sandstone Group from a major river system across the southern UK fed by monsoonal rains (Hobbs et al., 2002b). The lower-middle fluvial Sherwood sandstone passes laterally and upward into interbedded sandstones, siltstones and mudstones of the upper Sherwood Sandstone (Howard et al., 2008) (Figure 2.4).

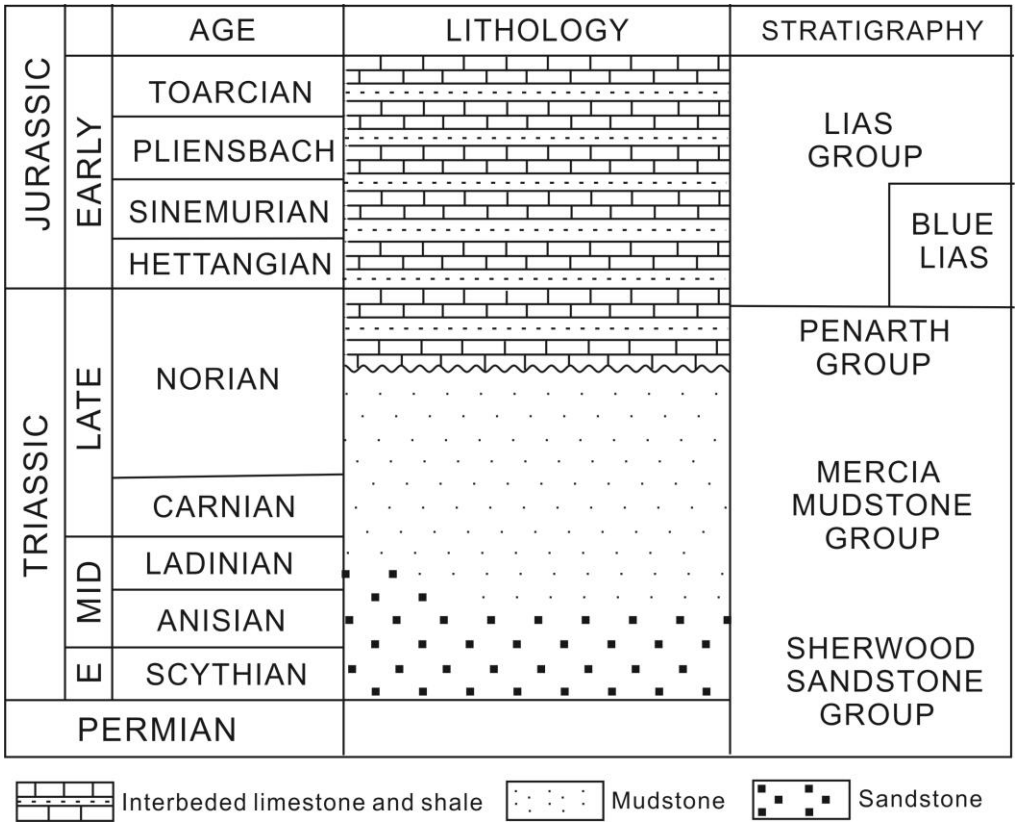


Figure 2.4 Stratigraphic column of the Triassic and Jurassic of the Bristol Channel Basin. Modified from Glen et al. (2005) and Hobbs et al. (2002b).

During the Anisian, the Mercia Mudstone was deposited in subaqueous, hypersaline and evaporitic mudflats that replaced the southward retreating fluvial environment of the early Triassic (Dart et al., 1995; Tucker, 1977). The Mercia Mudstone mainly includes reddish-brown, less commonly green and grey, mudstones and marls with beds of halite in Somerset (Howard et al., 2008; Whittaker and Green, 1983) (Table 2.1). The BCB received sediment infill from mudflats from four sources including mud and silt settled-out in playa lakes; silt and fine sand transported by flash flood; aeolian dust accumulated on wet mudflat surfaces, and salt precipitated from marine-sourced hypersaline water bodies and from contemporary groundwater (Hobbs et al., 2002b;

Talbot et al., 1994; Warrington et al., 1994). Subsequent transgression in the Late Triassic to Early Jurassic was accompanied by the deposition of grey to black marine mudstone of the Lower Penarth Group and interbedded mudstones and thin limestones of the Blue Lias Group (Howard et al., 2008; Whittaker and Green, 1983).

Table 2.1 Detailed Triassic Lithostratigraphy. Based on Whittaker and Green (1983), Tappin et al. (1995) and Glen et al. (2005).

Group	Formation	lithology
Penarth Group	Lilstock Formation	Calcareous mudstone and siltstone, including white lias-type limestone and marl
	Westbury Formation	Passing into interbedded limestone and shale
Mercia Mudstone Group	Blue Anchor Formation (Grey and Tea Green Marl)	Grey-green calcareous mudstone and marl
	Lower Mercia Mudstone (Keuper Marl)	Reddish-brown marl and siltstone with gypsum veins

2.2.3 Local geology

The studied outcrop is located in Warren Bay in the Watchet area, Somerset (Figure 2.5), where Triassic and Lower Jurassic strata are exposed in the 1.5 km E-W trending cliffs. The investigation of the local geological context focuses on the stratigraphy, geological and sedimentary structures.

2.2.3.1 Stratigraphy

The coastal cliffs near Watchet mainly expose the Triassic strata of the Mercia Mudstone and the Lower Jurassic Blue Lias (Figure 2.1). The Mercia Mudstone is subdivided into the Keuper Marl Formation and the Blue Anchor Formation.

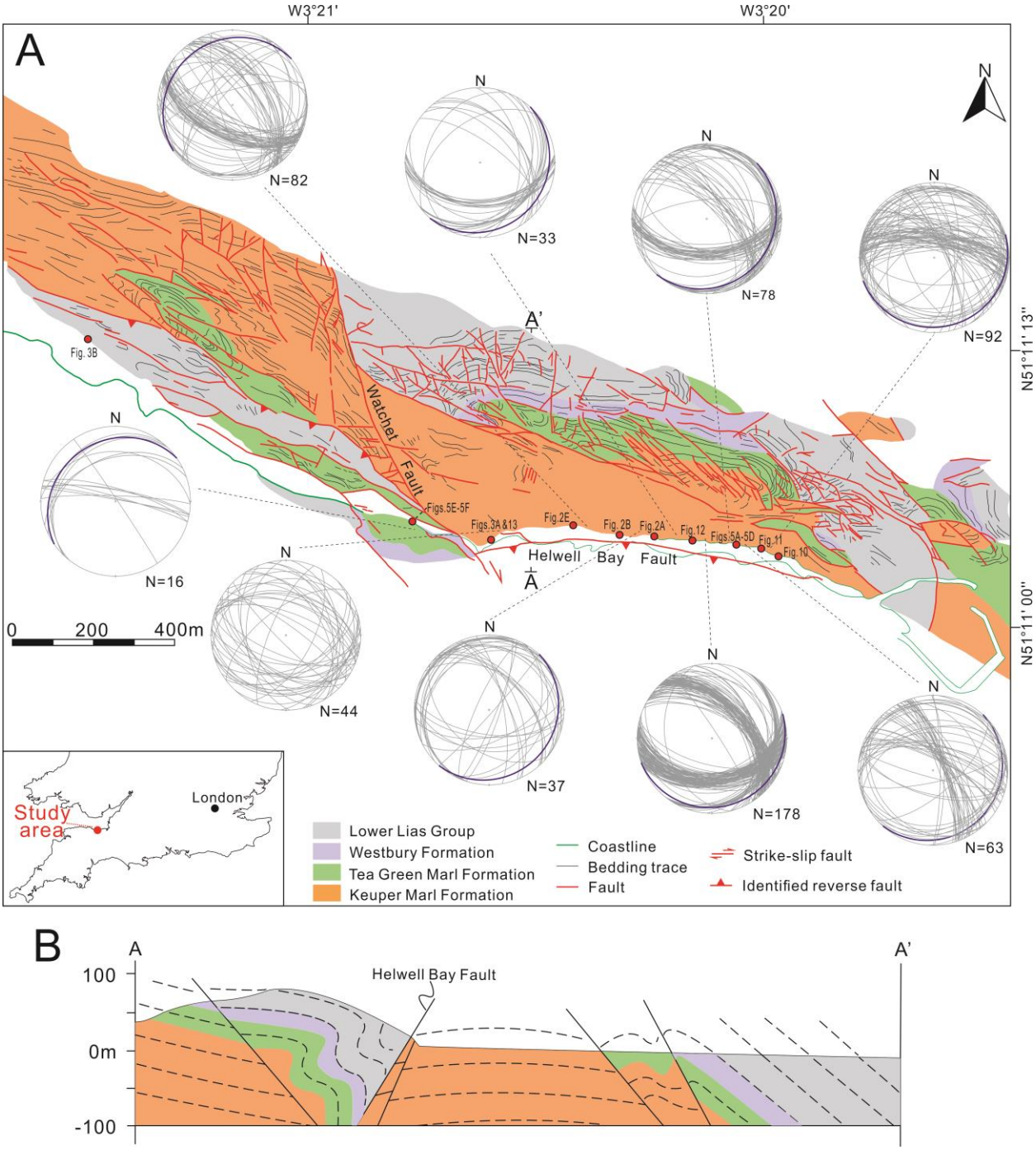


Figure 2.5 Geological map of the Watchet area (A) and cross-section along B-B' line. Modified from Dart et al. (1995) and Glen et al. (2005). Lower hemisphere stereonet projections show vein orientations (black circle) and bedding (purple circle) in nine sites.

The Keuper Marl Formation

The Keuper Marl is the oldest stratigraphic unit exposed in the outcrop, mainly consisting of red, reddish and brown unfossiliferous marl (Figure 2.7). The red marls are blocky, without apparent laminations. The multiple green siltstone bands and nodular gypsum horizons are regarded as indicators for bedding orientations. The beds are gently southeast dipping at less than ten degrees. The rock lithology is laterally homogeneous; however, it shows clear vertical variations. Based on gross lithological character and the content of gypsum, the exposed section of the Keuper Marl is here subdivided into five units (Figure 2.6).

Unit 1, as the lowermost part of the Keuper Marl, comprises three meter thick red marls (Figure 2.7B). An exposed 8 meter long and 1.5 meter thick sandstone body lies at the base of the marls (Figure 2.6A). The grey-green sandstones represent a brief episode of deltaic or estuarine deposition (Hobbs et al., 2002a).

Unit 2 overlies Unit 1, consisting of 10.5m thick grey-reddish silty marl (Figure 2.7C-D). The rocks are highly gypsiferous. Two groups of nodular gypsum horizons occur in this unit, ~1.0 m and ~1.5m thick respectively.

Unit 3 mainly contains reddish calcareous marl (Figure 2.7B-C). Four groups of nodular gypsum horizons occur in this unit. Each nodule group includes 4-5 horizons. Although rich in gypsum nodules, gypsum veins are not observed in nodule-free layers.

Unit 4 consists of red gypsiferous marls and three green siltstone bands (Figure 2.7A-B). Nine nodular gypsum horizons are observed, which help bedding correlation in fault-bounded blocks. Unit 5 is the uppermost unit of the Keuper Marl Formation (Figure 2.7A). The rocks comprise 6m homogenous red marls, lacking sedimentary structures. Neither gypsum nodules nor gypsum veins are observed in this unit.

The Blue Anchor Formation

The Blue Anchor Formation is exposed in the hangingwall of the Hellwell Bay Fault to the east of the Watchet Fault and also outcrops to the west of the Watchet fault. The formation consists of 22m thick laminated reddish, green and grey marls. Three lithological units are recognized in the Blue Anchor Formation (Figure 2.8). Unit 1 is the lowermost part of the Blue Anchor Formation (Figure 2.8A). This Unit contains a 4m thick laminated grey, reddish and green marl and limestone. Gypsum nodules and veins are absent.

Unit 2 consists of 16.5m interbedded dark mudstone and limestone (Figure 2.8A-B). This unit is observed to both the east and west of the Watchet Fault. The striking feature of this unit is the occurrence of groups of nodular gypsum horizons and veins (Figure 2.8C). To the east of the Watchet Fault, the layers of Unit 2 are tightly folded in the hanging wall of the south-dipping Helwell Bay Fault (Figure 2.8D). To the west of the Watchet fault, the layers that are striking NW-SE and dipping at ~20° are slightly deformed.

Unit 3, on top of Unit 2, exposes ~2m thick interbedded dark shale and grey-yellow limestone (Figure 2.8B). No gypsum veins and nodules occur in this unit.

The Blue Lias Formation

The Lower Jurassic Blue Lias consists of inter-bedded grey limestone, and dark grey to black bituminous shale. It is observed on top of Unit 3, Unit 4 and Unit 5 of the Keuper Marl. These layers are flat lying to the west of the Watchet fault; however, the dip of bedding varies from ~20° to nearly vertical above Unit 2 and Unit 3. Folded layers of the Blue Lias that appear as a detachment fold are also observed 500m to the west of the Watchet Fault. Well-preserved ammonites are frequently observed in this formation.

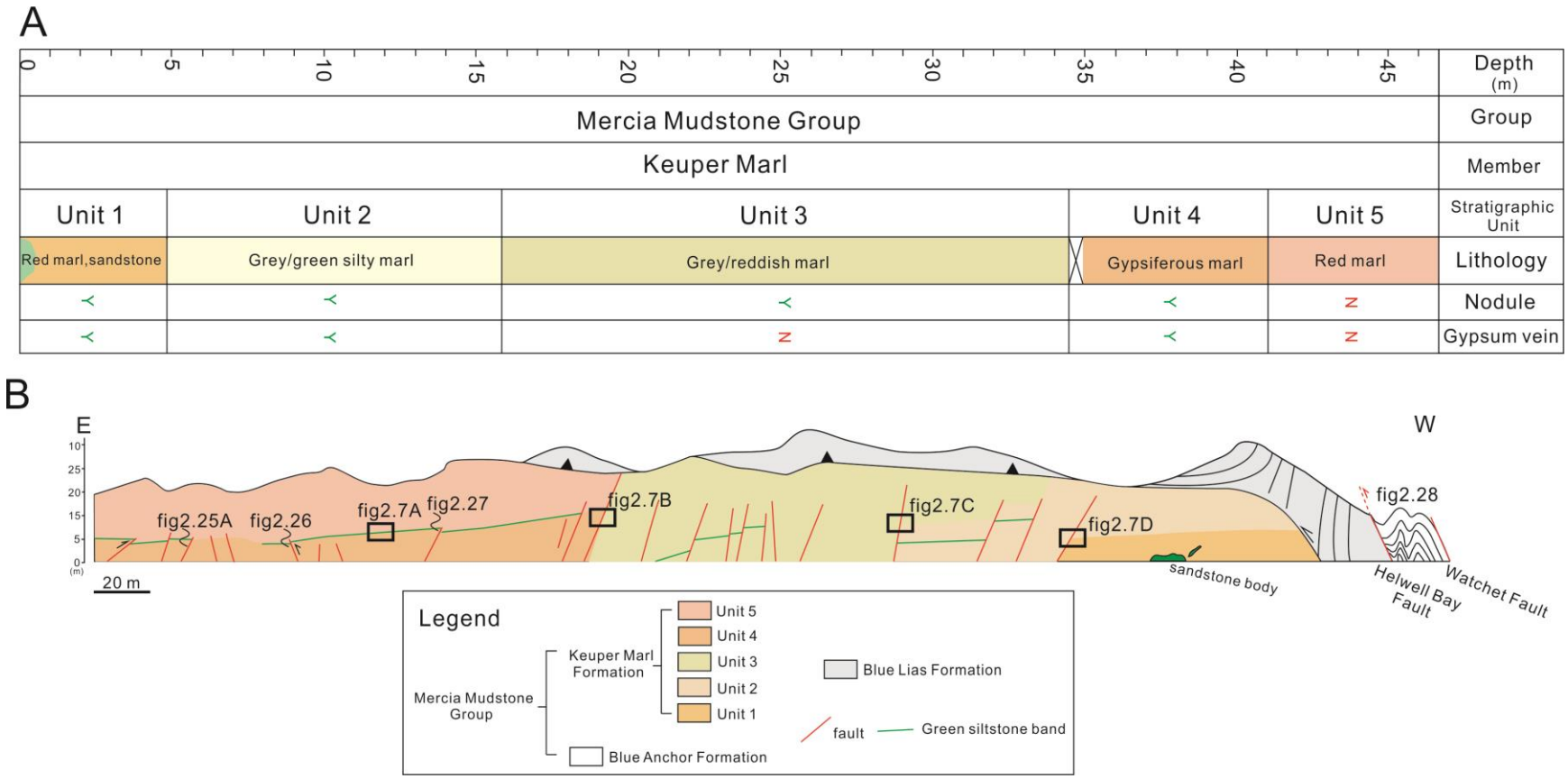


Figure 2.6 (A) Fracture stratigraphy in the Keuper Marl of the Mercia Mudstone. (B) E-W cross section of the cliffs on the Warren Bay. The arrows mark the reverse displacement of four faults. All the other faults have a normal displacement.

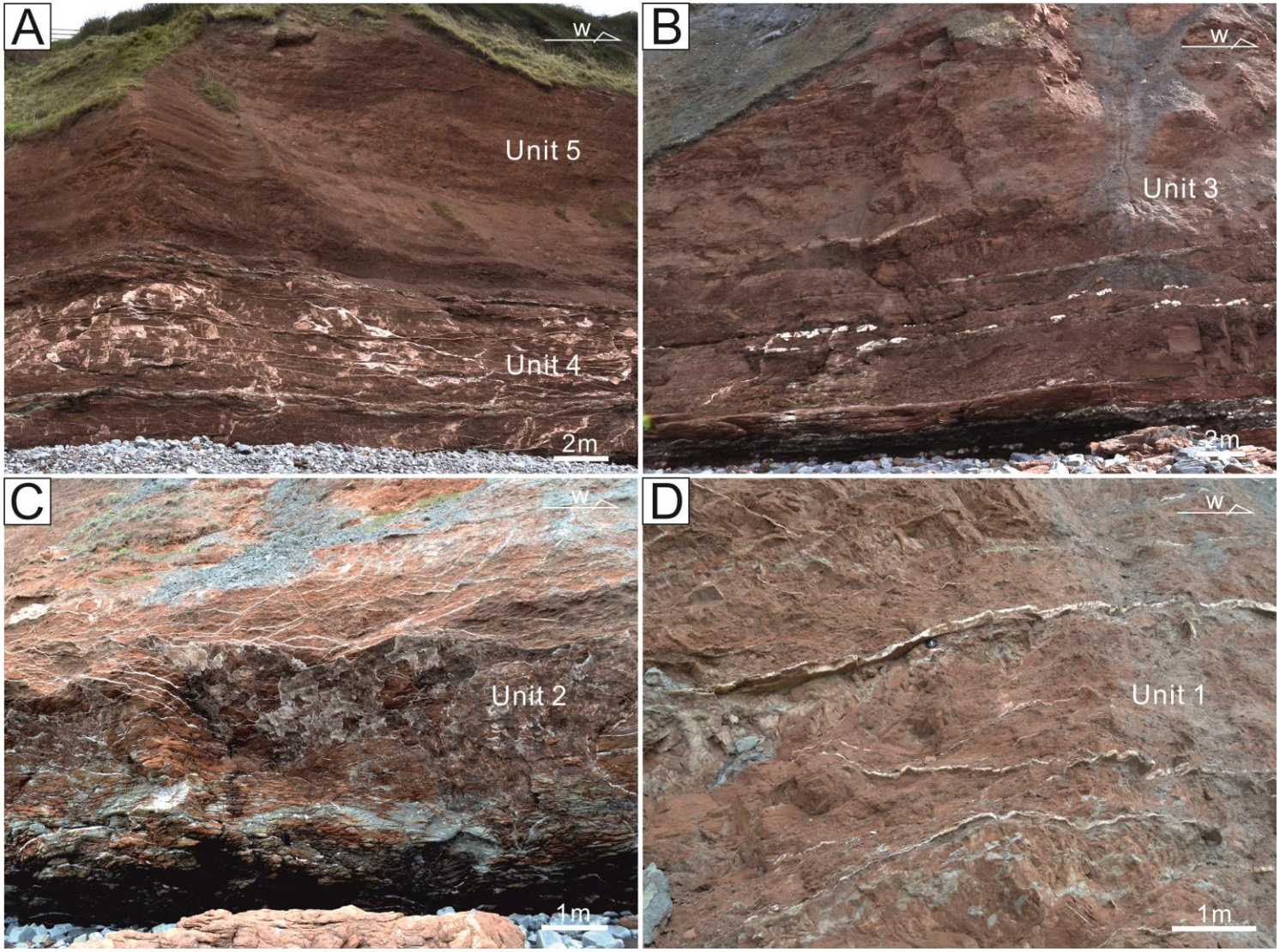


Figure 2.7 Fracture stratigraphy of the Keuper Marl Formation. (A) Unit 5 and Unit 4. (B) Unit 3. (C) Unit 2. (D) Unit 1.

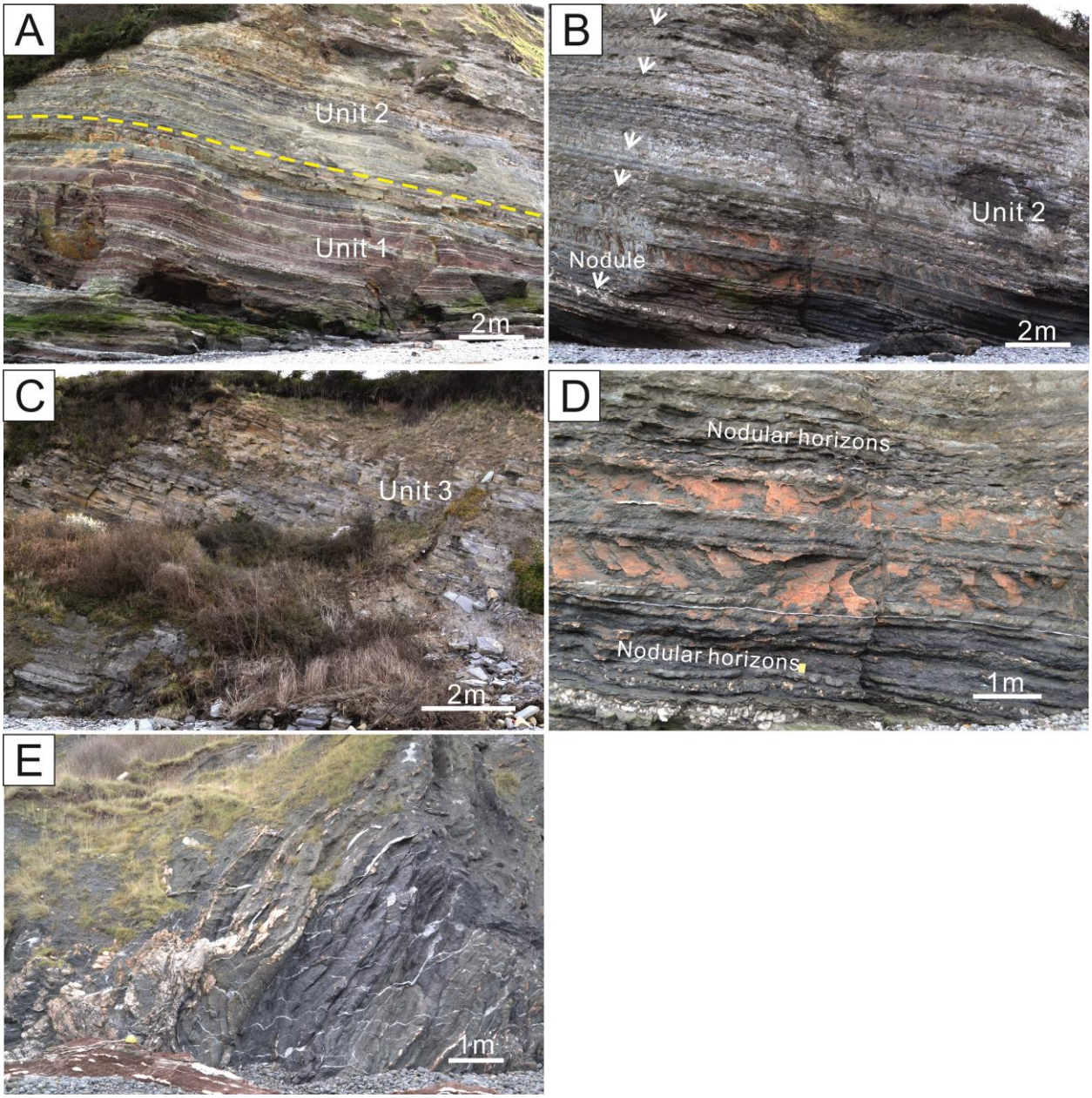


Figure 2.8 Gypsum vein distribution in the Blue Anchor Formation. (A) Unit 1 and Unit 2. (B) Unit 2. The arrows show the multiple nodular horizons. (C) Unit 3. (D) Slabs of numerous gypsum veins exposed in Unit 2. (E) Gypsum veins in the folded layers of the Blue Anchor Formation to the east of the Watchet Fault.

2.2.3.2 Structures

Numerous normal faults are exposed in the outcrop of the Mercia Mudstone (Figure 2.9). These faults mostly strike E-W and NW-SE and dip at moderate to high angles (37°-83°). Three reverse faults cut the Mercia Mudstone with reverse displacement ranging from 0.15 to 1.1m. The thrust motion is recorded by the gypsum fibres in the fault veins. The reverse faults are possibly normal faults that were reactivated as reverse faults to accommodate basin shortening during basin inversion (Kelly et al., 1999). The Blue Lias and the Mercia Mudstone in a horst is bounded by the E-W striking Hellwell Bay Fault (Figure 2.5). The horst is cut by the NW-SE Watchet strike-slip fault that transects the Mesozoic structures and possibly initiated as a Variscan structure (Holloway and Chadwick, 1986). Numerous NW-SE striking, deep-seated strike-slip faults are also recognized in the bay area (Figure 2.9B). Those faults have experienced strike-slip/oblique-slip with both sinistral and dextral motions throughout their evolution (Dart et al., 1995). The strike-slip faults are dominated with transtensional sinistral motions during basin extension, and transtensional dextral motion during compression. The strike-slip fault systems were reactivated during the Oligocene to Miocene, and are dominated by a phase of dextral motion (Rawnsley et al., 1998; Van Hoorn, 1987). The splay of the Watchet Fault in the Watchet area mainly exhibits a dextral sense of motion, transecting the Triassic and Liassic sediments with a displacement of 275m (Whittaker, 1972).

Buttress anticlines are observed in the hangingwall of reactivated normal faults as the result of accommodation of basin shortening during Alpine compression and flexural flow with bed-parallel slip (Engelder and Peacock, 2001; Nemčok et al., 1995). The anticlines verge towards the horst, which show locally overturned forelimbs. The fold axes mainly strike NNW-SSE. Axial surfaces may dip as low as 20°. Intense buttressing occurs in the hangingwall of the Helwell Bay Fault to

the east of the Watchet Fault, where complex parasitic anticlines and synclines develop around the crest (Figure 2.10A). The folds are cut by numerous minor faults which are sub-parallel to the main faults. Roll-over buttress folds are observed in the Lower Lias strata of the horst, whose fold axes trend approximately E-W (Figure 2.10B). The beds in the outcrop exposures dip at low angles to north, which increases sharply to be sub-vertical to the south. The folds are also cut by minor reverse faults. The Watchet Fault and several other strike-slip faults are accompanied with drag folds along fault traces. Axes of the drag folds are mostly at high angles to the displacement vector of the faults.

2.2.3.3 Nodular gypsum

Nodular gypsum is commonly observed in multiple horizons in both the Keuper Marl and the Blue Anchor Formation (Figure 2.11). The calcium sulphate nodules are primarily generated as syndepositional evaporites in the capillary and upper phreatic zones beneath the sabkha surface (Nichols, 2009). When burial depth exceeds several hundred meters, all $CaSO_4$ is present as anhydrite. The exact depth is controlled by the salinity and temperature of the pore waters (Jowett et al., 1993). However, on uplift to the telogenetic zone, anhydrite rehydrates to gypsum when it comes in contact with the low salinity, low temperature pore waters. Thus, the diagenetically regenerated gypsum present as gypsum nodules and veins is regarded as secondary gypsum (Tucker, 2009).

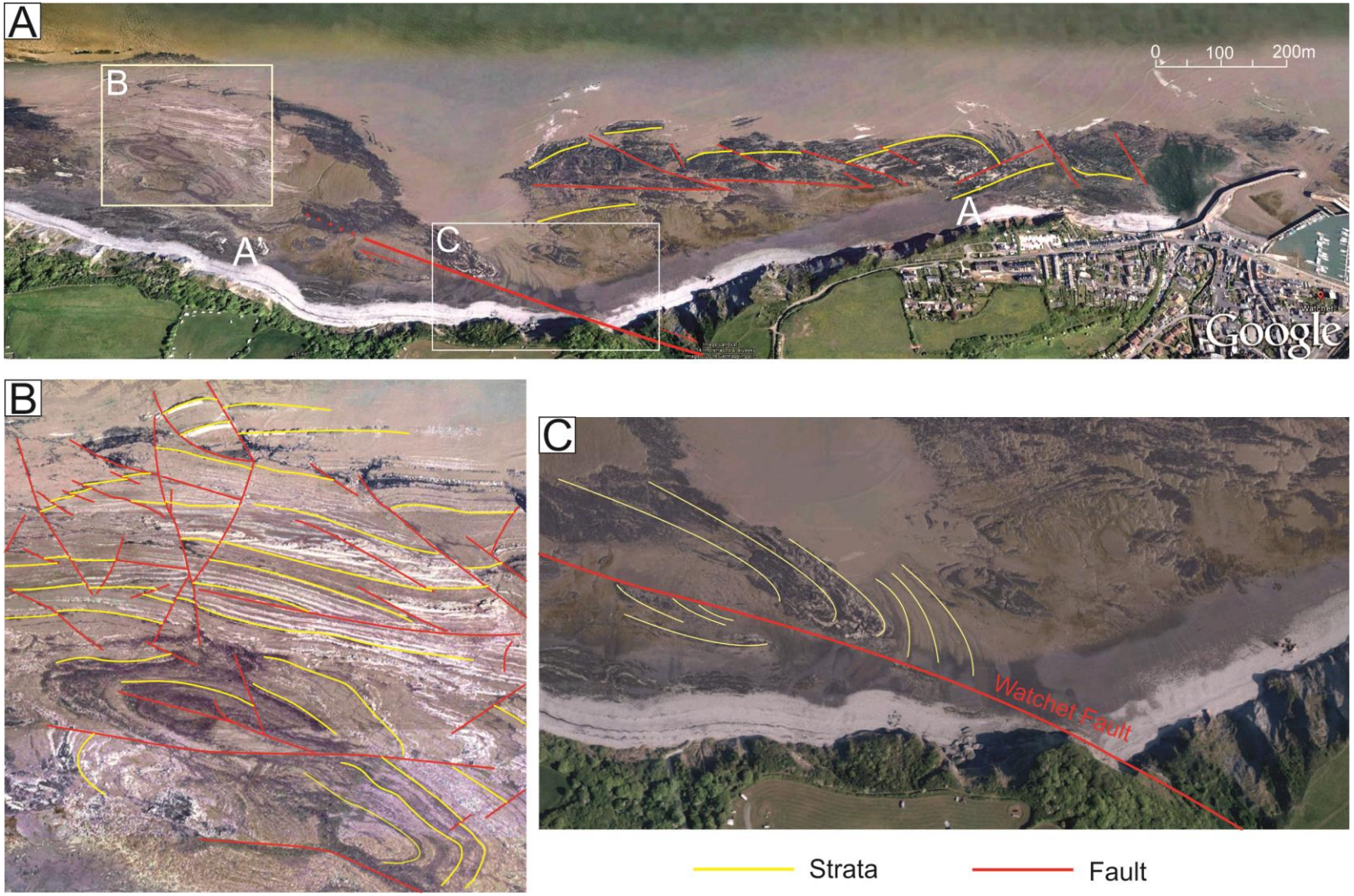


Figure 2.9 Satellite image showing the traces of strata and faults on the foreshore of the Warren Bay (A). (B) Numerous strike-slip faults and associated buttress folds. (C) The exposure of dextral Watchet strike-slip fault and its drag folds.

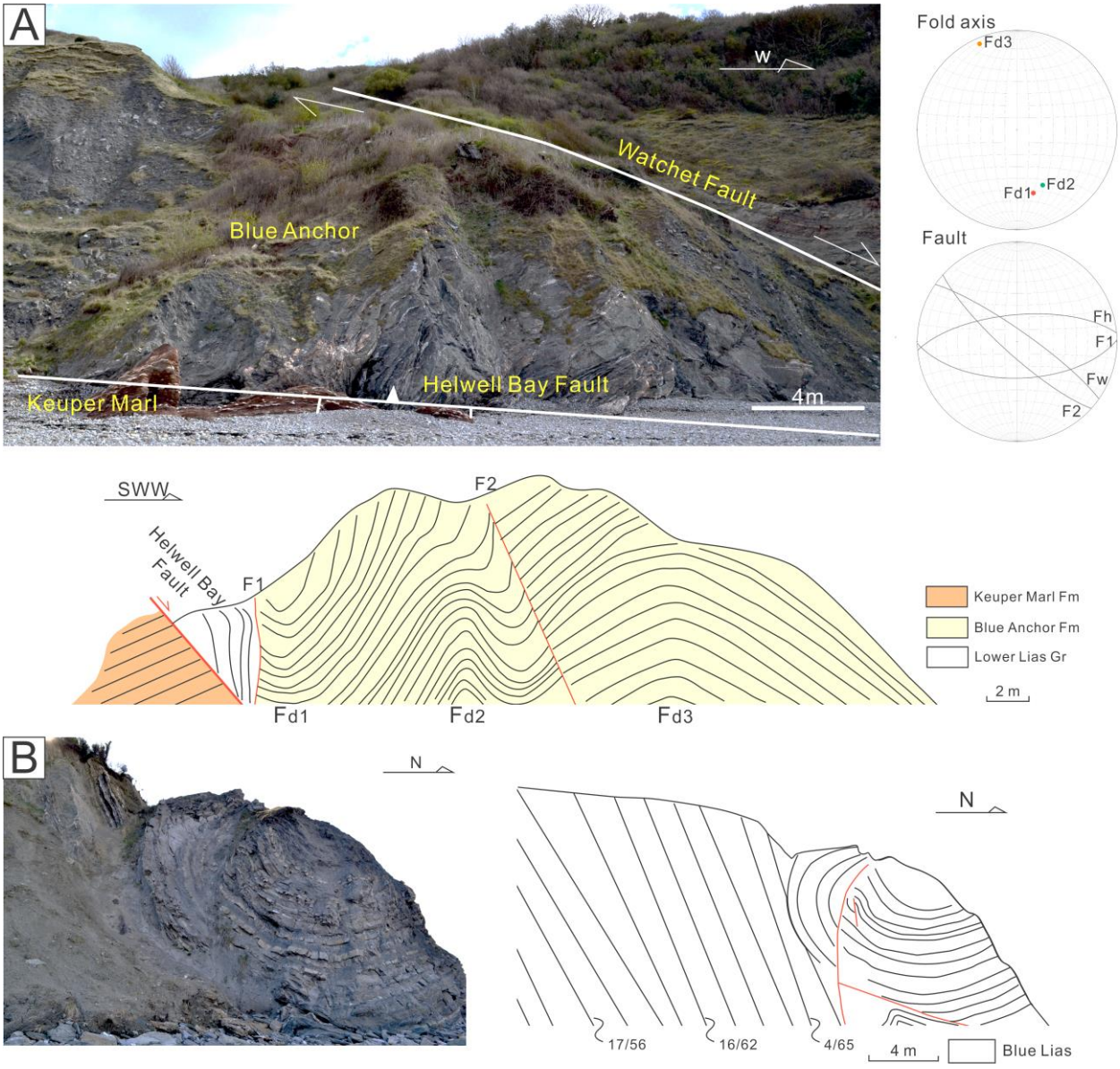


Figure 2.10 (A) Intense buttress anticlines in the hangingwall of the Warren Bay Fault and the sketch. Fold axes and fault orientations are projected in the lower hemisphere of stereonet. (B) Detachment fold in the Blue Lias Formation (left) and its sketch (right).

The gypsum nodules are spherical, ellipsoidal or irregularly shaped (Figure 2.11A-C). The long-axis dimension of the gypsum nodules varies from millimetres to 1.6m. Gypsum nodules are mainly restricted to certain horizons instead of being randomly distributed (Figure 2.11D-F), and therefore used as markers for stratigraphic correlation across faults in the rather homogeneous mudstone. Several gypsum nodule horizons that occur with a short vertical distance (usually less than 0.5 m) from each other form closely-spaced groups of nodule horizons (Figure 2.11E), which are both observed in the Keuper Marl and the Blue Anchor Formation. Nine groups of nodular gypsum horizons occur in the Keuper Marl, including four in Unit 3, two in Unit 2 and three in Unit 1. Gypsum nodules are only present in the interbedded limestone and dark mudstone of Unit 2 of the Blue Anchor Formation as three groups of nodule horizons.

Gypsum nodules are developed in clusters or independently, sometimes together with green bands of siltstone in the outer rims. The gypsum nodules commonly exhibit a white, reddish isotropic body. The bodies sometimes contain chicken wire structures, which are linear segments of the red host rock or the green siltstones (Figure 2.11B-C). The chicken wire structures exhibit a polygonal framework and divide the whole nodule into multiple parts, which are suggested as a result of nodule growth and coalescence in highly saturated pore waters of the capillary zone (Nichols, 2009). The gypsum nodules are mostly interconnected by sub-horizontal fibrous veins with no median lines. These satin spar veins do not cross-cut the nodules; instead, they are developed along the margins of nodules (Figure 2.11A).

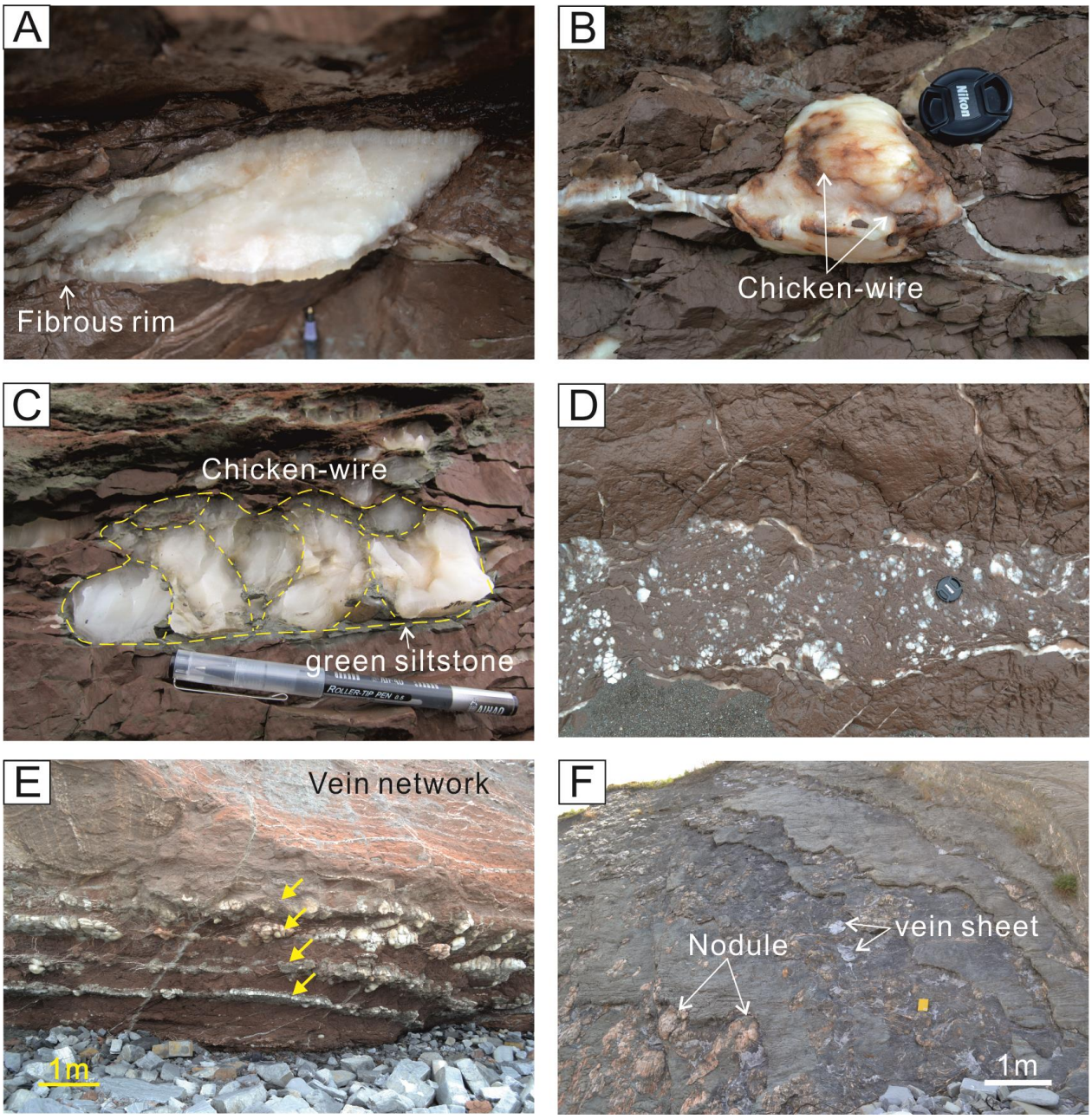


Figure 2.11 Outcrop exposure of nodular gypsum in the Mercia Mudstone. (A) A lenticular gypsum nodular with fibrous outer rim and rather homogeneous inner core. (B) Gypsum nodular with chicken-wire texture. Note the horizontal gypsum veins on both sides. (C) Strings of grey/green bands of siltstones segmenting nodular gypsum as chicken-wire texture. (D) Plan view of a nodular gypsum horizon. (E) Four closely spaced nodular gypsum horizons as a group in Unit 2. (F) Plan view of a nodule-rich horizon in the Blue Anchor Formation.

2.2.3.4 Sandstone body and sandstone dyke

The sandstone body at the base of the Keuper Marl includes a sub-horizontal main body and an inclined wing, both composed of gypsum cemented gritstone (Figure 2.12). Sedimentary structures include ripples and wavy horizontal laminations. The sands are coarse-grained and well sorted. Sub-horizontal and high-angle gypsum veins are widespread in the main sand body and the inclined body.

Twelve sandstone dykes are observed in the Keuper Marl, mostly NNW-SSE striking and medium to high angle dipping (37°-84°) (Figure 2.12D, Figure 2.32). The sandstone dykes are composed of gypsum cemented, coarse sandstones that are compositionally identical to the sandstone body. Thus, the sandstone body is interpreted to have acted as the source of sand for the sandstone dykes. The dykes exhibit variable aperture, ranging between 0.8-14.6 cm. The dykes mostly show a curved shape, which have been interpreted as buckled hydraulic fractures that formed during early burial and diagenesis (Cosgrove, 2001). A normal fault is observed to offset a sub-vertical sandstone dyke with a throw of 0.8m, whilst the correlated nodular horizons indicate a maximum fault throw of 2.1m (Figure 2.12D). This suggests that the sandstone dyke was intruded during the active period of the normal fault. The dykes are all cross-cut by gypsum veins. Some dykes contain dense gypsum veins, one of which includes a red host rock fragment trapped within the dyke.

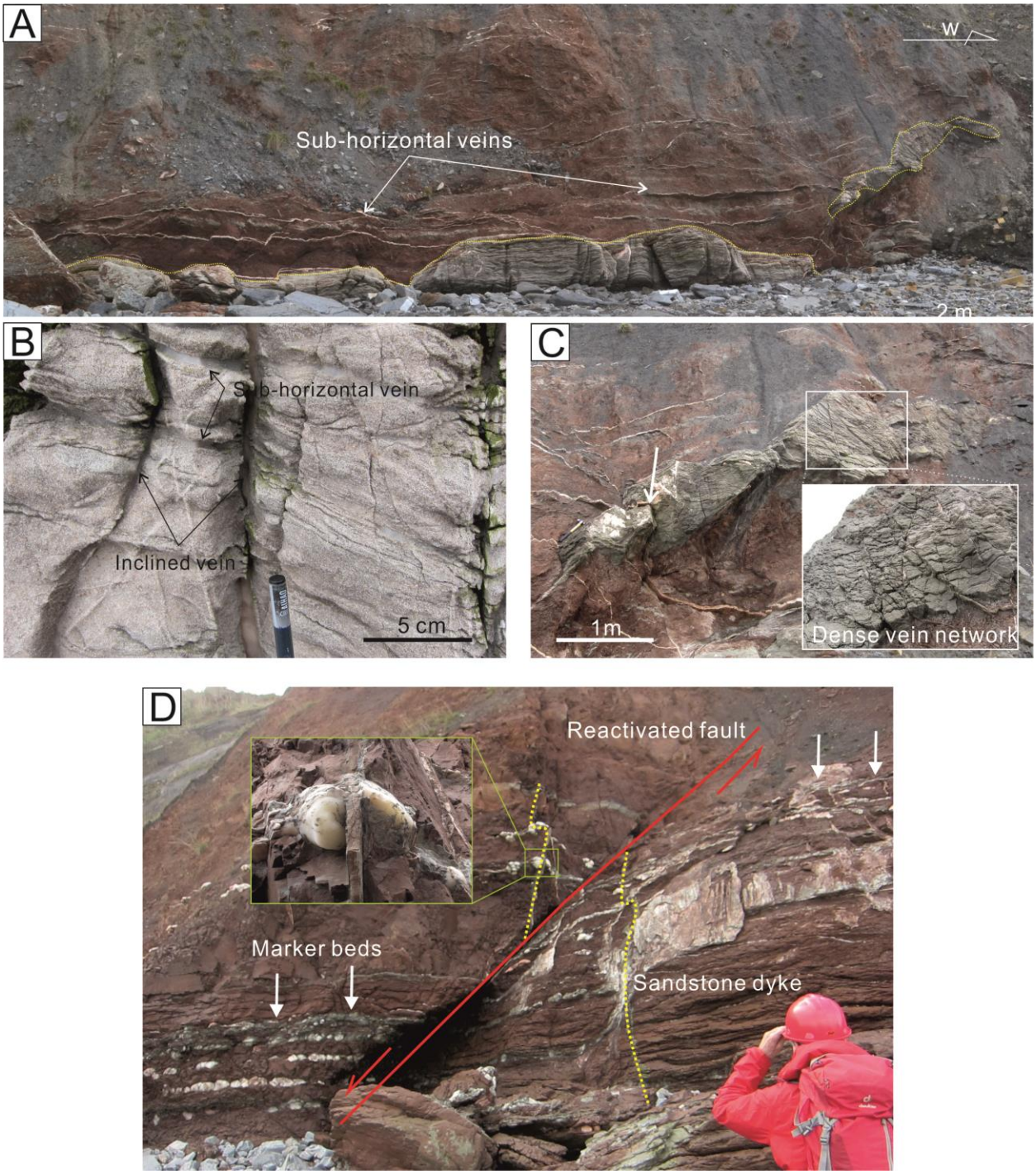


Figure 2.12 Exposure of the sandstone body at the base of the Keuper Marl (A). (B) Horizontal and inclined gypsum veins in the gypsum-cemented sandstone. (C) The highly fractured oblique wing of the sandstone body along a fault. Note the much higher vein density in the sandstone body than that in the host red marls. (D) A fault cross-cutting a sub-vertical sandstone dyke. The sandstone dyke also cross-cuts gypsum nodules. Note the lower throw of the dyke than that of the fault, suggesting that the fault has been reactivated with a reverse displacement. The arrows show the markers of four closely spaced nodular horizons for bedding correlation.

2.3 Vein characterization

2.3.1 Fracture stratigraphy

Gypsum veins are developed in both the Keuper Marl Formation and the Blue Anchor Formation. Importantly, the vein distribution and abundance are highly heterogeneous along the outcrop. The fracture stratigraphy is subdivided into five units in the exposed Keuper Marl, three units in the Blue Anchor Formation, according to the vein extent and intensity.

The Keuper Marl Formation

Unit 1, as the lowest unit of the Keuper Marl, mainly contains sub-horizontal gypsum veins (Figure 2.12A). The veins are mainly laterally persistent, and do not link with others. The sandstone body at the base of Unit 1 is highly fractured. The fractures are all filled with gypsum veins. The vein intensity in the sandstones is much higher than that in the surrounding marls.

Unit 2 overlies Unit 1 and contains the highest amount of gypsum veins of all the five units (Figure 2.7C, Figure 2.11E). The rocks are reddish, grey or green, comprising a high content of silts and sands. The gypsum veins show multiple orientations and a high connectivity. The intensity of gypsum veins is higher in the nodule-free horizons than the nodular gypsum horizons.

Unit 3 is located in the hangingwall of a normal fault and contains much less gypsum veins than Unit 2 (Figure 2.7B). The rocks are pale grey, reddish and green. Gypsum veins mainly occur within the nodular gypsum horizons or along faults. Veins are absent in the nodule-free horizons.

Unit 4 is also exposed in the hangingwall of a normal fault, which shows densely developed gypsum veins (Figure 2.7A). The red marls are more gypsiferous that Unit 3. The bedding parallel veins and inclined veins constitute a highly connected vein network.

Unit 5 as the topmost unit of the Keuper Marl, in contrast to Unit 4, shows no gypsum veins at all (Figure 2.7A). Gypsum nodules are also absent in Unit 5. The rocks are red and rather homogenous. Fissures without cement may be observed in the marls.

The Blue Anchor Formation

Unit 1 of the Blue Anchor Formation is highly bedded, consisting of numerous red, green and grey beds. Neither gypsum veins nor nodules are observed in this unit (Figure 2.8A).

Unit 2 and Unit 1 are bounded by a dark shale bed. Unit 2 contains 16.5 m thick grey-dark interbedded dolomite and marls. Both bedding-parallel and inclined gypsum veins are observed in this unit (Figure 2.8C). The bedding parallel veins are mainly concentrated in dark marls rather than grey marls or dolomites. This unit can also be observed in the hangingwall of the Hellwell Bay fault. Gypsum veins are intensively developed in the folds.

Unit 3 overlies Unit 2 and lacks both gypsum veins and nodules. The rocks are mainly interbedded dolomite and marls with a much lighter color than rocks in Unit 2.

In summary, gypsum veins are mainly developed in Unit 2, Unit 4 and Unit 5 of the Keuper Marl, and in Unit 2 of the Blue Anchor Formation. Gypsum veins also occur in Unit 3 of the Keuper Marl; however, the vein intensity is significantly lower. The veins are totally absent in Unit 5 of the Keuper Marl, and in Unit 1 and Unit 3 of the Blue Anchor Formation.

2.3.2 Orientation

The gypsum veins show multiple orientations in the Mercia Mudstone. A survey of vein orientations in the outcrop was carried out using 2D circular window method (Mauldon et al., 2001; Mauldon et al., 1999) that enables a complete sampling of multiple vein orientations in a selected area.

The gypsum veins can be rather curvy, thus only the representative orientations was chosen for measurement (Figure 2.13). For generally straight veins (deviation <20°), a tip to tip orientation is selected to represent the overall orientation. If the veins are rather curvy (deviation >20°), representative orientations were all measured. For branched veins, the branches were seen as new veins if the angle between the branch and the parent veins is higher than 20°. If one tip or both tips of the gypsum vein extend out of the circle, the orientation is only sampled from the part within the circle. Orientation data was collected in eight sites of the Keuper Marl, and two in the Blue Anchor Formation.

The results show that the gypsum veins exhibit three major preferred orientations (Figure 2.14-2.15), which include the NW-SE striking and north dipping veins (set 1), E-W striking and south dipping veins (set 2) , and sub-horizontal veins (set 3).

The veins of set 1 that dip northward at 60° are parallel to the E-W striking, basin-bounding normal faults along the southern margin of the basin and are presumably fault-controlled tectonic fractures (Cosgrove, 2001). The veins of set 2 are parallel to the Helwell Bay Fault and interpreted to have formed in the stress shadow of the fault, either during the formation or the reactivation of the fault. The sub-horizontal veins of set 3 are interpreted as newly-formed fractures along bedding planes.

It is notable that many other veins do not fall into the three sets, which exhibit near random orientations. Those veins are mainly curved veins whose propagation is significantly influenced by local pre-existing structures (see section 2.3.3.3). The ratio of population of each vein set revealed in the result may contain a systematic error due to the limited sampling area and different spacing of each vein set.

The gypsum veins in the Blue Anchor Formation are more consistently oriented and may be subdivided into two main sets, including an E-W striking, sub-vertical set (set 1), and a bedding-parallel set (set 2) (Figure 2.14). Veins of set 1 are red and rather evenly spaced. Those veins possibly have the same origin as the veins of set 1 of the Keuper Marl. Veins of set 2, which are mainly concentrated in dark marls are white and bedding-parallel.

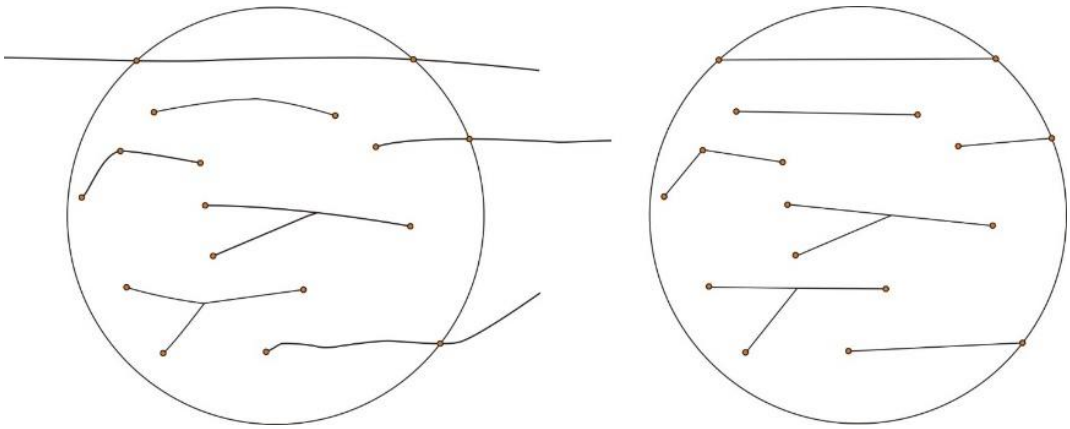


Figure 2.13 2D circular scanline method used for collection of vein orientation. See text for detailed explanation. The dots represent vein tips. The lines represent vein traces.

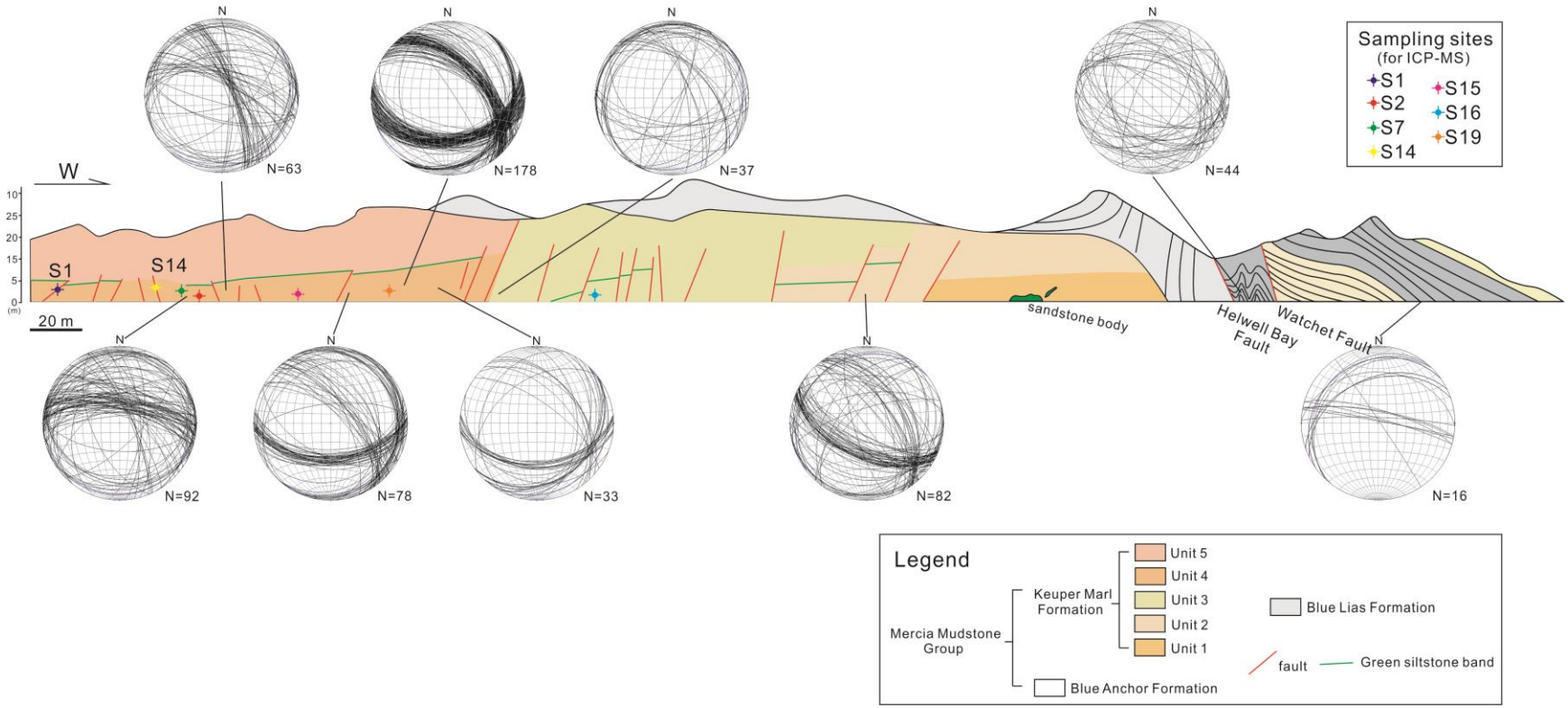


Figure 2.14 Stereonet projection of vein plane orientation along the cliffs on the Warren Bay. Lower hemisphere. Vein plane, black circle. Bedding plane, blue circle.

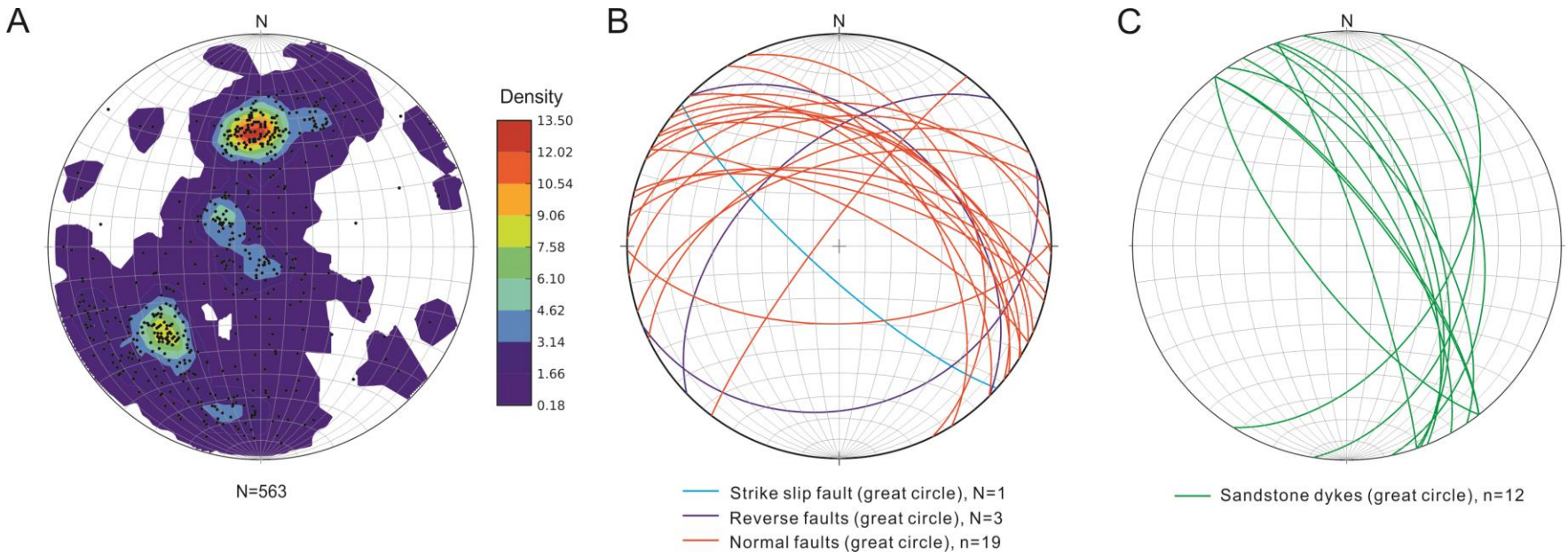


Figure 2.15 Stereonet projection of orientation of gypsum veins (A), faults (B) and sandstone dykes (C). Lower hemisphere

2.3.3 Geometry

2.3.3.1 Bedding-parallel veins

Although the gypsum veins in the Keuper Marl exhibit varied orientations, the bedding-parallel veins appear as the predominant set (Figure 2.16). Such veins follow the sub-horizontal bedding, exhibiting varied length and aperture. The sub-horizontal veins either occur as individual veins that are not visibly linked with any others veins (Figure 2.16C), or as clusters of closely-spaced veins with frequent interactions with neighbouring veins (Figure 2.16D-2.16G). The traces of bedding-parallel veins are frequently wavy with high local curvatures. Hence, intersection of those veins with adjacent sub-horizontal/inclined veins is common.

The bedding parallel veins often lie at the horizons where the host rock lithology shows variations (Figure 2.16F). Those gypsum veins are commonly more persistent and thicker than the intervening veins.

The persistent bedding parallel gypsum veins often exhibit a consistent aperture. However, the short veins with tapering tips pinch out in the red marls, whose maximum aperture is present in vein centre. Vein tips that mark the propagation direction of the veins commonly exhibit interactions with adjacent veins (see section 2.3.4).

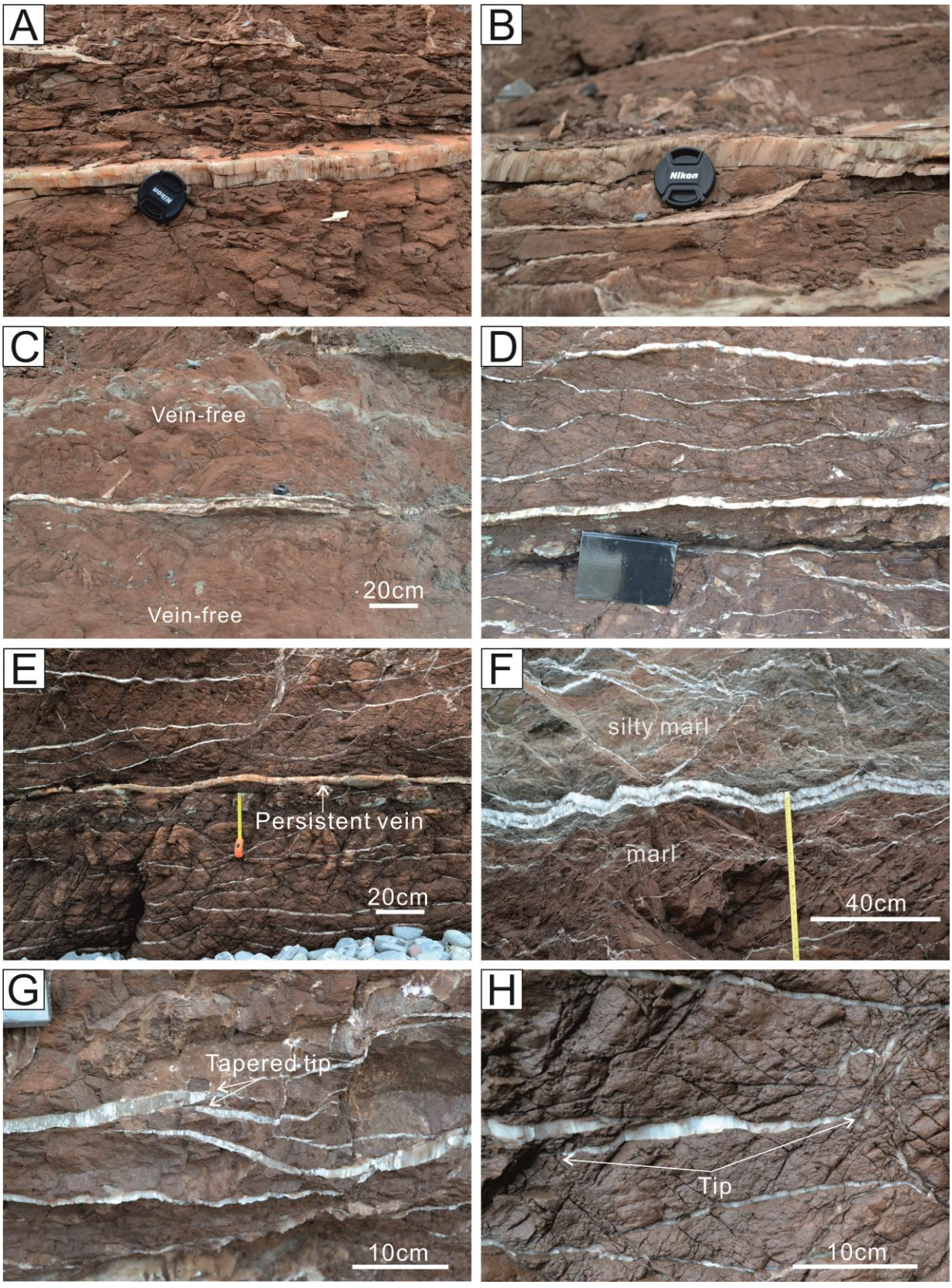

A
B
Nikon
C
Vein-free
20cm
Vein-free
D
E
Persistent vein
20cm
F
silty marl
marl
40cm
G
Tapered tip
10cm
H
Tip
10cm

Figure 2.16 (A) A horizontal gypsum vein with sub-vertical fibres. (B) A horizontal gypsum veins with fibres oblique to vein walls. (C) An isolated, horizontal gypsum vein in the red marl. (D) Multiple closely spaced horizontal gypsum veins. (E) Numerous gypsum veins with varied aperture. (F) A thick gypsum vein bounding two lithological units. (G) A cluster of small gypsum veins. Notice the tapered vein tips. (H)A short gypsum vein with both tapered tips exposed in the cliff.

Sub-horizontal gypsum veins are also abundant within the horizons that contain gypsum nodules (Figure 2.17). Those veins lie parallel to the long-axes of nodules which they are rooted in, and thus do not cross-cut the nodules. Single or multiple horizontal veins link adjacent gypsum veins. Vein tips are occasionally observed at the vein front, which pinch out in the red marls. Some nodule-rooted inclined veins are also observed, which propagate towards the upper/lower nodules (Figure 2.17D); however, the intensity of such veins is much lower than the horizontal veins.

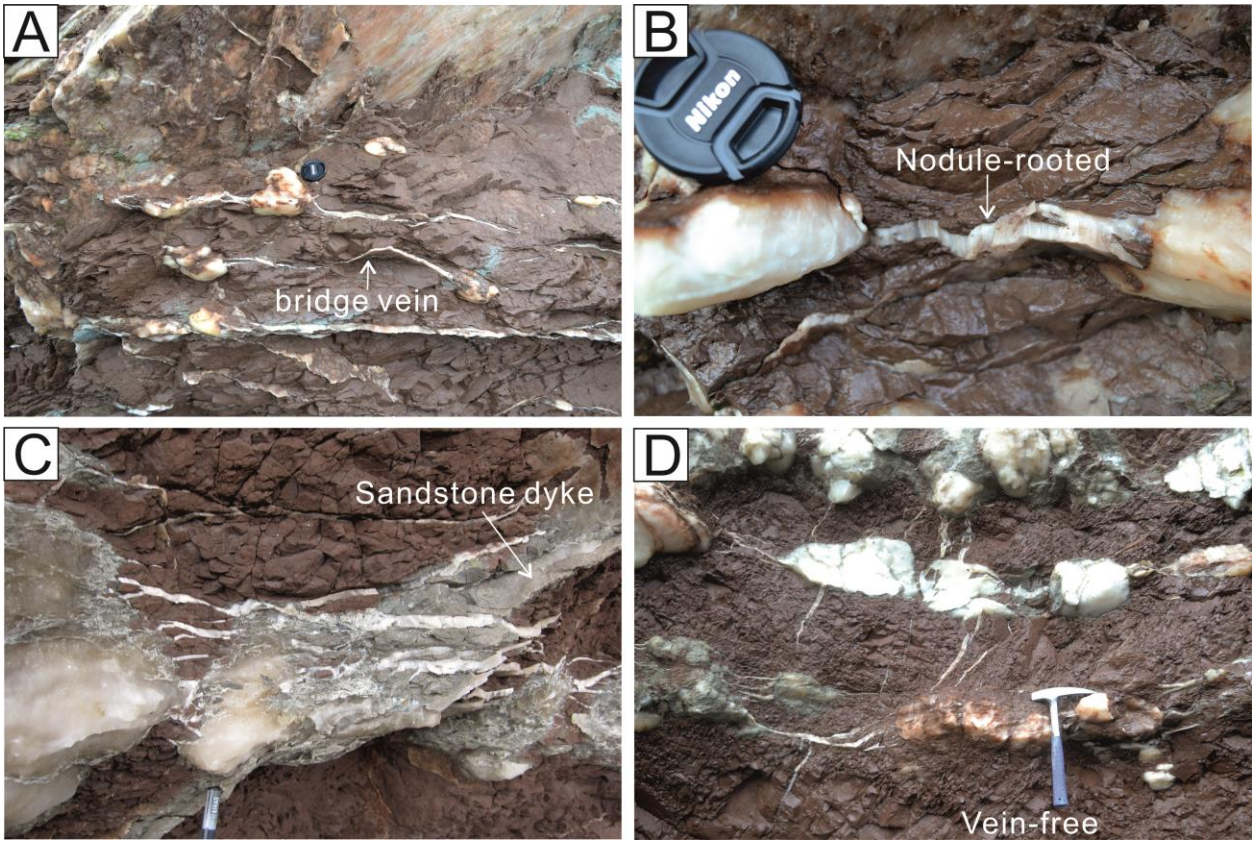


Figure 2.17 (A) Adjacent nodular gypsum linked by horizontal gypsum veins. (B) A horizontal gypsum vein coalescing with two gypsum nodules rather than cross-cutting them. (C) Nodule-linking gypsum veins cross-cutting an inclined sandstone dyke. (D) Multiple high-angle gypsum veins rooted in gypsum nodules.

The bedding parallel veins frequently appear as sets of en echelon veins (Figure 2.18). Such veins are parallel aligned, bounded by thin bands of wall parallel host rock fragments. The tips of single veins are commonly linked with walls of neighbouring veins. Multiple linkages of the en echelon veins results in more persistent sub-horizontal veins which contain multiple oblique host rock inclusion bands (Figure 2.18D). Some sub-horizontal gypsum veins terminate as a set of gently inclined en echelon veins (Figure 2.18C). The en echelon veins also display sigmoidal shapes, whose tips are sub-horizontal (Figure 2.18B, D). The linkage of neighbouring veins leaves rhombic host rock fragments enclosed by satin spar.

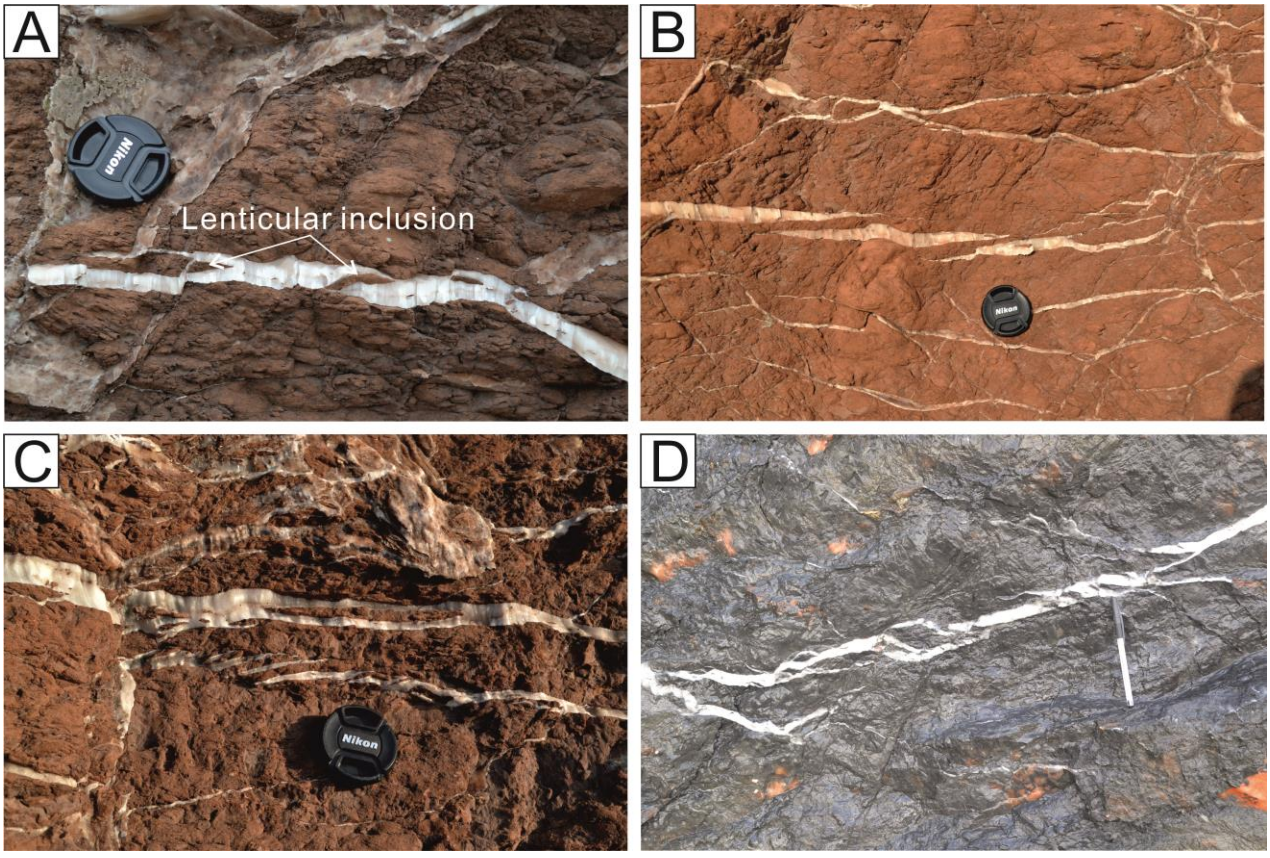


Figure 2.18 Outcrop exposure of en echelon gypsum veins. (A) En echelon veins with tips coalescing with the neighbouring vein. Note the oblique fragments of host rocks trapped between the tips. (B) En echelon veins with tapered tips. (C) Horizontal veins terminating as a set of en echelon veins. (D) Sigmoidal en echelon veins in dark grey limestone. Note the rhombohedral host rock inclusions between two adjacent veins.

Bedding parallel veins are also well developed in the interbedded grey dolomite and dark marls of the Blue Anchor Formation (Figure 2.19). The gypsum veins are gently inclined, strictly following bedding planes. The gypsum veins are mainly concentrated in the dark marls, exhibiting a contrasting white colour to the hosts. These veins are commonly laterally persistent and can be traced along the outcrop exposures for tens of meters.

The bedding parallel veins, except those nodule-rooted veins, are interpreted as the result of fracturing along bedding as weak planes. The origin of fracturing is discussed in section 2.6.2. The formation mechanism of nodule-rooted veins is discussed in section 3.8.5.

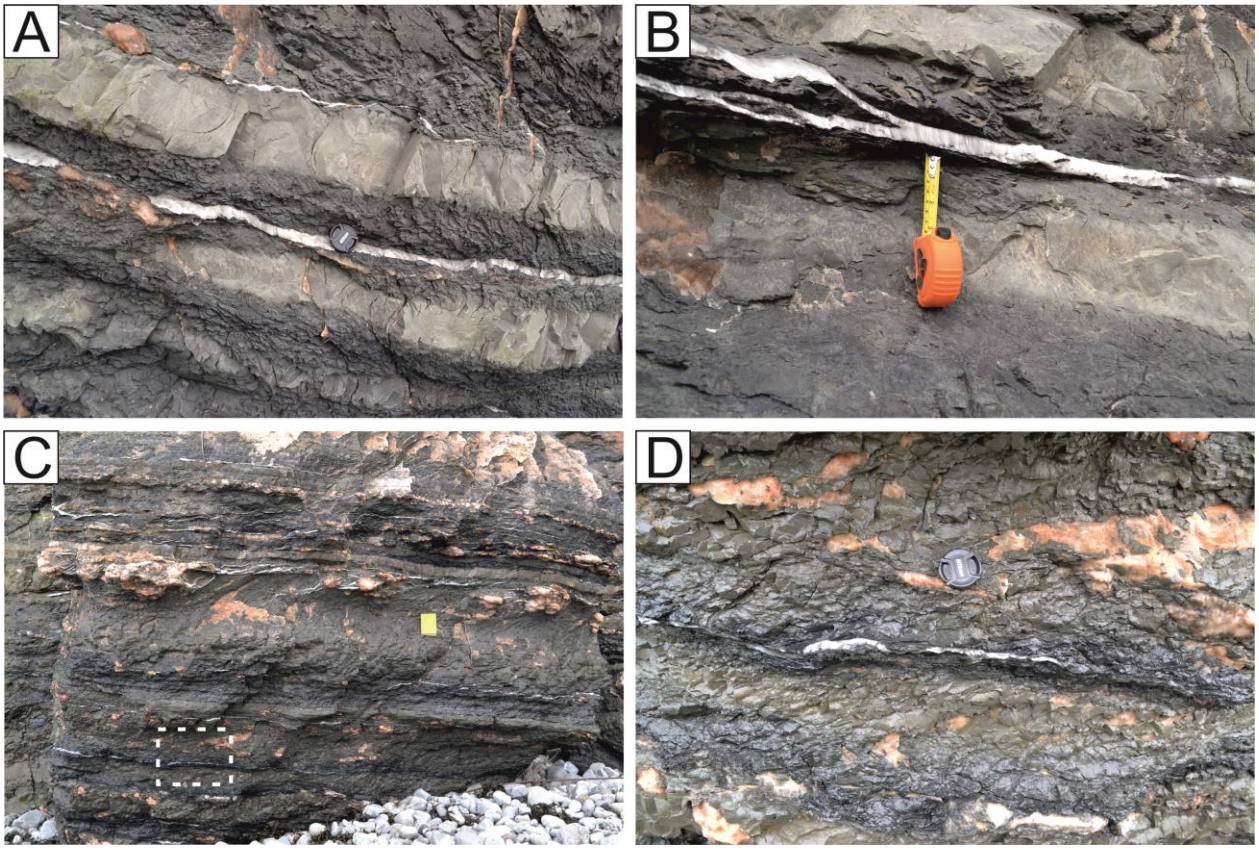


Figure 2.19 Bedding-parallel gypsum veins in the black marl of the Blue Anchor Formation. (A) and (B) showing the traces of those veins with an aperture of ~2cm. Note the branching of the vein in figure B. (C) and (D) showing the concentration of such veins in black marls. Figure 2.19D shows the enlarged area of the dashed box in figure 2.19C.

2.3.3.2 Inclined veins

The anastomosing gypsum vein network in the Keuper Marl consists of horizontal veins and inclined veins that show a high connectivity. The inclined gypsum veins are widespread in Unit 2 and Unit 4 of the Keuper Marl, mainly including veins with preferred orientations of set 1 and set 2 (Figure 2.20A-D).

Some small inclined veins are parallel-aligned along walls of sub-horizontal veins. Such veins are rooted in the horizontal veins with their aperture gradually decreasing towards the host rocks (Figure 2.20D, E). Those veins are interpreted to be wing-cracks that formed as a result of the propagation of their affiliated horizontal veins. In contrast to the horizontal veins, the wing-cracks commonly contain sub-horizontal fibres. Some inclined veins occur at vein front and link two parallel veins as tension gashes (Figure 2.20F).

The red veins in the Blue Anchor Formation exhibit strongly preferred orientations (Figure 2.20G-H). Those veins are often rooted in gypsum nodules and cut multiple beds.

2.3.3.3 Curved veins and vein steps

Some veins exhibit highly curved traces, whose dip can change dramatically over 60° (Figure 2.21A-D). The unstrained vein geometry is a growth feature rather than the result of deformation, which is evident from the uniform fibre orientations in different segments of the veins. Fibre orientation is largely sub-vertical and not affected by vein wall orientations (see more detailed description in Section 2.4), hence the angles between fibres and their contacting vein-walls decreases when vein dip decreases.

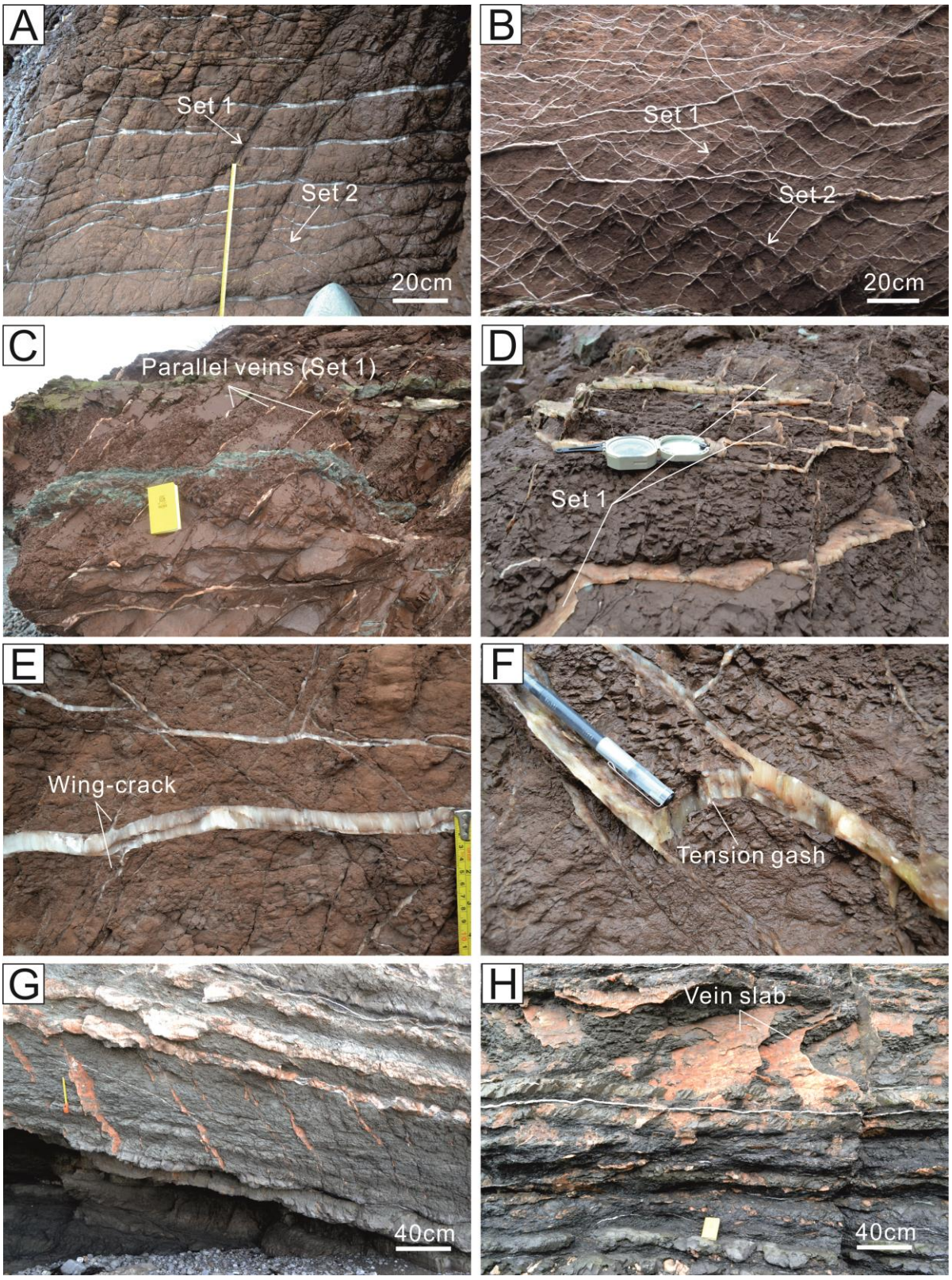


Figure 2.20 Outcrop exposures of inclined gypsum veins. (A) Dense gypsum vein network in the red marl. Note the much thicker horizontal veins than inclined veins. (B) Stockwork of gypsum veins with high

connectivity. (C) NW-SE striking, north dipping veins in the red marl. (D) Connection of inclined veins and horizontal veins. Note the non-cross-cutting relationship. (E) Inclined veins rooted in sub-horizontal veins. (F) A bridging vein connecting two parallel inclined veins. (G) E-W striking, high-angle dipping gypsum vein in the Blue Anchor Formation. (H) Exposure of vein planes of the incline veins in the Blue Anchor Formation. Note the bedding-parallel vein cross-cutting those inclined veins.

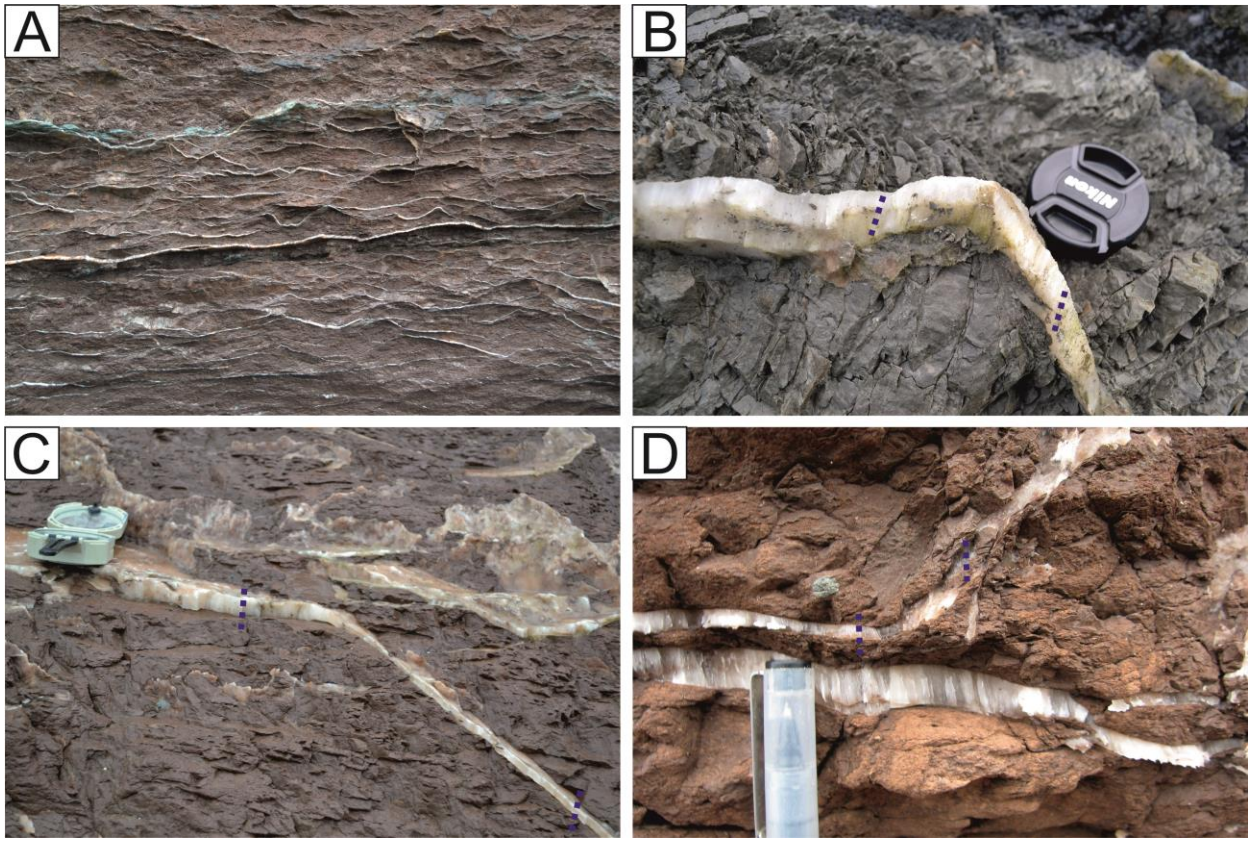


Figure 2.21 Curved gypsum veins in the Mercia Mudstone. (A) Traces of numerous wavy gypsum veins. (B) A curved gypsum vein with consistent fibre orientation. (C) and (D) showing curved gypsum veins with consistent sub-vertical fibres. The dashed lines highlight the fibre orientation.

Inclined vein steps are commonly observed to link sub-horizontal gypsum veins in different horizons (Figure 2.22). Such steps exhibit a much shorter length. The vein steps are parallel to numerous cemented or uncemented fractures, and are interpreted as the segments of pre-existing fractures that have been reopened. It is notable that the fibre orientations in the steps are consistent with those in the horizontal veins, possibly indicating a simultaneous opening and cementation in the steps and the horizontal veins. This is in contrast to the fibres in inclined veins that have formed as tension gashes (Figure 2.20F).

The adjustment of a vein propagation path is common where the veins intersect pre-existing structures in the adjacent areas (Figure 2.23). The orientations of gypsum veins change to be parallel to the walls of sandstone dykes as the veins approach the dykes (Figures 2.23A-B). Horizontal veins also curve to follow the fault planes as they encounter pre-existing faults (Figures 2.23C-D). Interestingly, minor gypsum veins gradually curve to be orthogonal to the wall of larger veins and intersect with them (Figures 2.23E-F).

Some of the red gypsum veins in the flat-lying beds of the Blue Anchor Formation exhibit a sigmoidal shape (Figures 2.24A-B). The axial surfaces of those folded veins are approximately E-W striking. The gypsum veins are intact without signs of modifications. Curved fractures are prevalent in the severely damaged host rocks. The fracture traces are parallel to the sigmoidal veins. The red veins are interpreted to have formed as the result of flexural slip folding of the individual beds that have different shortening and amplification rates. The beds that contain folded veins are folded weak layers.

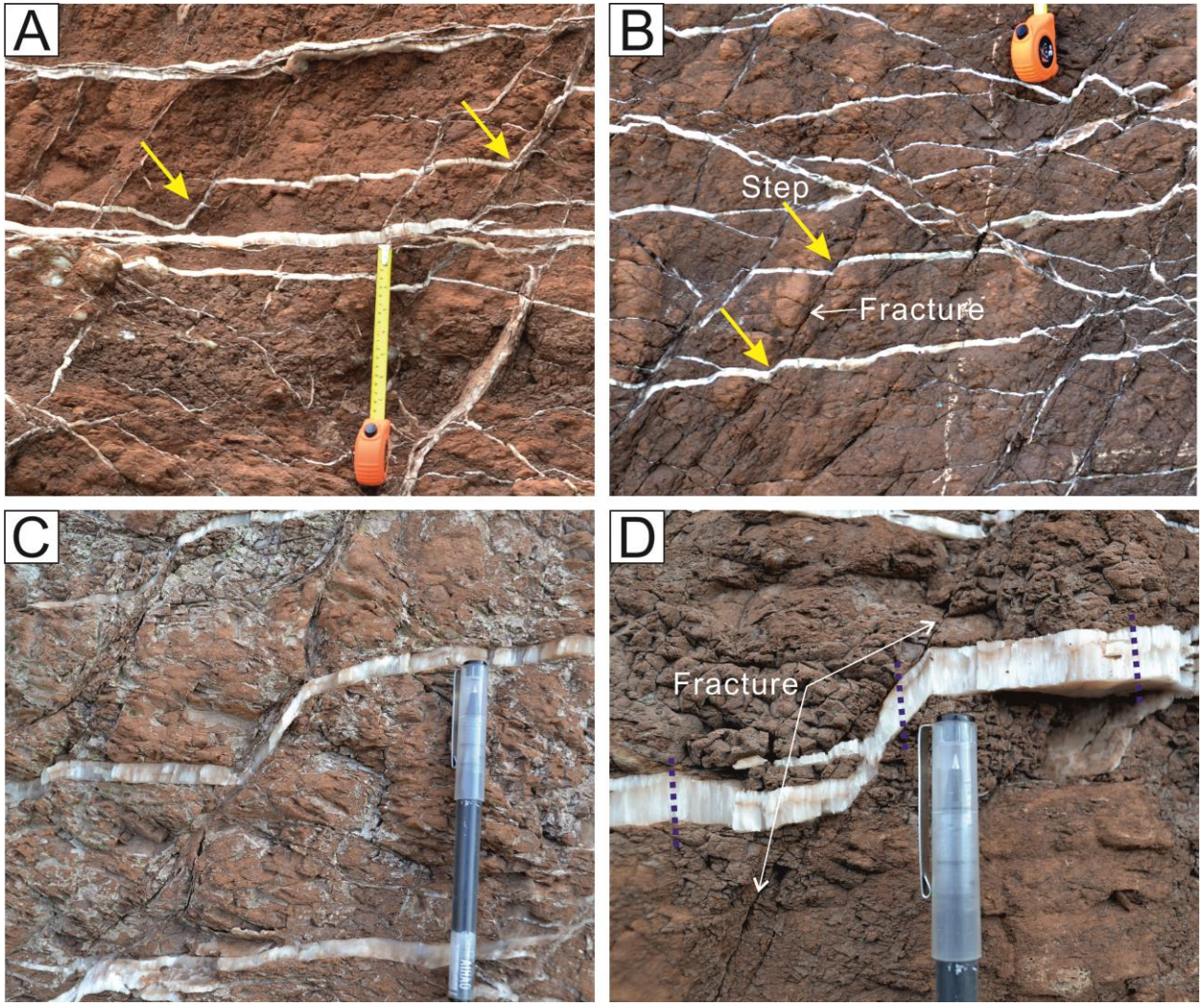


Figure 2.22 Steps in sub-horizontal gypsum veins. (A) and (B) showing relative large and small vein steps respectively. (C) and (D) showing vein steps taking advantage of inclined fractures. Note the consistent fibre orientations (dashed lines) in the inclined vein step and the sub-horizontal veins in figure 2.22D.

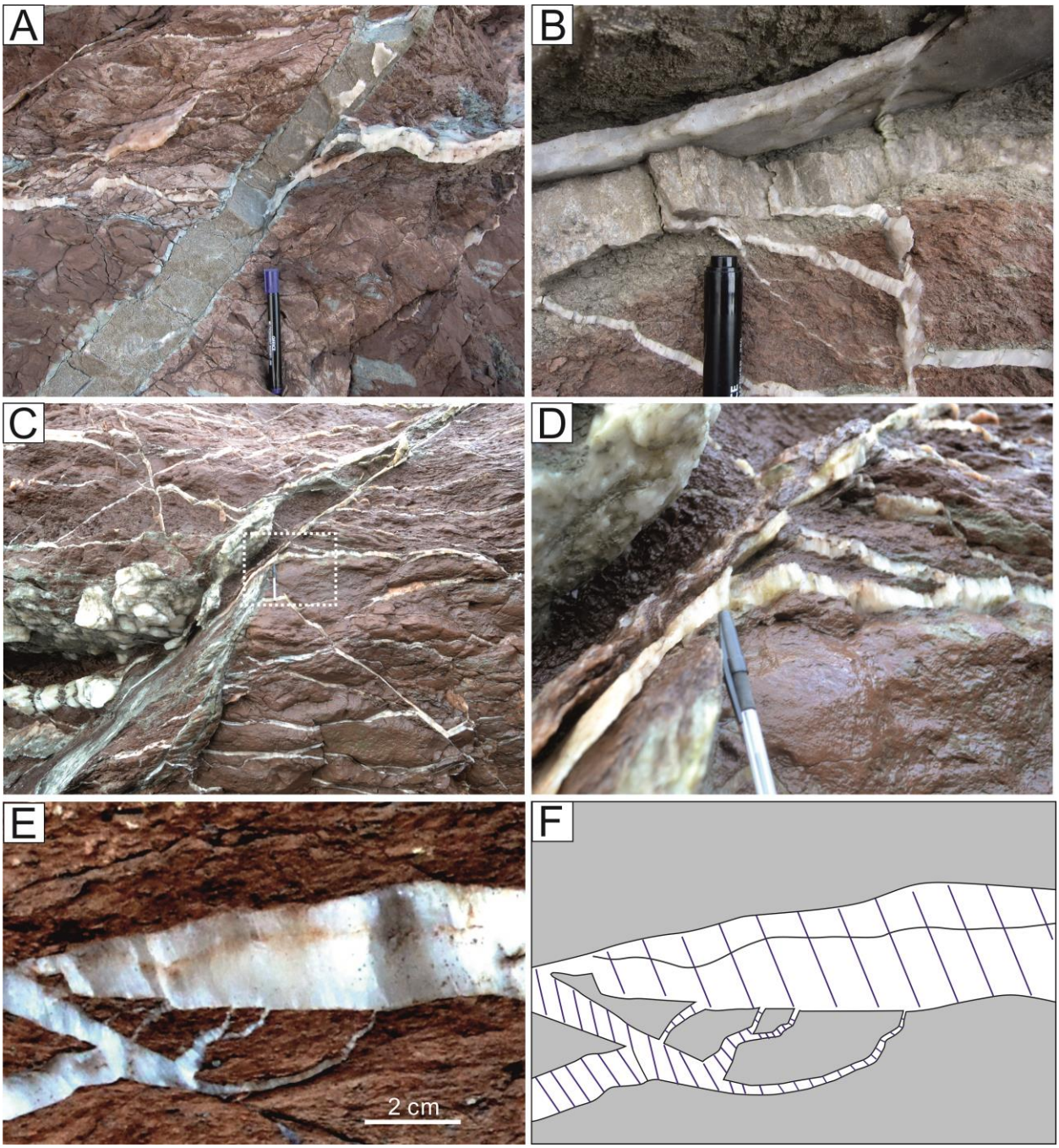


Figure 2.23 Curved gypsum veins propagating against pre-existing structures. (A) Horizontal gypsum veins curving to follow the planes of a sandstone dyke. (B) Multiple gypsum veins curving to cross-cut a sandstone dyke. (C) and (D) showing horizontal gypsum veins curving to follow the plane of a pre-existing fault. (E) and (F) showing multiple minor gypsum veins curving gradually to be normal to a much larger horizontal vein.

The gypsum veins in the folding zone on the west of the Watchet fault are predominately wavy (Figure 2.24C-D). They are either sub-horizontal or parallel to inclined bedding planes. These veins cross-cut multiple folded beds, implying that the formation of the veins postdates the folding of the host rock.

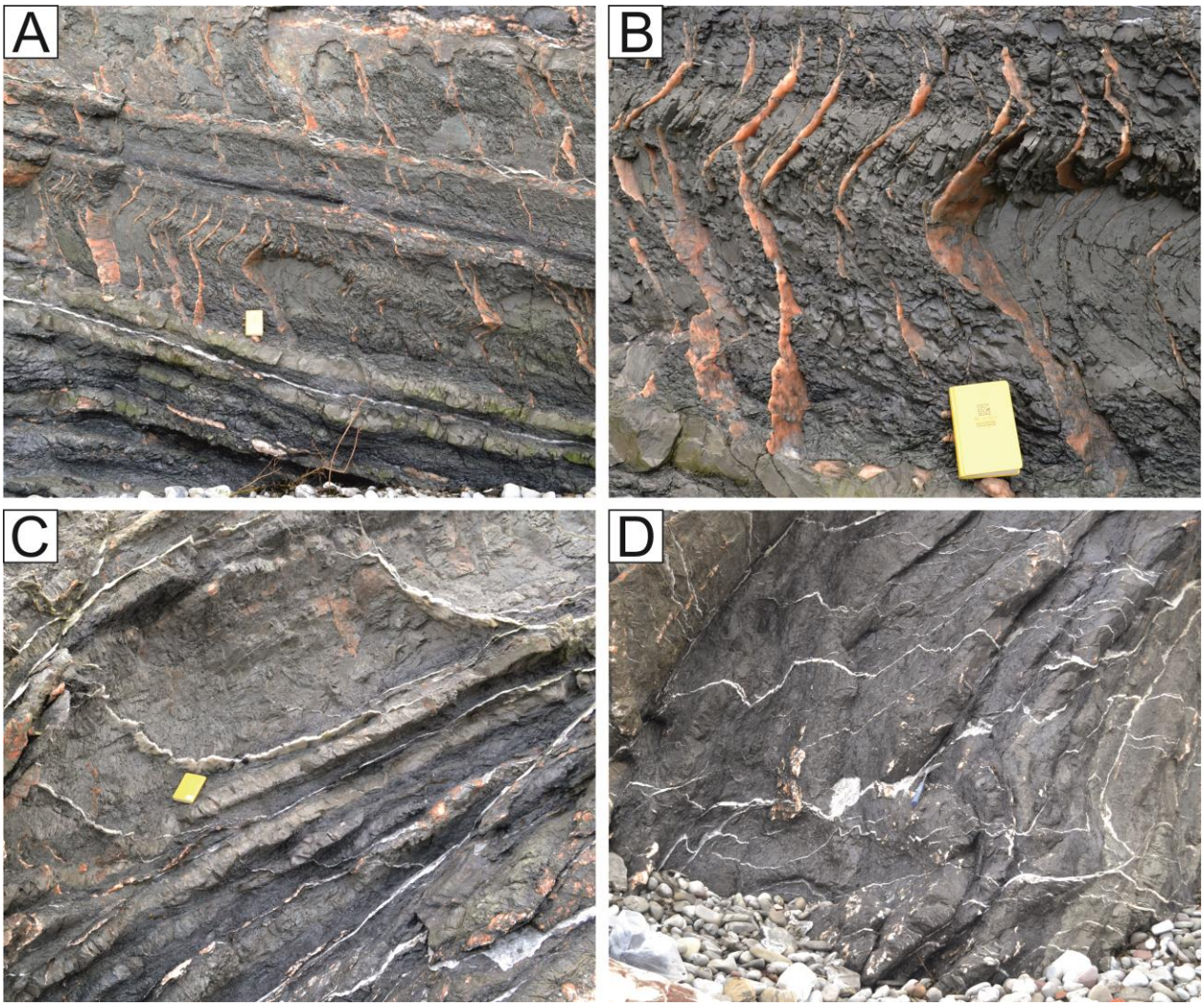


Figure 2.24 Curved gypsum veins in the Blue Anchor Formation. (A) and (B) showing the sigmoidal gypsum veins in the dark marls. (C) and (D) showing curved gypsum veins in the folds in the hangingwall of the Helwell Bay Fault.

2.3.3.4 Fault veins

All the faults exposed in the outcrop of the Mercia Mudstone are cemented by gypsum veins (Figure 2.25). The E-W striking faults commonly exhibit slabs of white fault veins dipping north. The vein width varies from several centimetres to 16.8 cm. The median zones of the fault veins contain a large amount of host rock inclusions and impure gypsum masses (Figures 2.25A, 2.25C). Similarly to the satin spar veins in the rock matrix, the fault veins also contain two outer fibrous parts that are rather pure in composition.

Fault 5 (316°/52°, dip direction/dip), as one of the faults with a reverse displacement, contains a 6 cm thick fault vein that exhibit a fibrous texture and cross-cuts the horizontal gypsum veins in the rock matrix (see section 2.3.4.1). Importantly, fibre lineations are observed on vein surfaces, which exhibit a sub-parallel direction (332°/48°, plunge direction/plunge) to the fault plane. Those fibre lineations are also parallel to striations on the slip surfaces of fault walls. It is interpreted that the fibre lineations reveal the sense of slip, whose direction reflects the dip-slip of the fault. Depressions that are filled with centimetre-scale host rock fragments are observed on fault vein surfaces. Those rock fragments occur ahead of numerous fibres that exhibit a higher relief than the fragments, resulting in point asperities on vein surfaces. The fibre fronts also commonly exhibit irregular traces and varied surface relieves, which are possible slickenside steps or the result of weathering.

More observations of fibre lineations are from Fault 9, which is a reverse fault and contains a 4 cm thick gypsum fault vein (Figure 2.27). The fault vein consists of linear fibres in the median zone that is parallel to the fault plane, and two outer fibrous parts. The fibres are sigmoidal-shaped, with the plunge gradually increasing to be sub-normal towards vein walls. Fibre lineations are observed on vein surfaces, which resemble those in Fault 5. The lineation front exhibits a crescent-shaped trace, which has a higher relief than the vein surface ahead and is interpreted as a

slickenside step. Hence, the reverse slip of Fault 9 is interpreted to be revealed by the fibre lineations on fault vein surfaces.

The gypsum cements in the Helwell Bay Fault appear as straight fibres parallel to fault planes (Figures 2.28E-F). Those fibres are needle-like and coarser than those in the satin spar veins in the bulk rock. The fault vein offsets sub-horizontal veins in the marls, leaving fibre-parallel slickenlines on the sections of transected veins in the marls. Hence, the fibres in the fault vein are interpreted to form during the slip of the fault, which postdate the development of satin spar veins in the marls. Due to the severe weathering of the fault vein and the marls, it is difficult to obtain additional information of the sense of fault slip during the formation of the fibre lineations. However, according to the reverse displacement of the horizontal satin spar vein, it is interpreted that the fibre lineations are associated with a reverse dip-slip of the Helwell Bay Fault. The fibre lineations in the fault veins have formed either by means of syn-kinematic recrystallization or dissolution/precipitation (Fossen, 2010) that reshaped the gypsum crystals on vein surfaces in the preferred orientation of fault slip.

Based on the observations above, the formation of fault veins is interpreted to have experienced three major stages of evolution (Figure 2.29). During the first reverse reactivation of faults due to tectonic compression, fibre lineations were produced on fault planes and aligned parallel to the fault slip direction. Such lineations are especially rich in the jogs that result from the asperities of fault planes. Those straight fibres serve as the median zone for the final fault veins. Then gypsum fibres start to grow towards vein walls during tectonic relaxation and the inactive state of the faults. The origin of curved geometry of fibres is discussed in section 3.8.3. Finally, the second phase of fault reverse reactivation commenced, with fibre lineations generated on vein surfaces that recorded the slip.

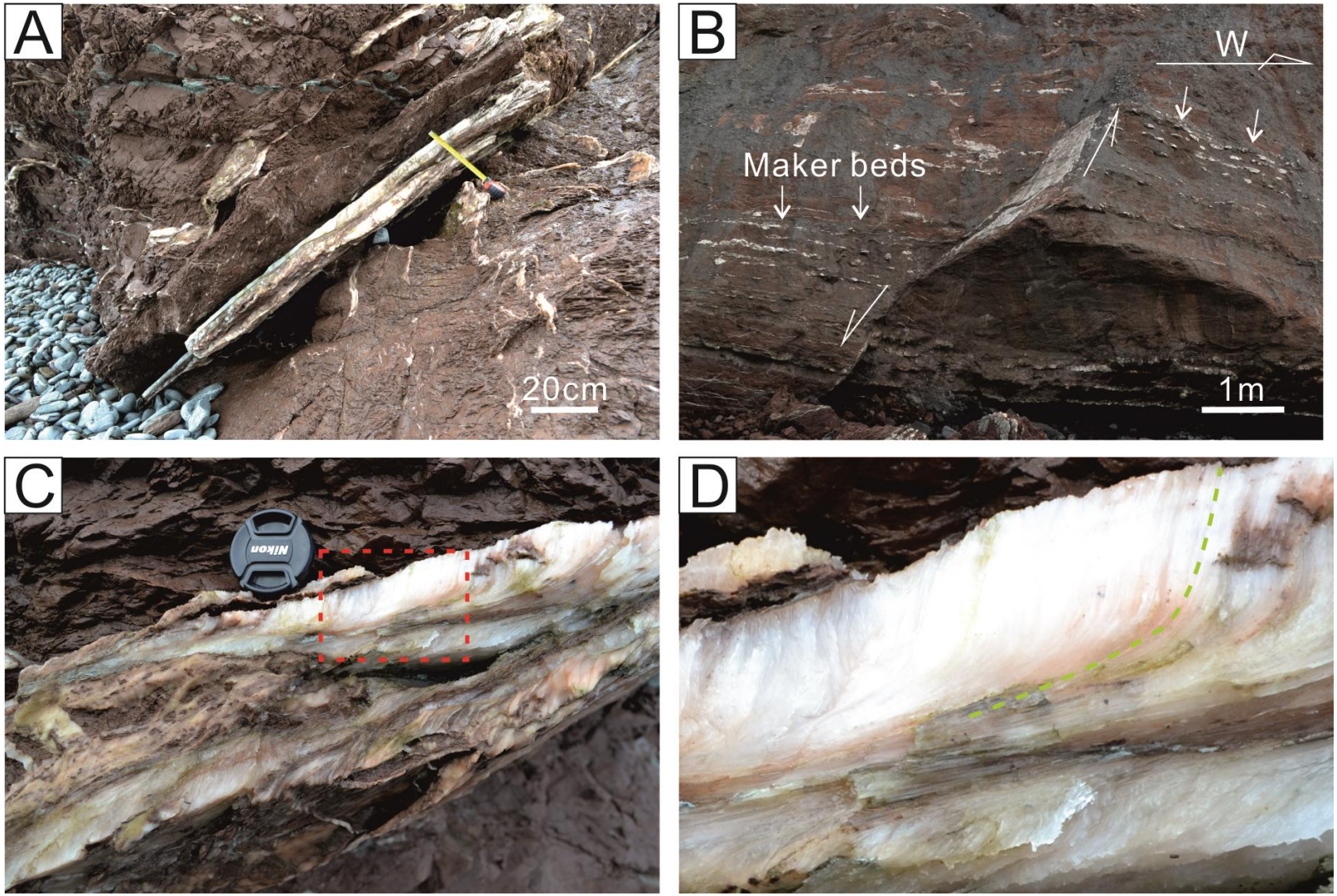


Figure 2.25 Exposures of fault veins in the study area. (A) A 16.8 cm thick fault vein. See location in figure 2.6. (B) A fault vein in a normal fault with vein slabs exposed. (C) Complex texture of the fault vein in figure 2.25A. (D) A closer view of the box area in figure 2.25C. Note the dashed line highlighting the curved fibre geometry.

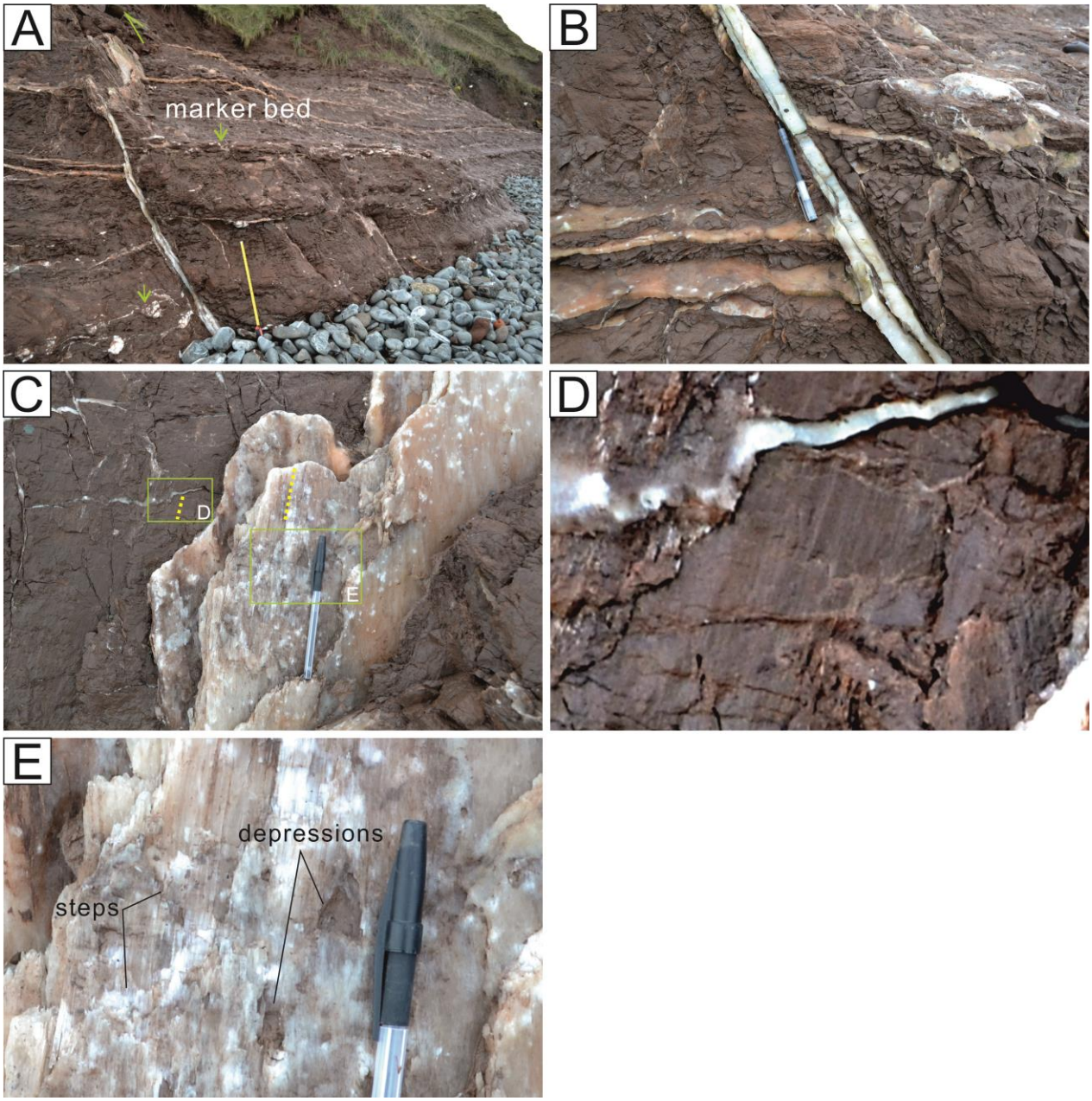


Figure 2.26 Photograph of Fault 5 in the study area. See location in figure 2.6. The taper measure is 1m as scale bar. (A) The overview of the fault vein. (B) A closer view of the fault cross-cutting two horizontal satin spar veins. (C) Fibre lineations on the surface of the fault vein. The dashed lines mark the striations and fibre lineations that are parallel. (D) A closer view of the striations shown in the box area of figure 2.26C. (E) A closer view of the fault vein plane in the box area in figure 2.26C. Note the occurrence of depressions and possible slickenslide steps.

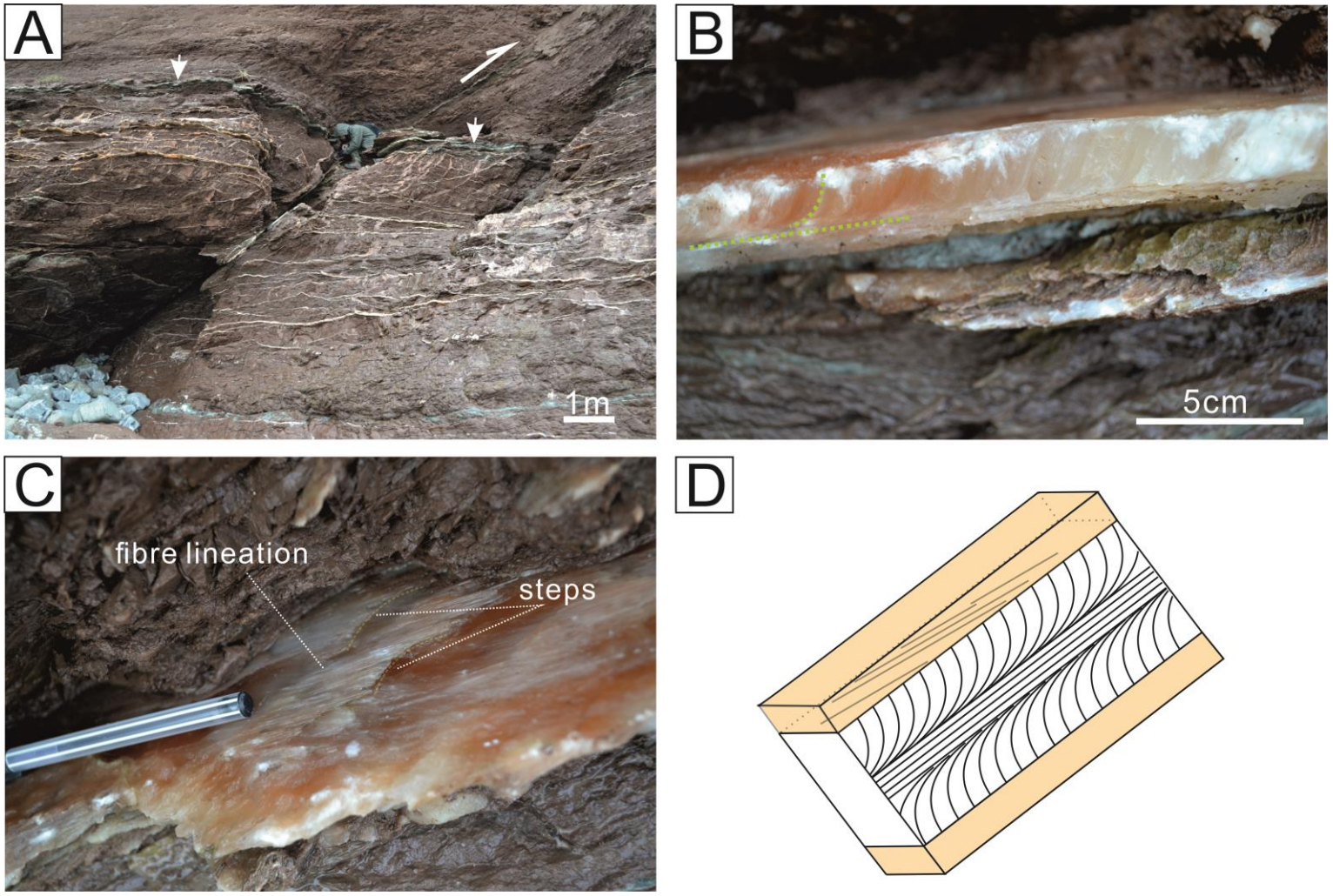


Figure 2.27 (A) Photograph showing the exposure of Fault 9. See location in figure 2.6. (B) The fault vein in Fault 9. The dashed lines mark the fibre orientations. (C) Fibre lineations on vein surface. (D) Schematic sketch showing the texture of representative fault veins in the study area.

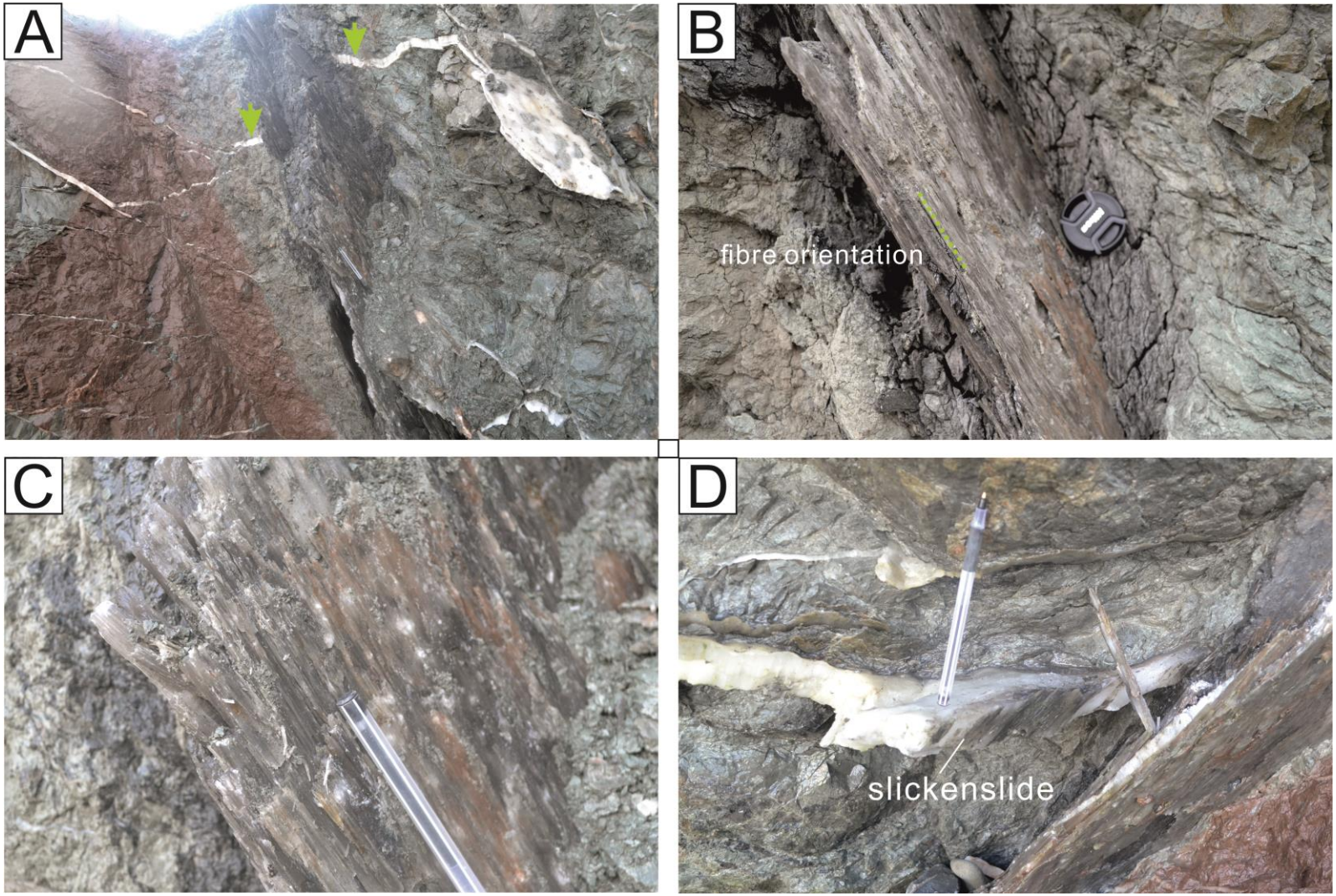


Figure 2.28 Photographs showing the fault vein in the Helwell Bay Fault. See location in figure 2.6. The arrows mark a horizontal vein cross-cut by the fault. (B) Fibre lineations showing the slip direction of the fault. (C) A closer view of the fibres. Note the fibre direction marked by the pen. (D) Slickenslides on the section of a horizontal satin spar vein in the marls.

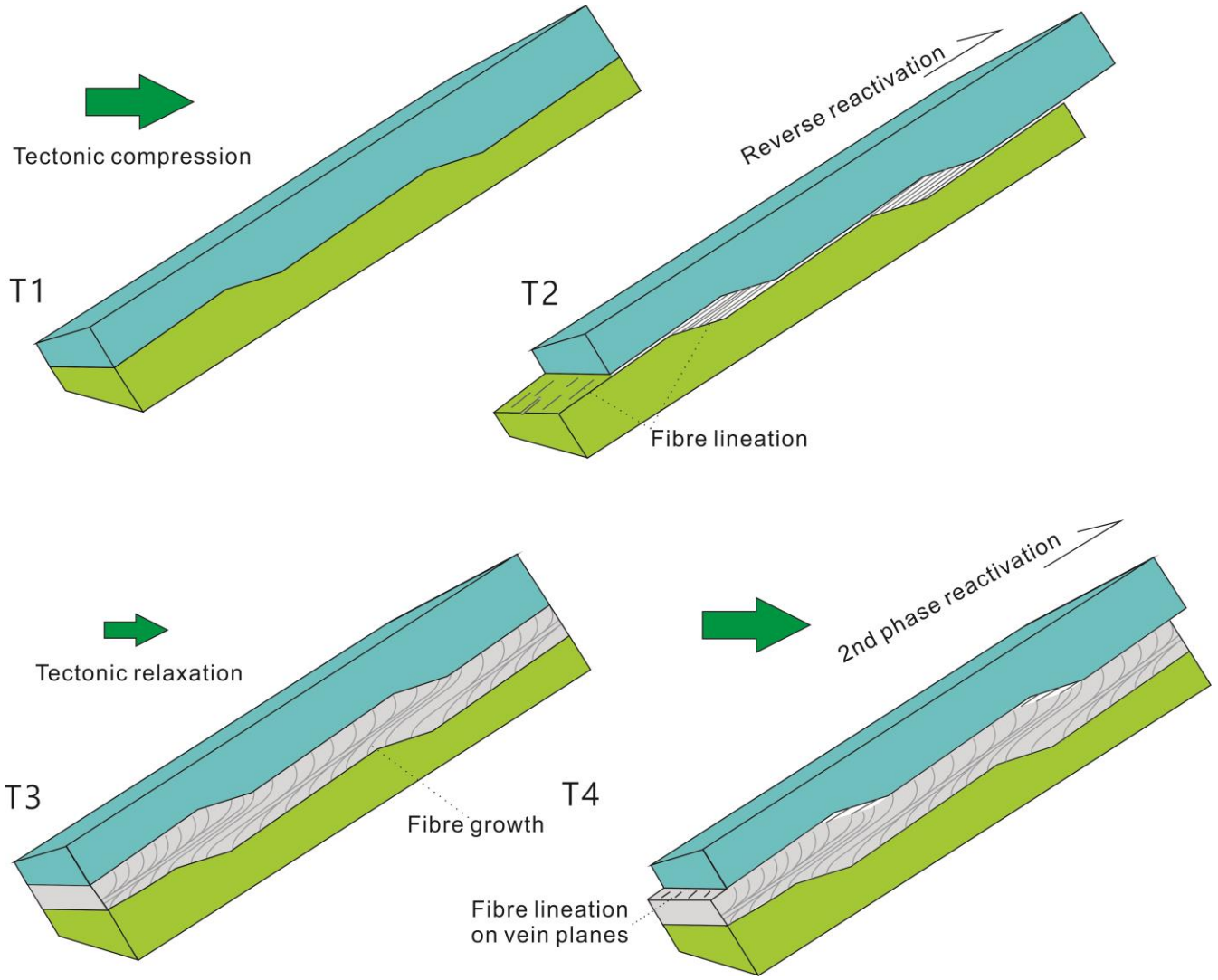


Figure 2.29 Schematic sketches illustrating the formation process of typical fault veins in the Mercia Mudstone. See text for explanation.

2.3.4 Interaction

2.3.4.1 Cross-cutting relationships

Veins

Intersection of differently oriented gypsum veins is commonly observed in the red marls. Although the intersecting veins may form ‘x’ shaped geometries, they do not cross-cut each other (Figure 2.30A-D). As shown in figure 2-26A, vein *c* and vein *d*, which are branches of vein *a* and vein *b* respectively, are not cross-cut by vein *a* and vein *b*. Vein *a* and vein *b* intersect at the junction e, where vein *c* and vein *d* deviate from the original orientation.

Similiar geometrical relationships that can be misinterpreted as vein cross-cutting is shown in Figure 2.30B. Vein *a* and vein *c* are segments of the upper curved vein. Vein *b* and vein *d* are segments of the strongly curved lower vein. Vein *b* and vein *c* are not cross-cut by vein *a* and vein *d*. The two veins both contain consistently oriented fibres, indicating the vein morphology as a growth feature. The vein walls coalesce for 2 cm and split during later propagation.

Coalescence of curved veins occurs between sub-horizontal veins and the NW-SE striking veins (Set 1) in the Keuper Marl (Figure 2.30C). Sub-horizontal vein *a* and vein *c* are not segments of a single vein, neither are the inclined veins *b* and *d*. However, vein *a*, vein *d* and vein *f* form an intact gypsum vein, which show smooth curves when vein-dip changes, so do vein *b* and vein *c*. Thus, vein *d* serves as a vein step that links vein *a* and vein *f*, which lies in different horizons with a vertical distance of 30 cm. Fibre orientations remain constant in single veins and are not affected by vein-wall orientations.

Thus, coalescence commonly occurs between differently oriented gypsum veins instead of cross-cutting when they are intersected, which is especially common between sub-horizontal veins and set 1 veins (Figure 2.30E-J).

Veins vs faults

Fault veins cross-cutting sub-horizontal gypsum veins is observed in two reactivated reverse faults, including the Helwell Bay Fault (Figure 2.31A-D). The layers in the hangingwalls and footwalls of the two faults can be correlated by nodular gypsum horizons and persistent gypsum veins with the same aperture, color and internal texture. Two closely spaced, horizontal veins are offset by the paler fault vein with a vertical throw of 0.8m (Figure 2.31A). Fibres in the fault vein are sub-orthogonal to the fault plane whilst the fibres in the horizontal veins are sub-vertical. The offset of sub-horizontal white veins in the hangingwall and footwall of the Helwell Bay Fault suggests a reverse motion with a throw of 12 cm (Figure 2.31C). The linear needle-like fibres as mineral lineation mark the direction of dip slip of the hangingwall.

In the majority of examples of faults, horizontal veins in the bulk rock are not cross-cut by faults, and instead the gypsum veins curve to follow fault planes (Figures 2.23C-D). It is interpreted that such veins progressively propagated to adjacent faults from the rock matrix and subsequently followed the walls of fault veins as weak planes.

Veins vs folds

The gypsum veins in the intensively folded layers of the Blue Anchor Formation are commonly wavy, however, their general orientations are sub-horizontal or slightly inclined. The veins frequently cut the inclined beds regardless of the position and curvature of the folded layers (Figure 2.31). Some veins have both sub-horizontal segments that cross-cut inclined beds, and also inclined segments that deviate from the horizontal direction to follow bedding. The other veins are observed to occur in dark marls in minor synclines or anticlines, whose traces are in accordance to their host folds. However, fibres in those veins remain consistently in the sub-vertical direction, indicating that the growth of fibres in single veins have occurred as post-folding features, otherwise the fibres would have exhibited multiple orientations depending on the geometry of the folded vein-walls. Hence, the generation of the veins is interpreted to postdate folding of the layers.

Veins vs dykes (sandstone body)

The sandstone dykes are considered as early-formed hydraulic fractures, which is evident from the bulked geometry as the result of subsequent compaction (Cosgrove, 2001). The sands with little cohesion are likely to have been fluidized at the early stages of burial and diagenesis when overpressure was achieved. The intact captive body of red marl fragment within the sandstone dyke suggests that the marls possibly possess a higher cohesion than the sands (Figure 2.28). When the differential stress is less than four times of the tensile strength of the marls, extensional fractures occurred in the marls, which were filled and preserved by the sands.

Other evidence for the early timing of sandstone dykes comes from the reactivated fault that cross-cut a sub-vertical dyke (Figure 2.12). The intrusion of the dyke is interpreted to have occurred

during the active period of the normal fault. This is based on the shorter displacement of the dyke than the fault, which is resulted from the reverse reactivation of the fault during basin inversion.

As described in section 2.2.3.4, the sub-horizontal gypsum veins cross-cut the high-angle sandstone dykes and also the sandstone body at the base of the Keuper Marl. Some gypsum veins curve to follow the dyke walls instead of cross-cutting them when they encounter the sub-vertical dykes (Figure 2.32B). Hence, the sandstone dykes are early-formed structures during burial, and predate the gypsum veins.

Veins vs nodules

The gypsum nodules in evaporite-rich beds are suggested as syn-depositional structures (Nichols, 2009; Whittaker and Green, 1983). The nodules are cross-cut by the early-formed sandstone dykes (Figure 2.12), suggesting an even earlier timing than the dykes.

As described in section 2.3.3.1, nodule-rooted gypsum veins do not cross-cut the gypsum nodules. Those veins exhibit the maximum aperture in the nodule-vein contacting sites and a tapering tip that vanishes in the marls or coalesces with neighboring veins or nodules. Such veins are interpreted to have formed during anhydrite-gypsum transition stage and derived materials from the excess gypsum from the rooted nodules (see section 3.8.5). Other gypsum veins commonly split into branches when they encounter nodules, and envelope them along the nodule margins. As a result, the gypsum nodules commonly show a blocky, homogeneous core and a thin fibrous rim. Thus, the nodules as the earliest sedimentary structures in the Mercia Mudstone clearly predate gypsum veins.

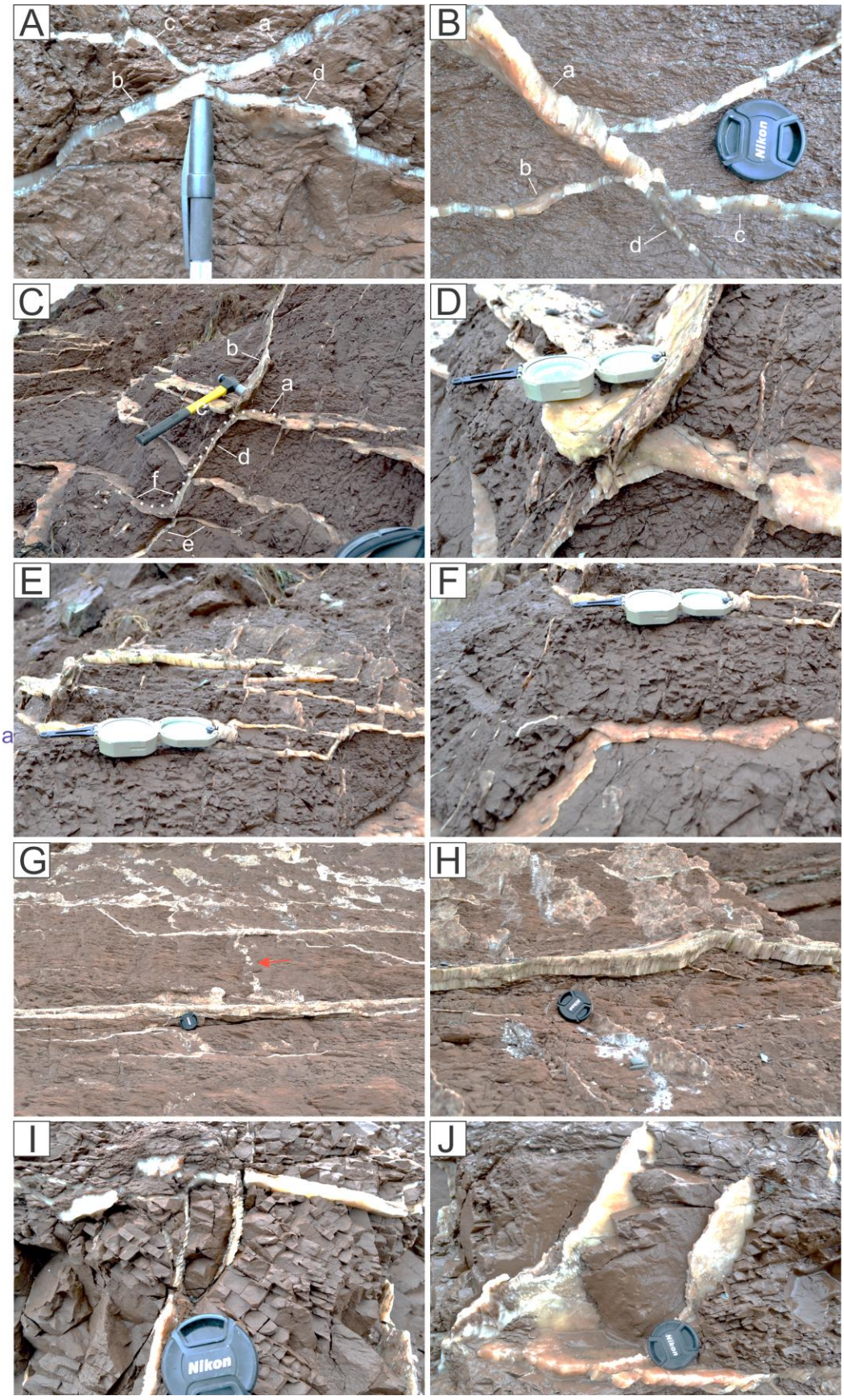

A
c
a
b
d
B
a
b
d
c
C
b
a
c
d
f
e
D
E
F
G
H
I
Nikon
J
Nikon

Figure 2.30 Coalescence of differently oriented gypsum veins. (A) and (B) showing vein branching and coalescence. (C) and (D) showing the inclined steps of horizontal veins. See text for explanation. (G) and (H) showing the inclined veins as tension gashes of large horizontal veins. (I) showing a steep gypsum vein as tension gashes of horizontal veins. Note the sub-horizontal fibres in the inclined veins. (J) Coalescence of NW-SE striking veins (Set 1) and horizontal veins.

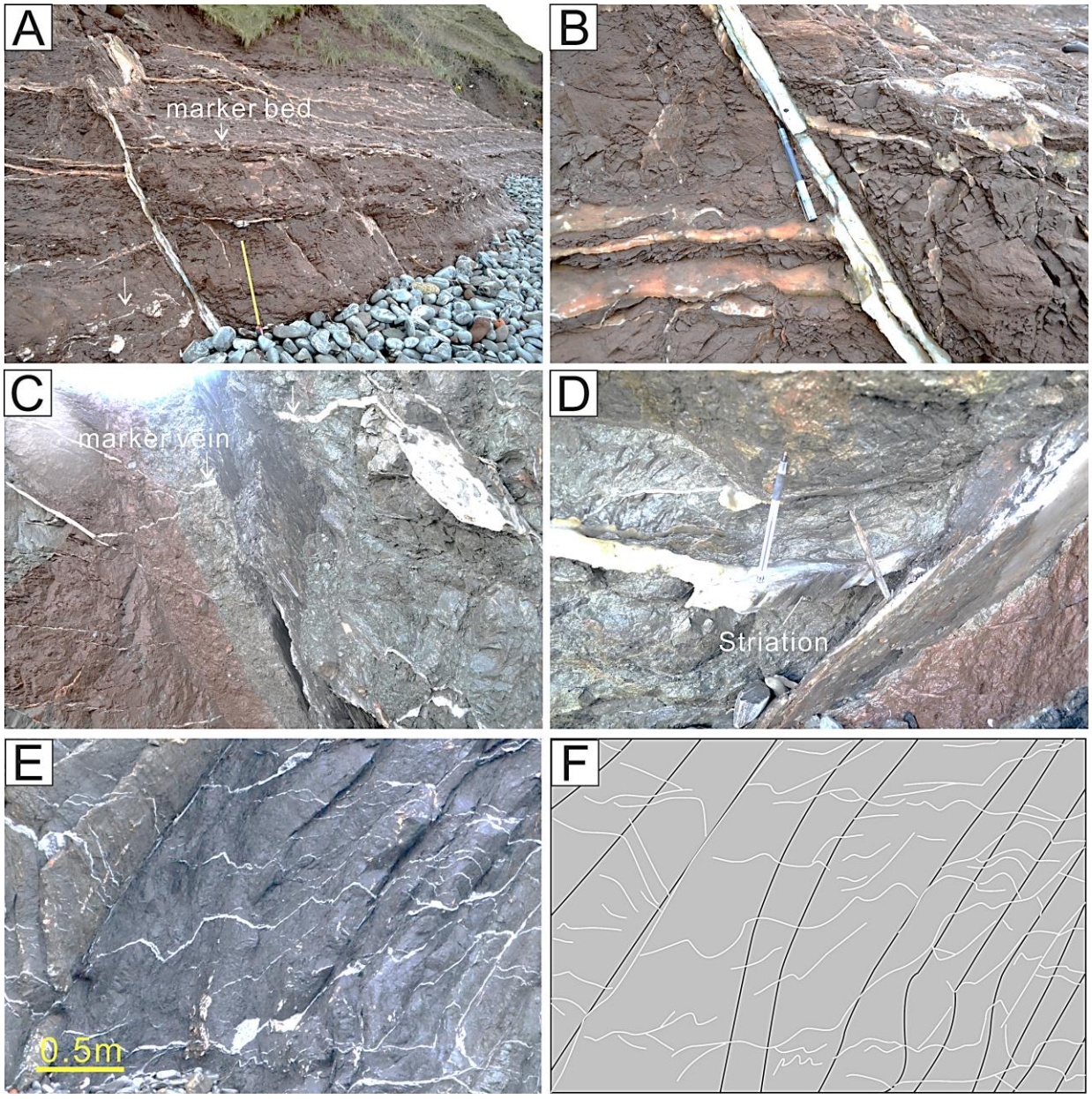


Figure 2.31 (A)-(D) showing horizontal veins cross-cut by a reactivated fault. Note the reverse displacement of the faults using markers of horizontal gypsum veins and nodular horizons. (E) and (F) showing the curved veins cross-cutting the folded beds in the hangingwall of the Hellwell Bay Fault.



Figure 2.32 Photo showing a folded sandstone dyke cross-cut by horizontal gypsum veins (left) and the sketch (right).

2.3.4.2 Branching

The gypsum veins commonly split into two or three branches during propagation (Figure 2.33). The sum of aperture of the branches is approximately the same as the original veins. Either one or none of the branches remains in the original orientation, while the other branches turn away. The branch that shares the same orientation as the parent vein commonly inherits the median zone that is consistent with that in the parent vein. Thus, the bifurcations where the parent veins split are not located in the median zones. The median zones may be straight and persistent in the branched veins, which are not affected by the decrease of vein aperture. The angles between the branches vary from a few degrees up to near ninety degrees.

Branching can occur at different sides of single gypsum veins, which is especially common in the sub-horizontal veins (Figure 2.33B). Branching is interpreted to have occurred during the progressive growth of fibres rather than a post-growth process of vein-splitting. The inclined

branches often coalesce with the adjacent horizontal veins, which significantly contribute to the formation of complex gypsum vein stockworks.

2.3.4.3 Coalescence

Coalescence, instead of cross-cutting occurs when same or differently oriented gypsum veins intersect with each other (see section 2.3.5.1), which can be distinguished from vein branching by the decrease in vein aperture towards the bifurcation point. Sub-horizontal gypsum veins are frequently observed to terminate against the walls of inclined veins (Figure 2.34A-B). Tips of horizontal veins may also curve to follow the direction of inclined veins at the junction where they coalesce. The inclined veins between the horizons of two thick neighbouring horizontal veins are intersected by the wall of horizontal veins (Figure 2.34C), which is evident from the persistent and continuous median zones in the veins. Petrographic patterns of vein coalescence are descried in section 3.4.4. The coalescence of veins gives rise to the backbone of the vein network and also enhances the vein connectivity (Figure 2.34D).

2.3.5 Connectivity

The common interaction and intersection of differently oriented gypsum veins in the Keuper Marl result in a complex vein stockwork with a high connectivity. The inclined branches of horizontal veins and also tension gashes and wing-cracks clearly enhance the vein connectivity by linking horizontal veins in adjacent horizons. Some isolated veins exhibit no linkage to other veins, whose tips pinch out in the hosts as blind tips. The tips of some veins are close to veins in the adjacent areas; however, no visible intersections are observed. Such vein tips are identified as diffusely connected tips.

To quantify the connectivity of the gypsum vein network, the number of blind and diffusively connected tips, and vein-coalescence sites are counted in nine selected sites in Unit 4 (site 1-5) and Unit 4 (site 6-9) (Figure 2.35). The sampling sites are 50cm*50cm sized boxes, containing identifiable gypsum veins in multiple orientations. High resolution digital images were taken for image analysis of vein traces. The results show that the ratio of the population of vein-coalescence ranges from 43.6% to 65.9% (Figure 2.35C), which is significantly higher than that of blind tips and diffusively connected tips. Vein connectivity in Unit 2 is higher than Unit 4, reflected by the larger number of vein coalescences.

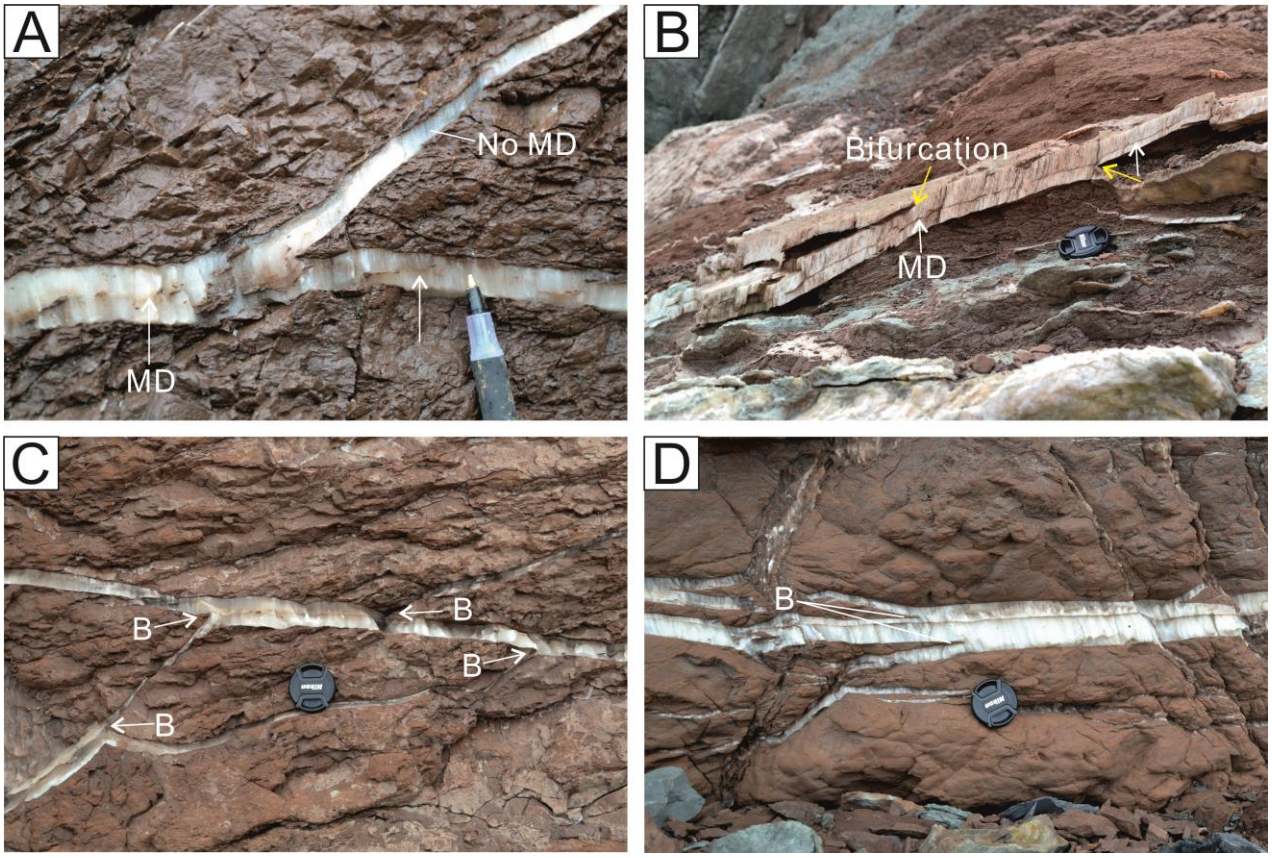


Figure 2.33 Branching of gypsum veins. (A) Branching of a sub-horizontal gypsum vein into two differently oriented veins. (B) Branching of a thick gypsum vein on both the left and right. (C) Branching of a thick horizontal gypsum vein with one branch coalescing with an adjacent vein. (D) A thick horizontal gypsum vein splitting into three branches. Note (1) the median line occuring in the vein that remain in the original orientation of the parent veins; (2) the sum of branches approximately equal to the parent vein. B, branching. MD, median zone.

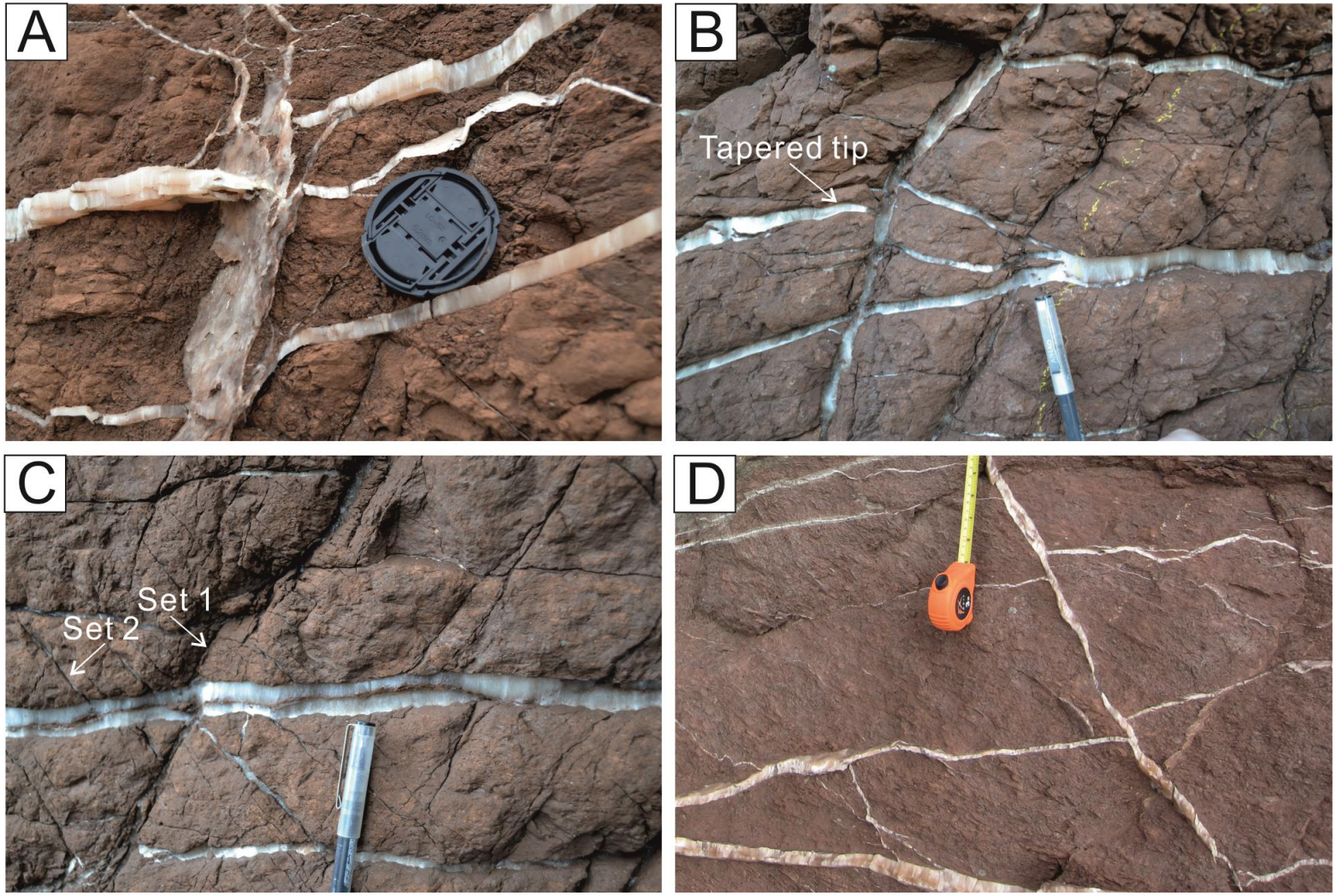
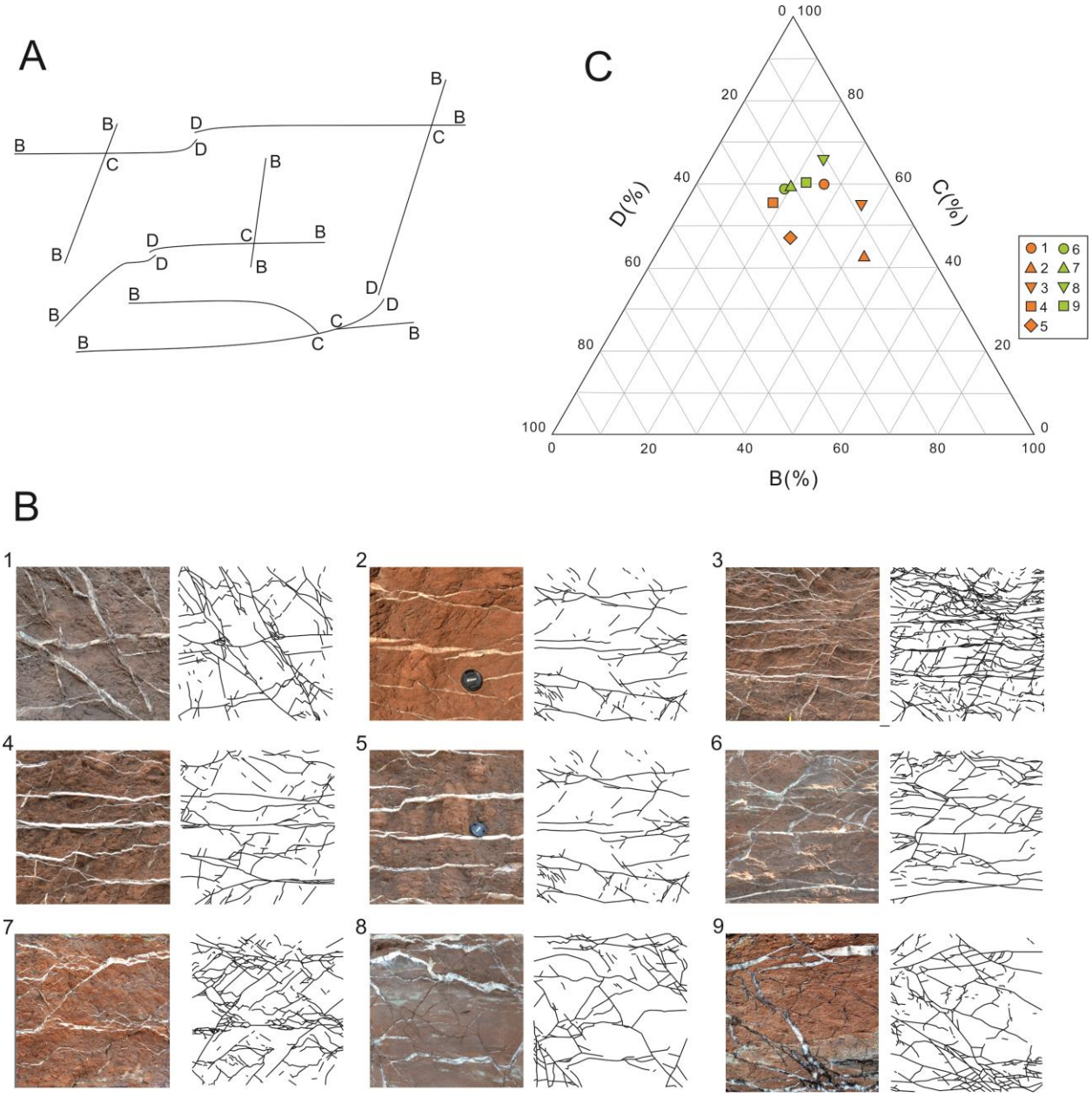


Figure 2.34 Coalescence of horizontal veins and inclined veins. (A) and (B) showing the coalescence of multiple horizontal veins coalescing with a pre-existing sub-vertical vein. Note the tapered tips of the horizontal veins showing their propagation direction. (C) Coalescence of horizontal veins and inclined veins of set 3. (D) Multiple horizontal veins coalescing with a high-angle dipping vein.


A
B
C
D
B
C
D
B
C
D

2.3.6 Aperture

The satin spar fill of the gypsum veins permits a precise measurement of vein aperture. For single veins, only the maximum aperture is measured, which may reveal the complete cementation history. The plot of vein orientation versus aperture shows that vein attitudes do not clearly influence vein aperture (Figure 2.36). However, the average aperture of sub-horizontal veins (dip<30°, n=130) is 4.14mm, much higher than that of the inclined veins, 1.89 mm (n=513). Sub-horizontal veins also exhibit a wide range of maximum aperture from 0.14mm to 22mm. Apertures greater than 10mm do not occur in steep veins (dip>60°).

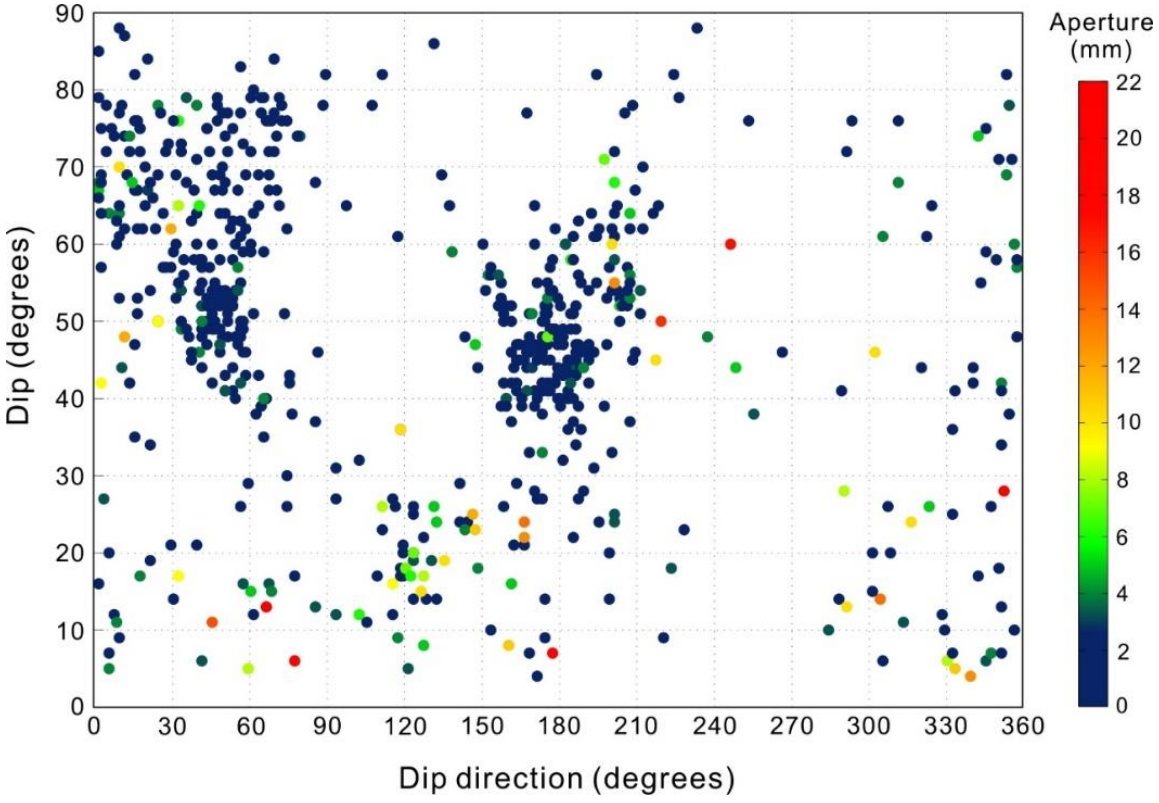
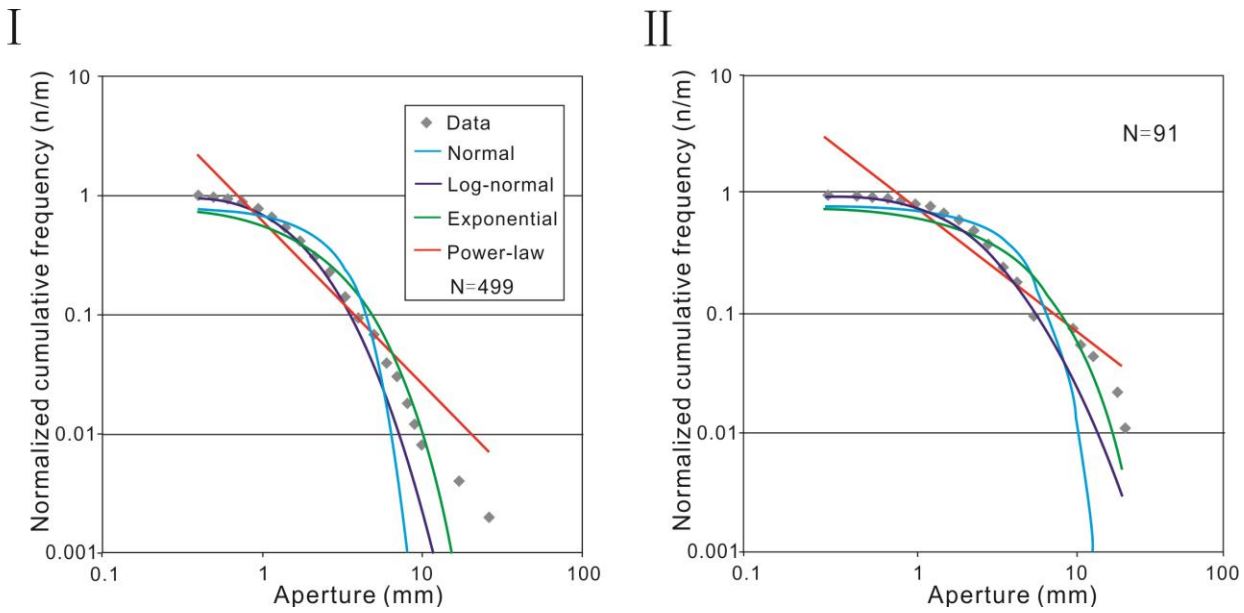


Figure 2.36 Scatter plot of coloured vein-aperture with dip direction and dip. N=643.

A systematic sampling of the vein aperture in a selected area was carried out in seven circular areas, to investigate the aperture distribution. The cumulative frequency of veins versus aperture and the best-fit trendlines are plotted (Figure 2.37). The cumulative frequency is normalized to eliminate the influence of sampling size and comparison of different data sets. A fracture-aperture comparator introduced by Ortega et al. (2006) is used for aperture measurement of thin veins (aperture <1mm). The minimum aperture documented is 0.05 mm. The trendlines of the most common distribution patterns that include power-law, log-normal, normal and exponential distribution are plotted. The chi-square test method is applied to evaluate the goodness of fit of each of each distribution (Table 2.2), where the lowest χ^2 indicates the best fit distribution (Hooker et al., 2013).

The results show that the trendlines are all best fit to a log-normal distribution with the lowest χ^2. The aperture of thick veins (aperture>10mm) are frequently higher than the expected values in the trendlines, i.e. the actual population of thick veins is higher than the value extrapolated from smaller fractures.



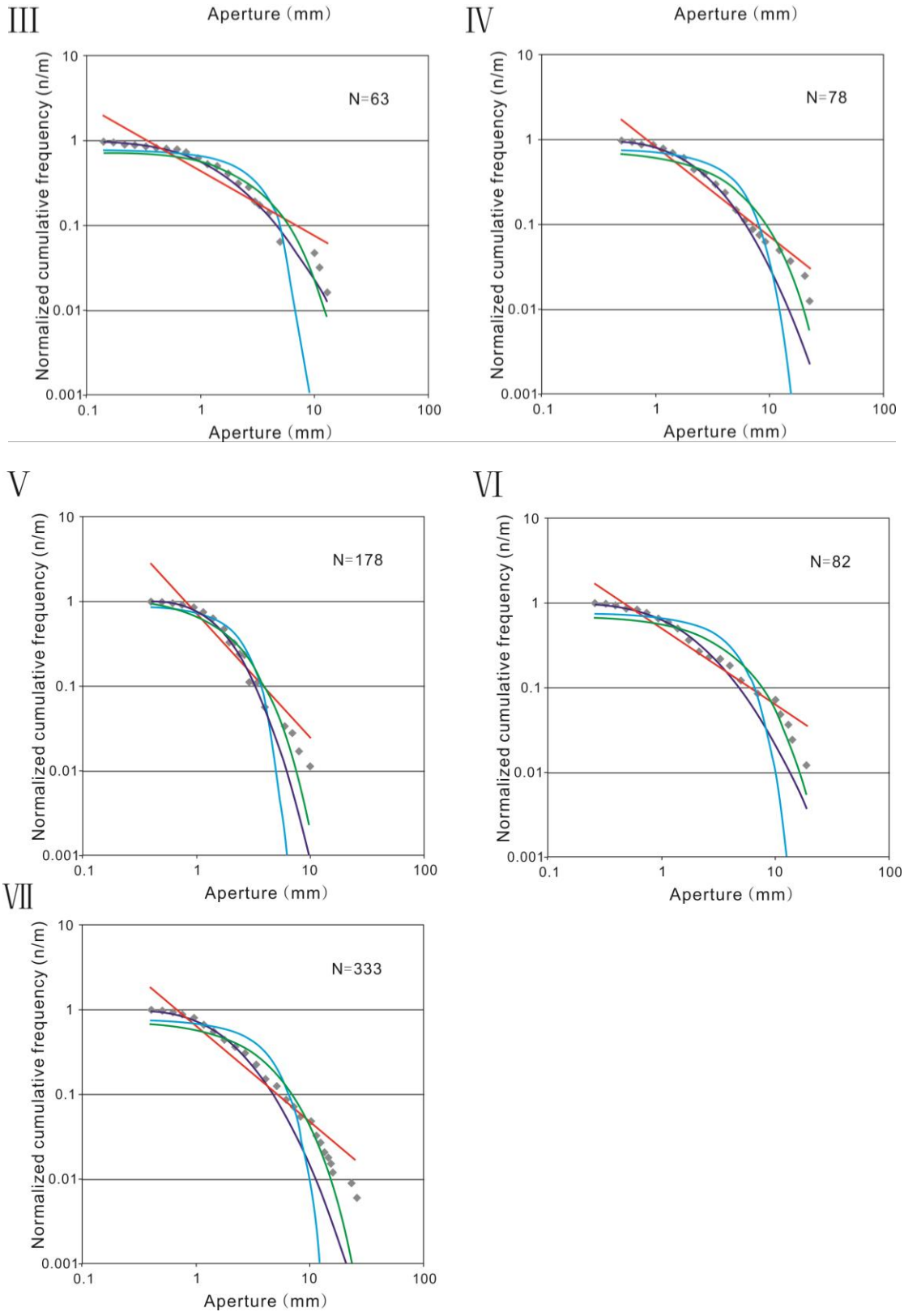


Figure 2.37 Plot of vein aperture versus normalized cumulative frequency.

Table 2.2 Statistics of goodness-of-fit of the distribution of vein aperture.

Outcrop number	Number	Size distribution χ^2 error[a]			
		Power law	Exponential	Normal	Log-normal
I	499	17.444	16.840	1.904E+09	0.295
II	333	7.953	13.798	38149771.86	0.357
III	91	6.128	3.213	673.651	0.359
IV	78	2.155	3.049	509.065	0.609
V	178	10.857	2.752	20602.29	0.931
VI	63	4.058	1.509	94.079	0.462
VII	82	1.889	3.495	373.312	0.806

[a] Lowest χ^2 error value best fit the distribution.

2.3.7 Median zone and host rock inclusions

Most gypsum veins show a thin band of median zone enclosed by upper and lower gypsum fibres (Figure 2.38). The median zone is not strictly within the central part of the gypsum veins, and can be closer to either the upper or the lower vein walls. The median zone is mainly composed of host rock inclusions that exhibit a darker colour than the white fibres (Figure 2.38A-B). The width of the median zone commonly varies in single veins from millimetres up to centimetre scale. Locally, the median zone may contain large lenticular host rock fragments with their long axes sub-parallel to vein walls (Figure 2.38C). The host rock fragments exhibit varied sizes and are commonly thicker than the median zones (Figure 2.38D).

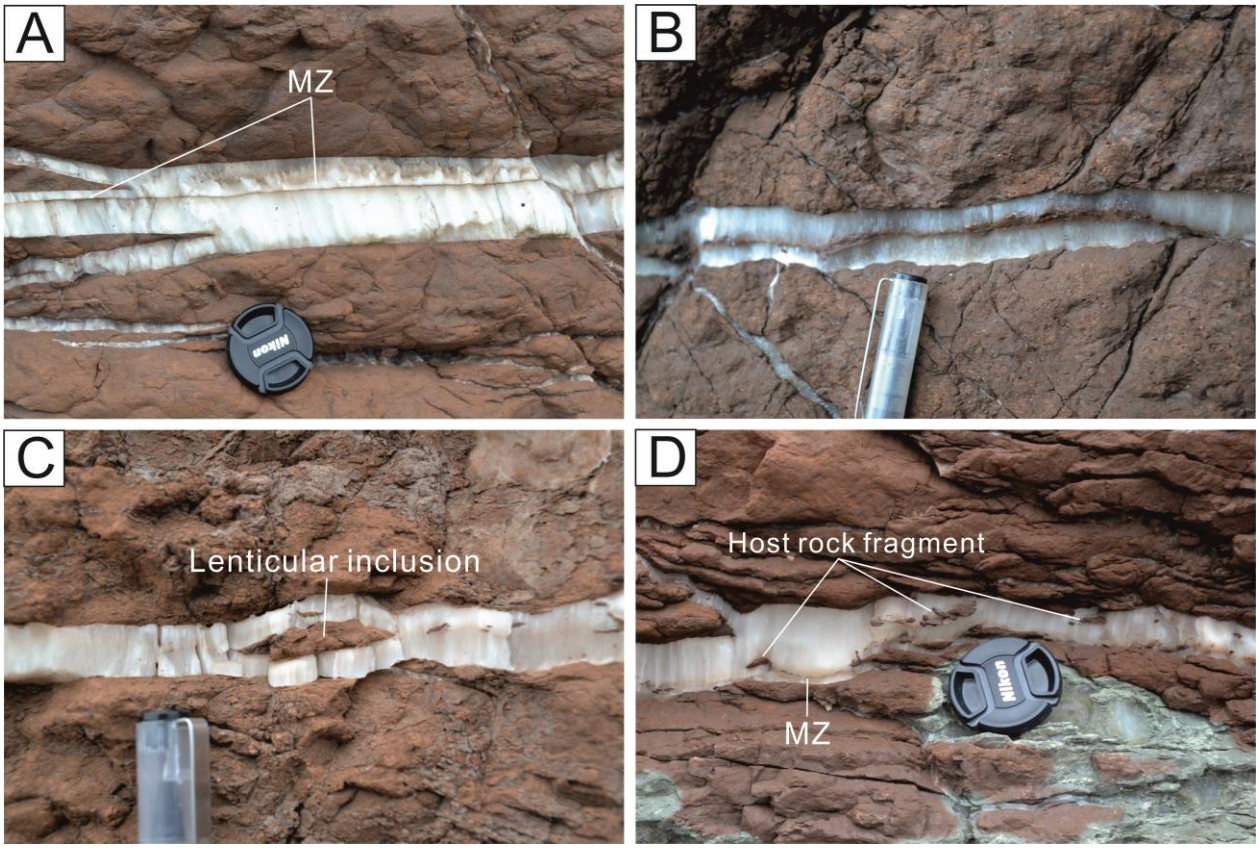


Figure 2.38 Median zones and host rock inclusions in satin spar veins. (A) A consistently horizontal median zone in a thick, branched gypsum vein. (B) A median zone with relative thick host rock inclusion bands. (C) Host rock fragments trapped within the median zone of a gypsum vein. (D) Pieces of host rock fragments enclosed by fibres in a gypsum vein.

The median zones are sub-parallel to vein walls in general; however, they can be rather curvy (Figure 2.39). As the vein width is normally constant, the fibres on different sides of the curvy median zones exhibit asymmetrical geometries. The length of upper and corresponding lower fibres thus show high variations. Locally, frequent fluctuation in the levels of median zones appears, whilst the vein wall geometry receives little influence from the curved median zone.

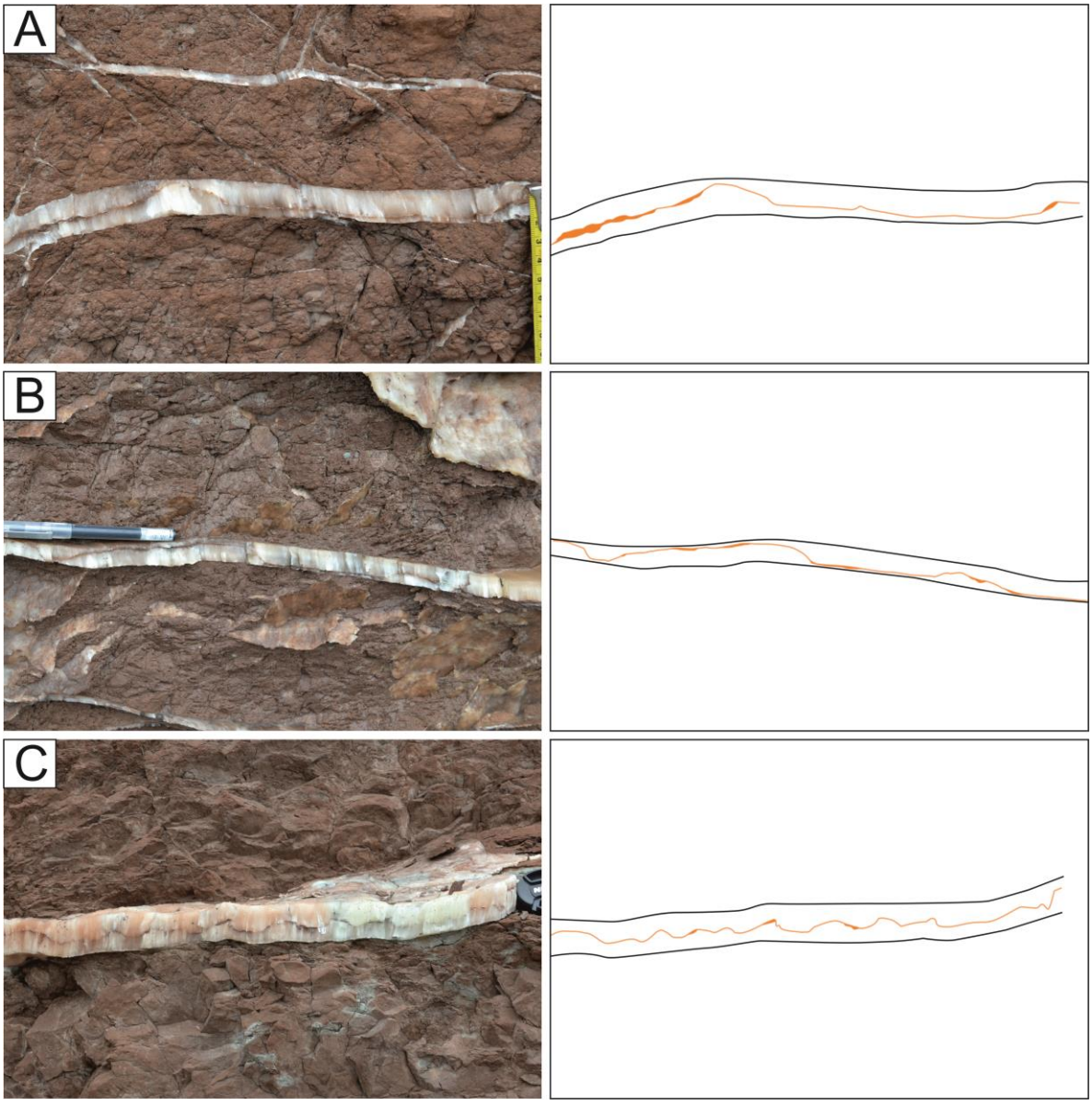


Figure 2.39 Traces of curved median line in single gypsum veins and their sketches in Unit 4 (A-B) and 1 (C).

2.4 Gypsum fibres

2.4.1 Observations

The satin spar veins in the Mercia Mudstone consist of parallel-aligned, needle-like gypsum fibres.

The fibres extend from the median zone to vein walls continuously, and are predominantly oblique

to vein walls. The vein networks that comprise variably oriented gypsum veins display varied fibre orientations (Figure 2.40).

2.4.1.1 Sub-vertical fibres in horizontal veins

Sub-horizontal gypsum veins are the most commonly observed vein set in the red marls, consisting of sub-vertical fibres (Figure 2.41). The angles between gypsum fibres and vein walls are usually greater than 45°. The closely spaced sub-horizontal gypsum veins contain fibres in the same orientations, which is not affected by vein sizes (Figure 2.41B-C). Fibres in curved segments of single wavy veins are parallel to those in the flat segments.

2.4.1.2 Sub-vertical fibres in inclined veins

Some inclined gypsum veins are filled with sub-vertical fibres (Figure 2.42). Such veins commonly occur as inclined segments of horizontal veins that contain sub-vertical fibres. The gypsum fibres in different parts of single curved veins are consistently oriented, regardless of vein-wall curvature and orientation.

A cluster of linked, differently oriented gypsum veins may contain gypsum fibres in the same direction (Figure 2.42E). All fibres are consistently parallel and not affected by vein orientation, size and curvature. The angles between fibres and the contacting vein-walls thus show high variations in differently oriented veins from 1° to 60°.

2.4.1.3 Sub-horizontal fibres in inclined veins

Sub-horizontal gypsum fibres are also observed in inclined veins, especially set 1 veins (Figure 2.43). Due to weathering and erosion of slabs of incline gypsum veins, some of the horizontal

fibres are exposed to the air. The plunges of those fibres are significantly lower than the dips of their host veins. These fibres also show different orientations from those in the adjacent sub-horizontal veins (Figure 2.43A).

Some inclined veins, curving towards larger sub-horizontal veins, contains fibres normal to local walls (Figure 2.43C). Thus, the fibres show gradual decrease in plunges during propagation. The fibres are sub-horizontal where the vein wall is sub-vertical.

2.4.1.4 Fibres in vein branches

Gypsum fibres in different vein branches exhibit different orientations from other branches (Figure 2.44). The branch that shares the same orientation with the parent vein contains the same or similarly oriented gypsum fibres as the parent vein. However, fibres in the other branch are in different orientations from the parent vein. For example, vein *b* in Figure 2.44A contains the same oriented fibres as those in the parent vein *a*, which are left-lateral relative to vein walls. Branch *c* deviates from the original direction of vein *a*, containing fibres at the right-later direction relative to vein walls.

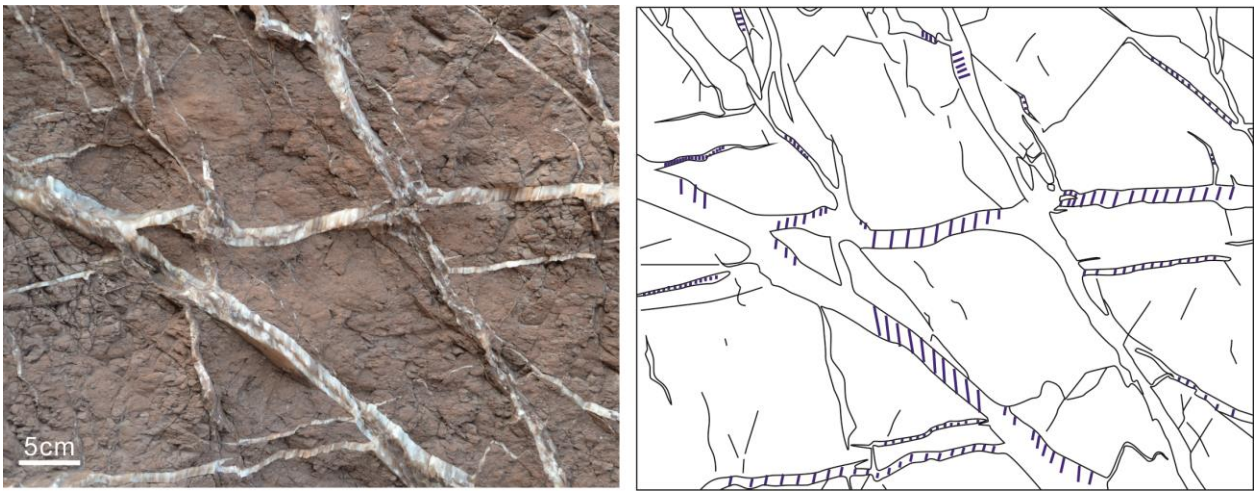


Figure 2.40 A network of satin spar veins with high connectivity. Note the varied fibre orientations.

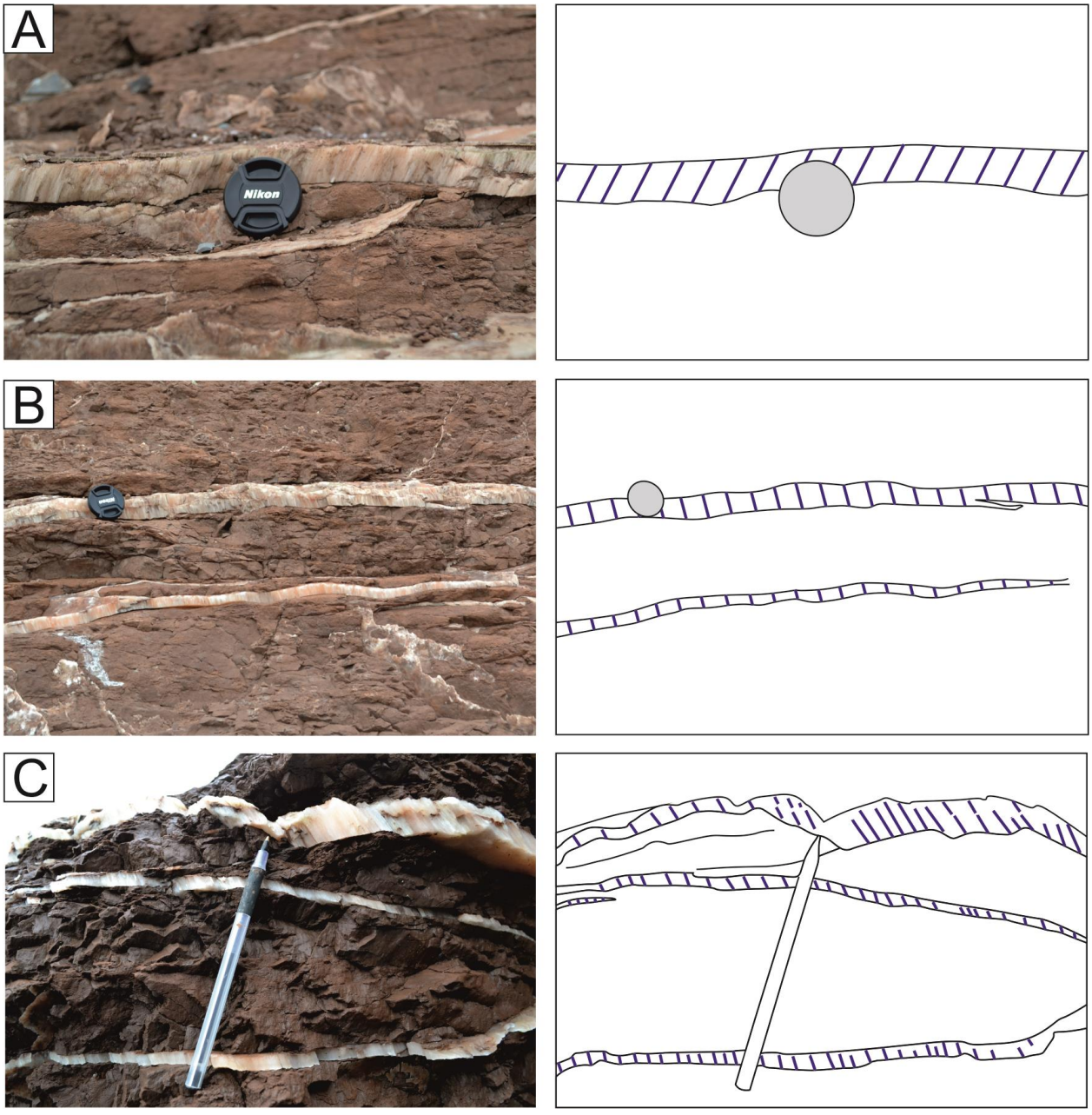


Figure 2.41 Sub-vertical fibres in sub-horizontal gypsum veins. (A) Oblique fibres. (B) and (C) Consistent fibre orientations in adjacent horizontal gypsum veins.

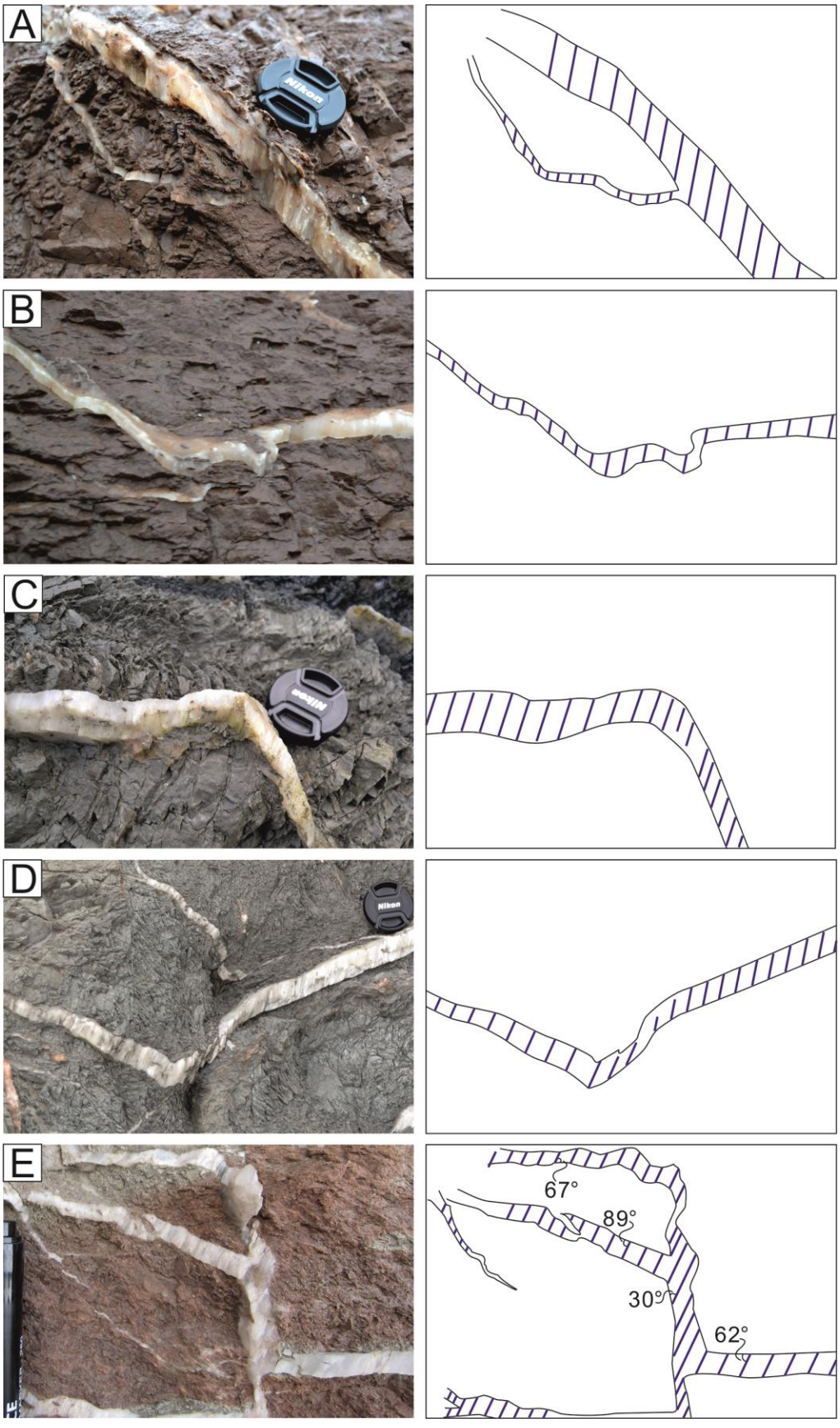

A
B
C
D
E
67°
89°
30°
62°

Figure 2.42 Sub-vertical fibres in inclined gypsum veins. (A) showing the consistent fibre orientation in the inclined vein and its branch. (B) - (D) showing consistent fibre orientations in curved veins. (E) showing consistent fibre orientation in a vein cluster. Note the different angles between fibres and vein-walls.

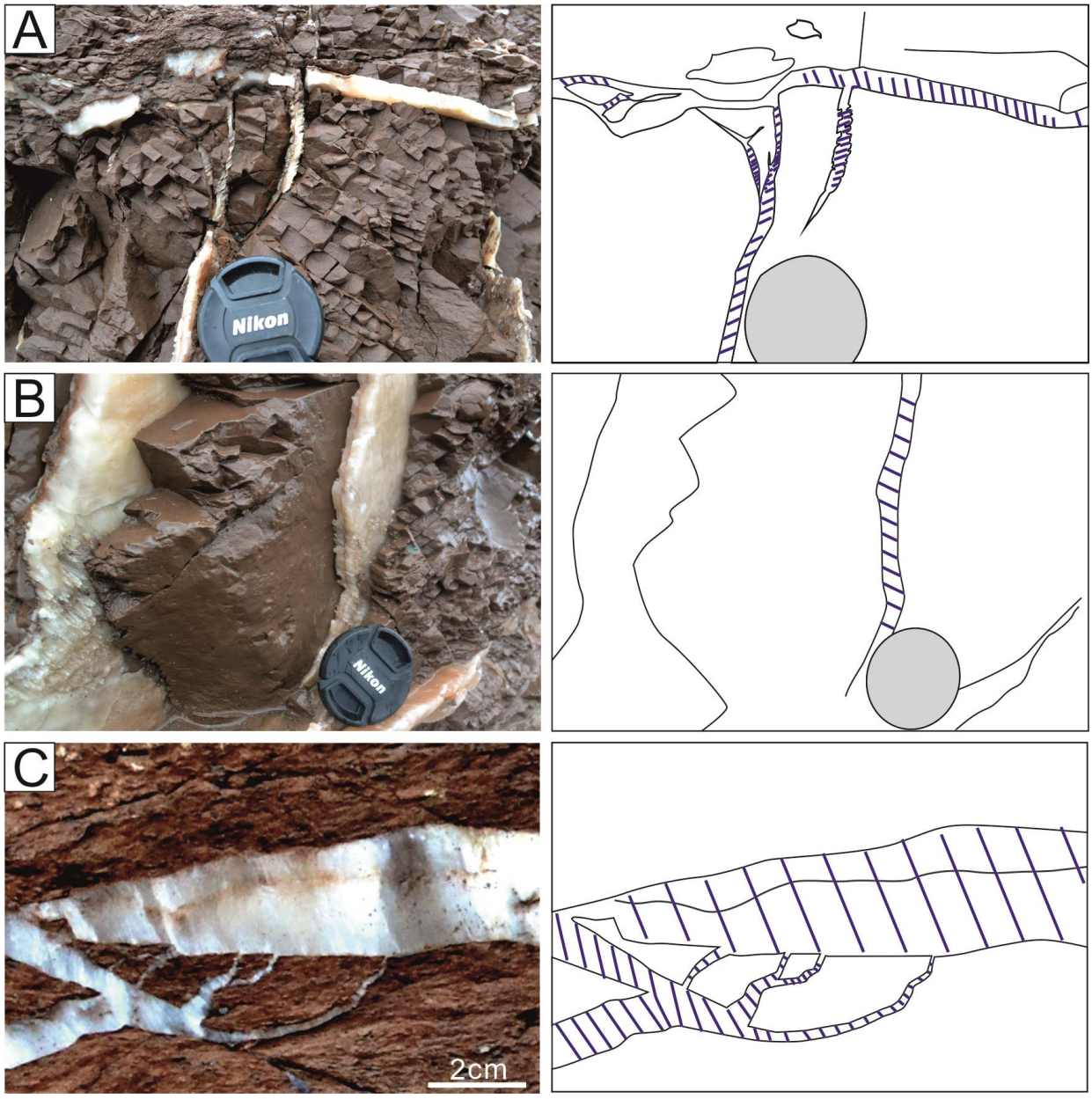


Figure 2.43 (A) and (B) showing sub-horizontal fibres in sub-vertical veins. (C) showing gypsum fibres that remain at an high angle to vein-walls regardless of vein orientation and curvature.

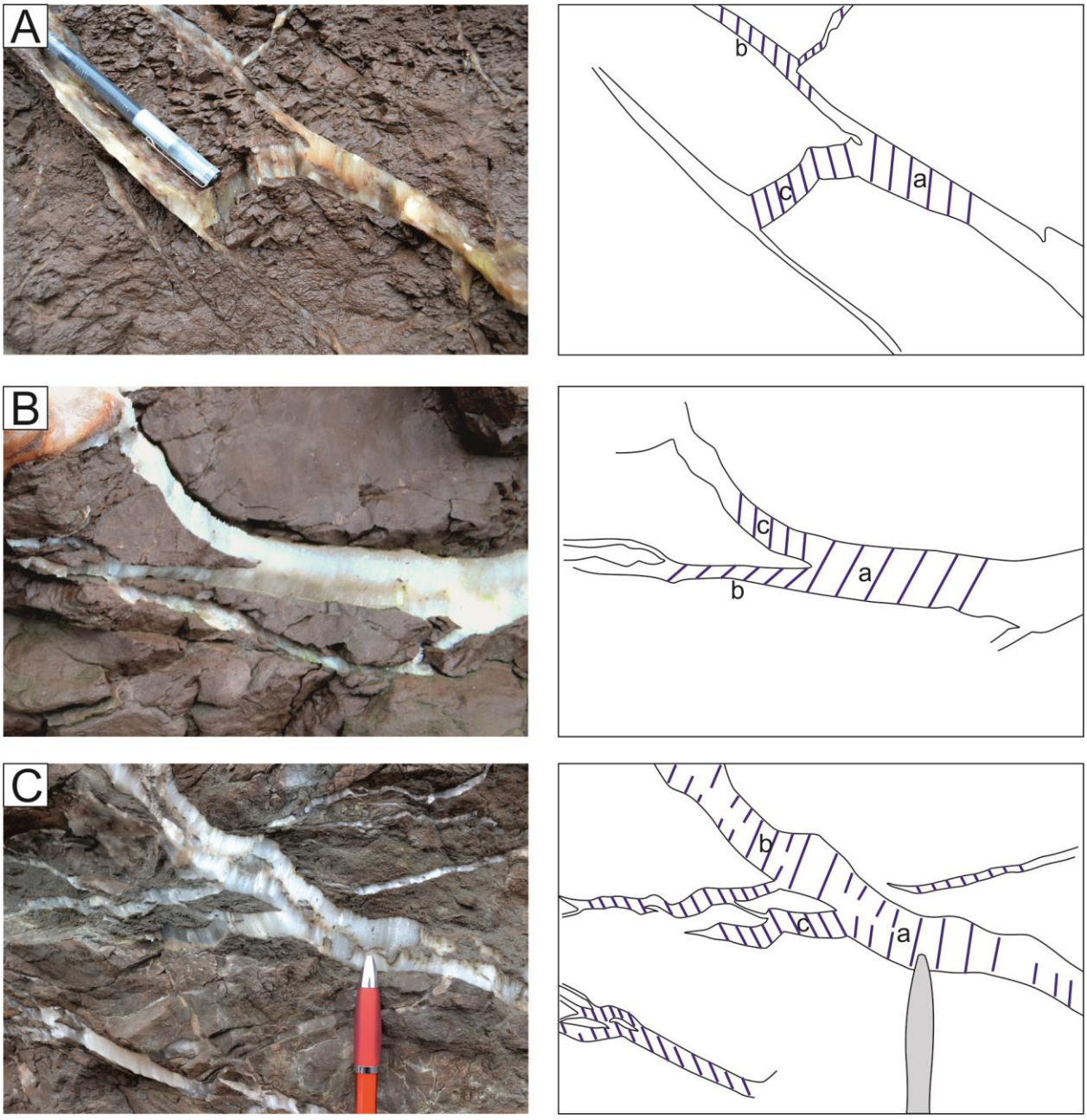


Figure 2.44 Varied fibre orientation in vein branches. See text for detailed description.

2.4.1.5 Curved fibres

Gypsum fibres are predominately linear and straight, however they can exhibit sigmoidal shapes in some persistent, horizontal veins (Figure 2.45). The curved fibres are gently plunged at the median zone, whose plunges gradually become steeper and finally sub-orthogonal to horizontal vein walls. The fibre traces are smoothly curved, whilst the vein walls remain flat and undeformed. The median zones in such veins can also be curvy, giving rise to the asymmetric vein structure.

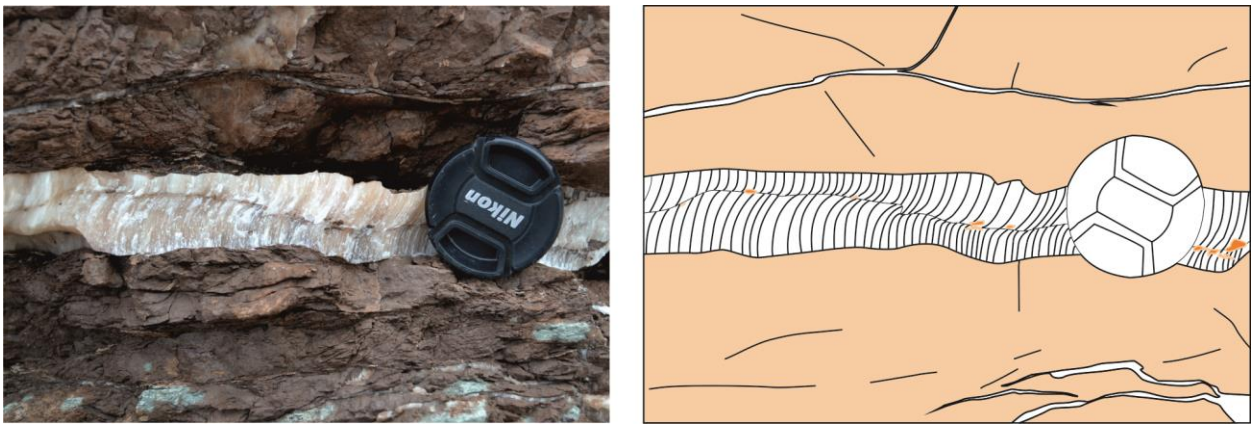


Figure 2.45 Curved fibres with gradually increased angles between fibre and vein-walls from the median zone to the host rocks.

2.4.2 Apparent angle between gypsum fibre and vein wall

As described in section 2.4.1, the gypsum fibres are oblique to vein walls rather than purely orthogonal to walls. 380 apparent angles between gypsum fibres and their contacting vein walls, as well as vein dips, were measured to verify the control of vein-wall direction on fibre direction (Figure 2.46). The vein sections selected for data collection are fresh planes that strike normal to fibre trends. The result shows that 93.9% of the angles are over 50°, while angles between 60°-70° are the most abundant (29.7%). There is no clear correlation between the angles and vein dips.

Plunges of fibres may be either lower or higher than dips of their vein-walls. Greater angles between fibres and vein-walls frequently occur in veins described in section 2.4.1.2, whilst lower angles are observed in sub-horizontal veins and veins described in section 2.4.1.3.

2.4.3 Fibre orientation

Fibre morphologies and orientations are identifiable in horizontal veins in the Mercia Mudstone, especially those with large apertures (>2cm) (Figure 2.16B). However, it is difficult to distinguish fibre boundaries and true orientations in thinner veins at outcrop. Fibre attitudes were measured in forty three thick, sub-horizontal gypsum veins in the Keuper Marl, and seven bedding parallel veins in the Blue Anchor Formation. The fibre orientations are presented in contoured stereonets using small circle count (1% area) method (Figure 2.47). The results show that the maximum density of poles to fibres occurs at 200°/73.7° in the sub-horizontal veins (the Keuper Marl), 200°/74° in the bedding parallel veins (the Blue Anchor). The fibres in the sub-horizontal veins in the red marls and the bedding parallel veins in the interbedded dolomite and marls exhibit similar attitudes.

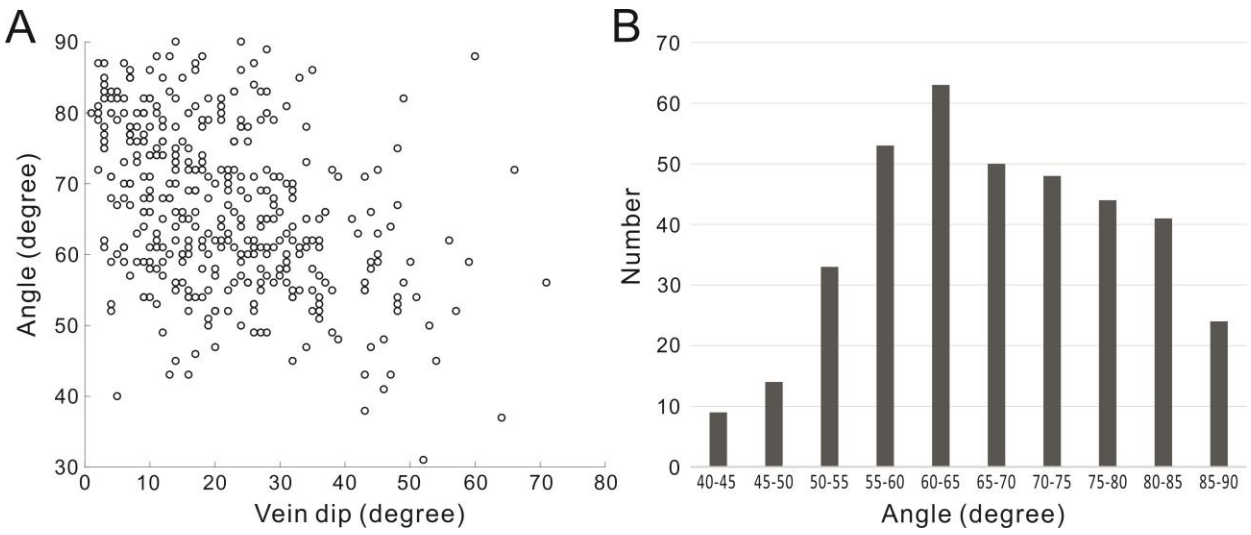


Figure 2.46 (A) Scatter plot of the dip of veins versus the apparent angle between fibre and vein-walls. (B) Histogram showing the distribution of number of angle between fibre and vein-walls.

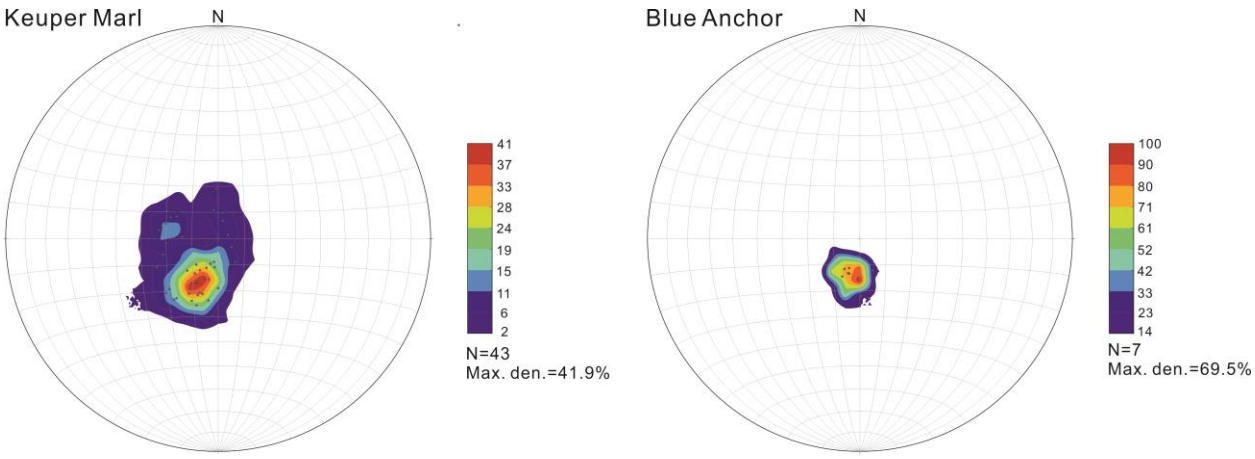


Figure 2.47 Contoured stereonet projection of fibre orientations in sub-horizontal gypsum veins in the Keuper Marl (left) and the Blue Anchor (right). Lower hemisphere.

2.5 Element concentrations

The gypsum veins in the bulk rock and faults along the outcrop exhibit varied colors, patterns and textures. It is necessary to derive the compositional information of different veins and nodules in order to clarify their relationships, vein material sources and also diagenetic fluids. In this study, the inductively coupled plasma mass spectrometry (ICP-MS) technique (Thomas, 2013) is used to determine high quality elemental concentrations in different gypsum vein/nodule samples.

Samples for analysis of chemical constituents of gypsum veins and nodules were collected from different fault veins (sample 1 and 14), nodules (sample 2 and 16) and fibrous veins hosted by red marls (sample 7, 15 and 19) (Figure 2.48). The samples show varied colors, textures and host locations, permitting a representative and comparative study. Sample 2 and 15 are reddish/red.

Sample 16 is greenish/white. Other samples show a white color. Sample 16 was collected from Unit 3, and others from Unit 4. Multiple samples were drilled in single gypsum veins (nine from sample 7, five from sample 15 and three from sample 19) from centre to margin, which allows a study of cement sequence and changes in diagenetic conditions.

The samples were dissolved in a mixture of hydrochloric, nitric, and hydrofluoric acids, followed by diluting them in 2% nitric acid for measurement on the Elan quadrupole ICP-MS at the department of Earth Sciences, University of Oxford. The measurement has a high precision to ±<0.01%.

The nodular gypsum, fault veins and satin spar veins hosted by red marls show rather similar and pure chemical constitutes of calcium sulphate, containing one major cation, Ca^{2+} (Figure 2.49). Numerous other cations occur in trace amounts. The most abundant elements include manganese, aluminum, sodium, silicon, manganese, titanium and iron.

Mg abundance is high in chlorite, smectite clay minerals (Harder, 1972) and dolomites. Al is the second most abundant chemical constituent for mudstones. The content of Al is particularly high in feldspar, micas and clay minerals (Boggs, 2009). Na abundance is related to both clay minerals (e.g. smectites and illite) and the content of albite. Si is the most abundant chemical constituent in mudstones, which is most strongly affected by the presence of quartz. Ti is contained in some clay minerals and heavy minerals (e.g. ilmenite, rutile, brookite and anatase) (Sterte, 1986). Mn occurs mainly as a substitute for iron in iron oxide minerals, although minor amounts of manganese oxide may occur (Loganathan and Burau, 1973).

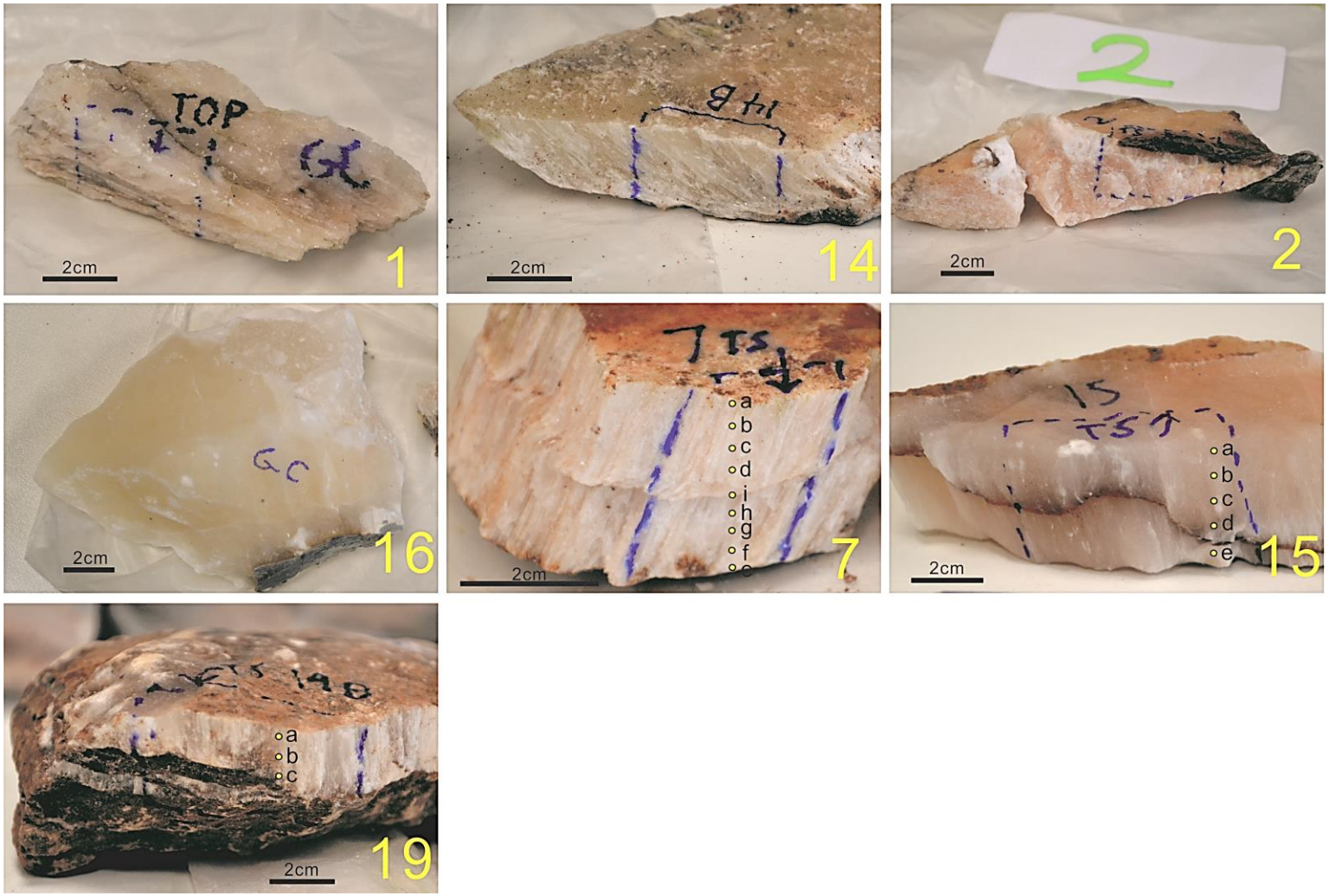


Figure 2.48 Sample photos showing the texture and color of the gypsum veins and nodules. Yellow dots show the drilling localities in single veins. See location of samples in figure 2.14.

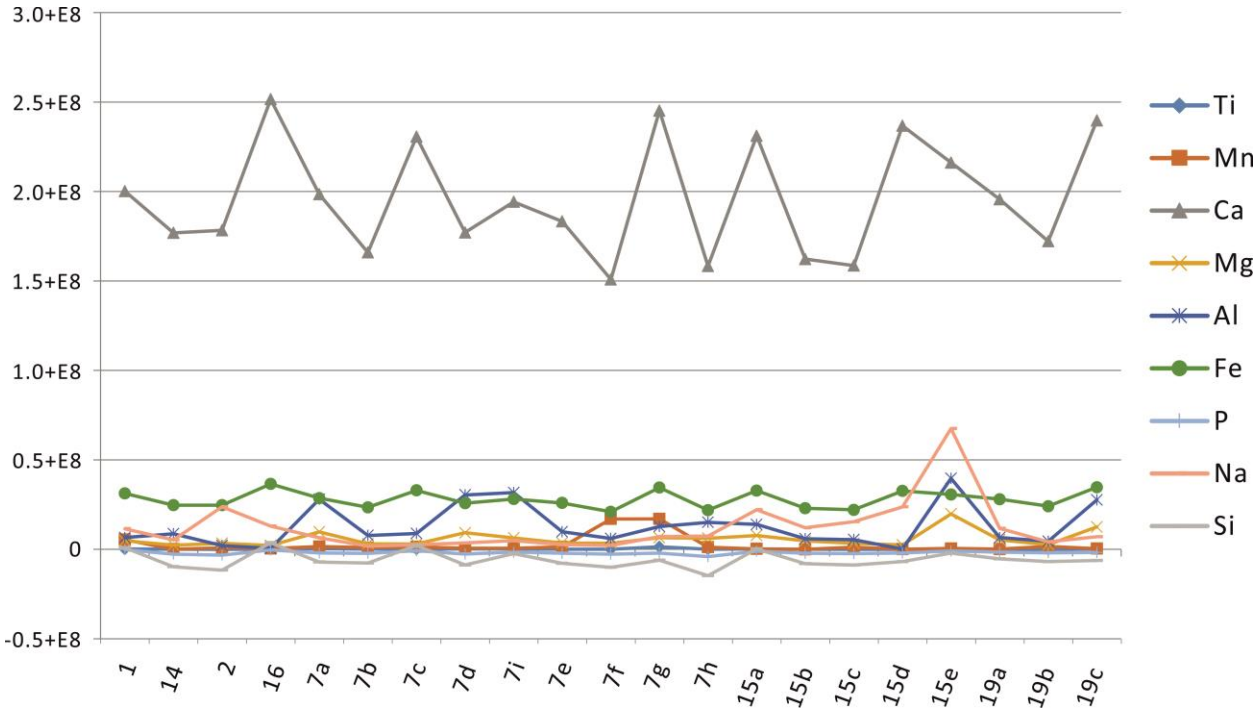


Figure 2.49 Chemical constitutes of gypsum nodules, faults veins and fibrous veins. The concentrations of elements is present in parts per billion (ppb).

Sample 15e contains the most abundant Al, Mg and Na (Figure 2.50), which is possibly caused by the occurrence of impurities of clay minerals and albite. Sample 7, especially 7a, 7d and 7i, are more abundant in Al and Si but less Na than other samples, indicating that the anomalies are mainly results of clay minerals. Sample 7f and 7g both contain much higher Mn than others. 7g also contain the most abundant Ti. The occurrence of high Mn and Ti may suggest inclusions of clay or heavy minerals in fibres close to vein lower margins of sample 7.

Iron is the most common constituent of many minerals, occurring both in the ferrous (Fe^{2+}) and ferric (Fe^{3+}) states (Boggs, 2009). Ferrous iron is important in chlorite, biotites, carbonates and sulfides (pyrite and marcasite). It may also occur in minor quantities in some silicate minerals, e.g. feldspar. Ferric iron is the most abundant in the iron-oxide minerals, including hematite, goethite and lepidochrocite. Ferric iron is also important for many heavy minerals such as magnetite. The

color of mudstones appears to be a function of the carbon content and the oxidation state of iron (McBride, 1974). The progression of colors from greenish grey to red through purple correlates with the increasing ratios of Fe^{3+}/Fe^{2+}, where Fe^{3+} iron gives red colors, Fe^{2+} iron gives green colors. The color of mudstones is associated with depositional environment in a general way. Red mudstones normally form in shallow-water, estuarine environments, and the muds are in contact with oxidizing bottom waters for a long period of time (Calvert and Pedersen, 1993). However, the color of mudstones is not a reliable indicator for depositional conditions as it can change during diagenesis and uplift if the sediments are brought into a different chemical environment. Green colors can be changed to red if the initial conditions are followed by oxidizing conditions, while red colors can be changed to green if ferric iron is reduced to ferrous iron during diagenesis (Grim, 1951).

Iron abundance in all samples shows minor fluctuations. All samples contains similar content of iron, which is not affected by their colors. Vein 15, which is reddish/red, contain similar amounts of iron to other white samples such as nodule 16 and vein 7. The red color is possibly caused by the concentration of Fe^{3+}. Accordingly, vein 15 has the highest content of Na, which possibly indicates a drier environment and a high-salinity pore water during the formation of red veins.

Single veins do not reveal significant variations in chemical constitutes (especially iron) from the median zone to margins, except those containing impurities of clay minerals and feldspars between fibres. This suggests a uniform environment and fluid condition during vein vertical accretion.

In summary, the gysum nodules, veins in the marls and faults all contain rather pure calcium sulphate. The anomalies in chemical abundance is likely to be caused by the solid inclusions of clay minerals, feldspar or heavy minerals. The iron content is similar in all samples, which is not

associated with their colors. Samples in reddish/red colors contains more Fe^{3+} and Na^{+}, and possibly formed in drier conditions and high-salinity pore waters. White/greenish samples contain more Fe^{2+}.

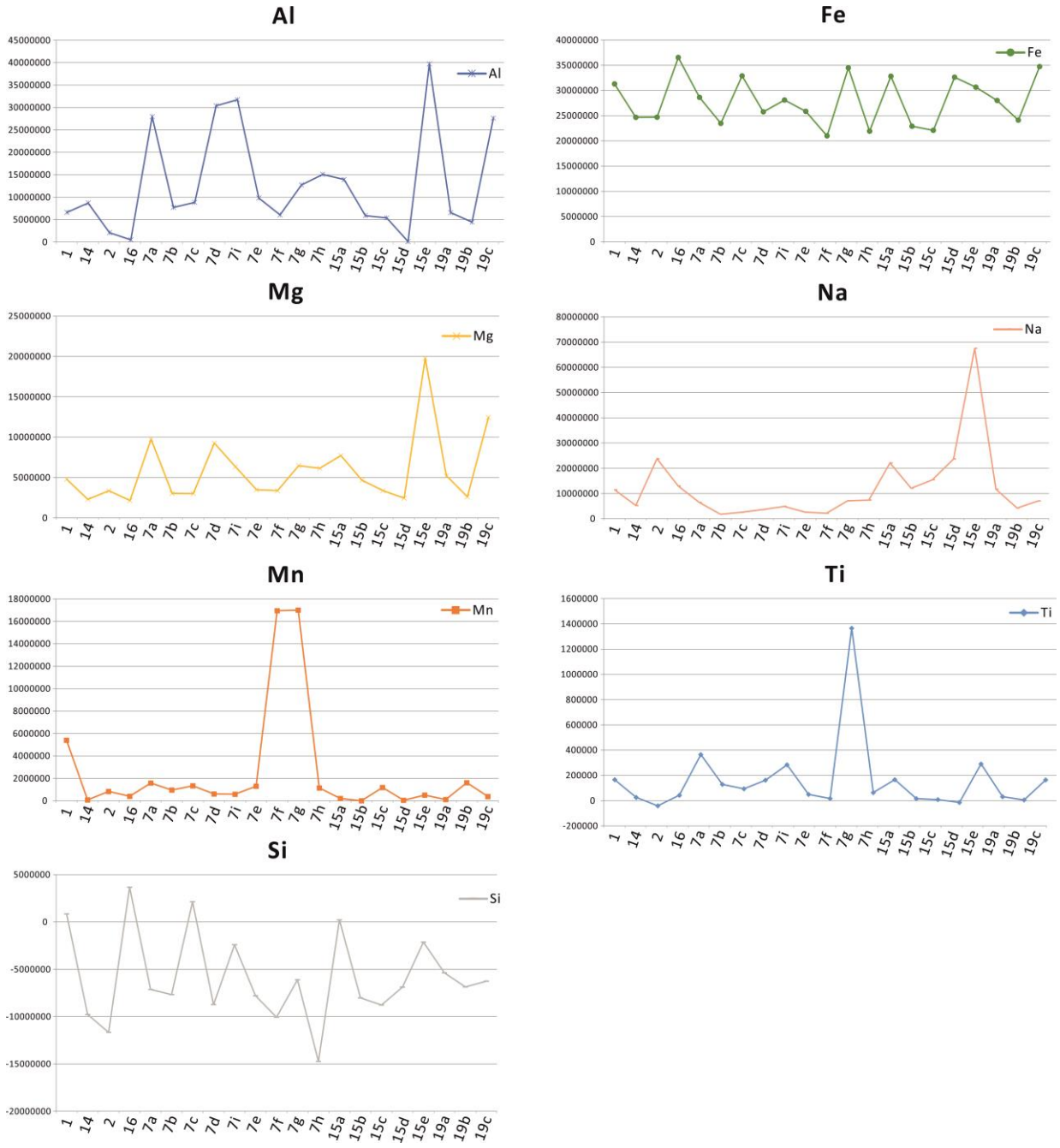


Figure 2.50 Plot of chemical concentrations of Al, Fe, Mg, Na, Mn, Ti and Si in gypsum nodules, faults veins and fibrous veins. The concentrations of elements is present in parts per billion.

2.6 Discussion

2.6.1 Timing of vein generation

Subsurface gypsum readily dehydrates and converts to anhydrite when the ambient temperature rises up to 50-60℃ (Testa and Lugli, 2000). The depth of mineral transformation depends on the geothermal gradient, lithostatic pressure and pore brine salinity, normally ranging from a few meters to a kilometre (Nichols, 2009). Hence, the genesis of satin spar veins presumably occurs at a relative shallow depth and a low ambient temperature. Coupled with the subsidence curve of the Mercia Mudstone Group in the Bristol Channel Basin, the development of gypsum veins is constrained to be during the last uplift stage of the basin evolution (Figure 2.51). It is interpreted that when the evaporite beds entered the telogenetic zone and came into contact with the low salinity waters, hydration of anhydrite to diagenetic regenerated gypsum occurred. The dissolution and redistribution of evaporite by meteoric flushing could lead to gypsum precipitation in pore spaces, cavities and fractures in adjacent non-evaporite beds. The gypsum veins were then filled with satin spar gypsum that can be considered as one of the indicators for basin uplift.

The reactivation of the Hellwell Bay Fault and two other faults are evident from their reverse displacement and gypsum-filled fault veins (Figure 2.27). Those fault veins contain slickenslide fibres on vein planes and cross-cut sub-horizontal veins in the bulk rock, indicating a multiple slip activities (≥ 2), which could even postdate the development of the gypsum veins in the marls.

Importantly, the numerous sub-horizontal gypsum veins that cross-cut the folded layers in the Blue Anchor Formation are unlikely to have formed as fold-related fractures. The wavy geometry of

those veins are not caused by folding after primary formation as the fibres in single veins exhibit consistent orientations (Figures 2.38C-D).

The homogeneous chemical composition of gypsum veins in different colors and the unclear cross-cutting relationships make it difficult to identify the phases of fracturing in the red Keuper Marl. However, the white bedding-parallel veins cross-cutting red high-angle veins in the Blue Anchor Formation indicates a minimum of two phases in the formation process. The E-W striking red veins in grey/dark marls possibly formed as tension gashes during flexural slip folding of the layers by the N-S compressional stress (Figure 2.52). The shear strain was accommodated by fracture dilation and rotation as slip along layer interfaces continued. Such a flexural slip resulted in the sigmoidal shapes of the fractures, which were later filled with gypsum fibres.

Given the cross-cutting relationships between gypsum veins and other structures, and the timing of basin uplift and inversion from Lower Cretaceous to Tertiary (Dart et al., 1995), fault reactivation and buttress folding from late Oligocene to Miocene (Glen et al., 2005; Engelder and Peacock, 2001) as constraints, it is suggested that the gypsum veins formed during the Miocene (Figure 2.53).

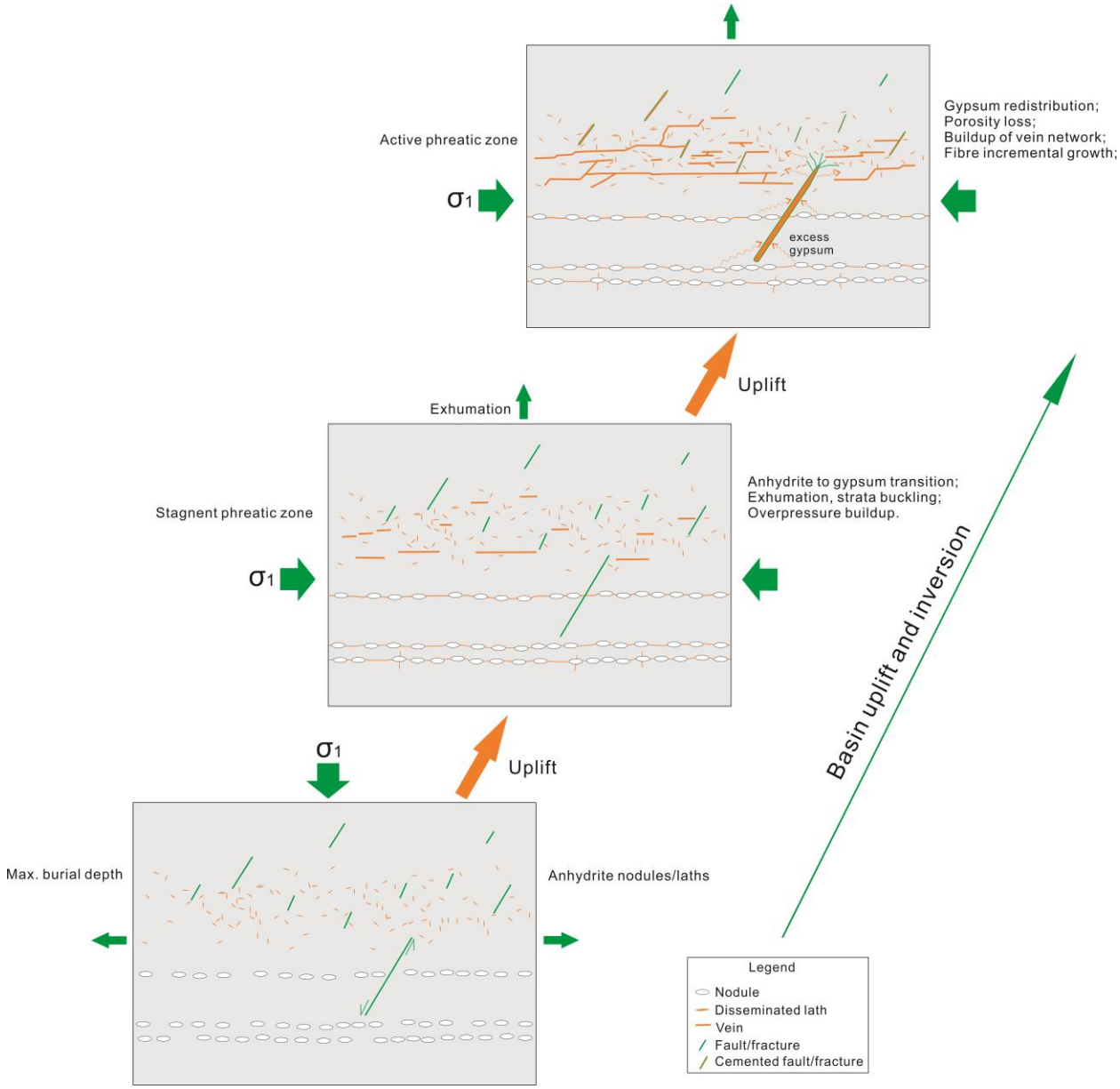


Figure 2.51 Simplified cartoon illustrating the process of gypsum vein network formation during basin uplift.

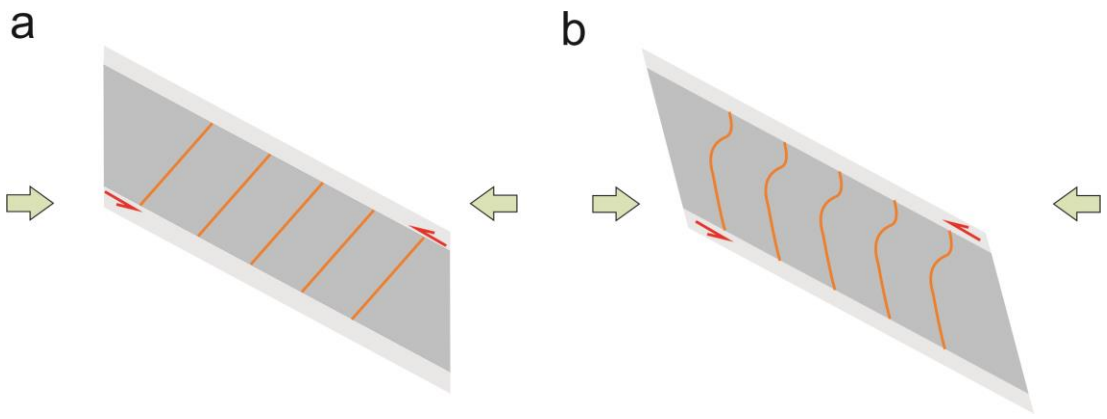


Figure 2.52 Cartoon illustrating the formation process of the sigmoidal fractures (shown in figures 2.24A-B) in the Blue Anchor Formation. Note that cementation of the fractures postdate the fracture generation.

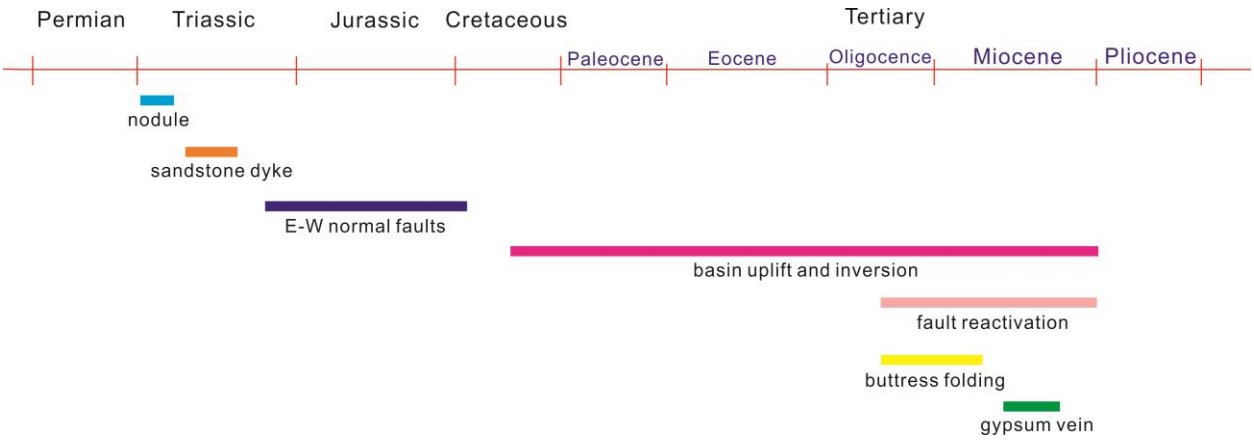


Figure 2.53 Consequences of major geological events in the study area and the approximate timing.

2.6.2 Mechanics of fracturing

The BCB was subjected to intense N-S basin compression during basin inversion, which is evident from widespread rock deformation in the Watchet area and other adjacent areas (Glen et al., 2005; Van Hoorn, 1987). At depth of several hundred meters, all total stresses are compressive. The formation of tension fractures relies on the fluid pressure to push aside the wall rocks against the

total rock pressure (Mandl, 2005). In addition, the formation of gypsum veins requires the precipitation of gypsum from sulphate-rich fluids. Thus, the paleofluids and fluid pressure have been significantly involved in vein generation and responsible for fracturing in some way.

The hydraulic fractures occur when the Mohr circle touches the failure envelope. The size of Mohr circle is controlled by effective stress $\bar{\sigma}$, i.e. the difference between remote stress and fluid pressure:

$$\bar{\sigma} = \sigma - p_f$$

In three dimensions, the effective stress is expressed as:

$$\begin{bmatrix} \bar{\sigma}_{11} & \bar{\sigma}_{12} & \bar{\sigma}_{13} \\ \bar{\sigma}_{21} & \bar{\sigma}_{22} & \bar{\sigma}_{23} \\ \bar{\sigma}_{31} & \bar{\sigma}_{32} & \bar{\sigma}_{33} \end{bmatrix} = \begin{bmatrix} \sigma_{11} - p_f & \sigma_{12} & \sigma_{13} \\ \sigma_{21} & \sigma_{22} - p_f & \sigma_{23} \\ \sigma_{31} & \sigma_{32} & \sigma_{33} - p_f \end{bmatrix}$$

The newly-formed bedding parallel gypsum veins are widespread in multiple horizons in the Mercia Mudstone as the predominant vein set. The initiation of these veins appears to be associated with Tertiary basin exhumation and sediment unloading. Previous work suggests that the BCB underwent at least 1 km of exhumation (Cornford, 1986; Holford et al., 2005a; Menpes and Hillis, 1995). The decrease of overburden possibly contributed to a vertical expansion and the fracture opening horizontally. The fluid pressure responsible for the horizontal fracturing is expressed as:

$$p_f > \sigma_v + s$$

Where σ_v is the overburden; *s* is the tensile strength of the host rock. The hydraulic fractures could take advantage of bedding parallel weak planes, including bedding fissures and bedding planes

(Shearman et al., 1972). The persistent bedding-parallel gypsum veins developed at the boundaries of different lithological units where *s* is the lowest particularly favour this explanation.

The build-up of overpressure in the Mercia Mudstone is likely to have resulted from tectonic compression during basin inversion (Cosgrove, 2001). The extremely low bulk permeability of the marls (commonly 10nD) (Seedhouse and Racey, 1997) does not permit fluid to expel fast enough, which gave rise to a pervasive increase in pore pressure Δp (Figure 2.54). Given the non-uniform vein geometries and the tension mode of veins, a low differential effective stress can also be inferred.

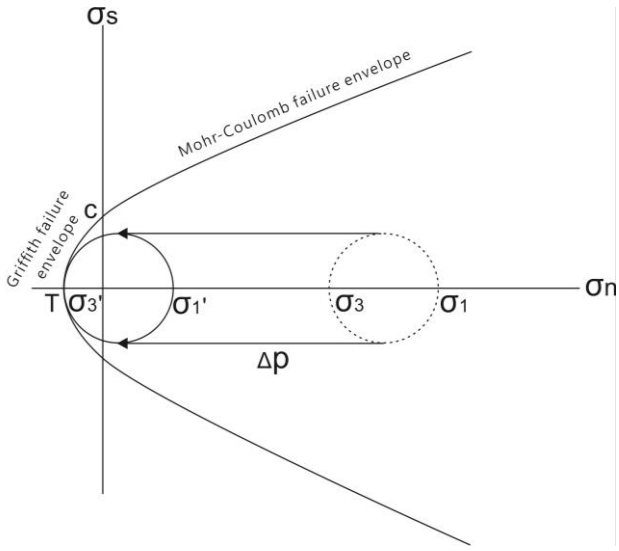


Figure 2.54 Mohr circular illustrating mechanics of overpressure for the generation of tension mode veins.

In summary, a combination of tectonic compression, overpressure and sediment unloading resulted in the newly-formed fractures, especially the sub-horizontal veins, in the Mercia Mudstone. The

associated textures in those veins that formed during this stage are summarized and discussed in section 3.8.1.

2.6.3 Reactivation of pre-existing faults/fractures

The inclined veins, including parts of set 2 and set 3, exhibit rather regular and systematic patterns, and are interpreted to have occurred under the influence of local major faults. Although some of the inclined fractures may have formed prior to the basin inversion as pre-existing tectonic fractures, it is difficult to distinguish those fractures from newly-formed veins during basin inversion.

Similar to reactivated normal faults, the pre-existing tectonic fractures were reactivated during basin inversion, when the critical value of coefficient of sliding friction μ_f is achieved. Given a cohesive strength of a pre-existing fracture is C_f, μ_f is expressed as

$$\mu_f = \frac{\sigma_s - C_f}{\sigma_n}$$

The magnitude of C_f is usually low and can be reduced significantly when fluid is injected to the fractures (Figure 2.50). Fracture opening and sliding then occur at shallow burial depth when the σ_s reaches the critical value. Thus, the cementation of such veins occurs in a passive mode as a result of hydrologically driven and mineral dissolution-precipitation processes.

In contrast with pre-existing fractures, the newly-formed fractures could have resulted from simultaneous fluid injection, vein opening and gypsum precipitation in an active mode. Fluid overpressure is responsible for pushing aside crack-walls for propagation of those fractures. Linkage of pre-existing and newly-formed fractures is enabled through mobile hydrofracturing

(Bons, 2001). The pre-existing fractures were reactivated as pathways for fluid migration, which were passively dilated by fluid pressure. This could explain the absence of cross-cutting relationships between differently oriented veins, especially those as vein steps linking horizontal veins at different levels.

2.6.4 Vein interaction

The inclined veins, except those described in section 2.5.3, contain gently plunged fibres in contrast to the sub-horizontal veins (Figures 2.39A-B). Because the fibre direction is argued to follow the opening trajectory of vein walls (see chapter 3, section3.8.3), the fibres suggest a normal displacement of the vein walls. Likewise, the fibres that exhibit a higher plunge than the dip of their host veins suggest a sense of displacement to be reverse. Such inclined veins are normally rooted in the sub-horizontal veins, with the greatest aperture at the bifurcation site and pinching out in the host rock. Those veins are interpreted to form as tension gashes or wing cracks as mode II fractures during propagation of horizontal fractures. Tensile stress may be concentrated at tips of horizontal fractures that underwent shearing, resulting in opening of tension fractures along horizontal fractures (Figure 2.55). This explains the non-cross-cutting relationships between the tension gashes (wing-cracks) and sub-horizontal veins. Unlike the pre-existing fractures, the formation of such inclined fractures occurred in an active mode. Their initiation and growth are accommodated by sliding along the horizontal fractures.

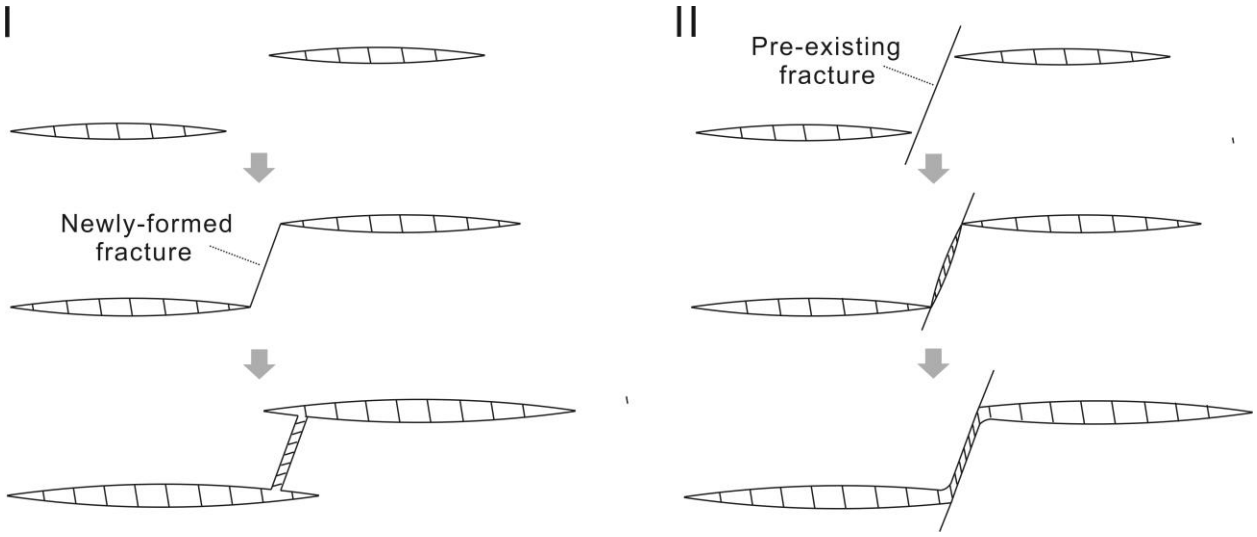


Figure 2.55 Cartoon illustrating the formation of inclined veins with sub-horizontal fibres (I) and sub-vertical fibres (II). Inclined veins in figure I are newly-formed tension fractures, whilst those in figure II are pre-existing fractures.

Other active veins include those curving towards older veins (section 2.3.3.3). Local stress perturbation may occur around tensile gypsum veins. When the elastic strain fields around two veins overlap, the newer vein may be interfered by the local stress field and adjust its orientation towards the direction of local maximum principle stress $\sigma 1$. Local $\sigma 1$ is normal to walls of the older vein as it continues opening and growth. Gypsum fibres in such curved veins are consistently sub-orthogonal to their host veins, recording the progressive opening process. Tips of sub-horizontal veins curving towards neighbouring veins and coalescing with them lead to the formation of more persistent veins (Figure 2.56).

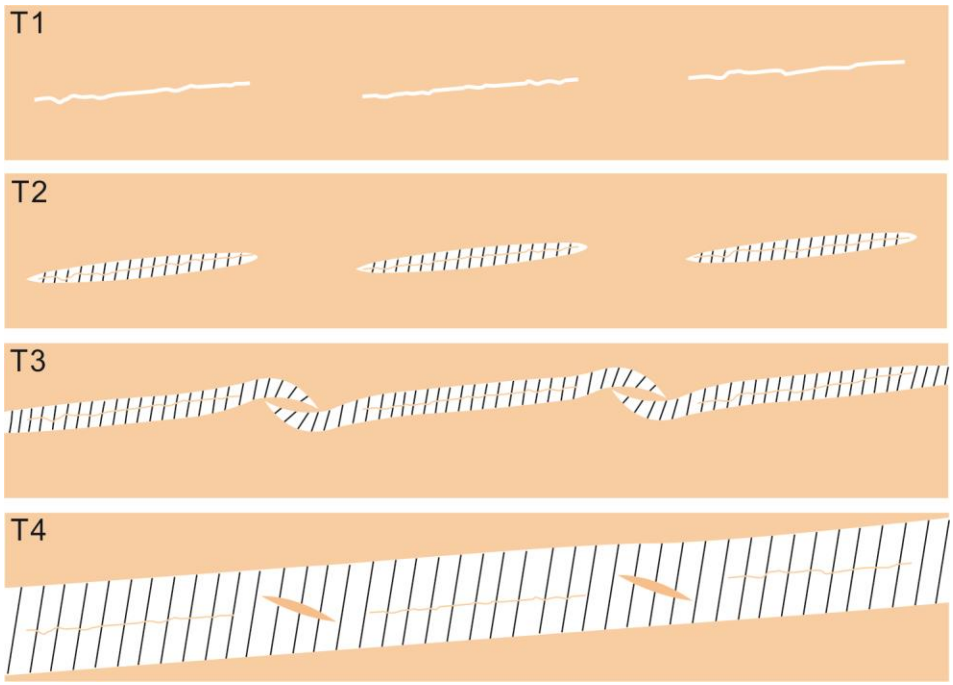


Figure 2.56 Cartoon illustrating the formation of persistent fibrous veins with multiple oblique host rock inclusions. T1: Initiation of en echelon fractures. T2: Fracture cementation. T3: Vein lateral propagation. T4: Vein coalescence.

In summary, the inclined gypsum veins comprise both passive and active fractures. The passive veins are reactivated pre-existing fractures that are simultaneously filled with same oriented fibres as newly formed horizontal hydraulic fractures. The active veins are newly formed tension fractures as by-product of growth of hydraulic fractures.

2.6.5 Hydraulic fracturing in closed systems

The distribution and abundance of gypsum veins is highly heterogeneous in the Mercia Mudstone along the cliffs. Unit 2 and Unit 4 both exhibit saturated, highly connected vein stockworks. The veins are prevalent in the low-permeability marls as a result of pervasive overpressure and reactivation of pre-existing fractures by fluid injection. In contrast, no gypsum veins are developed

in Unit 5, indicating that the circulation of fluid responsible for mineral transport is mainly restricted within the vein-rich units.

The calcareous marls in Unit 3 exhibit a high content of carbonates as pore cements that result in a low matrix porosity and an enhancement of mechanical strength. Hence, fluid circulation and transport in the rocks is difficult. Besides, the high strength increases the threshold of the differential effective stress required for hydraulic fracturing.

Unit 1 mainly contains discrete sub-horizontal gypsum veins, whose generation requires fluid pressure to exceed the sum of rock tensile strength and overburden. As Unit 1 is subjected to the highest overburden among all units, it is more difficult to produce hydraulic fractures in this unit.

Element data can provide data on the minerals that supplied the material and therefore the source and pathways of the fluids (Bons et al., 2012). Given the similar concentrations of minor and trace elements in single gypsum veins from the median zone to veins margins, it is suggested that the gypsum veins continuously obtained nutrient for fibre growth from single sources, i.e. adjacent disseminated gypsum (see section 3.8.5), with little input of external fluids.

Given the co-existence of gypsum veins and nodules in Unit 2 of the Blue Anchor Formation and the absence of gypsum in the rock matrix, the gypsum nodules are interpreted to serve as the nutrient source for the gypsum veins in this unit. The through-going red veins in the Blue Anchor Formation commonly cut multiple layers and likely acted as migration paths for fluids. The excess gypsum during anhydrite-gypsum transition could have been transported to other beds over a longer distance than that in the red marls. Nevertheless, the extent of sulphate redistribution is confined within Unit 2.

In summary, the heterogeneity in gypsum vein distribution and consistency in chemical compositions in single veins suggest that the generation of hydraulic fractures and nutrient transport for fibre growth occurred in a rather closed paleohydrologic system.

2.6.6 Implication of vein-aperture distribution

Vein (fracture) aperture is a critical scaling parameter for analysing vein size, growth and their relationships (André-Mayer and Sausse, 2007; Clark et al., 1995; Hooker et al., 2013; Monecke et al., 2001), which is best described by log-normal, power-law, negative exponential and normal distribution (Bonnet et al., 2001). Different vein-aperture distributions have been reported in multiple studies, which remain incompletely explained (Dershowitz and Einstein, 1988; Hooker et al., 2013). However, it is generally believed that different aperture distributions can be caused by incomplete data sampling, e.g. truncations of inferior values, or the maturity of vein network, e.g. the different development stages of vein network (Rives et al., 1992).

If natural fractures are randomly generated in a unifrom stress field at the early stage of rock deformation and fracture development, the aperture may be best fit to a negative exponenetial distbution (Cowie, 1998; Dershowitz and Einstein, 1988). The early fractures may show low connectivity and interaction (Cowie, 1998). Negative exponential distribution may also result from sampling bias of missing large-value data or truncated data at inferior values (Huang and Angelier, 1989; Kulatilake and Wu, 1984). Normal distributions are widely reported in natural and social sciences (Limpert et al., 2001), but rarely represented in fracture attributes (Huang and Angelier, 1989; Kulatilake and Wu, 1984). This is possibly due to the mechanical interaction that inhibits further generation of new fractures when fracture saturation has been achieved in a fracture network. Power-law distributions, which are represented as a linear trendline in a log-log plot, is

one of the most widely reported law of statistical distribution of fracture attributes (André-Mayer and Sausse, 2007; Cowie, 1998; Gross and Engelder, 1995; Marrett et al., 1999; McCaffrey et al., 2003; Sanderson et al., 2008). The fractures follow a power-law distribution normally show a self-similar geometry with sizes covering up to six magnitudes (Marrett et al., 1999).

Log-normal distributions are found across a wide range of scientific disciplines (Limpert et al., 2001) as a continous probability distribution of variable with their logarithm normally distributed. Log-normal distribution is suggested to appear when fractures interacted (Dershowitz and Einstein, 1988) or are saturated (Becker and Gross, 1996; Narr and Suppe, 1991). The growth and linkage of fractures are accompanied with overlaps of stress shadows and mechanical interaction, which may hinder the generation of new fractures (Becker and Gross, 1996; Narr and Suppe, 1991; Wu and Pollard, 1995) and localize growth to the largest fractures in the fracture system (Renshaw and Park, 1997).

In this study, the aperture of gypsum veins in the Mercia Mudstone is best fit a log-normal distribution. Large veins (aperture > 10mm), especially the sub-horizontal veins, occupy a very limited propotion in the overall vein population; however, their occurrence changes the distribution pattern significantly. Microveins (aperture below um scale) are not observed under microscope (see section 3.4), indicating a non-self-similar vein geometry.

A generic model for gypsum vein network evolvement is introduced to explain the origin of a log-normal aperture-distribution (Figure 2.57), based on the theories introduced above. At the primary stage, gypsum veins were randomly generated in a uniform stress field due to overpressure. The veins are mostly isolated with a low connectivity and interaction. Vein growth rate is mainly controlled by the degree of supersaturation with respect to gypsum in the fluid. Sub-horizontal

veins are possibly larger than others as they took advantage of bedding weak planes. Small sized veins take over a great majority in the vein population. At a later stage, sub-horizontal veins started to link with neighbouring bedding veins during growth, resulting in even large veins and a decrease of proportion of large veins. The aperture of all initial veins increases, regardless of their orientation and sizes. Vein nucleation continued, leading to a higher vein density and maturity of vein network. Inclined veins, including wing cracks and reactivated fractures, then coalesced with sub-horizontal veins, forming the highly connected backbone of the vein network. The mutual interference and mechanical interaction inhibit a future nucleation of new veins and favours the growth localized to the largest veins, particularly the sub-horizontal veins. The greater extrapolated number of the largest veins is possibly due to the existence of small veins with blind tips that indicate a potential further growth. The development of relatively small veins thereby reduce the proportion of the largest veins.

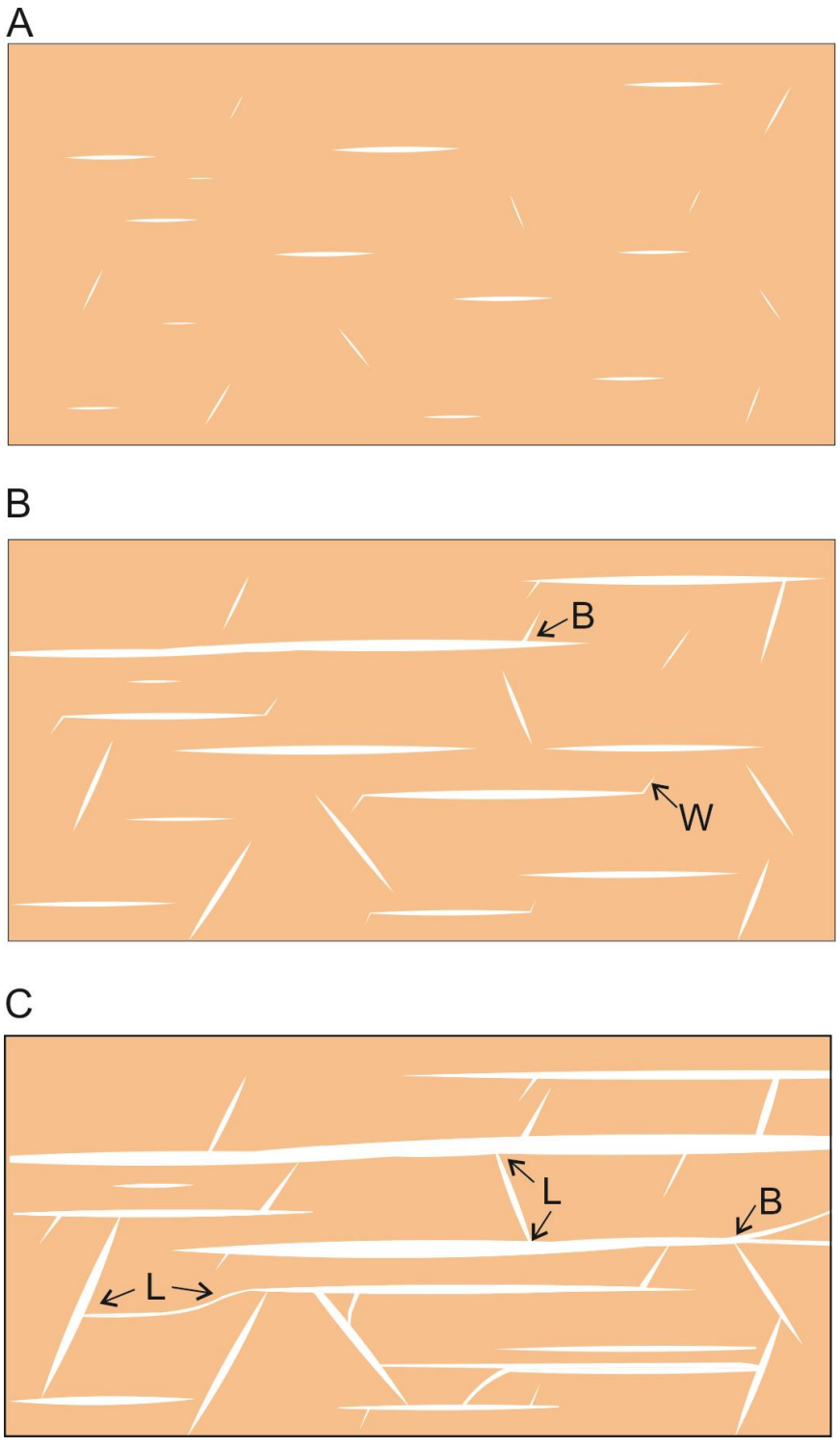


Figure 2.57 A generic model for model for the developed of gypsum vein network. (A) The initiation of primary hydraulic fractures. (B) Vein propagation and linkage. Notice the formation of wing-cracks and branches of sub-horizontal veins during propagation. (C) The linkage of sub-horizontal veins and inclined veins. B, branch; L, linkage; W, wing-crack.

2.7 Conclusions

(1) The satin spar vein network in the marls of the Mercia Mudstone was generated during basin uplift in early Cenozoic as indicators for basin inversion.

(2) A combined tectonic compression, overpressure and sediment exhumation resulted in the initiation of sub-horizontal fractures.

(3) The gypsum veins can be subdivided into active veins and passive veins. Active veins are newly formed hydraulic fractures or tension fractures as by-product of the growth of hydraulic fractures. Passive veins are reactivated pre-existing fractures, which are filled with gypsum fibres in the same orientations as those in the hydraulic fractures.

(4) Inclined fibres in bedding-parallel gypsum veins in both the Keuper Marl and the Blue Anchor Formation, which can be used as a shear sense indicator, record NWW-SEE shearing in the Mercia Mudstone in the Watchet area.

(5) The gypsum veins were produced and fed in closed systems, which are reflected in the anisotropic vein distribution and homogeneous chemical compositions.

(6) The aperture of gypsum veins in a vein stockwork is best fit a log-normal distribution as the result of vein connection and mechanical interaction.

Chapter 3 Petrographic characterization of satin spar veins in the Triassic Mercia Mudstone, the Bristol Channel Basin

3.1 Introduction

Some fibrous mineral veins are suggested to grow antitaxially, i.e. from the median zone towards vein walls (Bons, 2000; Bons and Montenari, 2005; Hilgers and Sindern, 2005; Hilgers and Urai, 2002). The median zone commonly consists of a thin band of host rock inclusions that marks the sites for primary nucleation of fibres (Bons et al., 2012; Hilgers and Urai, 2002). Individual veins may contain one or multiple median zones, which serve as records of cracking events (Cox and Etheridge, 1983a; Ramsay, 1980). During each cracking episode, the host inclusion bands may have been detached from the vein walls, providing sites for a new phase of fibre growth. The linear host rock inclusions are thus passively incorporated into the veins, aligned parallel to vein walls. Such a process of vein formation is attributed to the 'crack-seal' mechanism (Andreani et al., 2004; Cox and Etheridge, 1983b; Laubach et al., 2004; Matsumura et al., 2003; Ramsay, 1980; Toriumi and Hara, 1995). However, it is also suggested that crack-sealing may not be applicable in various cases, especially for antitaxial veins (Bons et al., 2012; Bons and Montenari, 2005; Hilgers and Urai, 2002; Passchier and Trouw, 1996).

Many veins consist of wall-oblique straight fibres or curved fibres (Urai et al., 1991; Williams and Urai, 1989). It is sugested that such fibres potentially contain essential information on vein opening as the fibres reflect the opening vectors of corresponding extension (Hilgers and Urai, 2002; Means and Li, 2001). This gives fibrous veins a promise as a tool for deducing the progressive deformation in the host rocks. Hence, the textural patterns and crystal morphology provide a

snapshot of the tensile strain in the bulk rock, vein-wall interaction and accretion process of the veins.

Numerous factors can control the pattern, frequency and distribution of fractures, including lithological characteristics (lithology, sedimentary structures, lithological competence, bed thickness, depositional composition, rock texture) (Cooke, 1997; Erickson, 1996; Huang and Angelier, 1989; Ji and Saruwatari, 1998; Ladeira and Price, 1981; Lamarche et al., 2012; Laubach et al., 2009; Lavenu et al., 2013; Narr and Suppe, 1991; Wennberg et al., 2006; Wu and Pollard, 1995), structural controls (tectonic setting, structural position, pre-existing structures, paleo-stress, subsidence and uplift history) (Blenkinsop, 2008; Brogi, 2011; Cosgrove, 1999; Holland et al., 2011; Narr et al., 2006; Peacock and Mann, 2005; Reyer et al., 2012; Van Noten et al., 2013; Walker et al., 2011), and fluid pressures (Cartwright, 2010; Cartwright, 1994; Cosgrove, 2001; Davies et al., 2012; Osborne and Swarbrick, 1997; Stoneley, 1983). To determine the controlling factors of fracture development in the context of the regional and local geological setting is increasingly appreciated by structural geologists, especially for fracture characterization and subsurface fracture prediction (Gillespie et al., 1993; Nelson, 2001).

This chapter reports a further study of satin spar veins and the host rocks mainly through a petrographic study. The chapter firstly describes a variety of forms of gypsum as pore cement in the rock matrix. Secondly, the chapter focuses on characterization of geometrical features of single gypsum veins and their internal textures and compositions. Then, the chapter presents the observations of differently oriented fibres in single curved veins and vein clusters. Finally, the chapter discusses the growth mechanism and kinematic implications of gypsum fibres, lithological control on vein development and the active mode of vein extension by force of crystallization.

The aims of this chapter are as follow:

(1) to present the textural patterns of the median zone and fibrous parts of gypsum veins and their structural implications;

(2) to investigate the controls on crystal morphology and kinematic implications of fibre growth in fine-grained rocks;

(3) to get a better understanding of how lithology affects the gypsum -vein distribution and abundance;

(4) to discuss the role of crystallization in fracturing and tensile straining in the host rocks;

(5) to develop genetic models for the formation and growth paths of satin spar veins.

3.2 Method

The distribution and characteristics of gypsum in the red marls were examined by hand specimen and petrographic observations. 56 thin sections of gypsum veins, nodules and their host rocks were cut. Optical examination was made in cross-polarized light with a Nikon Optophot Microscope fitted with a high resolution digital camera. A gypsum plate was inserted in the optical path between the sample and the polarizing filter, which helps determine the distribution of gypsum in the rock matrix. Polished thin sections were also examined using a FEI Quanta 650 FEG Scanning Electron Microscope (SEM) at voltage of 20kV, working distance of 10 mm and spot size of 5. Backscattered electron (BSE) images were produced to reveal micro-textures and mineral compositions. Elemental analysis was performed using energy dispersive X-ray spectroscopy (EDS) that is attached to the SEM.

3.3 Diagenetic gypsum

The calcium sulphate in the marls of the Mercia Mudstone was originally precipitated from interstitial brines or shallow water, hypersaline sabkha environments (Hobbs et al., 2002), which was later remobilized to form nodules (Leslie et al., 1993). The formation of gypsum nodules normally occurs during early diagenesis of the host rock before the main phase of compaction; however, it may occur at various stages during diagenesis and burial (Stow, 2005). Original gypsum readily dehydrates to anhydrite during burial when the ambient temperature exceeds 50-60℃ (Heard and Rubey, 1966; Jowett et al., 1993). Anhydrite pervasively rewatered to gypsum during basin uplift when the evaporite beds come into contact with low salinity and temperature fluids (Holliday, 1970; Testa and Lugli, 2000). Thus, it is inferred that the outcropping calcium sulphate in the red marls of the Mercia Mudstone are almost entirely composed of diagenetically regenerated gypsum. In thin sections, the diagenetic gypsum is present as gypsum veins, nodular gypsum, laths and diffusely disseminated gypsum as pore cement in the rock matrix. This section focuses on the petrographic descriptions of the three types of diagenetic gypsum, which are nodular gypsum, gypsum laths and diffusely disseminated gypsum.

3.3.1 Nodular gypsum

Macro nodules that can be identified at outcrop contain a series of densely-packed, poorly defined crystals of alabastrine gypsum (Figure 3.1A). The crystal aggregates exhibit a mosaic texture without apparent porosity. Single crystals are either blocky or elongated, many with irregular extinctions. The long dimension of crystals ranges from several to 200 μm. Those characteristics above are interpreted to represent anhydrite-gypsum replacement (Tucker, 2009).

Crystal aggregates of alabastrine gypsum with a diameter ranging from 500 μm to 2 cm are scattered in the clay matrix (Figures 3.1B-H). Such gypsum masses, or mini nodules, occur either individually or in clusters, commonly exhibiting little connectivity. Some mini nodules have clear boundaries in clay-rich regimes. Others exhibit non-uniform distinctions, especially where the enclosing sediments are silt-rich (Figures 3.1E-H).

Larger gypsum porphyrotopes are occasionally observed in the center of gypsum nodules, with a long axis in the scale of several millimeters (Figure 3.1F). Such crystals are interpreted to have formed as an earlier form of diagenetic gypsum during basin uplift before alabastrine gypsum (Murray, 1964).

3.3.2 Gypsum laths

Needle-like, elongate laths as another form of alabastrine gypsum are widespread in the marls of Unit 2 and Unit 5 (Figure 3.2). Single laths exhibit tapering tips and varied length ranging from several to 200 μm. The laths are either loosely scattered in the rock matrix or closely packed as aggregates. The aggregates of laths are often sub-parallel to the peripheries of gypsum nodules (Figures 3.1B-C). Some aggregates exhibit rounded or lenticular shapes, which resemble nodules. The laths described here are similar to those reported by Ortí et al. (2010) and Gibert et al. (2007).

The gypsum laths exhibit random orientations when their density is low (Figure 3.3A). However, the laths tend to have a preferred orientation when the lath density as well as connectivity increases (Figures 3.1B-E). The common coalescence of multiple closely spaced, parallel laths gives rise to a lath framework. Locally, the clay matrix is segmented by the lath framework, whist the detrital minerals of quartz and feldspar, and authigenic dolomites remain intact and are cemented by gypsum.

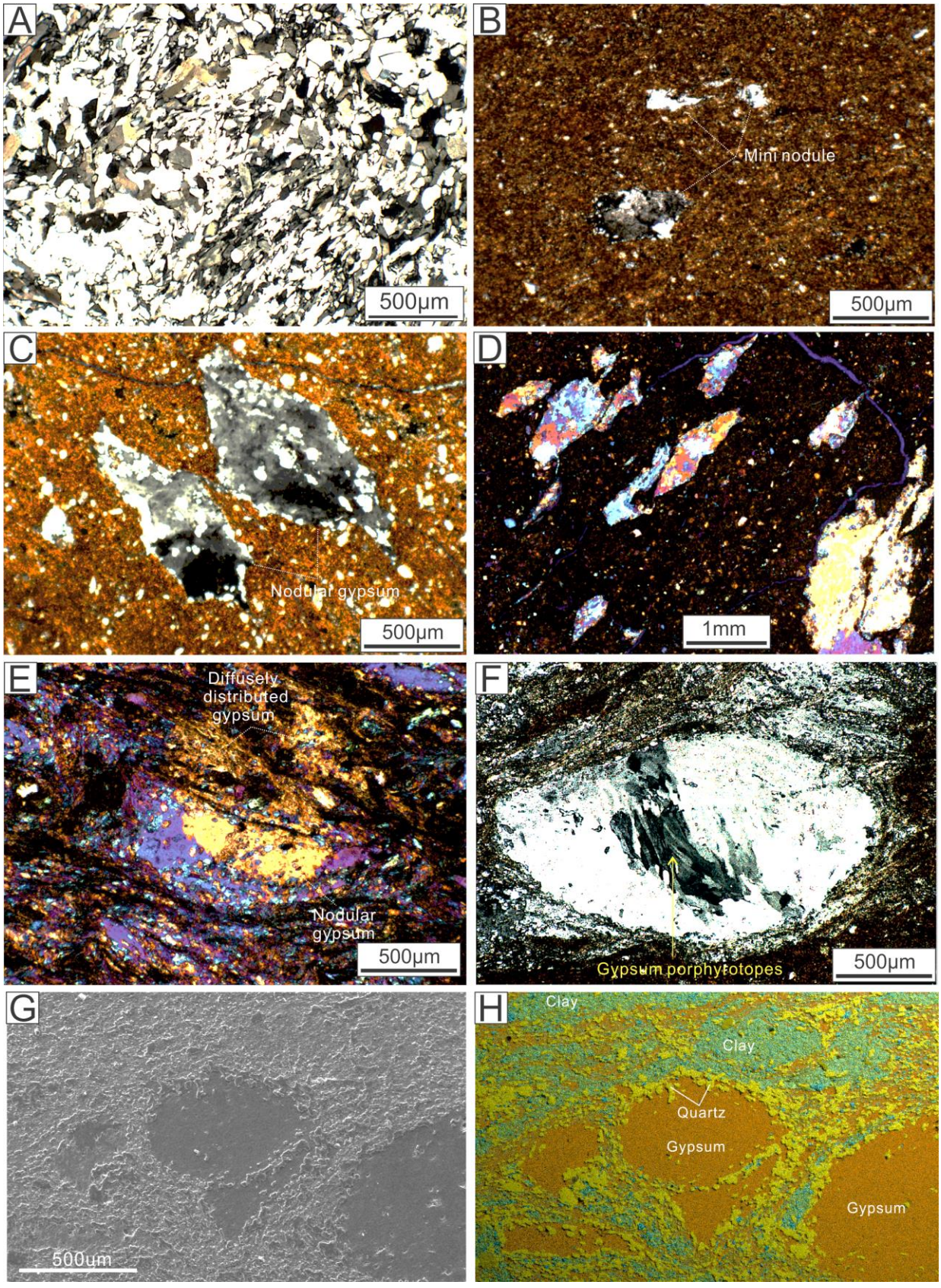

A
500μm
B
Mini nodule
500μm
C
Nodular gypsum
500μm
D
1mm
E
Diffusely distributed gypsum
Nodular gypsum
500μm
F
Gypsum porphyrotopes
500μm
G
500um
H
Clay
Clay
Quartz
Gypsum
Gypsum

Figure 3.1 (A) Alabastrine gypsum in macro gypsum nodules. Cross-polarized light. (B) - (D) Micro nodules in varied sizes. (E) Disseminated gypsum around a micro-nodule as pore cements. (F) An elliptical gypsum nodule consisting of gypsum porphyrotopes in the center. (G) Nodular gypsum enclosed by silt-rich sediments.

3.3.3 Diffusely disseminated gypsum (DDG)

Diagenetic gypsum is also commonly present as diffusely disseminated gypsum (DDG), exhibiting poorly-defined geometries and irregular extinctions (Figure 3.4). The DDG often appears in a flowing fabric, which can evolve into a convex morphology (Figures 3.3B-E). Similar features have been described by Ortí et al. (2010). Dense gypsum laths are often associated with the DDG, especially at the margins. Reorganization and rotation of the laths is identifiable through the regularly curved traces. The DDG is more prevalent in silt-rich areas, where the gypsum serves as the main pore-filling cementing agent and does not exhibit distinct textures and sizes (Figure 3.3F).

The fabric of diagenetic gypsum is associated with the content of silts in the host rock. In silty marls, gypsum mainly occurs as densely-packed lath-aggregates (Figure 3.5A), which evolves into prevalent DDG in siltstone as the predominant cement (Figure 3.5B). Siltstones around nodules of alabastrine gypsum contain abundant DDG in the rock matrix, with little porosity unfilled (Figure 3.5C). Similar to siltstones, sandstones at the base of Unit 1 are fully cemented and supported by DDG in the intergranular pore spaces (Figure 3.5D). The sandstone dykes (see section 2.2.3.4) are also cemented by DDG. However, gypsum is strictly restricted within the dykes and missing in the enclosing marls (Figure 3.6).

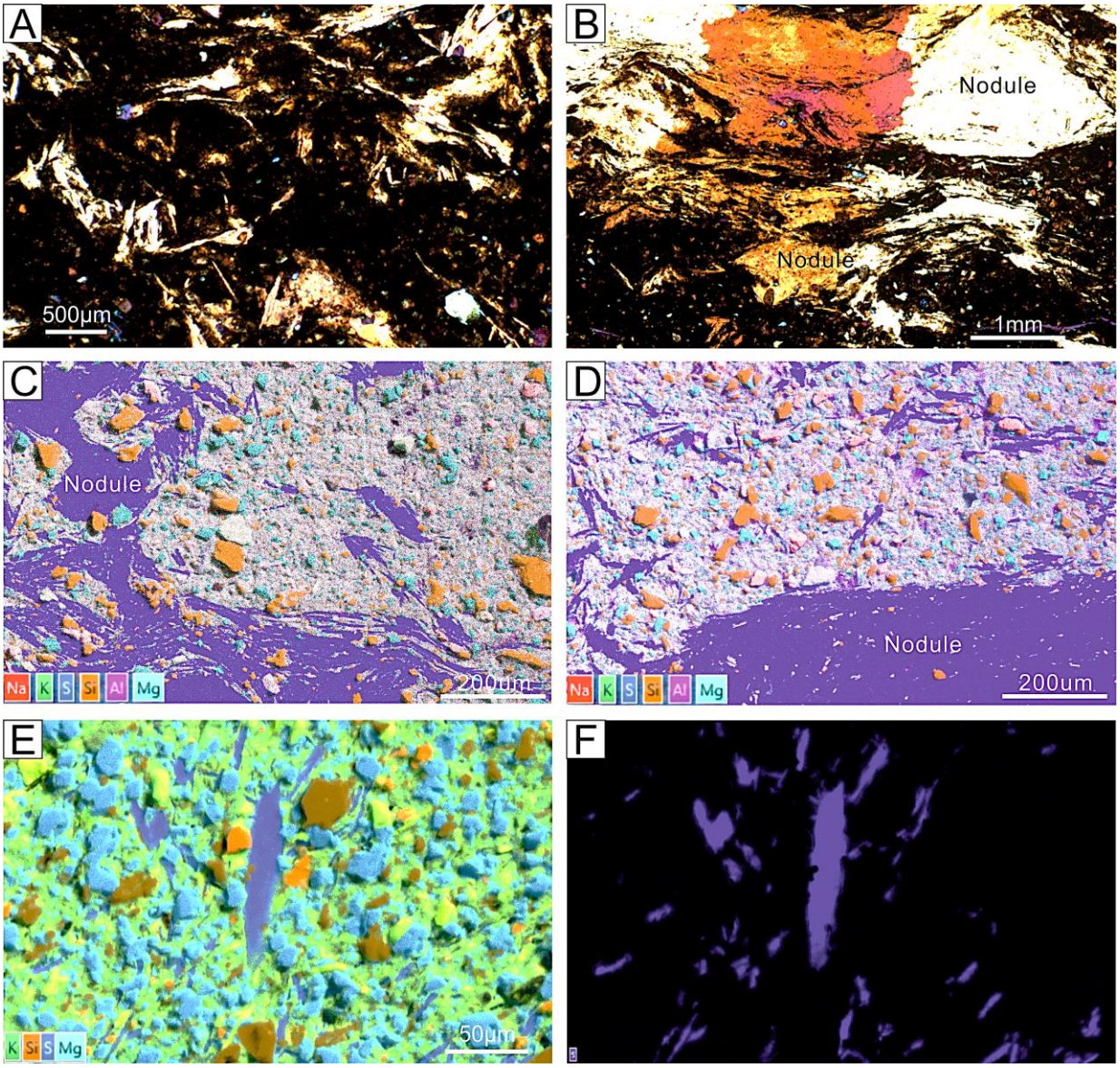


Figure 3.2 (A) Widely dispersed gypsum laths in marls. (B) Aggregates of gypsum laths sub-parallel to the long axis of a nodule. (C) Aggregates of gypsum laths and associated nodules. (D) Randomly scattered gypsum laths in the adjacent area of a nodule. (E) Isolated gypsum laths in the rock matrix. (F) Distribution of gypsum laths shown in figure 3.2E.

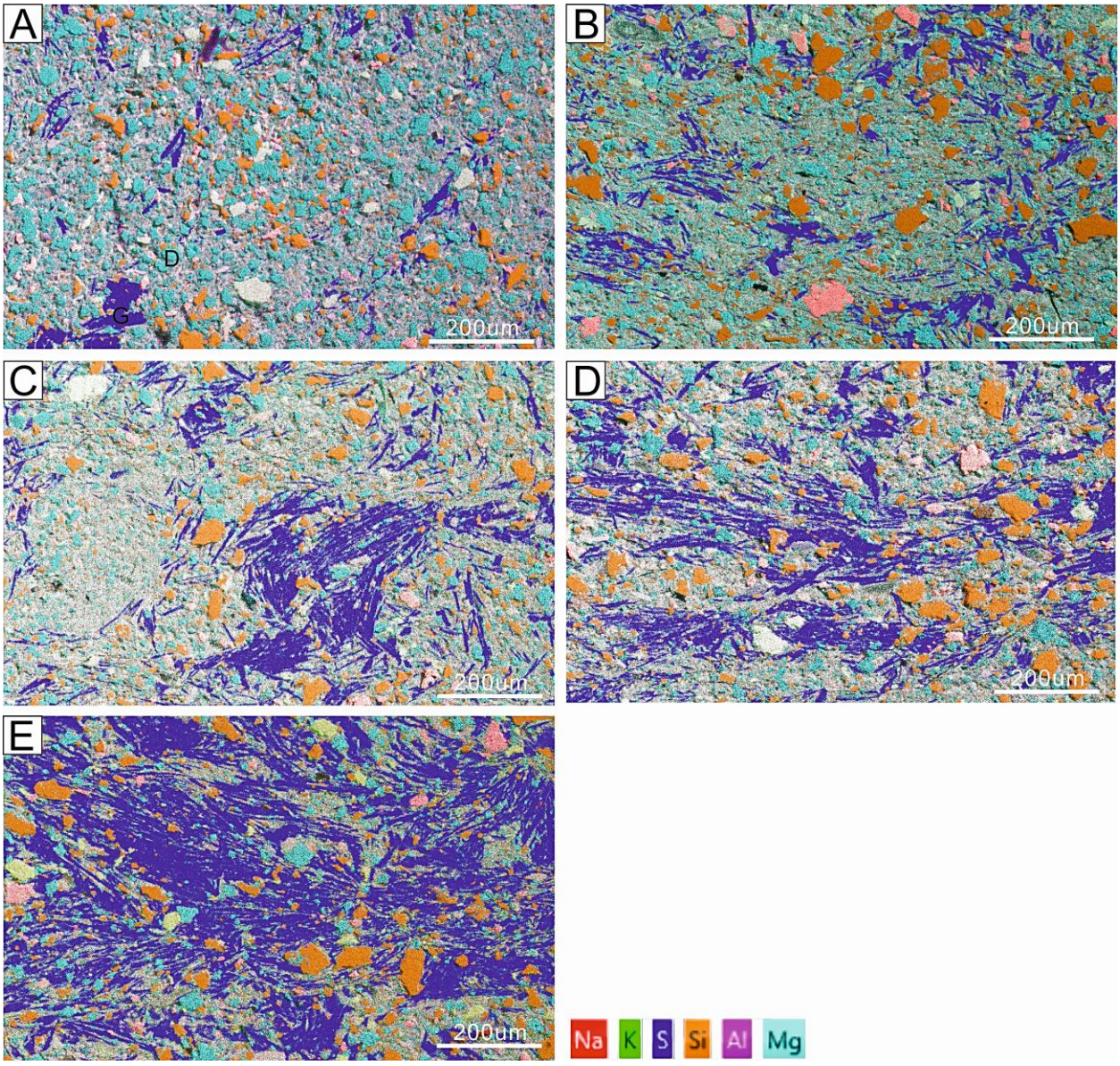


Figure 3.3 EDS maps showing gypsum laths with increased density and connectivity from (A) to (E). Note the random orientations of laths in figures 3.3A-B and sub-parallel laths in figures 3.3C-E. Samples in figure 3.3sA-D are from Unit 4. Sample in figure 3.3E is from Unit 2.

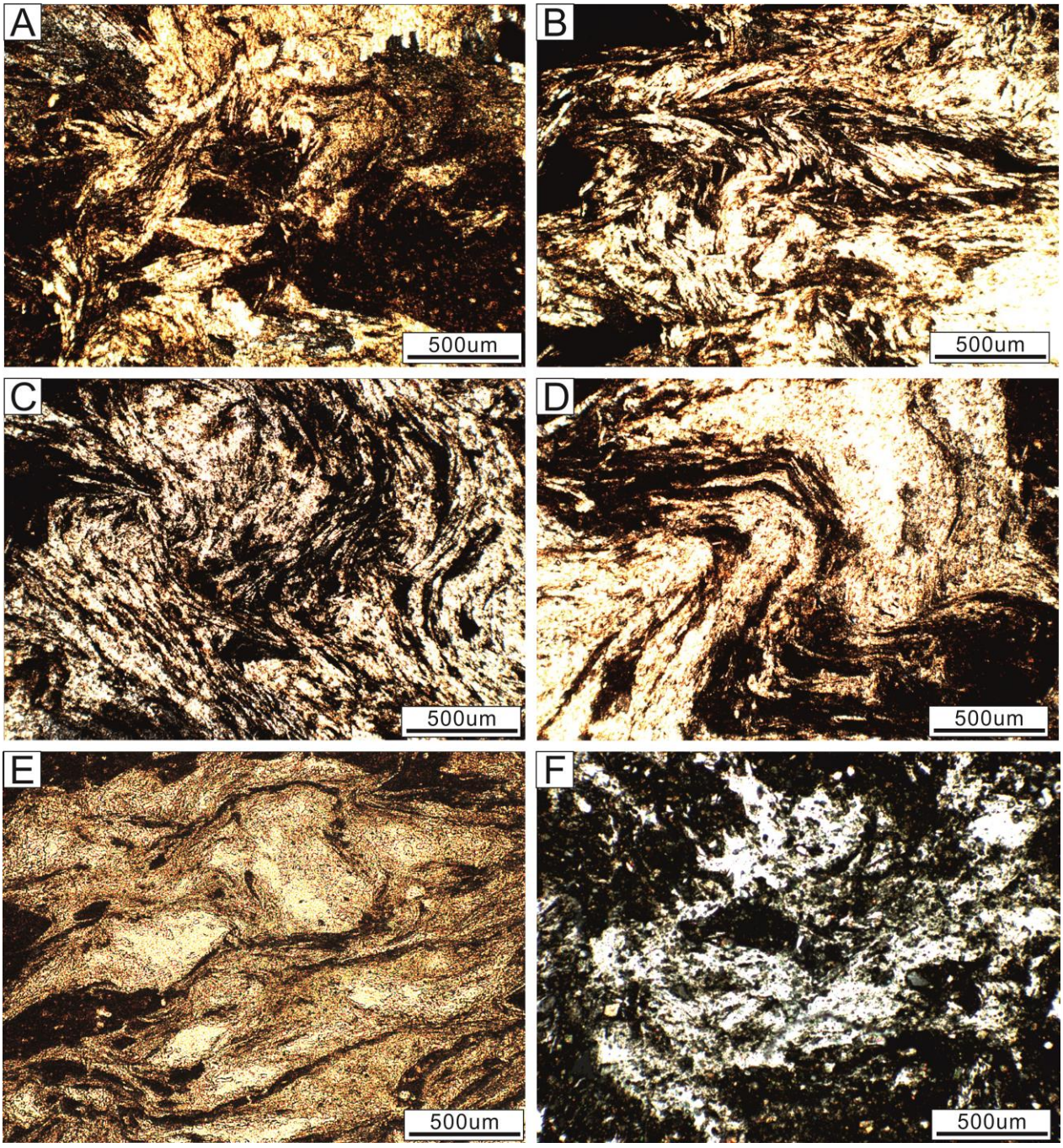


Figure 3.4 Diffusely disseminated gypsum as pore cements. (A) Aggregates of gypsum laths associated with DDG. (B) Anastomosing of abundant gypsum laths and gypsum cements. (C) and (D) Aggregates of gypsum laths and cements exhibiting sigmoidal traces. (E) DDG as the main cement. (F) Localized gypsum cements in silty marls. All samples are from Unit 2.

Interestingly, the DDG is intimately associated with the occurrence of silty grains. DDG is mainly concentrated where the silt grains are concentrated and clustered (Figure 3.7). In contrast, little gypsum is present in the adjacent areas of clay-dominated marls. Hence, a higher content of silts in the rocks commonly corresponds to a higher content of diffusely disseminated gypsum.

3.3.4 Relation to gypsum veins

Aggregates of gypsum laths, DDG, and non-prismatic gypsum masses are commonly associated with gypsum veins, appearing in the host rocks (Figure 3.8). The long axes of the gypsum aggregates are aligned parallel to the adjacent veins. The DDG are often attached to vein walls, contacting with satin spar crystals (Figure 3.8D).

Nodule-rooted micro satin spar veins (Figures 3.9, 3.10) with an aperture of ～150 μm are observed in polished hand specimens and also thin sections that resembles to those at outcrop (Figure 2.17B). The veins exhibit contrasting fibrous textures to the nodules that are rather homogeneous and non-prismatic. These veins commonly exhibit the maximum aperture at the roots that gradually decreases towards vein tips. Many veins pinch out in the marls whist some coalesces with neighboring nodules. It is interpreted that the nodules provide nutrient for the growth of the associated veins.

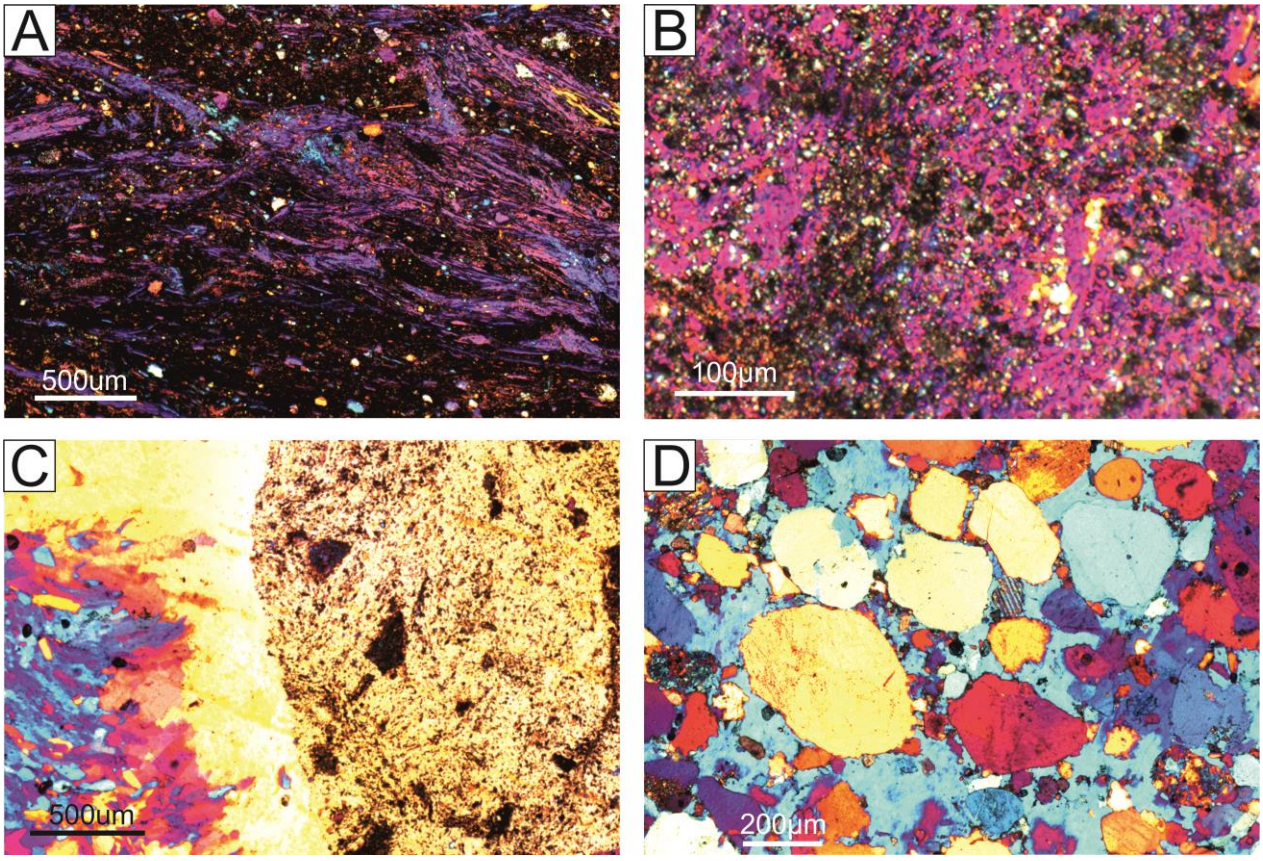


Figure 3.5 Diagenetic gypsum in silty marl (A), siltstone (B and C), and sandstone (D) as cement.

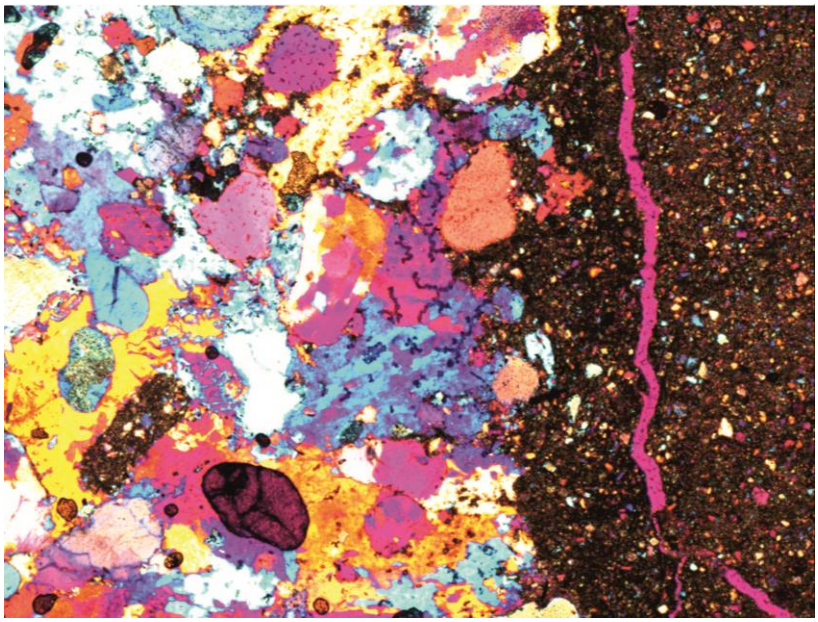


Figure 3.6 A sandstone dyke cemented by DDG. Note the absence of gypsum in the country rock.

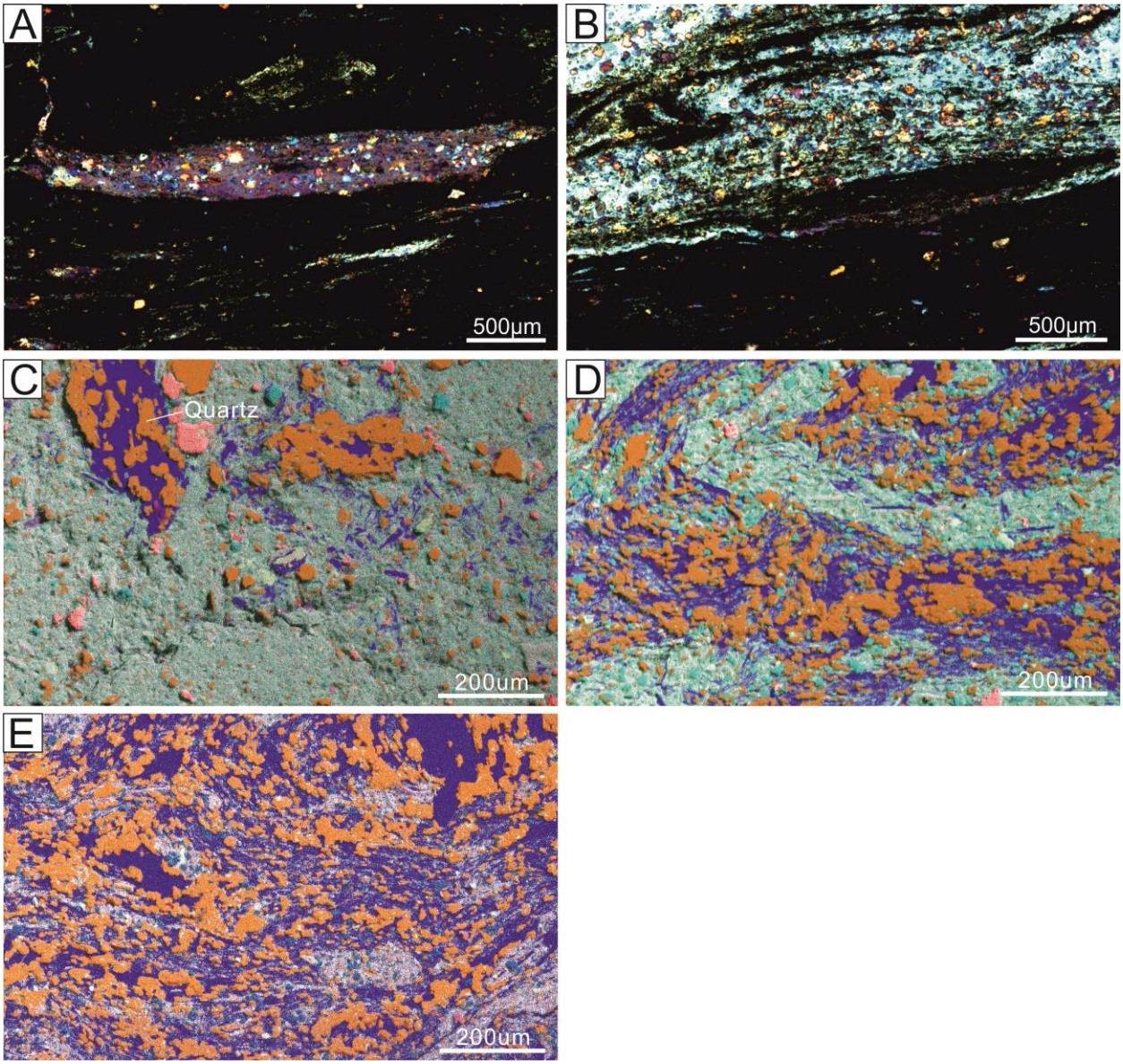


Figure 3.7 Preferential occurrence of gypsum cements in the marls. (A) A lenticular gypsum body cementing silty grains. (B) Localized gypsum in silt-rich zones. (C)- (E) EDS maps showing preferential distribution of gypsum in silt-rich zones. The silt content increases from figures 3.7C-3.7E.

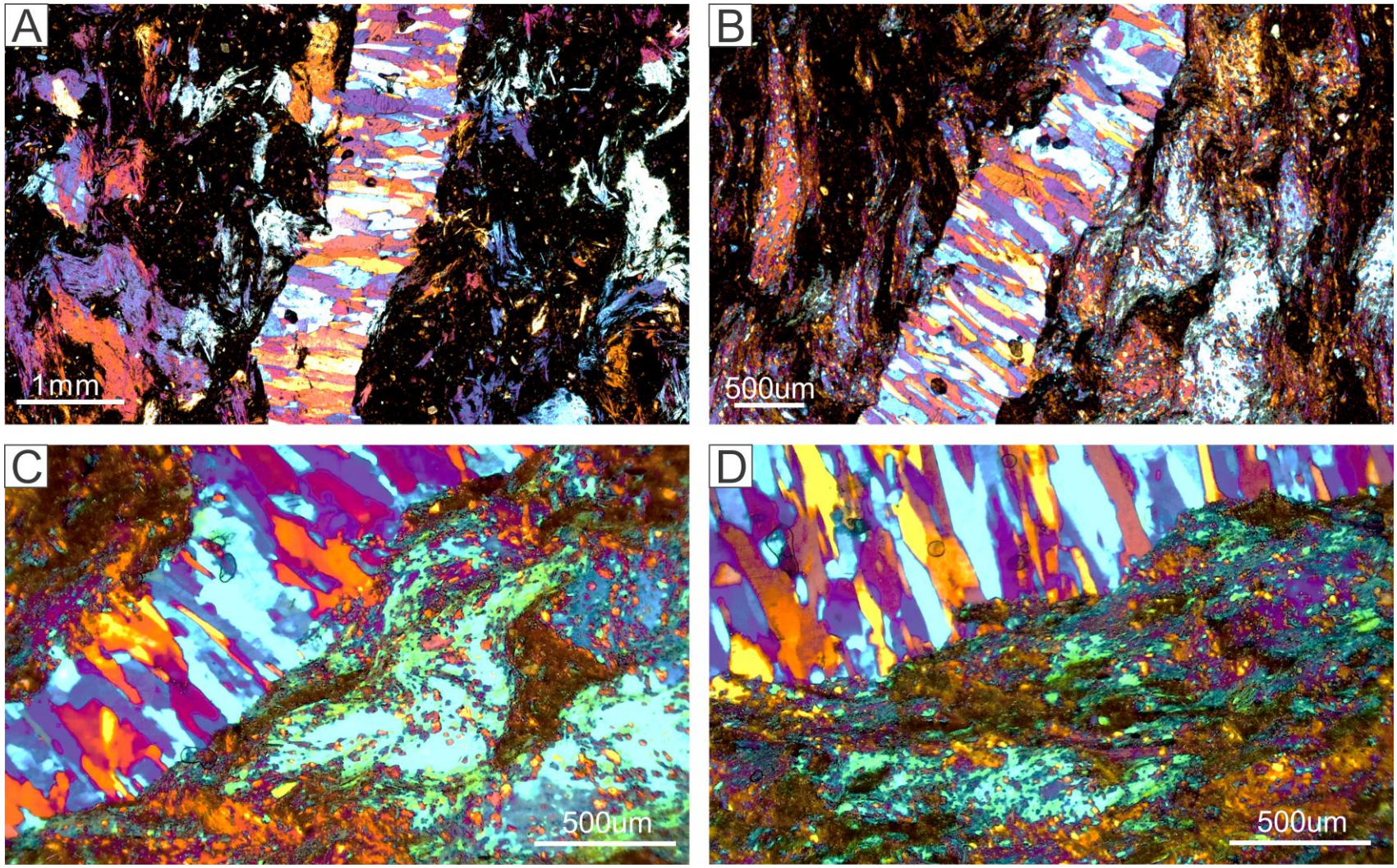


Figure 3.8 Photomicrographs showing the concentration of gypsum cements around gypsum veins. (A) Gypsum laths and irregular shaped gypsum aggregates near a fibrous vein. (B) Gypsum aggregates with long axes sub-parallel to a satin spar vein. (C) and (D) Diffusely disseminated gypsum near vein-walls.

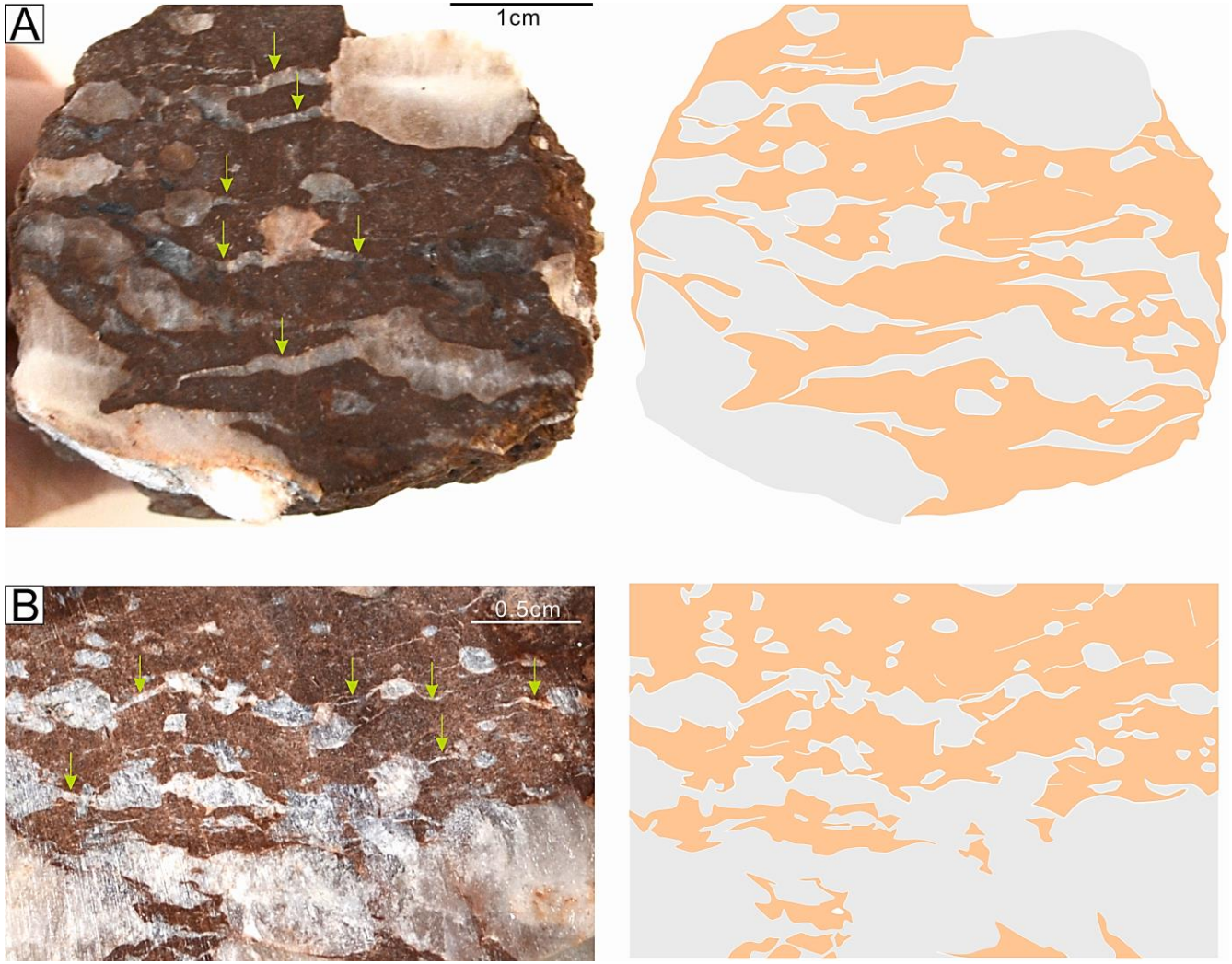


Figure 3.9 Photographs showing polished hand specimens from an evaporite-rich horizon in Unit 4 of the Keuper Marl. The arrows highlight the nodule-rooted veins.

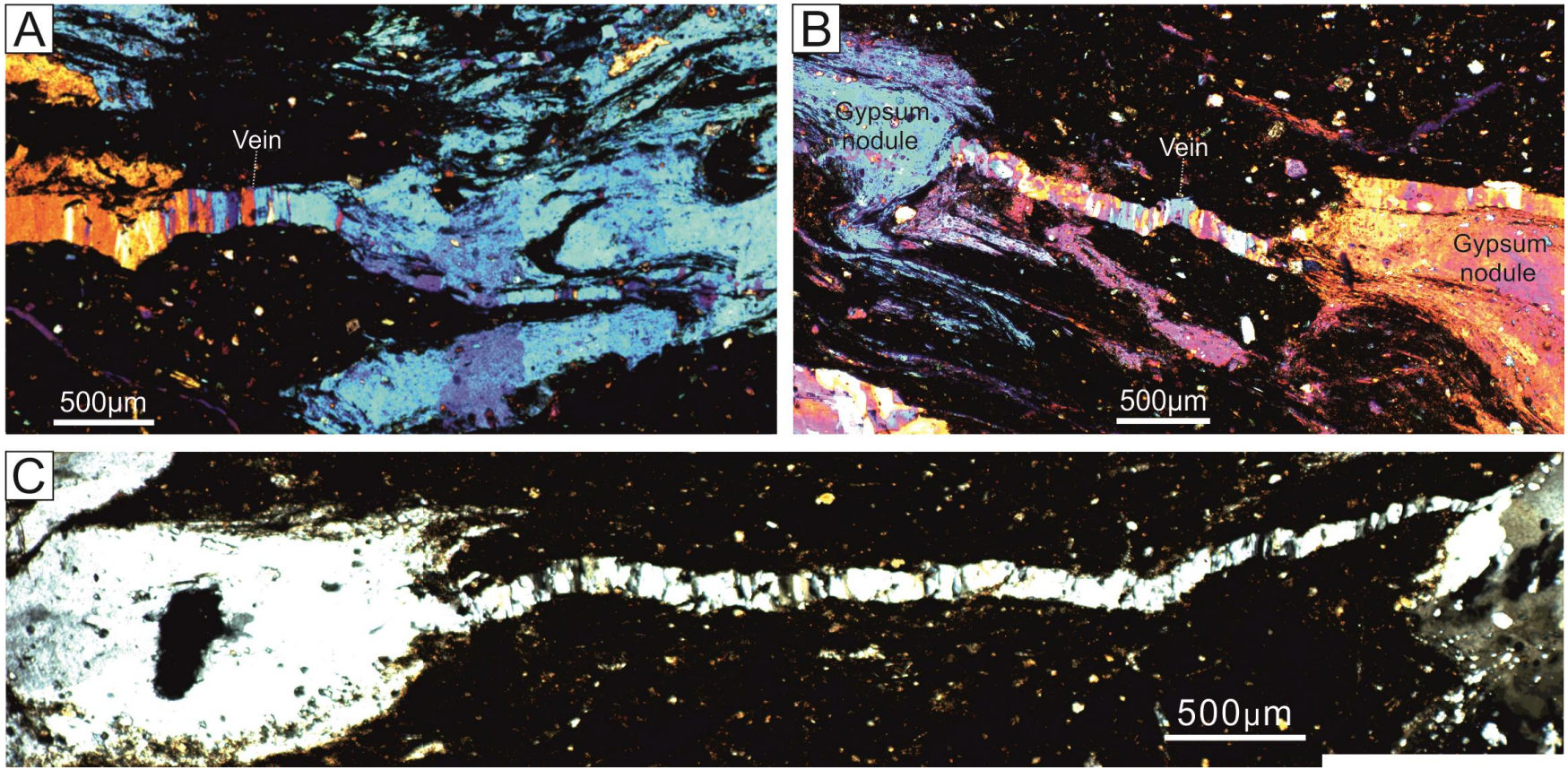


Figure 3.10 Photomicrographs showing the nodule-rooted satin spar veins. (A) A satin spar vein rooted in a gypsum nodule. (B) A satin spar vein linking two adjacent nodules. (C) A satin spar vein with a tapered tip to the right between two nodules.

3.4 Gypsum veins

Gypsum veins in the Mercia Mudstone exhibit varied geometries and internal textures in thin sections. In this section, the description focuses on the characteristics of single veins, en echelon veins, and vein behaviors of branching and coalescence.

3.4.1 Geometry

Single veins are often blocky, exhibiting structureless textures (Figure 3.11). Some veins consist of equant gypsum crystals in varied sizes that are tightly interlocked (Figure 3.11B). Satin spar veins are more often observed, whose aperture commonly exceeds 150 μm. The veins often exhibit irregular traces and variable widths, especially the blocky veins. The veins are either developed individually or associated with other gypsum masses.

3.4.2 En echelon veins

A series of short and parallel satin spar veins appears in the marls as en echelon veins. The veins exhibit sigmoidal shapes that reflect a left-stepping sense. Tips of single veins are often curved towards the neighboring veins and even coalesce with them. The maximum principal stress σ_1 responsible for the generation of the en echelon veins in figure 3.12A is interpreted to be horizontal. However, the very local σ_1 at the tip regions may be parallel to the walls of tips, which is evident from the wall-orthogonal fibres at vein tips that represent the direction of vein extension (Figure 3.12B). It is observed that some large veins terminate as a set of small en echelon veins (Figure 3.12C).

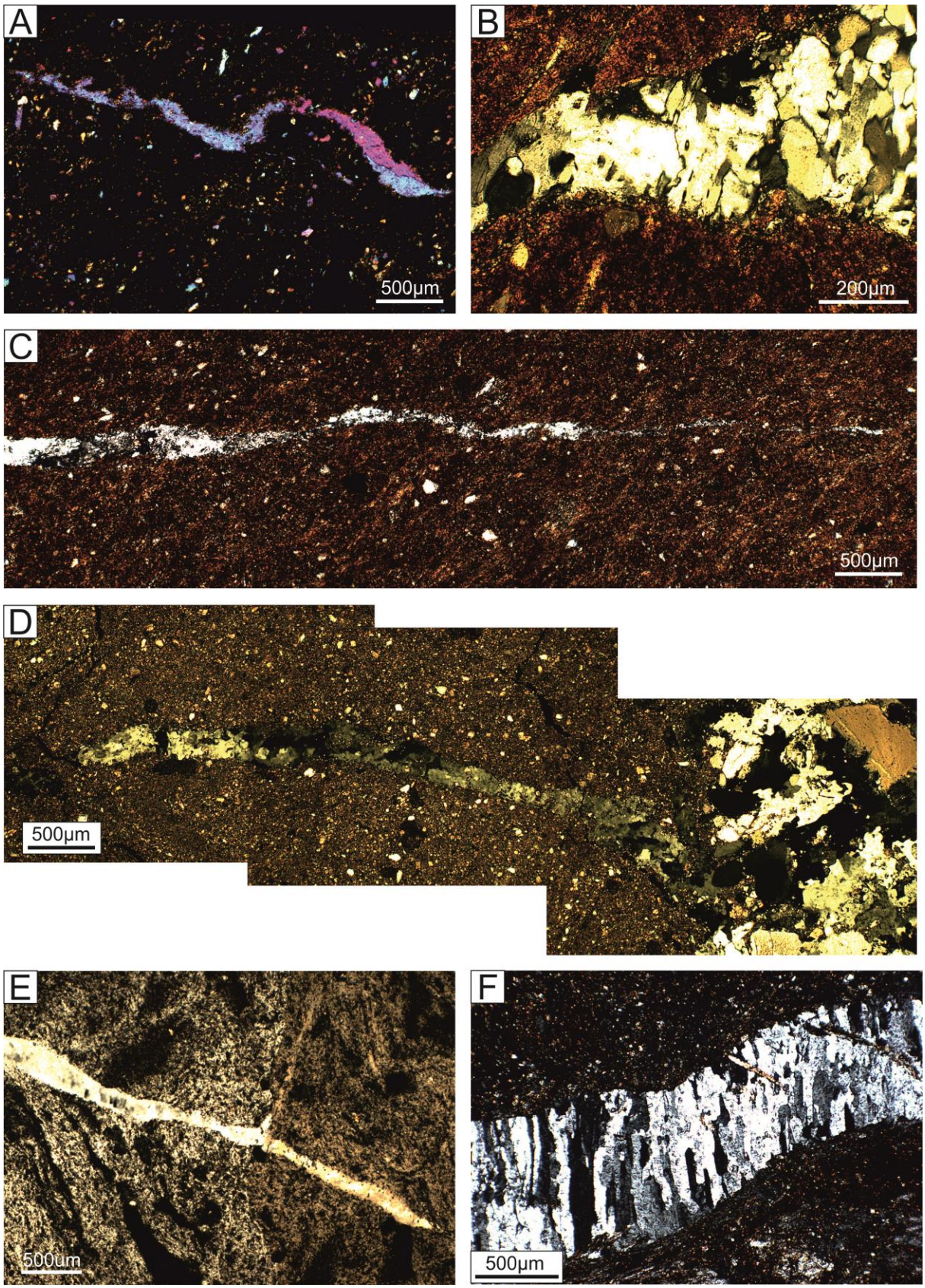

A
500µm
B
200µm
C
500µm
D
500µm
E
500µm
F
500µm

Figure 3.11 Photomicrographs showing the geometry and texture of single gypsum veins. (A) A blocky, curved gypsum vein. (B) A blocky gypsum vein with decreased aperture to the left. (C) A micro gypsum vein pinching out in the red marl. (D) A blocky gypsum vein rooted in a gypsum nodule. (E) A blocky gypsum vein with fuzzy boundaries in silty marl. Note the abundant gypsum disseminated in the surrounding rock. (F) A silightly curved, elongate-satin spar vein with oblique solid inclusions.

3.4.3 Vein branching

The branching behavior of micro veins during propagation resembles that at outcrops (see section 2.3.4.2) (Figure 3.13). The fibre orientation in the branches remains the same as that in the parent veins (Figures 3.13A-D), which represents the displacement direction of the vein walls. Repeated branching, i.e. splitting of the branches, of veins is observed, and accompanied with the decrease in the aperture of individual branches (Figures 3.13E-F).

Vein branching is presumably the result of the local stress perturbation by the appearance of adjacent veins. The branches are interpreted to form as tension gashes at the propagation front of veins (Figure 3.14). The sub-vertical expansion of veins could induce a wall-orthogonal compressional stress in the country rock, which modifies the local σ_1 to deviate from the original direction and then produces the branch of the adjacent vein.

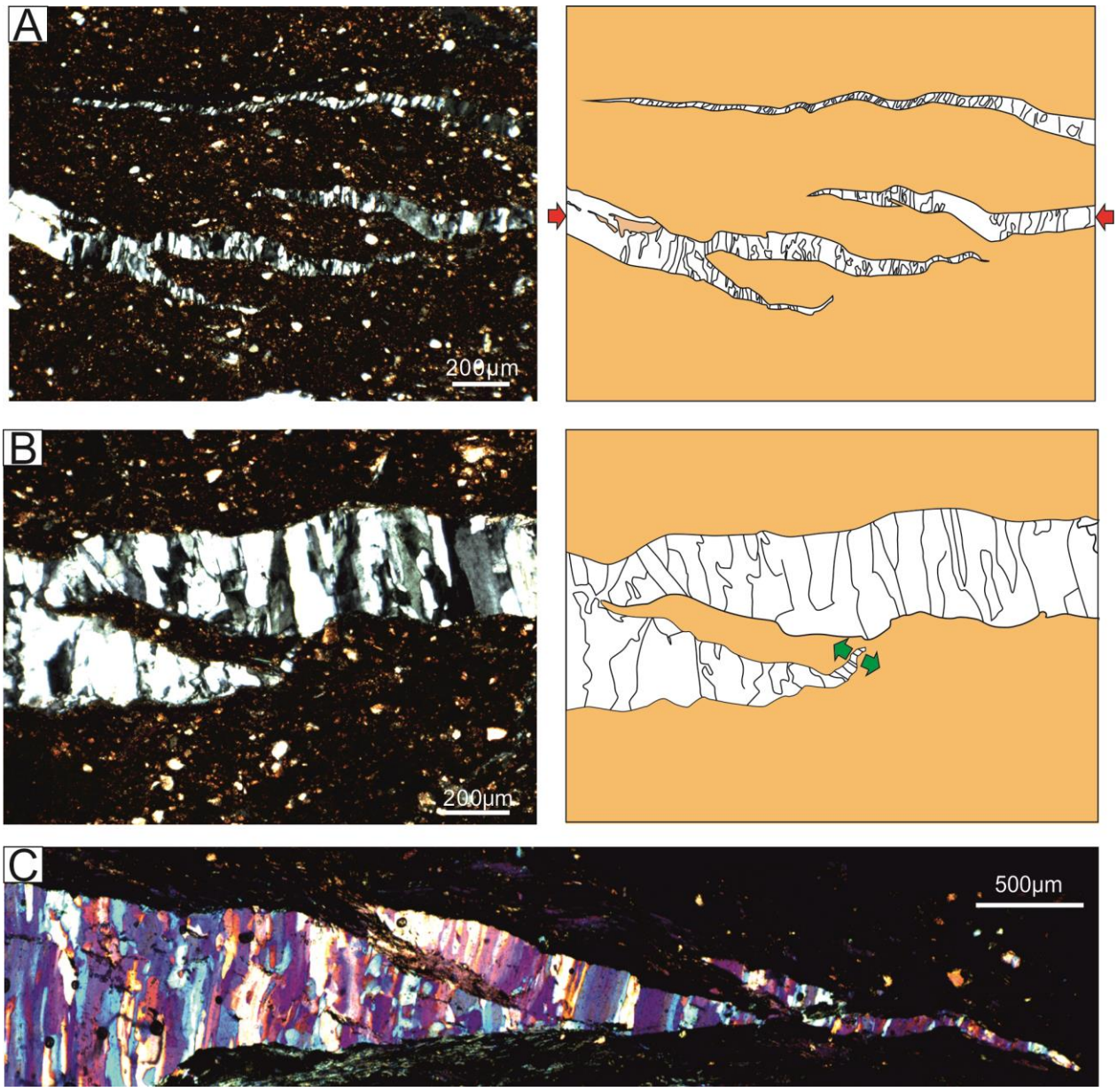


Figure 3.12 Photomicrographs showing en echelon veins. (A) A set of en echelon veins exhibiting sigmoidal geometries. (B) Coalescence of two adjacent en echelon veins. Note the curved vein tip. (C) A vein terminating as a set of en echelon veins. Samples are from Unit 4.

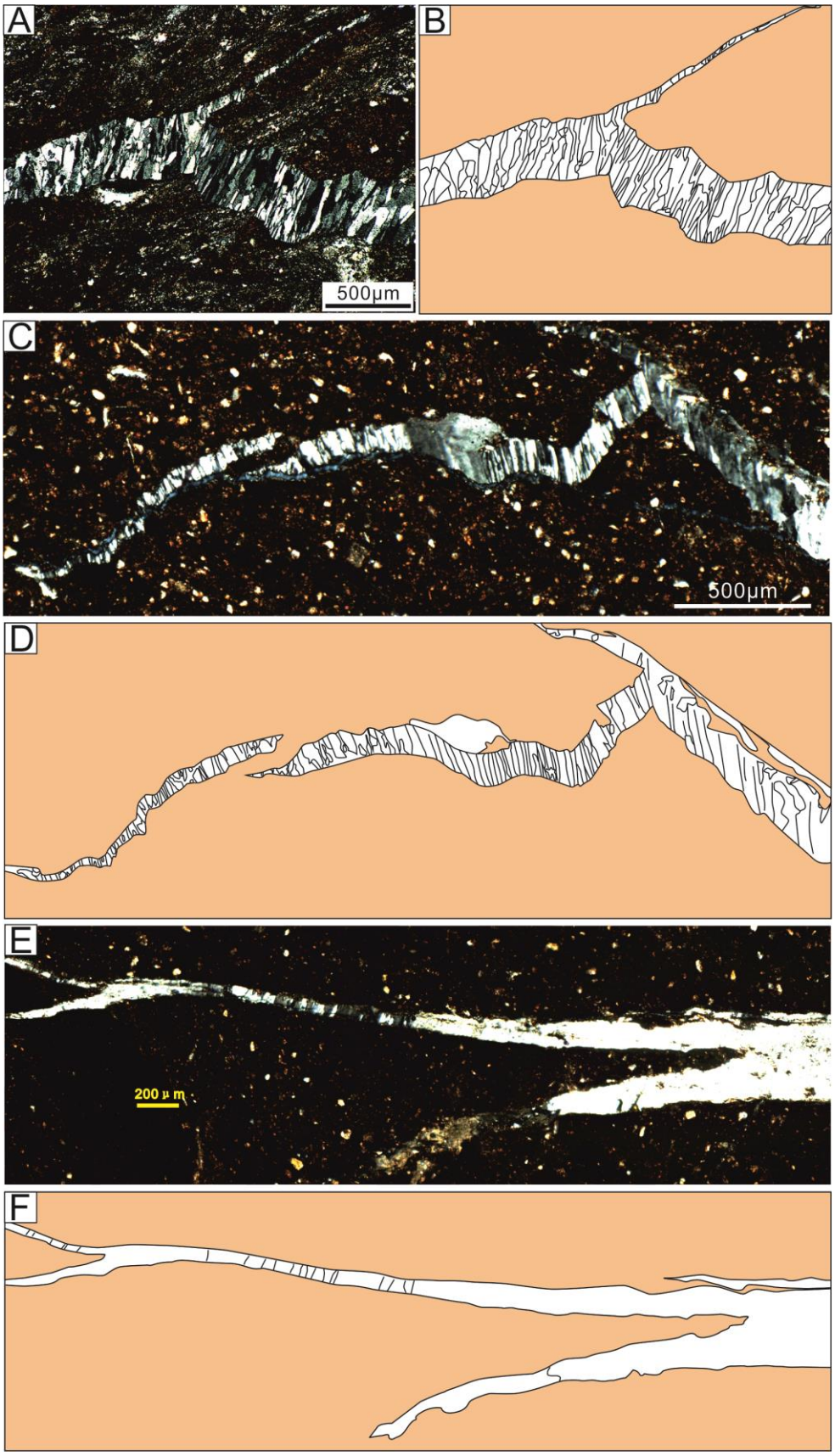

A
500μm
B
C
500μm
D
E
200 μ m
F

Figure 3.13 Photomicrographs showing branching of gypsum veins. (A) and (B) Two branches of a gypsum vein with varied aperture and orientation. (C) and (D) Gypsum branch deviating from the original direction of the parent vein. Note the branch is approximately orthogonal to the parent vein. (E) and (F) Repeated vein branching. Samples are from Unit 4.

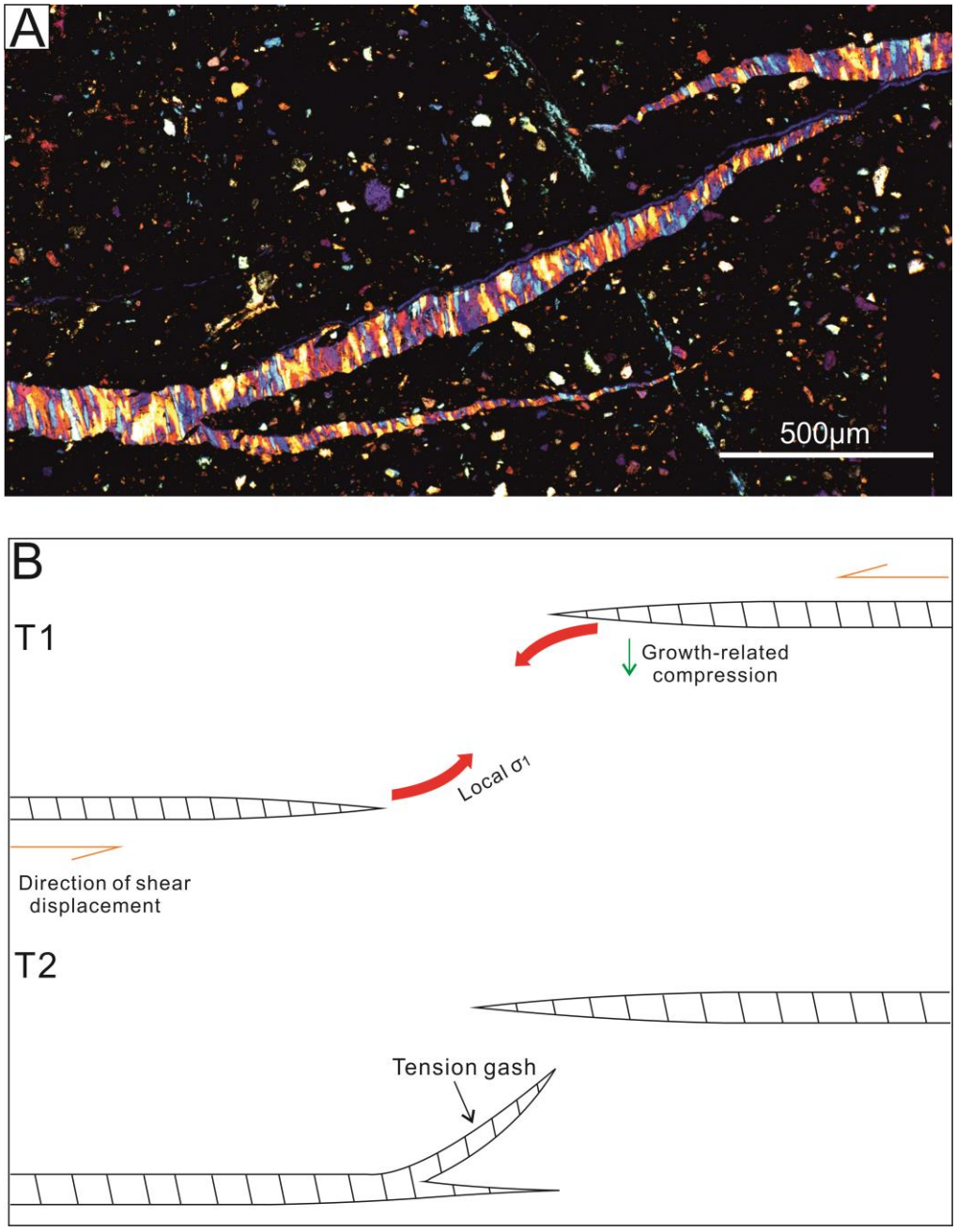


Figure 3.14 (A) Photomicrograph showing the branching of a gypsum vein. (B) Cartoons illustrating the mechanism of branching of the vein in figure 3.14A.

3.4.4 Vein coalescence

Single or multiple parallel trails of host rock fragments are observed to align oblique to vein walls (Figure 3.15). Those trails are interpreted to originate from the coalescence of adjacent parallel veins or en echelon veins rather than a later injection of the fragments. During the propagation and widening of parallel veins, the tips coalesce with the adjacent vein, leaving the in-situ host rock fragments entrapped between the tips. The direction of the inclusion trails are thus determined by the inner walls of the veins.

Intersection of differently oriented veins occurs when one vein propagates towards the wall of an adjacent vein (Figures 3.16, 3.17). The propagating vein is either oblique or normal to the pre-existing vein at the intersection site. The traces of the propagating vein can be straight or curved. The propagation path of the later vein can be influenced by the pre-existing vein. Figure 3.16F illustrates the interaction of two parallel veins, where the minor vein changed the orientation to be approximately normal to the larger vein during propagation.

Interaction also occurs between gypsum veins and nodular gypsum masses (Figure 3.18). Such veins are commonly rooted in larger veins and propagate towards the adjacent nodules. The fibre orientation in those veins exhibit high angles relative to that in the larger veins. It is interpreted that veins of this type form as tension gashes during the propagation of the large veins and also the possible expansion of the nodules.

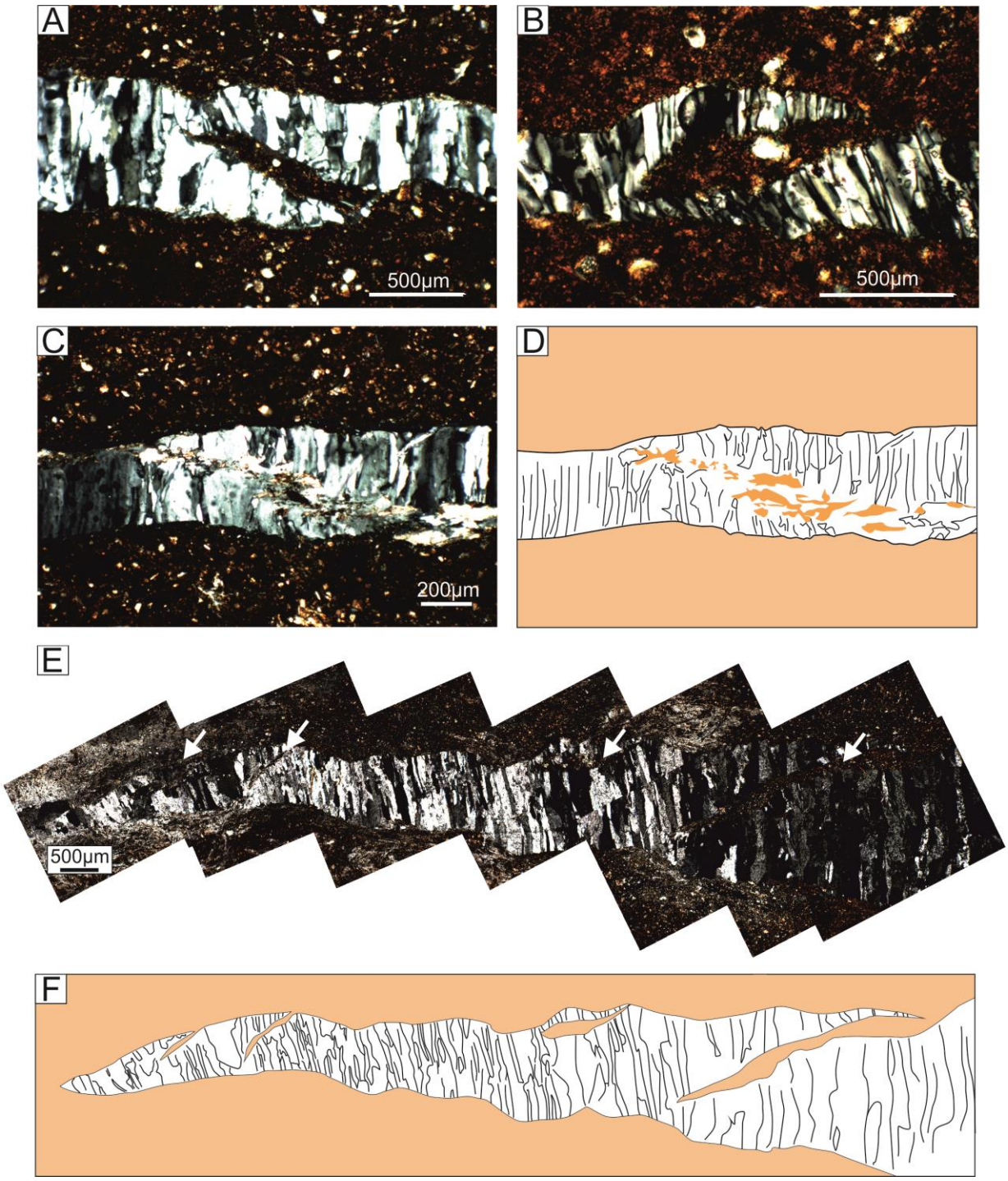


Figure 3.15 Photomicrographs showing the coalescence of parallel veins. (A) and (B) The coalescence of vein tips. (C) Solid inclusion trails that are oblique to vein walls. (D) Sketch of the gypsum vein in figure 3.15C. (E) A horizontal gypsum vein with multiple parallel lenses of solid inclusions.

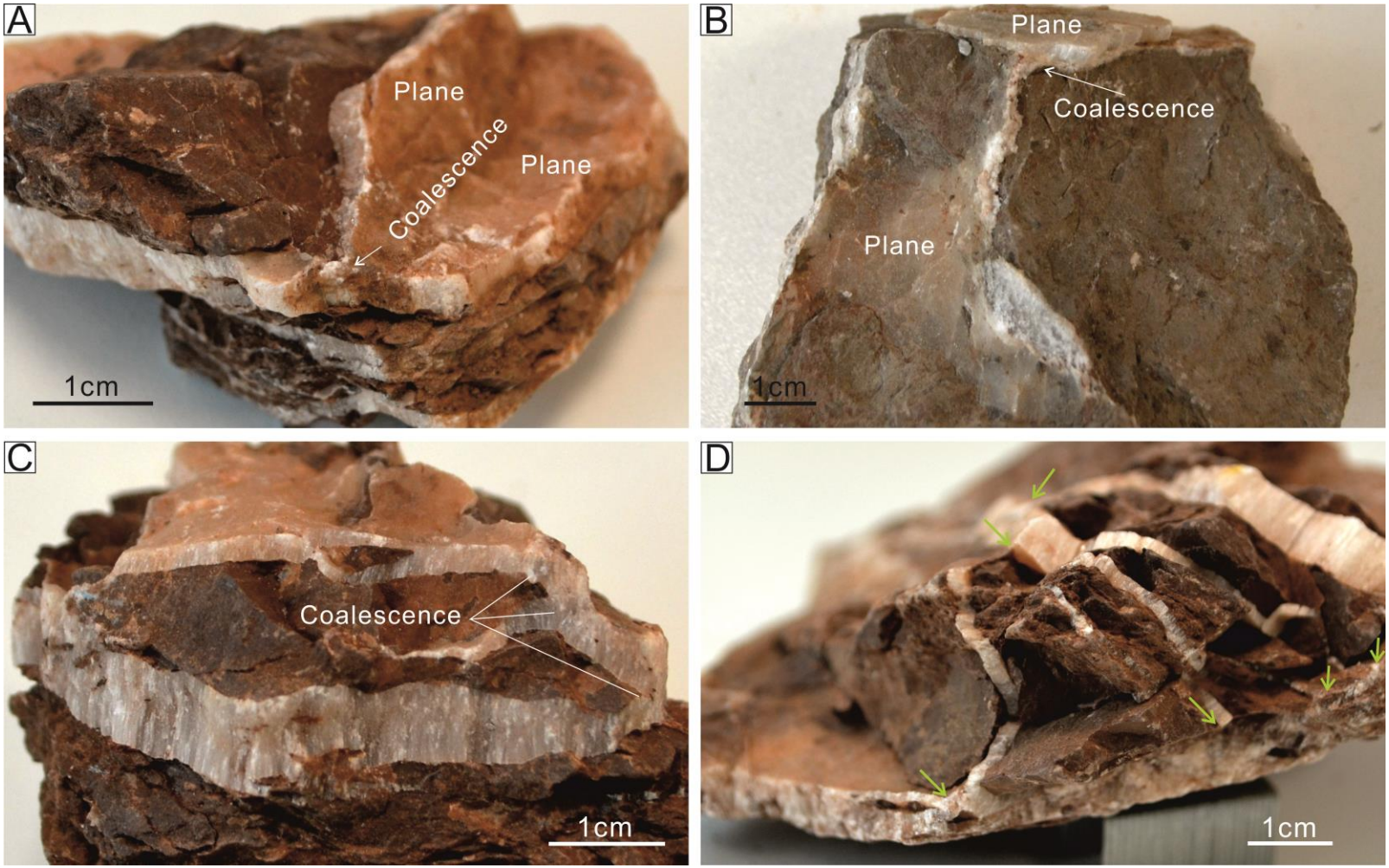


Figure 3.16 Photographs showing intersections of differently-oriented veins in 3D view. (A) and (B) Interaction of two sub-orthogonal veins. (C) Intersection of the inclined segment of a horizontal vein with another horizontal vein. (D) Intersection of multiple inclined veins with a horizontal vein. The arrows highlight the bifurcations. Samples in figure 3.16A, C-D are from Unit 4. Sample in figure 3.16B is from Unit 2.

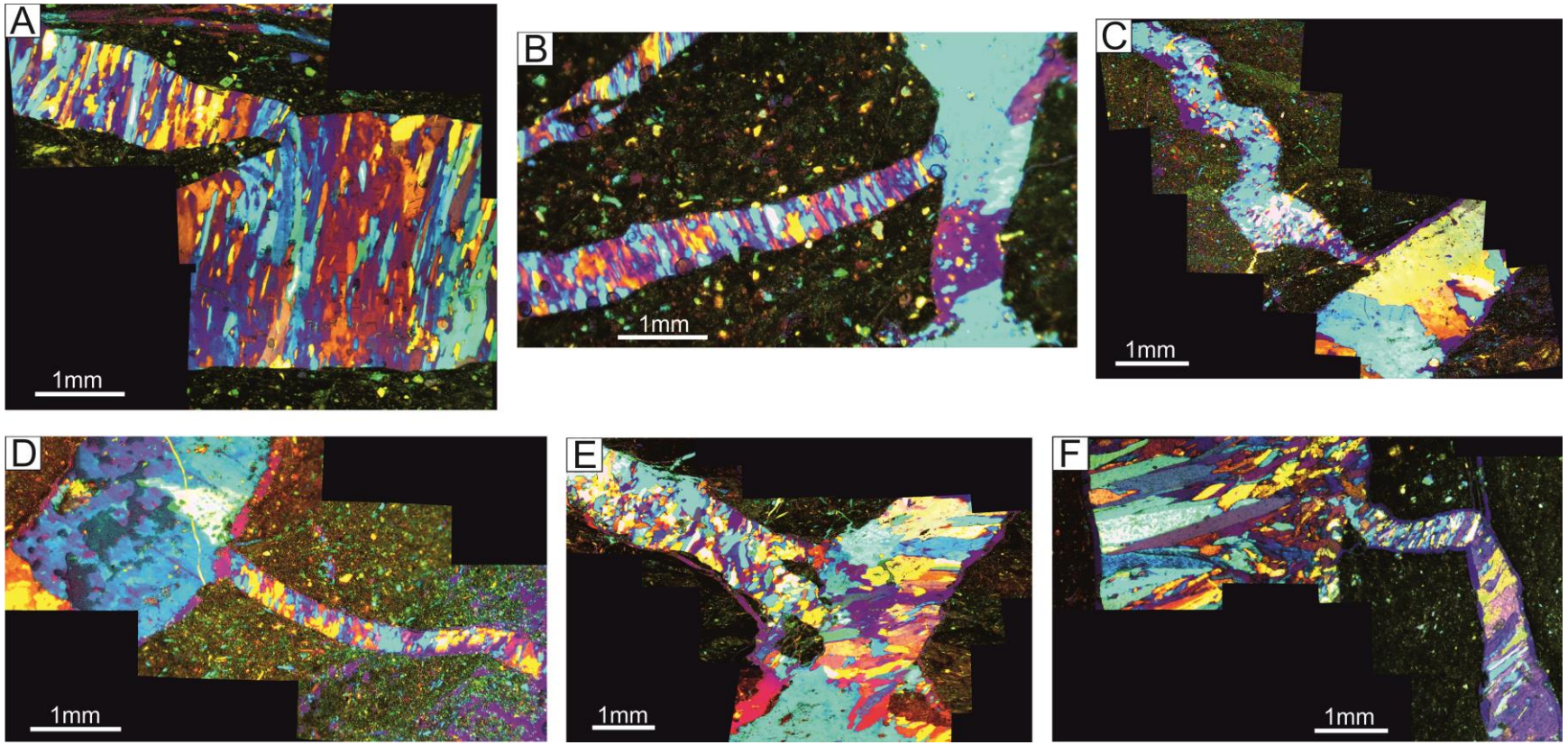


Figure 3.17 Photomicrographs showing the intersections of differently-oriented veins. (A) and (B) Intersection of two veins at an acute angle relative to the other vein. (C) Intersection of a wavy vein with a tapering tip and a thicker vein. (D) and (E) Two intersected veins that are orthogonal to each other. (F) A vein curving towards a larger vein.

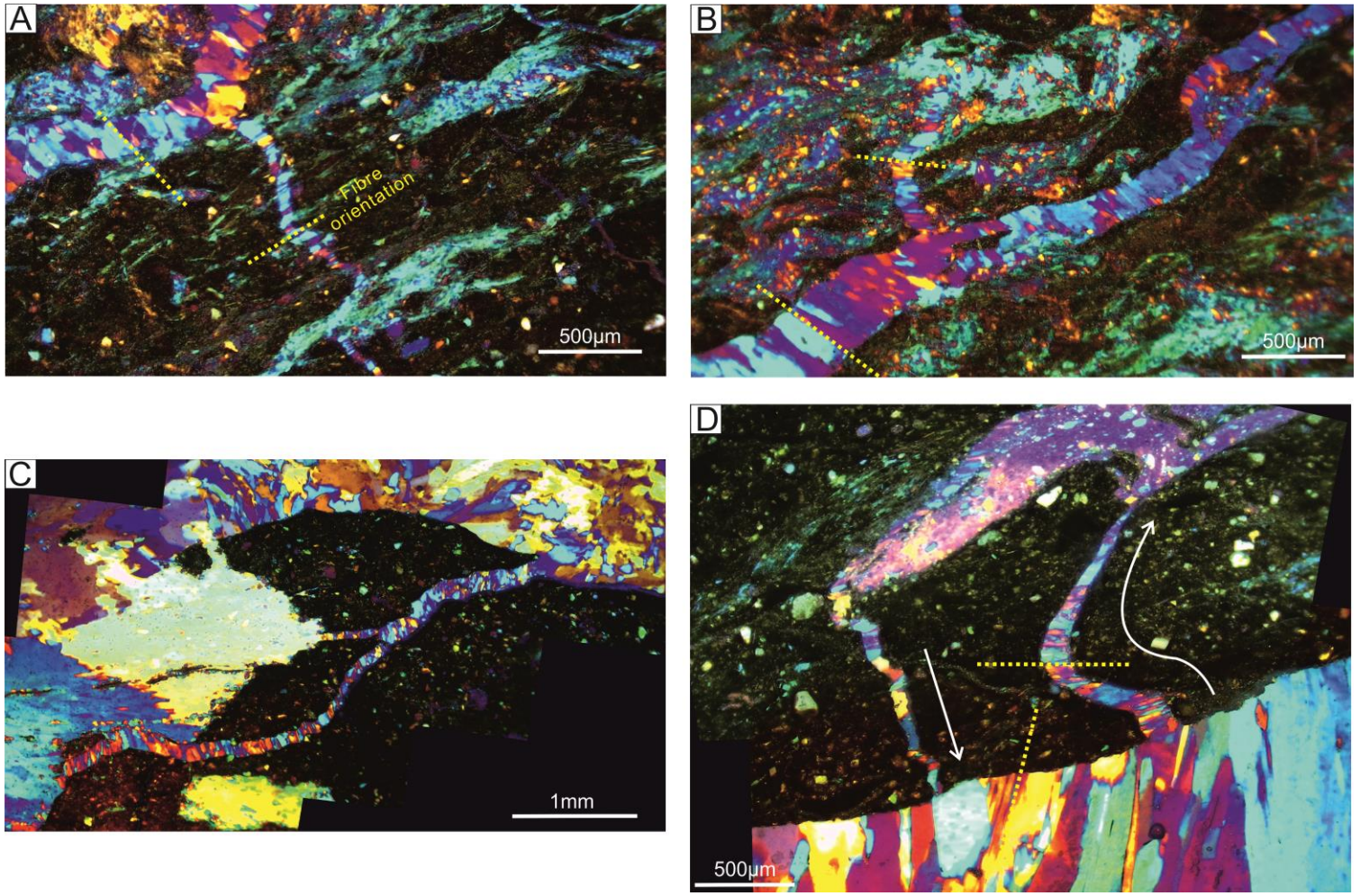


Figure 3.18 Photomicrographs showing the intersection of gypsum veins and nodular gypsum masses. The dashed lines highlight the fibre orientations. The arrows in figure 3.18D marks the propagation of the gypsum veins.

3.4.5 Vein network

The rock hand specimen permits a 3D view of the vein network in the host rocks (Figures 3.19-3.21). The samples reveal a dense vein stockwork, consisting of numerous veins of varying sizes, orientations and shapes. The vein network exhibits a high connectivity, which is established by the vein coalescence and intersection. Similar to the outcrop features, cross-cutting relationships are rarely observed.

Smaller veins commonly curve towards larger veins in the adjacent areas. It is interpreted that the stress shadows of larger veins play a more important role in controlling the propagation direction of smaller veins than the remote stress. Moreover, a low differential stress is inferred, which is evident from the non-systematic orientations of the veins.

It is notable that the oblique veins of vein branches and tension gashes significantly enhanced the connectivity of the vein stockwork (Figure 3.21). They are especially important for linking neighboring horizontal veins. Tension gashes are distinguishable from the branches by low fibre plunges, which marks the opening directions of those veins.

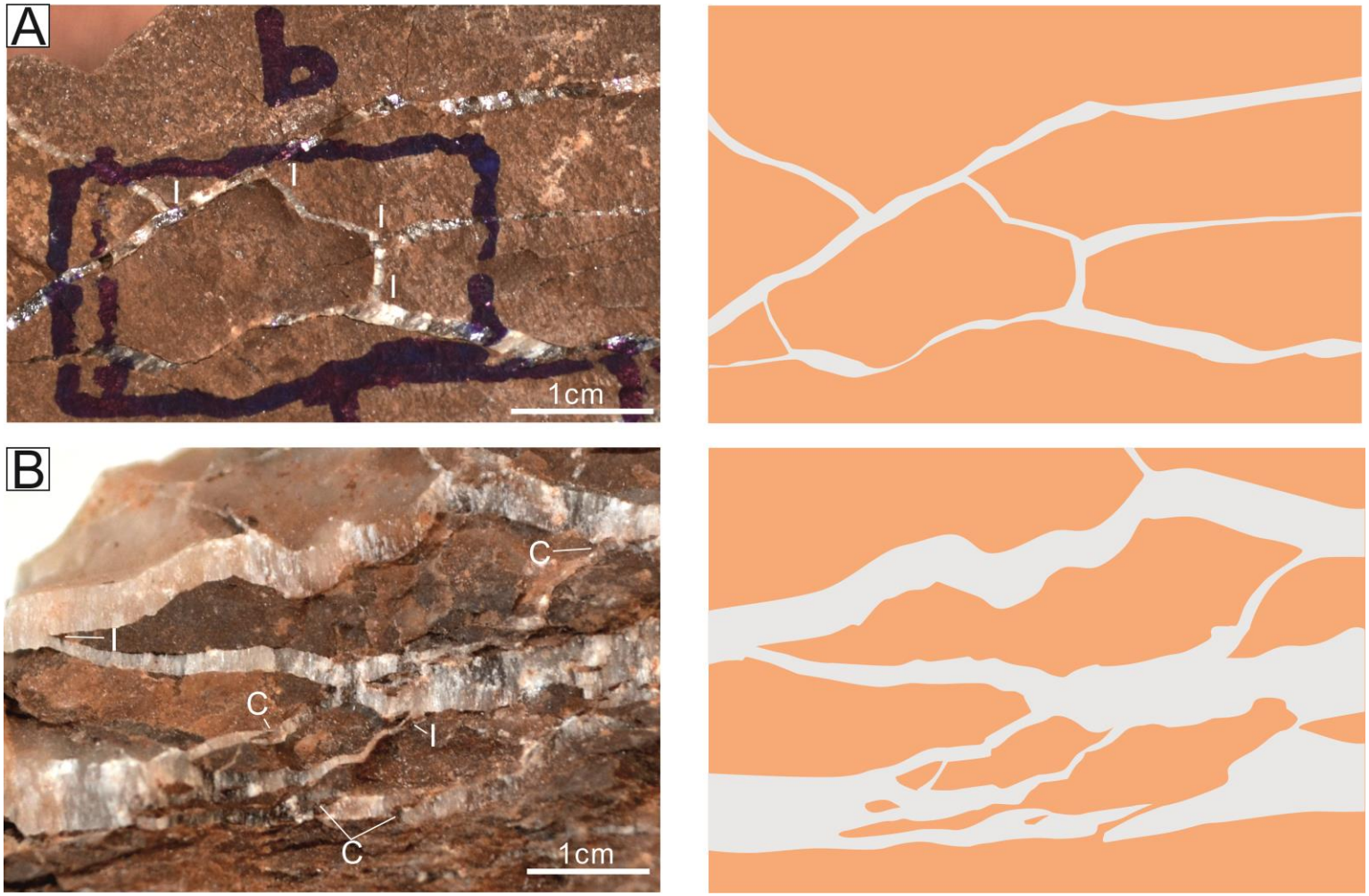


Figure 3.19 Photographs showing the vein stockwork in red marls. Figures on the right are the sketches of the veins. (A) Intersections of veins at high angles relative to the adjoining vein. (B) Vein stockwork resulted from intersection of differently oriented veins and coalescence of parallel-aligned veins. I=intersection. C=coalescence. Samples are from Unit 4.

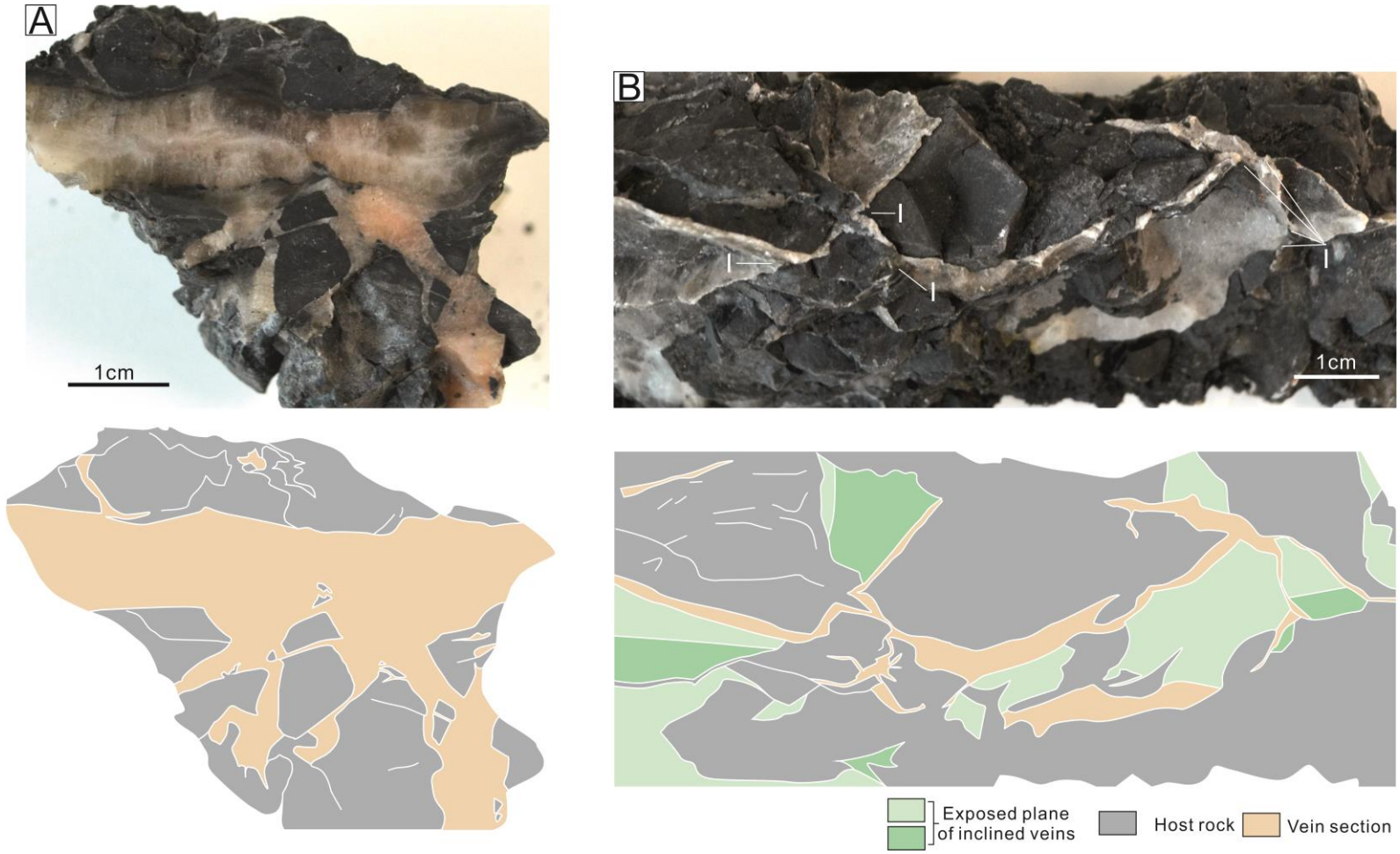


Figure 3.20 Photographs and sketches showing the 3D view of the vein stockwork in the hand specimen of gypsiferous dolomite from the Blue Anchor Formation. I=intersection.

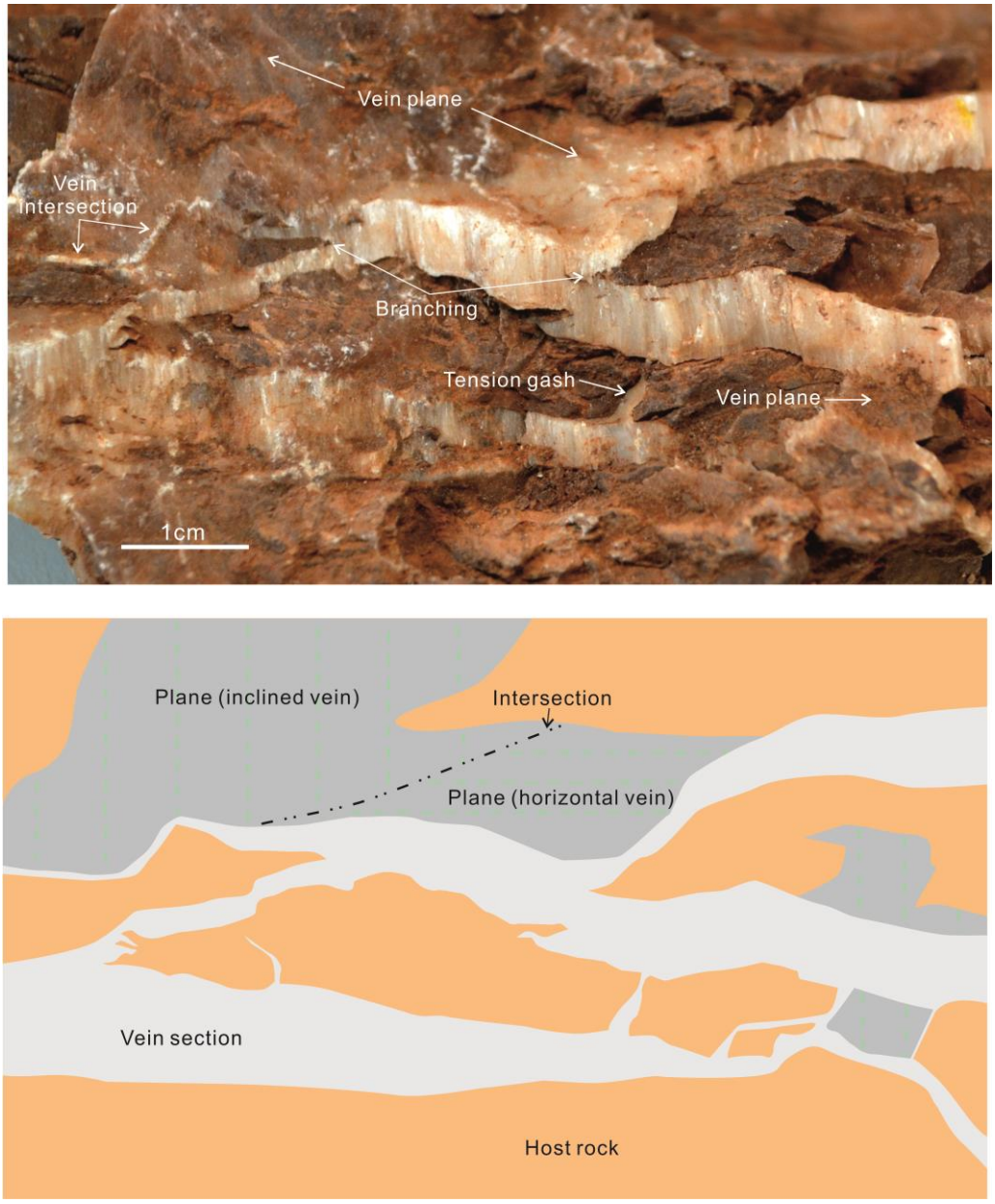


Figure 3.21 Photograph showing the 3D view of the vein stockwork with a high connectivity. Note the inclined veins as branches and tension gashes that link horizontal veins. The sample is from Unit 4.

3.5 Microtexture of gypsum veins

The gypsum veins are filled with densely packed aggregates of equant, elongate or fibrous crystals, thus exhibiting varied textures. This section focuses on the detailed characterization of the composition, crystal morphology, size and arrangements of blocky, elongate and fibrous veins.

3.5.1 Blocky veins

Blocky veins contain numerous interlocked, poorly defined gypsum crystals, exhibiting an overall blocky texture (Figure 3.22). Such veins are commonly irregularly shaped, with fuzzy boundaries. Single crystals are equidimensional and randomly oriented, which rarely extend from one wall to the other.

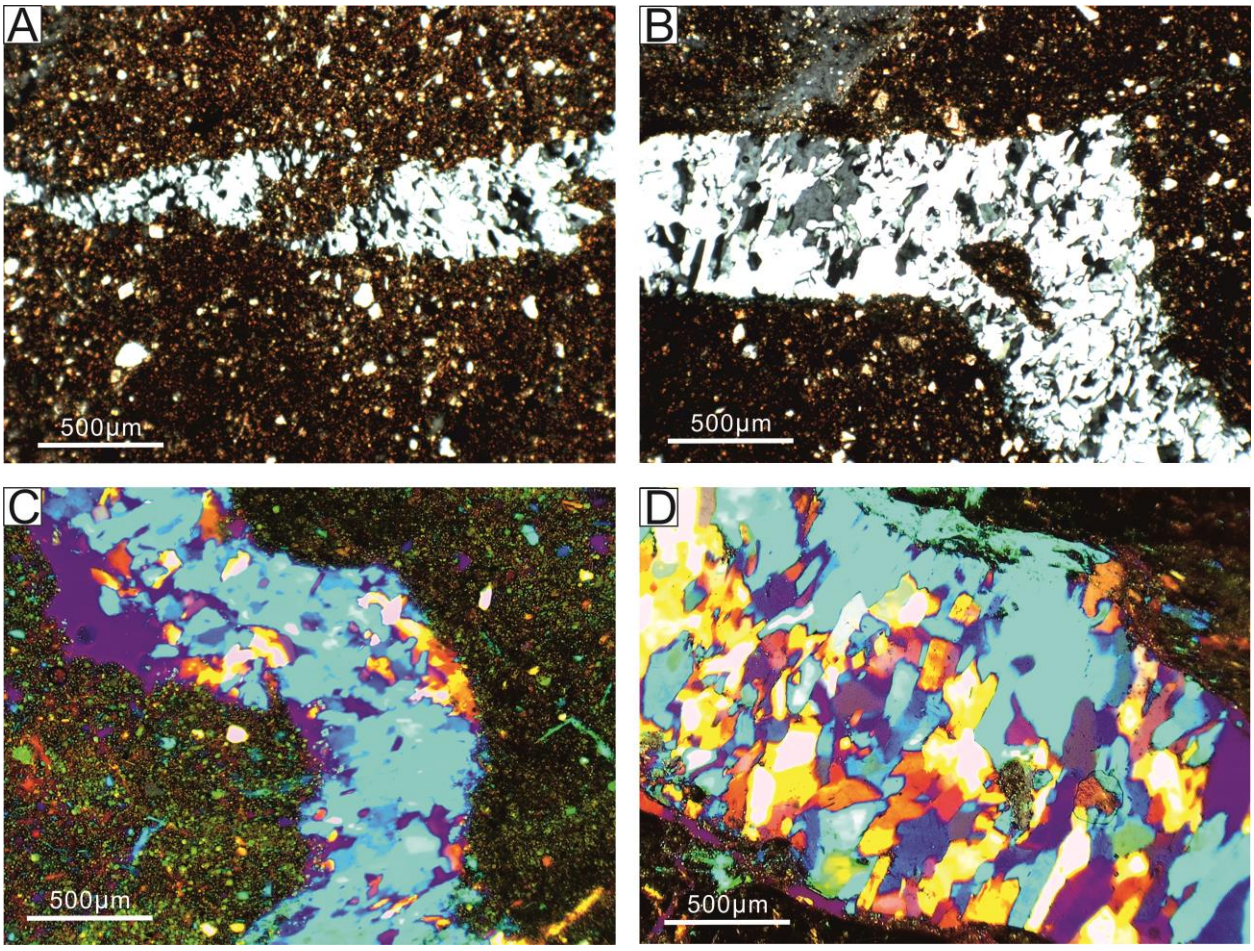


Figure 3.22 Photomicrographs showing the texture of blocky veins. (A) Two veins with irregular shapes and fuzzy boundaries. (B) A curved blocky vein with a clay lens trapped within it. (C) A wavy blocky vein. (D) Interlocked equant crystals in a blocky gypsum vein.

3.5.2 Elongate-fibrous veins

Elongate-fibrous veins mainly consist of gypsum crystals with an elongate shape (Figure 3.23). Compared to the blocky crystals, the elongate crystals exhibit a higher aspect ratio, and occasionally extend from one wall to the other. This is interpreted to be resulted from the suppressing of the growth competition (Hilgers and Urai, 2002). Many crystals become thin and end where they make contact with the neighboring crystals. Equant crystals are commonly developed at the ends of elongate crystals, and exhibit much smaller sizes.

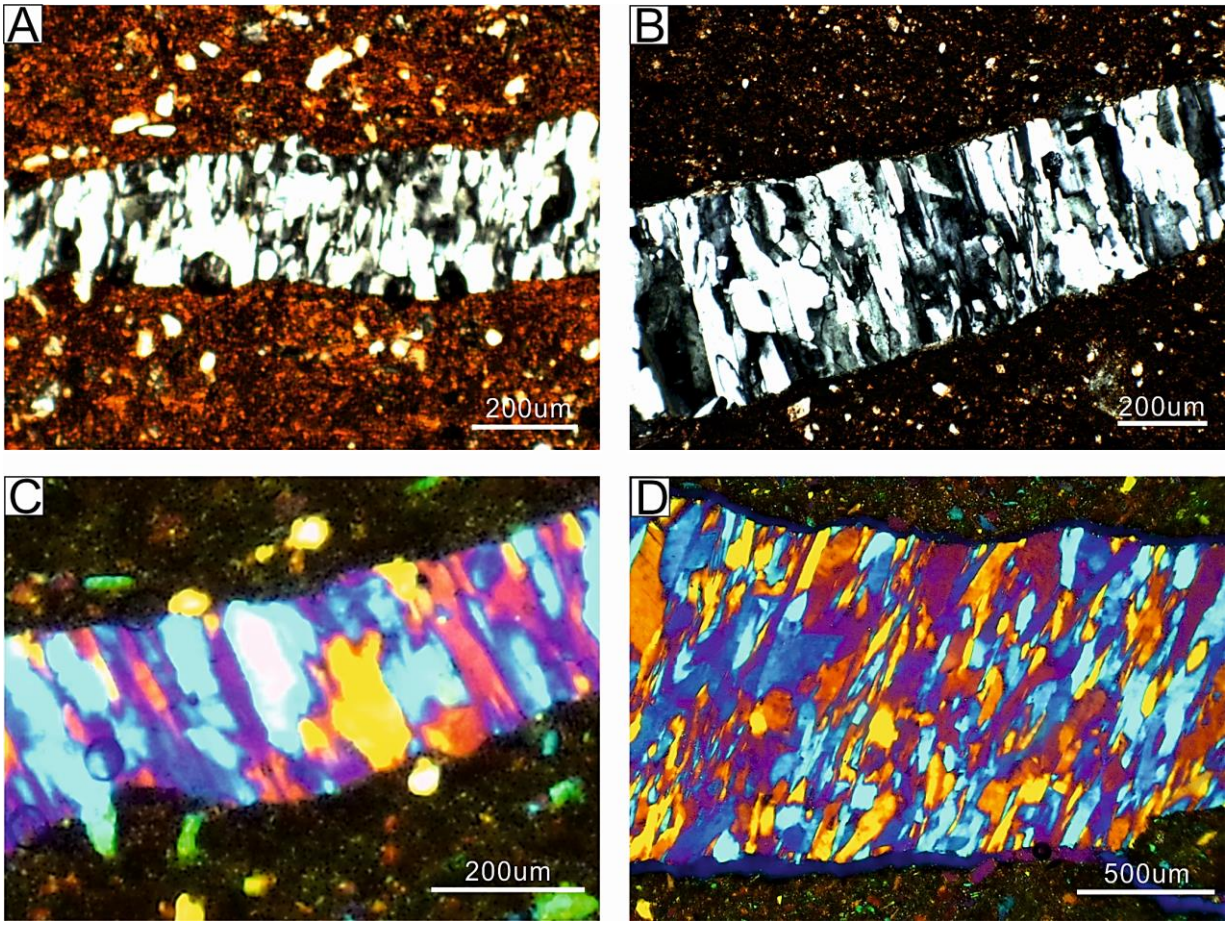


Figure 3.23 Photomicrographs showing the texture of elongate-fibrous veins. (A) Right-lateral elongate crystals in an elongate-fibrous vein. (B) Elongate crystals aligned normal to vein walls. (C) Left-lateral elongate crystals. (D) Numerous blocky crystals between elongate crystals.

3.5.3 Fibrous veins

Fibrous veins can be distinguished from the blocky veins and the elongate-fibrous veins by the presence of needle-like fibres as the main vein-fill (Figures 3.24, 3.25). The fibres are strictly aligned parallel and exhibit clear and smooth crystal boundaries. Single fibres have a high optical continuity with the aspect ratios ranging from 10 to 120.

Unlike the other types of veins, fibrous veins commonly contain a median zone having a blocky texture and a finite width (also see section 2.3.7). The median zone consist of blocky crystals and multiple thin bands of host rock inclusions (Figure 3.24B). The inclusion bands are parallel to the boundaries of the median zones, which are interpreted to have been detached from vein walls during cracking (Hilgers and Urai, 2005). The median zone exhibits typical characteristics of crack-seal veins (Cox and Etheridge, 1983a; Ramsay, 1980) and is interpreted as the result of crack-seal events. The blocky textures were produced in opened fractures by the injection of fluids during each cracking event. Some crystals in the median zones are also fibrous (Figure 3.24C), which could have formed by recrystallization. Fibres are developed on both sides of the median zone, which is interpreted to have grown from the median zone towards the host rock rather than inward growth as the source of gypsum for fibres comes from the enclosing host rock (see section 3.8.5).

Interestingly, fibres on one side of the median zone exhibit smoother fibre boundaries than those on the other side (Figure 3.25C). This is presμmably related to different growth rates and also the degrees of supersaturation of gypsum in the contacting host rocks (Bons, 2001). A faster growth rate and a higher degree of supersaturation contribute to the formation of a more fibrous vein. It is notable that some fibrous veins do not contain median zones (Figure 3.25B), which are especially

common in the tip regions and also vein branches. In those veins, fibres extend from one wall to the other. The absence of the median zone in satin spar veins indicates that such regions in single veins lacks the essential evidence of hydraulic fracturing. The initiation of such fibrous zones is likely to be driven by the growth of fibres in the vein propagation front by the force of crystallization (see section 3.8.4).

The median zones in fibrous veins in siltstones are represented by numerous discrete quartz grains that separate fibres on both sides (Figure 3.24D). The quartz grains occur either as individual or densely-packed aggregates, which are interpreted as residues of the host rock and have been incorporated into the veins during the early stage of fibre growth.

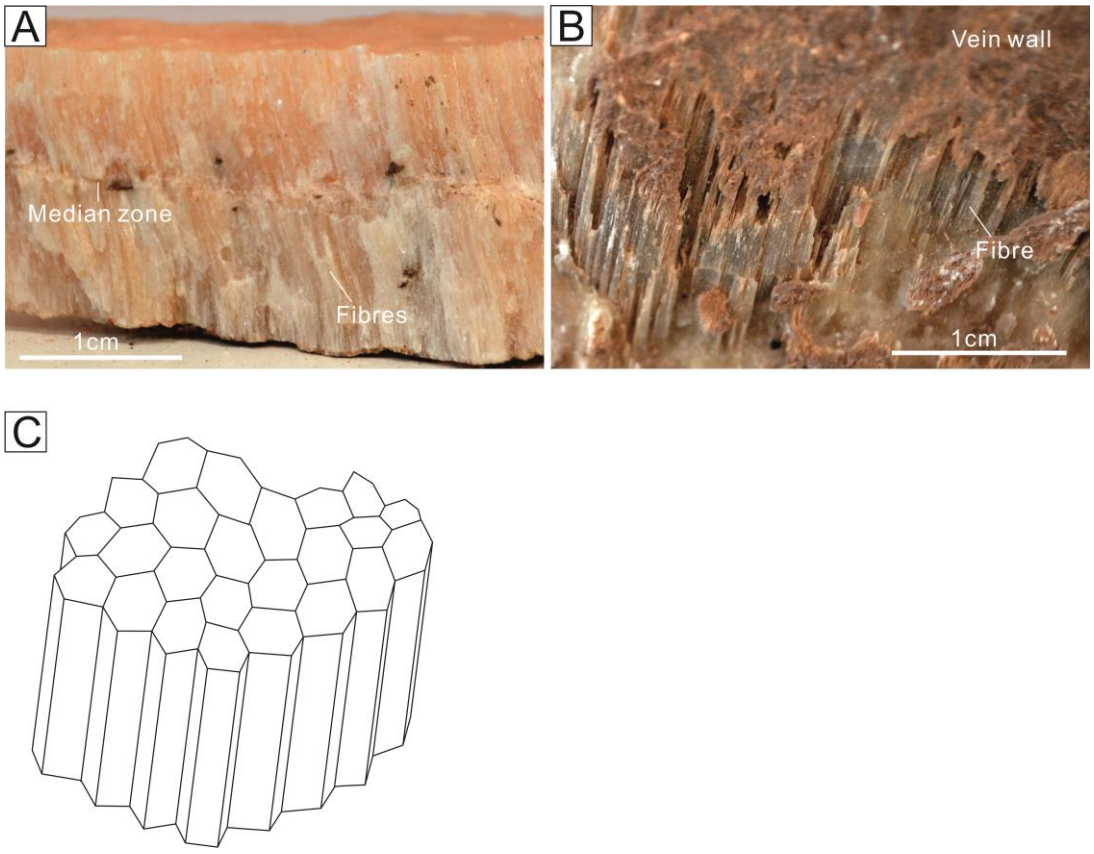


Figure 3.24 (A) Photograph of the section of a representative satin spar vein collected in Unit 4. (B) Photograph showing the vein-wall interface. Note the exposed fibres in 3D due to weathering. (C) Schematic sketch showing the 3D geometry of fibre aggregates of gypsum.

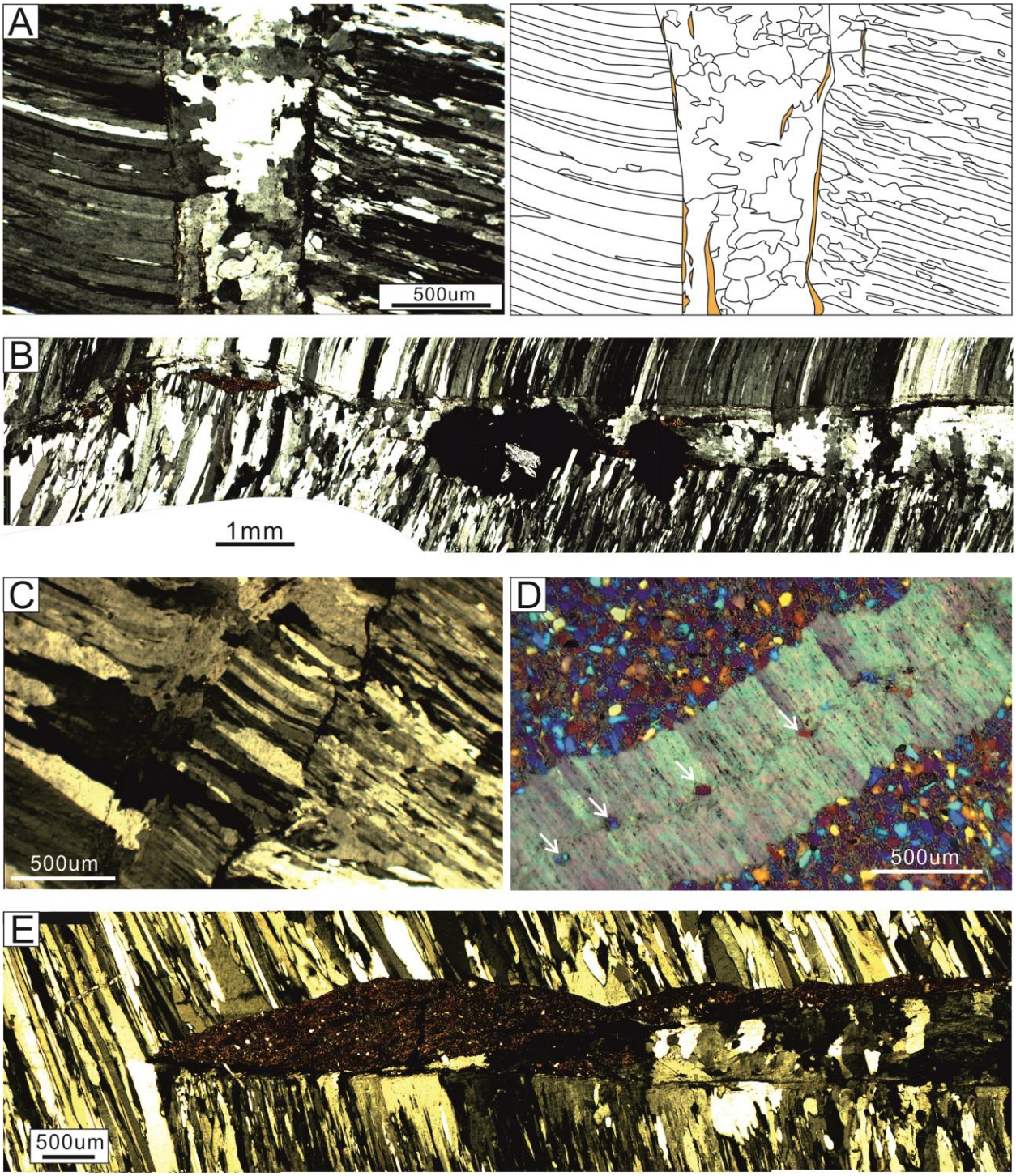


Figure 3.25 Photomicrographs showing the texture of the median zone of satin spar veins. (A) A median zone with thin bands of host rock inclusions. The right figure shows the sketch of the vein in figure 3.25A. Note the yellow bands showing the occurrence of host rock inclusions. (B) A curvy median zone with a varied width. Note the change in the width. (C) The median zone of a satin spar vein exhibiting fibrous texture. (D) A satin spar vein with the median zone filled with discrete quartz grains in the host rock of siltstone. (E) The termination of a median zone in a satin spar vein.

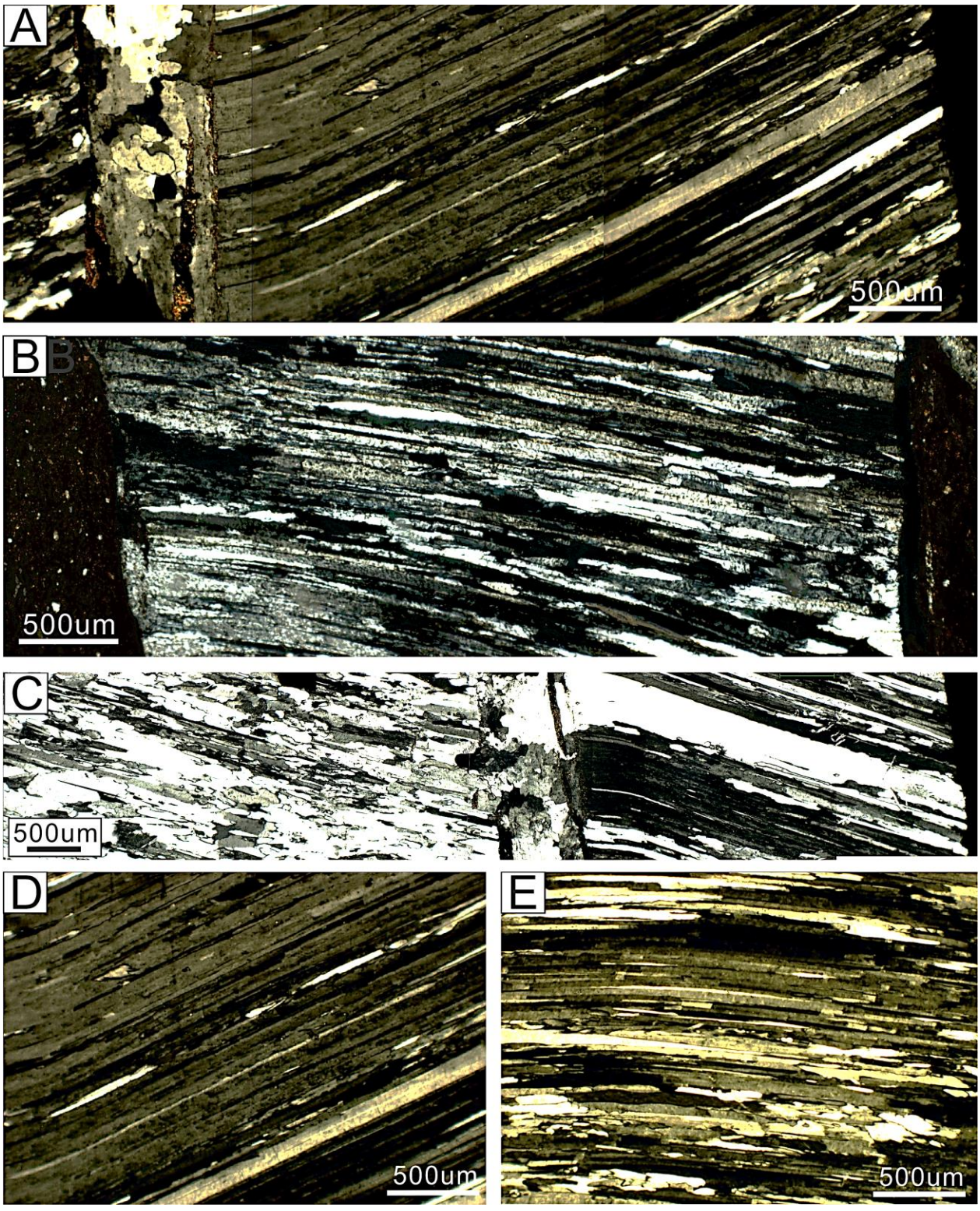

A
500um
B
500um
C
500um
D
500um
E
500um

Figure 3.26 Photomicrographs showing the morphology and arrangement of gypsum fibres within satin spar veins. (A) Gypsum fibres on one side of the median zone. (B) Gypsum fibres in a vein without median zones. (C) Gypsum fibres on both sides of the median zone. Note the crystals on the right are more fibrous than those on the left. (D) Fibres with smooth boundaries and constant width. (E) Occurrence of elongate-blocky crystals within fibrous veins. All samples are from Unit 4.

3.6 Rock segmentation and associated fibres

The walls of fibrous or elongate-fibrous veins are separated by elongate-fibrous crystals that lie at a high angle to the walls (Figure 3.26). In single veins, the fibre orientations commonly remain constant, regardless of the vein orientation. The unevenness of the walls can be matched by their curved traces, which are linked by the associated fibres.

Fibrous veins in siltstones exhibit less smooth vein walls than those in marls. Similarly, the fibres are aligned parallel at a high angle to the walls. It is demonstrated that the dilation direction of the vein, reflected by the jogs, is parallel to the fibre direction (Figure 3.27A). However, the minor unevenness of vein planes can be influenced by discrete quartz grains, which is represented by the quartz grains partially embedded in the vein planes (Figure 3.27B).

Interestingly, some host rock fragments are enclosed by satin spar, which is especially common at vein bifurcations (Figures 3.28, 3.29). Those fragments are partially or completely segmented from the rock matrix. However, the gashes are fully filled with parallel, minor gypsum fibres that exhibit different orientations from those in other veins. The displacement of the segmented rock lenses can be clearly inferred by the associated fibres (Figure 3.28D).

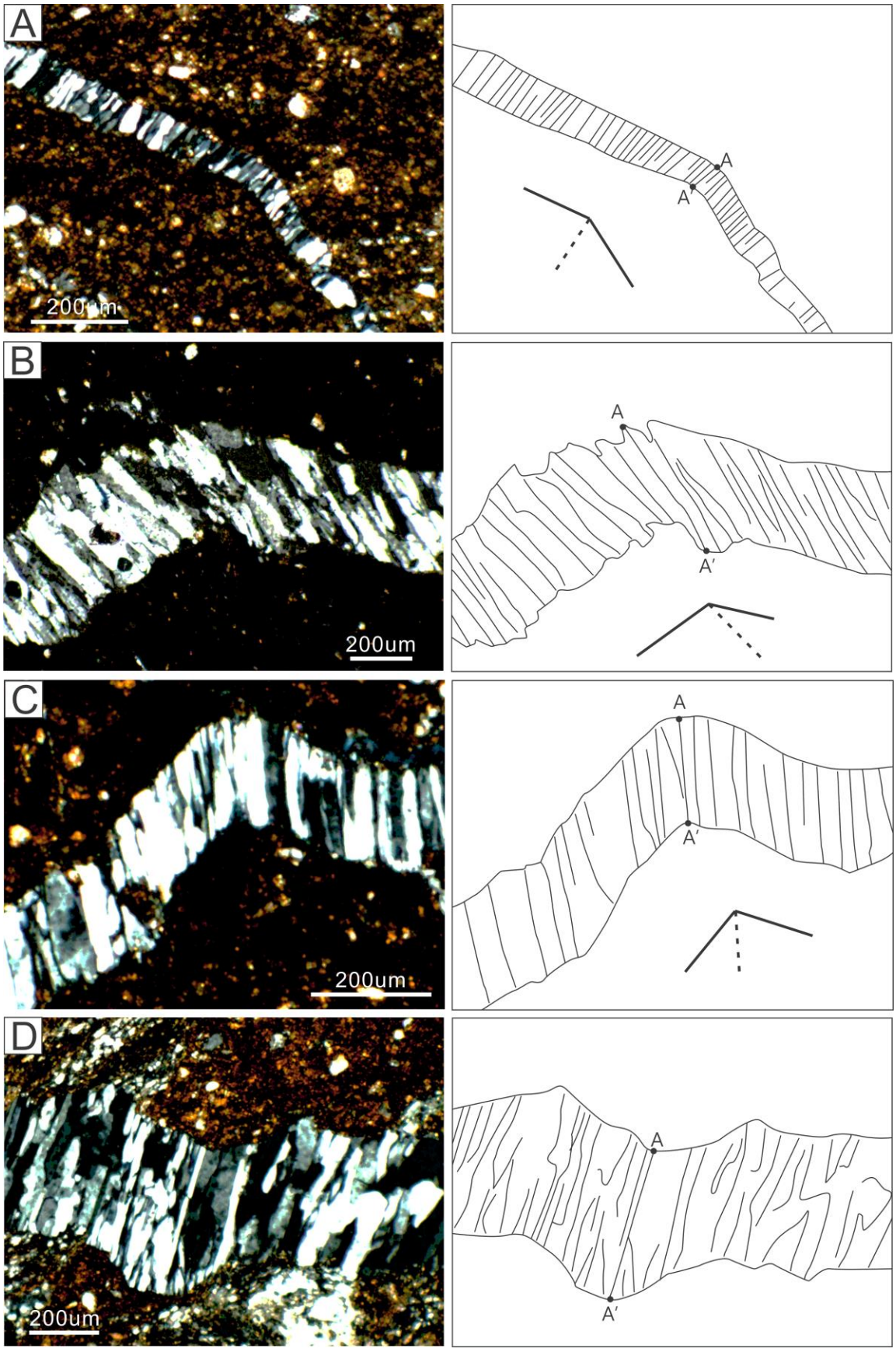

A
200um
A
A′
B
200um
A
A′
C
200um
A
A′
D
200um
A
A′

Figure 3.27 Photomicrographs and their sketches showing consistently oriented fibres in single gypsum veins. (A) A gently curved gypsum vein. Vein and fibre orientations are highlighted by bold and dashed lines respectively. (B) Another gently curved vein with left-lateral fibres. (C) A intensively curved vein. (D) A curved vein with wavy margins. A and A' in all figures are markers that can be matched using fibres.

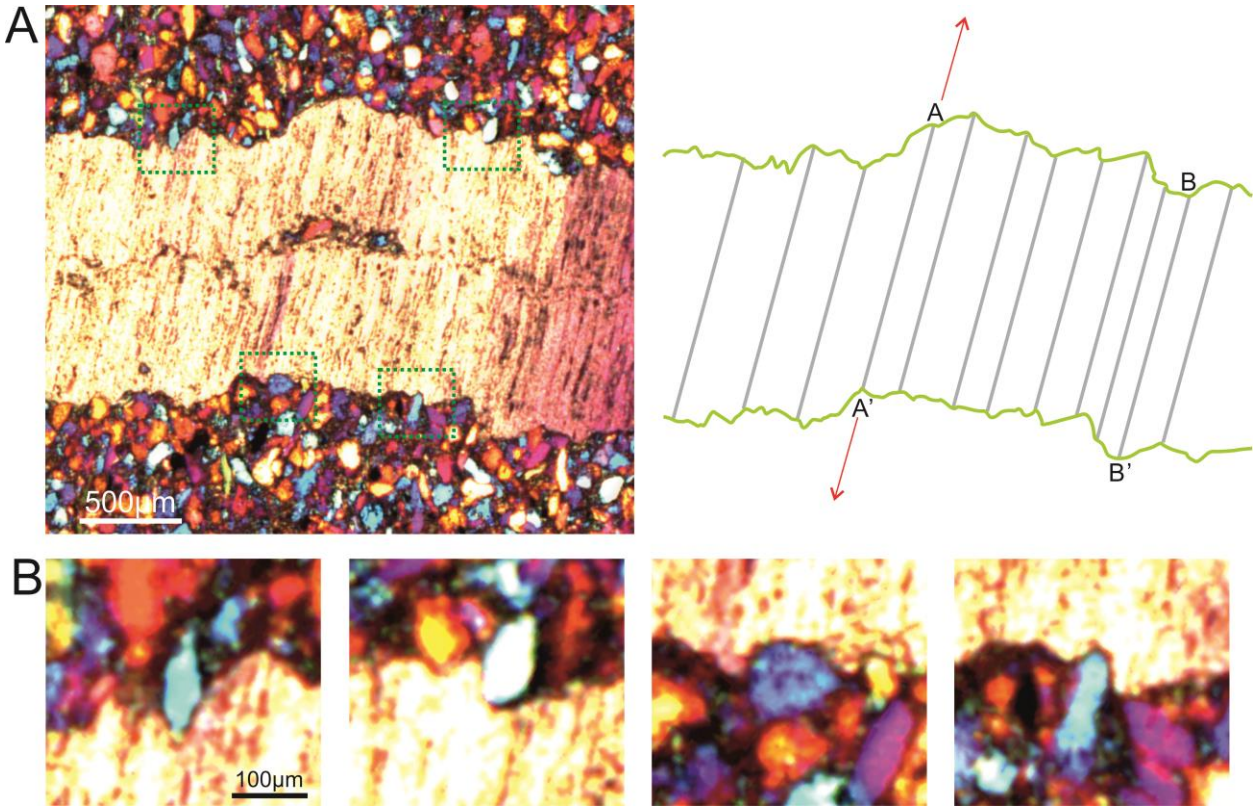
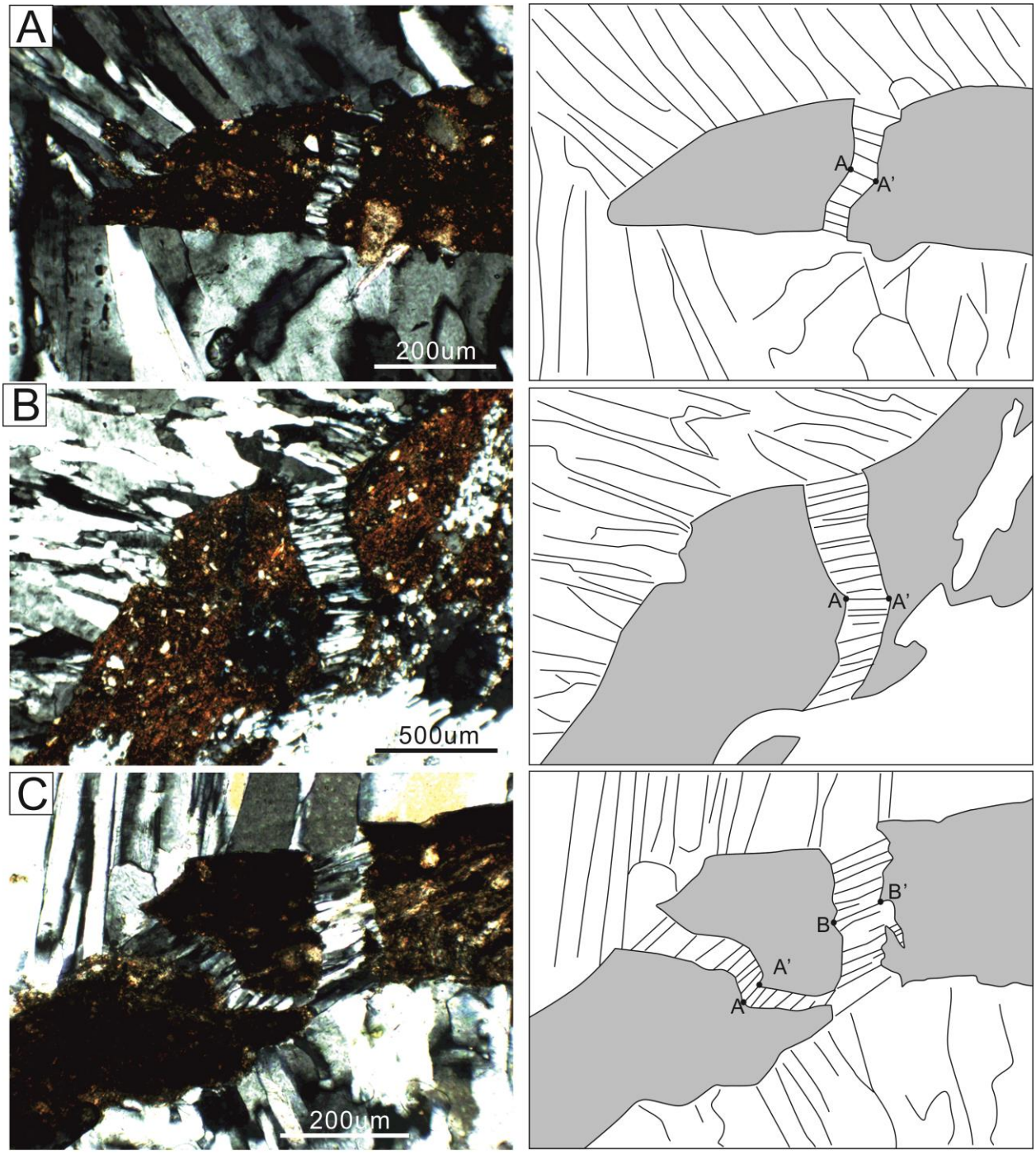


Figure 3.28 Photomicrograph showing a fibrous vein in siltstone. The sketch illustrates the fibre orientation and the walls. Note A and A', B and B' are markers that can be matched. (B) Quartz grains embedded in vein planes. The four figures share the same scale bar. The sample is from Unit 2.


A
200um
A
A'
B
500um
A
A'
C
200um
B'
B
A'
A

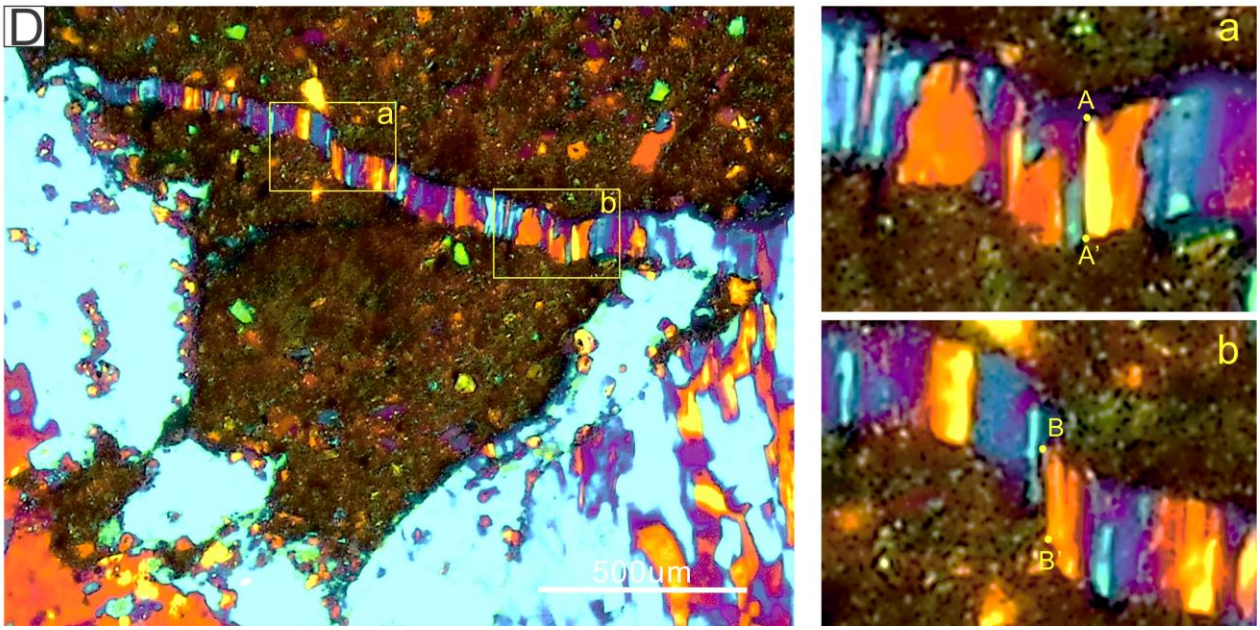


Figure 3.29 Photomicrographs and their sketches showing consistently oriented fibres in minor veins that link segmented host rock blocks. Note the different fibre orientations in the minor veins and the surrounded large fibres. (A) Short gypsum fibres linking a triangle shaped host rock block and the parent block. (B) Fibres linking two separated host rock blocks. (C) Two minor fibrous veins linking a segmented triangle host rock block from the parent blocks. (D) Host rock blocks segmented by a curved fibrous vein. Note the dilation direction of the vein is parallel to the fibre direction.

Figure 3.30A illustrates the segmented rock blocks at a bifurcation where two veins coalesce. The rock block exhibits a right-lateral rotation, indicated by the rock shape and crack-filling fibres. The minor veins that severely damage the host rocks contain fibres in varied lengths and orientations, which are determined by the displacement of the rock fragments.



Figure 3.30 Photomicrographs and their sketches showing partially or completely segmented host rock fragments that are linked with the parent blocks by minor fibrous veins. Note the different fibre orientations in the minor veins and the enclosing large fibres. (A) A triangle shaped host rock block segmented by two minor veins. (B) Several host rock fragments that are linked by satin spar.

Some clay lenses are scattered within satin spar as captive bodies (Figure 3.30). It is sometimes observed that some lenses are segmented by minor fibres which exhibit varied orientations from the enclosing, larger fibres. Similarly, the opening of jogs are indicated by the orientation of the minor fibres.

The backscattered electron image in figure 3.32 illustrates the microfabrics of multiple segmented rock fragments linked by satin spar. The host rock is separated into five major blocks. The unevenness in vein walls of all blocks can be well matched. In the section, block a13, a21 and a22 are completely separated from others, which are bounded by gypsum fibres in varied length and orientations. The long axes of the host rock blocks are generally sub-vertical, while a22 is slightly right-lateral rotated. The large gypsum fibres on the left of the host rock blocks are generally sub-horizontal and slightly tilted to the right. However, gypsum crystals on the right of the rock blocks are predominantly blocky.

Veins c1 and c4 are generally sub-horizontal, while the fibres in both veins are right-laterally inclined at high angles relative to vein walls. Veins c2 and c3 are both inclined and contain left-lateral fibres. The fibres in veins c1-c4 show varied orientations and record the displacement of each rock blocks relative to their primary locations. The vein widths of c3 and c4 both decrease gradually to the right. The width of vein c2 decreases downward till the bifurcation where the crack is not opened. A sub-horizontal crack c5 occurs in block a11 and remains closed.

It is interpreted that the cracking and right-rotation of the rock fragments have been induced by the growth of fibres on the left. All the minor veins formed in a hybrid mode, with the oblique fibres implying a shear component. Fibres in single minor veins, which are parallel to opening directions of jogs, directly indicate the displacement of vein walls.

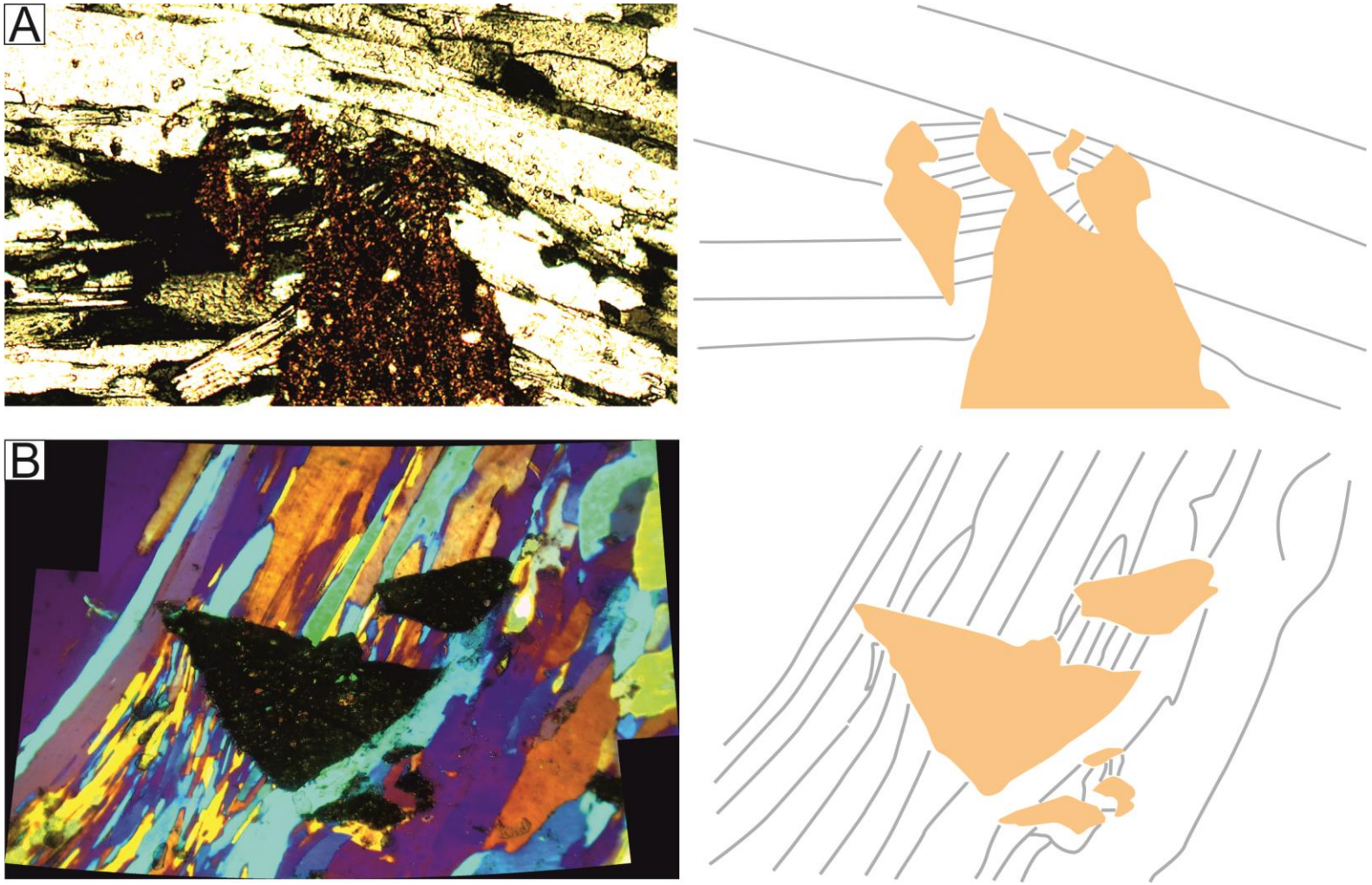


Figure 3.31 Photomicrographs and sketches showing clay lenses enclosed by gypsum fibres. (A) A clay lenses detached from the parent rock block. (B) Multiple clay lenses scattered within satin spar. Note the fibres linking the jogs of the two large lenses.

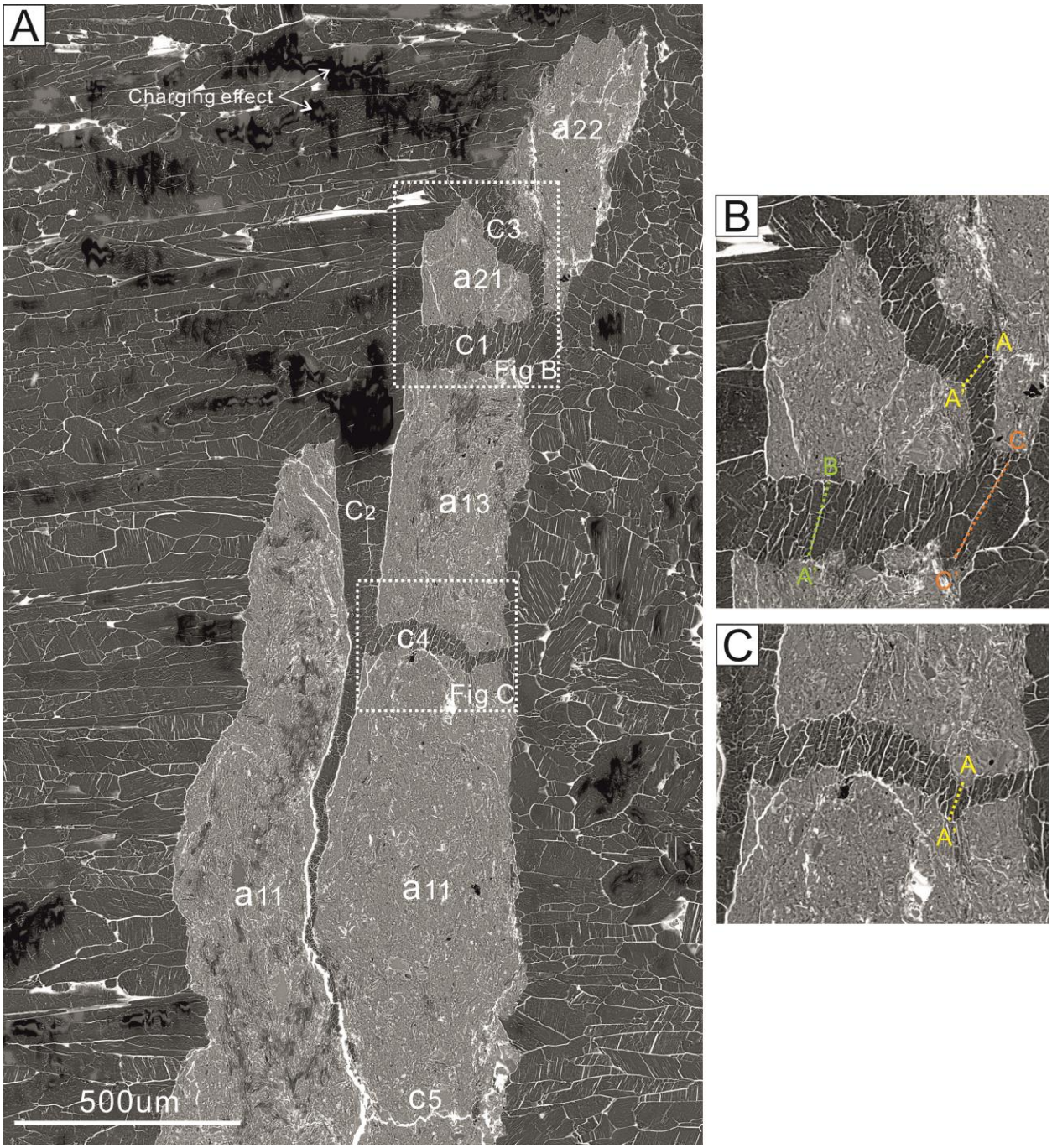


Figure 3.32 SEM images showing multiple host rock fragments that are linked by satin spar. Note the consistent fibre orientations in single veins, which are different from others. The dashed boxes are enlarged in figure (B) and (C). A/A', B/B' and C/C' are matching points. The dashed lines highlight the representative fibre orientations. Note the minor differences in fibre orientations in different veins.

3.7 Mineral composition of the host rock

The lithological characteristics of lithological units are as follows. The rocks in all the units consist mainly of clay minerals, carbonates, quartz, albite and K-feldspar (Figure 3.33). All mineral grains are mainly smaller than 50 μm, i.e. silt sized. Quartz is present throughout all units in the Keuper Marl. It is the main silt-sand sized detrital mineral and may be poorly to well-sorted. The grain shapes vary between angular and sub-rounded. Dolomite and calcite are important components of the marls as the main cementing agents. Dolomite is the most common carbonate in all units and may locally comprise up to 30% of the carbonate- rich beds. Calcite mainly occurs in Unit 3, where gypsum is absent in the rock matrix (Figure 3.33C). The carbonate particles in Unit 3 are more closely spaced, commonly showing linear-contacts. Dolomite may occur as euhedral rhombs in this unit.

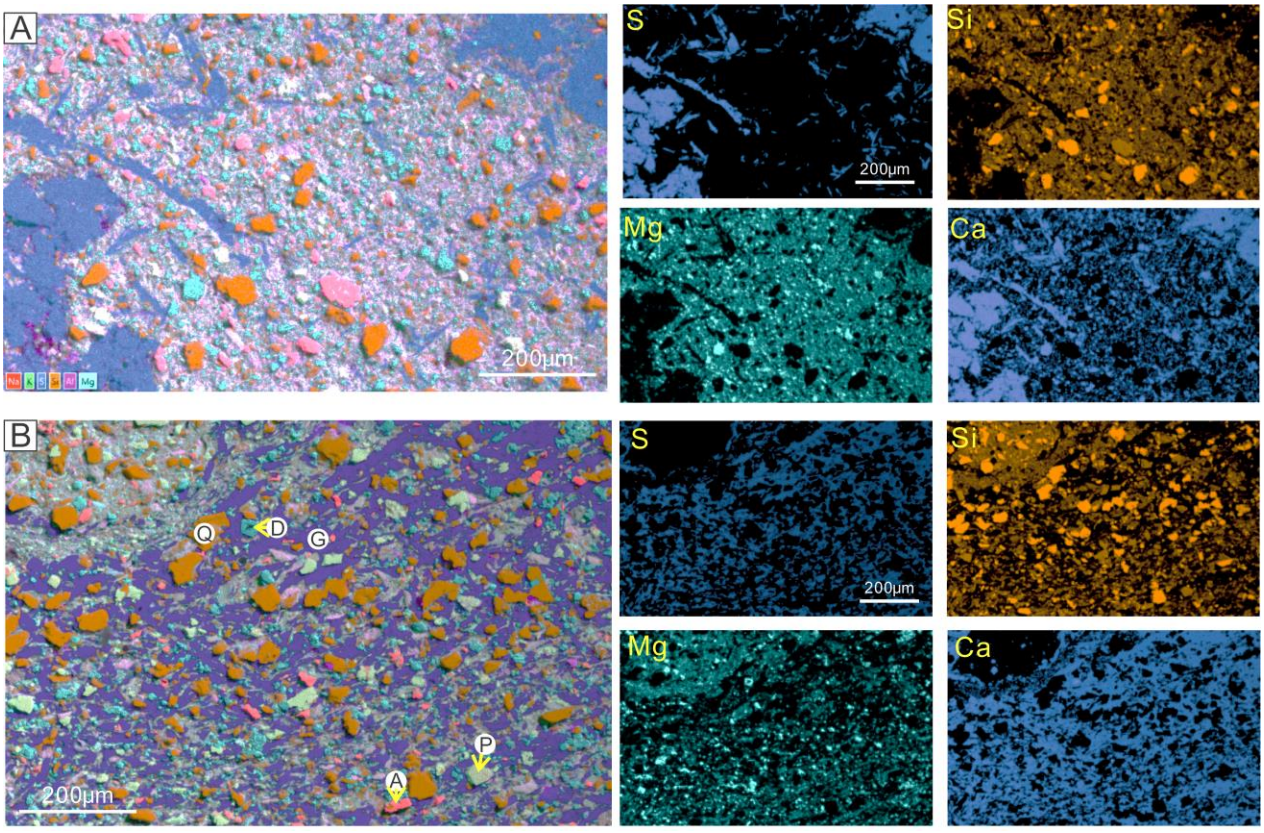
The Keuper Marl Formation

Gypsum appears in Units 1, 2 and 4, while it is absent in Unit 3 and 5. Gypsum mainly occurs as needle-like laths individually or in clusters. The long axes of such crystals are mostly lower than 200 μm and near-randomly oriented when they are isolated from others. Gypsum also occurs as deposits of mini nodules. The gypsum crystals are frequently sub-parallel to the adjacent nodules. However, gypsum with high intra-connectivity is widely disseminated in Unit 4, locally serving as the matrix that supports other minerals. The content of gypsum in Unit 4 is significantly higher than other units.

Halite is absent in all units. As halite is highly soluble and usually removed by groundwater within 40-60 m of the subsurface, it is interpreted that the halite in the outcrop have been dissolved by

meteoric flushing during basin uplift. Other non-clay minerals are present as minor constituents of the marl, including feldspar and heavy minerals such as titanium-iron oxides, apatite, zircon and monazite (Hobbs et al., 2002; Jeans, 1978). The main clay minerals in the Mercia Mudstone are illite, chlorite and mixed clay clays (illite-smectite, chlorite-smectite) (Jeans, 1978). Detrital illite is the main component of the clay mineral assemblage (Leslie et al., 1993).

Porosity is extremely low in all the units except Unit 5 (Figure 3.34). The pores in Unit 5 occur either as discrete individuals or in clusters that show high connectivity. The total porosity may reach up to 30% locally.



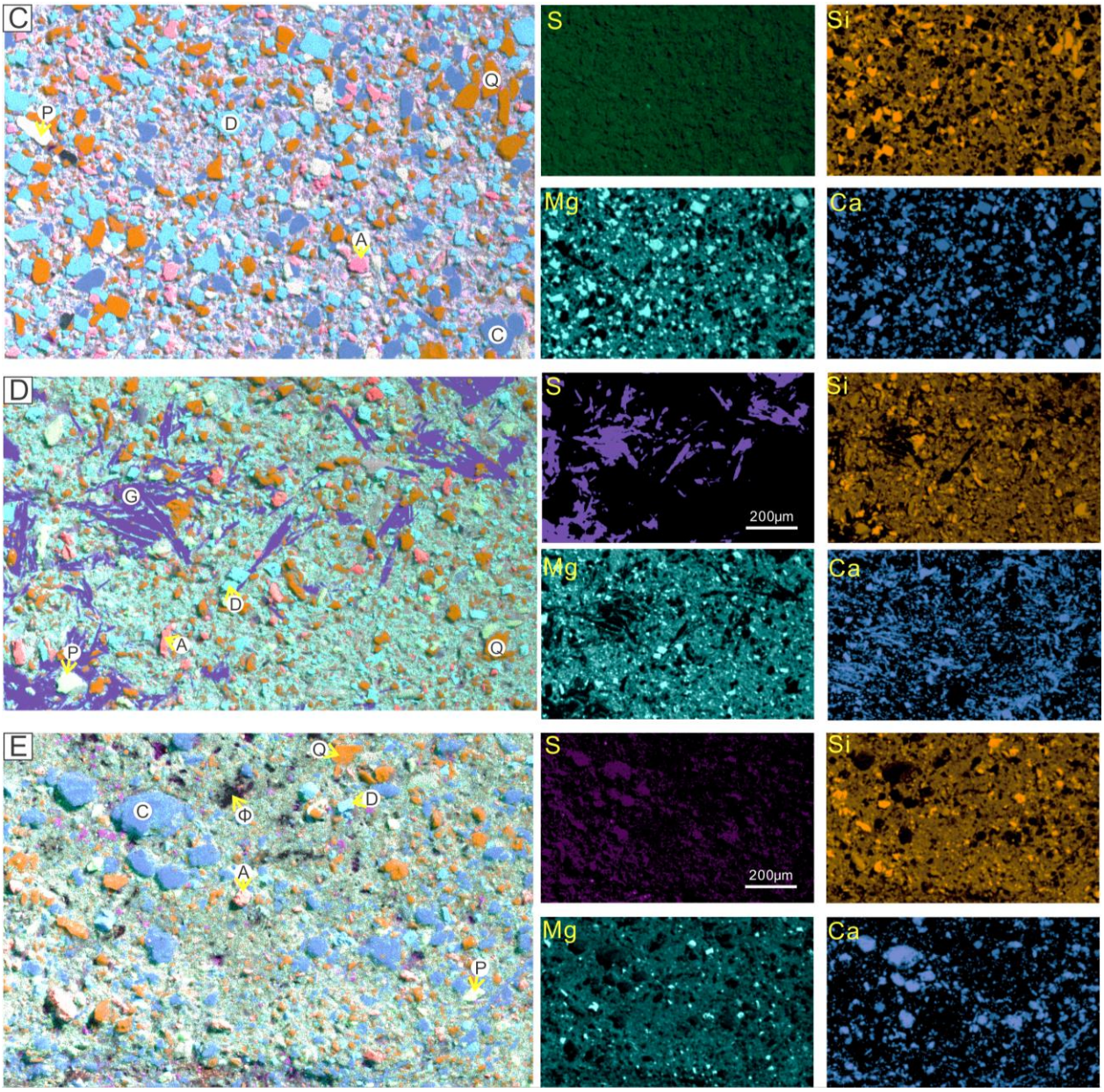


Figure 3.33 EDS images showing representative rock texture and mineral composition of different lithological units of the Mercia Mudstone. (A)–(E), Unit 1 – Unit 5. A, albite; C, calcite; D, dolomite; K, K-feldspar; Q, quartz; Φ, pore.

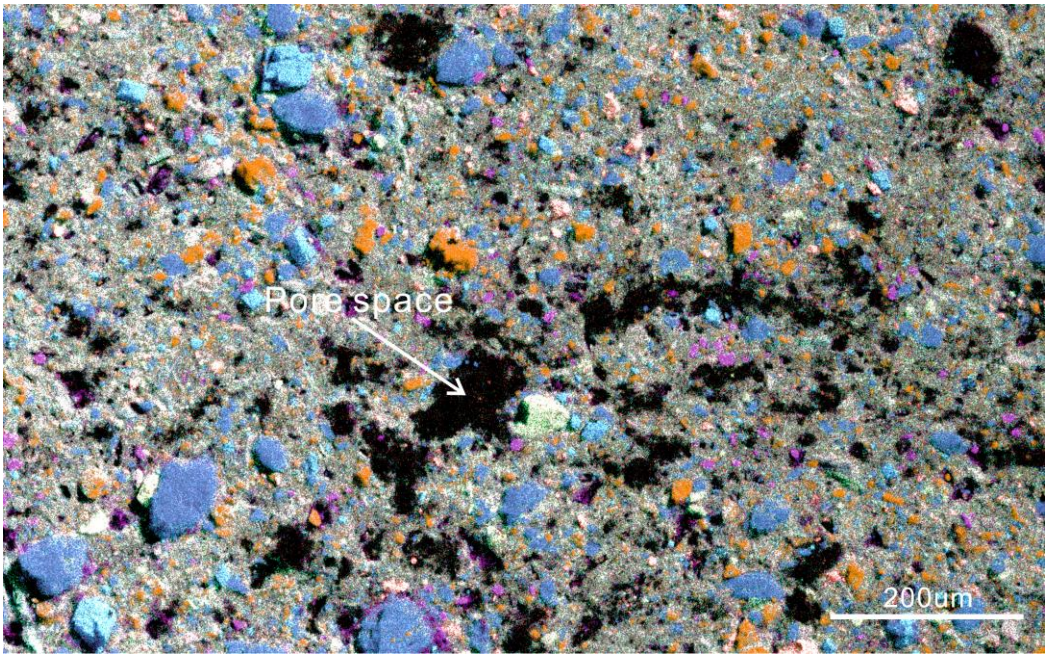


Figure 3.34 EDS image showing the pore spaces in the rock matrix of Unit 5.

The Blue Anchor Formation

The Blue Anchor Formation consists of interbedded dark silty marls and dolomites (Figure 3.35). The marls mainly consist of clay minerals, quartz, dolomite, albite and K-feldspar. The dolostone mainly comprises dolomite, quartz, K-feldspar and albite. All non-clay mineral grains are below silt-sized. The striking difference of rock mineralogy in the Blue Anchor from the Keuper Marl is that gypsum rarely occurs as disseminated crystals or cements in the rock matrix. Gypsum is localized within veins as the main cement.

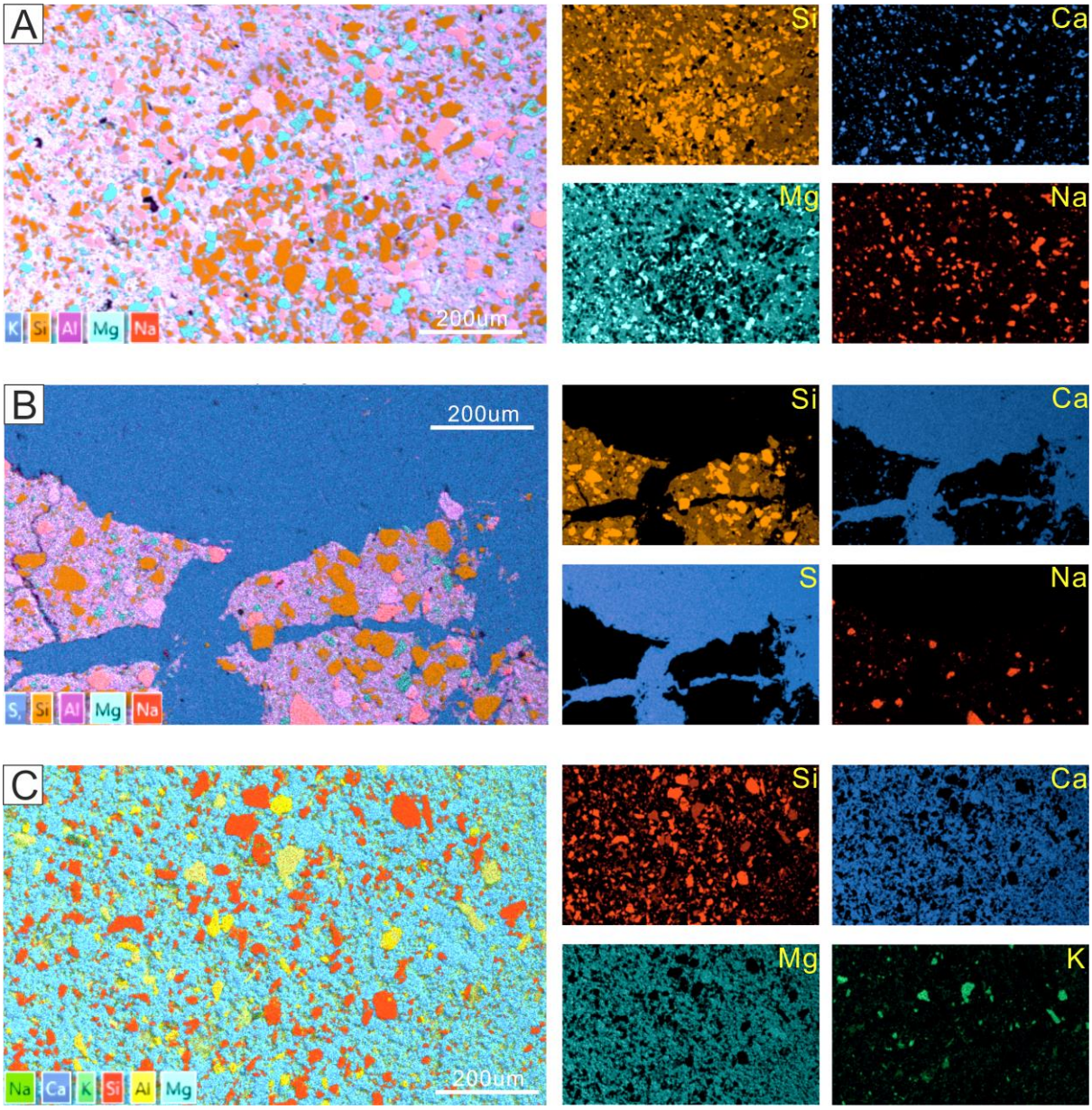


Figure 3.35 EDS images showing representative rock texture and mineral composition of rocks in the Blue Anchor Formation. (A) The dark marl. (B) Gypsum vein and the wall rocks of dark marls. (C) Dolomite.

3.8 Discussion

The discussion focuses on the origin of the microtextural characteristics of gypsum veins, the fibrous habit, vein opening mechanisms, the kinematic implications of fibre orientations, and also the lithological control on vein development, from the microscopic observations in this chapter, coupled with the corresponding macroscopic features at outcrops.

3.8.1 Microtextural expressions of hydraulic fracturing

As is discussed in section 2.6.2, the gypsum veins have initially been produced as hydraulic fractures due to overpressure. Petrographic evidence for this explanation lies in the blocky microtextures exhibited in some blocky veins and the median zones of fibrous veins. It has been suggested that blocky crystals form when growth competition leads to some crystals overgrowing others, which occurs in fluid-filled vugs or fractures (Bons, 2001; Fisher and Brantley, 1992) (Figure 3.36). The growth competition takes places with only a few favourably oriented grains surviving (Passchier and Trouw, 1996), and is responsible for the equidimensional crystal morphology. Such a phenomenon has been frequently observed in the field and verified by experimental and numerical studies (Hilgers et al., 2003; Hilgers et al., 2001).

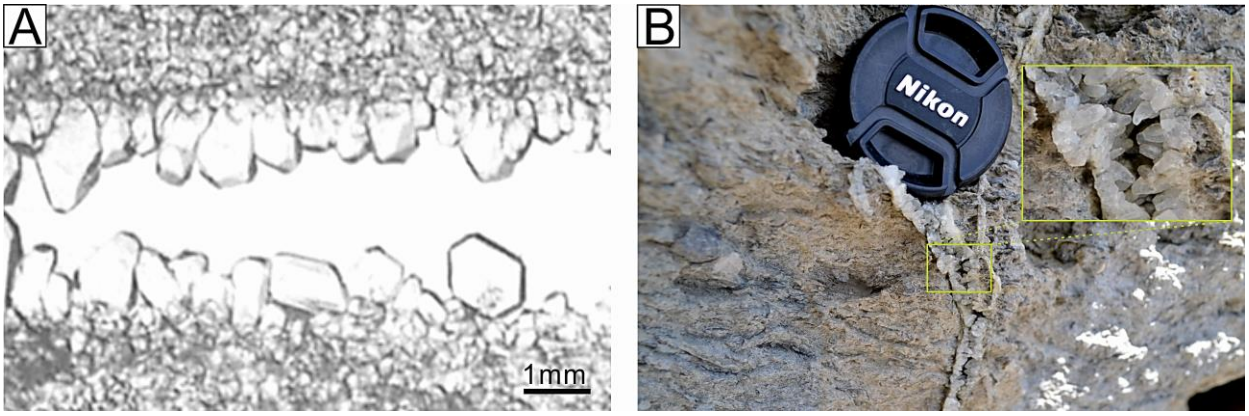


Figure 3.36 Experimental syntaxial growth of alum crystals in a channel of advective supersaturated solution. Adopted from Hilgers et al. (2003). (B) Photograph showing a blocky calcite vein in the Purbeck Group in the Wessex Basin. Note the vugs in the vein.

Because the median zones are considered as the seed vein and form the substrate for subsequent vein growth (Oliver and Bons, 2001), their blocky texture indicates a fracture opening by fluid injection. However, the filling of the median zone with a width up to 500 μm could not have been accomplished in a single phase, indicated by the occurrence of multiple host rock inclusion bands. The wall-parallel inclusion bands are believed to result from the detachment of vein-wall interfaces by the changes in the adhesion between the host rock and the vein (Hilgers and Urai, 2005). This is likely to be caused by dilation of pore spaces as a result of evaluated pore pressure. Crystal nucleation would subsequently occur between the wall rock and the inclusion band that has been fragmented off from the wall. Hence, the inclusion band is arranged parallel to the vein wall. However, the incorporation of another inclusion band seems unlikely during crystal continuous growth (Means and Li, 2001). It is suggested that the alignment of multiple inclusion bands can be given rise to by crack-seal events (Cox and Etheridge, 1983a; Holland and Urai, 2010; Laubach et al., 2004; Ramsay, 1980).

Crack-seal refers to a process of repeated increments of microcrack opening under accumulation of elastic strain associated with fluid pressure, followed by sealing of the microcrack by precipitation of minerals from solution (Ramsay, 1980). Each crack episode preferentially takes place along the vein-wall interface due to the low tensile strength and weak bonding between the mineral grains in the veins and grains in the host rock (Gale et al., 2007), which potentially triggers

the detachment of host rock inclusions and a subsequent incorporation into the veins (Figure 3.37A).

The periodically re-opened gypsum veins can serve as conduits for fluid flow (Rustichelli et al., 2016), with a much higher permeability than the intact wallrock of marls. This is accompanied with the decrease in the fluid pressure and also the resulting drop in solubility of gypsum (Henderson and McCaig, 1996; Phillips, 1972), which could possibly lead to a rapid supersaturation and instantaneous precipitation.

The fluid pressure within the cracks is generally lower than the average pore pressure in the country rock with a differential stress acting on the rock, which help suck pore fluid into the crack (Oliver and Bons, 2001). When inflow outweighs outflow, the crack increases in volμme and becomes unstable and ascends as mobile hydraulic fractures (Bons, 2000; Weertman, 1980). This process could significantly enhance vein network connectivity by linking neighboring fractures as weak planes, including horizontal fractures, en echelon fractures, and reactivated pre-existing fractures.

Another episode of overpressuring could be resulted from sealing of veins and the associated decrease in permeability that help buildup overpressure again (Figure 3.37B). The sudden fracturing, release of fluid and reduction in fluid pressure can be explained by the fault-valve model or seismic pumping (Cox, 1995; Sibson, 1992). This is especially evident from the complex fault-vein fabrics with abundant host rock fragments in the median zones (see section 2.3.3.4) and multiple phases of fault activities (see section 2.6.1).

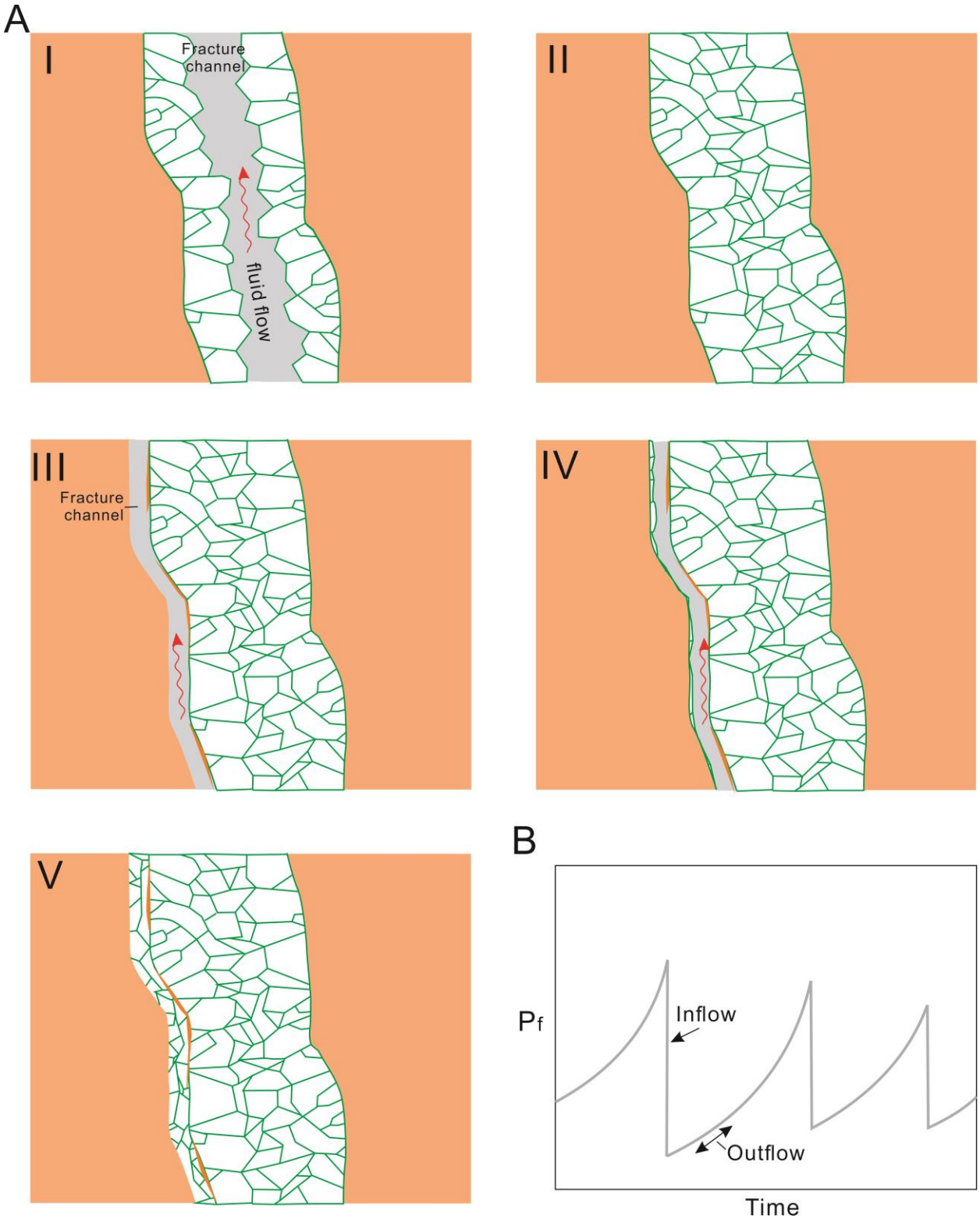


Figure 3.37 Cartoon illustrating one episode of crack-seal event and the process of incorporation of solid inclusion band in the vein. I: Fracture opening by fluid injection. II: Fracture sealing by blocky crystals.

III: Vein re-opening by overpressure. IV: Detachment of wallrock and crystal nucleation in the fluid channel. V: Vein sealing. (B) Cyclic overpressure and subsequent pressure drop due to cracking. Modified from Oliver and Bons (2001).

3.8.2 Growth of fibres

The different crystal morphology, size and orientation of gypsum fibres from blocky crystals indicate that they do not share the same formation mechanism (Bons and Montenari, 2005). The nucleation and growth of fibres cannot occur in fluid-filled fracture channels for the following reasons:

(1) The lack of overgrowth between neighboring fibres suggests that the growth competition is suppressed. This could only take place if fibres grow in an extremely limited space with width less than 10 μm (Hilgers and Urai, 2002) or on an essentially closed surface (Bons and Jessell, 1997; Hilgers et al., 2001; Means and Li, 2001).

(2) Unlike the median zones with abundant solid inclusions, the fibres are pure in composition. As is argued in section 3.8.1, the inclusions have been incorporated during cracking by fluid injection. The lack of such inclusions in fibres is thus incompatible with hydraulic fracturing.

(3) It is suggested that only if the potential growth rate of crystals exceeds the opening rate of vein walls can the crystals be fibrous (Hilgers et al., 2001). This idea is reasonable as the neighboring crystals will grow at the same rate under this condition, which help avoid overgrowth.

(4) The optical continuity and smooth boundaries of single fibres indicate a continuous growth process. Such features do not appear in crack-seal fibres with an incremental growth.

(5) Fibres could grow symmetrically on both sides of the median zone. If the fibre growth occurs in fluid-filled fractures, there would be two simultaneous fracturing on both sides of the median zone. Such a condition is unlikely as the release of pressure by fracturing on one side of the median zone would prevent fracturing on the other side (Bons and Montenari, 2005).

(6) Fringe structures with mineral fibres growing around a rigid object demonstrate that fibre growth does not necessarily involve fracturing (Figure 3.38). The formation mechanism of such structures is beyond the scope of this study. Readers may refer to Koehn et al. (2000), Koehn et al. (2003), Passchier and Trouw (1996) and Bons et al. (2012) for explanations.

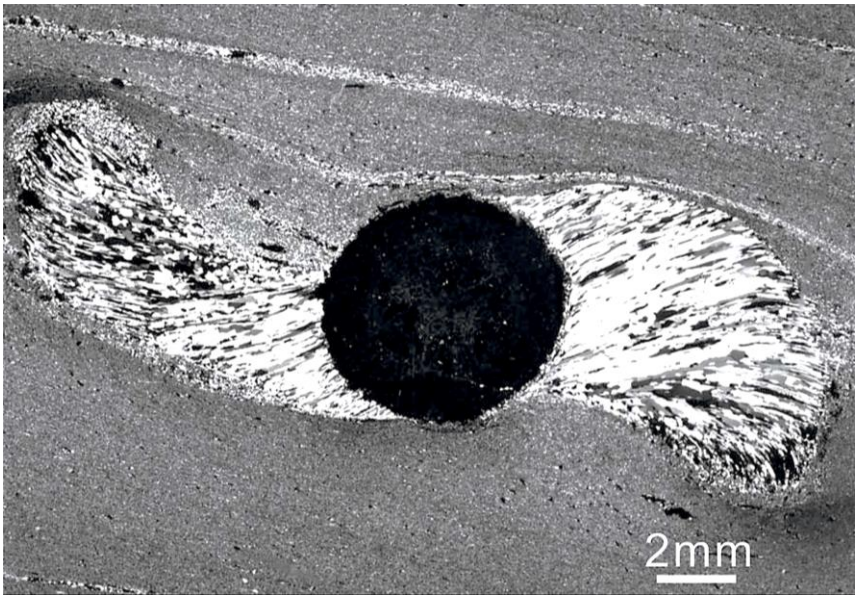


Figure 3.38 Photomicrograph showing strain fringes of quartz around a pyrite framboid. Note the fibrous texture of quartz. The image is from Passchier and Trouw (1996).

According to the arguments above, the fibres are suggested to grow continuously without fracturing. In this case, the fibres are most likely to derive nutrient from the wallrocks rather than

from channelized fluid flow in fractures. It is suggested that the nutrient transport is largely through diffusion from the mineral dissolution site to the precipitation site rather than advection, especially in fine-grained rocks with low permeability (Fisher and Brantley, 1992; Wiltschko and Morse, 2001). This could potentially explain why fibrous veins are much more prevalent in shaly rocks in sedimentary basins worldwide (Cobbold et al., 2013). Diffusion could also account for the transport of gypsum for fibre growth. Firstly, due to the fine grain size and extremely low permeability of the Mercia Mudstone (commonly 10nD) (Seedhouse and Racey, 1997), advective transport in the rocks driven by hydraulic head could only occur in faults and fractures as fluid pathways. Once the faults and fractures have been completely sealed, diffusion is largely responsible for transporting minerals in the intact rocks, without the movement of pore fluid. Secondly, the much thicker fibrous parts in fibrous veins than the median zones require a larger amount of source of gypsum. If gypsum is transported by fluid flow, the volume of the fluid flow would be extremely large due to the low solubility of gypsum, which is unlikely when the fractures are sealed. Moreover, the abundant mobilized gypsum masses that are diffusely disseminated in the country rock could serve as the nutrient supplier for adjacent veins.

Diffusional transport is driven by chemical potential. The difference in chemical potential ($\Delta\mu$) on a vein surface and the wallrock is given by (Paterson, 1973):

$$\Delta\mu = \mu_{(\text{vein surface})} - \mu_{(\text{rock})} = \Omega\,(\sigma_n - P)$$

Where Ω is the molar volume of the solid; σ_n is the normal stress acting on the grain boundary; P is the average stress in the rock. μ is approximately proportional to the concentration in a dilute solution, hence the equation can be written as (Bons and Montenari, 2005):

$$\Delta C = b(\sigma_n - P)$$

Where ΔC is the difference between the average equilibrium concentration in the rock and on the vein surface; b is a proportionality constant. The pressure difference between the host rock and the thin fluid film in the vein-wall interface could cause chemical disequilibrium (Bons et al., 2012). The resulting concentration gradient will lead to gypsum transport towards vein walls as the result of a geochemical self-organization.

It is notable that diffusion is only relevant within a small scale (<1m) in rocks (Bickle and McKenzie, 1987). This is evident from the heterogeneous vein distribution at outcrops, especially the vein-free Unit 5 of the Keuper Marl (see section 2.3.1). However, diffusion can play a significant role in vein formation and produce veins up to 10 cm in thickness (Fisher et al., 1995). This is verified by experimental simulation of fibrous growth of soluble salts when forcing a chemical concentration gradient (Bons and Jessell, 1997). As illustrated in figure 3.8, the diffusely disseminated gypsum around fibrous veins could contribute to vein growth driven by diffusional mass transfer.

The precipitation of gypsum on vein planes requires the pore fluids to be supersaturated. The question then arises regarding what factors could drive the supersaturation. It is suggested that the most likely origin of supersaturation is pressure solution (Wiltschko and Morse, 2001), which can be achieved either by applying differential stress in the rock (see section 3.8.4). The pressure could act on the anhydrite particles in the surrounding rock matrix, and lead to an increase in the equilibrium concentration of anhydrite (Serafeimidis and Anagnostou, 2014). Due to the greater solubility of anhydrite compared to gypsum at low temperatures, low salinities and shallow depth, any further anhydrite hydration and solution must result in supersaturation (Gustavson et al., 1994).

The expulsion of gypsum saturated fluids from the evaporitic beds to other beds may also result in localized supersaturation with the addition of anhydrite.

Pressure-driven dissolution-precipitation can also be related to the decreased P-T during basin uplift, as minerals generally have a higher solubility and are deposited at lower ambient P-T conditions (Bons et al., 2012). Besides, the near-instantaneous release of fluid pressure by the generation of hydraulic fractures, especially mobile hydraulic fractures, can give rise to a rapid supersaturation (Bons, 2000).

It has been demonstrated that the presence of small, strained grains and limited pore spaces in mudrocks could inhibit mineral precipitation and contribute to supersaturation (Putnis et al., 1995). Moreover, the mixing of NaCl brines with gypsum -saturated fluids will lead to a higher solubility of gypsum as long as the chloride concentration remains below its saturation (Gustavson et al., 1994).

3.8.3 Kinematic implications of fibres

It is demonstrated in section 3.6 that the material points on the wallrock surfaces that were once adjacent to each other are connected by gypsum fibres, i.e. fibres track the opening direction of the wall surfaces. Besides, the length of fibres reflect the displacement field of the relative motion of both walls. The observations agree with the idea that fibrous veins can record the opening trajectory of veins (Bons and Montenari, 2005; Durney and Rausay, 1973; Fisher and Brantley, 1992; Passchier and Urai, 1988; Ramsay, 1980; Spencer, 1991). The growth of fibres keeps pace with the progressive motion of vein walls simultaneously, suppressing the growth competition and producing fibres with constant width and smooth boundaries. Hence, it is suggested that fibre

morphology and orientation are intimately associated with wall displacement paths and are displacement-controlled (Fisher and Brantley, 1992), which can be used as an important tool for analyzing progressive deformation in the host rock (Ramsay and Huber, 1987; Spencer, 1991). This hypothesis has been verified by laboratory simulations of synthetic mineral fibres (Means and Li, 2001). In the experiments, mineral fibres of ammonium thiocyanate grow between the interfaces of two brine-soaked, porous ceramic substrates with a pore size less than 10 μm. The fibre axes exactly follow the opening direction of guided blocks by experimental setup. The growth of fibres is successive at a given degree of supersaturation of the fluid, which is different from the incremental and periodic growth of crack-seal veins.

This idea has been challenged by Cox (1987) and Urai et al. (1991), who suggested that the fibre orientations are not necessarily associated with vein wall displacement. According to kinematic reconstruction of grain boundary propagation in fibrous veins, the authors argued that the growth of fibres are more likely to be face-controlled rather than displacement controlled (Figure 3.39). The growth increments of individual fibres are suggested to be associated with the contacting wall morphologies. This arguments is based on two key prerequisites:

(1) The vein is opened along vein-wall contacts by the injection of fluid, i.e. fibres grow in free spaces.

(2) The growth rate of all fibres in single veins are strictly equal, regardless of the crystallographic orientations.

However, this hypothesis is not applicable for the satin spar veins in this study, as evident from four lines of evidence:

(1) Given the discussion in section 3.8.2 and the experiments by Means and Li (2001), reopening of veins is not necessarily required for the growth of fibres in veins. Besides, the lack of inclusion bands in the fibres with pure composition is not compatible with the case of fluid injection.

(2) This model will lead to crystal overgrowth and termination as a result of the differences in the relative sealing time of vein walls.

(3) An equal growth rate of all fibres will give rise to equal fibre length on the same side of the median zone and a symmetrical structure of veins, which is clearly against my observations.

(4) Assuming the growth of fibres is face-controlled, the increments on fibre tips would be normal to the walls, which would produce curved and non-parallel fibres when the walls exhibit rough surfaces. All fibres growing towards vein walls with a high asperity would terminate during vein expansion. However, this hypothesis cannot explain the smooth fibre boundaries illustrated in figure 3.26A. Moreover, our samples (Figure 3.29) and observations by Cox (1987) (Figure 3.40) demonstrate that fibres in single veins are parallel to each other, regardless of their positions and wall morphologies.

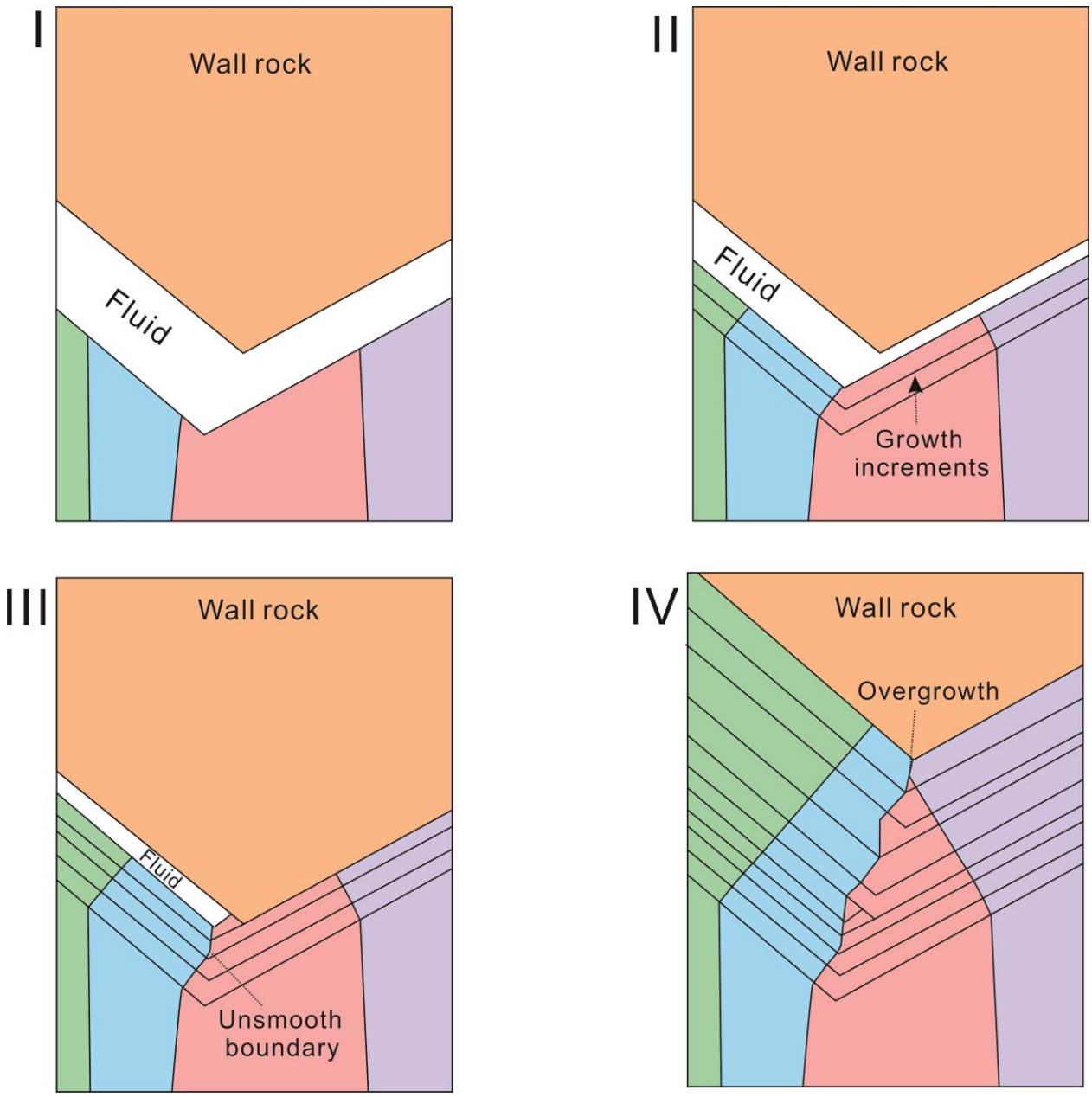


Figure 3.39 Cartoons illustrating the process of incremental growth of fibrous veins. I: Immediately after a cracking event, the vein is reopened by fluid along vein-wall contacts. II: All fibres grow at the same rate in fracture-channelized fluid. III: The vein is partially sealed due to the unevenness of vein walls. IV: Complete sealing of the vein after several cracking events. Modified from Urai et al. (1991).

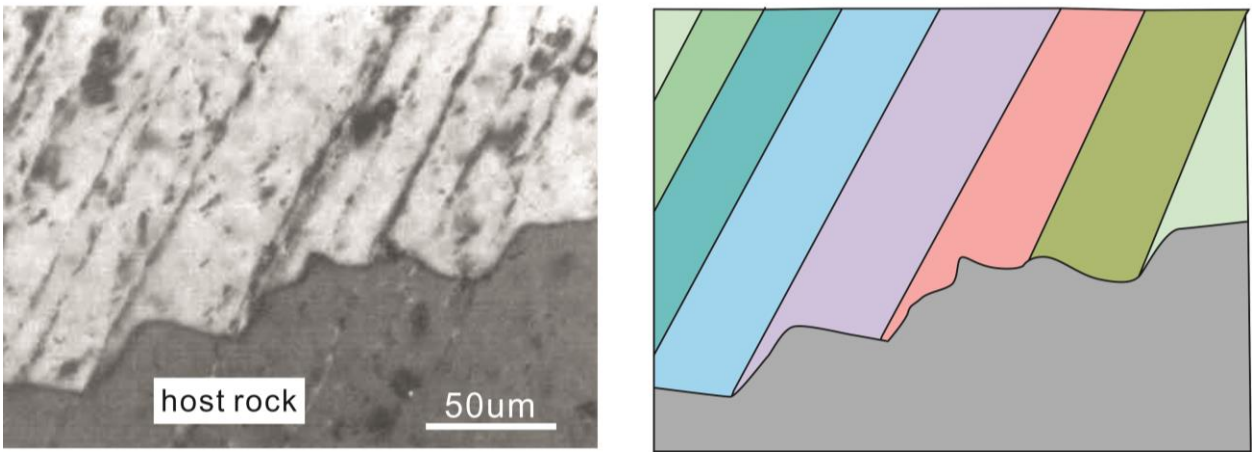


Figure 3.40 Morphology of vein walls and the associated fibres. Note the inherited morphology of crystal faces at vein-wall interfaces. Adopted from Cox (1987).

Based on the argument presented above and the matchable asperities on both vein walls, it is possible to reconstruct the kinematic history of the segmented rocks using associated fibres as kinematic indicators. Figure 3.41 illustrates the process of formation of several minor veins with different fibre orientations and the motion of host rock fragments presented in figure 3.32. Initially, the host rock block a is an intact piece that is enclosed by gypsum crystals on both sides. Due to the loading of crystallization pressure of exerted by sub-horizontal fibres on the left, crack c1 and c2 are generated, which are parallel and normal to those fibres respectively. This is followed by crack-propagation and satin spar precipitation in the cracks, resulting in block a separating into a1 and a2. Meanwhile, more cracks (c3 and c4) are produced. At a later stage, block a2 is segmented into a21 and a22 by c3 with oblique fibres. Crack propagation of c2 and c4 partially separate block a1 into a11, a12 and a13. Finally, all cracks are fully filled with gypsum fibres. Block a13, a21 and a22 are completely isolated from the parent rock block, whose displacement vectors are recorded by fibres in crack c1, c3 and c4. The three blocks all have a tendency of moving up and right. Crack c2 has approached the base of the rock block. A new sub-horizontal crack c5 is nucleated at

the crack front of c2. The geometry of vein wall margins in each vein is well preserved, which can be matched by oblique fibres that are in constant orientations in single veins but different from those in other veins.

In previous studies, non-coaxial (curved) fibres in mineral veins exhibit similar features to the gypsum fibres documented in this study (see section 2.4.1.5) (Bons, 2000; Bons and Montenari, 2005; Means and Li, 2001; Spencer, 1991; Williams and Urai, 1989). In some cases, the fibre curvature can be explained by vein deformation or grain boundary migration (Williams and Urai, 1989). However, in most cases the curved fibres are not bent because the crystal lattice is not bent (Bons and Montenari, 2005; Williams and Urai, 1989). The absorption of impurities (Mg^{2+} and Cd^{2+}) is also suggested as one cause of crystal curvature of gypsum (Rinaudo et al., 1989). However, this idea remains questionable in our case. Firstly, this idea may not explain the co-existence of straight fibres and curved fibres in the same chemical environment. Secondary, the distinct and parallel orientation of multiple curved fibres cannot be satisfactorily explained by this idea.

The laboratory simulation of curved mineral fibres provides the direct evidence for the displacement-tracking, growth origin of continuous fibres (Means and Li, 2001) (Figure 3.42). The fibres grow vertically when the upper ceramic block move upward. When the block is enforced to move along an oblique guided block, the synchronized increments of fibres follow the same orientation of the block motion.

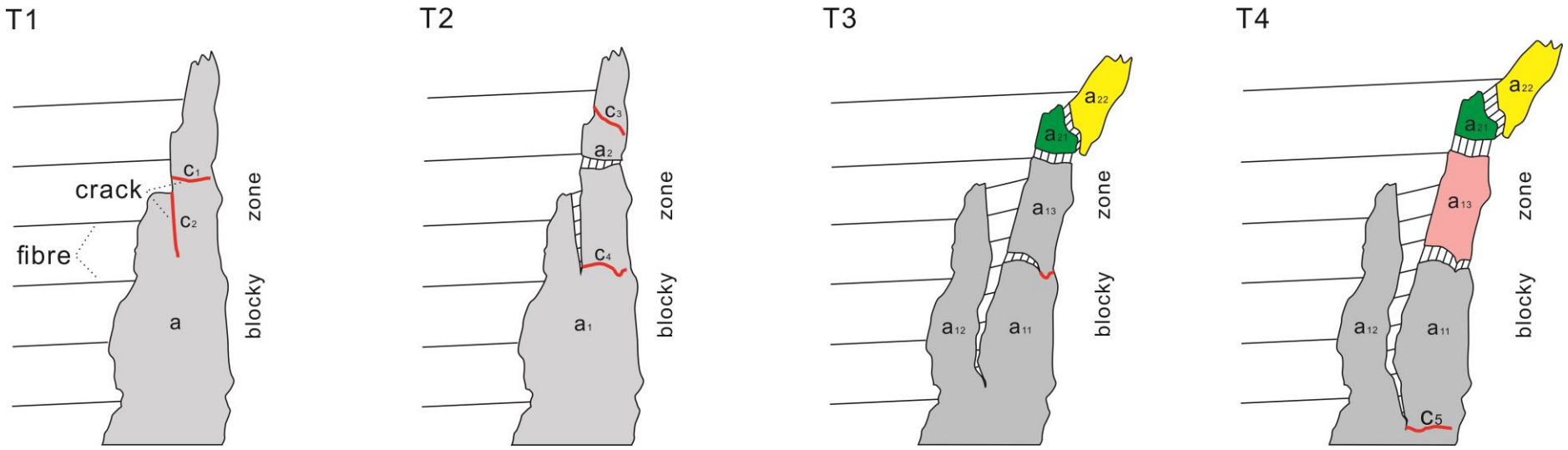


Figure 3.41 Cartoon illustrating process of segmentation of the host rock by multiple satin spar veins. See text for detailed explanation.

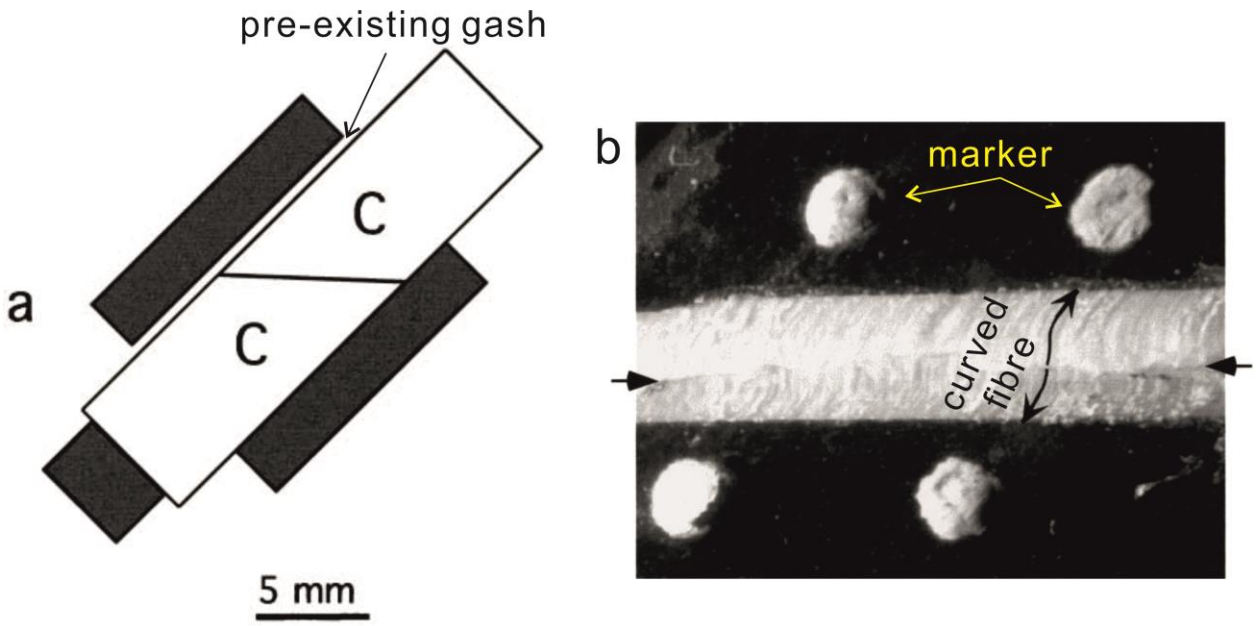


Figure 3.42 (A) Laboratory setup for the growth of fibrous crystals using guide ceramic blocks. (B) Result of fibrous mineral vein generated between the two ceramic blocks. Adopted from Means and Li (2001).

Hence, the fibre curvature is interpreted to have a growth origin (Spencer, 1991). The strain-free curved fibres are interpreted to represent the changes in the growth direction when kinematic axes rotate relative to the fracture (Means and Li, 2001; Ramsay, 1980).

Figure 3.43 illustrates the simplified process of the formation of curved fibres presented in this study. Initially, two marker points were adjacent to each other on different sides of a fracture at the co-ordinate of (0, 0), which is later displaced to (x_0, y_0) by the growth of oblique fibres. The fibres have a length of L_0. The angle between fibres and vein walls is *a*. Here, $x_0=L_0*\cos a$, $y_0=L_0*\sin a$. If the fibres continue to grow in the original direction with an increment of ΔL_1, the co-ordinate of the marker point becomes (x_1, y_1). Then, $x_1=x_0+\Delta L_1*\cos a= (L_0+\Delta L_1)*\cos a$, $y_1=y_0+\Delta L_1*\sin a= (L_0+\Delta L_1)*\sin a$. At the final stage, fibres grow in the direction perpendicular to vein walls, with a vertical increment of ΔL_2 and the resulting co-ordinate of the marker point at (x_2, y_2),

where $x_2=x_1=(L_0+\Delta L_1)*\cos a$, $y_2=y_1+\Delta L_2=(L_0+\Delta L_1)*\sin a+\Delta L_2$. It is notable that the vein walls exhibit varied degrees of roughness, which influence neither the fibre orientation nor the tracking ability of wall displacement.

It is notable that the fibres in the bedding parallel veins in both the Keuper Marl Formation and the Blue Anchor Formation are tightly clustered in similar orientations. The 200° trend of the fibres lies sub-parallel to the Watchet Fault, whose strike ranges from 195° to 220°. The fibres could reflect a shear in the direction of NEE-SWW in their host rocks. It is likely that the fibre orientations have been influenced by the local stress field under the stress shadow of the Watchet Fault. Reactivation and the transtensional dextral motion of the Watchet Fault during basin inversion (Dart et al., 1995) could have deflected the local stress field in the sediments around the fault, which is evident from the drag folds along the fault (Figure 2.9). The bedding parallel shear by loading the local σ_1 in the NEE-SWW direction is then responsible for the inclined fibres.

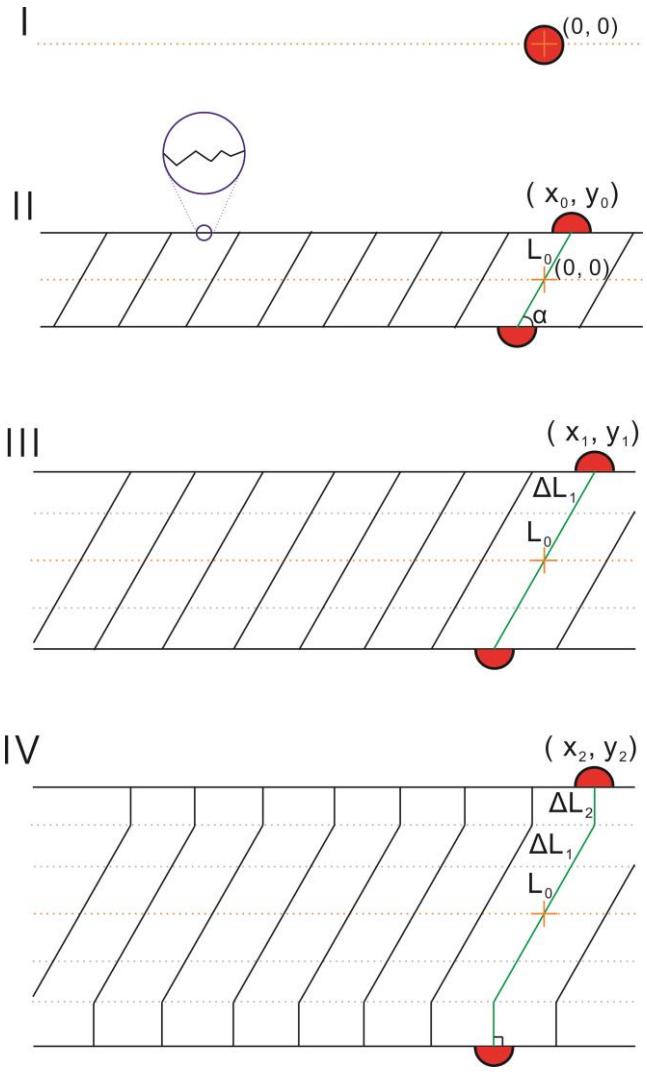


Figure 3.43 Cartoon illustrating the formation process of curved fibres. I: Initial fracturing. II: Fibre growth in the oblique direction and associated vein wall displacement. III: Continued fibre growth in the original direction. IV: Vertical fibre growth. See text for detailed explanation.

3.8.4 Force of crystallization

The continuous growth of satin spar could be maintained when the pore fluids remain supersaturated with respect to gypsum. The supersaturation is likely to be attributed to several factors (see section 3.8.2), and is proportional to the precipitation rate (Bons and Montenari, 2005). The precipitation of gypsum at fibre face would produce a crystallization pressure exerting on its

surroundings as a result of mechano-chemical interaction between minerals in the host rock and the solution (Maliva and Siever, 1988; Weyl, 1959). Quantitative calculation of crystallization pressure using the concepts of equilibrium thermodynamics can be expressed as (Winkler and Singer, 1972) :

$$P_C = \frac{RT}{V}\ln\Omega$$

Where Pc is the pressure exerted by growing crystals; R is the gas constant; T is the absolute temperature; V is the molar volume in the growing crystalline phase; Ω is the degree of supersaturation. Thus, the value of crystallization pressure is determined by the degree of supersaturation of the fluid at a given temperature. It has been demonstrated that the growth of crystals could induce a crystallization pressure greater than the overburden and lift the rocks above or cause intense fracturing in the country rock when Ω is high enough. (Gratier et al., 2012; Noiriel et al., 2010). Crystallization pressure of gypsum during anhydrite-gypsum conversation reaches up to 15 MPa (Keulen et al., 2001). A Ω value of 2 for the degree of supersaturation of gypsum can result in an approximate 34.5 MPa pressure at 25℃ (Keulen et al., 2001). Gypsum crystallization is also one of the main reasons for deteriorations of porous construction materials in urban environment, such as stone, bricks, concrete in buildings, tunnels and other civil engineering structures (Charola et al., 2007; Flatt, 2002; La Iglesia et al., 1997; Saidov et al., 2015; Scherer, 2004).

The external agent of forces, i.e. fluid pressure, is considered unlikely to account for the vein expansion and the associated bulk extension, given the lines of evidences presented in section 3.8.2. The internal agent from crystallization itself could uplift the overburden if the degree of supersaturation is sufficiently high. In order that the satin spar veins could expand and deform the

host rock, the force of crystallization is required to exceed the sum of overburden and the tensile strength of the Mercia Mudstone:

$$Pc \geq Tm + \rho gh$$

Where Tm is the tensile strength of the Mercia Mudstone, 0.4MPa (Hobbs et al., 2002); ρ is the density of the mudstone, $2.6*10^3 kg/m^3$; h is the maximum depth, 300-700 m. P is thus between 8.2-29 MPa. According to equation 1, the degree of supersaturation is

$$\Omega = \exp(\frac{PV}{RT})$$

R=0.082 liter-atm/mole°k. V=54.80 cm^3/mole. Assμme a surface temperature of 20℃ and a geothermal gradient of 50℃/km, the temperature T at the depth of 300/700 m is 35/55 ℃ (308/328 k) respectively. Thus, the degree of supersaturation of the pore fluid is estimated to be no less than 1.02-1.06. A higher degree of supersaturation above the threshold leads to a higher tensile stress which is substantially larger than the overburden and the tensile strength of the host rock.

Another possible evidence for the force of crystallization lies in the curved median zones, but that has been rarely reported in previous studies. It is notable that both vein-walls in single veins are straight and parallel to each other, whereas they are non-parallel to the median zone. It is difficult to match vein walls that were once adjacent to each other due to the absence of asperities on both walls. The current traces of median zones can represent either the shape of the initial fracture or a deformed structure that was initially straight. If we assume the curved median zone retains the original shape, the fibres must have pushed the rough walls to varying distances, so that the current vein walls could be flat and smooth. This would have been accommodated by a growth-related differential compaction in the consolidated surrounding rocks.

The other interpretation is that the median zone was originally straight, which was enforced to be curved during the growth of fibres. The different fibre lengths on the same side of the median zone possibly reflect different growth rates. Gypsum precipitation from pore fluids with a higher degree of supersaturation is faster, which exerts a larger crystallization pressure accordingly. The nonhomogeneous crystallization pressure exerted by fibres in varying length could have forced the median zones to be folded so that the volume of fibres can be accommodated. In either case, the progressive crystallization of fibres acts as the driving force for the associated deformations.

3.8.5 Lithological control on vein development

The dense gypsum veins in the red marls of the Mercia Mudstone occupy a large portion of the bulk volume, which requires vast quantities of gypsiferous solutions for vein-filling due to its low solubility (Porta, 1998). It is thus argued that the veins could have been largely locally sourced by the adjacent nodular masses through the reactivated fault systems (Philipp, 2008) when the evaporite beds entered the telogenetic zone during basin uplift and underwent dissolution. This explanation is applicable for Unit 1, 2 and 4 that contain both nodular beds and gypsum veins in the adjacent beds, and Unit 5 that does not contain neither veins nor nodules. However, it is difficult to explain the absence of gypsum veins in the non-evaporite beds of Unit 3. This indicates that the occurrence of nodular gypsum is not a necessary condition for the genesis of gypsum veins in the adjacent beds.

The volumetric increase during the transition of burial anhydrite to secondary gypsum is suggested to exert a crystallization pressure sufficient to produce brecciation and distortion of the surrounding rock (Keulen et al., 2001; Shearman et al., 1972), and is thus considered as the main cause of gypsum veins in the surrounding marls (Hobbs et al., 2002; Shearman et al., 1972).

However, little deformation around gypsum nodules, except for nodule-linking horizontal veins, indicates that expansion is necessarily involved in the mineral transition (Gustavson et al., 1994). The nodule-linking veins could have been resulted from stress concentration at the long-axis ends of the elliptical nodules (Philipp, 2008), where local stress is sufficient to break atomic bonds and cause growth and propagate of microcracks in the non-porous medium. Continued cracking in such active process zones may also provide sites for precipitation of the excess gypsum derived from the vein-rooted nodules.

As discussed in section 3.8.2, the growth of fibres relies on diffusional transport of nutrient from the surrounding host rock to vein-wall interfaces, i.e. the local diffusely disseminated gypsum masses, including laths and crystal aggregates, serve as the main source for adjacent veins. This is demonstrated by the co-existence of diffusely disseminated gypsum and veins within the same horizons (see section 3.7). Continuous accretion of fibres is enabled by the remobilization of gypsum in the low-permeable rock matrix through diffusion as the result of chemical potential.

The gypsiferous marl, silty marl, siltstone and sandstones in different units of the Mercia Mudstone, which can be defined by different mechanical properties as the result of mineral composition, rock texture and diagenesis (Di Naccio et al., 2005; Laubach et al., 2009), could respond mechanically differently to stress and significantly influence the development of fractures. Sandstone and siltstone contain the most abundant gypsum veins, followed by silty marl and then gypsiferous marl, whilst carboniferous marl contains the least amount. Sandstone/siltstone are generally stronger than marl, which means they can support a larger differential stress (Twiss and Moores, 1992). Hybrid fractures tend to occur more easily in the sandstone/siltstone than marls as a smaller pore fluid pressure is required in sandstone/siltstone for the Mohr circle to touch the failure envelope.

Given the dominant mode of nutrient transport as diffusion in marls (see section in 3.8.2), solute transport via advection as the other basic means of material transport is considered less important. The importance of advection relative to diffusion is expressed by the Péclet number (Pe) (Bear, 2013):

$$Pe = vL/D$$

Where v is the fluid flow velocity; L is the characteristic length scale, such as the grain size in a porous granular material; D is the efficient diffusion coefficient. Diffusion dominates when Pe is close to zero, whist advection dominates at high Pe, roughly above ten (Bons et al., 2012).

During the episodes of failure, fracture permeability increases dramatically and permits dominant advective flow (high Pe) in fracture channels in both the marls and siltstone/sandstone. However, once the fractures are healed by mineral precipitation and pressure drop, stagnation of flow leads to a dominance of diffusion (low Pe) in the marls. A higher Pe for siltstones and silty marls than marls is anticipated due to the much higher permeability (10^{-4}-10^{0} darcies). This enables a more efficient mass transport in the intact rock and fluid-rock interaction due to the larger interfacial area (Oliver and Bons, 2001), which is evident form the more prevalent diffusely disseminated gypsum in the rock matrix of siltstone than marls. Hence, the fractures in siltstone and silty marls could be fed by material sources more efficiently after their closure than the veins in clay-rich marls.

The concentration of satin spar veins in the evaporite rich-horizons in Unit 2 in the Blue Anchor Formation and the absence of disseminated gypsum in the rock matrix suggest that the veins derive nutrient from the nodular beds. Gypsum is likely to have been transported to adjacent veins by advective flow in fractures. The maximum distance of gypsum transport depends on the

development and connectivity of fractures as fluid conduits, especially mobile hydraulic fractures. The localization of bedding parallel veins within dark marls rather than in dolomite (see section 2.3.3.1) is presumably the result of the much lower tensile strength (0.4MPa) that favors the generation of mode-I fractures when loading a sub-horizontal maximum principal stress.

3.9 Conclusions

(1) The satin spar veins have experienced a syntectonic stage, which are indicated by the crack-seal textures in the median zones.

(2) Fibre growth is a post-tectonic, continuous process without the involvement of re-opening by fluid injection. Mobilized gypsum, which is transported to vein-wall interfaces largely via diffusion, precipitates from supersaturated pore fluids.

(3) Fibres track the opening displacement of vein walls and can be used as indicators for kinematic analysis.

(4) The growth of fibres exerts a force of crystallization on the surrounding rock and can be responsible for the fracture opening.

(5) The gypsum fibres are mainly sourced from local disseminated gypsum in the rock matrix rather than gypsum nodules in the evaporite beds. Siltstone and silty marls exhibit a higher degree of vein development, due to their mechanical properties and the more efficient mass transport.

Chapter 4 Fibrous calcite veins in the Lower Jurassic shales of the Charmouth Mudstone Formation, the Wessex Basin

4.1 Introduction

According to crystal arrangement and textural patterns, fibrous calcite veins are mainly identified as two main types calcite "beef" veins and cone-in-cone structures (Cobbold et al., 2013). Calcite beef veins contain parallel-aligned fibres with smooth crystal boundaries and constant widths (Bons and Montenari, 2005; Hilgers and Urai, 2002; Passchier and Trouw, 1996). Cone-in-cone structures consist of nested, conical bundles of calcite fibres (Cobbold et al., 2013; Selles-Martinez, 1996; Woodland, 1964).

Fibrous calcite veins are commonly occurring in over 110 sedimentary basins worldwide (Cobbold and Rodrigues, 2007; Cobbold et al., 2013) (Figure 4.1). Such veins predominantly occur in marine shales as bedding parallel structures, whose age ranges from Cambrian to Palaeogene (Cobbold et al., 2013). Cone-in-cone structures are also frequently reported to occur along the outer rims of carbonate concretions (Kiriakoulakis et al., 2000; Selles-Martinez, 1996).

Calcite beef veins and cone-in-cone structures in fine-grained sediments have received considerable attention from geologists since the 1850s, because they offer insights into the deformation in the host rock, fluid pressure, paleostress and diagenetic conditions (Al-Aasm et al., 1995; Bons et al., 2012; Kowal-Linka, 2010; Marshall, 1982; Passchier and Trouw, 1996; Sorby, 1859; Tarr, 1922). The veins, as former fluid conduits, can also help reveal either basin scale fluid advection or local scale diffusional processes in sedimentary basins (Hilgers and Sindern, 2005; Oliver and Bons, 2001; Worden et al., 2015; Yardley, 1986).

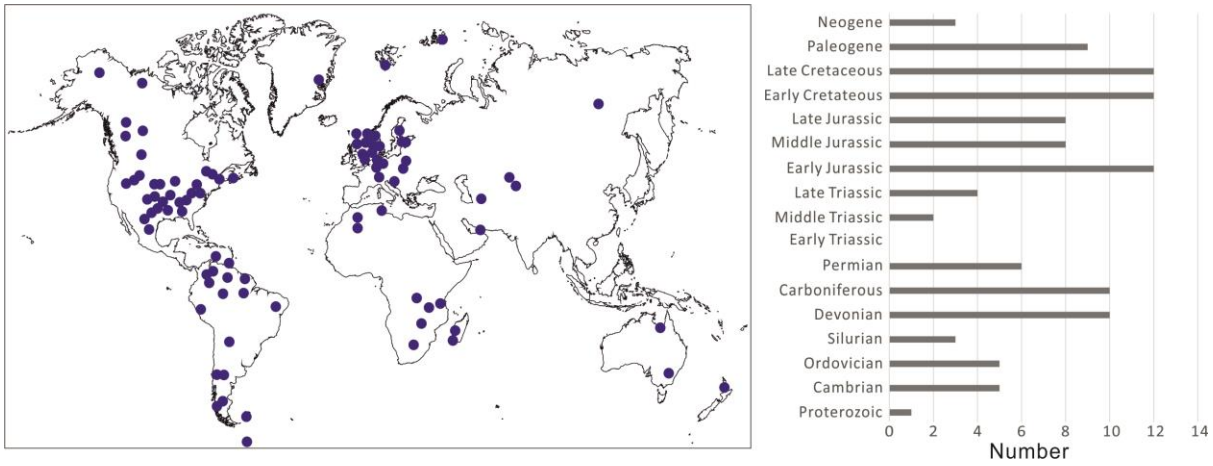


Figure 4.1 Worldwide distribution of fibrous calcite veins and the ages of their host rocks. Modified from Cobbold et al. (2013).

It has been demonstrated that carbon and oxygen isotopes (^{13}C and ^{18}O) are efficient tools for analysing material sources of carbonates as well as fluid circulation in chemical systems (Al-Aasm et al., 1993; Cox et al., 1987; Dietrich et al., 1983; Evans and Battles, 1999; Hilgers and Sindern, 2005; Oliver and Bons, 2001; Richards et al., 2002; Worden et al., 2015). The isotope compositions can also help reveal vein growth processes and fluid–rock interactions (Barker et al., 2006; Bebout, 1991; Bons et al., 2012; Cox et al., 1987; Elburg et al., 2002; Evans and Battles, 1999; Hilgers et al., 2004; Vrolijk, 1987).

In this chapter, the fibrous beef veins and cone-in-cone structures of the Lower Jurassic black shales of the Charmouth Mudstone Formation in the Wessex Basin have been investigated using combined field and geochemical methods. The studying area provides ideal outcrops, with intensively developed calcite beef veins and cone-in-cone structures in a relative thick shale succession (Gallois, 2008; Jenkyns and Weedon, 2013; Lang et al., 1923; Tarr, 1933), allowing a thorough and systematic study of the spatial distribution, pattern and geochemistry of fibrous calcite veins in black shales.

This chapter first describes the vein distribution as well as structural and sedimentary features of their host rocks. Then, the chapter presents the isotope data of calcite veins and their host rocks from four sites. Finally, the chapter discusses various questions, regarding vein generation, growth and controls on distribution. The aims of this chapter are:

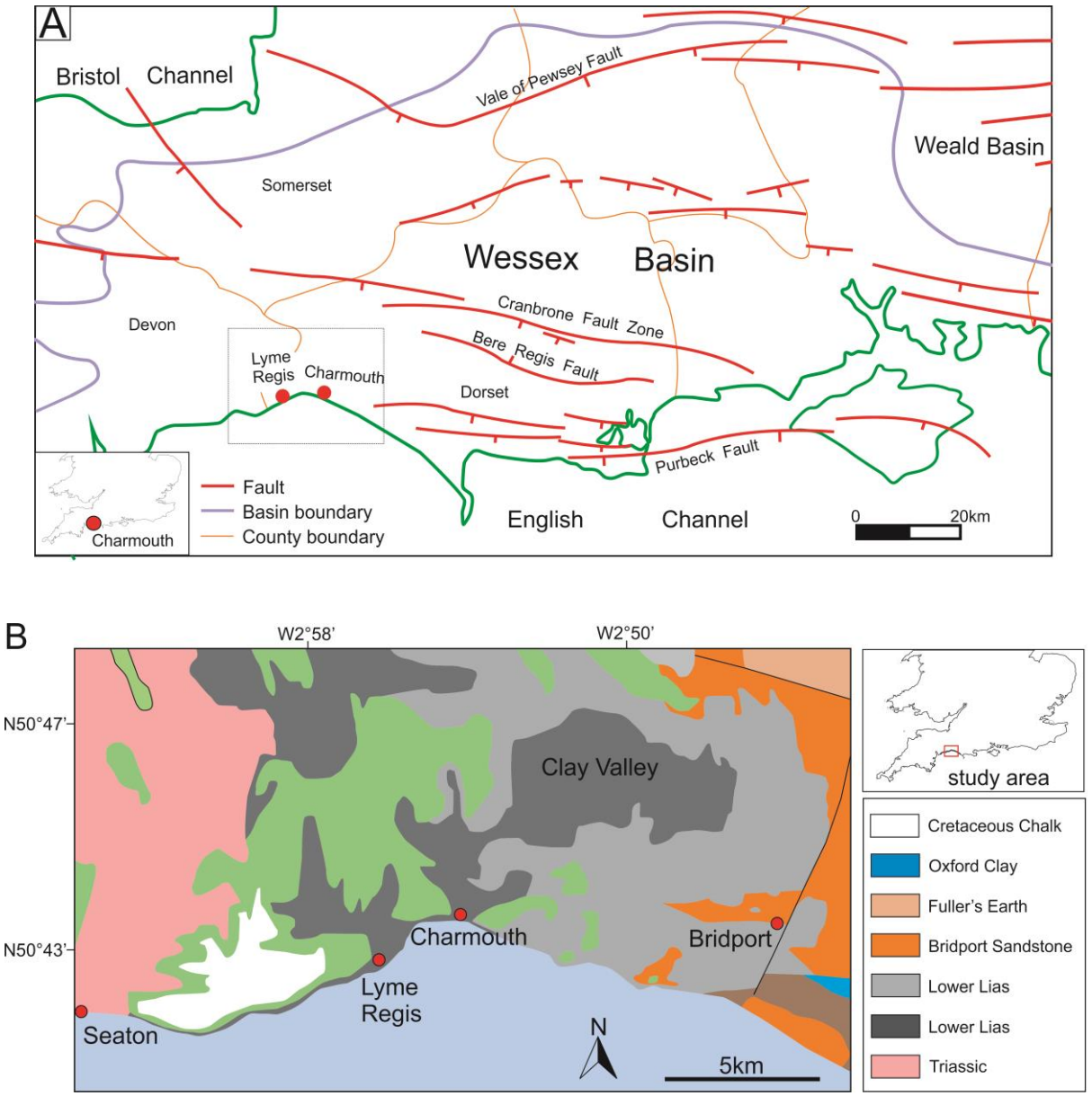
(1) to provide constraints on the timing and diagenetic conditions of vein formation;
(2) to determine the geological controls on vein distribution and material sources for vein growth;
(3) to reveal the fluid conditions and fluid-rock interactions during vein generation;
(4) to refine the understanding of structural diagenesis in black shales during burial.

4.2 Geological setting

4.2.1 Location

The study area is located on the coast at Charmouth, the southern margin of the Wessex Basin (

4.2). The Wessex basin comprises four half graben sub-basins, including the Channel sub-basin, Dorset sub-basin, Mere-Portsdown sub-basin and Pewsey sub-basin, which are bounded by roughly E-W trending normal faults (Stoneley, 1982; Swann and Munns, 2003; Underhill and Stoneley, 1998). The Wessex Basin covers an onshore area of more than 20,000 km^2, encompassing the Pewsey sub-basin to the east and the Dorset sub-basin in the west (Chadwick, 1986; Simms, 2004). The northern margin of the Wessex Basin is defined by the southern flanks of the Welsh Massif and the Mendip High in the west and the London platform to the east, which lies approximately along the Variscan front (Simms, 2004). To the west Palaeozoic basement is exposed in Devon, and to the east beneath the lower Jurassic strata in Kent (Donovan et al., 1979).



4.2 (A) Structural framework of the Wessex Basin and the adjacent areas in Southern England. (B) Geological map of the study area in southern Dorset. See location in figure 4.1A. Modified from Chadwick (1986) and Barton et al. (2011).

4.2.2 Basin setting

4.2.2.1 Structural evolution

The Wessex Basin is a Mesozoic intracratonic basin as one of the extensive networks of basins that cover much of NW Europe (Ziegler, 1982). The basin formed during Mesozoic extension and was subsequently modified by Cretaceous uplift and "Alpine" inversion (Buchanan, 1998; Chadwick, 1986; Karner et al., 1987; Stoneley, 1982; Underhill and Stoneley, 1998).

The Wessex Basin is divided into a series of grabens and half-grabens by E-W striking, south dipping normal faults that are associated with reactivation of the Variscan thrust faults in the basement (Swann and Munns, 2003). Deposition of the Permian and Mesozoic sediments is strongly influenced by these E-W faults (Chadwick, 1986). The basin underwent continued extension from the early Permian to the Late Jurassic, resulting in a cumulative deposition of sediments of about 3 km (Worden et al., 2015).

The basin experienced uplift in the Cenozoic with the southern part of the basin uplifting more than 1 km in some regions (Chadwick, 1993; Law, 1998). Basin inversion occurred due to the N-S compression related to the Alpine Orogeny at this stage, largely facilitated by a reverse movement of pre-existing E-W normal faults and intense folding (Chadwick, 1986; Karner et al., 1987; Lake and Karner, 1987). The basin underwent a greater burial and heating towards the south and east of the basin, in the offshore region of the east of Portland and south of the Purbeck Fault (Chadwick, 1986).

4.2.2.2 Stratigraphy

The basin unconformably overlies a basement of Lower Palaeozoic to Carboniferous rocks. The basin consists of ~2km Permian to Tertiary sediments (Underhill and Stoneley, 1998), which are represented by three megasequences, (1) the Permian-Lower Cretaceous megasequence, (2) the Upper Cretaceous megasequence and (3) the Tertiary megasequence (Underhill and Stoneley, 1998) (Figure 4.3). The following descriptions of the sediments and stratigraphy are mainly based on Lake and Karner (1987), Simms (2004), Stoneley (1992), Swann and Munns (2003) and Worden (2015).

The Permian and Triassic sediments are dominated by continental facies. The Permian sediments comprise alluvial conglomerates, Aeolian sandstones and mudstones. The Triassic sections consist of the Lower-mid fluvial sandstones of the Sherwood Sandstone Group and the Mid-upper Triassic lacustrine mudstones and local halite of the Mercia Mudstone Group.

The end of the Triassic is marked by shallow marine interbedded shales and limestones of the Lower Lias Group during the major global major transgression. The Jurassic section is dominated by marine and epicontinental sediments. The marine Lower Lias Group is mainly represented by the interbedded limestone and mudstone of the Blue Lias Formation and the organic-rich mudstone of the Charmouth Mudstone Formation.

The Upper Jurassic sediments consist of the marine Bridport Sandstone, which forms an important hydrocarbon reservoir in the Wytch Farm oilfield, Dorset. The Middle Jurassic section is represented by a series of limestones and mudstones. The Upper Jurassic sediments include the Corallian series of sandstone, limestone and mudstone, among which the mudstone-dominated Kimmeridge Clay Formation is highly organic-rich and serves as one of the major potential source rocks in the region. The end of the Jurassic is marked by a major regression that results in the deposition of non-marine sediments in the early Cretaceous. The Lower Cretaceous succession is presented by the Wealden Group of a fluvial origin.

The Upper Cretaceous megasequence is separated from the underlying Permian-Triassic megasequence by the Albian-Aptian unconformity, which is marked by the progressive truncation of the Permian and the Mesozoic sediments towards west. The lower part of this megasequence comprises westerly-onlapping marine sandstones, which passes into the Chalk Group.

The Tertiary megasequence is distinguished from the Upper Cretaceous megasequence by a subtle and regional unconformity. The succession consists of near-shore marine and non-marine sediments, and is mainly confined to the area east of Dorchester.

4.2.3 The black shale

The Wessex Basin has been intensively studied due to the exceptional exposure of the entire Jurassic succession, which contains all of the potential source rocks for hydrocarbon reservoirs in this region (Chadwick, 1986; Jenkyns and Weedon, 2013; Karner et al., 1987; Stoneley, 1983; Underhill and Stoneley, 1998; Worden et al., 2015).

The Lower Jurassic Lias Group of England and Wales extends southwards from Redcar in the Cleveland Basin, through the east Midlands Shelf, the Cotswords and Somerset, to the Lyme Regis region of the Wessex Basin (Kemp et al., 2005) (Figure 4.4A). It consists of shallow marine interbedded shales and limestones that were deposited in an extensive epicontinental sea during the major global transgression (Anderton et al., 1979). The Charmouth Mudstone of the Lower Lias comprises dark grey shales, paler grey blocky mudstone and marls, sporadic limestone concretions and tabular limestone beds (Jenkyns and Weedon, 2013; Simms, 2004).

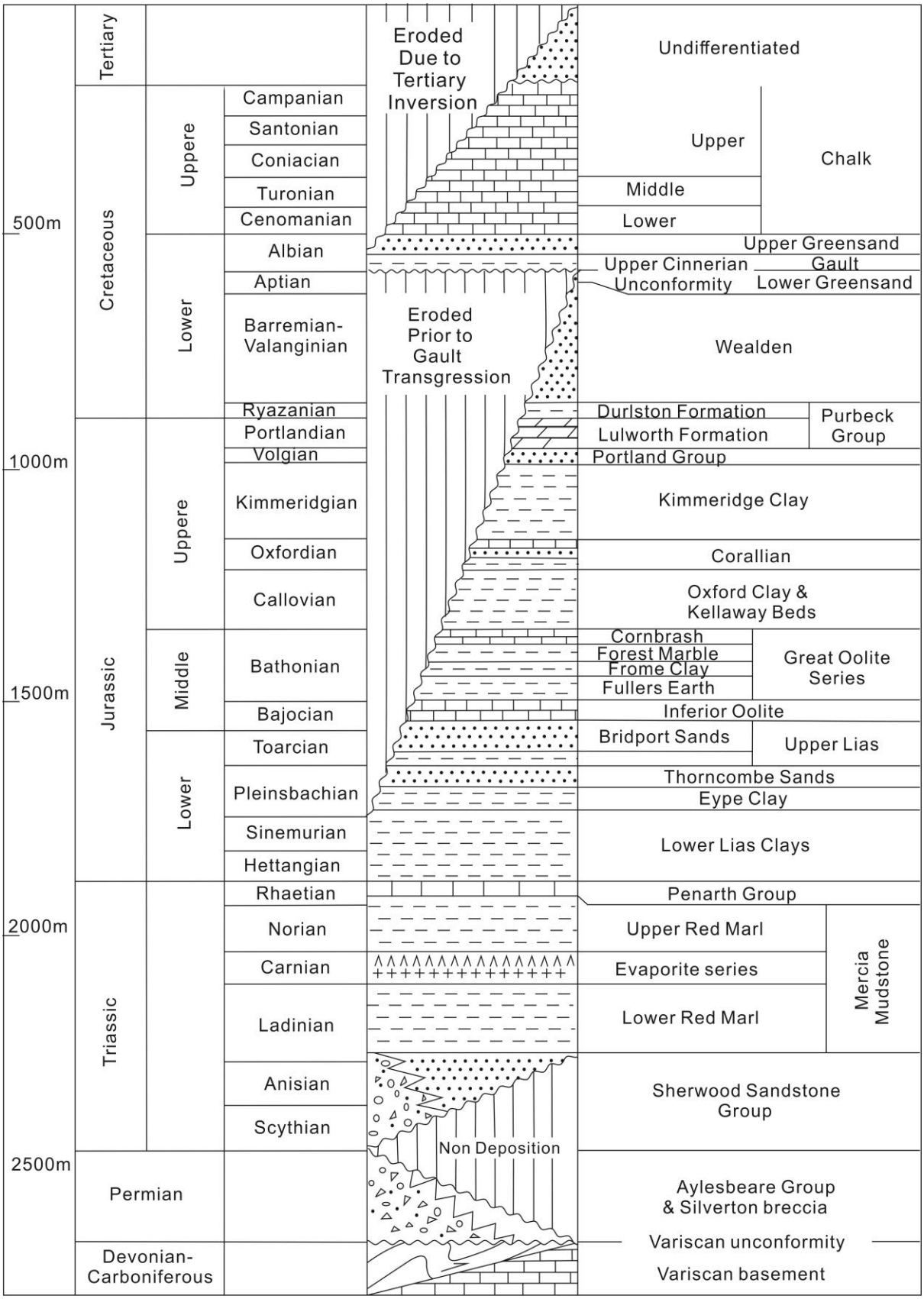


Figure 4.3 Stratigraphic column of the Wessex Basin. Modified from Swann and Munns (2003) and Underhill and Stoneley (1998).

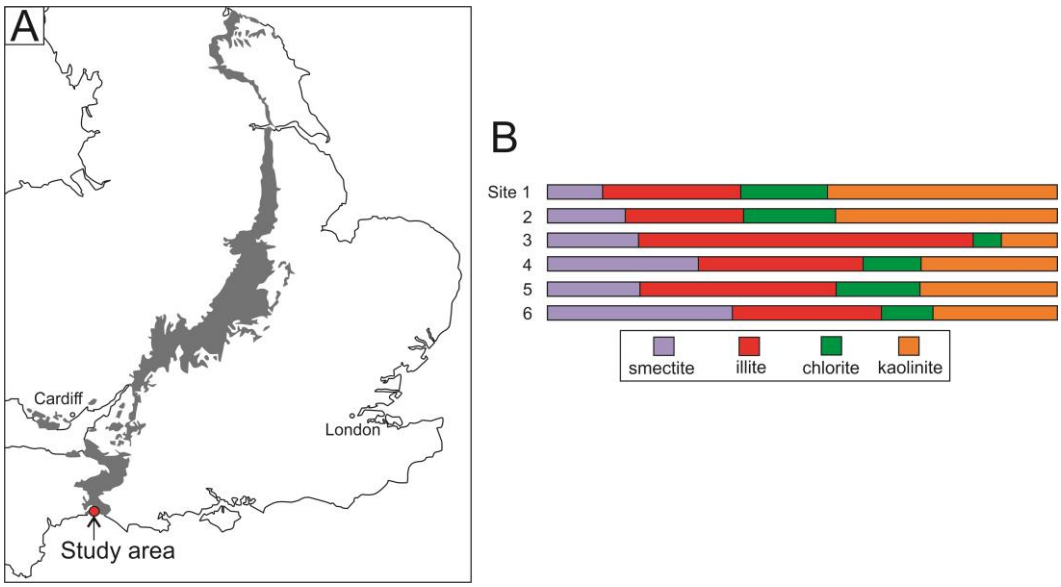


Figure 4.4 (A) Map showing the distribution of outcrops of the Lias Group in the UK. The arrow shows the study area on the coast of Dorset. Modified from Hobbs et al. (2012). (B) Clay mineral composition in mudstones of the Charmouth Mudstone Formation. Sampling site 1 and 2 are located in Northcot, Gloucester; Site 3, 4 and 5 in Stonebarrow Hill, Dorset; Site 6 in Lyme Regis, Dorset. Note the absense of illite/smectite (I/S). Adopted from Kemp et al. (2005).

Fibrous beef veins and cone-in-cone structures occur frequently in the black shales of the Shales-with-Beef Member of the Lower Charmouth Mudstone. The Shales-with-Beef Member consists of 33m laminated black shales with interbedded impersistent limestone beds (Hesselbo and Jenkyns, 1995) (Figure 4.5). The shales are organic rich and are prominent in the lower and middle part of the member (Gallois, 2008). The limestones occur frequently as decimetre-scale nodules, which often contain well preserved ammonites (Simms, 2004). The shales consist of numerous thin beds (<10cm) of fibrous calcite veins, referred to as 'beef', which give the member its name (Lang et al., 1923; Tarr, 1933). The Shales-with-Beef Member is overlain by the Black Ven Marl that consists of 43m dark-grey thinly interbedded and organic-rich mudstone, with a few thin beds of muddy limestone (House, 1989) (Figure 4.5).

The black shales in the Shales-with-Beef Member are richly fossiliferous, containing ammonites, belemnites, brachiopods and bivalves (Jenkyns and Weedon, 2013). The shales contain a total organic carbon (TOC) up to 10.4%, serving as the source rocks for the hydrocarbons in the Wytch Farm oilfield in Dorset (Buchanan, 1998; Jenkyns and Weedon, 2013). The organic matter is predominantly type II algal material (Underhill and Stoneley, 1998). The shales are highly calcareous, with calcite, dolomite and aragonite. The non-clay mineral assemblages include carbonates, quartz, feldspar (albite and K-feldspar), pyrite, gypsum and jarosite (Kemp et al., 2005). Clay minerals include illite, smectite, kaolinite and chlorite (Figure 4.4B). However, mixed illite/smectite has not been detected. The existence of smectite and kaolinite indicates that the mudstones are immature (Kemp et al., 2005). The equivalent source rock units encountered the oil window in the Late Cretaceous prior to the basin inversion in Tertiary (Stoneley, 1992). Coupled with organic maturity analyses, the source rock shales are suggested to have experienced a maximum burial depth of 2 km and a peak paleotemperatures of 75℃ (Hower et al., 1976; Kemp et al., 2005). However, the source rocks exposed in the outcrop in the study area are immature, whose maximum burial depth is 900-1100m and equivalent vitrinite reflectance is only 0.35% (Ebukanson, 1985).

4.3 Methodology

As the upper part of the outcrop of the Shales-with-Beef Member in the Charmouth is variably weathered and covered with fallen muds due to landslides, the field observation of the calcite veins was made in the lower part of the section between the Fish Bed and Devonshire Head Limestone. Detailed stratigraphic logging was carried out in the successions that expose multiple horizons of calcite veins. Field observations mainly focus on vein distribution, geometry, size, interaction, internal texture, composition, surface morphology, and host rock deformation.

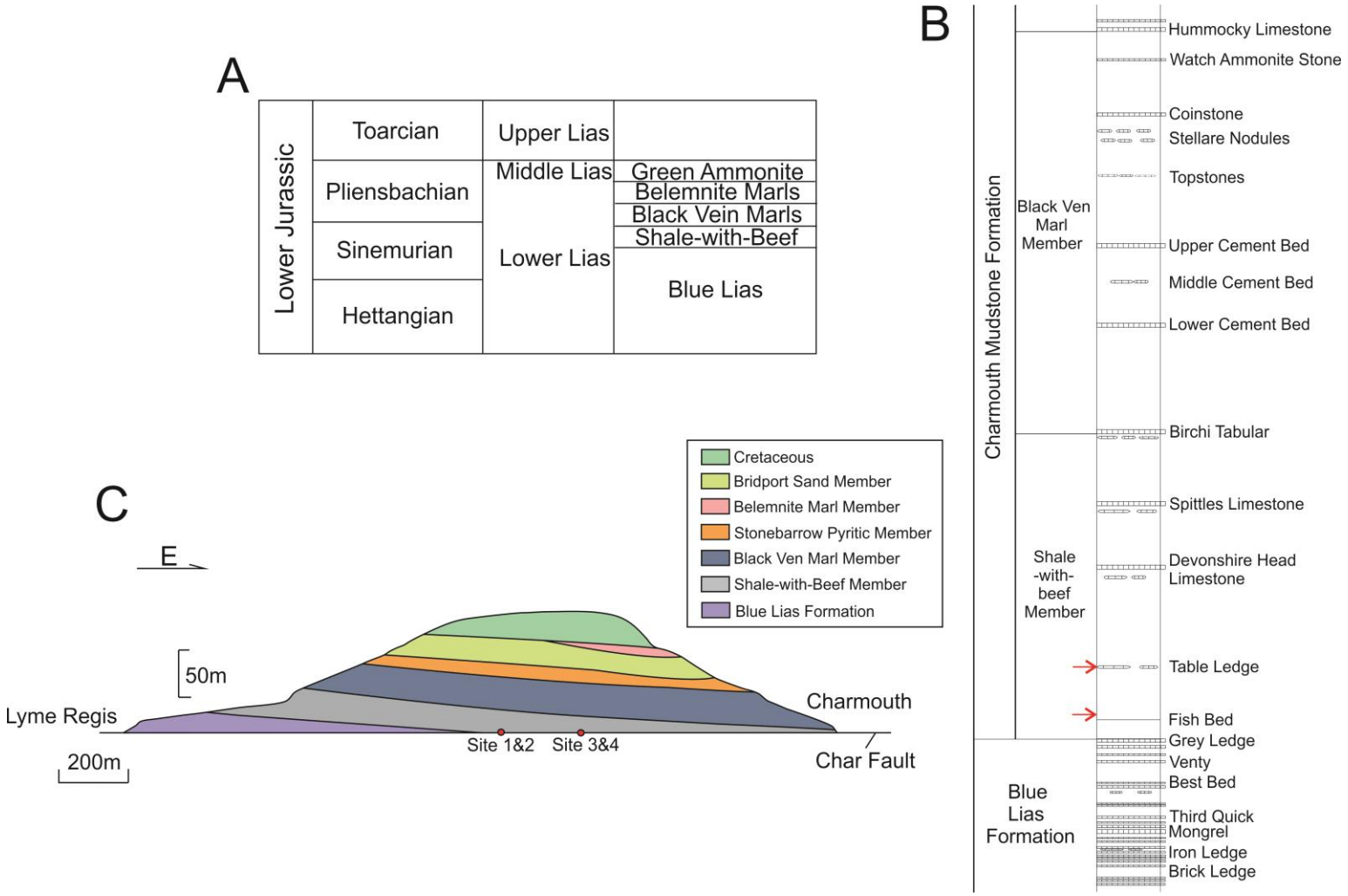


Figure 4.5 (A) General stratigraphy of the Early Jurassic exposed on the Dorset coast. Adopted from Jenkyns and Weedon (2013). (B) Simplified stratigraphic column of the Shales-with-Beef Member in the regions of Lyme Regis and Charmouth. (C) Cross-section of the outcrop between Lyme Regis and Charmouth. Modified from Gallois (2008).

Representative vein samples were collected in multiple sites for petrographic and geochemical analysis. Systematic sampling of rock samples in four sites (Figure 4.5C), including calcite veins and host shales, was carried out that permit a comparative study of the veins and their host rocks in different horizons.

Fifteen samples for determination of carbonate concentration and TOC (total organic carbon) content were collected from each shale bed in site 1, to analyse their control on vein development. The content of carbonate and TOC were measured using a Shimadzu TOC-5000A TOC Analyzer, following the principles of the 680 degrees centigrade combustion catalystic oxidation method (Benner and Strom, 1993). All samples are heated to 680℃ in an oxygen-rich environment inside combustion tubes that are filled with a platinum catalyst. The carbon dioxide generated during combustion is cooled and dehumidified, and then detected by an infrared gas analyser (NDIR) with a detection limit of 4μg/L. The concentration of TC (total carbon) in the sample can be obtained through comparison with a calibration curve formula. By subjecting the oxidized sample to the sparging process, the IC (inorganic carbon or carbonate) in the sample is converted to carbon dioxide. Then the IC concentration is obtained by NDIR. The TOC concentration is obtained by subtracting the IC concentration from the TC concentration.

Both stable isotopes of $\delta^{13}C$ and $\delta^{18}O$ were measured for studying the calcite veins and their host rocks. Samples were systematically collected from four sites in order to include a wide range of host rock lithologies and vein types. Site 1, 2 and 3 contain closely spaced calcite veins. In site 1, twelve vein and fifteen host rocks were sampled, four veins and six rocks in site 2, four veins and six rocks in site 3. Samples from site 4 were collected from a carbonate concretion with a fibrous outer rim. Ten samples were drilled from the core zone to the rim to reveal the variation in isotope compositions.

Powdered samples were extracted using a microdrill from both the upper and lower fibres in single veins. Distilled water and high pressure air were used to clean the equipment so as to avoid cross contamination. Concentrated phosphoric acids were added to the samples to produce the CO_2 to be analysed. The samples were run at the isotope laboratory of the Open University using MAT 253 mass spectrometer. The isotope composition was calculated relative to Pee Dee Belemnite (PDB) standard (Hoefs and Hoefs, 1997).

4.4 Vein characterization

4.4.1 Occurrence

Calcite beef veins and cone-in-cone structures are widespread in the black shales of the Shales-with-Beef Member. The veins are white or grey and can be easily distinguished from the black, fissile shales.

Multiple beds of carbonate concretions in this member are often accompanied with the occurrence of calcite veins in the adjacent beds. The lenticular concretions are observed to be enveloped with radial cone-in-cone structures in the outer rims, which exhibit distinctly different textures from the horizontal laminations in the inner core areas (Figure 4.6). The thickness of the cone-in-cone structures reaches up to several millimetres.

Beef veins and cone-in-cone structures that are not associated with concretions are scattered in the black shales. The shale succession between the Table Ledge and the Fish Bed with abundant calcite veins was selected for vein observation and sampling. The outcrop of site 1 exposes vertically clustered arrays of calcite beef veins and cone-in-cone structures. The veins are mainly distributed in 15 horizons, with an average vertical spacing of 19.8 cm (Figure 4.7).

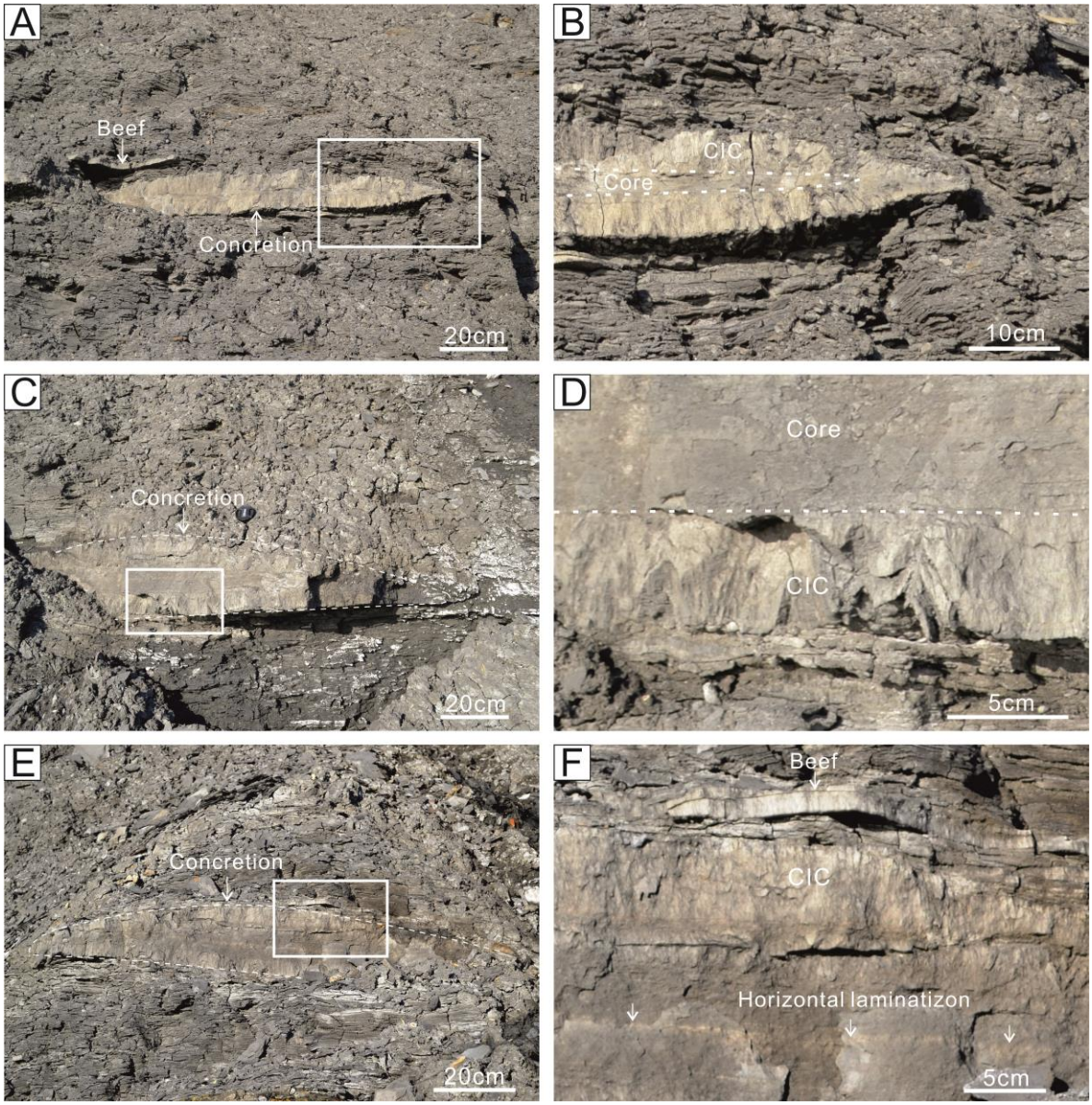


Figure 4.6 Outcrop exposures of carbonate concretions with associated cone-in-cone structures in the black shales of the Shales-with-Beef Member, Lower Lias Group. Figures A, C and E show single lenticular concretions. Figure 4.6B, 4.6D and 4.6F show the enlarged area of the boxes in figure 4.6 A, 4.6C and 4.6E, respectively. Note the horizontal laminations in the cores of concretions and cone-in-cone structures in the outer rims. CIC=cone-in-cone.

Cone-in-cone structures occur in horizons 8, 10, 18 and 26 (Figures 4.8C, 4.8E). These structures are all tabular and persistent along the outcrop for tens of meters. The maximum apertures of the structures are 8, 3, 6 and 1.8 cm respectively.

Calcite beef veins occur in eleven horizons. The veins in different horizons exhibit varied geometries, sizes and textural patterns. The length of single veins varies from several

millimetres to tens of meters. They occur either as isolated veins or closely spaced vein groups. The detailed descriptions are as follows:

Horizon 2 contains swarms of minor calcite beef veins (Figure 4.8A). The veins are closely spaced and bounded by thin shales.

Horizon 4 exposes multiple textureless calcite bands (Figure 4.8A). Each band has a width of 1-2 mm that is the lowest among all veins. All the bands are horizontal and closely spaced.

Horizon 6 includes two types of beef veins (Figure 4.8B). Type one of the veins are 2-3 metres long, with a maximum aperture of 1cm. Type two of veins are 10-15 cm long, with a maximum aperture of 0.4-1 cm. The larger veins are always approximately 2 cm above the small veins.

Horizon 12 and 22 both contain a persistent calcite beef vein (Figure 4.8F). The maximum aperture of the vein is 0.4 and 0.6 cm respectively.

Horizon 14, 16 and 24 contain clusters of short horizontal calcite beef veins (Figures 4.8D, E and G). The length of the veins ranges from several centimetres to decimetres. Vein length varies from several centimetres to 40 cm. The maximum vein aperture is 1.4 cm. The vertical spacing of the calcite veins is commonly lower than 1cm. All veins exhibit similar geometries and textures.

Horizon 20, 22, 28 and 30 consist of multiple closely spaced horizontal beef veins as groups (Figures 4.8F, H). All veins are persistent in length. The vertical spacing of the veins in single groups is between 1-2 cm. Vein aperture ranges between 1-1.5 cm.

The host rocks are entirely black shales. Rock colours are grey/black; however, it is difficult to distinguish the minor variations in rock colors due to weathering. The bedding is generally horizontal above and below vein planes, however, it is often curved in the vein tip regions.

An elliptical carbonate concretion occurs in horizon 27, with the horizontal long axis of 18.9 cm and the short axis of 9.8 cm.

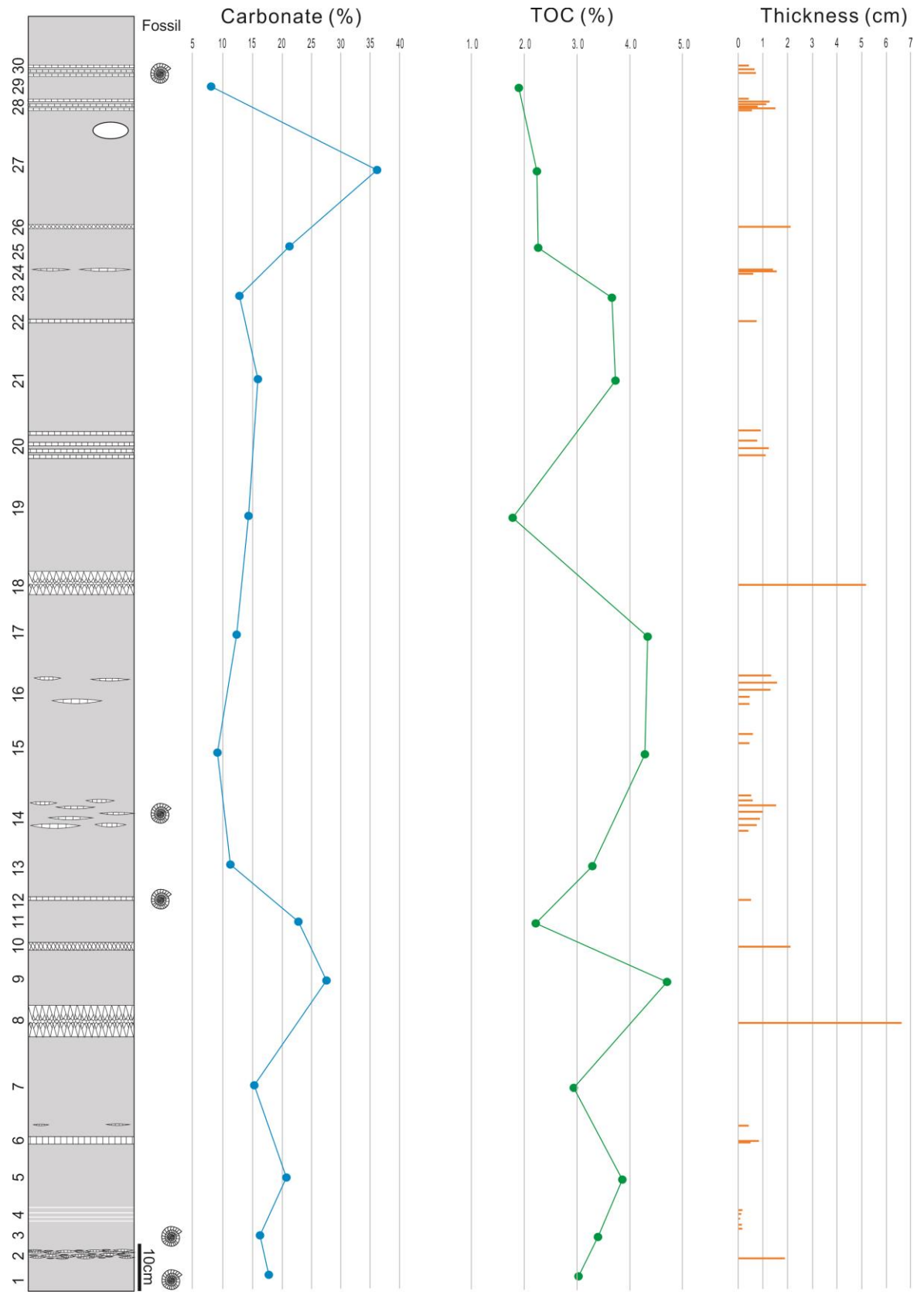


Figure 4.7 Stratigraphic column, carbonate concentration, TOC content and vein thickness of site 1.

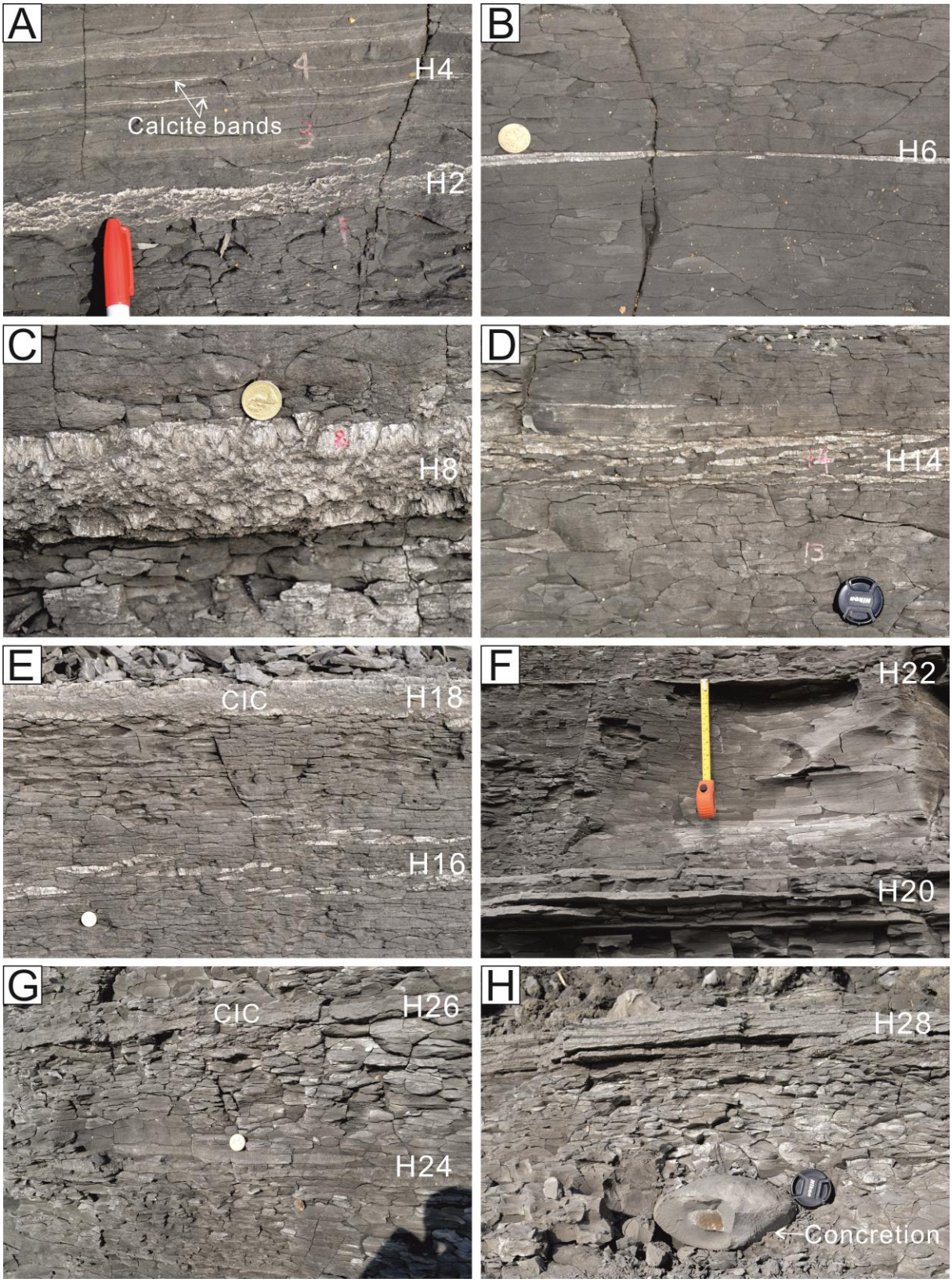


Figure 4.8 Outcrop photographs showing the patterns of calcite veins in different horizons in site 1. See text for detailed descriptions.

4.4.2 Vein pattern

4.4.2.1 Geometry and size

The fibrous veins are predominantly tabular and bedding-parallel, regardless of their size. Cone-in-cone structures are all persistent, with a higher aperture than beef veins. Two different groups of veins are recognized, including lenticular veins with length ranging from several centimetres to 2m, and sheet veins with a persistent length that can be traced along the outcrop for tens of metres (Figure 4.9). Lenticular beef veins commonly exhibit two tapering tips. Vein length and aperture measurement is feasible in these veins. The measurement of vein sizes reveals that aspect ratios (length/aperture) of single impersistent veins range from 3.6-38.6, with an average value of 12.1 (Figure 4.10). Most veins have an aspect ratio between 5-15, 40% between 5-10, 32.9% between 10-15.

4.4.2.3 Solid inclusions

Fibrous beef veins commonly contain one or two dark horizontal median zones of host rock inclusions that bound the upper and lower fibres (Figure 4.11). The median zones often extend from tip to tip. However, they are occasionally absent in the tip regions, especially those exhibiting a planar-concave shape (see section 4.4.2.5).

An interesting feature of fibrous beef veins is the appearance of clay lenses enclosed by fibres (Figure 4.12). These clay lenses are often completely sealed by fibres and show no connection to the host rock. The long axes of such clay lenses are parallel to the median lines. The length varies from millimetres to 2.5cm. The occurrence of clay lenses is accompanied with an elevation on vein surfaces as ridges (see description in section 4.4.2.4).

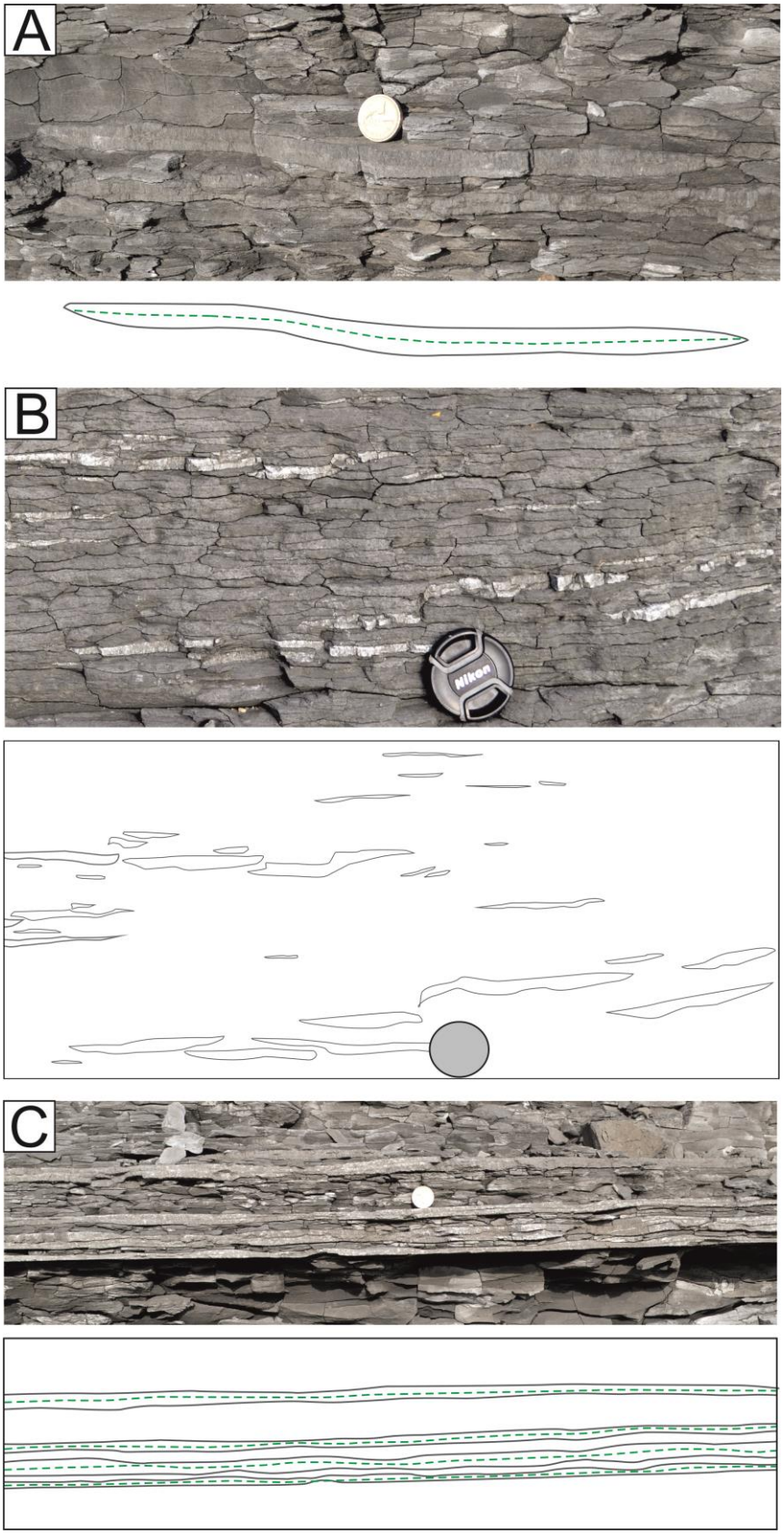


Figure 4.9 Outcrop photographs and the line drawing showing the geometry of isolated beef veins (A), closely spaced vein clusters (B) and persistent beef veins (C). Green dashed lines show the median zones.

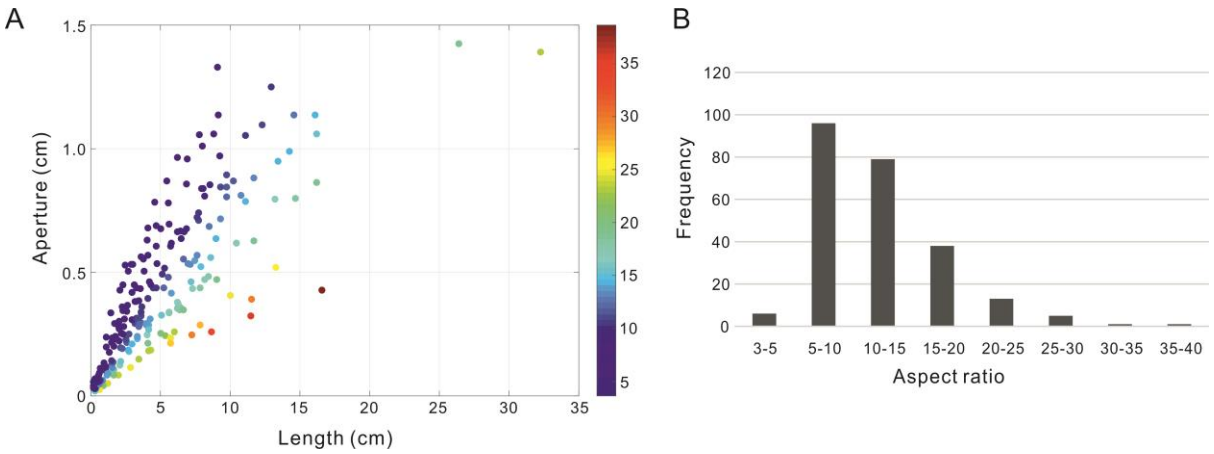


Figure 4.10 (A) Plot of length versus aperture of calcite beef veins with tips in bed 14, 16 and 24. The colour bar shows aspect ratio. (B) Histogram showing the distribution of aspect ratios of calcite beef veins. N=240.

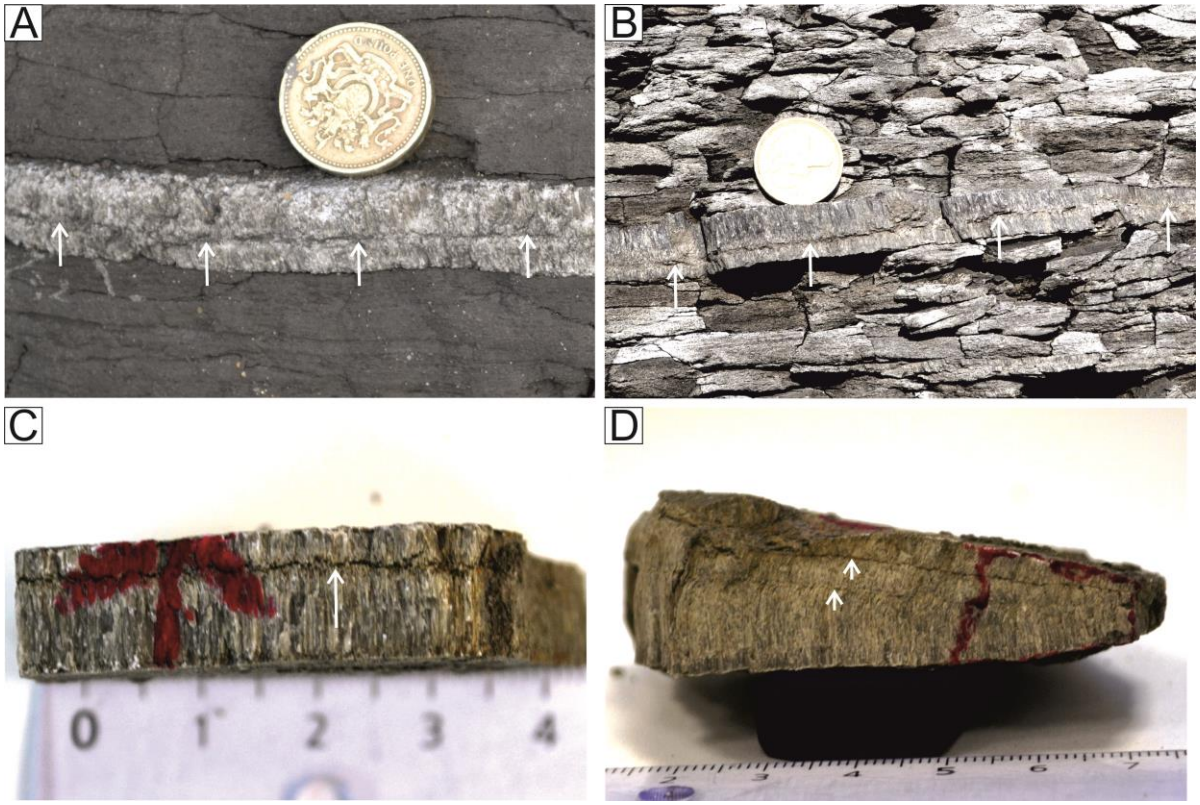


Figure 4.11 Outcrop (A and B) and hand specimen (C and D) photographs showing the linear bands of median zones in beef veins (pointed by whtie arrows). Note the two median zones in the vein in figure 4.11D.

The cone-in-cone structures generally contain a larger proportion of clay inclusions due to the distinct arrangement of calcite crystals (Figure 4.13). The gaps between adjacent cones are filled by abundant clay minerals. The clay inclusions mainly occur as linear bands that follow the boundaries of cones, whose dips depend on the apical angles of the affiliated cones. Similar to fibrous beef veins, the cone-in-cone structures also contain a median zone that comprises dark host clays and minor crystal aggregates of calcite. The median zone is not visible as linear traces. Instead, it is distinguished by the oppositely oriented cone apices on either side that marks the zone margins. The cone-in-cone structures enveloping carbonate concretions do not contain median zones.

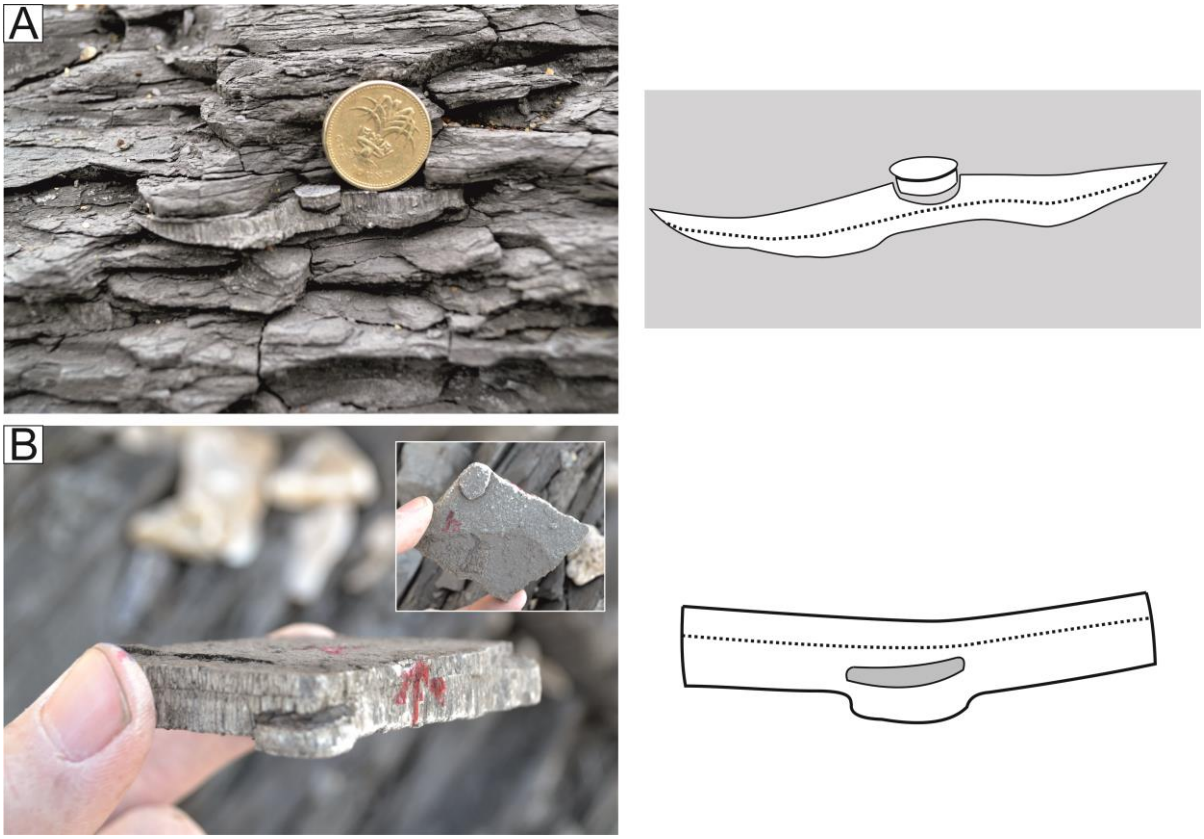


Figure 4.12 Outcrop exposures of solid inclusions in the fibrous calcite veins and their sketches. (A) A short calcite vein with a horizontal clay lens trapped within the upper fibres. The median zone is shown by the dashed line. (B) A clay fragment in the lower part of a calcite vein and the associated circular ridge in the lower surface.

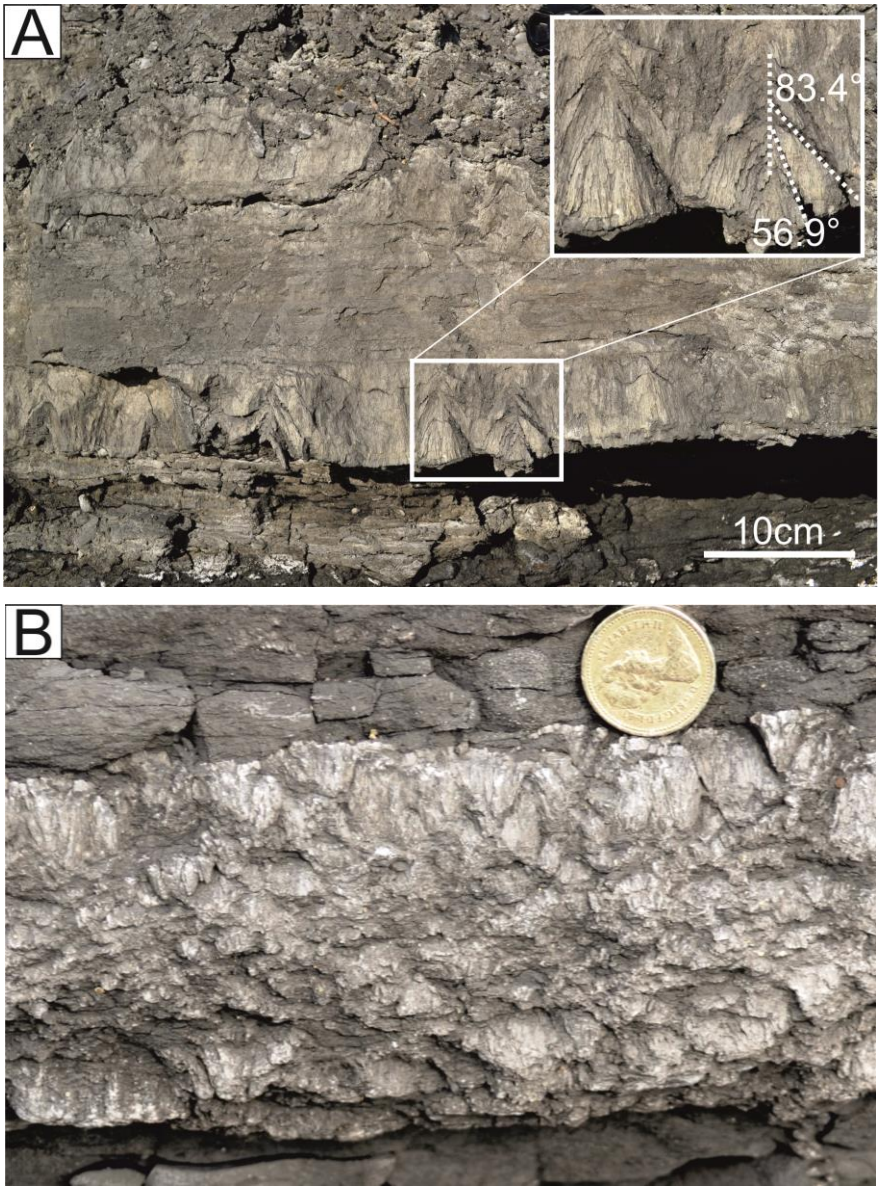


Figure 4.13 Calcite cone-in-cone structures consisting of stacks of conical crystal aggregates. Notice the apical angles decrease towards the host rocks. (B) Close shot of 8 cm thick cone-in-cone structure consisting of nested cones and dark host rock inclusions.

4.4.2.4 Surface morphology

The surfaces of fibrous beef veins are commonly smooth and flat. However, circular ridges with a higher relief occur where there are clay fragments incorporated within fibres (Figures 4.14A-C).

In contrast, cone-in-cone structures exhibit rough surfaces that contain numerous annular ridges in much larger sizes than the beef ridges (Figure 4.14D). Those rings are the surface expressions of the individual cones (Selles-Martinez, 1996). The radii of the rings is commonly on a scale of centimetres. The depressions between the annular ridges are filled with host clays.

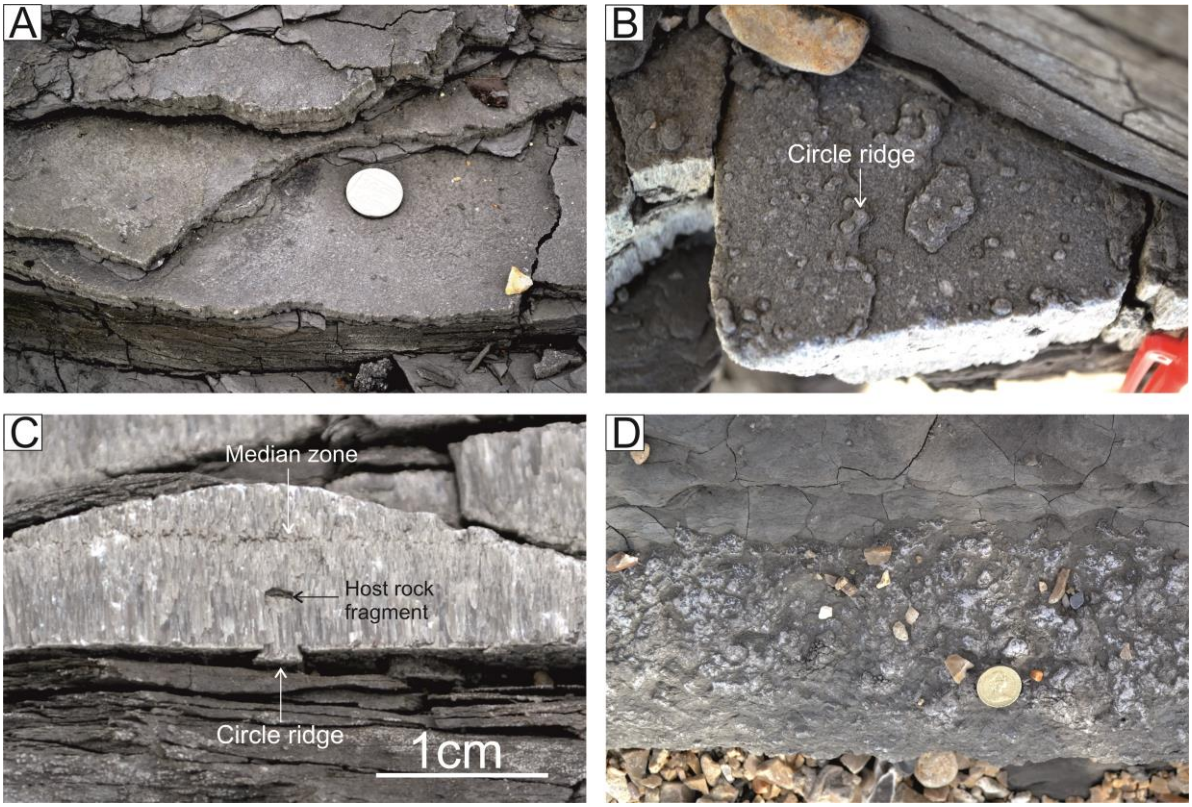


Figure 4.14 (A) Smooth surfaces of calcite beef veins. (B) Minor circular ridges on planes of beef veins. (C) Cross-section of beef vein showing the circular ridge. Note the small host rock fragment trapped above the ridge. (D) Uneven surfaces of cone-in-cone structures.

Interestingly, fossil ammonites with well-preserved morphology are observed on the surfaces of some short beef veins (Figure 4.15). The morphologies of ammonites on both the upper and lower surfaces are symmetrical. The skeletons of ammonites, which are representative of ammonite morphology, exhibit a higher surface relief that the smooth vein surfaces. Single veins commonly contain clusters of ammonites in varied sizes.

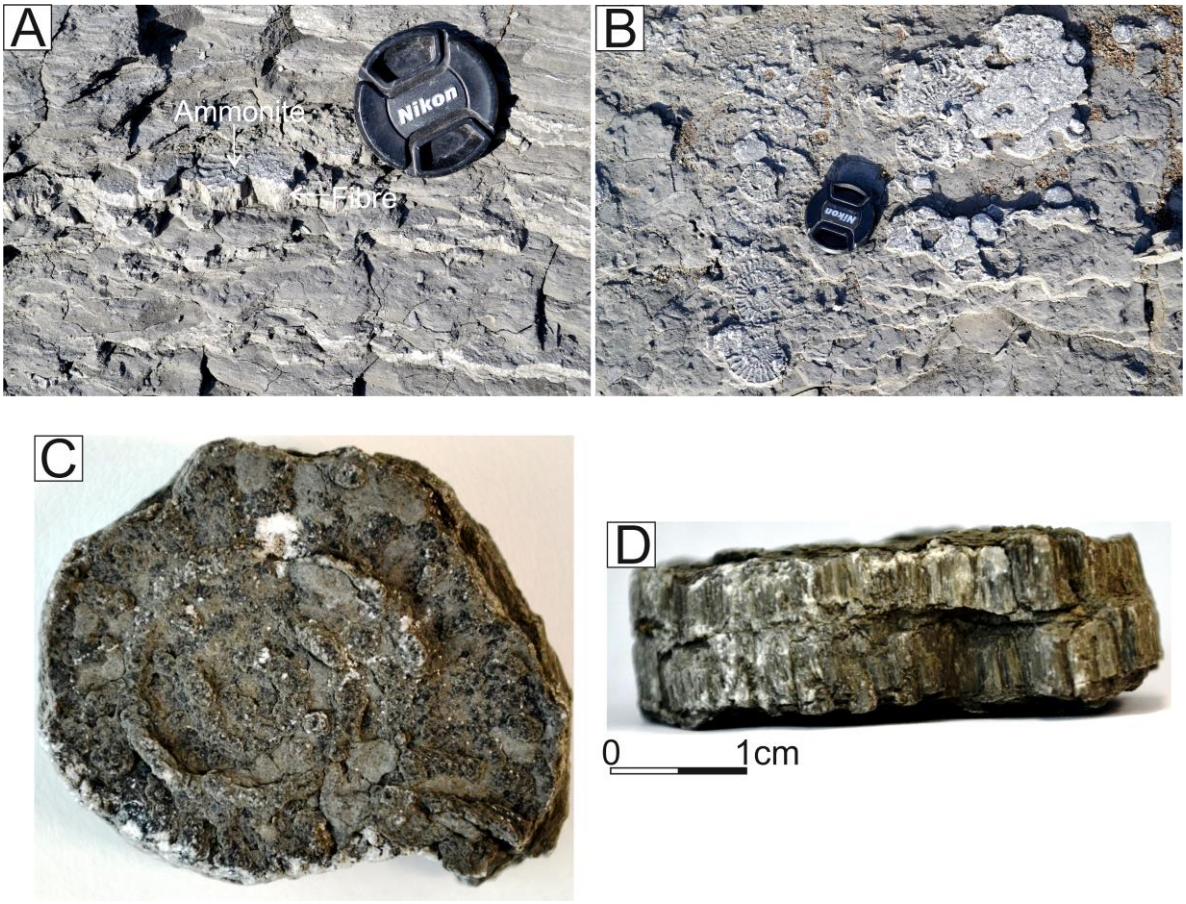


Figure 4.15 Well preserved ammonites on surfaces of beef veins. (A) 3D exposure of a short beef veins with ammonites on the surfaces. Note that the diameters of ammonites are shorter than the length of their host veins. (B) Numerous ammonites occur in single veins. (C) Plane view of the upper surface of a hand specimen of a calcite beef vein. (D) Cross section of the same beef vein shown in figure 4.15C.

4.4.2.5 Tip structure

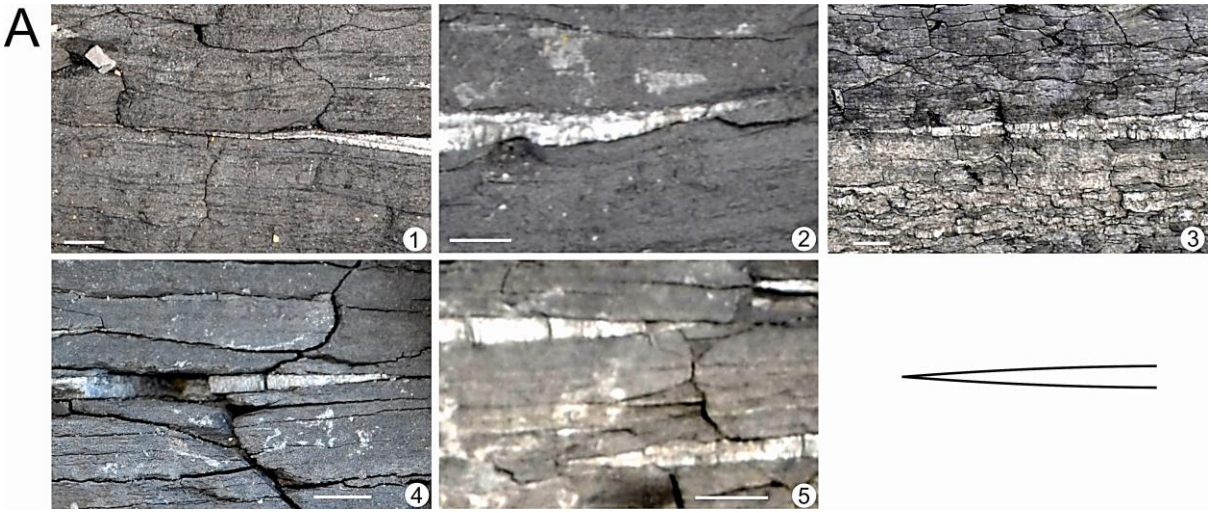
The tip structures of short beef veins exhibit varied geometries. In general, the tips mainly include gently tapering tips with acute angles and blunt tips with larger tip angles.

The veins containing gently tapering tips are mostly isolated veins that are free from vein interactions (Figure 4.16A). Those veins exhibit the maximum aperture in the centre (Figure 4.17). Vein aperture gradually decreases towards vein tips in a linear trend. The veins exhibit a symmetric structure, with both the upper and lower surfaces being planar.

Blunt tips commonly appear in closely spaced veins whose tips are adjacent to the neighbouring vein (Figures 4.16B-D). The mutual interfering of the veins is evident from the deformed host rock with curved laminations parallel to vein planes.

According to tip angles and geometries, the blunt tips can be subdivided into wedge tips, square tips and round tips. Wedge tips are observed in closely spaced veins with a vertical spacing less than 5 cm (Figure 4.16B). The adjacent veins vanish in the tip overlapping zones. Interestingly, such tips exhibit a planar-concave shape, with the outer walls being consistently planar and the inner walls curving outward. The veins with round tips exhibit a dramatic decrease in vein aperture in the tip region (Figure 4.16C). Unlike veins with wedge tips, round-tip veins display a symmetric structure. Square vein tips exhibit the largest tip angles (Figures 4.16D, 4.17). The veins that contain square tips vanish in the host rock abruptly. Such veins mostly occur in clusters in the same horizons.

The plot of vein maximum aperture versus tip angle shows that there is no clear control of vein aperture on tip angles. Most tip angles (86.9%) are between 5-25°. The average value of tip angles is 16.6°.



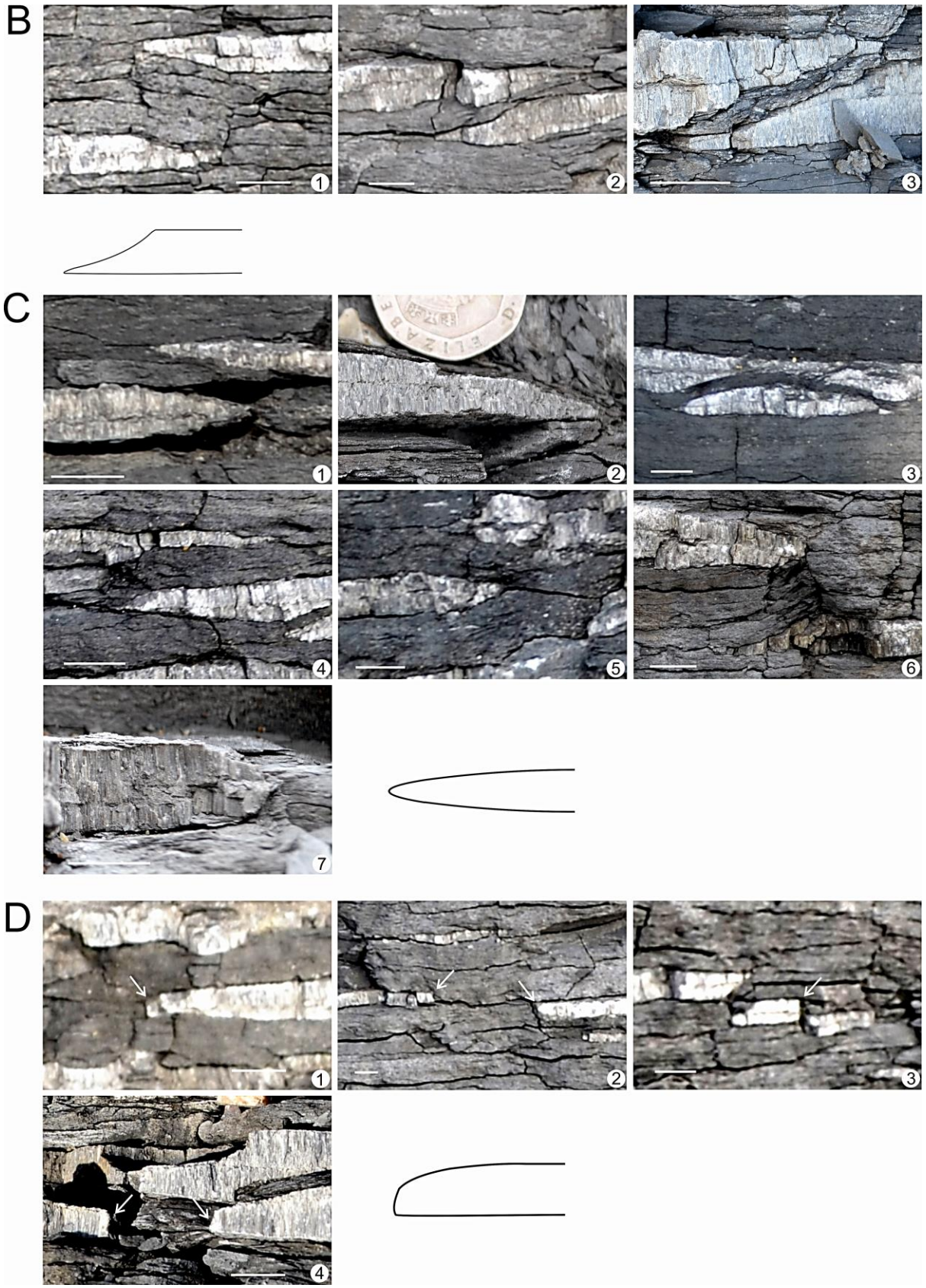
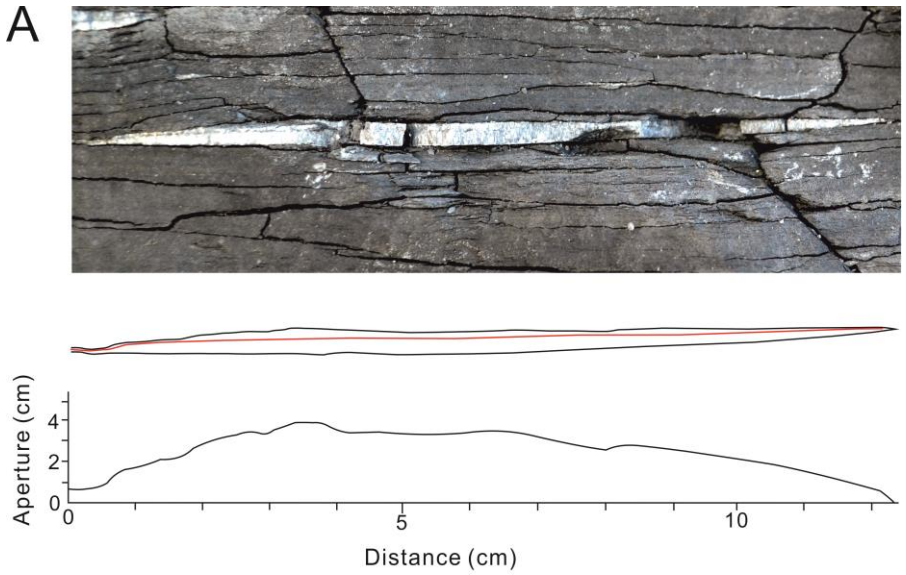
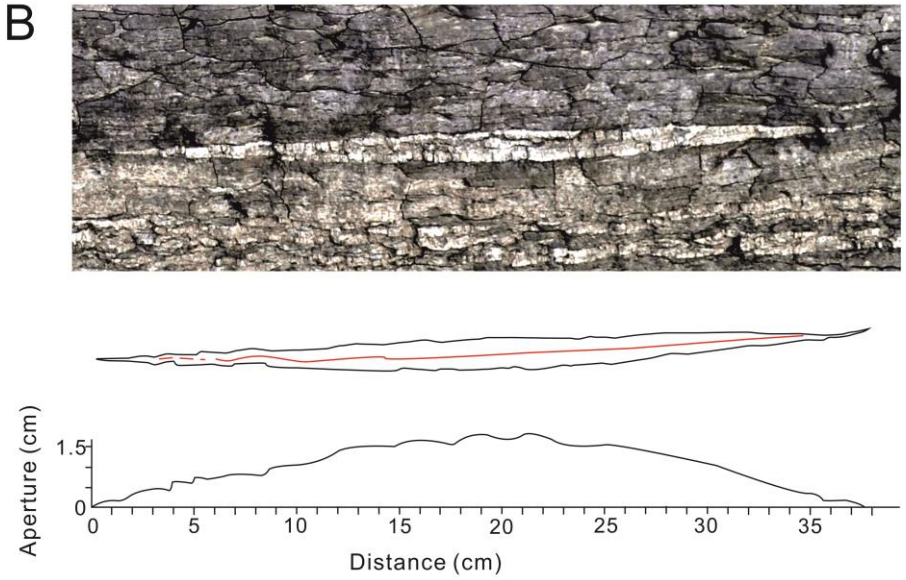


Figure 4.16 Gently tapering vein tips (A) and blunt vein tips (B-D). (B) Wedge tips. Note the planar-concave shape. (C) Round tips. (D) Square tips. The line drawings illustrate the simplified tip geometry. The scale bar is 1cm.


A
Aperture (cm)
4
2
0
0
5
10
Distance (cm)


B
Aperture (cm)
1.5
0
0
5
10
15
20
25
30
35
Distance (cm)

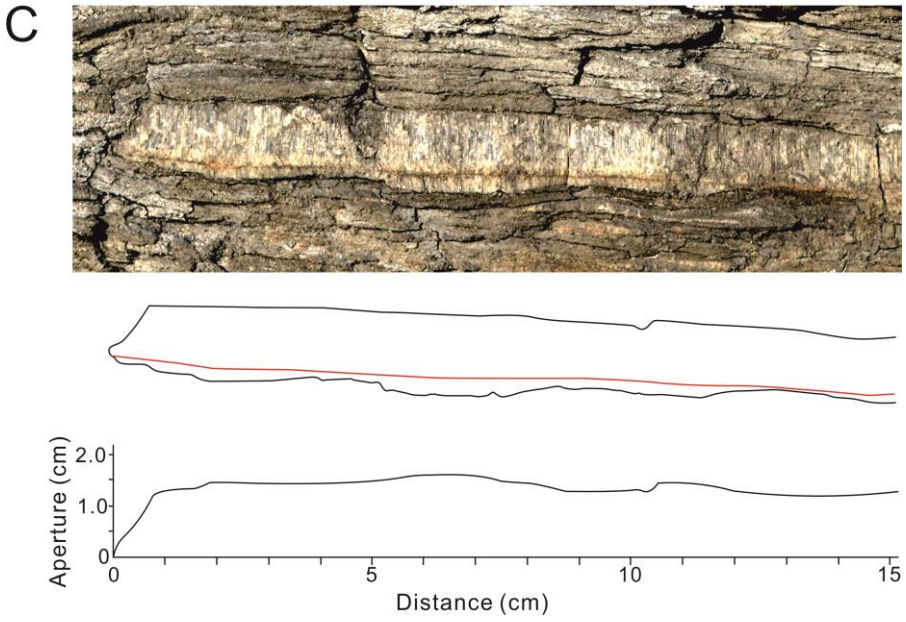

C
Aperture (cm)
2.0
1.0
0
0
5
10
15
Distance (cm)

Figure 4.17 Geometry and profile of single beef veins with gently tapering tips (A-B) and blunt tips (C). The red lines mark the median zones. Note the gradual decrease in vein aperture in figures 4.17A-B, and the sharp decrease in aperture in figure 4.17C.

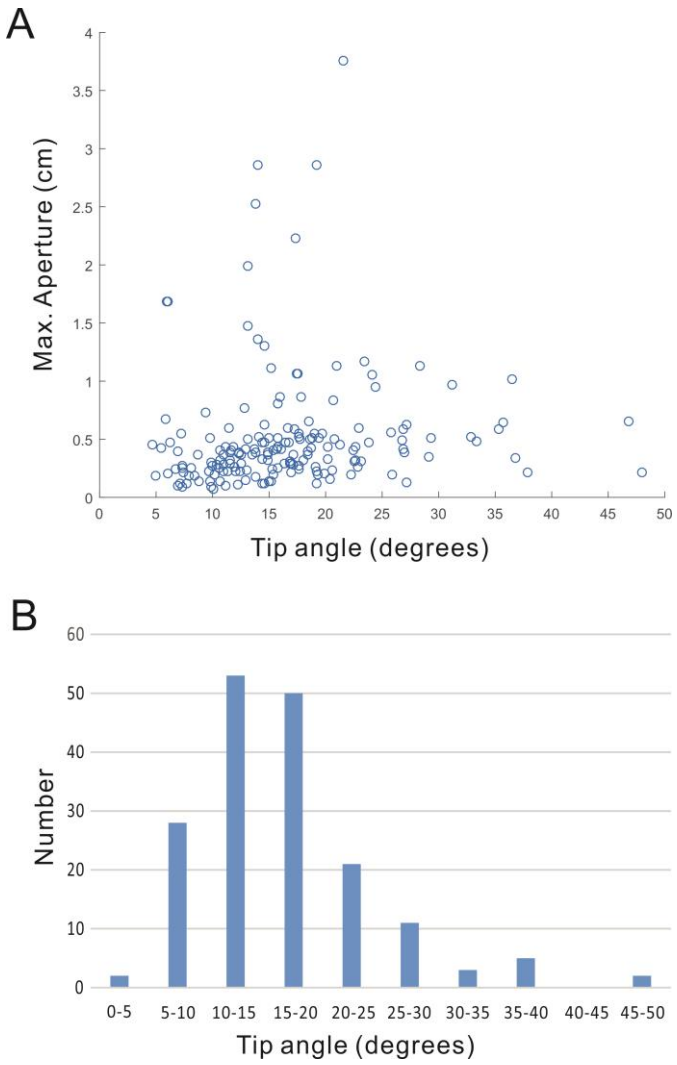


Figure 4.18 (A) Scatter plot of vein tip angles versus the maximum aperture of the veins. (B) Histogram showing the distribution of vein tip angles. N=175.

4.4.2.6 Interaction

Vein interactions are commonly observed in closely spaced vein sets. The interactions are represented by the change of vein aperture in the overlapping zones of adjacent veins (Figures 4.19-20).

Figure 4.19A illustrates typical interactions of closely spaced veins in the vertical direction. The upper vein exhibits a planar tapering tip and a curvy median zone. The trace of the median zone is generally sub-horizontal; however, it is curved and parallel to the upper plane of the lower vein in the overlapping zone. The lower vein exhibits a symmetric structure, blunt tips and a horizontal median zone. Interestingly, the aperture of the upper vein decreases gradually in the overlapping zone. Its lower margin is parallel to the median zone whist the upper wall remains consistently horizontal. However, the sum of aperture of the two veins in the overlapping zone is approximately equal.

A similar condition of vein interactions is presented in figure 19B. A minor difference is that all veins exhibit horizontal median zones. The decrease in aperture of the upper vein is equal to the aperture of the lower vein such that the cumulative aperture is largely constant laterally.

Interactions of closely spaced veins commonly occur in the tips, reflected by the decrease of aperture of both veins (Figure 4.20). The inner walls of vein tips exhibit a concave shape whist the outer walls remain planar. The sum of aperture of both veins remains approximately consistent in the tip overlapping region.

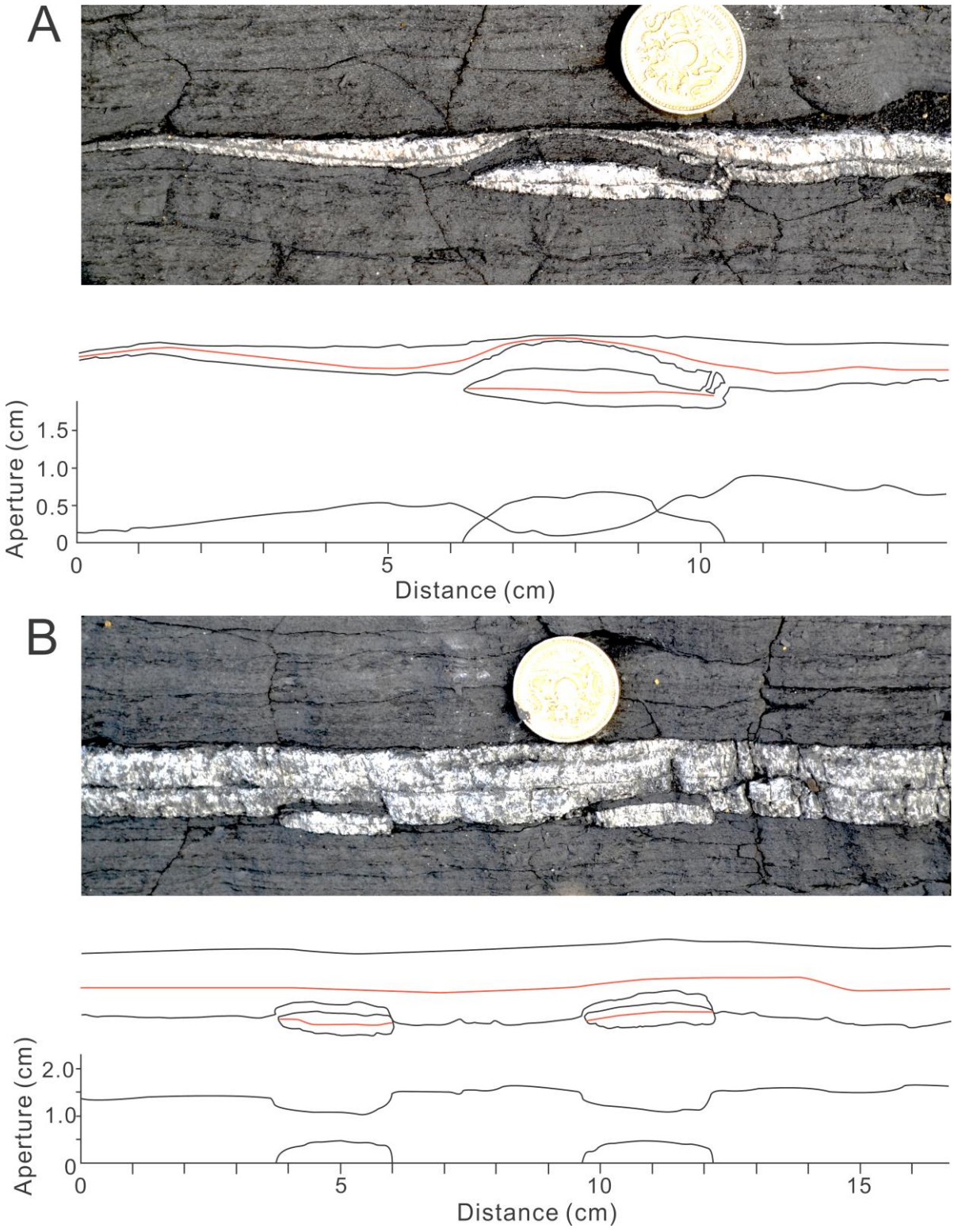


Figure 4.19 Interaction of closely spaced veins and vein profiles showing vein aperture. Note the curved median zone and thinning of the upper vein in the overlapping zone in figure 4.19A. The red lines mark the median zones.

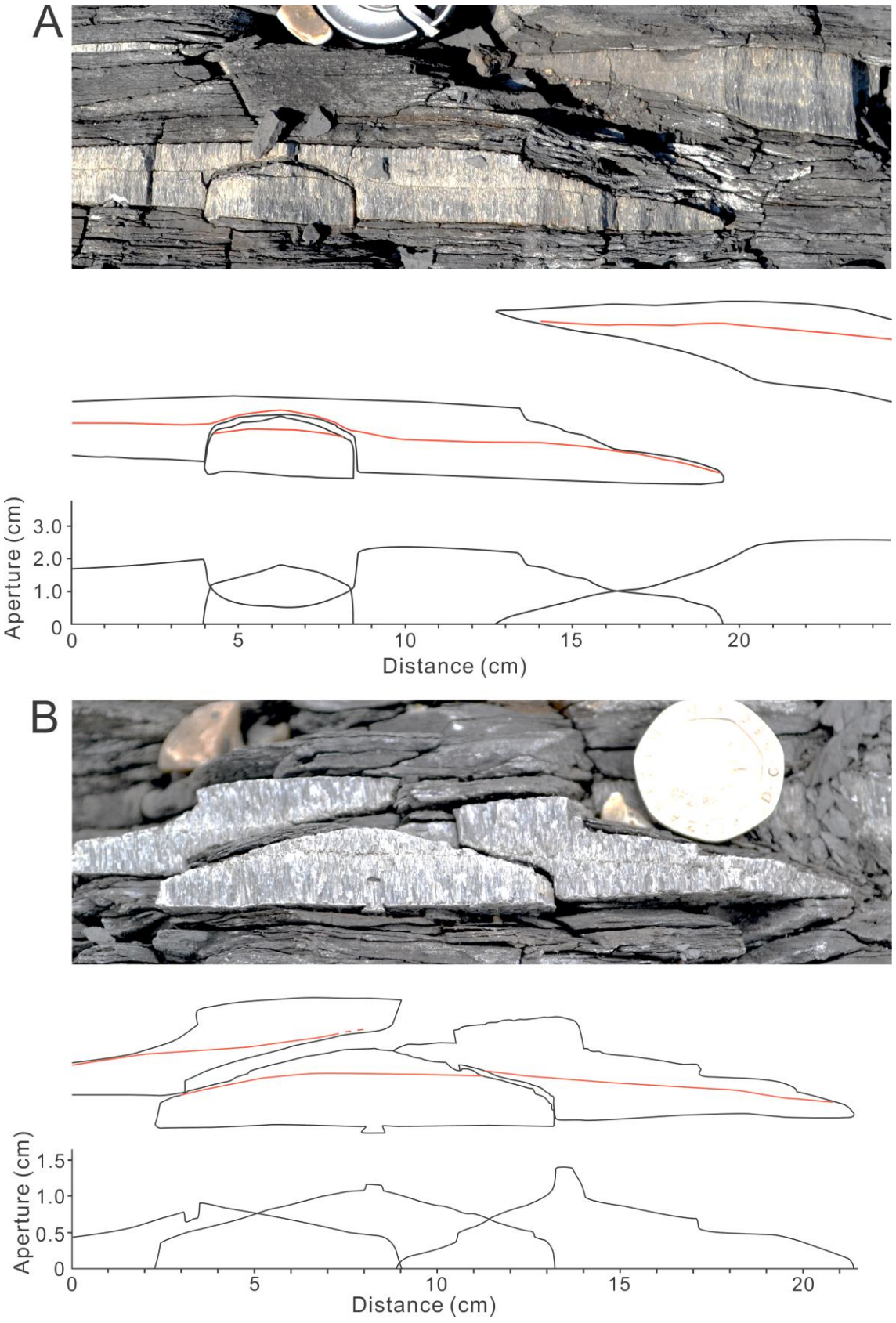


Figure 4.20 Interaction of tips of closely spaced veins and vein profiles showing the aperture. The red lines mark the median zones. Note the widening of the lowest vein in figure 4.20B due to the existence of the solid inclusion.

4.4.3 Host rock deformation

The growth of fibrous beef veins is accommodated by host rock deformation during the expansion of vein volume. The styles of host rock deformation can provide information on: (1) the relative timing of vein growth; (2) the extent of deformed rocks and vein-growth related compaction; (3) the rock mechanical properties and stress state (Maher et al., 2016); (4) whether the vein growth is displacive.

Deformation of the host rock is most easily recognized in the regions of vein tips and interactions. Figure 4.21 illustrates the typical features of host rock deformation around beef veins. Figures 4.21A and B show the curved shale laminations around beef veins. The laminations are folded and parallel to vein margins. However, the layers above the veins in figure 4.21A are horizontal, indicating little influence of the growth of the lower vein on the shales above the upper vein. Figures 4.21C-E illustrate the folds and associated fractures in the regions of blunt vein tips. Shear fractures are developed in the layers above the tip regions that exhibit the maximum curvature. The fracture mainly have a reverse displacement. By stratigraphic correlation, it is observed that the shale laminations above the veins have been uplifted to these horizons by vertical fibres. This is strongly indicative of the displacive growth of the beef veins.

Figure 4.22 illustrates the reconstruction of vein interaction and the deformation processes in the host shales. The lower vein is interpreted to have been initiated prior to the upper vein. This is reasonable because the growth of the lower vein could have caused vertical compaction in the enclosing clays with the laminations gently folded to accommodate the expansion. This explains the curved median zone in the upper vein. The formation of the upper vein commenced along the curved bedding fissure at a certain time during the continued growth of the lower vein. The extent of rock deformation is mainly restricted to the

overlapping areas of the two veins. The shales between the two veins have experienced the highest degree of growth-related compaction.

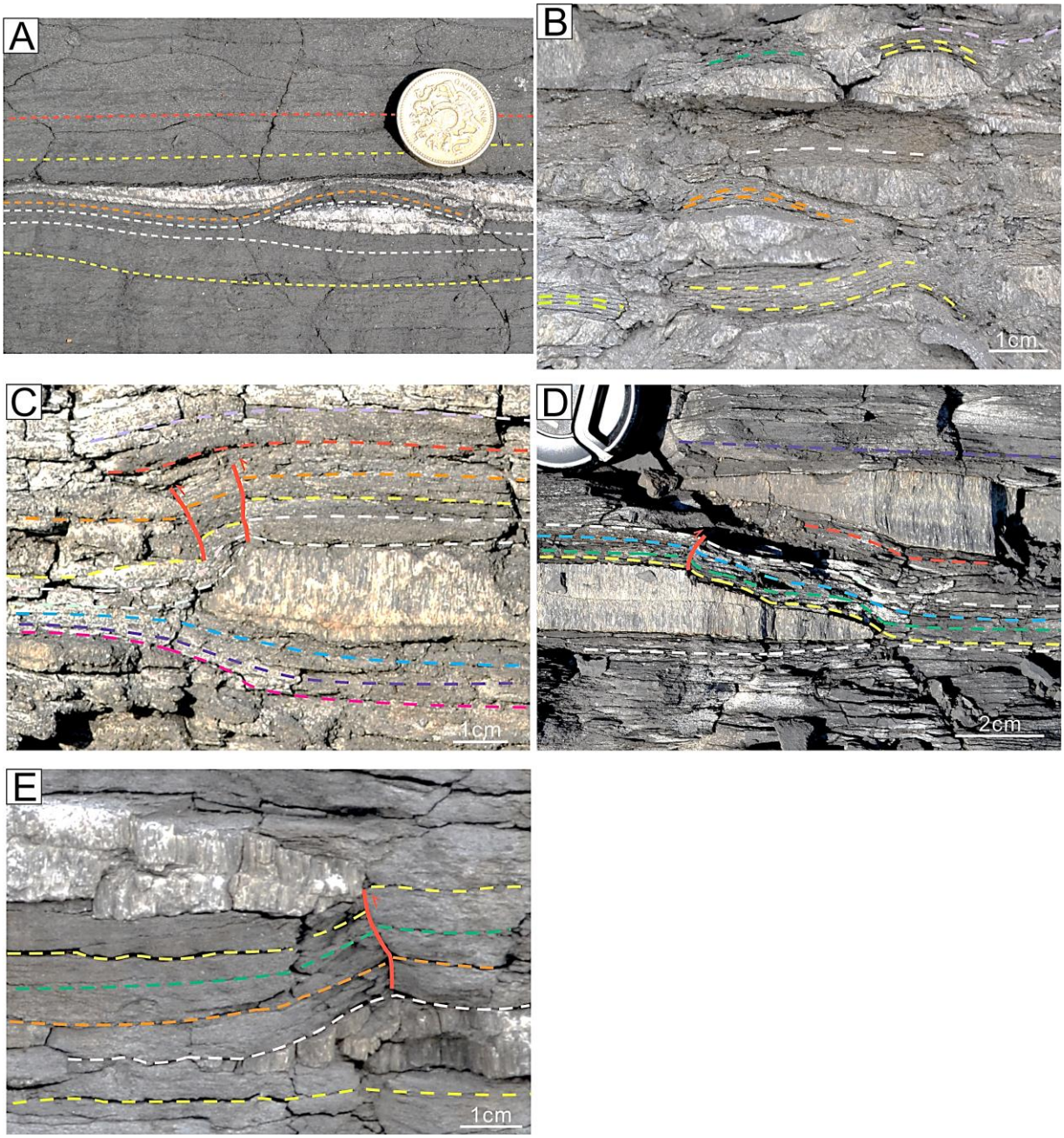


Figure 4.21 Deformation of shales in the regions around beef veins. (A) Curved shale laminations following the traces of vein margins in the overlapping zone of two closely spaced veins. (B) Curved laminations showing varied traces around a cluster of small beef veins. (C) Folding and fracturing in the shale in the tip region of a blunt vein tip. (D) and (E) Vein expansion-related compaction and the associated fracturing. The dashed lines mark the bedding. The red solid lines mark the shear fractures with a reverse displacement.

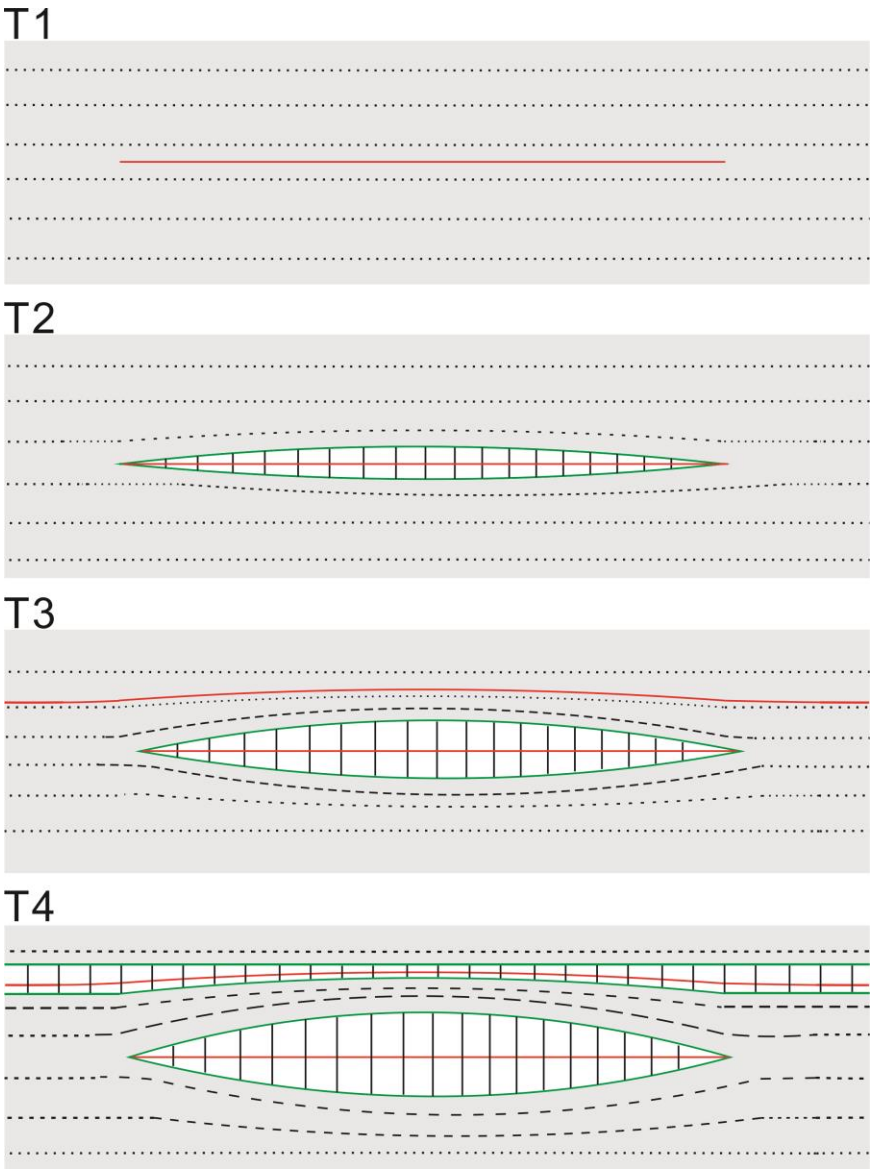


Figure 4.22 Cartoon illustrating the processes of growth of two closely spaced veins and the related host rock deformations. See text for detailed explanation.

Figure 4.23 illustrates reconstruction of the processes of tip interactions and the ductile/brittle deformation in the host shales. Primarily, two veins were initiated in two different horizons with a short vertical distance between them. Fibre growth in both veins caused vertical squeezing of both the upper and lower shales and finally led to shear fracturing in the tip region with the maximum curvature. The shales in the relay zone of two veins have suffered compressive stresses from both the veins. The shales overlying the upper vein and underlying

the lower vein have experienced vertical compaction during vein growth, however, they remain horizontal. The displacive growth of the veins can be highlighted by the folding in the tip regions that marks the growth-related displacement of the shales.

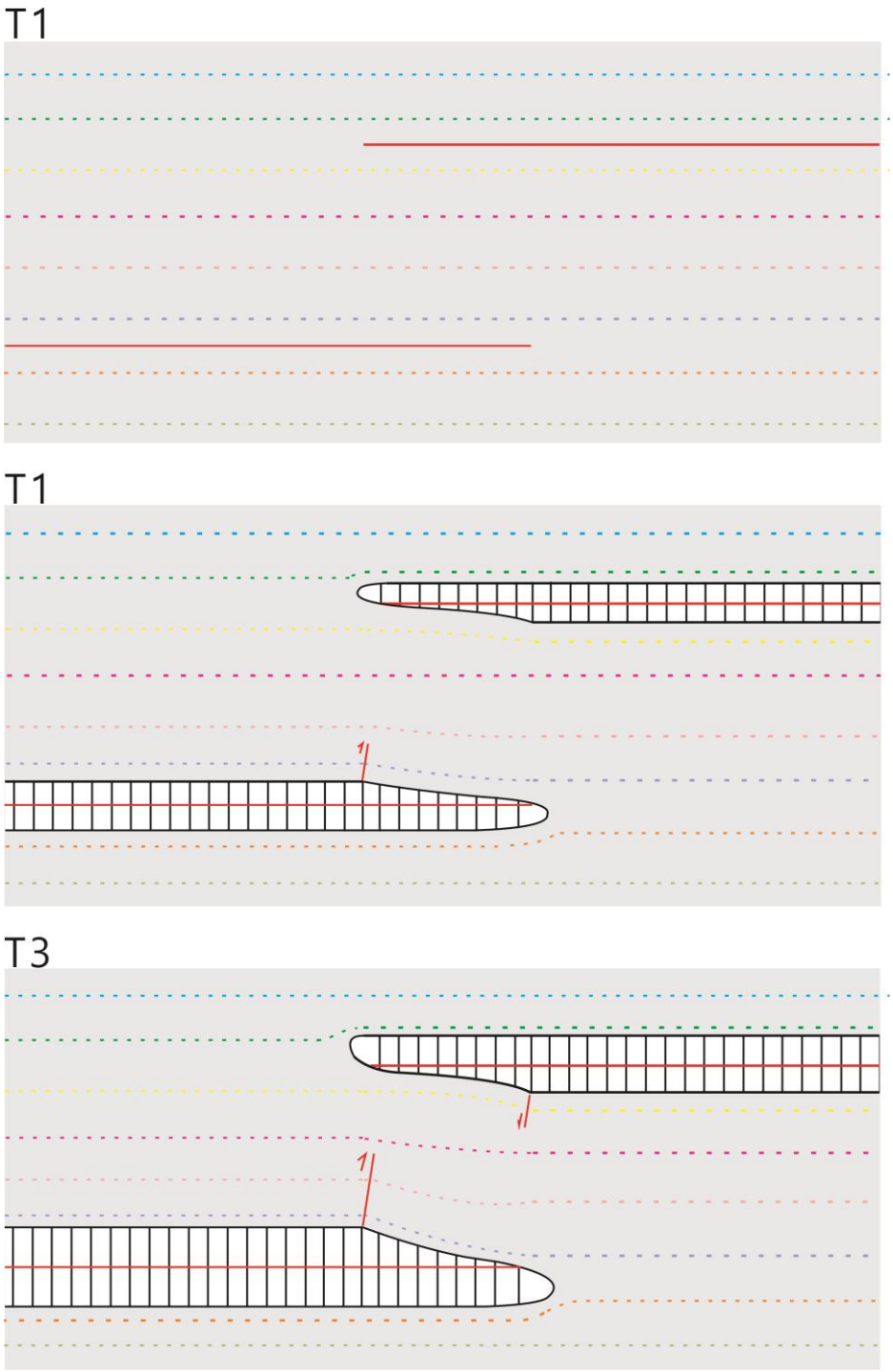


Figure 4.23 Cartoon illustrating the processes of interaction of tips of two closely spaced veins and host rock deformations in the relay zones. See text for detailed explanation.

The formation process of beef veins with parallel median zones shown in figure 4.19 is illustrated in figure 4.19B. The veins are interpreted to have formed synchronously or within a relative short time-interval, such that the extent of host rock deformation induced by vein growth was beyond the horizons where the median zones of both veins lie. Hence, the median zones as primary fractures occurred along undistorted bedding planes and exhibit sub-horizontal traces. During the progressive growth of both veins, the adjacent host rocks have been squeezed, especially those between the overlapping zones of the veins have underwent two-way growth-related compaction. Later, the lower fibres of the upper vein reached the horizon of the lower vein. Further growth was inhibited in the overlapping zone as the space have been accommodated by the lower vein. Calcite fibres above the overlapping zone exhibit varied length due to the lenticular shape of the lower vein, whilst those above the tip regions of the lower vein are longer than those near the central regions. The fibre growth beyond the overlapping zone were not affected by the lower vein. Finally, the upper vein and the lower vein are bounded by a thin band of host rocks with curved laminations parallel to vein margins.

The observations and interpretations above demonstrate that (1) the synkinematic deformation of the host rock is plastic during vein expansion; (2) vein growth led to a finite displacement of the layers above/below and a growth-related compaction; (3) the physical state of the host rock was possibly during the stage of ductile-brittle transition as evident from the shear fractures (Figure 4.23). The mechanism of vein displacive growth is discussed in section 5.8.5.

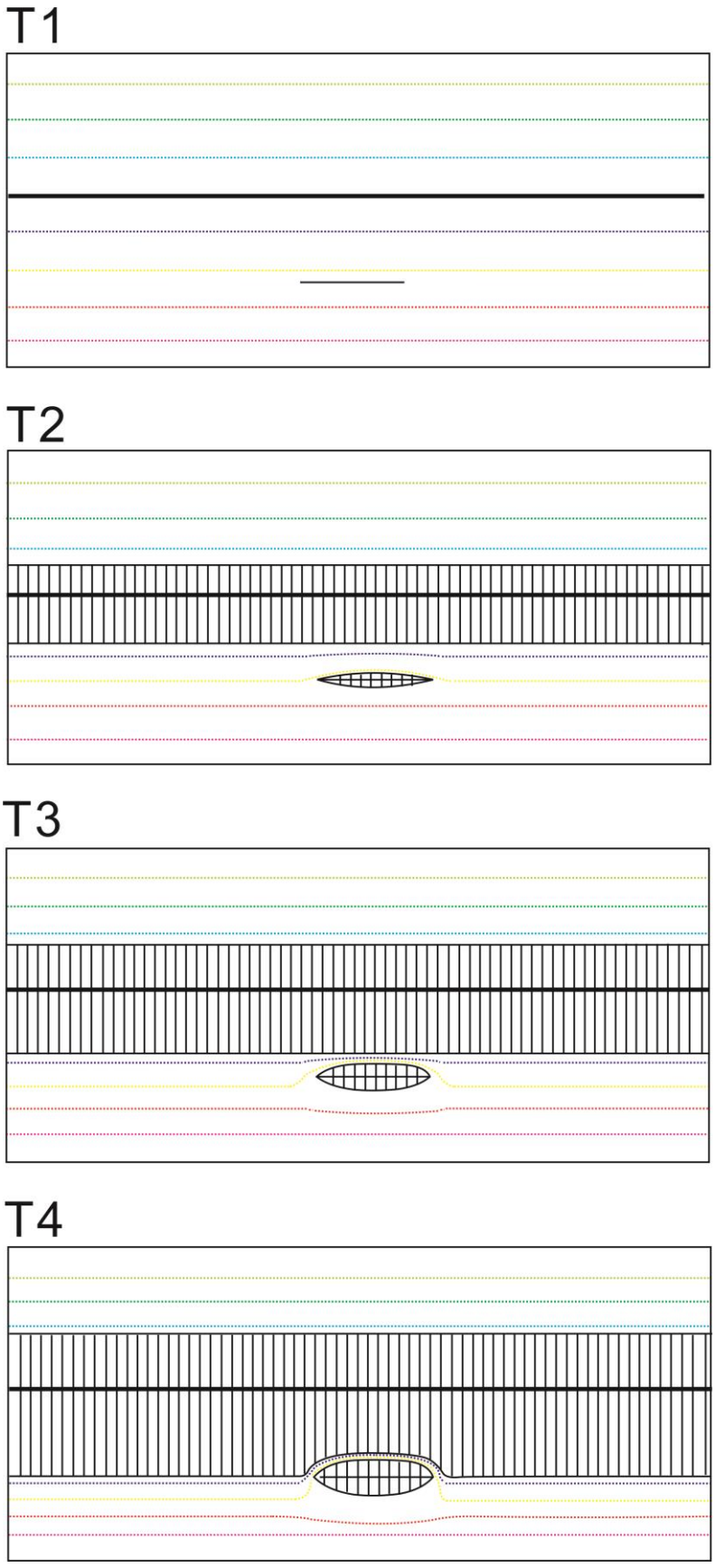


Figure 4.24 Cartoon illustrating the formation process of two closely spaced veins with horizontal median zones. See text for explanation.

4.5 Geochemistry

The geochemical studies in this project mainly focus on the carbonate concentration and total organic carbon of the host rocks, the carbon and oxygen isotope composition of the veins. Previous analysis of stable isotope signatures of beef veins in the study area by Marshall (1982) and Worden et al. (2015) yielded information on vein formation and diagenesis of the host shale; however, a further investigation is still needed due to the lack of data from the veins exhibiting varied patterns, the host rocks, and samples from different horizons. This study presents the geochemical data of calcite beef veins, cone-in-cone structures, and their host rocks that were sampled from four sites. The results provide new clues on fluid-rock interactions, diagenetic conditions and fluid movement during vein formation.

4.5.1 Carbonate concentration

The carbonate concentration in the shale samples of different horizons in site 1 without macroscopic veins ranges from 8.25% to 36.17% by weight (Figure 4.7). The average value is 17.58%. Horizon 9 and 27 contain the highest content of carbonate, which reaches up to 26.67% and 36.17% respectively.

4.5.2 Total organic carbon

The total organic carbon (TOC) in shales in site 1 ranges from 1.78% to 4.70%, with an average value of 3.18% (Figure 4.7). The peak value appears in horizon 9. Negative excursions occur in horizon 11 and 19, whose TOC values are 2.22% and 1.78% respectively.

4.5.3 Carbon isotope data

Site 1

The $\delta^{13}C$ values of the fibrous calcite veins in site 1 range from -1.180‰ to 2.462‰, with an average value of 0.353‰ (Figure 4.26). Most of the $\delta^{13}C$ values are positive. The negative values mainly occur in the cone-in-cone structures in horizon 8, 10 and 18. The beef veins predominantly exhibit positive $\delta^{13}C$ values. $\delta^{13}C$ values in the beef veins with well-preserved ammonites on the surfaces range from 0.156‰ to 0.726‰. In single beef veins, the upper parts and the lower parts reveal either similar or varied $\delta^{13}C$ values. The thin calcite bands in horizon 4 exhibit a $\delta^{13}C$ value of -0.919‰.

In contrast to the calcite veins, the shale beds all reveal negative values of $\delta^{13}C$, excluding bed 119 (0.092‰). The negative $\delta^{13}C$ values range from -0.232‰ to -1.708‰, with a median value of -0.665‰ and an average value of -0.686‰. The shales with the lowest $\delta^{13}C$ values are in horizon 27 that contain discrete carbonate concretions.

The plot of $\delta^{13}C$ values of calcite veins versus that of their host rocks shows that the data points are widely scattered without showing a regular pattern (Figure 4.27). The linear trendline for the data set fits a low coefficient of determination R^2 of 0.1403.

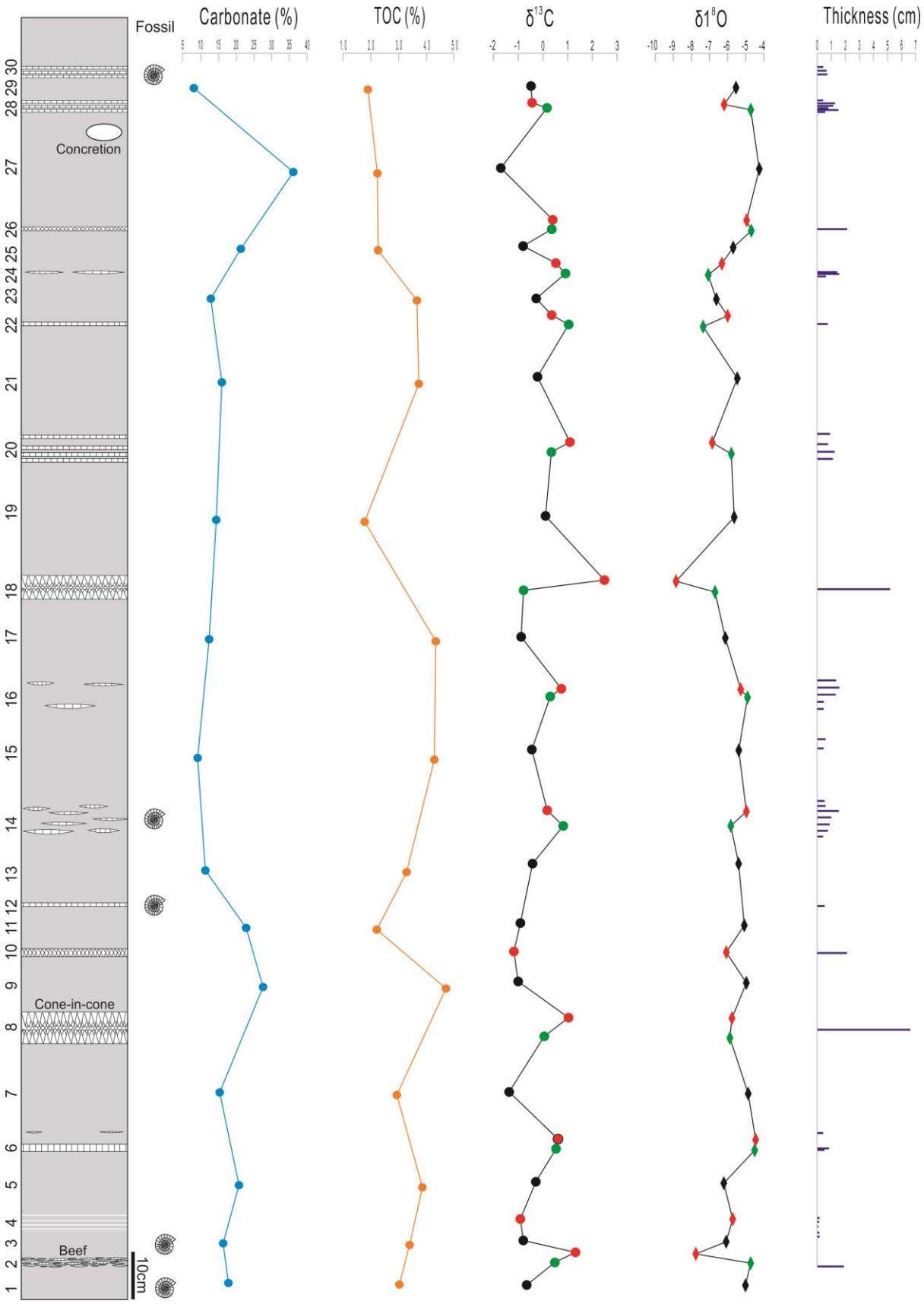


Figure 4.25 Plot of carbon and oxygen isotope composition of calcite beef veins and host rocks, TOC and carbonate concentration of the host rocks, and the maximum vein aperture in site 1. Green and red colours represent the lower and upper part of an individual vein.

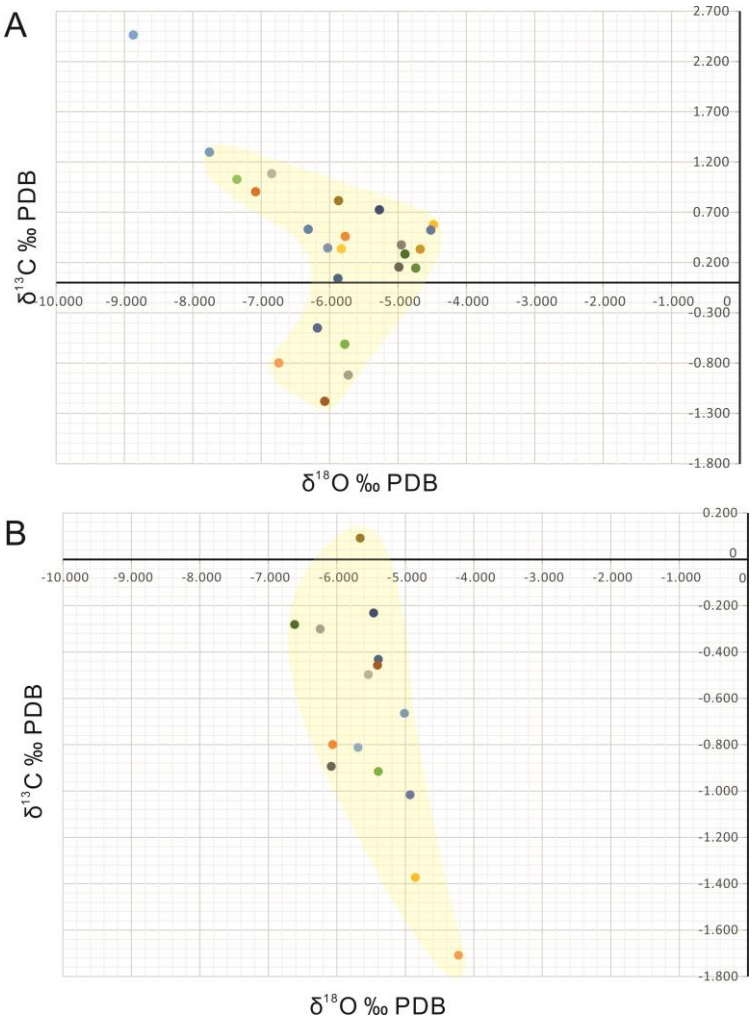


Figure 4.26 Carbon versus oxygen isotope composition in calcite veins (A) and the host rocks (B) in site 1. See original data in the appendix (Table 1).

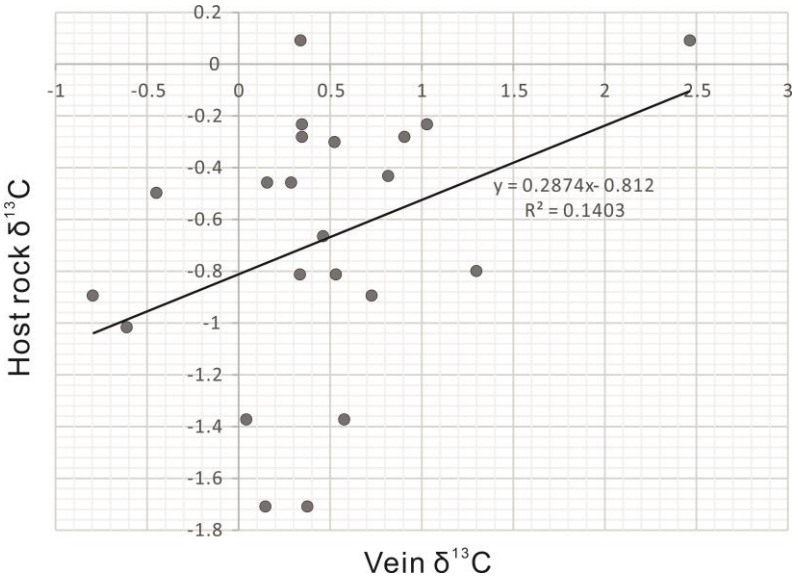


Figure 4.27 Carbon isotope composition of calcite veins versus host rocks in site 1.

Site 2

The $\delta^{13}C$ values show a rather regular pattern in site 2 (Figures 4.28-29). The $\delta^{13}C$ values of the closely spaced calcite veins are all positive, ranging from 0.244‰ to 0.888‰. The upper parts and the lower parts in single veins exhibit slightly different values (<0.5‰). The $\delta^{13}C$ values of the upper parts of two veins are lower than their lower parts respectively, while the value of the upper part is higher in the other vein. In contrast, the shales between these three veins all exhibit negative values in $\delta^{13}C$, ranging from -0.232‰ to -0.587‰.

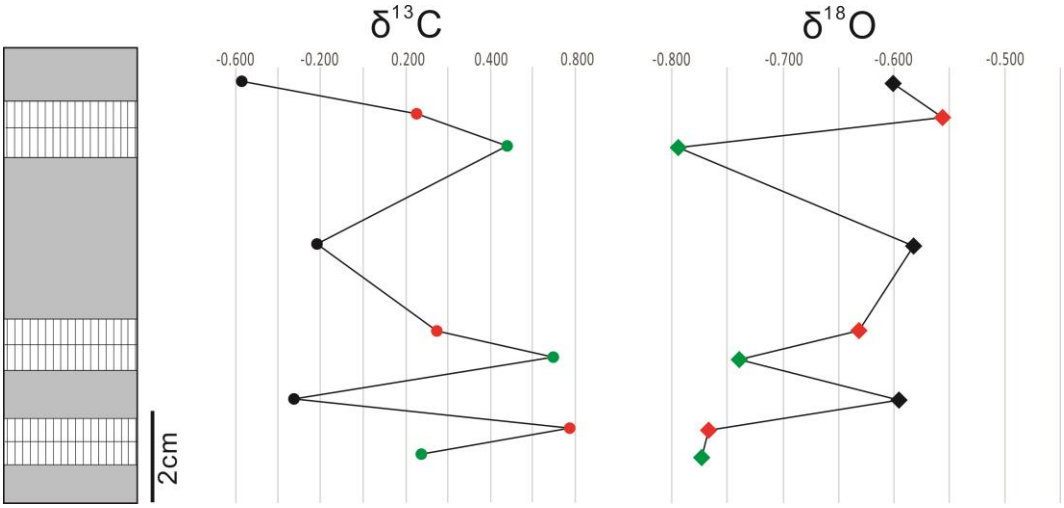


Figure 4.28 Carbon and oxygen isotope composition in calcite veins and the host rocks in site 2.

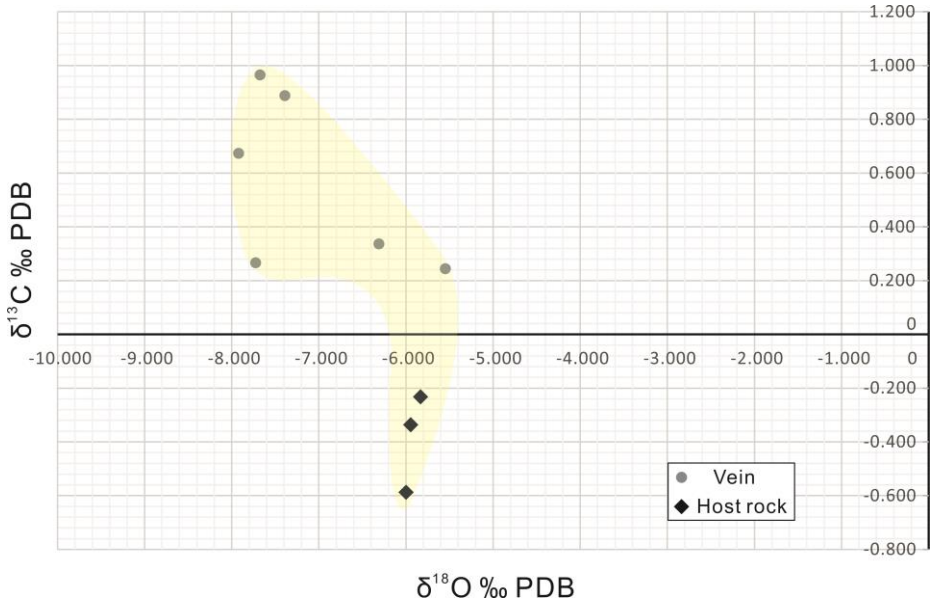


Figure 4.29 Carbon versus oxygen isotope composition in calcite veins and the host rocks in site 2. See original data in the appendix (Table 2).

Site 3

The $\delta^{13}C$ values of the upper calcite vein in site 3 are 0.154‰ and -0.113‰ for the upper and lower part respectively, whilst the $\delta^{13}C$ values of the lower vein are 0.125‰ and -0.262‰ (Figure 4.31). The upper parts of the two calcite veins both reveal higher $\delta^{13}C$ values, whilst their lower parts show lower values. Host rocks in horizons between the two calcite veins show varied values in $\delta^{13}C$. The values decrease gradually downward from 0.128‰ to -0.180‰.

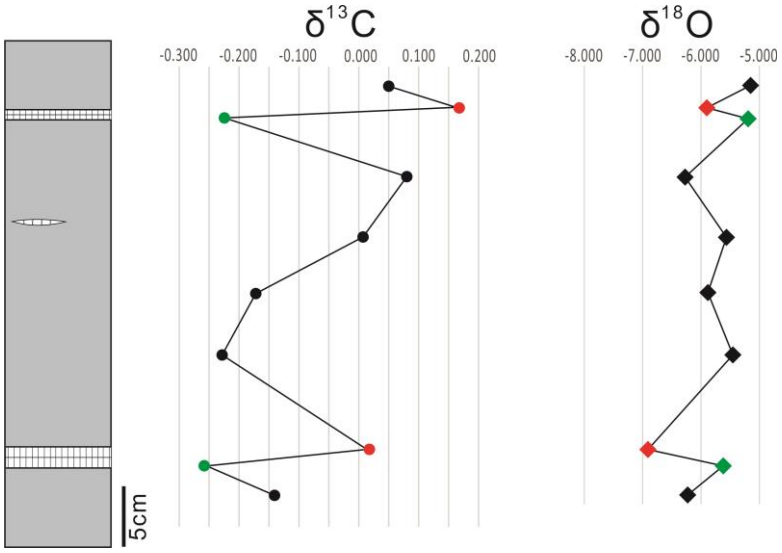


Figure 4.30 Carbon and oxygen isotope composition in calcite veins and the host rocks in site 3.

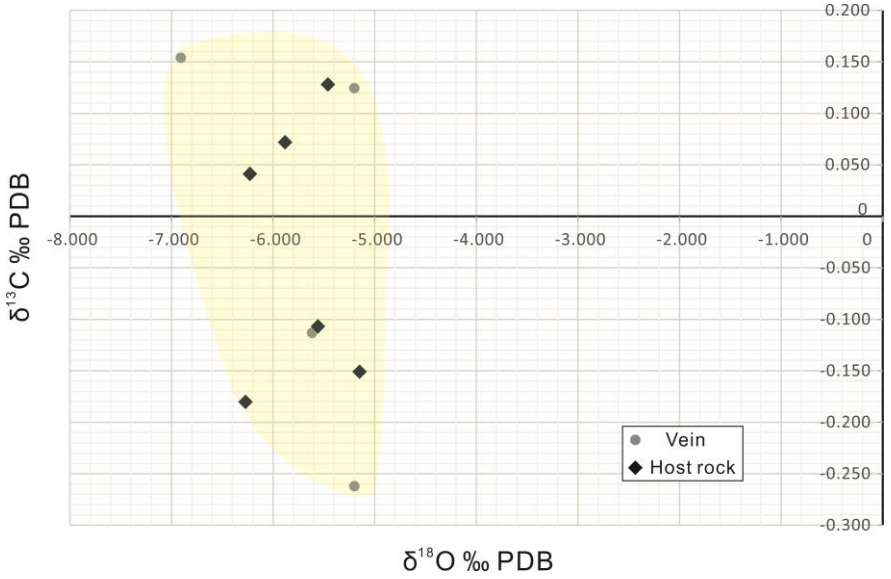


Figure 4.31 Carbon versus oxygen isotope composition in calcite veins and the host rocks in site 3. See original data in the appendix (Table 3).

Site 4

The $\delta^{13}C$ values revealed in the core of the carbonate concretion range from -8.783‰ to -7.117‰, which are much lower than the surrounding cone-in-cone structures and beef veins (Figures 4.32-33). The cone-in-cone structures in the lower rim of the concretion exhibit a negative $\delta^{13}C$ value of -1.515‰, whist those in the upper rim exhibit positive values. A $\delta^{13}C$ measurement of 2.723‰ is obtained in a beef vein above the concretion. The $\delta^{13}C$ values of dark shales above and below the concretion are 0.461‰ and -0.063‰ respectively.

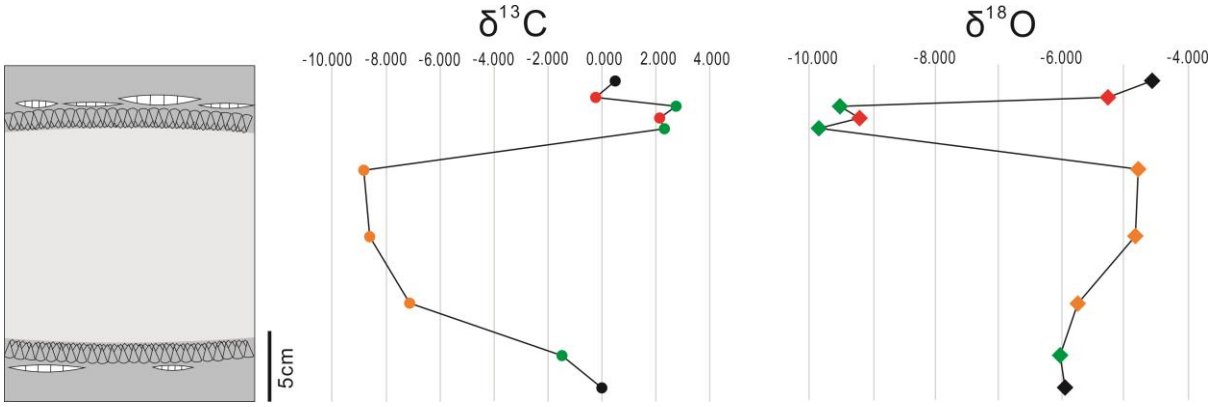


Figure 4.32 Carbon and oxygen isotope composition of the carbonate concretion, enveloping cone-in-cone, beef vein and host shales.

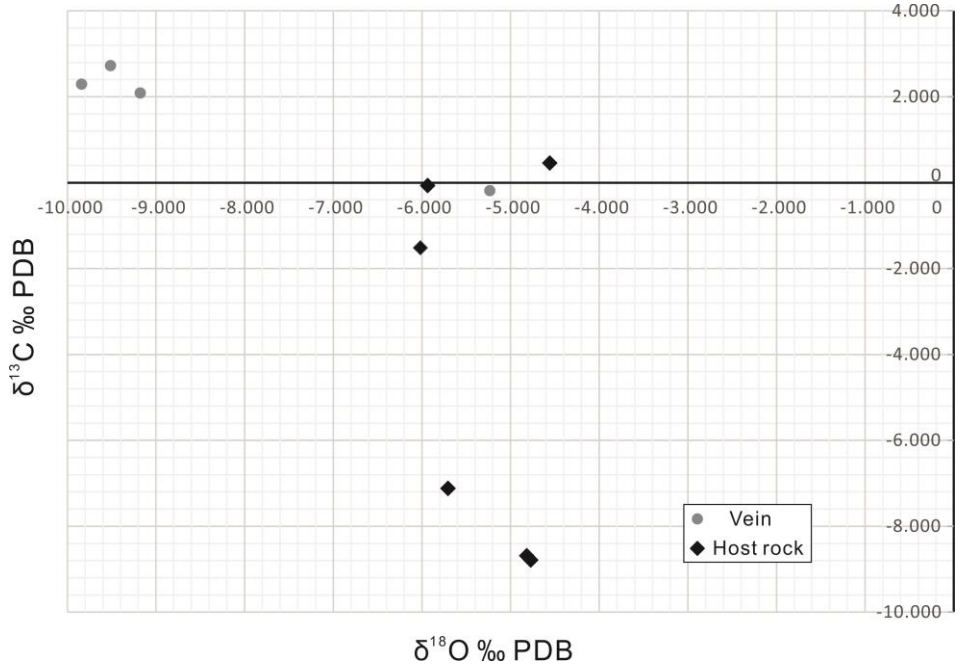


Figure 4.33 Carbon versus oxygen isotope composition in samples from site 4. See original data in the appendix (Table 4).

4.5.4 Oxygen isotope data

The $\delta^{18}O$ composition of calcite veins in site 1 are all negative, ranging from -8.872‰ to -4.521‰. Most $\delta^{18}O$ values are between -6.5‰ to -4.5‰. The $\delta^{18}O$ values of the host rocks exhibit a narrower range from -6.616‰ −4.224‰. The $\delta^{18}O$ compositions are mostly between -6‰ and -5‰.

The $\delta^{18}O$ values of calcite veins in site 2 ranges from -7.921‰ to -5.547‰. The samples from the three shale horizons exhibit $\delta^{18}O$ values of approximately -6‰, which is higher than most vein $\delta^{18}O$ compositions.

The $\delta^{18}O$ composition of the beef veins in site 3 ranges from -6.910‰ to -5.200‰. The measurement of host shales exhibits a similar range of $\delta^{18}O$ values from -6.273‰ to -5.461‰.

The core of the carbonate concretion in site 4 exhibit $\delta^{18}O$ values from -5.705‰ to -4.772‰, which are higher than the surrounding cone-in-cone structures and beef veins. In contrast to the concretion and the host shales, the $\delta^{18}O$ composition of cone-in-cone structures in the upper rim of the concretion exhibits the lowest values.

Plots of carbon versus oxygen isotope compositions of samples demonstrate the covariations of oxygen and carbon isotope signatures in the calcite veins, especially in the samples from site 4 (Figure 4.31). Lower $\delta^{18}O$ values commonly correspond to higher $\delta^{13}C$ values.

4.6 Discussion

The field characteristics and stable isotope signatures of fibrous calcite veins in the Lower Jurassic Charmouth Mudstone shed light on the timing and mechanism of vein formation, source of carbonate materials and the fluids involved in the calcite precipitation process. The

timing, paleostress and growth mechanism of the calcite veins is discussed in Chapter 5, coupled with new detailed petrographic observations.

4.5.1 Source of carbonates

The fibrous calcite beef veins and cone-in-cone structures are ubiquitous throughout the succession of thinly bedded organic-rich shales in Charmouth, occupying approximate18.9% ($vein\ cumulative\ aperture/whole\ thickness$) of the total volume in site 1. The question arises as to the sources of carbonates involved in the precipitation, which are largely reflected in the carbon isotope signatures revealed in vein samples (Coleman and Raiswell, 1981; Irwin et al., 1977; Marshall, 1982).

Importantly, the local dissolution of fossil shells could have provided bicarbonate with a $\delta^{13}C$ value of $\sim$0‰ (Marshall, 1982). The skeletal remains of calcium-secreting fossils on vein surfaces could be volumetrically important components of the calcite veins (see discussion in chapter 5) and possibly even contribute to a component of up to 80% to the calcite veins (Hendry et al., 1995). However, the variations in $\delta^{13}C$ values suggest a mixture of material sources from organogenic carbon in the country rock (Irwin et al., 1977).

The initial carbon isotope composition of the pore fluid at the sediment-water interface would be that of sea water, which is later modified by CO_2 generation from the decomposition of organic matter due to the increase of burial depth and temperature (Conybeare and Shaw, 2000; Irwin et al., 1977; Tissot et al., 1974).

The carbonate concretion in site 4 is isotopically zoned, with the core presenting the most negative $\delta^{13}C$ values. Such an isotopically light carbon is suggested to be derived from in situ decomposition of organic matter during bacterial reduction in an anaerobic environment (Kiriakoulakis et al., 2000; Raiswell and Fisher, 2004). Sulphate reducing produces carbonate

depleted in ^{13}C ($\delta^{13}C \approx$-20‰ to -25‰) (Hudson, 1978; Mclane, 1995). Summary reaction for production of carbonate by sulphate reduction is:

$$SO_4^{2-} + 2[CH_2O] \rightarrow H_2S + 2HCO_3^-$$

This idea has been verified by the presence of biomarkers of abundant unsaturated fatty acid in the lower Jurassic concretions (Kiriakoulakis et al., 2000). The bicarbonate derived during this stage gives rise to the negative carbon isotope composition of the concretion core. The formation of concretions in the Lower Jurassic shales in the study area is suggested to have commenced during early burial, possibly in the first tens of metres, which are evident from the preservation of labile organic matter in the concretion and well-preserved ammonites within the concretions (Allison and Pye, 1994; Marshall and Pirrie, 2013; Stewart, 1986).

However, the enveloping cone-in-cone structures and beef veins have heavier carbon isotope compositions than the concretion core. This shift in carbon isotope signature suggests the weakening of the role of sulphate-reduction in providing carbonate materials during later calcite precipitation. Nevertheless, biomarkers of fatty acid for bacterial activity have also been observed in calcite beef veins, although they are much less abundant than those in the concretions (Kiriakoulakis et al., 2000; Pearson et al., 2005). This demonstrates that bacterial activity has at least contributed to some of the precipitated carbonate in the calcite veins and may primarily control the distribution of the veins.

An important feature of carbon isotope signatures is that the $\delta^{13}C$ values of the host shales are commonly lower than those in the veins. The calcite veins mostly have positive $\delta^{13}C$ values (ca. 0‰-2‰), suggesting the carbonate may have been originated from a source with heavy carbon.

CO_2 produced in the methanogenesis zone, which usually underlies the sulphate-reducing zone in the sediment column, is suggested to reveal heavy carbon isotope signatures ($\delta^{13}C \approx 0‰$ to 15‰) (Raiswell, 1987; Wolff et al., 1992). The precipitation of the upward migrating methanogenic CO_2 results in authigenic carbonate with positive carbon isotope compositions (Krylov et al., 2008; Whiticar, 1999). Hence, the methanogenic bicarbonate contributes to an overall heavier carbon isotope signature. The mixing of methanogenic CO_2 with that derived from bacterial sulphate reduction results in a balance in the overall isotope composition of the veins.

The upper parts of veins in horizon 2 and 18 in site 1 show higher $\delta^{13}C$ values and lower $\delta^{18}O$ values than the contacting host rocks and other veins. Their isotope compositions can thus result from a greater component of CO_2 derived from methanogenesis than other veins at a deeper burial depth and a higher formation temperature.

Another possible source of carbonate is the CO_2 generated by oxidation of CH_4 above the zone of methanogenesis. However, this process give rise to carbonate with extremely light carbon isotope compositions ($\delta^{13}C \approx -70‰$-$60‰$) (Gautier and Claypool, 1984). Hence, this hypothesis can be ruled out as an important source of CO_2.

It is thus suggested that the calcite beef veins and the cone-in-cone structures mainly derived carbonate from seawater inorganic carbon and bioclasts.

4.5.2 Diagenetic conditions

The oxygen isotope composition of carbonate minerals is the function of primary isotope composition and the specific temperature of the water in which the carbonates are precipitated (Boggs, 2009; Grossman and Ku, 1986). However, the $\delta^{18}O$ values of the black shales do not reveal the primary $\delta^{18}O$ composition due to the resetting of oxygen isotope

values during burial and diagenesis in the sediments (Worden et al., 2015). Hence, the oxygen isotope signatures of calcite veins can provide information on the source of formation fluid and the clues to physical and chemical processes that may have affected the original fluid composition (Conybeare and Shaw, 2000; Longstaffe, 1986).

The oxygen isotope composition of the calcite veins falls within a narrow range (ca. -7‰ - -5‰), which is similar to or slightly below the range of host shales. Such an oxygen isotope signature is too negative to reflect carbonate precipitation in equilibrium with the early Jurassic marine pore waters (-1.2‰) (Marshall, 1982).

The negative shift of the oxygen isotope compositions is mainly ascribed to several mechanisms, including the influence of isotopically light meteoric waters (Carpenter et al., 1991), $\delta^{13}C$ depleted waters generated by the decomposition of organic matter (Sass et al., 1991) or by water-rock interactions (Longstaffe, 1986; Zheng and Hoefs, 1993), and the increase of pore-water temperatures (Al-Aasm et al., 1995; Longstaffe, 1986).

The negative $\delta^{18}O$ values of calcite veins in different horizons exhibit similarities, suggesting that the veins grew in burial rather than in depositional waters (MacKenzie, 1972; Marshall, 1982). The $\delta^{18}O$ depletion can be attributed to the increasing temperature during burial (Conybeare and Shaw, 2000; Longstaffe, 1986). The fractionation factor for calcite has been derived by experimental studies (Friedman and O'Neil, 1977):

$$1000ln\alpha = 2.78*10^{6}T^{-2}-2.89$$

Applying the oxygen isotope values of Jurassic sea water and the calcite veins in this study results in a temperature range of 27-45 ℃ for vein formation. Although there is no independent measurement of the $\delta^{18}O$ value of the sea water from which the calcite veins grew, the vitrinite reflectance data suggests a maximum burial depth of the Liassic shales of

900-1100 m in the Charmouth area and a maximum temperature of 30-50℃ (Ebukanson and Kinghorn, 1986). Hence, the assumed temperature is possibly too high to reflect the realistic temperature at which calcite was precipitated.

A flux of meteoric waters with depleted ^{18}O could presumably account for the negative shift of $\delta^{18}O$ value in the calcite veins. However, there is a limit to how much meteoric water could have been mixed with original sea waters to deplete the $\delta^{18}O$ values (Al-Aasm et al., 1995). In addition, the narrow variations of carbon and oxygen isotope values indicate only a minor influence of meteoric waters which could have generated a range of water compositions between two end member fluids that have distinct ^{18}O and ^{13}C signatures (Zheng and Hoefs, 1993).

It is suggested that the decomposition of organic matter can produce $\delta^{18}O$ depleted fluids by sulphate reduction (Sass et al., 1991). However, this model is based on very organic-rich sediments (TOC>50%) and the induced $\delta^{18}O$ shift is relatively small, which may not be applicable to the sediments with a moderate or a low TOC in the present study.

Water-rock interaction during shallow to deep burial diagenesis of shales is possible to cause oxygen isotope fractions of pore waters and thus influence $\delta^{18}O$ signatures of authigenic carbonates (Longstaffe, 1986; Zheng and Hoefs, 1993). It is suggested that the gradual pore water evolution with burial can contribute to a systematic ^{18}O depletion in successive precipitates (Dickson and Coleman, 1980; Hodgson, 1966; Marshall, 1982). This model is especially applicable when the sediments contain volcanic materials (Morad and De Ros, 1994). Hydration and carbonization occur in the sediments, leading to a negative shift in $\delta^{18}O$ values of pore waters (Al-Aasm et al., 1995).

Although most veins exhibit similar oxygen isotope signatures in the upper and lower parts, variations occur in some of veins (e.g. cone-in-cone in horizon in site 1). This can be attributed to by several factors, mainly including the local input of bicarbonate from aragonitic shells, expulsion of pore waters from shales under compaction and mixing of external pore waters (Friedman and O'Neil, 1977; Marshall, 1982).

The dissolution of prevalent aragonitic fossil shells in the shales would introduce abundant bicarbonate with $\delta^{18}O$ and $\delta^{13}C$ of approximately zero (Marshall, 1982), resulting in the mixing of original pore waters and a possible shift in the isotope signatures in precipitated calcite.

The isotope variations can also be induced by the ultrafiltration process in shales during compaction, which produces residual waters with enriched ^{18}O (Coplen and Hanshaw, 1973). However, it is difficult to assess the magnitude and validity of this explanation simply from the observed isotope signatures.

As mentioned above, the input of meteoric waters supplies a possible source of waters with different isotopical signatures from the original pore waters. The ^{18}O in meteoric waters can either be depleted or enriched (Boggs, 2009). Hence, their occurrence presumably gave rise to the variations in $\delta^{18}O$ values in the veins.

4.5.3 Vein formation

Horizontal fibrous beef veins and cone-in-cone structures in black shales are commonly considered to form as natural hydraulic fractures due to overpressure during primary oil migration (Rodrigues et al., 2009; Stoneley, 1983). This hypothesis is evident from the frequently observed hydrocarbon inclusions in the median zones of the veins that mark the primary crack opening (Dobes et al., 1999; Lash and Engelder, 2005; Suchy et al., 2002;

Zanella et al., 2014). Thus, vein formation commences along bedding planes when the shales enter the oil window and release abundant oil and gas (Cobbold et al., 2013; Lash and Engelder, 2005; Parnell et al., 2000; Rodrigues et al., 2009). This explanation is possibly reliable for shales as mature source rocks. However, uncertainties remain regarding the relative timing of vein formation and inclusion emplacement of hydrocarbons. Hydrocarbons may possibly migrate along pre-existing calcite veins as pathways rather than the low-permeable host shales. In this case, vein formation predates hydrocarbon migration. Moreover, the Charmouth Mudstone is not mature enough to produce oils (Ebukanson and Kinghorn, 1986; Kemp and McKervey, 2001; Kemp et al., 2005), and no hydrocarbons have been found in the veins. Overpressure can be generated in several ways (see Chapter 3). In this discussion, the question to be considered is the specific origin of overpressure in the Charmouth Mudstone.

As discussed above, the calcite veins could owe their authigenic carbonate materials partially to methanogenic CO_2 with positive carbon isotope values. The biogenic CH_4 and CO_2 generated in the megthanogenesis zone readily migrates upward. It is reasonable to suggest that gas migration results in overpressuring in the host sediments.

Previous studies have demonstrated that the generation of methane gas is an important, or even principle cause of overpressure and undercompaction in organic-rich shales (Flemings et al., 2003; Hedberg, 1974, 1980; Lacazette and Engelder, 1992; Osborne and Swarbrick, 1997). The corresponding decrease in fluid pressure during migration results in the exsolution of CO_2. This will be accompanied with a volume expansion in the relatively impermeable medium (Lacazette and Engelder, 1992). Meanwhile, the gas bubbles dispersed in pore waters will reduce the permeability of the bulk rock (Hedberg, 1974). Under such conditions, a catastrophic increase in fluid pressure may occur with minor changes in composition in a

fixed pore-volume rock mass. The free gas can produce three orders of magnitude more fracture volume than brines for a given pressure drop due to its greater compressibility (Lacazette and Engelder, 1992). Overpressure triggered by gas migration can exceed the sum of overburden and tensile strength of the sediments and may yield abundant tensile failures that vent the overpressured gas (Flemings et al., 2003; Liu and Flemings, 2007; Tréhu et al., 2004).

Given the narrow range of oxygen isotope values in the calcite veins in different horizons, a rather uniform paleohydrological system is inferred, where water movement seems to have been restricted. The primary migration of gases in the methanogenesis zone is highly likely to generate overpressure in the low permeability sediments (Rukin, 1990), which is evident from the covariations of carbon and oxygen isotope compositions. As the burial depth becomes deeper, $\delta^{18}O$ values of pore waters shift to be more negative as a function of ambient temperature, which corresponds to higher $\delta^{13}C$ values revealed in bicarbonate produced by methanogens.

It was also suggested that the rapid influx of sediments of the overlying Eype Clay and the Down Cliff Sand members may contribute to the overpressuring of the shales in the Shales-with-Beef Member in the study area (Rukin, 1990). The absence or poor development of calcite veins in other parts of the British Lias with a lower TOC reflects that the methanogenesis in the organic-rich shales is possibly responsible for the overpressuring and formation of vein seams.

Increases in pore pressure can also influence the chemical equilibrium in aqueous systems by increasing the solubility of minerals. It was suggested that as pore pressure increases in a closed system, more $CaCO_3$ is dissolved in the pore fluid (Shemesh et al., 1992). The dissolution reaches a maximum when the pore pressure reaches its maximum. When

hydraulic fracturing occurs, pore pressure drops drastically, leading to the pore fluids to become supersaturated (Shemesh et al., 1992). This results in a rapid precipitation of calcite in the fracture systems, giving rise to the vein filling.

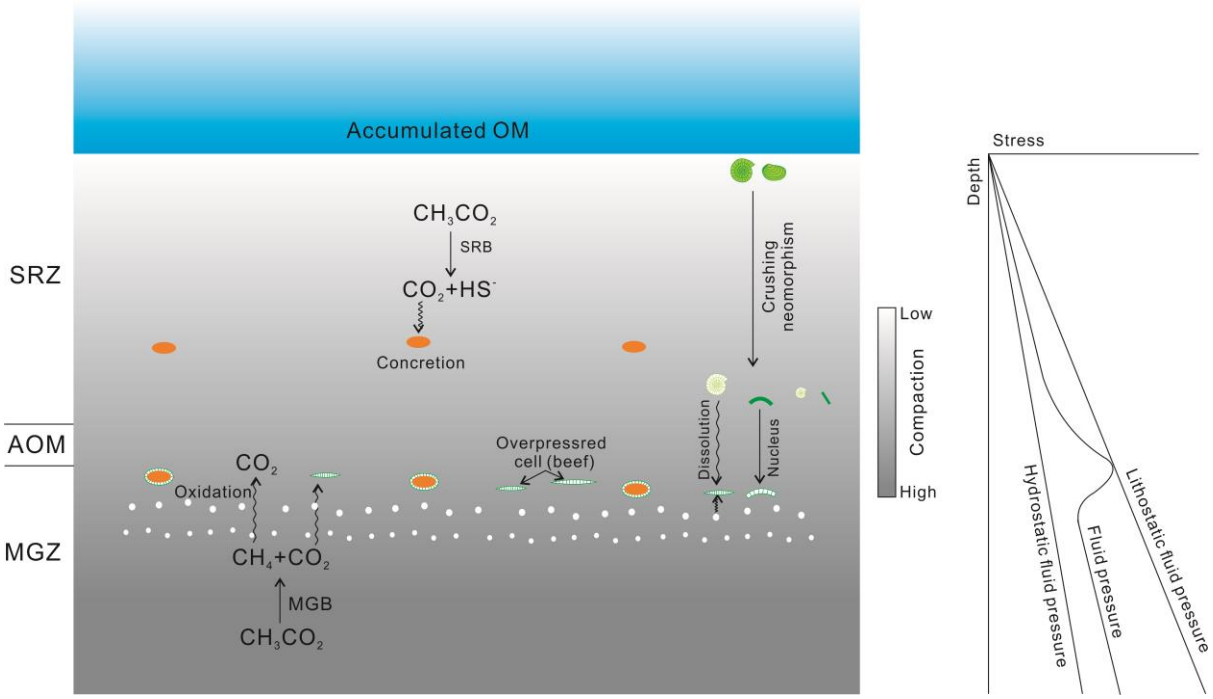


Figure 4.34 Cartoon illustrating the depth and material sources of fibrous calcite veins. See text for explanation. OM = organic matter. AOM = anaerobic oxidation of methane. SRZ = sulfate reduction zone. MGB = methanogenic bacteria. MGZ = methanogenic zone.

4.5.4 Controls on vein development

As discussed in section 4.6.1, the bicarbonate produced by bacterial sulphate reduction supplies materials for concretion cores and also partially for beef veins and cone-in-cone structures. Although no direct biomarkers for methanogenesis have been found in the calcite veins (Kiriakoulakis et al., 2000), their positive carbon isotope values, that are higher than their host rocks, suggest a component of methanogenic CO_2 in the composition. The covariations revealed in the measurement of carbon and oxygen isotope compositions in the calcite veins indicate the significance of $\delta^{13}C$ enriched methanogenic CO_2 to the precipitation

of authigenic carbonates at a deeper burial depth and temperature with a higher $\delta^{13}C$ value. Hence, the organogenic bicarbonate plays an important role in the precipitation of vein calcite.

The TOC in the shales in site 1 exhibits a positive correlation to vein thickness in multiple horizons, especially in horizons 8, 10 and 18 that are neighbouring to organic-rich shales (Figure 4.7). This indicates that the veins derive carbonates, at least partially, from organic matter. Hence, the thickness/volume of calcite veins are positively related to the TOC in the adjacent shale beds.

However, TOC in the host rock is not well correlated to vein thickness in all cases, e.g. the vein in horizon 28. The TOC values in horizon 27 and 29 are both low-moderate, however, the cumulative vein thickness is even higher than several other veins whose host rocks exhibit higher TOC values. It is notable that horizon 27 has the highest carbonate concentration (36.17%) among all shale horizons. Such a high carbonate content may have been resulted from precipitation of authigenic carbonates in pore spaces in the rock matrix. This is evident from the occurrence of carbonate concretions in this horizon that have been largely sourced from the decomposition of organic matter (Figure 4.8H).

The TOC in shales is also critical for the generation of overpressuring during methanogenesis (see section 4.6.3). A higher TOC favours the buildup of fluid pressure and carbonate saturation, which then contribute to the formation of hydraulic fractures by gas migration.

The distribution of short calcite veins in several horizons all contain fossil shells on vein surfaces. The veins are interpreted to follow the site of fossil preservation, where the shells act as a nucleus for calcite precipitation. The bicarbonate derived from the dissolved aragonitic fossils, having similar range of carbon isotope compositions to the veins, are highly likely to be responsible for the majority of the vein fills (Hendry, 2002; Hendry et al., 1995), although the component from organic matter decomposition should not be ignored.

4.8 Conclusions

(1) Calcite beef veins and cone-in-cone structures are prevalent in the black shales of the Lower Charmouth Mudstone in the Wessex Basin. Horizontal beef veins, consisting of vertical fibres and host rock inclusions, are developed in clusters. The length is either short or persistent. Well-preserved fossil skeletons of ammonites are found on vein surfaces. Cone-in-cone structures are developed either along the outer rims of carbonate concretions or as tabular, bedding-parallel structures in the shales, and contain conical bundles of calcite fibres and a much higher content of host rock inclusions than beef veins.

(2) The short beef veins exhibit either planar tapering tips where the veins are isolated from others, or blunt tips where the veins are interfered by adjacent veins. No clear correlation is found between the maximum vein-aperture and the angles of vein tips.

(3) The calcite veins exhibit moderate carbon isotope values, ranging from -1.515‰ to 2.732‰, the $\delta^{13}C$ values in the host shales are all negative. The core of the carbonate concretion in site 4 exhibits the most negative $\delta^{13}C$ values. The carbon isotope composition of calcite veins suggest a mixture of carbonate sources from aragonite skeletons and bicarbonate derived from both the early bacterial sulphate reduction and the later methanogenesis.

(3) The oxygen isotope composition of the calcite veins are all negative, ranging from -8.872‰ to -4.521‰, which is too negative to reflect the primary pore water oxygen isotope signatures. The oxygen isotope could be primarily caused by the increased temperature during burial, suggested by the narrow range of $\delta^{13}C$ values. Input of meteoric waters with depleted or enriched ^{13}C, release of bicarbonate from aragonitic fossils, or the ultrafiltration processes during shale compaction could also influence the oxygen isotope signatures and have caused the isotope fluctuations, however, the magnitude and validity is difficult to assess.

(4) The formation of calcite veins in the black shales could be attributed to early overpressuring when the clays enter the methanogenesis zone, which is evident from the covariations of carbon and isotope signatures. The drop of pore pressure by hydraulic fracturing results in fluid supersaturation and subsequent calcite precipitation in fractures.

(5) TOC is a critical factor for the formation and growth of calcite veins. The occurrence of fossil skeletons as crystal nucleus also affects the intra-layer distribution of some of the beef veins.

Chapter 5 Petrographic characterization of the fibrous calcite veins in the Lower Jurassic Charmouth Mudstone, the Wessex Basin

5.1 Introduction

Referred to as a geological puzzle (Clifton, 1957), the genesis of cone-in-cone structures has raised broad interest due to its great importance for understanding the diagenesis and stress conditions in the host sediments (Selles-Martinez, 1994; Selles-Martinez, 1996). Tarr (1922) first proposed that the volume expansion during transition of aragonite to calcite produced the conical calcite, which was also adopted by Gilman and Metzger (1967). Tarr (1932) suggested that the loading of sediments and overburden may result in conical shear fractures and preferential solution of calcite along the cleavage directions to account for the conical structures. More recent work suggested that the force of crystallization exerted by growing calcite crystals may possibly be responsible for the formation of cone-in-cone structures that have a diagenetic origin (Durrance, 1965; Franks, 1969; Kowal-Linka, 2010; Marshall, 1982; Woodland, 1964). Cone-in-cone structures possibly formed at the syngenetic stage when the host sediments are still plastic, which is evident from the intruded host rock inclusions within the cone-in-cone structures (Brown, 1954; Gilman and Metzger, 1967). Ábalos and Elorza (2011) argued that the cone-in-cone structures are induced by submarine propagation and amplification of seismic surface waves in soft sediments. It is also suggested that cone-in-cone structures might be analogous to fibrous beef veins, being formed as internal hydraulic fractures in the low-permeable host mudrocks when overpressure is achieved (Shearman et al., 1972; Stoneley, 1983). Cobbold et al. (2013) and Rodrigues et al. (2009) related the generation of fibrous calcite veins and cone-in-cone structures in the black shales to overpressure that is caused by hydrocarbon generation and migration. Although multiple

hypotheses have been brought up to interpret the formation mechanism of cone-in-cone structures, it remains subject to debate and poorly understood (Boggs, 2009; Tucker, 2009). Detailed examinations of cone-in-cone structures in organic-rich shales, especially those as immature source rocks, are needed. The common association of beef veins with cone-in-cone structures also requires a better explanation regarding their relationships and the geological implications.

Electron backscattered diffraction (EBSD) is a scanning electron microscope based technique that gives crystallographic information about the microstructure of a sample (Humphreys, 2004; Wright and Nowell, 2006). It has been applied widely in characterizing the deformation of rocks at the grain scale. The analysis of EBSD data is crucial for revealing and understanding the microstructures and deformation mechanisms in sedimentary and metamorphic rocks quantitatively (Lloyd, 2000; Prior et al., 1999; Schmidt and Olesen, 1989). Mörk and Moen (2007) used EBSD to examine compaction microstructures in quartz grains and cements in sandstone reservoirs. Ábalos et al. (2011) described microfabrics of pre-Cambrian deformation recorded in quartz pebbles by a series of EBSD based crystal preferred orientation (CPO) analyses. Rock seismic anisotropy has also been investigated by analyzing CPO derived from EBSD measurement (Bascou et al., 2001; Cossette et al., 2015). Although EBSD has become a powerful tool for microstructural-crystallographic characterization, little EBSD work has been reported on the beef veins and cone-in-cone structures.

This chapter starts with the description of the textural characteristics of calcite beef veins and cone-in-cone structures, the distribution, morphology and size of the components of skeletal fragments, amorphous organic matter and pyrite, and the microtextures of the clay inclusions. Then the EBSD analysis of c-axis orientations, crystal boundaries and size of calcite within the veins is presented, followed by the characterization of non-clay minerals (organic matter, pyrite, detrital and

authigenic carbonate) in the matrix of the host rocks. Finally, the important issues regarding the timing, paleostress, the formation and growth mechanisms of beef veins and cone-in-cone structures are discussed.

The aims of this chapter are:

(1) to demonstrate the diagenetic growth of cone-in-cone structures and beef veins;
(2) to examine the role of organic matter in the origin of the calcite veins;
(3) to investigate the crystallographic orientations of calcite quantitatively and the implications for crystal morphology and stress state;
(4) to reveal displacive growth of the veins and to address the significance of the force of crystallization for vein expansion;
(5) to get a better understanding of the relative timing and the genetic relationship between cone-in-cone structures and beef veins and their formation processes.

5.2 Methods

An integrated optical and scanning electron microscopy (SEM) based petrographic characterization method (see description in section 3.2) is applied in this study to reveal the composition, texture and crystallographic information of the calcite veins and their host clays. The samples for the petrographic study were systematically collected from the sampling sites described in Chapter 4, which allows documentation of the compositional and textural differences. A Centaurus cathodoluminescence detector was attached to the SEM that enables the production of digital CL images used for characterizing textural and chemical-zoning features. The crystallographic orientations were measured using an electron backscatter diffraction (EBSD)

detector attached to the SEM. The thin sections were mounted on a stage that was tilted at 70° with the median lines of calcite veins parallel to the X-axis of the SEM stage. A copper tape was attached to surfaces of the thin sections to reduce charging effects. The acquisition of electron backscatter patterns (EBSPs) was performed at 20 kV accelerating voltage and a working distance of 10mm. To obtain optimal EBSPs, the thin sections were not coated with a conductive layer and a low-vacuum mode was adopted. EBSD and secondary electron data were automatically collected using Aztec software package (Pérez-Huerta et al., 2014). The EBSD data was then analysed using HKL Channel 5 software package for orientation mapping and lattice pole plotting (Humphreys, 2004). Orientation maps are presented using Y direction IPF (Inverse pole figure) orientation maps by assigning a colour to each of the corners of the inverse pole figure. Y direction is true vertical, thus the maps shows colour indexed to crystallographic orientations that lies along vertical direction. The c-axes are presented in lower hemisphere, equal area stereographic projections.

5.3 Textural characteristics

The analysis of vein textures is focused on the crystal morphology and arrangement of calcite beef veins and cone-in-cone structures, which allows a comparative study of the calcite veins exhibiting varied textures.

5.3.1 Beef veins

The beef veins consist of parallel-aligned fibres with high aspect ratios and a median zone that bounds fibres on both sides. Two main types of beef veins are identified based on the composition and texture of the median zones. Type A contains bedding-parallel median zones with dark bands

of solid inclusions and numerous small and equidimensional calcite crystals. Veins of Type B contain a straight or a curved carbonate median zone with a finite width. The following sections describe the textural characteristics of the median zones and the fibrous zones in the beef veins.

5.3.1.1 Median zone

Type A

Veins of Type A contain a dark median zone with solid inclusions and equant-elongate calcite crystals. The calcite crystals are either randomly scattered individually or closely packed as aggregates (Figure 5.1). The length of single crystals ranges from several microns to 470 μm, which is much lower than the fibres. Interestingly, the crystal aggregates commonly exhibit similar geometries to beef veins and cone-in-cone structures, whose long axes are approximately horizontal.

The median zones often contain multiple lenticular host rock fragments. These clay lenses have long axes ranging from tens of microns to 2mm, and thicker width than that of the median zone. The clay lenses are gently inclined with both ends linking with the thinner bands of the median zone. Hence, the median zones on different sides of the clay lenses lie in slightly varied levels. A series of clay lenses are often observed to occur in the median zone of single beef veins, which are associated with frequent changes in the levels of the median zones. It is notable that the bands of median zones are generally straight and bedding-parallel, regardless of their levels and the geometry of the contacting clay lenses. The bands of median zones at different levels that contact with the same fragments occasionally exhibit an overlapping zone.

The occurrence of the clay lenses and the associated changes in the levels of the median zones are interpreted as growth features of the beef veins. The median zones at varied levels are interpreted as two closely spaced fractures that were initiated simultaneously. The host rock fragment was flat lying and possibly marked the tip regions of associated fractures. The subsequent antitaxial growth of calcite fibres along the initial fractures not only caused displacement of the adjacent host rocks, but also the rotation of the rock fragments. The driving force that pushed such a movement is discussed in section 5.8.4. Finally, the fibres in the overlapping zone of two fractures enclosed the clay lenses, resulting in the coalescence of the two neighbouring veins. The incorporation of the host rock fragment into the median zone of the final vein rather than being displaced upward/downward is due to the constaint from both the upper and lower veins.

Type B

Beef veins of Type B contain a carbonate median zone that is either straight or curved (Figure 5.4). The width of the median zone ranges from 15-70 μm. The composition of the median zone is homogeneous micrite, which is interpreted as residues of crushed fossil bivalves. These veins are randomly oriented, which follow the traces of their median zones.

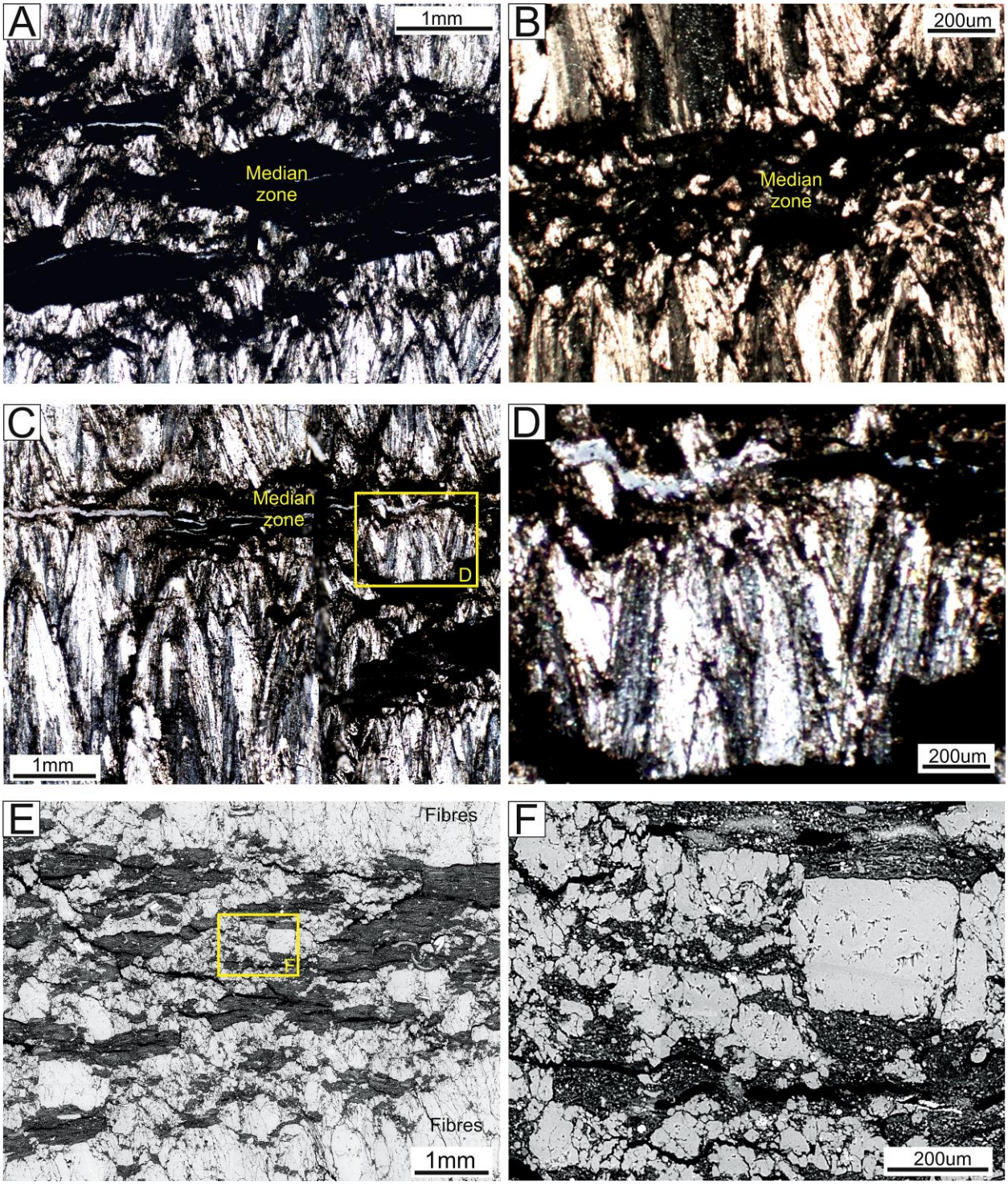


Figure 5.1 Photomicrographs showing the median zones that consist of crystal aggregates of calcite. (A) Beef - like crystal aggregates in the median zone of a fibrous calcite vein. (B) Equant calcite crystals scattered in the median zone. (C) Conical bundles of calcite crystals in the median zone of a beef vein. (D) Enlarged area in the box in figure 5.1C. (E) Backscattered electron image showing the distribution of crystal aggregates of calcite in the median zone. (F) Enlarged area in the box in figure 5.1E. Note the equant shapes of the crystals.

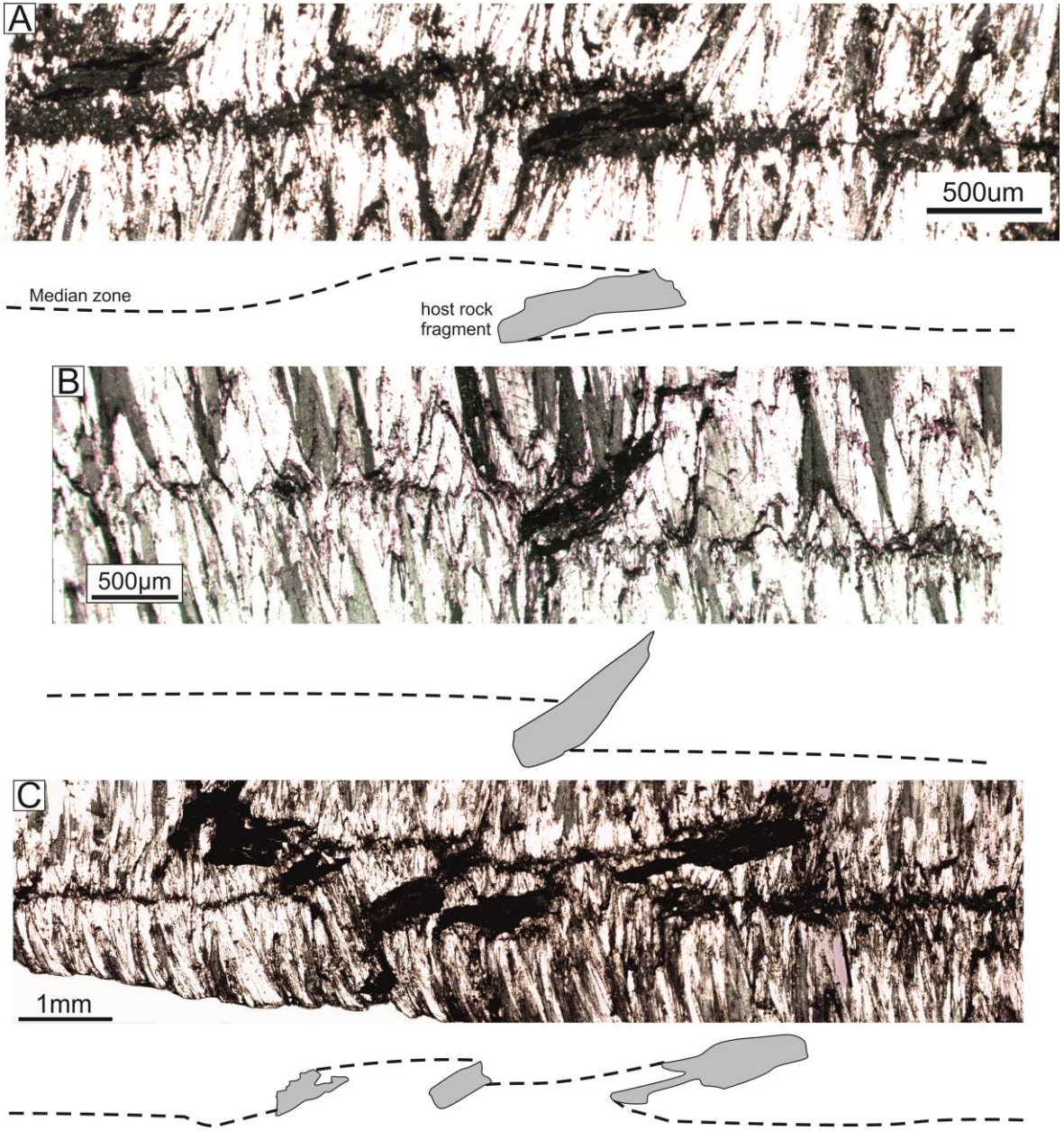


Figure 5.2 Photomicrographs and sketches showing the overlapping of median zones in one single fibrous calcite vein. Cross - polarized light. (A) Three overlapping areas of the median zones in a calcite vein with decreased aperture towards left in the figure. Notice the median lines are consistently sub-horizontal. (B) A lenticular host rock fragment trapped within the overlapping zone of the median lines. Notice the gentle dip of the clay fragment.

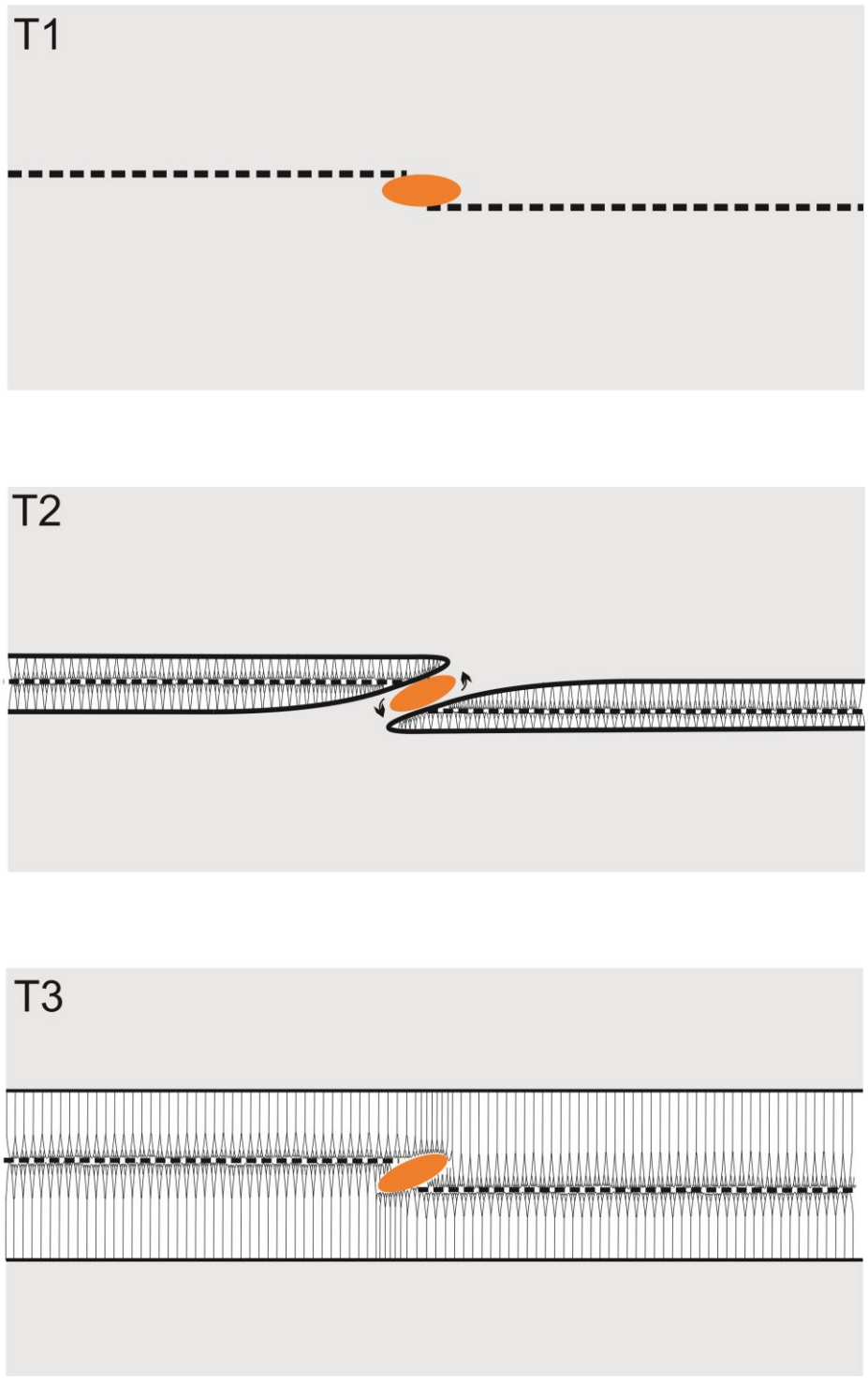


Figure 5.3 Reconstruction of the process of formation of calcite beef veins shown in figure 5.2. T1: Formation of two closely spaced bedding-parallel fractures. T2: Subsequent growth of fibres in the two fractures causing the anticlockwise rotation of the host rock fragment that is linked with the two veins. T3: Progressive growth of fibres finally led to the incorporation of the host rock fragment in the medina zone.

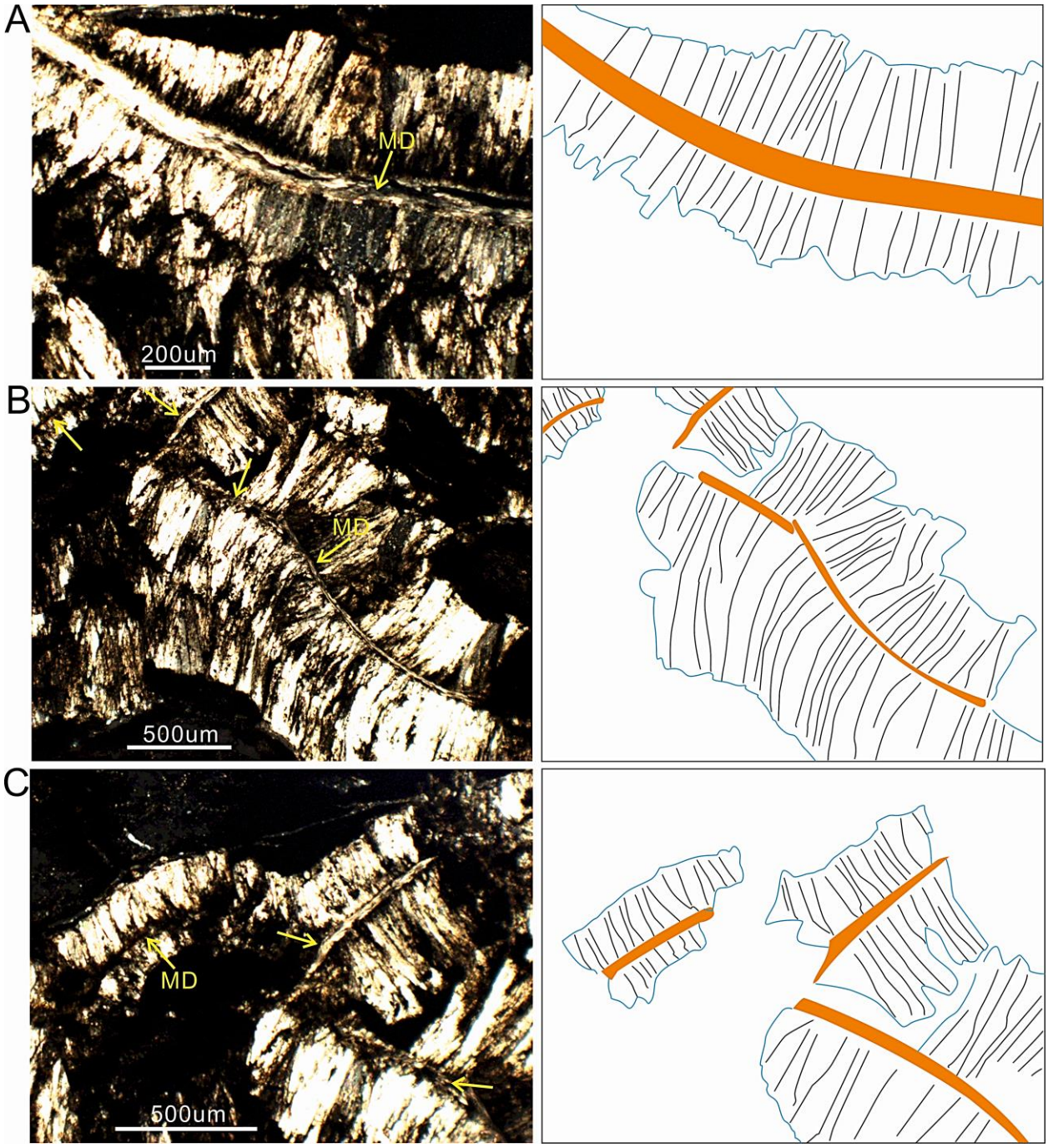


Figure 5.4 Photomicrographs and their sketchs showing randomly oriented beef veins with carbonate median zones. (A) gently curved beef vein with gradually decreased fibre plunge to the left of the figure. (B) and (C) showing clusters of beef veins with carbonate median zones.

5.3.1.2 Fibrous zone

The beef veins consist of two fibrous zones on either side of the median zone (Figure 5.5). The calcite fibres are parallel aligned and closely packed, with few solid inclusions entrapped between neighbouring fibres. Single fibres have planar-tapering tips. The crystal width gradually increases outward to a maximum of 500 μm. Fibre length are commonly constant on the same side of the median zone, which can be either similar to or different from those on the different side.

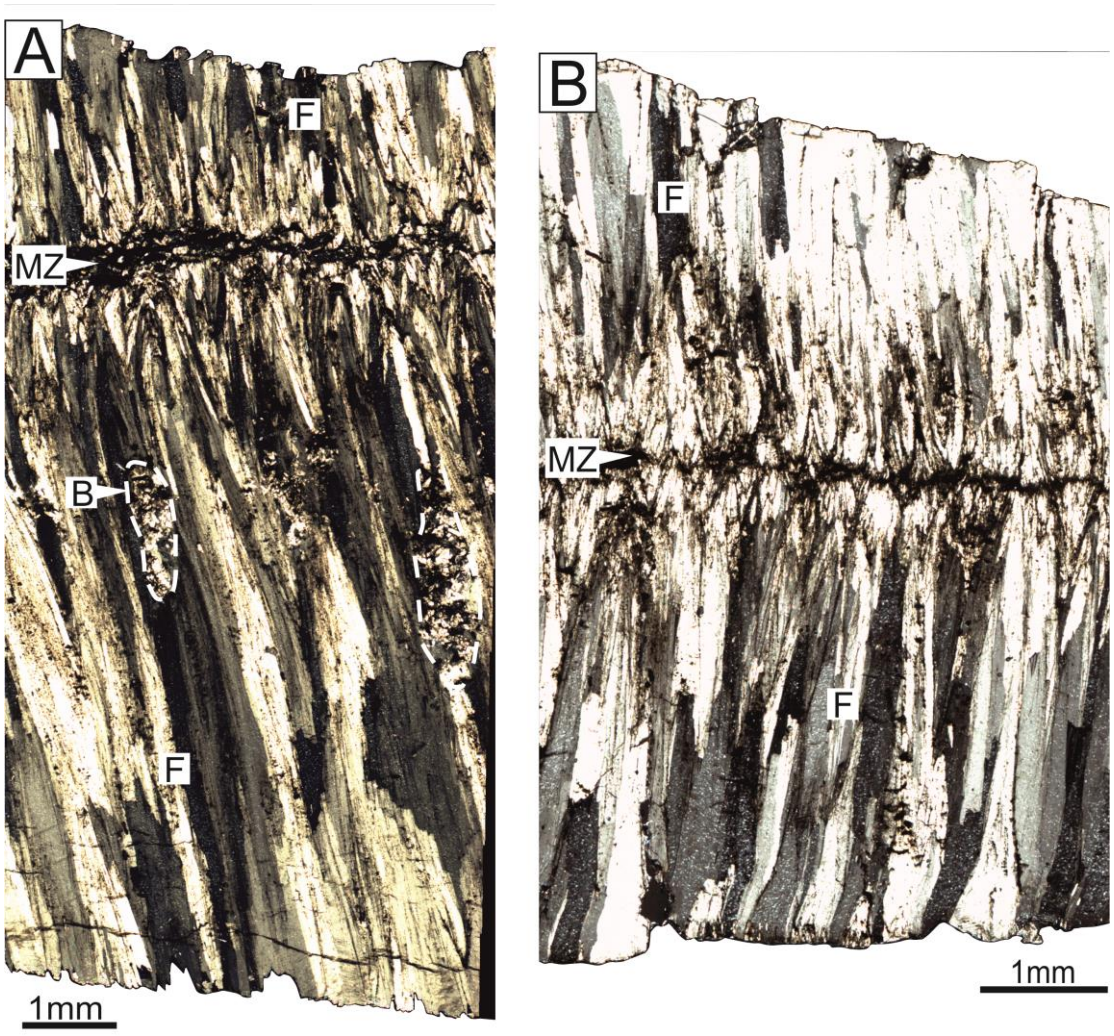


Figure 5.5 Photomicrographs showing the texture and composition of calcite beef veins. Cross polarized light. Note the varied fibre length on different sides of the median zone. F, fibre. B, blocky zone.MZ, median zone.

The fibres in beef veins of Type A are commonly arranged as cone-in-cone structures in the regions near the median zone (Figure 5.6). The apical angles of single cones gradually decrease towards vein margins. This is accompanied with a decreased amount of solid inclusions enclosed between adjacent fibres.

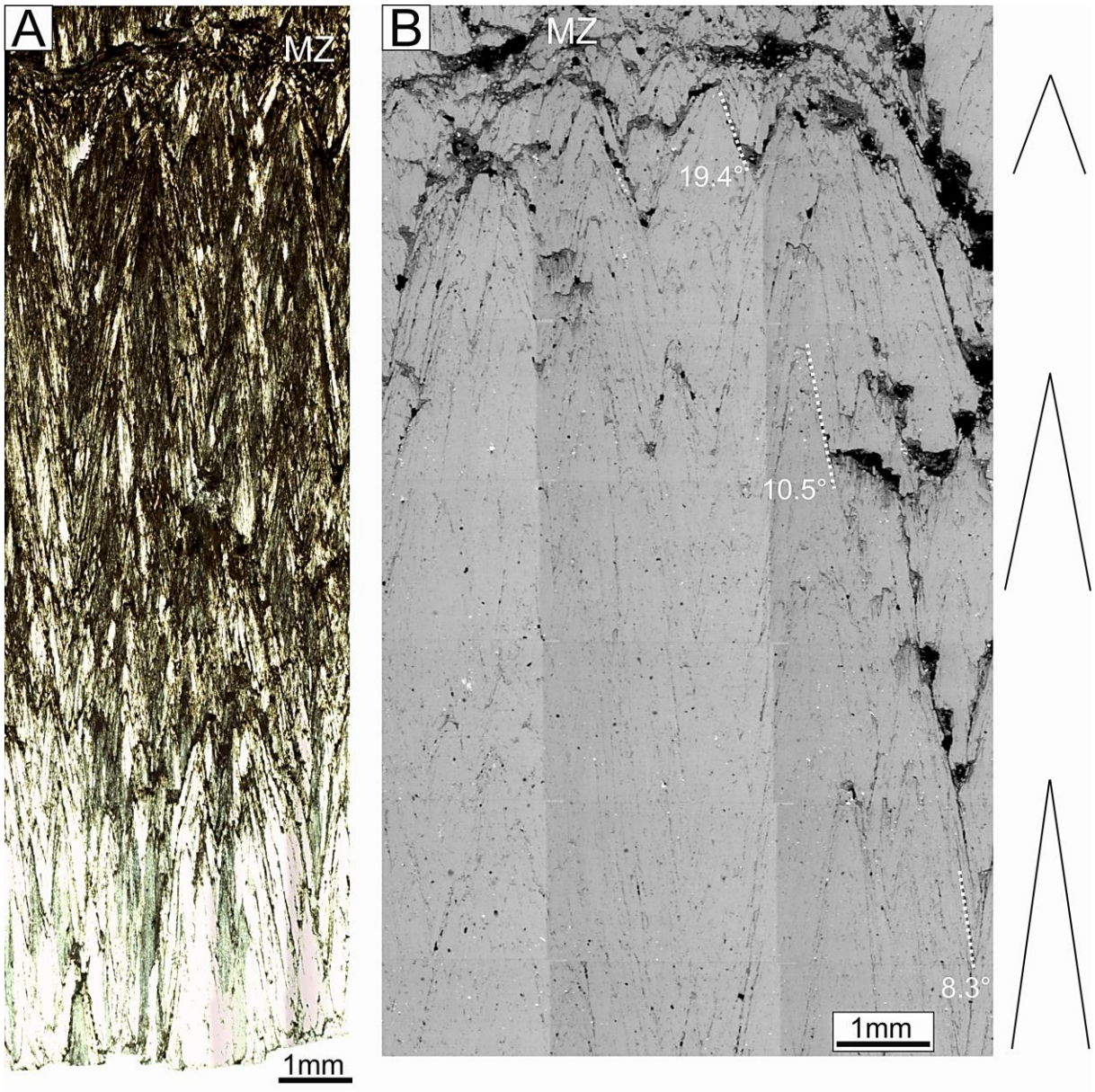


Figure 5.6 Textural features on one side of the median zone of beef veins. (A) Photomicrograph showing the gradual decreased amount of host rock inclusions towards the vein wall. Cross - polarized light. (B) BSE image showing the decreased apical angles of individual cones towards vein wall. MZ=median zone.

In contrast, the beef veins of Type B consist of fibres that are strictly orthogonal to the median zones (Figure 5.7). Hence, fibres exhibit varied orientations in single curved veins. A cluster of randomly oriented beef veins also contain complex fibre orientations that are determined by the median zone traces. It is notable that those beef veins often exhibit rather blunt ends. Calcite fibres are developed along the median zones, exhibiting limited changes in length.

5.3.1.3 Blocky zone

Blocky zones in this study refer to the regions within calcite veins that consists of numerous, small and equidimensional calcite crystals and clays minerals (Figure 5.8). Three major types of blocky zones are identified, which are all regularly shaped.

One type of blocky zone is spindle-shaped and completely enclosed by fibres. The second type of blocky zones are circular shaped, with a maximum diameter of 5 cm. Those blocky zones are associated with the circular ridges on vein surfaces (see Figure 4.14). Deformation twins are found in the upper calcite fibres that are in contact with the blocky zones. It is worth noting that the upper fibres terminate when they encounter the blocky zone. The nucleation of the lower fibres is interpreted to postdate the incorporation of the blocky zone. This is evident from the tapering tips of the lower fibres that point towards the blocky zone from below.

The third type of blocky zone exhibits a conical shape, and consists of both small and equant calcite crystals along the cone margins and fibres in the center (Figure 5.10). Fibres outside the cones terminate where they encounter the cones rather than penetrating them. Those blocky zones contain linear lateral bands of solid inclusions and widely-disseminated pyrite crystals within the fibre-free areas. CL imaging exhibits a clear zoning feature, where the fibres inside and outside

the cones are all dark and the rest of the areas within the cones are much brighter. This suggests a different timing of the formation of such blocky zones from the fibres.

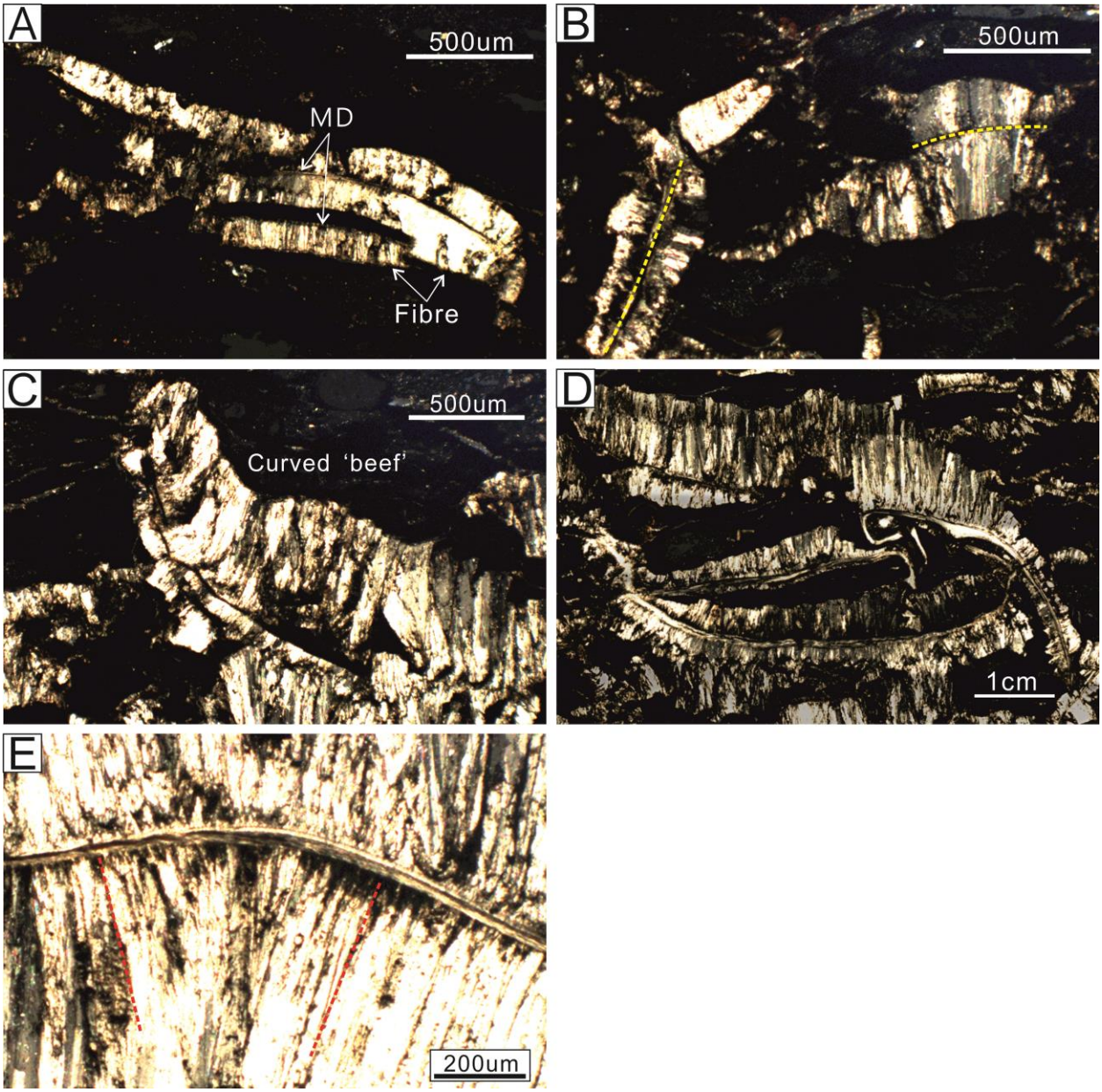


Figure 5.7 Photomicrographs showing beef veins of type two. Note the planar ends of beef veins in figure 5.7A and B, and the curved vein geometries in figures 5.7C-D. The varied fibre orientation is highlighted in figure 5.7E by dashed lines.

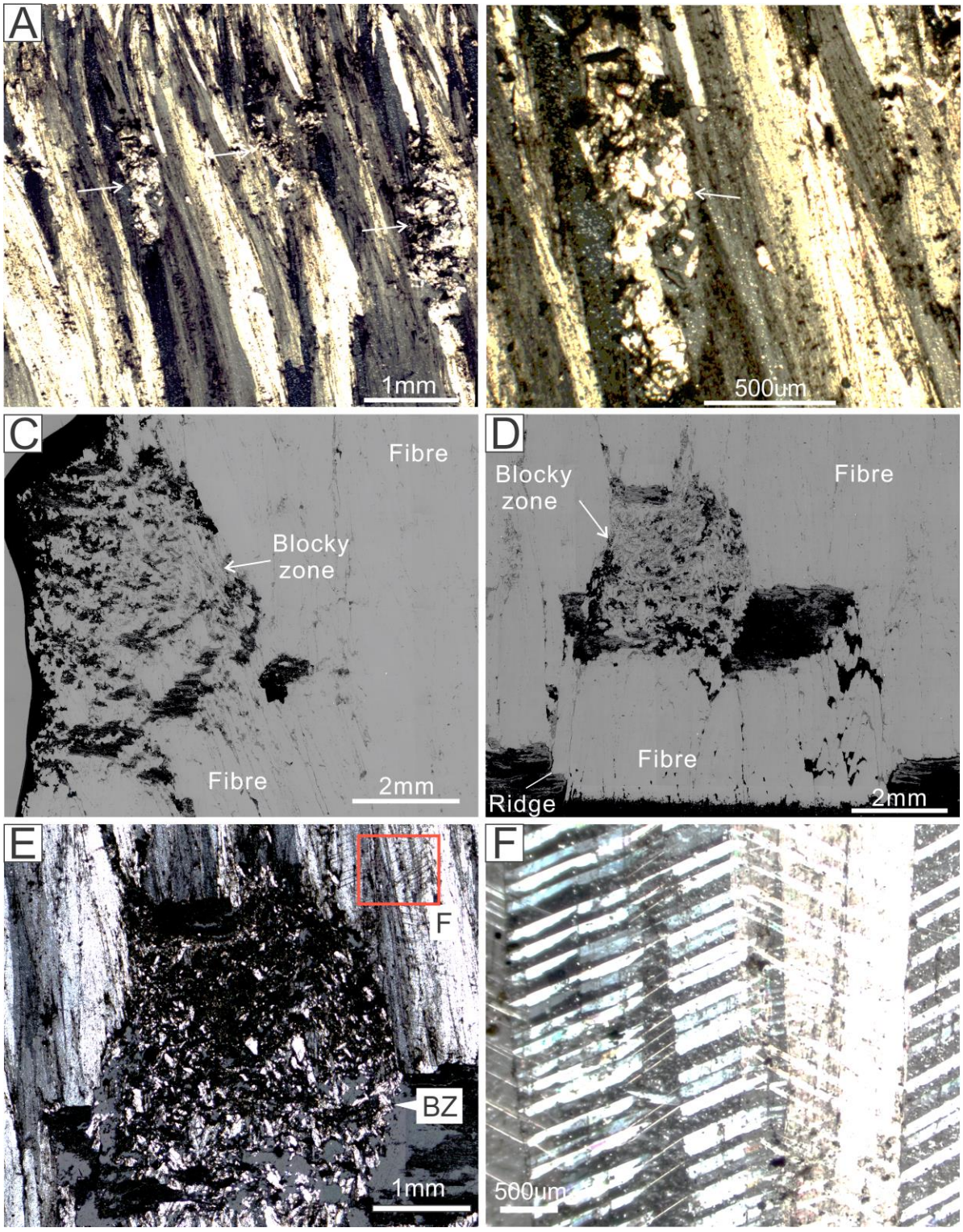


Figure 5.8 Blocky zones within calcite beef veins. (A)and (B) Photomicrograph showing the spindle-shaped blocky zone. (C) and (D) BSE image showing the circular blocky zone. (E) Photomicrograph of the same area as figure 5.8D showing the detailed texture. (D) Deformation twins in calcite fibres in the area shown in the box of figure 5.8E.

The blocky zones presented in this research are interpreted to be remains of fossil skletons. The fossil species possibly include ammonite, gastropod and belemnite that are prevalent in the Liassic shales (Jenkyns and Weedon, 2013), which are evident from the distinct internal textures. The occurrence of pyrite is likely to have formed during bacterial decomposition of organic tissues of the fossils. The high mechanical strength of the shells has prevented the fossils from distortion and being crushed by fibre growth. The appearance of twinning in fibres shown in figure 5.8D indicates an intercrystalline deformation. Those twins are interpreted to have formed as growth twins when fibres encountered rigid obstacles of fossil shells as the twinning is only observed within fibres around the blocky zones. The fossil chambers served as the fluid storage sites, allowing the precipitation of blocky calcite crystals in an open space. This explains the different crystal morphology of precipitated calcite in the blocky zones from the neighbouring fibrous zones.

The incorporation process of fossil skeletons into calcite beef veins is illustrated in figure 5.9. Initially, hydraulic fractures form along sub-horizontal bedding planes due to overpressure (see section 4.5.3. Subsequent growth of calcite fibres towards both the upper and lower walls occur in the fracture, which leads to a vertical displacement and a growth-related compaction of the adjacent host rocks. When the fibres have reached the skeletons, the growth of skeleton-contacting fibres terminates due to the high mechanical competency (Currey, 1976) that permits the skeletons to survive from being crushed by growing fibres. This enables the preservation of the morphologies of the skeletons and also different fluid conditions within the fossil chambers. Finally, the fibres exceed the levels where the skeletons lie and continue to grow as long as the pore fluids remain supersaturated. Simultaneous nucleation of new fibres below the skeletons commences with the carbonate skeletons serving as nucleus. Given equal time, the length of newly formed fibres is approximately equal to the increments of fibres whose growth is not influenced by the skeletons.

It is notable that the host rocks are displaced by the fibres during their progressive growth, which requires the host rock to be undercompacted. A high plasticity of the host rock allows (1) the accommodation of the expanded beef veins without uplifting the overburden; (2) the competent skeletons remain in-situ rather than being displaced, so that the incorporation into the beef veins is possible.

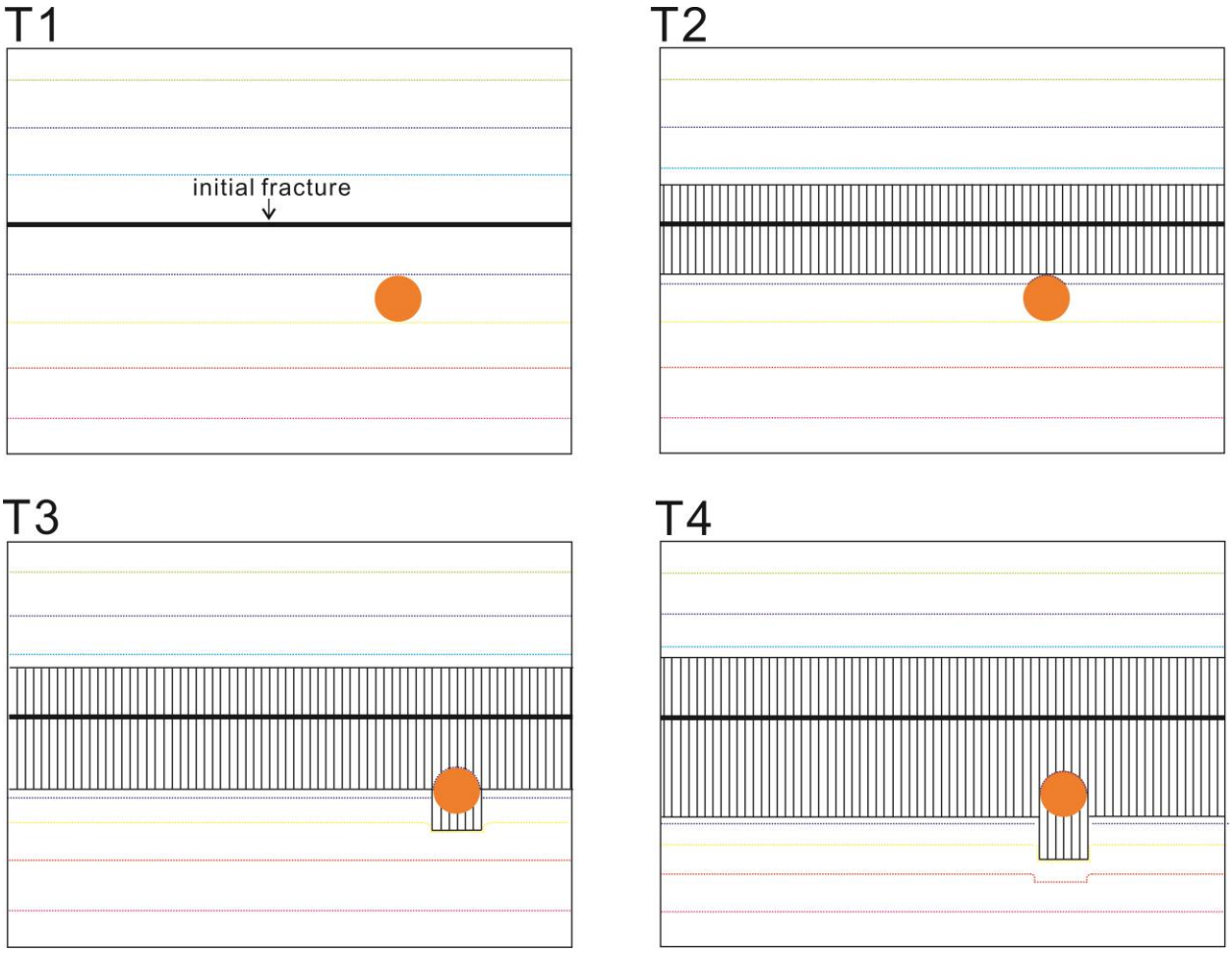


Figure 5.9 Schematic sketches illustrating the incorporation process of skeletons into a calcite beef vein. T1: Formation of initial fractures along bedding. T2: Subsequent growth of sub-vertical fibres within the fractures. Note that the fibres have not reached the levels where the skeleton lies. T3: Continuous growth of calcite fibres that leads to the enclosure of the fossil skeleton by fibres. The skeleton remains intact. T4: Complete incorporation of the fossil skeleton into the beef vein. Note the displacement of the host rocks by the beef vein during its incremental growth.

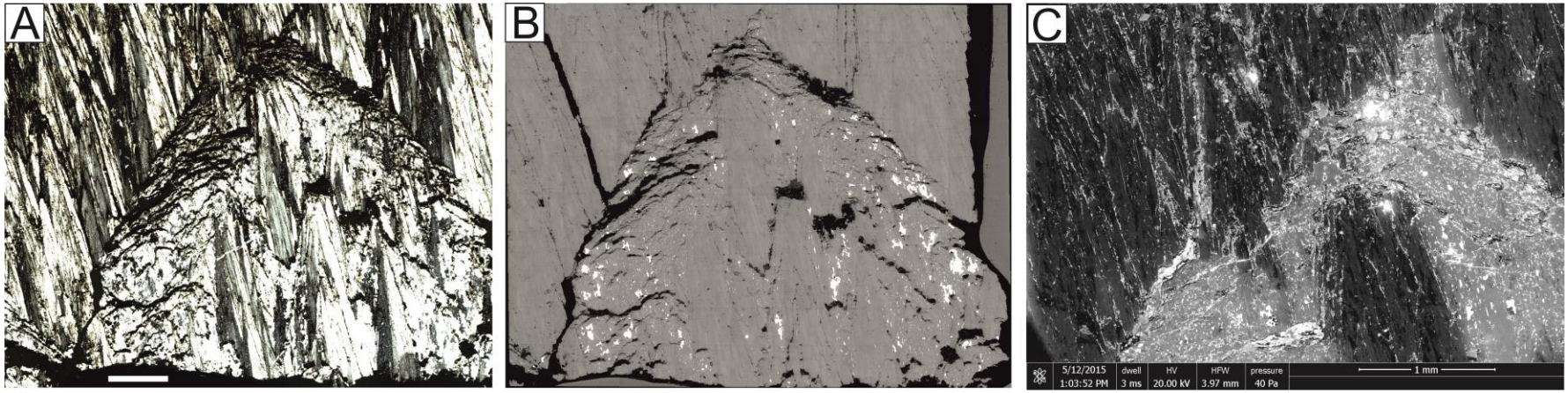


Figure 5.10 Texture and composition of the conical blocky zones within calcite beef veins. (A) Photomicrograph showing the textural patterns. The scale bar is 1cm. (B) BSE image showing the occurrence of pyrite within the blocky zone shown in figure 5.10A. (C) SEM-CL image showing the zoning feature of the blocky zone shown in figures 5.10A and 5.10B.

5.3.2 Cone-in-cone structure

5.3.2.1 Median zone

The median zones in cone-in-cone structures are defined as a curvy band of solid inclusions (Figure 5.11). Unlike in beef veins, the margins of median zones in cone-in-cone are frequently indistinct; however, they can be identified by the oppositely oriented apices of single cones on opposite sides of the median zone. The solid inclusions in the median zones are commonly distributed along the boundaries of individual cones, hence the median zones exhibit a wavy trace.

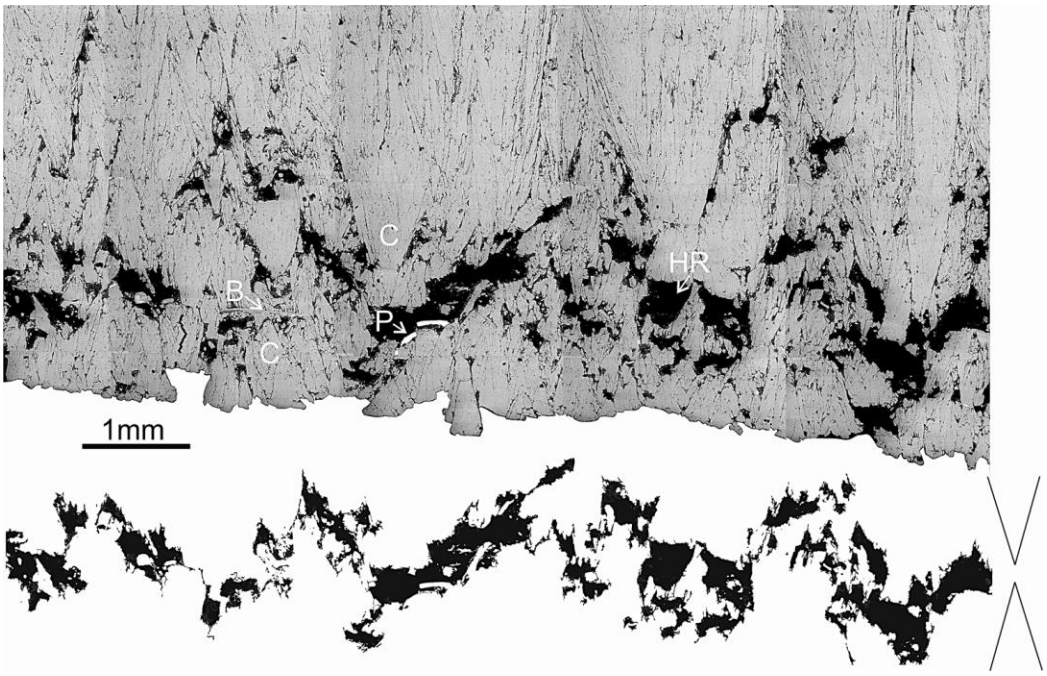


Figure 5.11 BSE image showing the median zone of a cone-in-cone structure. The lower image showing the wavy trace of the median zone. Note the opposite direction of cone apices. B=bivalve. C=cone. P=pyrite. HR=host rock.

5.3.2.2 Fibrous zone

The cone-in-cone structures consist of numerous nested conical bundles of calcite fibres (Figure 5.12). Individual cones exhibit similar geometries, with a height of 0.6-12 cm. Each cone contains

multiple vertical fibres that are arranged in a plumose aggregate. This results in angular patches of clay films filling the gaps between neighbouring cones. Cone boundaries can be distinguished by the opaque solid inclusions that separate adjoining aggregates. The distinct arrangement of calcite fibres also causes the undulose extinctions of vein margins and uneven surfaces of cone-in-cone structures. The features are identical to those described previously by Franks (1969), Woodland (1964), and Kowal-Linka (2010), among others.

Figure 5.13 illustrates the mutual interference of adjoining cones with their apices located at varied horizons. Some cones exhibit a complete conical geometry, which are bounded by neighbouring fibres that terminate against the cone margins. Other cones, especially those closer to the median zones, are commonly truncated by the neighbouring cones, exhibiting a step-like cone boundary.

The apical angles of individual cones range from 8.3° to 19.4° in figure 5.13. The cones closer to the median zones have a higher apical angle, however, these cones are shorter. Figure 5.14 illustrates numerous cones in a calcite vein with varied apical angles which reach up to 126°. Interestingly, the upper part of this vein contains vertical fibres and few solid inclusions, which are arranged in a uniform way similar to that in beef veins. In contrast, the lower part consist of stacks of cones and abundant clay inclusions, exhibiting a much more complex texture.

Figure 5.15 illustrates two major cone-in-cone structures that consist of more loosely spaced cones of fibre aggregates compared to those in figure 5.12. The cone apices exhibit a non-uniformly distribution in varied horizons. The size of individual cones varies significantly, with the height ranging from 0.1-1.7 cm. Multiple small cones are dispersed within the host shales, exhibiting a similar geometry to the larger cones. A cluster of small cones with their apices located in the horizons between the two cone-in-cone structures form a bridging vein.

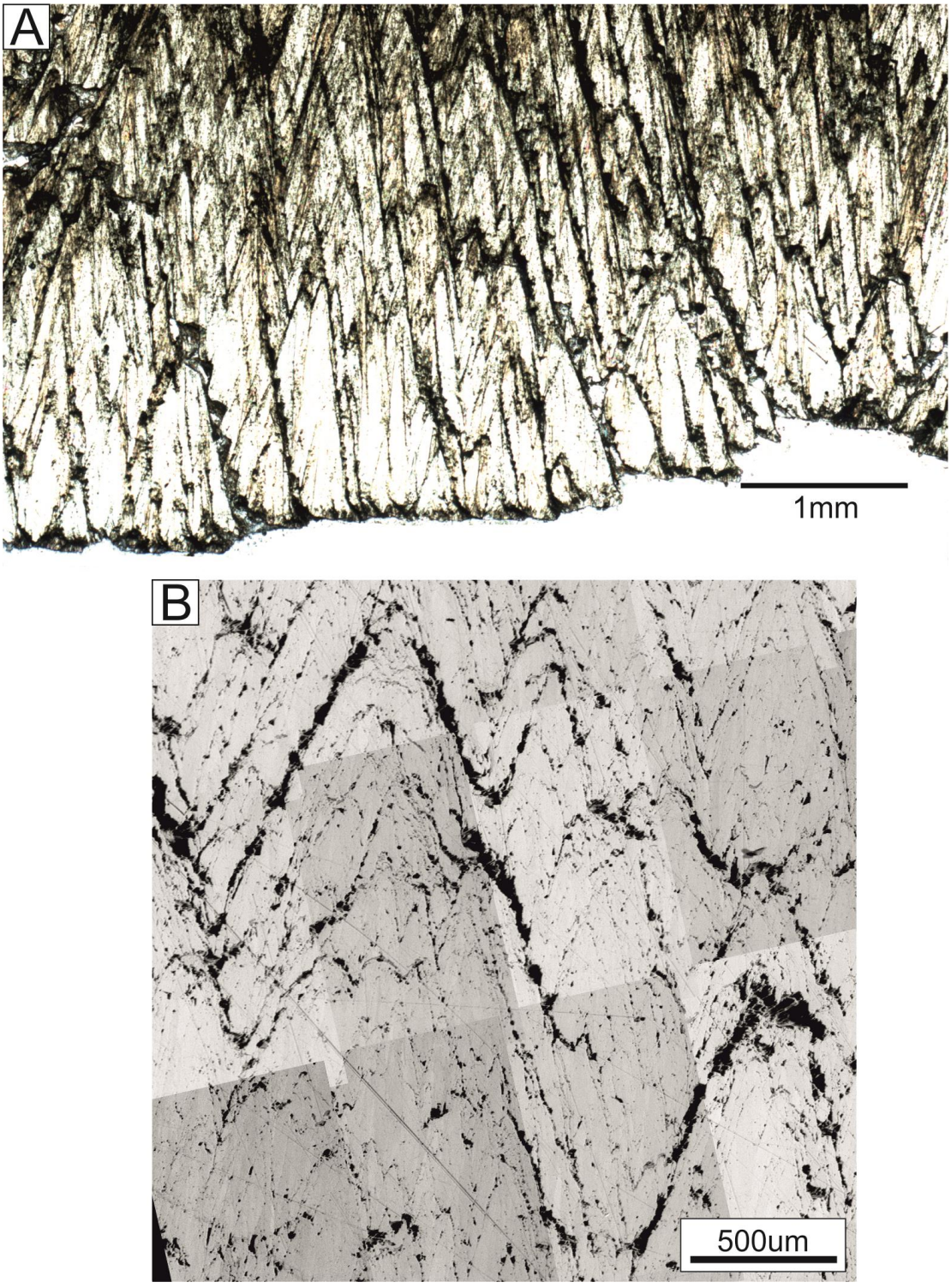


Figure 5.12 Texture and composition of cone-in-cone structures. (A) Photomicrograph showing the arrangement of conical bundles of calcite fibres. (B) BSE image showing the distribution of solid inclusions along margins of individual cones.

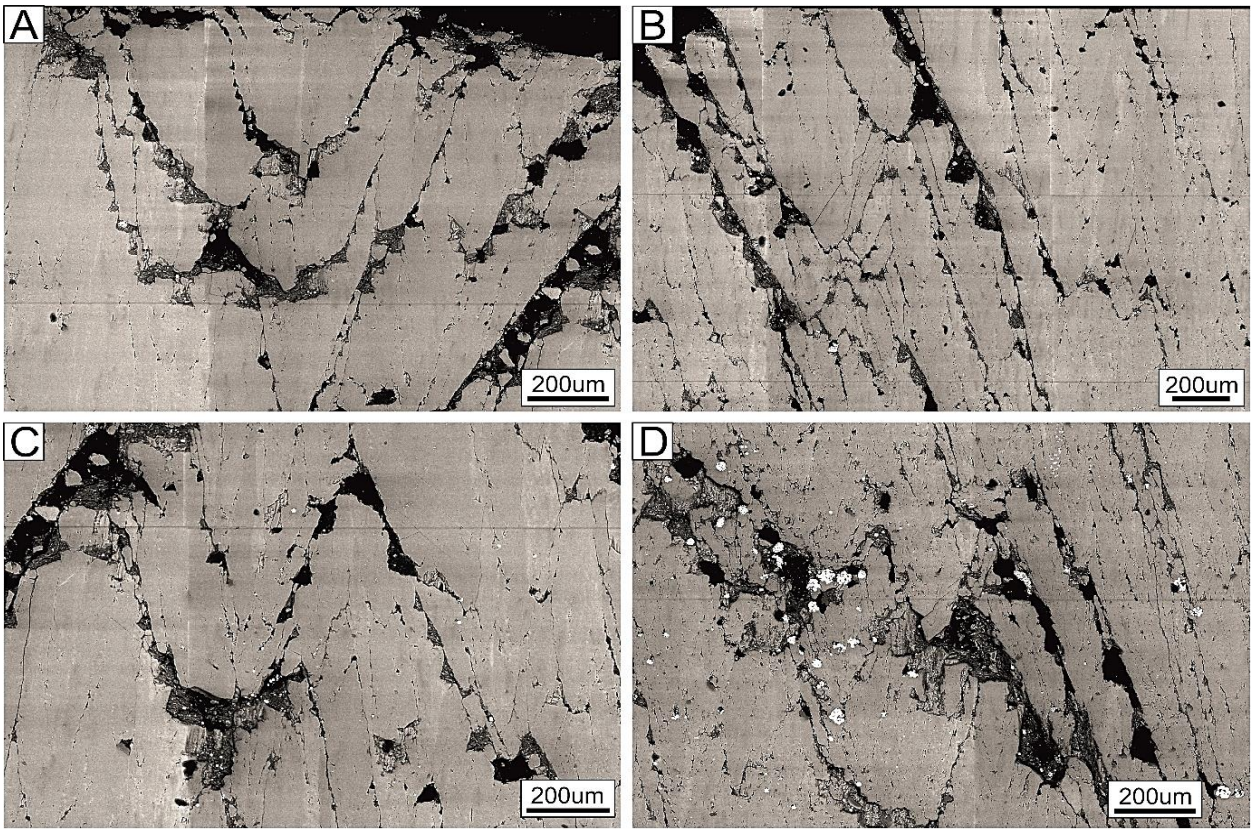


Figure 5.13 BSE images showing the mutual interference of adjoining cones. Note the occurrence of triangular solid inclusions along cone margins (B and C) and the spread of pyrite spheres in the cone-in-cone (D).

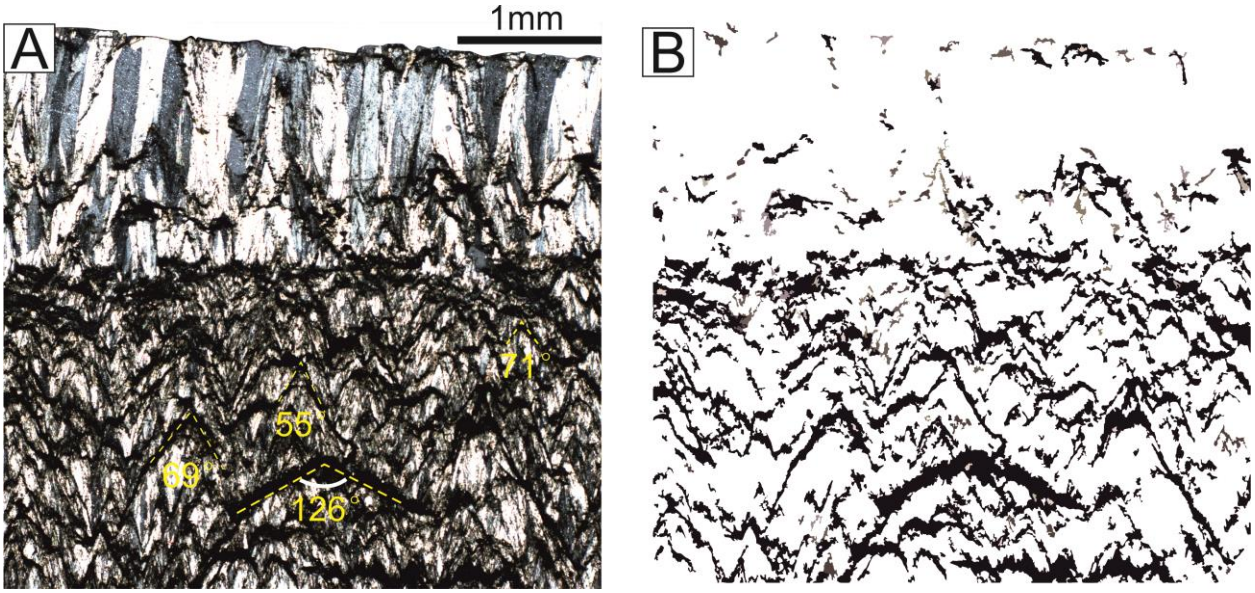


Figure 5.14 A calcite vein with an upper part of parallel-aligned fibres and a lower part of cone-in-cone structures (A) and the distribution of solid inclusions (B). Note the significant difference in the amount of solid inclusions between the upper and lower parts.

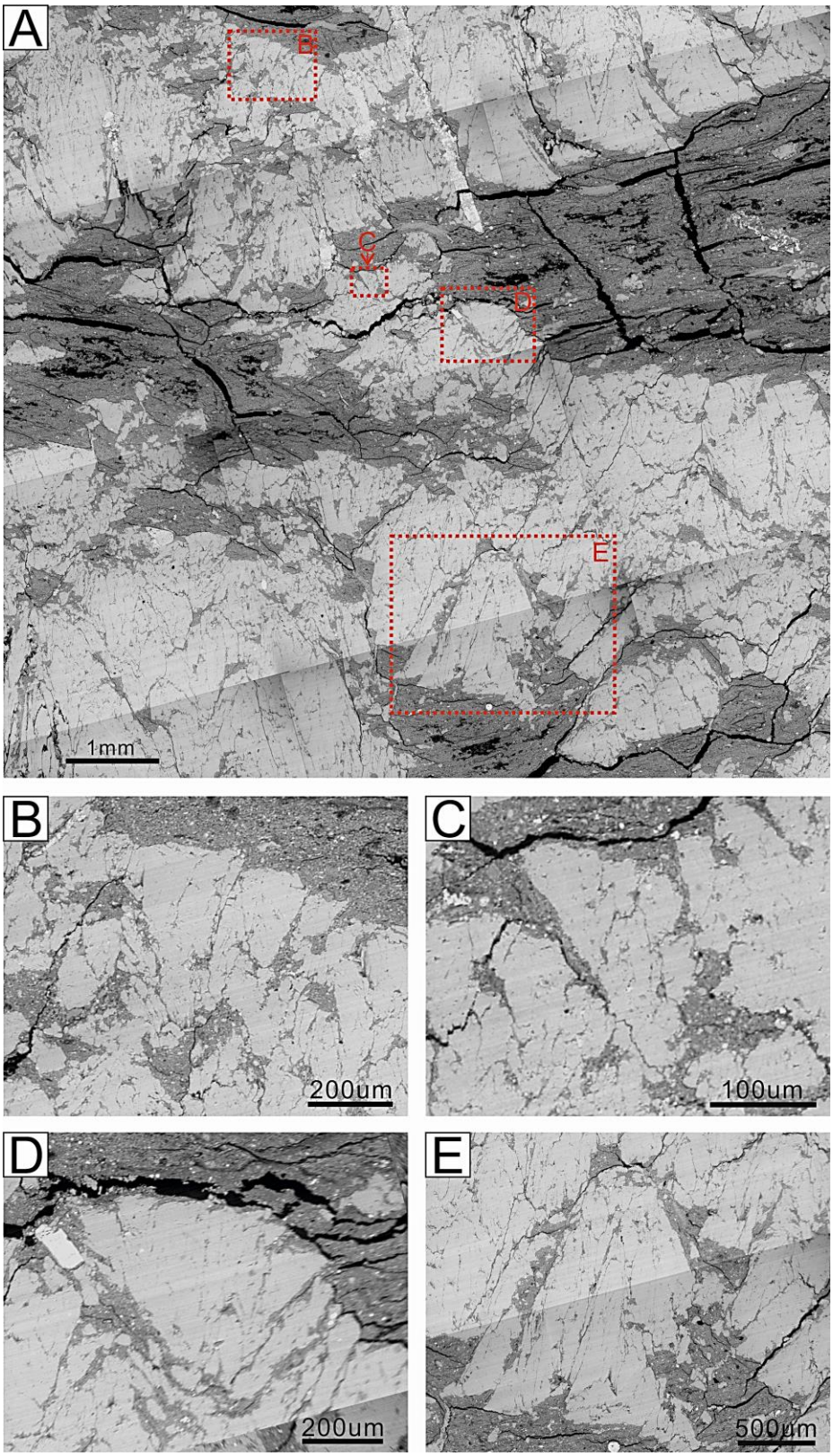


Figure 5.15 BSE images showing stacks of conical bundles of calcite fibres in varied sizes (A). Figures 5.15B-E are enlarged areas shown in the boxes in figure 5.15A.

Based on the observations above, the stacking of individual cones within a cone-in-cone structure is interpreted as a growth feature. The cone texture and the incorporation of the clay patches are presumably the results of displacive volumetric expansion of single conical units of fibre aggregates. The limited spaces between neighbouring cones prevent further growth of fibres as the adjacent areas have been accommodated by the development of other cones. The assumption that individual cones form along shear fractures during compaction (Kowal-Linka, 2010; Selles-Martinez, 1994) seems unlikely. First, it is difficult to explain the changes in apical angles in single cone-in-cone structures. Second, the assumed fractures are not observed in the host shales around the cones, especially the small sized cones that are scattered in the shales. The variance in cone sizes is interpreted to have been caused by the nucleation time of single cones. Larger cones presumably have formed earlier than the smaller cones. The cone apices mark the horizons and sites for primary cone nucleation.

5.4 Composition

The calcite beef veins and cone-in-cone structures are mainly formed of calcite fibres and solid inclusion of host clays. Detailed petrographic observations in this study reveal that the veins also contain abundant aragonitic skeletons, pyrite and organic matter. The following sections are focused on characterization of the distribution, morphology and size of those important components.

5.4.1 Skeletal fossil fragments

Skeletal fragments of whole fossils or bioclastic debris are observed within the median zones as the initial sites for fibre nucleation (Figure 5.16). The skeletal fragments mainly consist of calcite.

Some fragments have been partially or completely filled with pyrite. The fossils include ammonite, gastropod, bivalves, foraminifera and belemnite in varied shapes and degrees of preservation.

The circular skeletons are mainly enclosed by clay flakes and equant calcite crystals (Figures 5.17A-D). Some are partially wrapped by calcite fibres. The skeletons with higher aspect ratios are mostly sub-horizontal (Figures 5.17E-J). Those fragments serve as nucleus for the growth of fibres that occur either on one side or both sides.

The carbonate median zones in beef veins of type two mostly consist of calcite and pyrite, exhibiting either straight or regularly curved shapes (Figure 5.18). Such median zones are interpreted as skeletal fragments of bivalves. The skeletons are enclosed by fibres that are normal to them and determine the distribution of such veins.

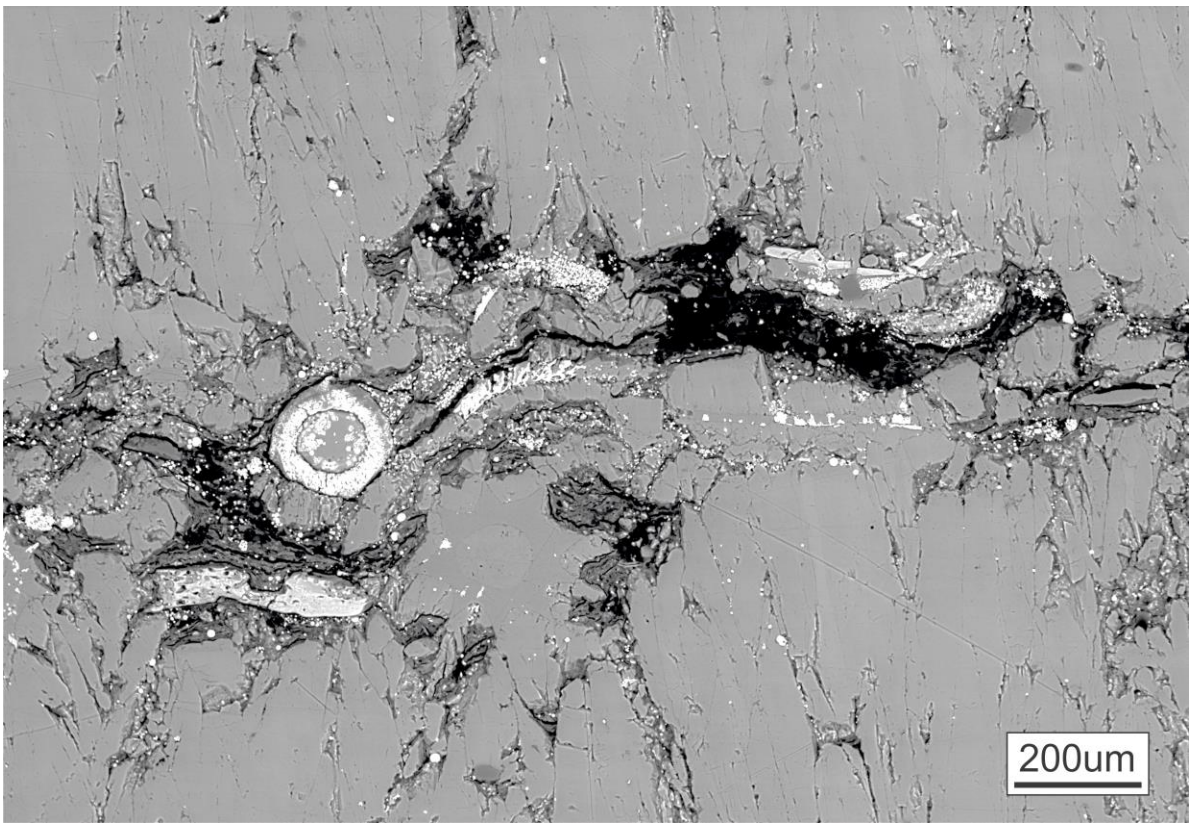
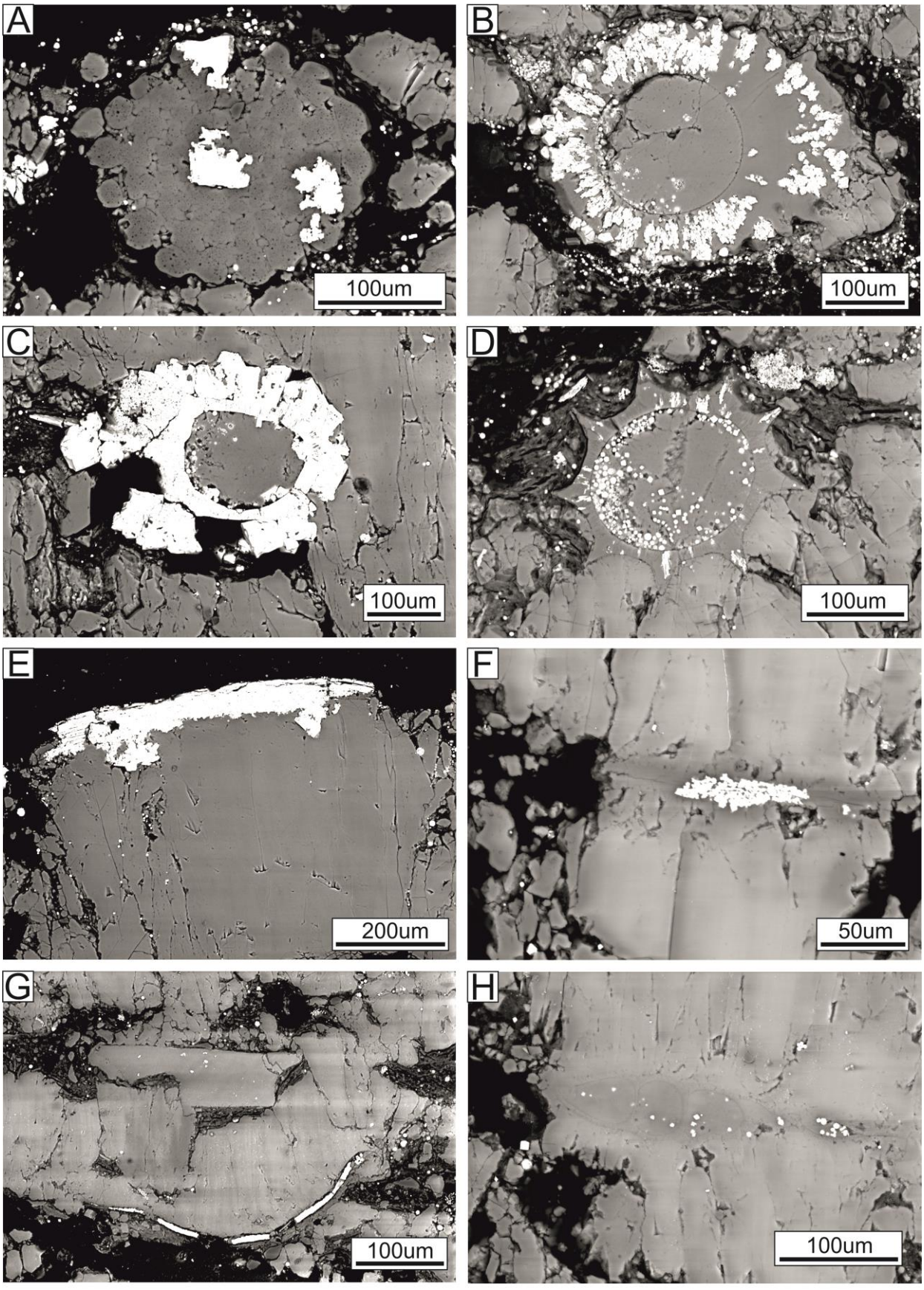


Figure 5.16 BSE image showing the occurrence of skeletal fragments in the median zone of a beef vein.


A
100um
B
100um
C
100um
D
100um
E
200um
F
50um
G
100um
H
100um

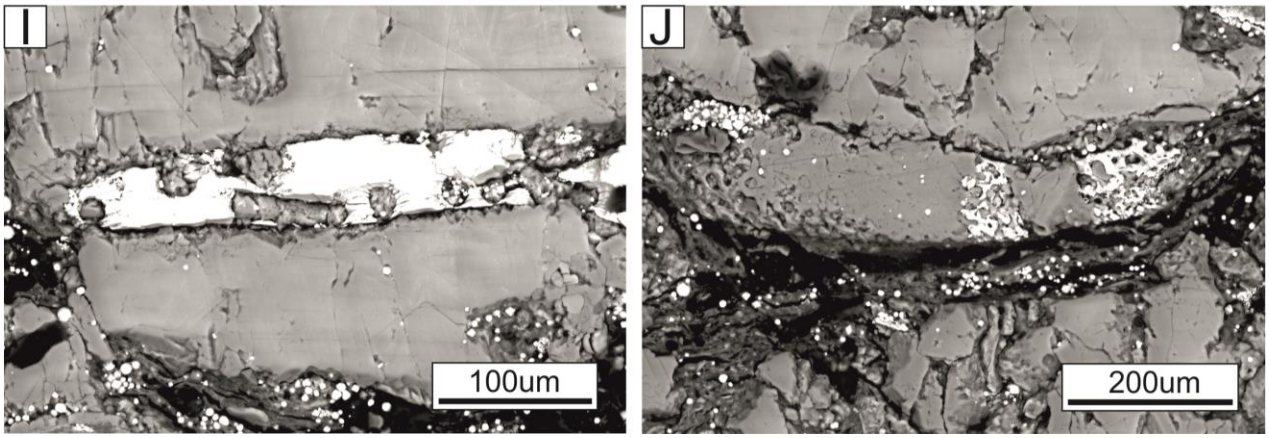


Figure 5.17 BSE images showing skeletal fragments of ammonites (A-D), bivalve (E-G), gastropod (H), belemnite (I) and foraminifera. Pyrite is white.

5.4.2 Amorphous organic matter (AOM)

Organic matter appears commonly within the calcite veins as amorphous kerogen (AOM) (Figure 5.19) that corresponds to degraded phytoplankton or bacterially-derived AOM, higher plant resins, and amorphous products by the diagenesis of macrophyte tissues (Tyson, 1995). AOM occurs as structureless particulate organic components. AOM mainly occurs as scattered patches in varied shapes, and sizes ranging from several to a maximum of 500 μm.

The AOM is widely disseminated within the beef veins and cone-in-cone structures, filling the spaces between neighbouring crystals (Figure 5.20). AOM is most prevalent in the median zones, intimately associated with clay particles, skeletal fragments and pyrite crystals. The AOM either appears as individual patches with little linkage with others or thin, curvy bands with varied width and embedded clay flakes and pyrite framboids.

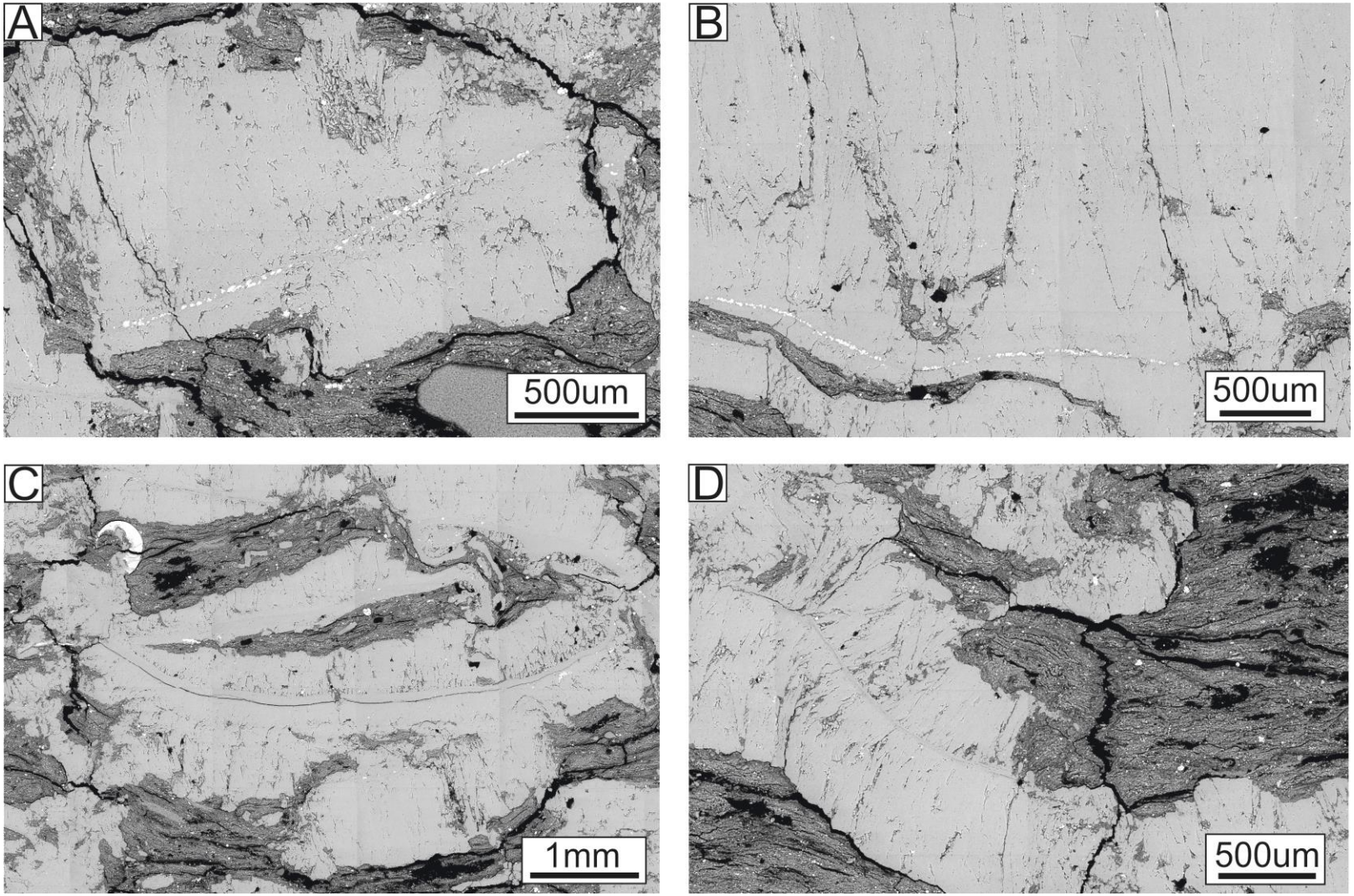


Figure 5.18 BSE images showing the skeletal fragments of bivalves as median zones of beef veins of type two. Note the skeletons in figure 5.18A and 5.18B are pyritized.

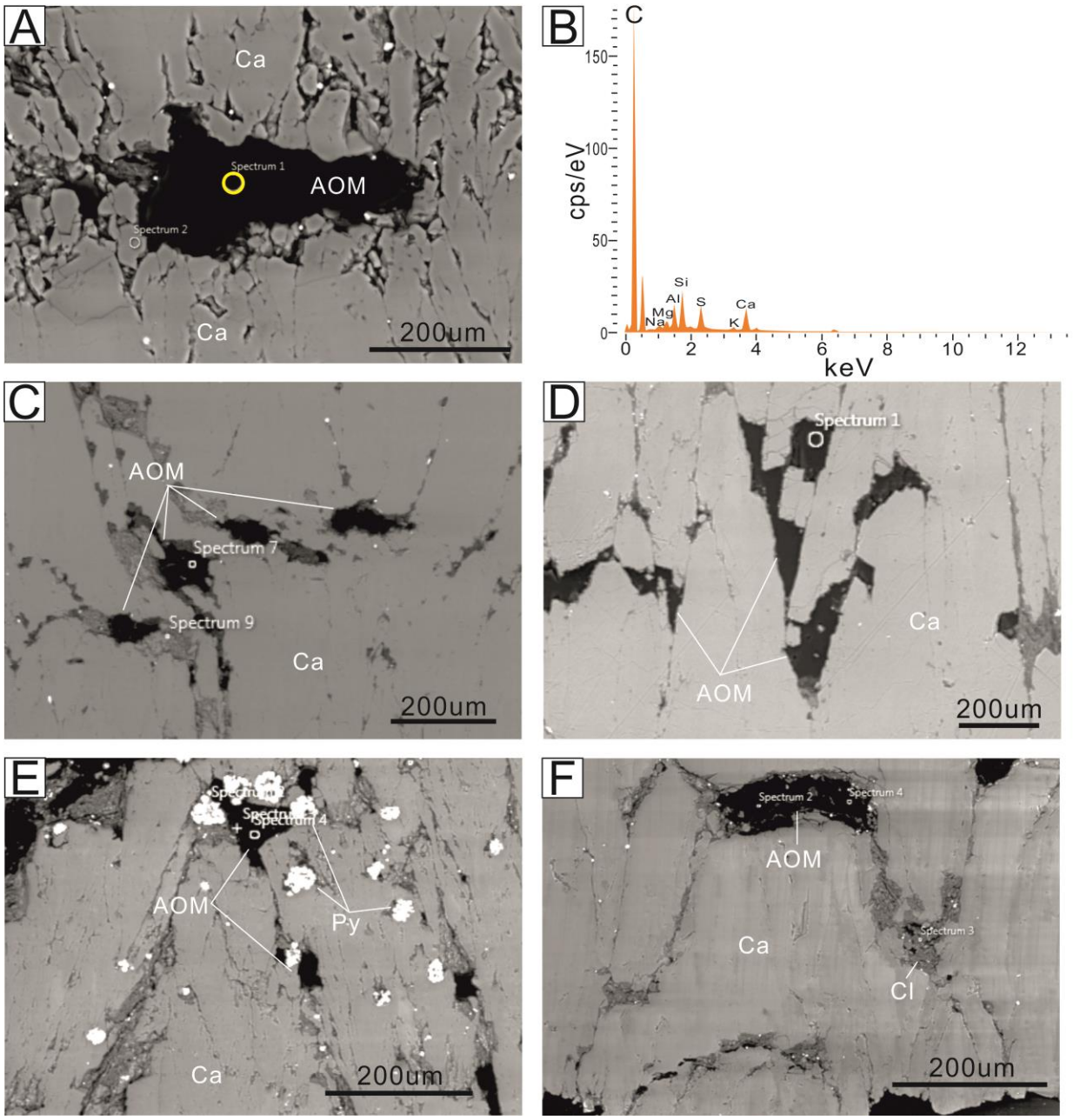


Figure 5.19 BSE images showing the occurrence of amorphous organic matter within calcite veins (A, C-F). (B) EDS spectra showing the chemical composition of the AOM in the selected sites (circle)in figure 5.19A. AOM in figures 5.19A and 5.19C are distributed in the median zone. AOM in figures 5.19D-5.19F are scattered along cone margins. AOM = amorphous organic matter. Ca = calcite. Cl = clay. Py=pyrite.

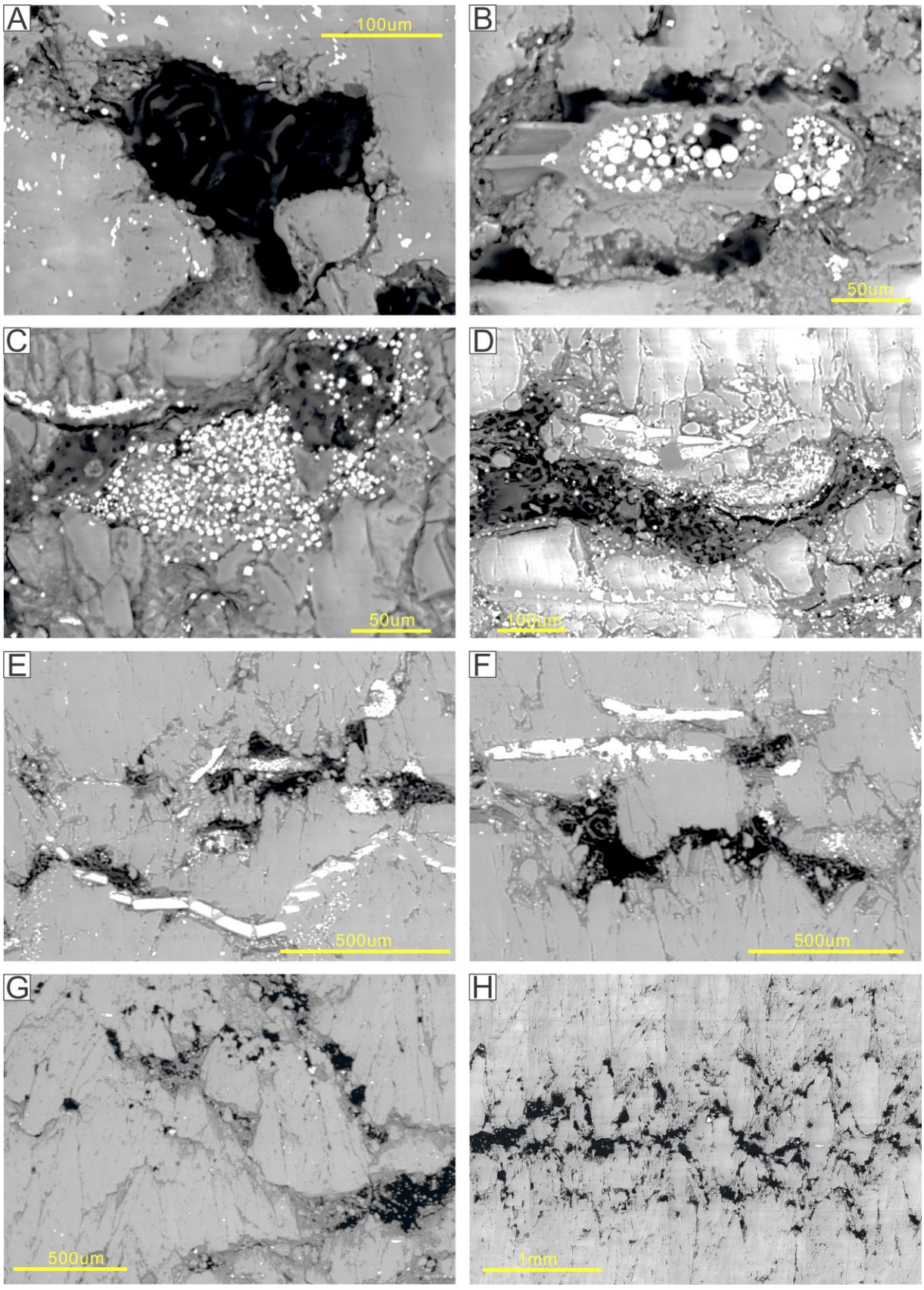

A
100um
B
50um
C
50um
D
100um
E
500um
F
500um
G
500um
H
1mm

Figure 5.20 BSE images showing the distribution of amorphous organic matter within calcite veins. (A) A single AOM patch (black) enclosed by calcite grains. (B) AOM around and within skeletal fragments. (C) AOM with embedded pyrite framboids (white) and clay flakes. (D) AOM in the median zone as the main component. (E) and (F) show AOM in the median zone. (G) Distribution of AOM in cone-in-cone structures. (H) Widely scattered AOM in the median zone of a beef vein. Note the increase in the amount of AOM towards the median zone.

The distribution of AOM is similar to that of clay minerals within the calcite veins. In beef veins, AOM is mainly concentrated within the median zone, and is rarely observed in the fibrous zones (Figure 5.20). However, AOM is more prevalent scattered in cone-in-cone structures, not only in the median zones but also the angular spaces created between neighbouring cones of plumose aggregate of fibres (Figure 5.21). The filling of those spaces often consists of argillaceous films.

5.4.3 Pyrite

Pyrite is one of the major components within the calcite veins, occurring as homogeneous fillings of skeletal fragments, single microcrystals of framboids, or spherical aggregates of densely packed framboids (Figure 5.22). Individual pyrite framboids are regularly shaped, with a diameter ranging from several up to 10μm. The pyrite spheres also exhibit a uniform morphology, consisting of aggregates of uniformly sized and shaped framboids. The diameter of those spheres varies from several to 80μm. Pyrite framboids and spheres are intimately associated with skeletal fragments, clay flakes and AOM, and localized to the sites with those components.

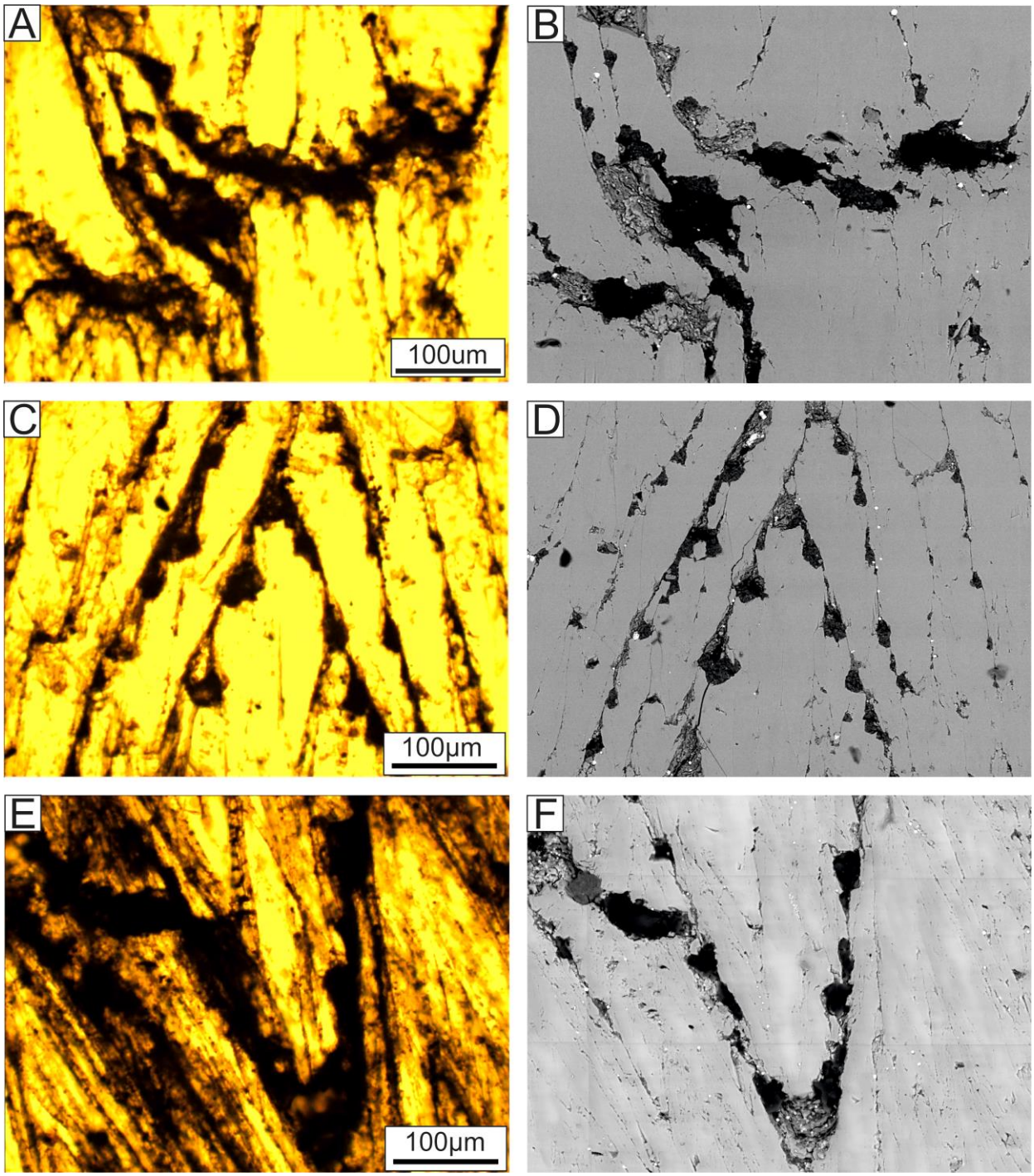


Figure 5.21 The distribution of AOM in the median zone (A and B) and along cone boundaries (C-F). Figure 5.21A, C and E are photomicrographs taken under plane light. Figure B, D and F are BSE images.

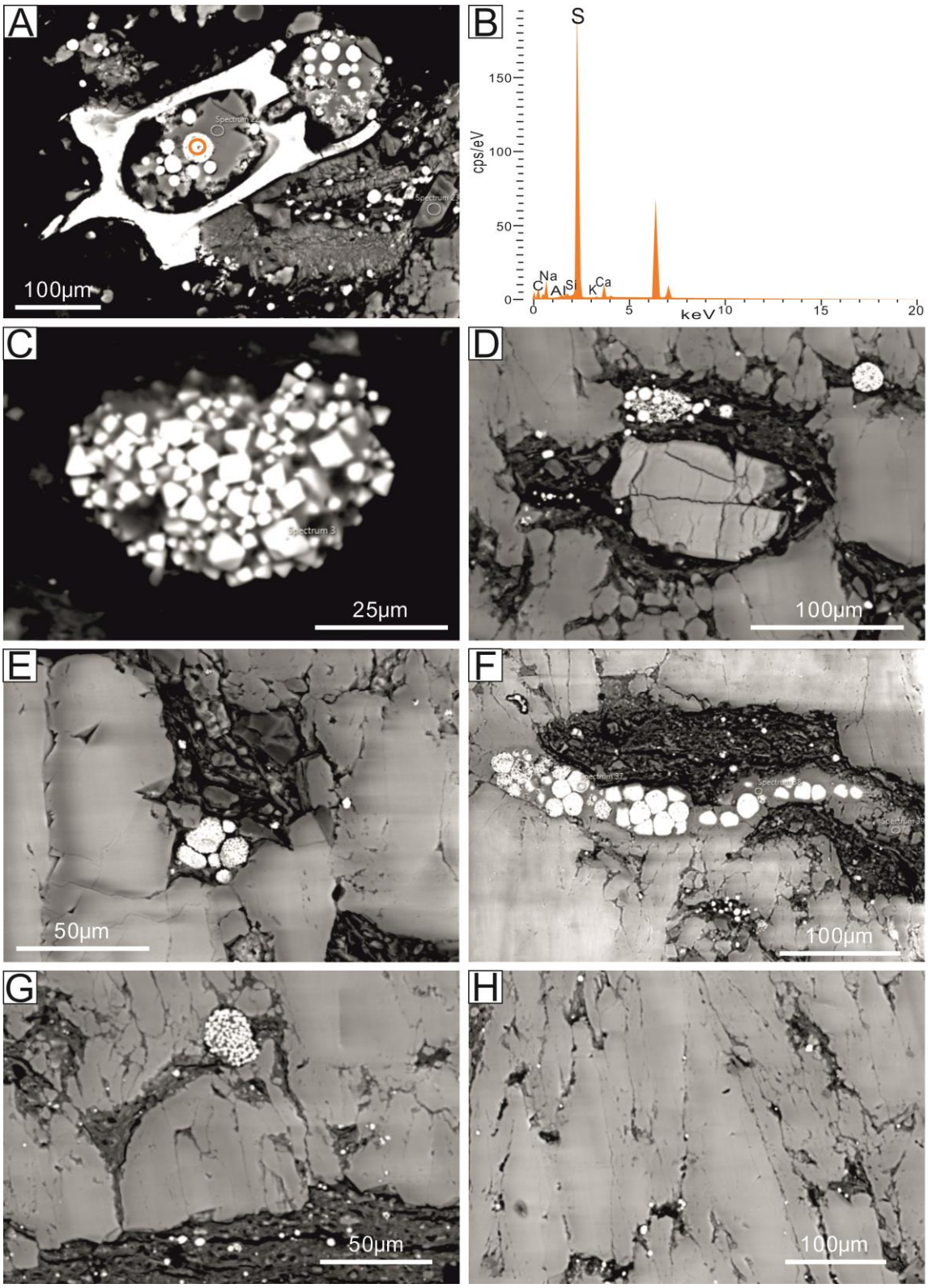


Figure 5.22 Occurrence of pyrite within calcite veins. (A) Pyrited skeleton and pyrite spheres within and round the skeleton. (B) EDS spectrum showing the chemical composition of the circular area in figure 5.22A. (C) Densely packed aggregates of pyrite crystals. (D) and (E) showing pyrite spheres associated

with clay particles. (F) A cluster of pyrite spheres concentrated within a possible skeleton. (G) A pyrite sphere on the top of a cone. (H) Microcrystals of pyrite (white spots) disseminated between neighbouring fibres.

5.5 Microtexture of clay inclusions

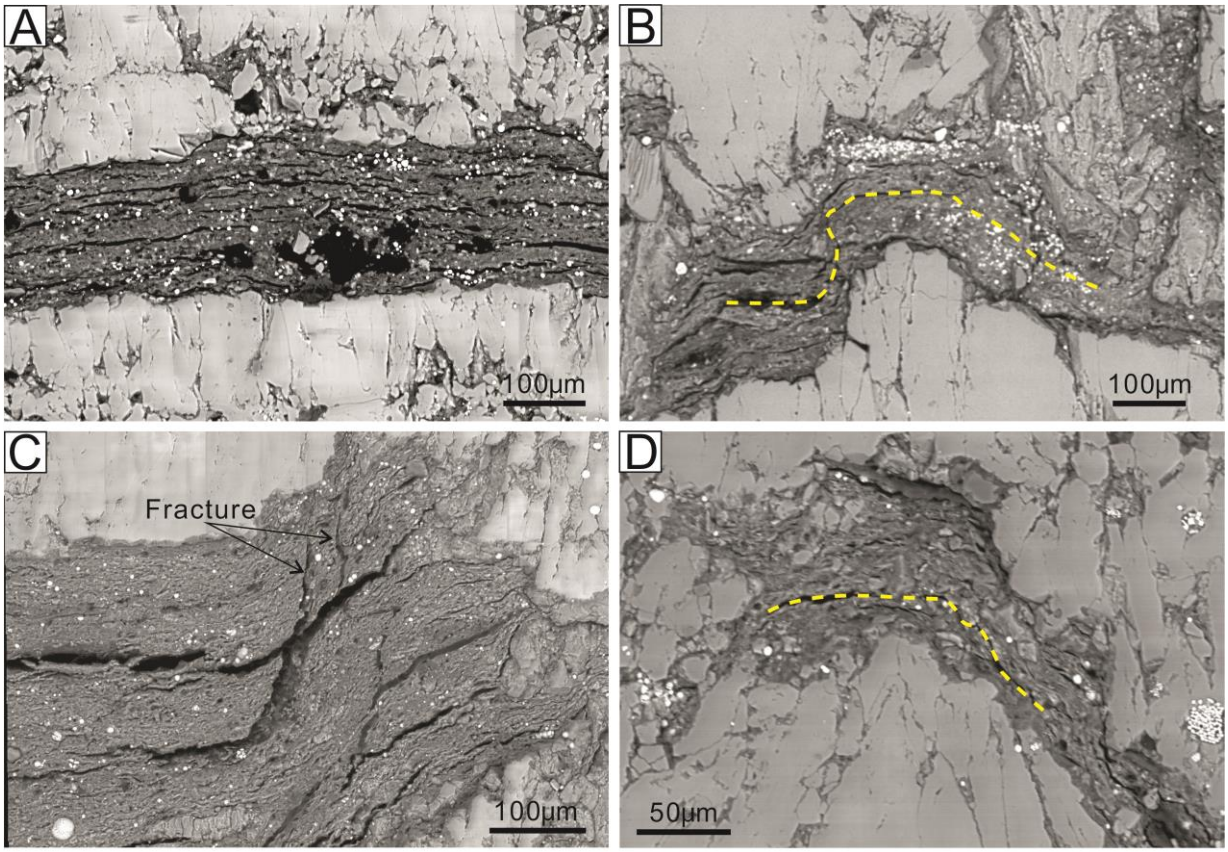
The study of the microtextural characteristics of clay inclusions within calcite veins is focused on the orientation of laminae of argillaceous materials, plastic and brittle deformation associated with the growth of adjacent fibres, which help reveal the information of timing of fibre growth, physical state of clays and the paleostress responsible for the strain in the clay inclusions (Franks, 1969; Tarr, 1933).

Clay inclusions are mainly localized in the median zone as the main component and in the spaces between adjacent fibres (Figures 5.23A-B). Those inclusions exhibit varied shapes and sizes, with the width ranging from several to 500 μm. Interestingly, the clays are thinly laminated and parallel to the contacting crystal margins of calcite. In the median zone, the clay laminae is generally horizontal. Locally, the laminae can be gently or severely folded due to the uneven crystal margins (Figures 5.23C-D). Shear fractures are often developed where the laminae exhibits the maximum curvature (Figure 5.23C).

Clay inclusions in cone-in-cone structures are more uniformly distributed and shaped, as patches filling the spaces between plumose aggregates of fibrous calcite (Figures 5.23E-H). Clay laminae are generally horizontal at cone apices, whose dip becomes steeper along cone limbs. The orientation of those clay flakes are parallel to the fibre ends. The laminations in a series of clay patches can be correlated by markers of bedding fissures (Figures 5.23F-G). Importantly, this suggests a uniform source of the clay patches that were originally an intact rock block with sub-horizontal laminations prior to the development of cone-in-cone structures. The growth of fibres

in different cones subsequently led to the separation of the rock block into multiple pieces, whose size was determined by the width of contacting cones. The displacement of each clay patch depends on the fibre length.

The microtextures of the clay inclusions also suggest that the growth of calcite fibres commenced during early diagenesis, prior to the full lithification of the sediments. The clays need to have partially been consolidated so that the nucleation of calcite fibres took place on the surfaces of clay lenses instead of homogeneously throughout a watery mud (Woodland, 1964). The contortion of clays by fibres indicates a plastic state of the sediments, which is possibly related to a high water saturation. As evident from relationship between the clay laminea and fibre ends, it is deduced that the growth of calcite fibres is responsible for the disruption and disposition of the clay flakes. Clay laminations parallel to fibre ends also suggests that the maximum compressional stress is parallel to the fibre directions, otherwise, the laminae would have been folded.


A
100μm
B
100μm
C
Fracture
100μm
D
50μm

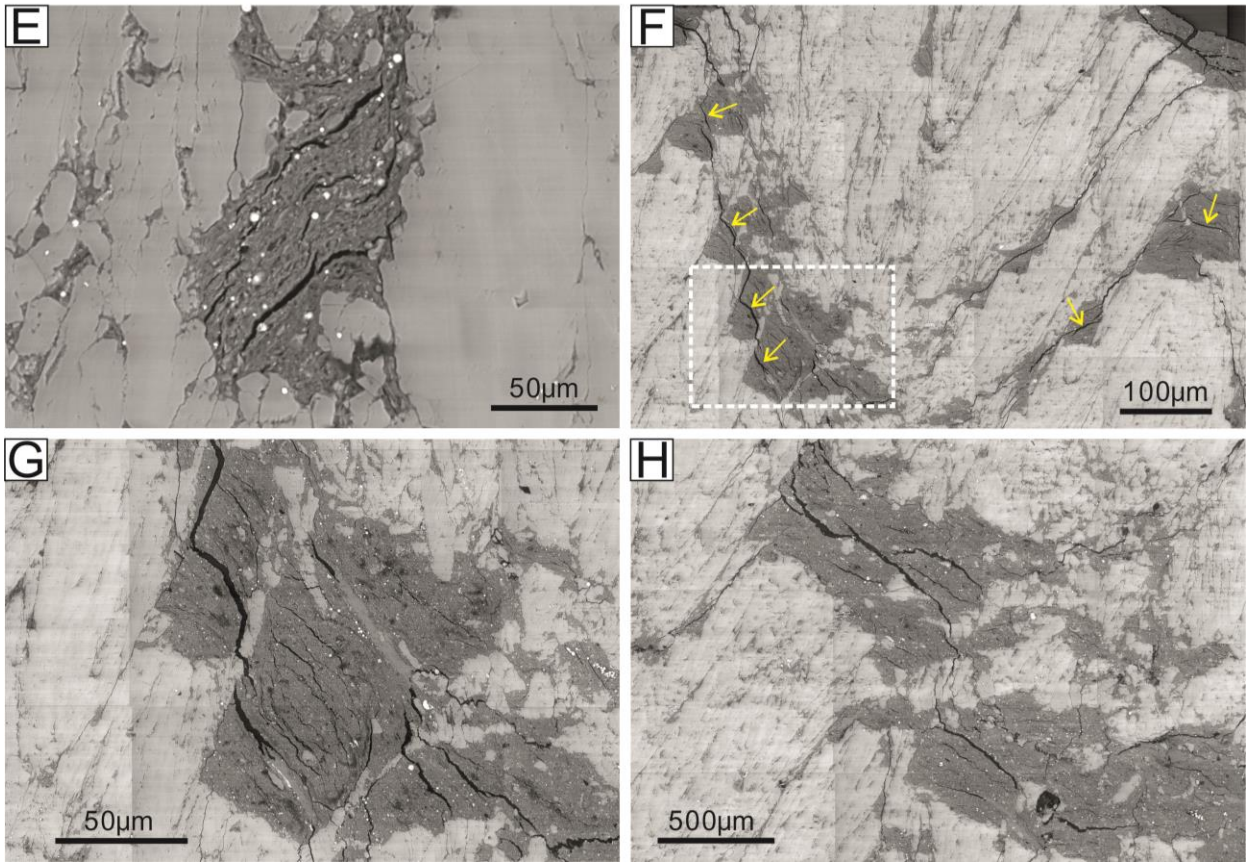


Figure 5.23 BSE images showing the microtextures of clay inclusions within beef veins (A-C) and cone-in-cone structures (D-H). (A) Horizontal clay laminations in the median zone. (B) Fold clay laminae parallel to fibre margin. (C) Fold related fracture within clay inclusions. (D) Fold laminae along the boundary of a cone. (E) Inclined clay laminae. (F) A series of clay inclusions in a saucer form. (G) Clay laminae parallel to the fibre ends. Note the feasible bedding correlation of the different patches of clay inclusions. (H) Varied orientations of clay flakes that are parallel to the ends of contacting fibres.

5.6 EBSD analysis

C-axis fabrics of calcite could reflect the growth kinetics and provide information of stress-strain state that are critical for the analysis of the growth mechanism of crystals (Paquette and Reeder, 1990; Woodland, 1964). It is suggested that c-axes of calcite are virtually parallel to the long axes of fibres in beef veins and cone-in-cone structures (Cobbold et al., 2013; Rodrigues et al., 2009). However, the universal stage (U-stage) measurements demonstrate that the c-axes of calcite fibres

in horizontal beef veins are by no means entirely vertical (Woodland, 1964). Although the U-stage is a useful tool to measure crystallographic orientations, it is generally laborious and time-consuming (Passchier and Trouw, 1996). Besides, the lower limit of mineral grains chosen for measurement is no smaller than 20 μm (Passchier and Trouw, 1996), preventing a systematic study of crystals of all sizes. Moreover, only one data point is often obtained per grain, which tends to be inaccurate and unrepresentative. The electron backscatter diffraction (EBSD) technique, which is a stage-of-the-art microstructural-crystallographic characterization technique to study crystal orientation and size and also allows orientation mapping (Instruments, 2005), was applied in this study. EBSD analysis of calcite beef veins and cone-in-cone structures focuses on quantitative measurement of the crystallographic c-axis orientations of calcite crystals in the median zones, fibrous zones, blocky zones and tip regions, as well as information of crystal boundaries, sizes and aspect ratios.

5.6.1 Beef veins

5.6.1.1 Median zone

The thin median zones contain numerous small calcite crystals that exhibit varied shapes and sizes (Figure 5.24A). The plot of c-axes of the crystals in a stereonet reveals a dispersed scattering, suggesting that the c-axes have a near random orientation.

Figure 5.24B illustrates the c-axes orientations of calcite crystals in the median zone shown in figure 5.1A. The randomly dispersed crystals are predominantly small and equant. Larger crystals are mainly closely packed as aggregates, which also exhibit random c-axis orientations. Differently, the c-axes of elongate crystals assembled in the form of cone-in-cone structures are quasivertical (red), which are similar to the fibres.

Median zones with a larger width consist of abundant small crystals in a quant habit (Figure 5.24C). The overall c-axis orientation is random. However, some elongate crystals that are densely packed exhibit higher c-axis plunges. Those crystals also have much larger sizes than the other crystals.

5.6.1.2 Fibres

Figure 5.25 illustrates a representative fibrous zone of a beef vein that consists of numerous vertical fibres. The EBSD data demonstrates that the fibres have a preferred c-axis orientation in the near-vertical direction. To examine the subtle variations in c-axis orientations of calcite fibres from the median zone towards vein margins, the upper fibrous part of the vein is subdivided into four zones for c-axis stereonet projections. The results reveal a trend of decrease in c-axis plunges towards the median zone. In zone one, the c-axes of crystals primarily plunge at 60°-90°. The plunges of c-axes in zone two ranges from 50°-90°. The lowest plunge of c-axes decreases to ~40°. In zone four, the calcite crystals cover a much wider range of c-axis orientations than the other zones. Hence, c-axis plunges of calcite gradually increase from the median zone towards vein margins.

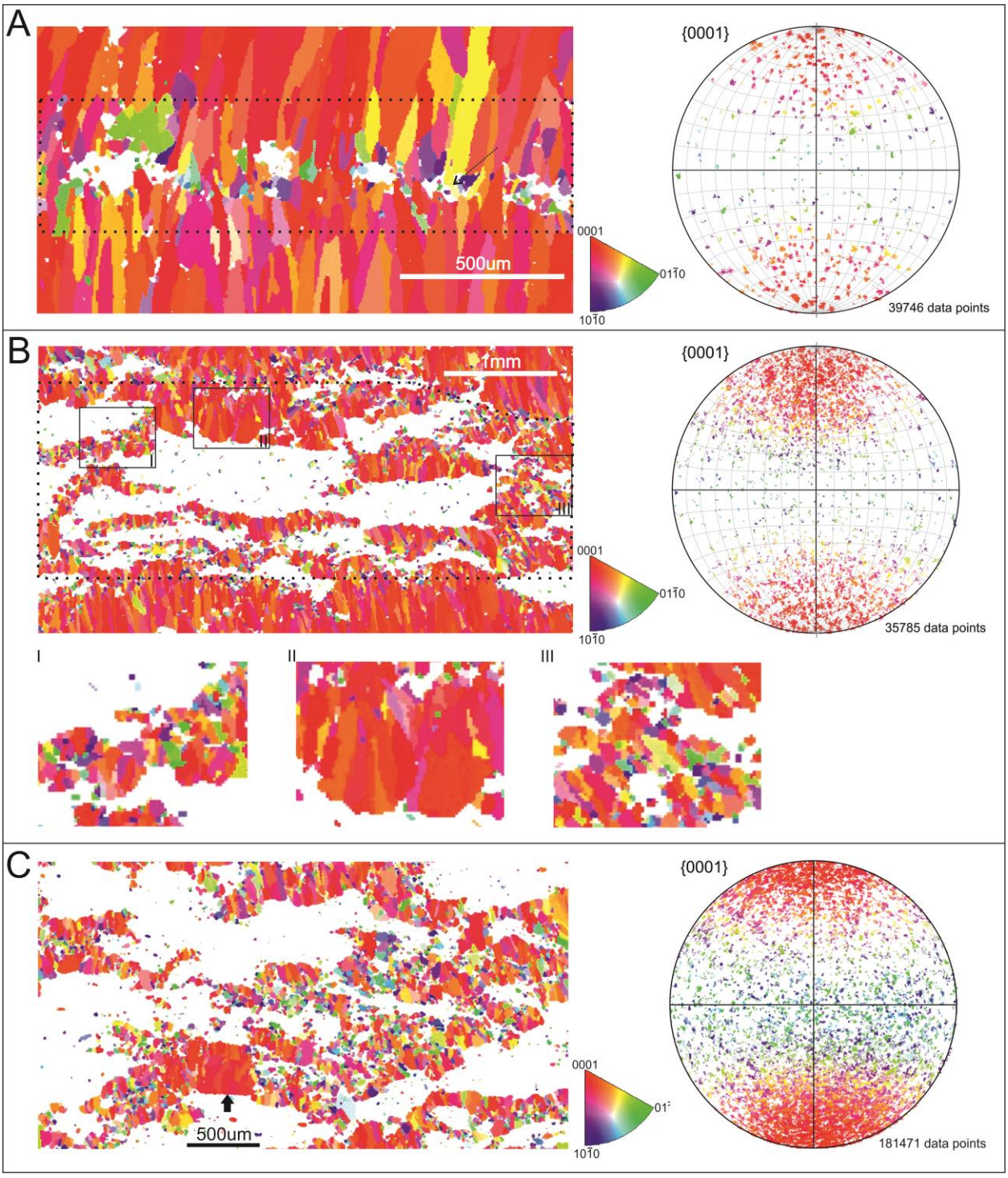


Figure 5.24 Y-direction IPF colouring orientation maps (IPF-Y) showing the crystallographic orientations in the median zones. The right figures show stereonet projections of the c-axis orientations of the crystals in the left figures.

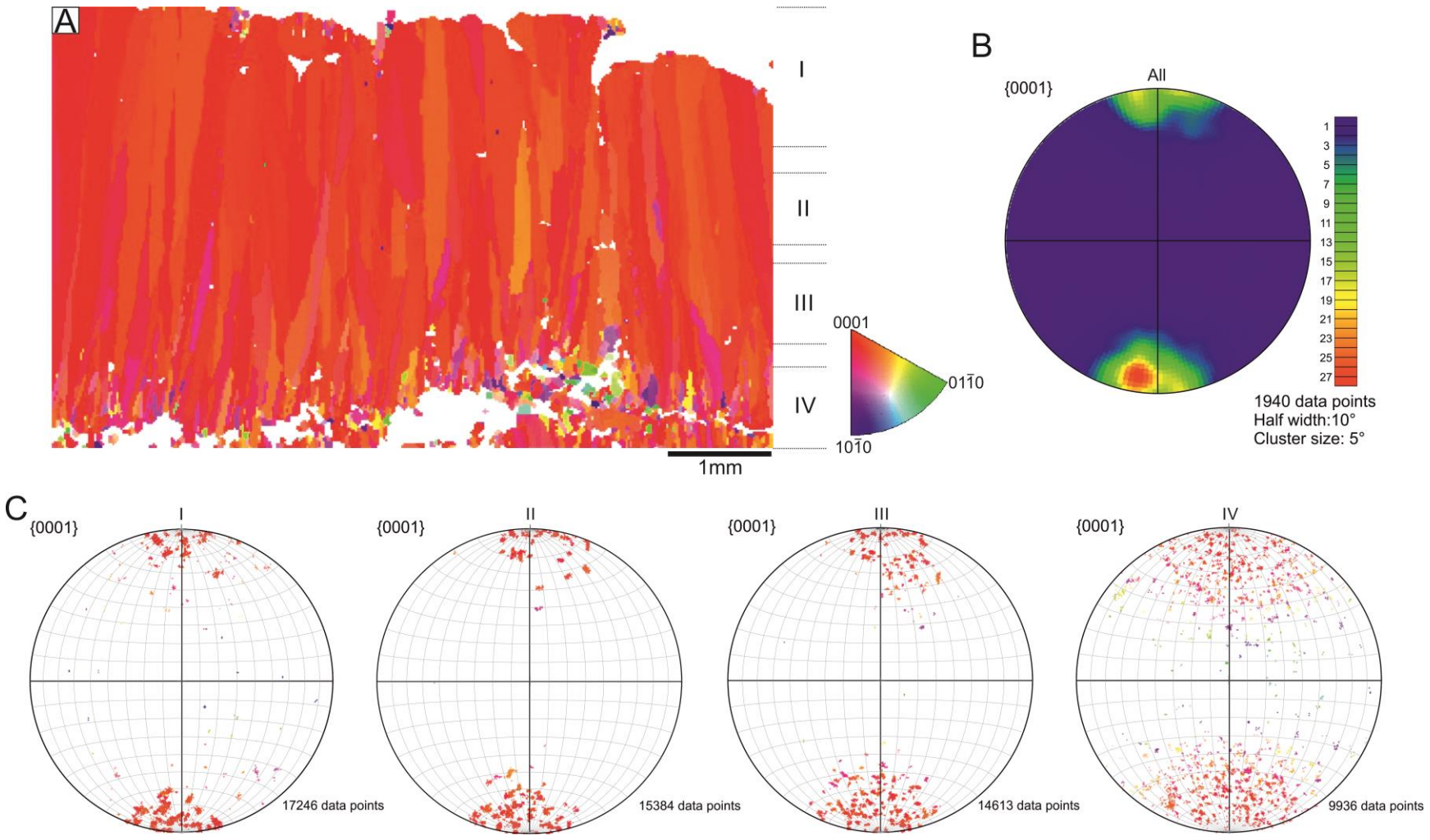


Figure 5.25 Y-direction IPF colouring orientation maps (IPF-Y) showing the crystallographic orientations of calcite fibres. (B) Contoured stereonet projection of c-axis orientations of the fibres in figure 5.25A. One data point per crystal. (C) Stereonet projections of c-axis orientations of the crystals in the four zones shown in figure 5.25A.

It is notable that single fibres rarely extend from the median zone to vein margins (Figure 5.26). Fibre overgrowth occurs frequently between neighbouring fibres, leading to the termination of some crystals, especially those with low c-axis plunges. Single fibres commonly exhibit a lenticular geometry and a sharp tip with the apices pointing towards the median zone. C-axis orientations are constant in single fibres, which are not in accord with the long axes orientations.

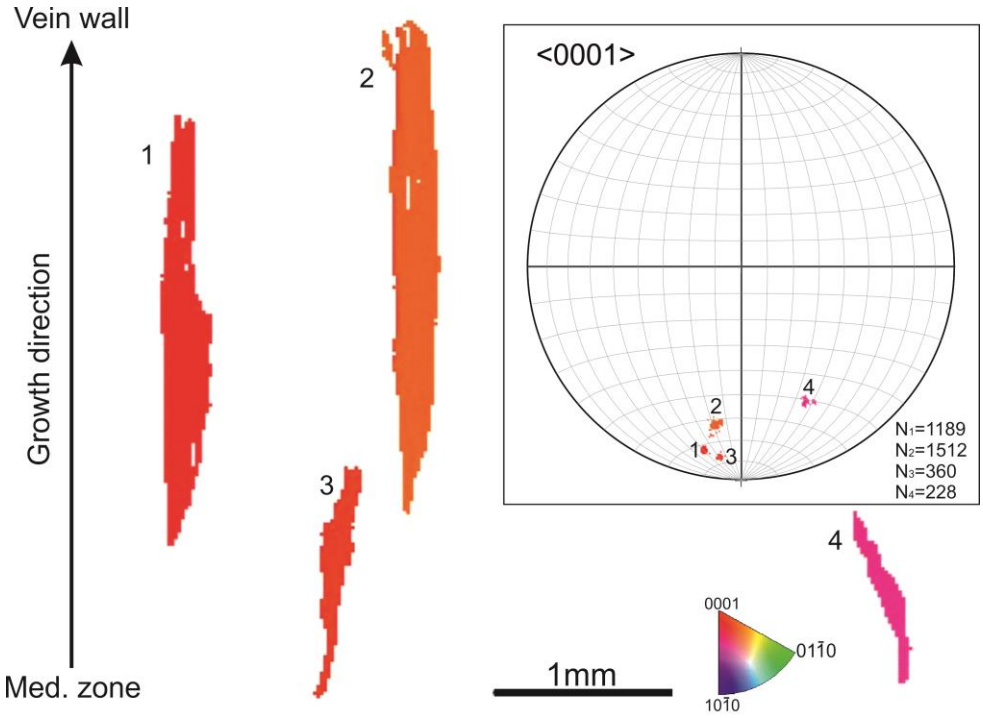


Figure 5.26 Y-direction IPF colouring orientation maps (IPF-Y) showing the crystallographic orientations of four calcite fibres (left) and the stereonet projections of their c-axes.

5.6.1.3 Blocky zone

The three types of blocky zones (see section 5.3.1.3) within the fibrous parts of beef veins share similar features of crystal shape, size and c-axis fabric, which are in contrast to the enclosing fibres. The calcite crystals are predominantly small and equidimensional, exhibiting randomly oriented

c-axes (Figure 5.27). However, the fibres in the centre of the conical shaped blocky zone have subvertical c-axes similar to those outside the cone.

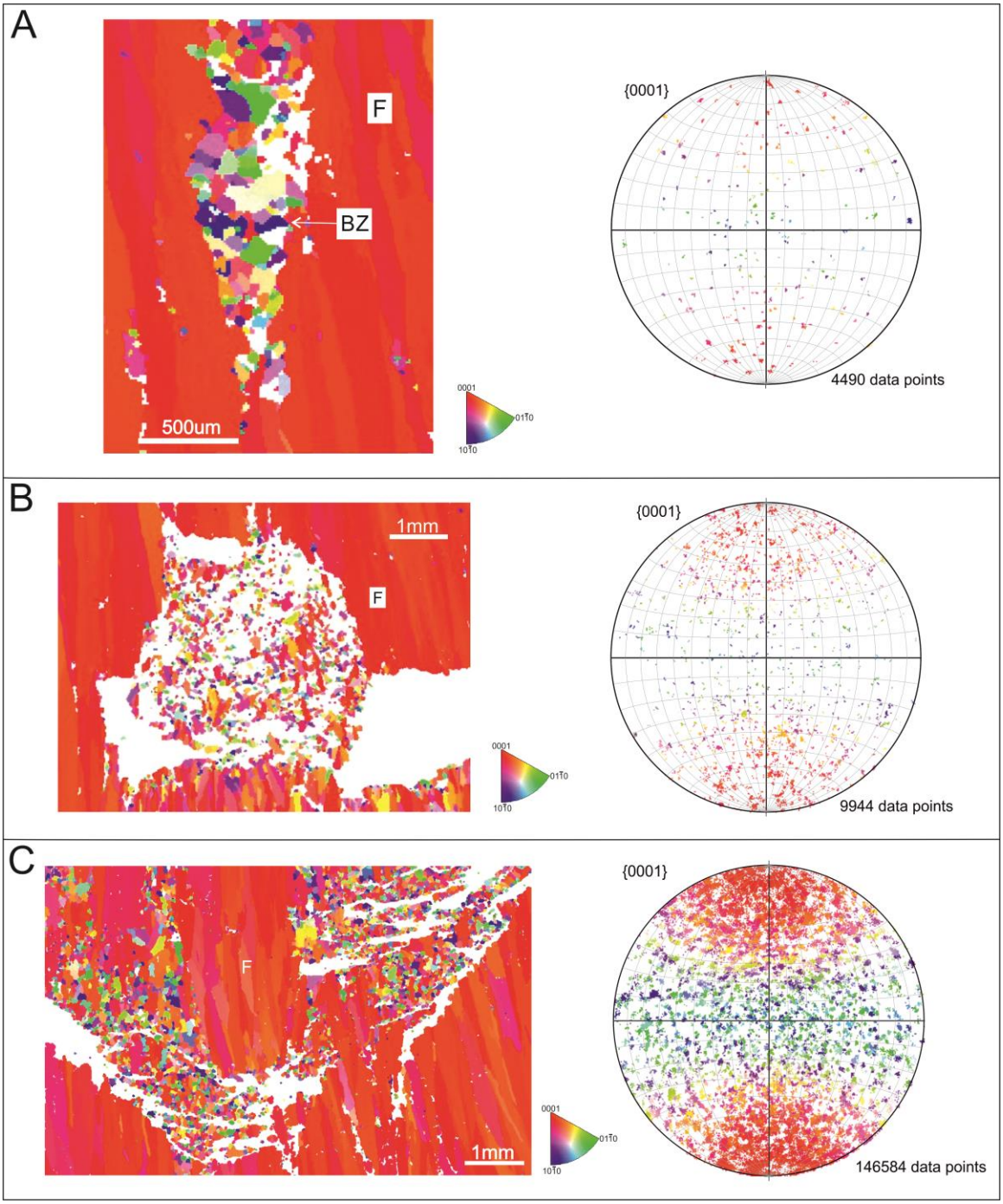


Figure 5.27 Y-direction IPF colouring orientation maps showing the crystallographic orientations of the spindle-shaped (A), circular (B), and conical shaped (C) blocky zones (left) and the stereonet projections of their c-axes.

5.6.1.4 Tips

It is difficult to sample the vein tip in a 2D section due to the 3D sheet-like geometry of single veins. In this study, vein tips were sampled at the vanishing point of a vein that crops out in the black shales. Figure 5.28 illustrates a representative vein tip that contains both equant and elongate-fibrous crystals of calcite. The equant crystals exhibit varied sizes and are mainly localized along vein margins. The elongate-fibrous crystals are orthogonal to the upper vein-wall, with a plunge of 60°. The stereonet projections of c-axes of calcite reveal a preferred orientation that is approximately parallel to the long axes direction of the fibers. C-axes of the equant crystals exhibit a random orientation, regardless of the localities and sizes.

5.6.1.5 Curved beef veins

The beef veins of Type B (see section 5.3.1.1) exhibit different characteristics of c-axis fabrics from veins of type one. The c-axes of fibres are only oriented vertically in the horizontal segments of single veins. In the inclined segments, the c-axes are approximately orthogonal to the contacting vein-walls. Hence, the fibres in the parts with the highest vein-dip have the lowest c-axis plunge. In figure 5.29, the c-axis orientations exhibit a trend of counterclockwise rotation. C-axes are closely associated with the vein-wall orientations.

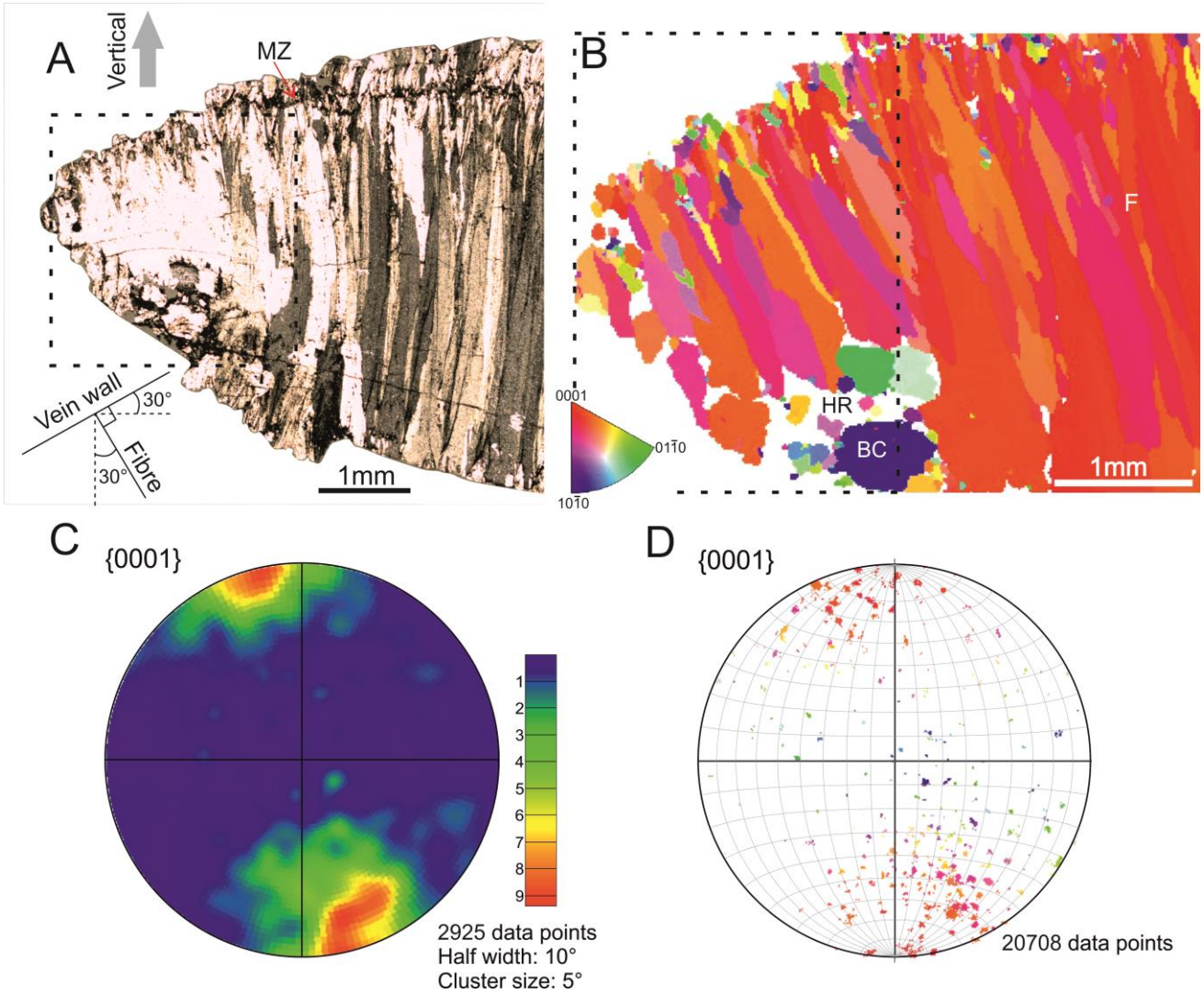


Figure 5.28 Photomicrograph showing the tip regions of a calcite beef vein. (B) Y-direction IPF colouring orientation maps showing the crystallographic orientations of the calcite in figure 5.28A (dashed box). (C) Contoured stereonet projection of the c-axis orientations of the calcite crystals in figure 5.28B. One data point per crystal. (D) Stereonet projection of the c-axis orientations.

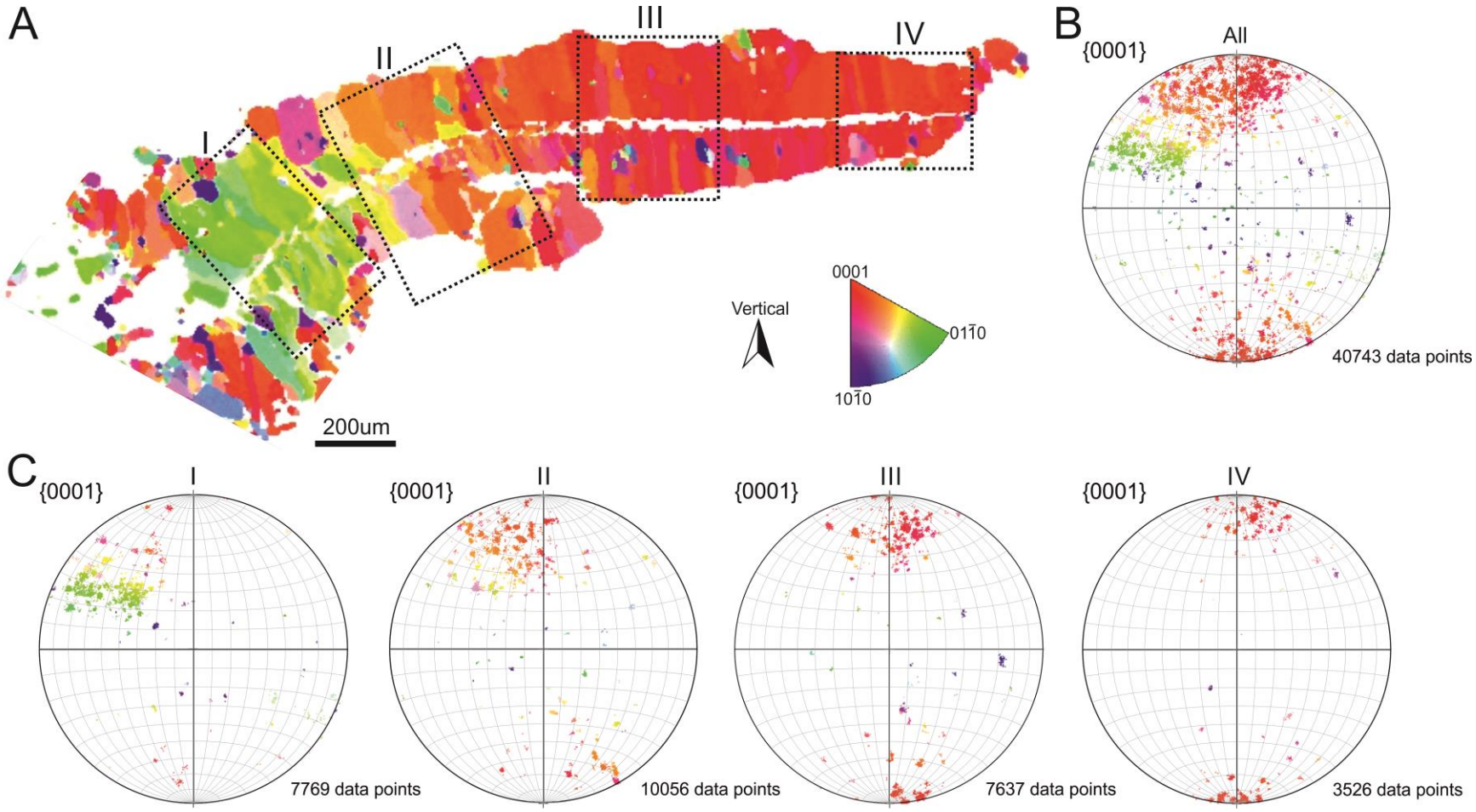


Figure 5.29 Y-direction IPF colouring orientation maps showing the crystallographic orientations of the calcite fibres in a curved vein. (B) Stereonet projection of the c-axis orientations of the calcite crystals in figure 5.29A. (D) Stereonet projection of the c-axis orientations of fibres in four different zones shown in the boxes in figure 5.29A.

5.6.2 Cone-in-cone structures

The cone-in-cone structures illustrated in figure 5.30 were examined by EBSD. The results show that single cones contain multiple elongate-fibrous crystals with the long axes aligned vertically. The c-axes exhibit a preferred vertical direction, which is not influenced by the angles of cone apices.

Figure 5.31 illustrates the crystallographic orientations of crystals in the cone-in-cone with lower apical angles. Similarly, the c-axes are preferential oriented in the vertical direction. However, numerous smaller, equant or elongate crystals at cone tips and along cone boundaries have randomly oriented c-axes.

The vein described in figure 5.32 exhibits slightly varied EBSD results. The fibres in the upper part have much larger sizes and a lower crystal number that those in the lower cone-in-cone structures. Although the contoured projections of c-axes reveal a preferred vertical direction, the crystals in the cones exhibit a more widely dispersed c-axis distribution.

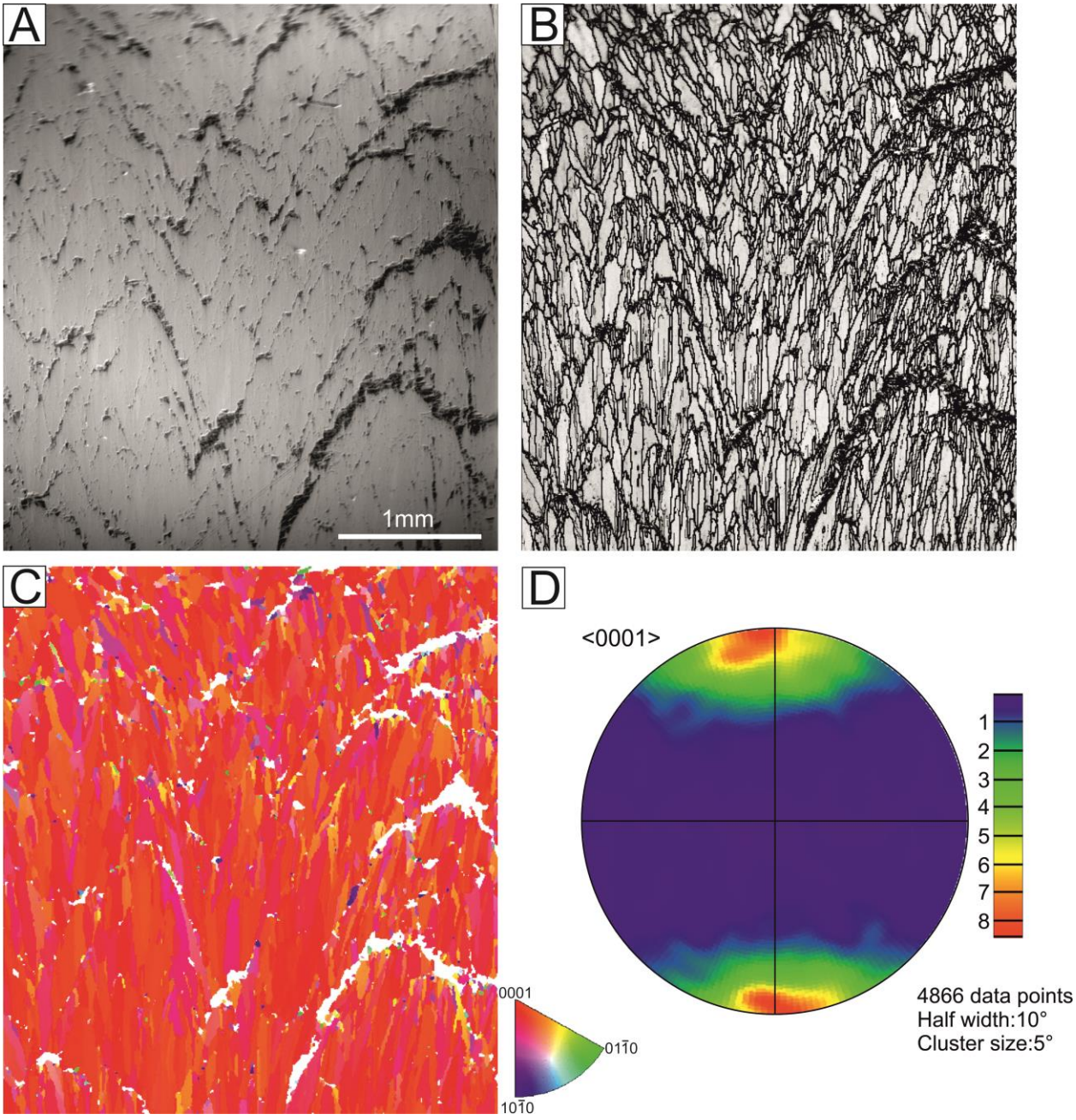


Figure 5.30 BSE image showing the microtexture of cone-in-cone structure. (B) Crystal boundaries identified by EBSD. (C) Y-direction IPF colouring orientation maps showing the crystallographic orientations of the calcite fibres. (D) Contoured stereonet projection of c-axis orientations of crystals shown in figure 5.30C. One data point per crystal.

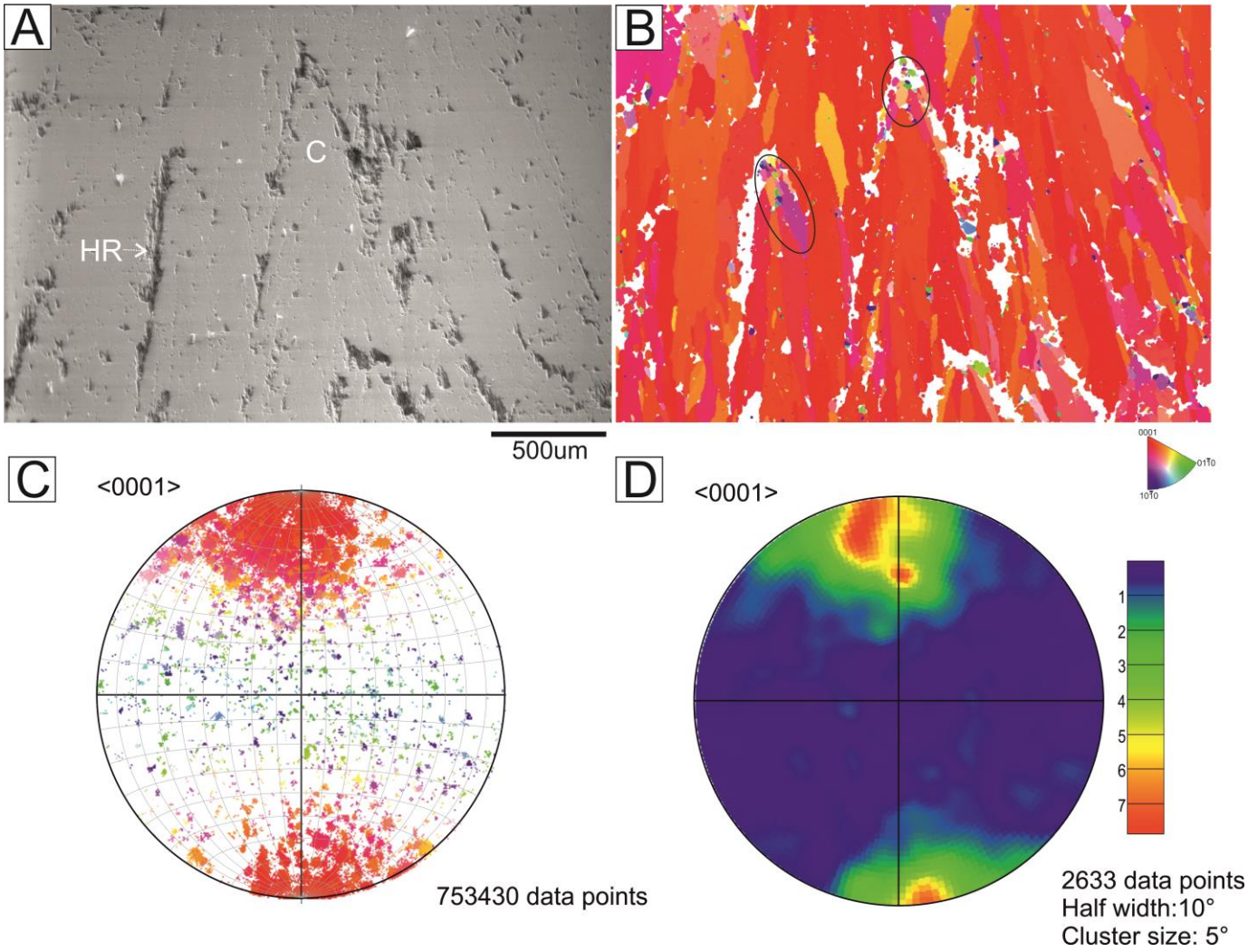


Figure 5.31 BSE image showing the microtexture of cone-in-cone structure with low apical angles. (B) Y-direction IPF colouring orientation maps showing the crystallographic orientations of the calcite fibres. (C) Stereonet projection of c-axis orientations of all crystals shown in figure 5.31B. (C) Contoured stereonet projection of c-axis orientations of all crystals. One data point per crystal.

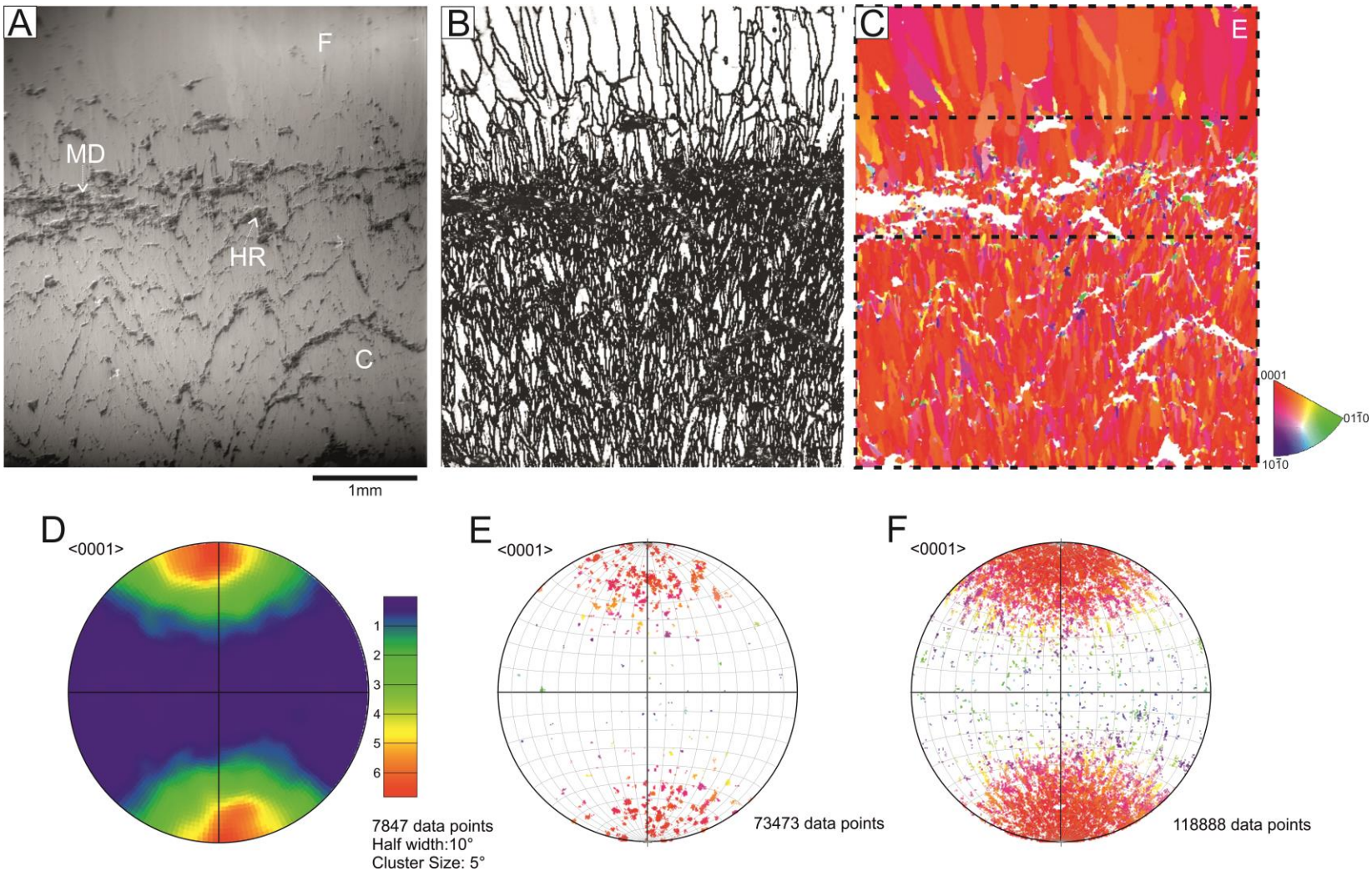


Figure 5.32 BSE image showing the microtexture of a calcite vein consisting of fibres in the upper part and cone-in-cone structures in the lower part. (B) Crystal boundaries. (C) Y-direction IPF colouring orientation maps showing the crystallographic orientations of the calcite crystals. (C) Contoured stereonet projection of c-axis orientations of all crystals shown in figure 5.32C. One data point per crystal. (E) Stereonet projection of c-axis orientations of the upper fibres. (F) Stereonet projection of c-axis orientations of the crystals in the lower cone-in-cone structures.

EBSD measurements of cone-in-cone structures with plumose margins reveal that their c-axes approximately plunge at 60°-90°, whilst trending in the direction orthogonal to their faces at fibre ends (Figure 5.33). This indicates the c-axes are orthogonal to the laminations of clay flakes trapped within the angulate spaces.

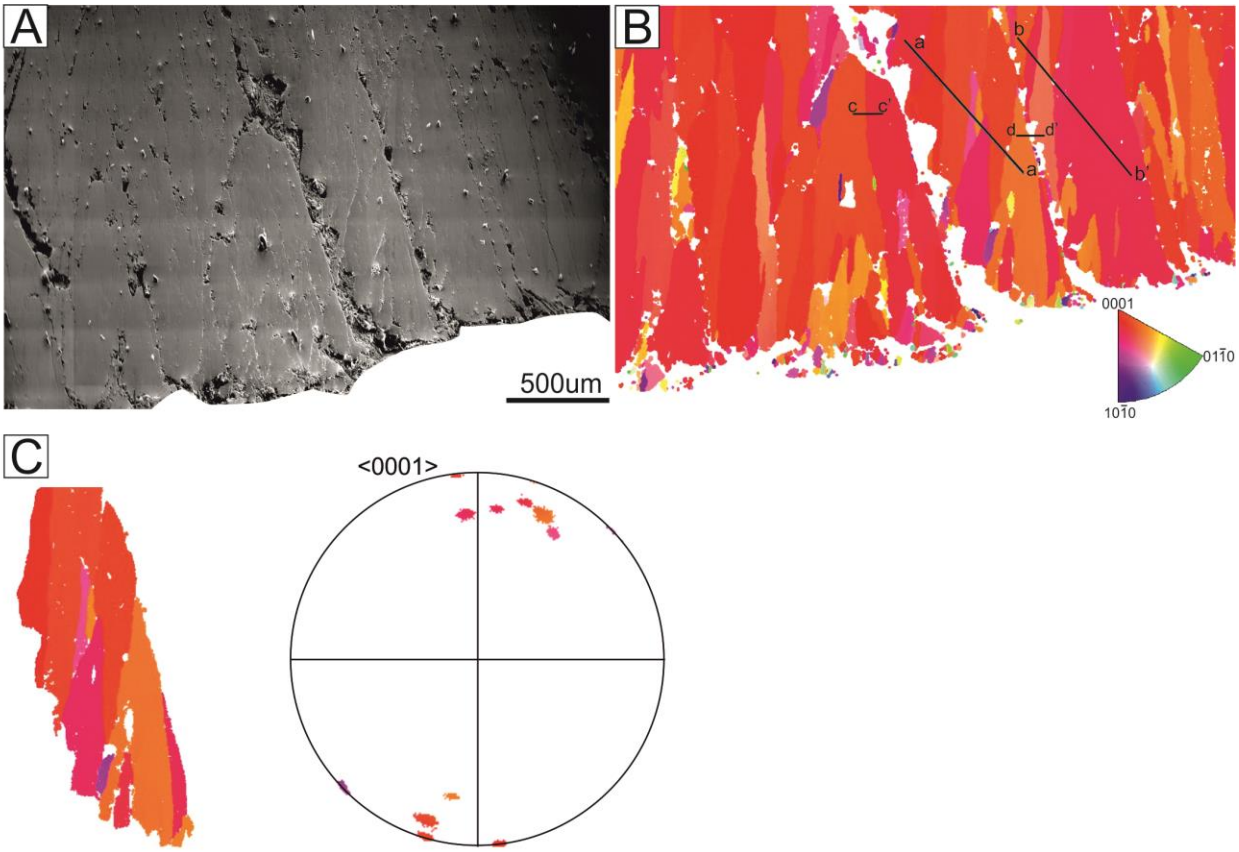


Figure 5.33 BSE image showing the microtexture of a cone-in-cone structure exhibiting a plumose geometry. (B) Y-direction IPF colouring orientation maps showing the crystallographic orientations of the calcite crystals. (C) Stereonet projection of c-axis orientations of the selected crystals.

To examine the variations of neighbouring crystals in cone-in-cone structures, the degrees of orientation change (or misorientation) along cross-lines were measured (Figure 5.34). The misorientation within single crystals is commonly below 2° and can be negligible, whilst the value rises up to be 35°-50° at crystal boundaries. The adjacent fibres within different cones also exhibit similar misorientation values to those within the same cones.

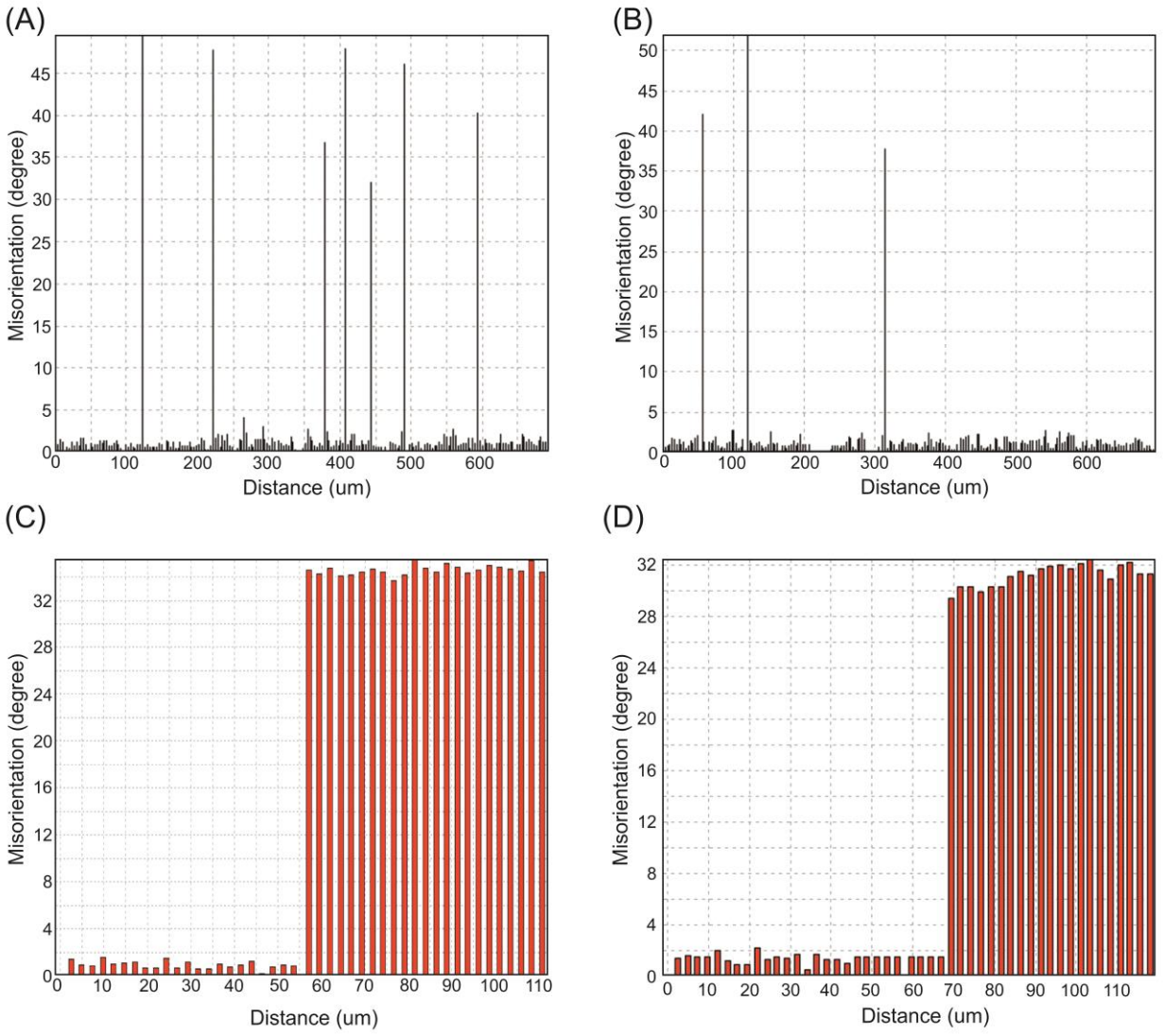


Figure 5.34 Misorientation along cross-lines in cone-in-cone structures in figure 5.33. Data in figures 5.34A -B is presented relative to the previous value. Data in figures 5.34C-D is presented relative to the previous crystal.

5.7 Non-clay mineral composition of the black shales

The petrographic characterization of the non-clay mineral compositions is mainly focused on AOM, pyrite, detrital and authigenic carbonates within the clay matrix, which allows a comparison with the composition of the solid inclusions within the calcite veins, and provides insights into shale diagenesis.

AOM is prevalent in the host shales in the studied sites. The distribution of AOM is commonly associated with calcium sulphate (Figure 5.35) which survived during bacterial sulphate reduction (Curtis, 1980). AOM is also enriched in the zones with abundant bioclasts.

Pyrite is widely disseminated within the clay matrix in the form of single framboids or aggregates as spheres (Figure 5.36). Pyrite spheres are often concentrated within the skeletal fragments, exhibiting a localized distribution. The occurrence of pyrite indicates the diagenetic modifications of the sediments by sulphate reduction (Berner et al., 1985).

Detrital carbonates are mainly skeletal fragments of aragonitic fossils and non-skeletal grains of peloids (Figure 5.37). The peloids are spherical, and silt sized with a diameter of 10-20 μm. They occur in clusters and are very well sorted. The peloids are generally white to grey in BSE images, containing a thin, darker outer rim of carbonate components. The cores of the peloids are structureless and symmetrical. The peloids are closely packed and concentrated within multiple horizons that appear as thin carbonate bands at outcrop (see section 4.4.1).

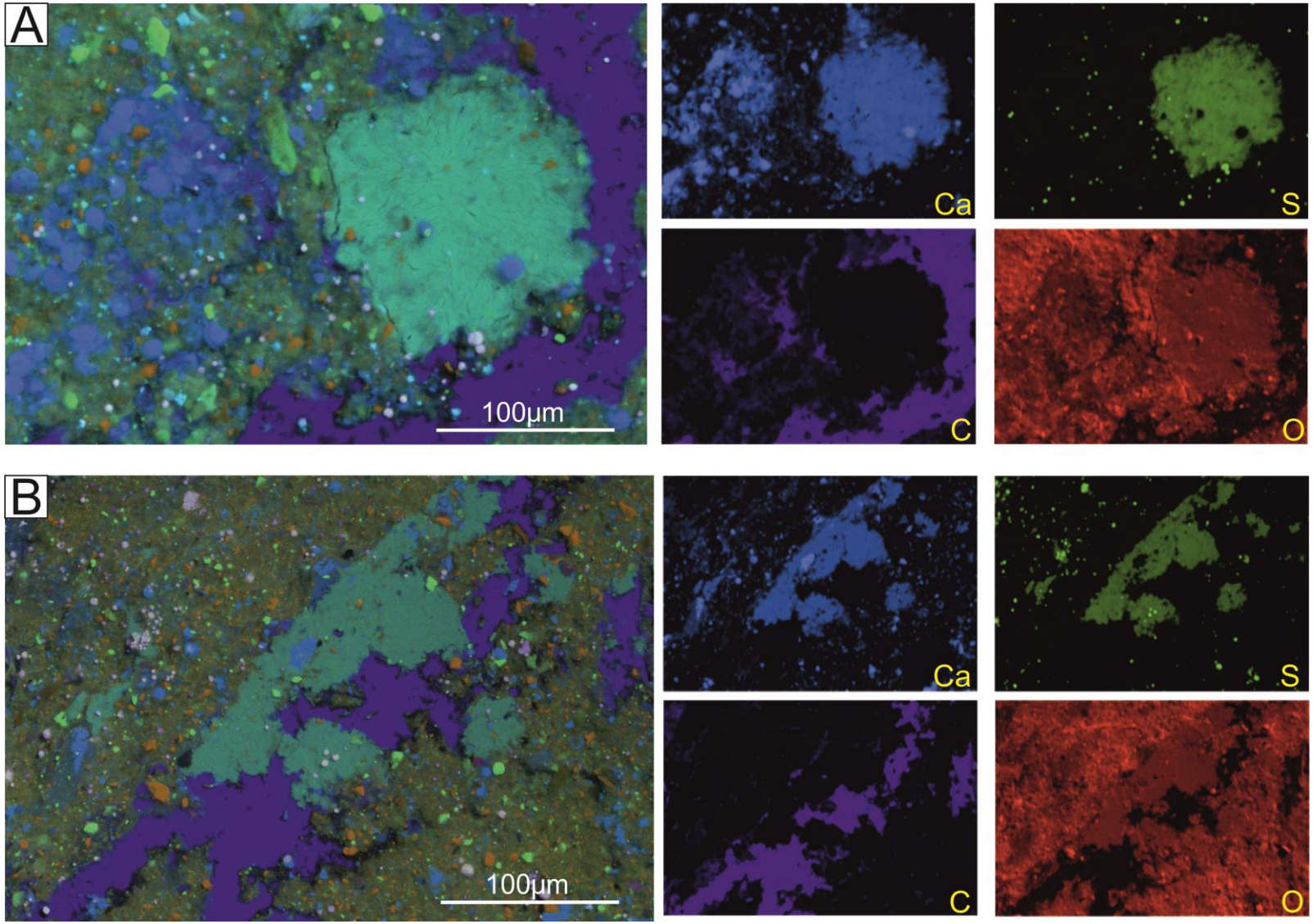


Figure 5.35 EDS images showing the mineral composition of shales and the in horizon 11 (A) and 23 (B) in site 1. Figures on the right show the elements of Ca, S, C and O.

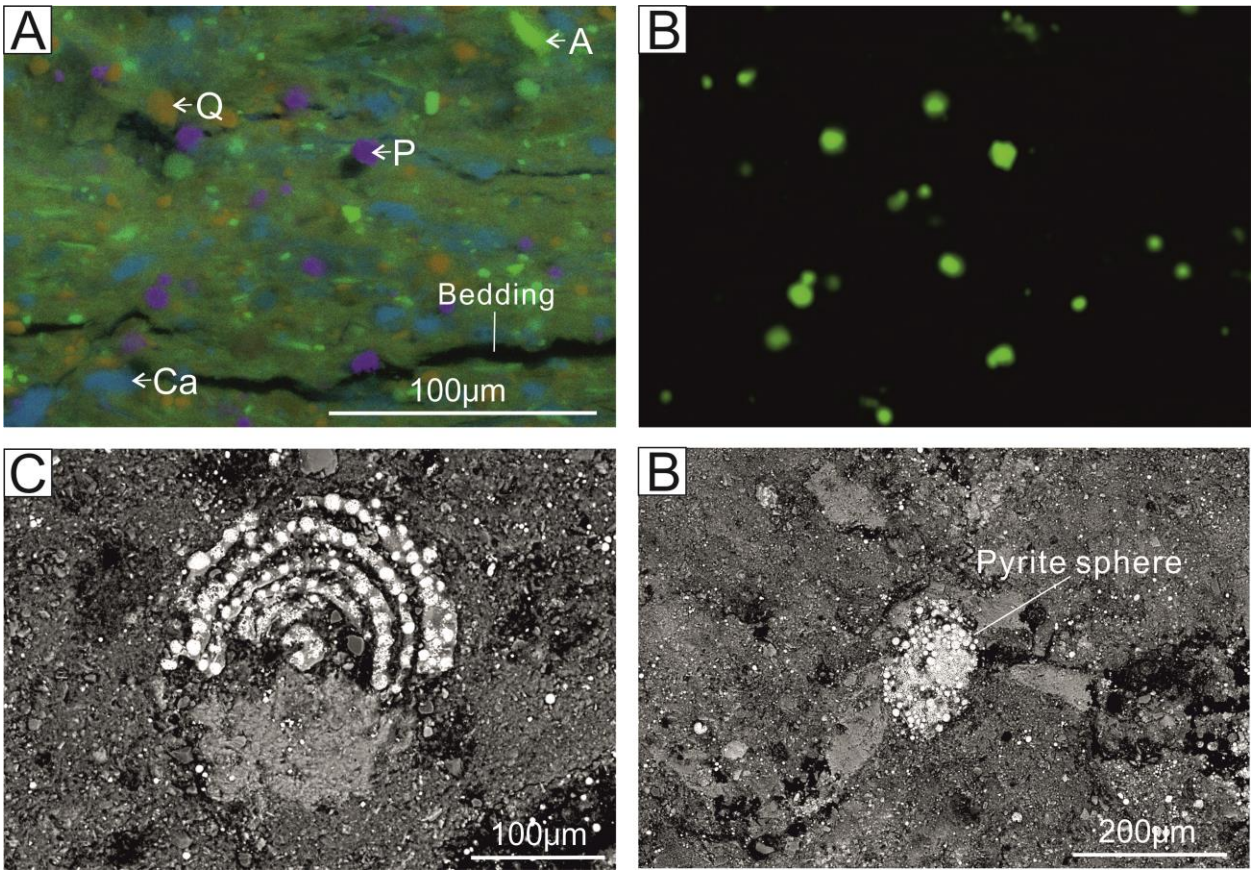


Figure 5.36 EDS image showing the mineral composition of the black shales in horizon 21 in site 1. A=albite. Q=quartz. P=pyrite. Ca=carbonate. (B) Distribution of pyrite framboids within the clay matrix in the area of figure 5.36A. (C) Pyrite spheres concentrated within skeletal fragments. (D) Spherical aggregates of pyrite in the rock matrix.

Peloids are suggested to have a fecal origin, produced by a variety of organisms while feeding on organic-rich sediments (Flugel, 2004). The environment is believed to be low-energy, in a quiet, marine water with muddy bottoms. It is also suggested that the rounded peloids could have formed as micritized bioclastic grains by alteration of skeletal fragments by microboring microbes and recrystallization (Samankassou et al., 2005).

EDS data demonstrates that the peloids are mainly composed of carbonate (Figure 5.38). Importantly, AOM patches in the sizes ranging from several to 200 um are developed in the clays adjacent to the peloids. Microcrystals of pyrite framboids are widely disseminated throughout the same horizons.

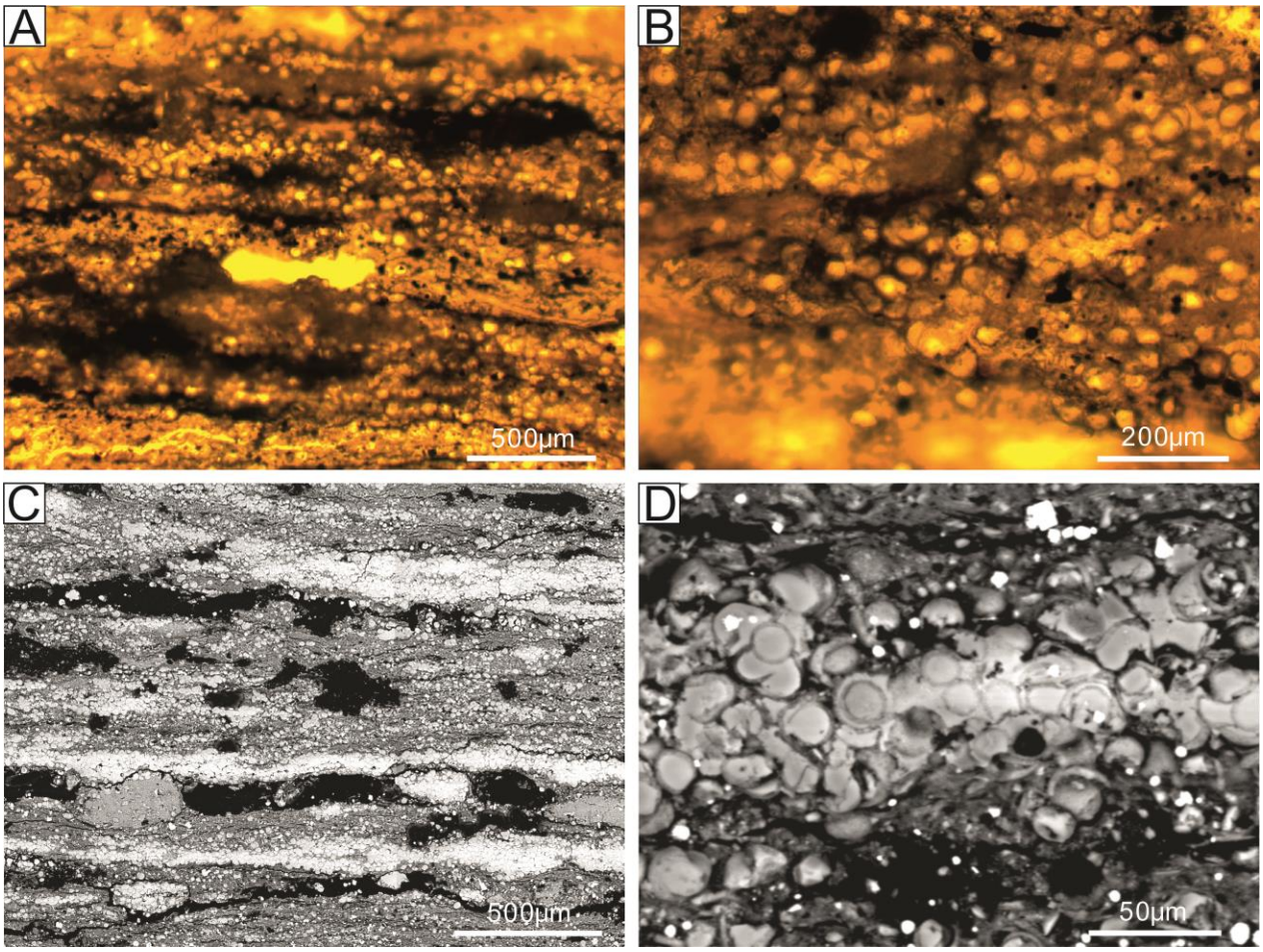


Figure 5.37 The occurrence of peloids in black shales. (A) and (B) showing the peloids with a darker envelop of carbonate component. Reflected light. (C) BSE image showing the concentration of peloids within three horizons. (D) BSE image showing the carbonate rim of peloids and structureless cores.

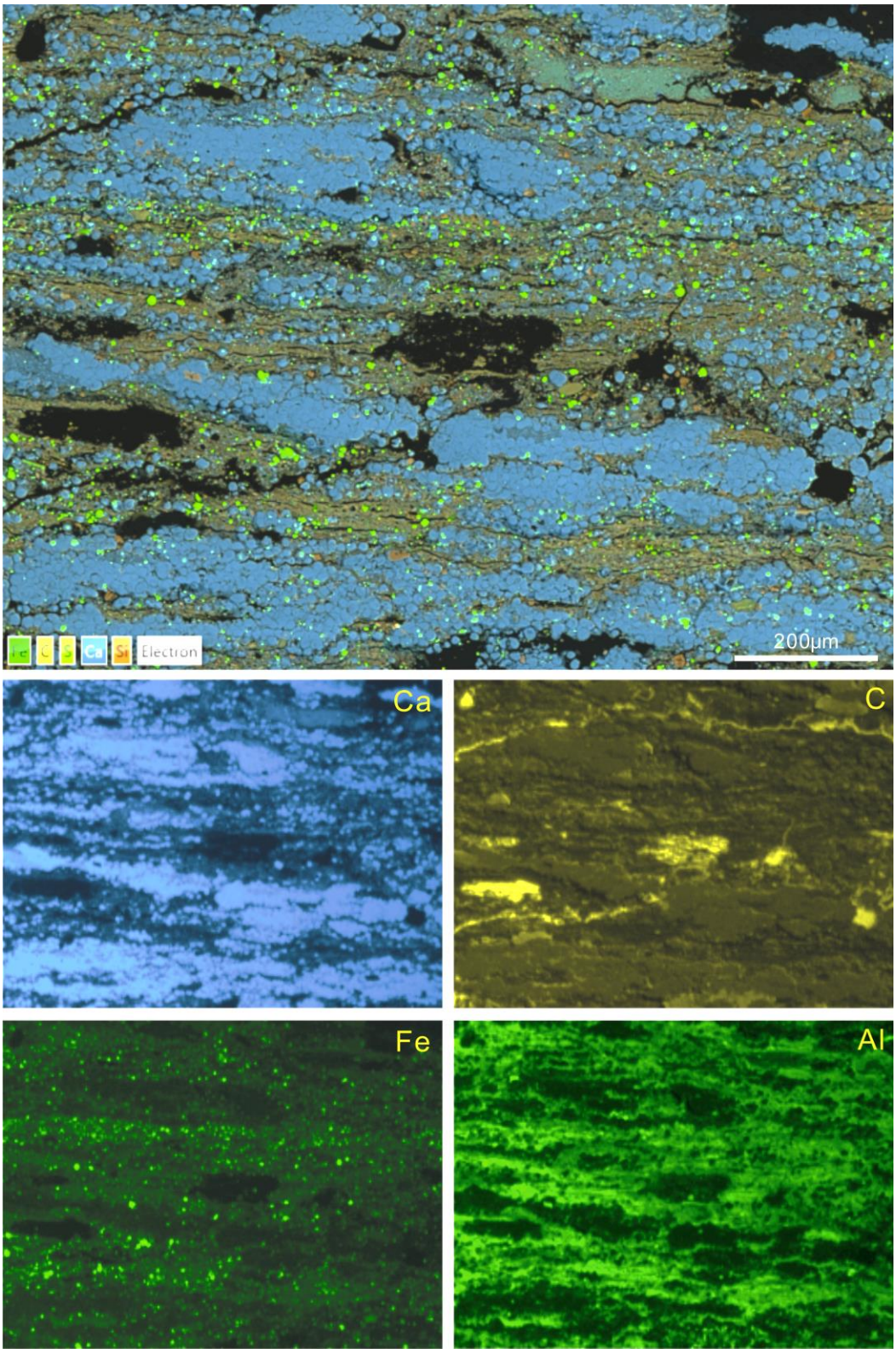


Figure 5.38 EDS image showing the mineral composition of the peloids and the host shales. The lower images show the elements of Ca, C, Fe and Al.

Authigenic carbonate occurs as pore-filling cements in the clay matrix, with a size of several to 200 μm (Figure 5.39). Their distribution is often closely associated with AOM. Elongate-fibrous calcite is observed to develop along pyrited skeletal fragments on one side. The crystal length reaches up to 500 μm.

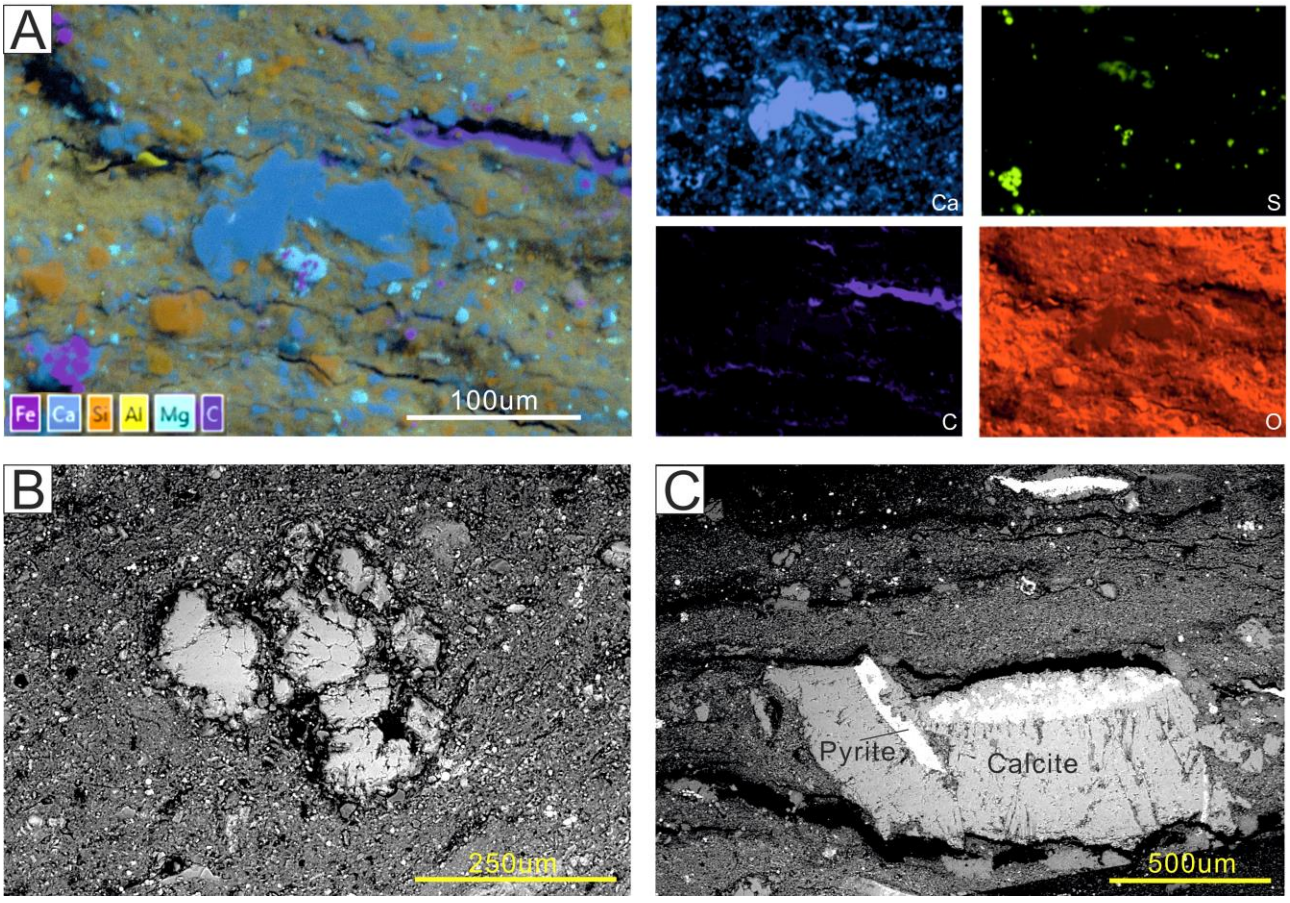


Figure 5.39 EDS image showing the occurrence of authigenic carbonates and AOM. The figures on the right show the elements of Ca, S, C and O. (B) BSE image showing a cluster of authigenic carbonate grains. (C) BSE image showing elongate-fibrous calcite along pyrited skeletal fragments.

5.8 Discussion

The discussion focuses on the diagenetic growth of fibrous calcite, the role of AOM, implication of c-axis orientations, evidence for the force of crystallization and, finally a synthesis of the formation mechanism of beef veins and cone-in-cone structures based on combined new petrographic observations and evidence presented in Chapter 4.

5.8.1 Diagenetic growth

The plastic deformation in the host shales (Figure 4.21) and laminated solid inclusions (Figure 5.23), as well as the displacement of clay particles to surfaces of individual cones, indicates that the growth of the fibrous veins commenced during early diagenesis, before the sediments were fully consolidated. The carbon isotope signatures of the calcite veins presented in section 4.5.3 provide a clue of timing of vein formation, which are interpreted to be after the cession of bacterial sulphate reduction.

The sediments were semi-lithified with a high water content so that the authigenic growth of fibrous crystals could be capable of inducing growth-related soft deformation in the shales around the crystals. Given the localization of mechanical twinning in the fibres around rigid skeletons, it is reasonable to argue that the enclosing sediments were mechanically weak with poor bonding between particles. However, the fold-related shear fractures in the host shales and clay inclusions may possibly indicate a transition from plastic to a later brittle deformation during incremental expansion of the veins.

More evidence for the timing hinge on the delicate fossil structures that have been so well preserved on vein surfaces and within the median zones (Hudson, 1978; Marshall and Pirrie, 2013).

The high degree of fossil preservation indicates 1) a rapid rate of deposition so as to avoid surface weathering; 2) cementation in fossil chambers predates actual compaction of the host sediments, which inhibits the mechanical crushing (Selles-Martinez, 1996).

The evidence above all lends support to the idea that the growth of calcite beef veins and cone-in-cone occurred during early diagenesis of the host sediments.

5.8.2 Role of organic matter

As argued in section 4.5.3, the release of CH_4 and CO_2 as products of organic matter decomposition during methanogenesis have initially caused hydraulic fracturing and the subsequent genesis of the calcite veins. This is further supported by the occurrence of scattered patches of amorphous organic matter in the median zones that may have given rise to overpressure in the horizons of the median zones.

Importantly, the very common occurrence of pyrite in the median zones, either filling skeletal fragments, or appearing as framboids/spheres, indicates the impact of early bacterial action on organic matter and activities of H_2S. On one hand, in addition to the release of CO_2, bacterial sulphate reduction may have caused destruction of SO_4^{2-} with concomitant increase in pH, which is essential for the precipitation of calcite by establishing a favorable chemical environment (Woodland, 1964) and modifications of calcite equilibria through the common ion effect (Franks, 1969).

Organic matter potentially plays a more important role in cone-in-cone structures than beef veins due to their alternative occurrence along the margins of plumose cones. The framboidal pyrite and organic matter located at cone tips (Figure 5.18D) represents an early nucleation of authigenic

carbonate by bacterial sulphate reduction. The organic matter may have possibly contributed to the supply of bicarbonate by bacterial decay and also to the chemical equilibrium of the microenvironments. However, it is notable that cone-in-cone structures are not universally associated with organic matter, e.g. those illustrated in figure 5.14. Moreover, the beef veins of Type B contains few solid inclusions as well as organic matter. Hence, the spatial distribution of cone-in-cone structures and beef veins is not necessarily determined by organic matter.

The carbon isotope compositions of the calcite veins are not compatible with those revealed in authigenic carbonates by microbial activities during burial (Feng et al., 2010; Stakes et al., 1999). It is suggested that the detrital carbonates, including skeletal fragments and peloids, are more likely to serve as the main source for fibrous calcite veins (see section 4.5.1), through aragonite neomorphism and dissolution (Maliva and Dickson, 1992). This is revealed by the carbon isotope signatures of the veins in this study and also the equivalently high Sr^{2+} concentration in both the fibrous veins and the skeletal fragments in the Chief Beef Member (the Wessex Basin) (El-Shahat and West, 1983).

The authigenic carbonates as pore-filling cements could have derived from decay of the organic matter in the clay matrix, which is demonstrated in figure 5.39. This is especially evident from horizon 27 (site 1) that contains the highest carbonate concentration, including abundant authigneic carbonate as pore cements and carbonate concretions, and the lowest ^{13}C.

Hence, the microbial decay of organic matter is argued here to be crucial for overpressure development in the undercompacted sediments. Organic matter may have provided an important source of bicarbonate for the cementation of pore spaces, but was much less important for the calcite veins.

5.8.3 Implications of C-axis orientations

As is discussed in section 3.8.2, the fibrous habit of calcite in beef veins and cone-in-cone structures must have resulted from limited growth space and a higher potential growth rate of fibres than the widening rate of the veins, which inhibited growth competition between neighbouring crystals.

The long axes of fibres are uniformly orthogonal to vein-walls, exhibiting radial growth in the outer rims of cone-in-cone structures and curved beef veins (Type B), parallel in straight veins (vertical in horizontal veins, inclined in oblique veins) (Figure 5.40). Orientations of calcite fibres is suggested to be the function of the local environment and a response to the directions of easiest crystal growth (Franks, 1969). A further explanation is then needed regarding the preferred fibre orientations and also their c-axes.

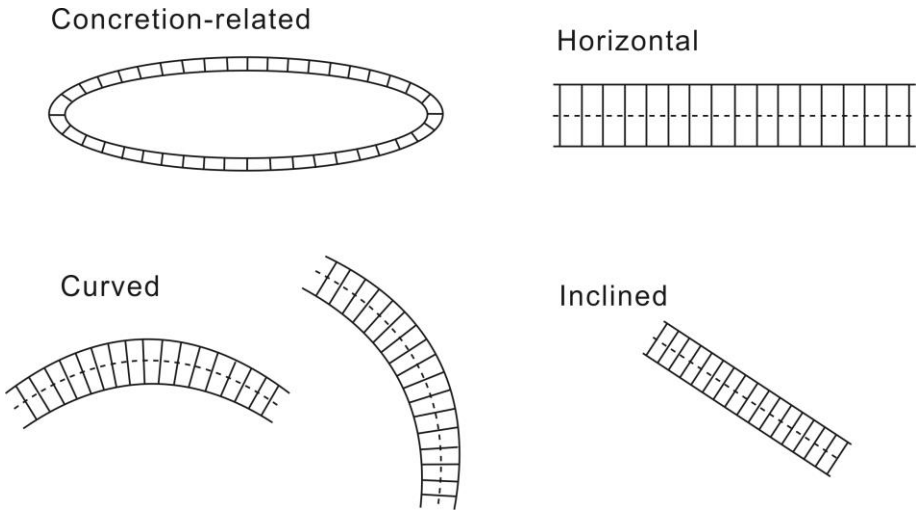


Figure 5.40 Fibre orientations in cone-in-cone structures enveloping carbonate concretions, horizontal, curved and inclined veins.

Under a hydrostatic stress in the blocky zones of fossil chambers as site for fluid storage, the calcite crystals exhibit distinctly equant morphologies and much smaller sizes than the fibres. Unlike fibres, the c-axis orientations do not have preferred orientations, indicating a non-hydrostatic stress under which the fibres grow.

Mechanically, the crystal lattice tends to have a preferred crystal orientation along the elastically weakest axis under non-hydrostatic stresses, which minimizes the chemical potential required for equilibrium for crystallization (Kamb, 1959). For calcite, c-axis is the weakest axis, along which the crystallization of calcite across the plane in a direction normal to the maximum principle stress σ_1 is favoured preferentially (Kamb, 1959; Larson and Tullborg, 1984; Milholland et al., 1980). Hence, across a given interface between crystals and fluid, calcite grows the fastest with its c-axis aligned with σ_1. Additionally, calcite is the most stable in-situ with the c-axis parallel σ_1 due to the preferential dissolution of calcite with c-axes not oriented to σ_1 under non-hydrostatic stresses (Adelseck et al., 1973; Carlson et al., 1983; O'Brien et al., 1993).

Combined with the theoretical considerations, it is suggested that the very local σ_1 that is orthogonal to vein walls promotes the growth of calcite with distinct fibre orientations. This σ_1 is presumably gravitationally established stresses that may have been modified by the growth of fibres. The growing of fibre aggregates could have set up a stress field by the force of crystallization (see section 3.8.6 and 5.8.4), which affected the local stresses more significantly than other factors, especially in the watery mud during early burial.

This explanation is inconsistent with the idea by Maher Jr et al. (2016), arguing that a sub-vertical minimum principle stress σ_3 should be responsible for the growth of vertical fibres in beef veins

and cone-in-cone structures. However, their suggestion remains unsatisfactory for the following reasons:

(1) The formation of beef veins and cone-in-cones have commenced during early burial in an extensional environment, inferring a horizontal σ_3. Only in such a stress regime can the concurrent normal faults be produced (Chadwick, 1986; Stoneley, 1982).
(2) It is difficult to explain the origin of wall-normal, non-vertical fibres in non-horizontal veins, especially the radial fibres in the rims of carbonate concretions.
(3) The internal agent of forces, i.e. the force of crystallization, that exerted on the host rocks and may have led to growth-related compaction, have been ignored.
(4) The fibre-orthogonal laminations in displaced clay lenses along the margins of plumose aggregates of fibres indicate a compressional stress parallel to the long axes of fibres.

It is notable that the c-axis orientations of fibres do not necessarily coincide with the directions of their long axes (Figure 5.26). Besides, crystal overgrowth occurs commonly, especially for cone-in-cone structures. It is suggested that growth of certain fibres could be favoured over others so that they could grow larger with their free surfaces expanding more readily normal to c-axes. This explains why the crystals in cone-in-cone structures exhibit a wider range of c-axis orientations than beef veins and smaller crystal sizes accordingly.

5.8.4 Displacive growth

The calcite beef veins and cone-in-cone structures exhibit a displacive growth of fibres, which is different from the characteristic calcite cement fabrics passively filled in voids. Field and petrographic evidence for vein displacive growth include the following:

(1) Distinct morphology and c-axis fabrics of calcite fibres suggest a different growth mode of fibres from the crystals cementing the pore spaces in the clay matrix, blocky and median zones.

(2) The presence of split and displaced fossils with impressions preserved on both surfaces of single veins (Figure 4.15).

(3) The localized compaction and folding in the enclosing clay flakes related to fibre growth.

(4) The square ends of some veins (Figure 4.17C) perhaps represent the shear surfaces separating the displaced and non-displaced areas.

(5) The distribution of clay films that are composed of original sediments along the margins of individual plumose aggregates of calcite suggests that the clay fills have been incorporated into the cone-in-cone structures, in keeping with the volumetric expansion.

Calcite crystals can grow displacively and exhibit distinct neomorphic fabrics (Watts, 1978). The displacive growth of calcite have been recognized by splitting fossils (Brown, 1954; Marshall, 1982; Woodland, 1964), disruption and brecciation of detrital fragments (El-Shahat and West, 1983; Maliva and Siever, 1988; Watts, 1978), displacement and incorporation of the host sediment particles (Woodland, 1964), the texture of the compacted domains of clay matrix separated by calcite crystals (Astin and Scotchman, 1988), and even uplift the overburden (Gratier et al., 2012; Wiltschko and Morse, 2001). Although displacive calcite has been frequently described, the implications have been largely ignored (Watts, 1978).

It is suggested that fibrous growth of calcite in black shales is only possible if the bedding planes were held apart against the confining pressure by fluid pressure (Parnell et al., 2000; Stoneley, 1983). Under such conditions, the clay films could have been injected into the spaces between adjacent cones by fluids (Selles-Martinez, 1994). However, the authors have underemphasised the

displacive growth of calcite fibres that can push aside the host rocks, especially when they were still soft and semi-lithificated. Besides, it is difficult to explain the retained clay laminations as well as their orientations parallel to the faces of fibre ends, during injection of fluid flow.

Given the self-similar geometries, the aspect ratio of the resulting mineral veins from hydrofracturing is suggested to reflect the static overpressure of the fluid, Δp, is given by (Gudmundsson, 1999; Philipp, 2012):

$$\Delta p = \frac{AE}{2L(1-v^2)}$$

Where *E* is the Young's modulus of the rock within which the vein occurs; *v* is the Poisson's ratio; *A* and *L* are the aperture and length of the vein respectively. Using a typical value of 10 for L/A, the current values of 2.55 MPa for *E*, and 0.25 for *v* (Hobbs et al., 2012), the Δp is 0.136 Mpa, which is possibly too low to yield tensile fractures in the sediments. Moreover, it is difficult to explain the origin of the shells that are bisected by fibres, considering their high mechanical strength.

As is discussed in section 3.8.6, crystals can grow against or exert a pressure on the surroundings, namely crystallization pressure. The value of crystallization pressure is positively related to the degree of supersaturaion of the pore fluid (Correns, 1949; Dewers and Ortoleva, 1990). In sea water, the crystallization pressure of calcite may reach up to $\sim$50 MPa at the degree of supersaturation of 2 (Wiltschko and Morse, 2001).

The lines of evidence for displacive growth of beef veins and cone-in-cone structures also indicate that the force of crystallization of calcite fibres could have been responsible for the development of the calcite veins. It is possible as the growth of the veins is syncompactional when the sediments

were still soft under relative shallow burial. Moreover, overpressuring in the sediments (see section 4.5.3 and 5.8.2) could enhance the degree of supersaturation with respect to calcite in pore fluids as well as the plasticity of the hosts (Kiriakoulakis et al., 2000; Wiltschko and Morse, 2001), allowing veins to grow displacively with a larger crystallization pressure.

However, the displacive growth of calcite fibres is not necessarily accompanied with a volumetric expansion of the bulk rock by uplifting the overburden. Firstly, the crystallization of calcite predates the compaction of the host clays, which is evident from the undeformed fossils on beef surfaces and plastic deformations in the sediments induced by fibre growth. The expansion of the veins could have been accommodated by a growth-compaction in the country rock. Such a localized strain is especially evident from vein tip regions (Figure 4.21). Furthermore, the sediments may suffer a volume loss during the mechanical compaction that is synchronous with diagenetic growth of the veins (Selles-Martinez, 1994).

5.8.5 Formation mechanism

Calcite beef veins and cone-in-cone structures are commonly associated in shales (Cobbold et al., 2013; Marshall, 1982), however, their composition and texture exhibit significant differences. A clear genetic relationship based on the relative timing of formation exists between beef veins and cone-in-cone structures, but this have been largely ignored in previous studies.

Four lines of evidence suggest that beef veins postdate cone-in-cone structures. Firstly, the cone-in-cone structures generally contain a lower $\delta^{13}C$ and a higher $\delta^{18}O$, which suggest a relative shallower burial depth and a lower ambient temperature (see section 4.5.2). Secondly, the

appearance of cone-in-cone structures as well as equant crystals in the median zones of beef veins indicates that the cone-in-cone structures predate the nucleation of fibres on both sides. Moreover, the arrangement of calcite fibres near the median zones resembles that in typical cone-in-cone structures, which reveals a trend to becoming more parallel aligned towards vein walls (Figure 5.6). Such a succession in crystal morphology demonstrates that beef veins possibly evolve from cone-in-cone structures during burial and diagenesis. Lastly, the higher content of solid inclusions in cone-in-cone structures, compared to beef veins, suggests a more viscous state of the sediments when they were incorporated into the cone-in-cone structures. The host sediments are presumably more brittle due to compaction during the genesis of beef veins, making it more difficult to keep up with the development of crystals, which gives rise to the purer composition of beef veins.

The formation of cone-in-cone structures is considered as a geological puzzle (Clifton, 1957; Selles-Martinez, 1996) due to the distinct conical arrangement of crystals. Some authors attribute the conical shape to shear fracturing that occurred either in the sediments for later crystal nucleation and fracture cementation (Conybeare and Shaw, 2000; Selles-Martinez, 1994) or in the pre-existing fibrous crystals (Kowal-Linka, 2010). However, uncertainties remain in the ideas, regarding the following aspects:

(1) Since the cone-in-cone structures and beef veins are believed to have occurred when the sediments were still plastic, it is difficult to explain why shear fracturing rather than plastic deformation occurs when loading pressures.
(2) The wide range of conical apical angles (8°-126°) (Figure 5.13) and the decrease in apical angles from the median zone towards vein walls (Figure 5.6) make the explanation unreasonable.

(3) The uniformly pointed orientation of individual cones on the same side of the median zone remains unexplained.

(4) Shear fractures are neither observed in the surrounding sediments of the individual conical aggregates that are loosely spaced in the clay matrix, nor in the cones (Figure 5.14), especially the fibres on the opposite side of cone-in-cone structures that are illustrated in figure 5.13.

(5) It is difficult to understand why the shear fracturing is localized, especially for the scattered individual cones.

It is suggested that the conical bundles of crystals form as a growth feature, which is in agreement with Woodland (1964) and Franks (1969). The individual cones presumably nucleated at numerous points randomly in overpressured horizons of watery mud. It is a nature of calcite to assemble as tuftlike aggregates (Hodgson, 1966; Selles-Martinez, 1994), which is observed in the median zones of beef veins in this study (Figure 5.1A). At a later stage, the growth of crystals is crystallographically controlled, resulting in the preferential growth of certain crystals with c-axes parallel to σ_1 and the termination of others. Such a growth competition leads to the small crystal sizes in cones.

Vein growth-related compaction of the enclosing sediments is evident from the rock deformational textures associated with displacive growth of fibres (see section 5.8.4). Such a compaction not only induces the transition of the physical state of the sediments from ductile to brittle and a lower amount of clays incorporated into the veins, but also a preferential lattice orientation of the crystals as a feedback mechanism. The decrease in apical angles from the median zones towards vein walls with correspondingly reduced solid inclusions (Figure 5.6) indicates that the physical properties of the host sediments are influenced by vein displacive growth and determine the apical angles of

cones. Cones with larger apical angles are established when the host clays remain a low degree of compaction.

Combined with the field, geochemical, petrographic and crystallographic data, a model is envisaged as follows for the development of cone-in-cone structures and beef veins in organic-rich shales. The generation of cone-in-cone structures commences at a relative shallow burial depth within the methanogenic zone when the horizons become overpressured by the generation of biogenic gas. The cones are nucleated at numerous points as overpressured cells which later develop into conical aggregates of crystals. During the growth of individual cones, the clay flakes are forced to be displaced by crystallizing calcite. Coarsening of grains with favorable lattice orientations towards cone margins gives rise to a plumose geometry. Beef veins are produced when the sediments possess a higher degree of compaction, sharing a similar formation mechanism to cone-in-cone structures. The crystals are more fibrous due to the alignment with free surfaces expanding normal to c-axes, permitting the easiest way for fibre growth. The force of crystallization of calcite is not only responsible for the displacive growth of veins and deformation/displacement of the host rock, but also the affecting the development of the structures themselves.

5.9 Conclusions

(1) The calcite beef veins and cone-in-cone structures in the black shales are of an early diagenetic origin.

(2) The decay of organic matter by methanogens gives rises to early overpressuring in the sediments. However, the carbonate materials for veins from organic matter is minor.

(3) The c-axis orientations of calcite are preferentially normal to vein walls in a stress field set up by crystallization pressure, favoring the growth of crystals with their free surfaces expanding normal to c-axes.

(4) The veins exhibit a displacive growth by the force of crystallization, which does not necessarily involve the consequence of bulk expansion.

(5) The cone-in-cone structures predate beef veins; however, they share similar formation mechanisms. The physical properties of the host rocks is responsible for the differences in the textural characteristics. The conical aggregates are growth features rather than shear fractures.

Chapter 6 Summary and discussion

6.1 Satin spar veins and calcite beef veins: a comparison

In this study, two types of fibrous mineral veins developed in mudrocks have been studied, including satin spar veins and calcite beef veins. Although these veins are composed of different materials, they exhibit rather similar vein geometry, internal texture and crystal arrangement, which indicates that they could share similar processes of kinetics of crystal growth and vein accretion.

The satin spar veins and calcite beef veins both grow antitaxially from the vein nucleation sites, namely the median zone towards wall-rocks. Their crystal morphologies are controlled by the fact that potential crystal growth rate exceeds vein opening rate, leaving rather limited spaces between crystal faces and enclosing rocks. They both derive nutrients from their host rocks by diffusion through the extremely low-permeability matrix, which enables crystals to grow incrementally. Neither of the two types of veins show typical crack-seal textures in the fibrous zones.

However, significant differences also occur between the two types of veins, in terms of vein orientation, size, concentration of solid inclusions, crystal morphology and vein interactions. These differences are results of different timing, paleostress, and physical states of the host rocks that are associated with the specific stage of basin evolution.

Although sub-horizontal veins predominate, the satin spar veins also exhibit multiple orientations. In contrast, the calcite beef veins mainly lie in the horizontal direction along bedding. The late timing of gypsum vein generation were accompanied with reactivation of pre-existing faults and

fractures that evolved into passive veins. The interaction of newly generated veins and reactivated fractures results in a dense and complex vein network.

In contrast, the calcite beef veins are early formed structures during burial of the host sediments. The fine-grained sediments are structureless with no suffering of tectonic compression and deformation. The beef veins are solely horizontal along the weakest planes of bedding. Different veins lie in different horizons, corresponding to different timing. This is because the vein generation are argued to be mainly restricted to the methangenesis zone where the enclosing hosts started to release CO_2 and CH_4. The development of beef veins occurred simultaneously with further consolidation of clay minerals by pushing the hosts aside.

The paleo-stress states also exhibit differences between the satin spar veins and the calcite beef veins, which are responsible for varied fibre orientations. Unlike calcite fibres that are strictly perpendicular to their median zones, the gypsum fibres are oblique to the median zones. In the environment of intense tectonic compression, the gypsum fibres act as shear-sense indicator for interlayer slip. The angles between vein walls and fibres reflect the relative displacement of two walls. However, the development of fibrous calcite occurred in an extensional stress field, receiving little interference from tectonism. Fibre growth is mainly controlled by geochemical self-organization, which caused local plastic deformation in the highly rheological hosts.

In summary, the satin spar veins in the Mercia Mudstone and calcite beef veins in the Charmouth Mudstone exhibit similarities in geometry, internal texture, kinetics of growth and mode of nutrient transport. Their differences in vein and crystal orientation, vein interaction, purity of composition and deformation in the hosts are the results of different stages of basin evolution, paleostress state, and mechanical properties of the host rocks.

6.2 Mechanisms of mineral vein generation during basin extension and compression

As former conduits of fluids, fibrous veins record fluid activities in the bulk rock during the time of vein generation at a specific stage of basin evolution (Kolb et al., 2004; Sibson and Scott, 1998; Vrolijk, 1987). In inverted rift basins, a pervasive increase in pore pressure and high-magnitude overpressure can be feasibly generated by tectonic compression, especially in fine-grained mudrocks (Cartwright, 1994; Japsen, 1998; Sibson, 1995, 2009; Turner and Williams, 2004). Tensional hydraulic fractures are produced under high fluid pressure and low differential stress and allow overpressure reduction (Giles, 1987). Hence, the mineral veins that take advantages of those fractures commonly form with a syntectonic origin.

In tectonic-relaxed or rift basins, the origin of overpressure that can give rise to mineral veins as hydraulic fractures is non-tectonic, which mainly include disequilibrium compaction, smectite-to-illite transformation, hydrocarbon maturation, fluid flow and buoyancy (Cosgrove, 2001; Osborne and Swarbrick, 1997). This can be poorly understood due to the geological complexities of the basins.

Calcite veins in organic-rich shales may derive a high component of bicarbonate from organic matter as either biogenic or thermogenic products at different burial depth and ambient temperature. In matured source rocks, the calcite veins can be produced as hydraulic fractures during primary migration of oil and gas, which are evident from hydrocarbon inclusions in the median zones (Cobbold and Rodrigues, 2007; Parnell et al., 2000; Rodrigues et al., 2009; Stoneley, 1983; Zhang et al., 2016).

However, if the source rocks are immature, i.e. at shallow burial depths, severe overpressuring may also occur as a response to (1) rapid deposition of sediments on top of the shales

(Gaarenstroom et al., 1993; Leynaud et al., 2007; Potter et al., 2005); (2) biogeneic methane generation (Flemings et al., 2003; Hedberg, 1974; Osborne and Swarbrick, 1997). The Eype Clay and Down Cloff Sand members on top of the Shales-with-Beef Member were deposited as one of the major ammonite subzones (Stokesi Subzone), which contain abundant, intact ammonite fossils (Hallam, 1975; Simms, 2004). The preservation of ammonites suggests a quick sedimentation rate at which the fossil assemblages remained a short time at the sediment-water interface before final burial and received little erosion and crushing (Potter et al., 2005). The rapid influx of sediments led to overpressuring in the Shales-with-Beef Member while their rich organic content survived oxidation in the sulphate-reduction zone to produce CO_2 for beef veins during methangenesis. The absence or poor development of calcite beef veins in the Lias elsewhere in the UK may suggest the unusually high sedimentation rate during the Stokesi Subzone (Simms, 2004). The poor development of beef veins in the Blue Lias could reflect generally lower organic-carbon contents than the Shales-with-Beef Member (Hallam, 1964; Morris, 1980; Simms, 2004), which does not provide enough gases essential for overpressure.

It is notable that the shales could be undercompacted at the relative shallow depth of methanogenic zone. The beef veins can be characterized as early hydraulic seals which may result in isolation of a cell of the basin, where normal compaction is inhibited and accumulation of abnormally high pressure is developed (Selles-Martinez, 1994; Selles-Martinez, 1996). The large volume expansion in the closed systems accompanied with gas release can also contribute to extreme overpressures (Osborne and Swarbrick, 1997).

In summary, overpressure related mineral veins can occur at various stages during basin burial and uplift. Multiple factors may cause overpressure in mudstones, which should be evaluated under the geological contexts of the basins.

6.3 Controls on mineral vein distribution in a chemically closed system

The mineral veins exhibit a heterogeneous distribution in the rather homogeneous successions of mudstones in this study. A closed system is inferred for the development of fibrous veins in which the vein masses are derived from the adjacent host rocks. The distribution of mineral veins is then closely associated with the material sources.

Both the satin spar veins and the calcite beef veins are predominantly horizontal along bedding planes. This is due to the low cohesive strength of bedding fissures which provide preferential sites for vein opening and dilation.

The host rock lithology (mineral composition) is a critical factor in controlling vein distribution and abundance. Mineral veins, especially the isolated ones, derive vein masses locally from the wallrocks by chemical potential within a scale of one meter. Only if the host rocks are composed of the vein material may the veins grow continuously with the oldest material precipitated in the median zone. This is evident from the dense gypsum veins in the beds of gypsiferous marls and also the thicker calcite veins in hosts with high TOC values.

Host rock lithology may also affect vein development in terms of mechanical properties of rocks and hence mechanical stratigraphy. A higher content of silt and sand in mudstones may require a smaller pore fluid pressure to cause hydraulic fracturing as sands can support a larger differential stress than muds. Hence, hydraulic fractures are preferentially developed in more coarse-grained beds.

In summary, the occurrence of mineral veins in a closed system relies on the abundant vein masses in the adjacent hosts and also favorable mechanical properties of the rocks for the generation of either shear or tensile failure.

6.4 Conditions for displacive crystallization by force of crystallization

From many previous studies, it has been demonstrated that displacive growth of crystals rather than replacive or passive growth is indeed possible during various stages of host rock diagenesis and basin evolution.

Given the evidence of vein formation during a relative late stage of basin uplift, it is argued that the gypsum veins caused intense brittle fracturing in the consolidated marls of the Mercia Mudstone and grew displacively, pushing the host rocks aside.

Unlike the gypsum veins, the calcite veins in the Charmouth Mudstone are argued to form when the hosts are still unconsolidated. The plastic deformation of the dark shales may have resulted from fluids that jack up fractures where calcite appears as passive cement precipitation (Selles-Martinez, 1994). However, some factors make this interpretation questionable. Firstly, it would be difficult to explain the fibres being oriented perpendicular to the nucleation surfaces rather than parallel to them. Secondly, the common square ends of calcretes, including sub-horizontal, inclined and curved ones, do not fit the geometry of hydraulic fractures with tapered tips. Their growth is more likely to postdate the closing of the fractures when fluid pressure drops. Moreover, the euhedral crystal faces of the calcite crystals in planar contact with the host clays strongly lend support of displacive growth.

Based on equilibrium thermodynamics, the relationship of magnitude of pressure and degree of supersaturation is (Dewers and Ortoleva, 1990):

$$\Omega = exp\left\{\frac{\Delta V(P-p)}{RT}\right\}$$

Where Ω is the level of supersaturation of pore fluid above that in equilibrium with the solid at hydrostatic pressure p; ΔV is the difference between the molar volume of solid and solute; R is the gas constant; T is temperature, and P is the normal stress applied across grain boundaries.

For Ω>1, P>p, then the crystallization pressure can be responsible for displacive growth of crystals. Thus, it is a prerequisite for P to be greater than hydrostatic when force of crystallization becomes valid.

Besides, for crystals to grow and exert pressure on the surroundings, a thin film of solution is required to be as low as several nanometers, which can have diffusional access to the bulk pore water in equilibrium with the bulk host sediments (Tada et al., 1987; Weyl, 1959). The solid-liquid interfacial energy can be totally neglected if the radii of pores exceeds 1 μm (Serafeimidis and Anagnostou, 2014). Moreover, the crystallization pressure P is highly sensitive to pore sizes, which is expressed as:

$$\mathrm{P} = 2\sigma(\frac{1}{\mathrm{r}} - \frac{1}{\mathrm{R}})$$

Where σ is the mineral-solution interfacial tension; r and R are the radii of small and coarse pores. For crystallization to occur in the smaller pores that are connected to larger pores filled with crystals, the crystallization pressure is required to resist the confining stress on the rigid crystals. In larger pores where crystals can grow freely, the necessary confinement condition for

crystallization will not be reached (Noiriel et al., 2010). Hence, crystal growth, which relies on the force of crystallization to resist confining stress, is favoured in small pores.

Calcite has a preferential growth along the c-axis orientation which is the weakest axis of a crystal. To minimize the chemical potential required for equilibrium across the plane normal to the maximum principle stress axis, c-axis tend to align parallel to σ_1 (Kamb, 1959). Besides, the calcite crystals with c-axes parallel to σ_1 are the most stable in-situ due to the preferential dissolution of calcite crystals with c-axes oblique to σ_1 (Bain, 1940; Carlson and Christensen, 1979; Carlson et al., 1983; O'Brien et al., 1993). Given the c-axes of calcite fibres orthogonal to the median zones of calcite veins regardless of vein orientation and curvature, it is deduced that the remote stress did not play an important role in controlling fibre growth and orientations. Instead, the normal stress loaded on crystal faces are locally parallel to c-axes of calcite fibres due to the enhancement of growth-related compaction in the enclosing clays and a significant reduction in porosity. This process also decreases viscosity of the hosts which are highly porous and not fully consolidated under relative shallow burial conditions, permitting displacive growth (Dewers and Ortoleva, 1990; Selles-Martinez, 1996). The displacive crystallization also enhances host-phase solution and supersaturation in the thin film of solution between hosts and calcite fibres. Thus, crystal displacive growth and crystallization pressure exhibit a positive feedback interaction.

In summary, the fibrous veins grow displacively by the force of crystallization rather than passive cementation of pore and fracture spaces, when (1) the normal stress P applied across grain boundaries is non-hydrostatic; 2) an extremely thin film of solution is present with a sufficient degree of supersaturation; 3) the host rocks are not very viscous.

Chapter 7 Conclusions and suggested future work

This research focuses on field, petrographic and geochemical characteristics of two types of fibrous mineral veins (satin spar veins and fibrous calcite veins) in mudrocks. Satin spar veins and fibrous calcite veins were generated during different stages of basin evolution; however, they both exhibit similar morphological patterns and help reveal fluid activities during their growth.

Satin spar veins in the Triassic Mercia Mudstone (the Bristol Channel Basin) are natural hydraulic fractures preserved through gypsum cementation. The evolution from fracture generation to vein filling by fibres is a dynamic process rather than a single syntectonic phase. Key innovative findings in this project are listed as follows:

· Multiple phases (≥2) of hydraulic fracturing occurred in the Triassic marls during basin inversion in the Miocene, which postdate the buttress folding. Sequential fault reactivation, recorded by fault veins, is evident from slickenslide fibres in the median zones and also on vein surfaces.

· Crack-seal events in the low-permeability marls are revealed in the median zones of fibrous veins by multiple wall-parallel host rock inclusion bands and alabastrine gypsum as the main components.

· The transition of blocky gypsum to fibrous gypsum marks the cessation of hydraulic fracturing. Vein growth is likely to be driven by crystallization pressure rather than overpressure, which in turn positively favors the fibrous morphology of crystals.

· Closed system fracturing and lithological variances in the bulk rock determine the degree of vein development. Mass transport by diffusion from adjacent diffusely disseminated gypsum to vein-

wall interfaces results in localized vein distribution and the incremental accretion of gypsum fibres with homogeneous chemical constitutes.

· Coalescence of differently oriented veins leads to the anastomosing vein network, exhibiting a high connectivity. Vein aperture is best fit to a long-normal distribution as a result of mechanical interference that inhibits a further nucleation of new fractures and localizes growth to the large veins.

· Fibres are demonstrated to track vein opening trajectories, which helps tectonic analysis of the bulk rock and also structural restoration of the host rock.

However, the satin spar veins remain incompletely understood, regarding (1) the source of fluid; (2) the variances in vein colors. Geochemical methods, such as oxygen and strontium isotopes are suggested to be applied to the veins and nodules in all lithological units for a comparative study of isotope composition and also the hydrologic systems. Sedimentary microfacies analysis of the Blue Anchor Formation and the redox environment during vein production also needs a further investigation, which helps the interpretation of the origin of vein colors.

More case studies of satin spar veins are suggested to carry out in different localities that permit a comparative study of similarities and differences. Recommended cases include the following: (1) the Lower Triassic mudstone of the Moenkopi Formation, Capitol Reef National Park, Utah, USA; (2) the Upper Permian mudstone of the Quartermaster Formation, Caprock Canyons State Park, Texas, USA; (3) the Yellowknife Bay Formation, the Yellowknife Bay, Mars.

The calcite beef veins and cone-in-cone structures in the Lower Jurassic black shales of the Charmouth Mudstone (the Wessex Basin) formed during early burial of the sediments. The

diagenetic growth of the calcite fibres in the unconsolidated clays gave rise to the distinct vein textures and associated deformations in the host rock. Key innovative findings in this project are as follows:

· The veins formed during methanogenesis and mainly derived nutrients from seawater inorganic carbon and skeletal fragments, with implications from the moderate $\delta^{13}C$ values and covariations of ^{13}C and ^{18}O signatures of the veins and their hosts.

· The hydraulic fractures in overpressured cells, which were induced by sediment degassing, allowed rapid precipitation of authigenic carbonates and served as seed veins for subsequent antitaxial growth of fibres.

· Calcite fibres exhibit a displacive growth**.** The preferred c-axis orientations of fibres, which are orthogonal to vein walls, are possibly associated with the force of crystallization.

· Cone-in-cone structures and beef veins share similar formation mechanisms. The differences in textures and the content of solid inclusions are attributed to the compaction degrees of the host sediments.

However, the validation of early overpressuring in the undercompacted sediments, as well as the formation depth, are still required in further studies using basin modeling method. Moreover, case studies on calcite beef veins in black shales as mature source rocks are needed. The recommended cases are the shale-gas shales in the gas producing fields, such as the Barnett shale in the Fort Worth Basin and the Marcellus shale in the Appalachian Basin in the USA.

Appendix

Table 1 Carbon and oxygen isotope values of the calcite veins and host rocks in site 1.

Sample number	Sample type	Load (mg)	δ13C VPDB (‰)	Standard deviation (‰)	δ18O VSMOW (‰)	Standard deviation (‰)	δ18O VPDB (‰)	Standard deviation (‰)
101	shale	1.99	-0.665	0.045	25.740	0.066	-5.012	0.066
102a	beef	0.79	1.300	0.038	22.910	0.103	-7.757	0.103
102b	beef	1.05	0.461	0.123	24.957	0.166	-5.771	0.166
103	shale	1.95	-0.799	0.029	24.659	0.066	-6.060	0.066
104	vein	1.76	-0.919	0.019	25.004	0.031	-5.726	0.031
105	shale	1.46	-0.300	0.016	24.470	0.037	-6.244	0.037
106a	beef	0.56	0.577	0.035	26.285	0.029	-4.483	0.029
106b	beef	0.76	0.523	0.042	26.246	0.024	-4.521	0.024
107	shale	2.39	-1.372	0.051	25.902	0.062	-4.855	0.062
108a	CIC	0.82	-0.612	0.043	24.951	0.037	-5.777	0.037
108b	CIC	0.61	0.042	0.023	24.845	0.024	-5.880	0.024
109	shale	2.06	-1.017	0.029	25.823	0.026	-4.931	0.026
110	CIC	0.52	-1.180	0.024	24.648	0.036	-6.071	0.036
111	shale	1.3	-0.915	0.020	25.639	0.063	-5.110	0.063
113	shale	3.87	-0.431	0.034	25.345	0.102	-5.395	0.102
114a	beef	0.56	0.156	0.043	25.765	0.022	-4.987	0.022
114b	beef	0.65	0.817	0.048	24.856	0.016	-5.869	0.016
115	shale	4.26	-0.457	0.031	25.334	0.057	-5.406	0.057
116a	beef	0.63	0.726	0.019	25.471	0.015	-5.272	0.015
116b	beef	0.56	0.286	0.015	25.857	0.028	-4.898	0.028
117	shale	3.22	-0.893	0.030	24.638	0.044	-6.081	0.044
118a	CIC	0.55	2.464	0.041	21.761	0.019	-8.872	0.019
118b	CIC	0.66	-0.798	0.038	23.955	0.030	-6.744	0.030
119	shale	2.82	0.092	0.024	25.072	0.070	-5.659	0.070
120a	beef	0.75	1.085	0.024	23.848	0.021	-6.847	0.021
120b	beef	0.63	0.338	0.054	24.898	0.035	-5.829	0.035
121	shale	2.76	-0.232	0.022	25.275	0.053	-5.463	0.053
122a	beef	0.77	0.345	0.083	24.693	0.042	-6.027	0.042
122b	beef	0.64	1.028	0.058	23.324	0.070	-7.355	0.070
123	shale	3.85	-0.281	0.041	24.086	0.088	-6.616	0.088
124a	beef	0.71	0.531	0.086	24.398	0.063	-6.313	0.063
124b	beef	0.59	0.905	0.047	23.605	0.040	-7.083	0.040
125	shale	1.73	-0.812	0.022	25.039	0.040	-5.692	0.040
126a	CIC	0.71	0.376	0.074	25.802	0.057	-4.951	0.057
126b	CIC	0.61	0.334	0.063	26.086	0.042	-4.676	0.042
127	shale	1.96	-1.708	0.100	26.552	0.075	-4.224	0.075
128a	beef	0.6	-0.450	0.098	24.538	0.059	-6.178	0.059

128b	beef	0.54	0.146	0.087	26.020	0.082	-4.740	0.082
129	shale	4.5	-0.497	0.022	25.194	0.075	-5.541	0.075

Table 2 Carbon and oxygen isotope values of the calcite veins and host rocks in site 2.

Sample number	Sample type	Load mg	δ13C VPDB (‰)	Standard deviation (‰)	δ18O VSMOW (‰)	Standard deviation (‰)	δ18O VPDB (‰)	Standard deviation (‰)
21	shale	3.23	-0.587	0.042	24.722	0.107	-5.999	0.107
22a	beef	0.64	0.244	0.099	25.188	0.109	-5.547	0.109
22b	beef	0.7	0.673	0.086	22.741	0.115	-7.921	0.115
23	shale	3.57	-0.232	0.029	24.895	0.084	-5.831	0.084
24a	beef	0.66	0.337	0.110	24.401	0.121	-6.311	0.121
24b	beef	0.62	0.888	0.083	23.288	0.126	-7.390	0.126
25	shale	3.15	-0.336	0.025	24.779	0.084	-5.944	0.084
26a	beef	0.65	0.965	0.110	22.995	0.131	-7.674	0.131
26b	beef	0.58	0.267	0.092	22.942	0.126	-7.725	0.126

Table 3 Carbon and oxygen isotope values of the calcite veins and host rocks in site 3.

Sample number	Sample type	Load mg	δ13C VPDB (‰)	Standard deviation (‰)	δ18O VSMOW (‰)	Standard deviation (‰)	δ18O VPDB (‰)	Standard deviation (‰)
31	shale	6.05	0.041	0.030	24.487	0.085	-6.227	0.085
32a	beef	0.74	0.154	0.086	23.783	0.056	-6.910	0.056
32b	beef	0.51	-0.113	0.078	25.114	0.064	-5.619	0.064
33	shale	4.98	0.128	0.038	25.277	0.090	-5.461	0.090
34	shale	5.2	0.072	0.032	24.844	0.093	-5.881	0.093
35	shale	5.55	-0.107	0.015	25.177	0.073	-5.558	0.073
36	shale	5.07	-0.180	0.039	24.439	0.061	-6.273	0.061
37a	beef	0.67	0.125	0.097	24.826	0.141	-5.898	0.141
37b	beef	0.56	-0.262	0.09	25.546	0.115	-5.2	0.115
38	shale	5.01	-0.151	0.056	25.598	0.060	-5.150	0.060

Table 4 Carbon and oxygen isotope values of the calcite veins and host rocks in site 4.

Sample number	Sample type	Load mg	δ13C VPDB (‰)	Standard deviation (‰)	δ18O VSMOW (‰)	Standard deviation (‰)	δ18O VPDB (‰)	Standard deviation (‰)
41	shale	3.06	0.461	0.026	26.210	0.095	-4.556	0.095
42a	beef	0.61	-0.187	0.085	25.512	0.107	-5.233	0.107
42b	beef	0.49	2.723	0.071	21.100	0.116	-9.513	0.116
43a	CIC	0.69	2.089	0.097	21.446	0.116	-9.177	0.116
43b	CIC	0.71	2.294	0.121	20.764	0.119	-9.838	0.119
44	concretion	0.74	-8.783	0.101	25.987	0.115	-4.772	0.115
45	concretion	0.76	-8.686	0.108	25.942	0.136	-4.816	0.136
46	concretion	0.78	-7.117	0.110	25.025	0.120	-5.705	0.120
47	CIC	0.69	-1.515	0.120	24.703	0.134	-6.018	0.134
48	shale	2.55	-0.063	0.037	24.787	0.061	-5.936	0.061

Bibliography

Ábalos, B., Elorza, J., 2011. Latest Cretaceous cone-in-cone structures and soft-sediment deformation (Basque-Cantabrian Basin, north Spain): A record of deep-marine paleoseismicity? Geological Society of America Bulletin 123, 427-438.

Ábalos, B., Elorza, J., 2012. Structural Diagenesis of Siderite Layers in Black Shales (Albian Black Flysch, Northern Spain). The Journal of Geology 120, 405-429.

Ábalos, B., Puelles, P., Fernández-Armas, S., Sarrionandia, F., 2011. EBSD microfabric study of pre-Cambrian deformations recorded in quartz pebbles from the Sierra de la Demanda (N Spain). Journal of Structural Geology 33, 500-518.

Adelseck, C.G., Geehan, G.W., Roth, P.H., 1973. Experimental evidence for the selective dissolution and overgrowth of calcareous nannofossils during diagenesis. Geological Society of America Bulletin 84, 2755-2762.

Al-Aasm, I., Coniglio, M., Desrochers, A., 1995. Formation of complex fibrous calcite veins in Upper Triassic strata of Wrangellia Terrain, British Columbia, Canada. Sedimentary Geology 100, 83-95.

Al-Aasm, I.S., Muir, I., Morad, S., 1993. Diagenetic conditions of fibrous calcite vein formation in black shales: petrographic, chemical and isotopic evidence. Bulletin of Canadian Petroleum Geology 41, 46-56.

Allison, P.A., Pye, K., 1994. Early diagenetic mineralization and fossil preservation in modern carbonate concretions. Palaios, 561-575.

Anderton, R., Bridges, P., Leeder, M., Sellwood, B., 1979. Dynamic stratigraphy of the British Isles: a study in crustal evolution. Allen & Unwin.

Andreani, M., Baronnet, A., Boullier, A.-M., Gratier, J.-P., 2004. A microstructural study of a "crack-seal" type serpentine vein using SEM and TEM techniques. European Journal of Mineralogy 16, 585-595.

André-Mayer, A.-S., Sausse, J., 2007. Thickness and spatial distribution of veins in a porphyry copper deposit, Rosia Poieni, Romania. Journal of Structural Geology, 29, 1695-1708.

Antonellini, M., 2000. A natural analog for a fractured and faulted reservoir in dolomite: Triassic Sella Group, Northern Italy. AAPG Bulletin 84, 314-344.

Astin, T., Scotchman, I., 1988. The diagenetic history of some septarian concretions from the Kimmeridge Clay, England. Sedimentology 35, 349-368.

Aydin, A., 2000. Fractures, faults, and hydrocarbon entrapment, migration and flow. Marine and petroleum geology 17, 797-814.

Baihly, J.D., Altman, R.M., Malpani, R., Luo, F., 2010. Shale gas production decline trend comparison over time and basins, SPE annual technical conference and exhibition. Society of Petroleum Engineers.

Barker, S.L., Cox, S.F., Eggins, S.M., Gagan, M.K., 2006. Microchemical evidence for episodic growth of antitaxial veins during fracture-controlled fluid flow. Earth and Planetary Science Letters 250, 331-344.

Barton, C., Woods, M., Bristow, C., Newell, A., Westhead, R., Evans, D., Kirby, G., Warrington, G., 2011. Geology of south Dorset and south-east Devon and its World Heritage Coast. British Geological Survey.

Bascou, J., Barruol, G., Vauchez, A., Mainprice, D., Egydio-Silva, M., 2001. EBSD-measured lattice-preferred orientations and seismic properties of eclogites. Tectonophysics 342,

61-80.

Bear, J., 2013. Dynamics of fluids in porous media. Courier Corporation.

Bebout, G.E., 1991. Geometry and mechanisms of fluid flow at 15 to 45 kilometer depths in an early Cretaceous accretionary complex. Geophysical Research Letters 18, 923-926.

Becker, A., Gross, M.R., 1996. Mechanism for joint saturation in mechanically layered rocks: an example from southern Israel. Tectonophysics, 257, 223-237.

Bello, R.O., Wattenbarger, R.A., 2010. Multi-stage hydraulically fractured horizontal shale gas well rate transient analysis, North Africa technical conference and exhibition. Society of Petroleum Engineers.

Benner, R., Strom, M., 1993. A critical evaluation of the analytical blank associated with DOC measurements by high-temperature catalytic oxidation. Marine Chemistry 41, 153-160.

Berner, R., De Leeuw, J., Spiro, B., Murchison, D., Eglinton, G., 1985. Sulphate reduction, organic matter decomposition and pyrite formation [and discussion]. Philosophical Transactions of the Royal Society of London A: Mathematical, Physical and Engineering Sciences 315, 25-38.

Bickle, M., McKenzie, D., 1987. The transport of heat and matter by fluids during metamorphism. Contributions to Mineralogy and Petrology 95, 384-392.

Blenkinsop, T., 2008. Relationships between faults, extension fractures and veins, and stress. Journal of Structural Geology 30, 622-632.

Boggs, S., 2009. Petrology of sedimentary rocks. Cambridge University Press.

Bonnet, E. et al., 2001. Scaling of fracture systems in geological media. Reviews of Geophysics, 39, 347-383.

Bons, P., 2001. Development of crystal morphology during unitaxial growth in a progressively widening vein: I. The numerical model. Journal of Structural Geology 23, 865-872.

Bons, P.D., 2000. The formation of veins and their microstructures. Journal of the Virtual Explorer 2, 12.

Bons, P.D., 2001. The formation of large quartz veins by rapid ascent of fluids in mobile hydrofractures. Tectonophysics, 336, 1-17.

Bons, P.D., Elburg, M.A., Gomez-Rivas, E., 2012. A review of the formation of tectonic veins and their microstructures. Journal of Structural Geology 43, 33-62.

Bons, P.D., Jessell, M.W., 1997. Experimental simulation of the formation of fibrous veins by localised dissolution-precipitation creep. Mineralogical Magazine 61, 53-63.

Bons, P.D., Montenari, M., 2005. The formation of antitaxial calcite veins with well-developed fibres, Oppaminda Creek, South Australia. Journal of Structural Geology 27, 231-248.

Bowker, K.A., 2007. Barnett shale gas production, Fort Worth Basin: Issues and discussion. AAPG bulletin 91, 523-533.

Brogi, A., 2011. Variation in fracture patterns in damage zones related to strike-slip faults interfering with pre-existing fractures in sandstone (Calcione area, southern Tuscany, Italy). Journal of Structural Geology 33, 644-661.

Brooks, M., Trayner, P., Trimble, T., 1988. Mesozoic reactivation of Variscan thrusting in the Bristol Channel area, UK. Journal of the Geological Society, 145, 439-444.

Brown, R.W., 1954. How does cone-in-cone material become emplaced? American Journal of Science 252, 372-376.

Bruce, C.H., 1984. Smectite dehydration--its relation to structural development and

hydrocarbon accumulation in northern Gulf of Mexico basin. AAPG Bulletin 68, 673-683.

Buchanan, J.G., 1998. The exploration history and controls on hydrocarbon prospectivity in the Wessex basins, southern England, UK. Geological Society, London, Special Publications 133, 19-37.

Caine, J.S., Evans, J.P., Forster, C.B., 1996. Fault zone architecture and permeability structure. Geology 24, 1025-1028.

Calvert, S., Pedersen, T., 1993. Geochemistry of recent oxic and anoxic marine sediments: implications for the geological record. Marine geology, 113, 67-88.

Carlson, R., Schaftenaar, C., Moore, R., 1983. Causes of compressional-wave anisotropy in calcareous sediments from the Rio-grande rise. Initial Reports of the Deep Sea Drilling Project 72, 565-576.

Carpenter, S.J., Lohmann, K.C., Holden, P., Walter, L.M., Huston, T.J., Halliday, A.N., 1991. $\delta^{18}O$ values, $^{87}Sr/^{86}Sr$ and Sr/Mg ratios of Late Devonian abiotic marine calcite: Implications for the composition of ancient seawater. Geochimica et Cosmochimica Acta 55, 1991-2010.

Cartwright, J., 2010. Regionally extensive emplacement of sandstone intrusions: a brief review. Basin Research 22, 502-516.

Cartwright, J.A., 1994. Episodic basin-wide fluid expulsion from geopressured shale sequences in the North Sea basin. Geology 22, 447-450.

Chadwick, R., 1986. Extension tectonics in the Wessex Basin, southern England. Journal of the Geological Society 143, 465-488.

Chadwick, R., 1993. Aspects of basin inversion in southern Britain. Journal of the Geological

Society 150, 311-322.

Charola, A.E., Pühringer, J., Steiger, M., 2007. Gypsum: a review of its role in the deterioration of building materials. Environmental geology 52, 339-352.

Chiaramonte, L., Zoback, M.D., Friedmann, J., Stamp, V., 2008. Seal integrity and feasibility of CO2 sequestration in the Teapot Dome EOR pilot: geomechanical site characterization. Environmental Geology 54, 1667-1675.

Clark, M.B., Brantley, S.L., Fisher, D.M., 1995. Power-law vein-thickness distributions and positive feedback in vein growth. Geology, 23, 975-978.

Clifton, H.E., 1957. The carbonate concretions of the Ohio Shale. Ohio Journal of Science 57, 114-124.

Cobbold, P.R., Rodrigues, N., 2007. Seepage forces, important factors in the formation of horizontal hydraulic fractures and bedding-parallel fibrous veins ('beef'and 'cone-in-cone'). Geofluids 7, 313-322.

Cobbold, P.R., Zanella, A., Rodrigues, N., Løseth, H., 2013. Bedding-parallel fibrous veins (beef and cone-in-cone): worldwide occurrence and possible significance in terms of fluid overpressure, hydrocarbon generation and mineralization. Marine and Petroleum Geology, 43: 1-20.

Coleman, M., Raiswell, R., 1981. Carbon, oxygen and sulphur isotope variations in concretions from the Upper Lias of NE England. Geochimica et Cosmochimica Acta 45, 329-340.

Conybeare, D., Shaw, H., 2000. Fracturing, overpressure release and carbonate cementation in the Everest Complex, North Sea. Clay Minerals 35, 135-149.

Cooke, M., 1997. Predicting fracture localization in folded strata from mechanical stratigraphy

and fold shape: case study of East Kaibab Monocline, Utah. International Journal of Rock Mechanics and Mining Sciences 34, 56.

Coplen, T.B., Hanshaw, B.B., 1973. Ultrafiltration by a compacted clay membrane—I. Oxygen and hydrogen isotopic fractionation. Geochimica et Cosmochimica Acta 37, 2295-2310.

Cornford, C., 1986. The Bristol Channel Graben: organic geochemical limits on subsidence and speculation on the origin of inversion. Proceedings of the Ussher Society, 6, 360-367.

Correns, C.W., 1949. Growth and dissolution of crystals under linear pressure. Discussions of the Faraday society 5, 267-271.

Cosgrove, J.W., 1999. Forced folds and fractures: An introduction. Geological Society, London, Special Publications 169, 1-6.

Cosgrove, J.W., 2001. Hydraulic fracturing during the formation and deformation of a basin: A factor in the dewatering of low-permeability sediments. AAPG bulletin 85, 737-748.

Cossette, É., Schneider, D., Audet, P., Grasemann, B., Habler, G., 2015. Seismic properties and mineral crystallographic preferred orientations from EBSD data: Results from a crustal-scale detachment system, Aegean region. Tectonophysics 651, 66-78.

Coward, M., 1995. Structural and tectonic setting of the Permo-Triassic basins of northwest Europe. Geological Society, London, Special Publications, 91, 7-39.

Cowie, P.A., 1998. Normal fault growth in three dimensions in continental and oceanic crust. Geophysical Monograph-American Physical Union 106, 325-348.

Cox, S., Etheridge, M., 1983. Crack-seal fibre growth mechanisms and their significance in the

development of oriented layer silicate microstructures. Tectonophysics 92, 147-170.

Cox, S., Etheridge, M., Wall, V., 1987. The role of fluids in syntectonic mass transport, and the localization of metamorphic vein-type ore deposists. Ore Geology Reviews 2, 65-86.

Cox, S.F., 1987. Antitaxial crack-seal vein microstructures and their relationship to displacement paths. Journal of Structural Geology 9, 779-787.

Cox, S.F., 1995. Faulting processes at high fluid pressures: an example of fault valve behavior from the Wattle Gully Fault, Victoria, Australia. Journal of Geophysical Research: Solid Earth 100, 12841-12859.

Curtis, C., 1980. Diagenetic alteration in black shales. Journal of the Geological Society 137, 189-194.

Curtis, J.B., 2002. Fractured shale-gas systems. AAPG Bulletin 86, 1921-1938.

Dart, C.J., McClay, K., Hollings, P.N., 1995. 3D analysis of inverted extensional fault systems, southern Bristol Channel basin, UK. Geological Society, London, Special Publications 88, 393-413.

Davies, R.J., Mathias, S.A., Moss, J., Hustoft, S., Newport, L., 2012. Hydraulic fractures: How far can they go? Marine and Petroleum Geology 37, 1-6.

Dershowitz, W., Einstein, H., 1988. Characterizing rock joint geometry with joint system models. Rock Mechanics and Rock Engineering, 21, 21-51.

Dewers, T., Ortoleva, P., 1990. Force of crystallization during the growth of siliceous concretions. Geology 18, 204-207.

Di Naccio, D., Boncio, P., Cirilli, S., Casaglia, F., Morettini, E., Lavecchia, G., Brozzetti, F., 2005. Role of mechanical stratigraphy on fracture development in carbonate

reservoirs: Insights from outcropping shallow water carbonates in the Umbria–Marche Apennines, Italy. Journal of Volcanology and Geothermal Research 148, 98-115.

Dickson, J., Coleman, M., 1980. Changes in carbon and oxygen isotope composition during limestone diagenesis. Sedimentology 27, 107-118.

Dietrich, D., McKenzie, J.A., Song, H., 1983. Origin of calcite in syntectonic veins as determined from carbon-isotope ratios. Geology 11, 547-551.

Dobes, P., Suchy, V., Stejskal, M., 1999. Diagenetic Fluid Circulation through Fractures: a Case Study from the Barrandian Basin (Lower Paloeozoic), Czech Republic. Geolines 8, 18-19.

Donato, J., 1988. Possible Variscan thrusting beneath the Somerton anticline, Somerset. Journal of the Geological Society 145, 431-438.

Donovan, D., Horton, A., Ivimey–Cook, H., 1979. The transgression of the Lower Lias over the northern flank of the London Platform. Journal of the Geological Society 136, 165-173.

Durrance, E., 1965. Cone-in-cone structures: A new investigation. Proceedings of the Geologists' Association 76, 83-89.

Duruey, D., Rausay, J., 1973. Incremental strains measured by syntectonic crystal growth. Gravity and Tectonics (KA Dejong & R. Scholten, eds.). J. Wiley & Sons, New York.

Ebukanson, E., 1985. Kerogen facies in the major Jurassic mudrock formations of southern England and the implication on the depositional environments of their precursors. Journal of Petroleum Geology 8, 435-462.

Ebukanson, E., Kinghorn, R., 1986. Maturity of organic matter in the Jurassic of Southern

England and its relation to the burial history of the sediments. Journal of Petroleum Geology 9, 259-280.

Elburg, M.A., Bons, P.D., Foden, J., Passchier, C.W., 2002. The origin of fibrous veins: constraints from geochemistry. Geological Society, London, Special Publications 200, 103-118.

El-Shahat, A., West, I., 1983. Early and late lithification of aragonitic bivalve beds in the Purbeck Formation (Upper Jurassic-Lower Cretaceous) of southern England. Sedimentary Geology 35, 15-41.

Engelder, T., 1985. Loading paths to joint propagation during a tectonic cycle: an example from the Appalachian Plateau, USA. Journal of Structural Geology 7, 459-476.

Engelder, T., Peacock, D.C., 2001. Joint development normal to regional compression during flexural-flow folding: the Lilstock buttress anticline, Somerset, England. Journal of Structural Geology, 23, 259-277.

Erickson, S.G., 1996. Influence of mechanical stratigraphy on folding vs faulting. Journal of Structural Geology 18, 443-450.

Evans, M.A., Battles, D.A., 1999. Fluid inclusion and stable isotope analyses of veins from the central Appalachian Valley and Ridge province: implications for regional synorogenic hydrologic structure and fluid migration. Geological Society of America Bulletin 111, 1841-1860.

Feng, D., Chen, D., Peckmann, J., Bohrmann, G., 2010. Authigenic carbonates from methane seeps of the northern Congo fan: microbial formation mechanism. Marine and Petroleum Geology 27, 748-756.

Fisher, D.M., Brantley, S.L., 1992. Models of quartz overgrowth and vein formation:

deformation and episodic fluid flow in an ancient subduction zone. Journal of Geophysical Research: Solid Earth 97, 20043-20061.

Fisher, D.M., Brantley, S.L., Everett, M., Dzvonik, J., 1995. Cyclic fluid flow through a regionally extensive fracture network within the Kodiak accretionary prism. Journal of Geophysical Research: Solid Earth 100, 12881-12894.

Flatt, R.J., 2002. Salt damage in porous materials: how high supersaturations are generated. Journal of crystal growth 242, 435-454.

Flemings, P.B., Liu, X., Winters, W.J., 2003. Critical pressure and multiphase flow in Blake Ridge gas hydrates. Geology 31, 1057-1060.

Flugel, E., 2004. Microfacies of carbonate rocks: analysis, interpretation and application. Springer.

Franks, P.C., 1969. Nature, origin, and significance of cone-in-cone structures in the Kiowa Formation (Early Cretaceous), north-central Kansas. Journal of Sedimentary Research 39, 1438-1454.

Freed, R.L., Peacor, D.R., 1989. Geopressured shale and sealing effect of smectite to illite transition. AAPG Bulletin 73, 1223-1232.

Friedman, I., O'Neil, J.R., 1977. Data of geochemistry: Compilation of stable isotope fractionation factors of geochemical interest. US Government Printing Office.

Gale, J.F., Holder, J., 2008. Natural fractures in the Barnett Shale: Constraints on spatial organization and tensile strength with implications for hydraulic fracture treatment in shale-gas reservoirs, The 42nd US Rock Mechanics Symposium (USRMS). American Rock Mechanics Association.

Gale, J.F., Holder, J., 2010. Natural fractures in some US shales and their importance for gas

production, Geological Society, London, Petroleum Geology Conference Series. Geological Society of London, 1131-1140.

Gale, J.F., Laubach, S.E., Marrett, R.A., Olson, J.E., Holder, J., Reed, R.M., 2004. Predicting and characterizing fractures in dolostone reservoirs: Using the link between diagenesis and fracturing. Geological Society, London, Special Publications 235, 177-192.

Gale, J.F., Reed, R.M., Holder, J., 2007. Natural fractures in the Barnett Shale and their importance for hydraulic fracture treatments. AAPG Bulletin 91, 603-622.

Gallois, R., 2008. The lithostratigraphy of the shales-with-beef member of the Charmouth Mudstone Formation, Lower Jurassic. Geoscience in south-west England: proceedings of the Ussher Society 12, 32-40.

Gautier, D.L., Claypool, G.E., 1984. Interpretation of methanic diagenesis in ancient sediments by analogy with processes in modern diagenetic environments, Clastic Diagenesis. Mem. Am. Assoc. Petrol. Geol, 111-123.

Gibert, L., Ortí, F., Rosell, L., 2007. Plio-Pleistocene lacustrine evaporites of the Baza Basin (Betic Chain, SE Spain). Sedimentary Geology 200, 89-116.

Gillespie, P., Howard, C., Walsh, J., Watterson, J., 1993. Measurement and characterisation of spatial distributions of fractures. Tectonophysics 226, 113-141.

Gillespie, P., Walsh, J., Watterson, J., Bonson, C., Manzocchi, T., 2001. Scaling relationships of joint and vein arrays from The Burren, Co. Clare, Ireland. Journal of Structural Geology 23, 183-201.

Gilman, R.A., Metzger, W.J., 1967. Cone-in-cone concretions from western New York. Journal of Sedimentary Research 37, 87-95.

Glen, R., Hancock, P., Whittaker, A., 2005. Basin inversion by distributed deformation: the southern margin of the Bristol Channel Basin, England. Journal of Structural Geology 27, 2113-2134.

Gough, D., Bell, J., 1982. Stress orientations from borehole wall fractures with examples from Colorado, east Texas, and northern Canada. Canadian Journal of Earth Sciences 19, 1358-1370.

Gratier, J.-P., Frery, E., Deschamps, P., Røyne, A., Renard, F., Dysthe, D., Ellouz-Zimmerman, N., Hamelin, B., 2012. How travertine veins grow from top to bottom and lift the rocks above them: The effect of crystallization force. Geology 40, 1015-1018.

Grim, R.E., 1951. The depositional environment of red and green shales. Journal of Sedimentary Research 21, 226-232.

Gross, M.R., Engelder, T., 1995. Strain accommodated by brittle failure in adjacent units of the Monterey Formation, USA: scale effects and evidence for uniform displacement boundary conditions. Journal of Structural Geology, 17, 1303-1318.

Grossman, E.L., Ku, T.-L., 1986. Oxygen and carbon isotope fractionation in biogenic aragonite: temperature effects. Chemical Geology: Isotope Geoscience Section 59, 59-74.

Gudmundsson, A., 1987. Geometry, formation and development of tectonic fractures on the Reykjanes Peninsula, southwest Iceland. Tectonophysics 139, 295-308.

Gudmundsson, A., 1999. Fluid overpressure and stress drop in fault zones. Geophysical Research Letters 26, 115-118.

Gustavson, T.C., Hovorka, S.D., Dutton, A.R., 1994. Origin of satin spar veins in evaporite

basins. Journal of Sedimentary Research 64, 88-94.

Harder, H., 1972. The role of magnesium in the formation of smectite minerals. Chemical Geology 10, 31-39.

Heard, H.C., Rubey, W.W., 1966. Tectonic implications of gypsum dehydration. Geological Society of America Bulletin 77, 741-760.

Hedberg, H.D., 1974. Relation of methane generation to undercompacted shales, shale diapirs, and mud volcanoes. AAPG Bulletin 58, 661-673.

Hedberg, H.D., 1980. Methane generation and petroleum migration. AAPG Special Volumes, 179-206.

Henderson, I., McCaig, A., 1996. Fluid pressure and salinity variations in shear zone-related veins, central Pyrenees, France: implications for the fault-valve model. Tectonophysics 262, 321-348.

Hendry, J.P., 2002. Geochemical trends and palaeohydrological significance of shallow burial calcite and ankerite cements in Middle Jurassic strata on the East Midlands Shelf (onshore UK). Sedimentary Geology 151, 149-176.

Hendry, J.P., Ditchfield, P.W., Marshall, J.D., 1995. Two-stage neomorphism of Jurassic aragonitic bivalves: implications for early diagenesis. Journal of Sedimentary Research 65, 214-224.

Hesselbo, S., Jenkyns, H., 1995. A comparison of the Hettangian to Bajocian successions of Dorset and Yorkshire. Field Geology of the British Jurassic. Geological Society, London, 105-150.

Hilgers, C., Dilg-Gruschinski, K., Urai, J.L., 2003. Microstructures grown experimentally from advectivesupersaturated solution and their implication for natural vein systems.

Journal of Geochemical Exploration 78, 221-225.

Hilgers, C., Dilg-Gruschinski, K., Urai, J.L., 2004. Microstructural evolution of syntaxial veins formed by advective flow. Geology 32, 261-264.

Hilgers, C., Koehn, D., Bons, P., Urai, J., 2001. Development of crystal morphology during unitaxial growth in a progressively widening vein: II. Numerical simulations of the evolution of antitaxial fibrous veins. Journal of Structural Geology 23, 873-885.

Hilgers, C., Sindern, S., 2005. Textural and isotopic evidence on the fluid source and transport mechanism of antitaxial fibrous microstructures from the Alps and the Appalachians. Geofluids 5, 239-250.

Hilgers, C., Urai, J.L., 2002. Microstructural observations on natural syntectonic fibrous veins: implications for the growth process. Tectonophysics 352, 257-274.

Hilgers, C., Urai, J.L., 2002. Experimental study of syntaxial vein growth during lateral fluid flow in transmitted light: first results. Journal of Structural Geology 24, 1029-1043.

Hilgers, C., Urai, J.L., 2005. On the arrangement of solid inclusions in fibrous veins and the role of the crack-seal mechanism. Journal of Structural Geology 27, 481-494.

Hillis, R.R., 1992. A two layer lithospheric compressional model for the tertiary uplift of the southern United Kingdom. Geophysical research letters 19, 573-576.

Hobbs, P., Entwisle, D., Northmore, K., Sumbler, M., Jones, L., Kemp, S., Self, S., Barron, M., Meakin, J., 2012. Engineering geology of British rocks and soils: Lias Group. British Geological Survey.

Hobbs, P., Hallam, J., Forster, A., Entwisle, D., Jones, L., Cripps, A., Northmore, K., Self, S., Meakin, J., 2002. Engineering geology of British rocks and soils: Mudstones of the Mercia Mudstone Group. British Geological Survey.

Hodgson, W., 1966. Carbon and oxygen isotope ratios in diagenetic carbonates from marine sediments. Geochimica et Cosmochimica Acta 30, 1223-1233.

Hoefs, J., Hoefs, J., 1997. Stable isotope geochemistry. Springer.

Holford, S., Turner, J., Green, P., 2005a. Reconstructing the Mesozoic–Cenozoic exhumation history of the Irish Sea basin system using apatite fission track analysis and vitrinite reflectance data, Geological Society, London, Petroleum Geology Conference series. Geological Society of London, 1095-1107.

Holland, M., Urai, J.L., 2010. Evolution of anastomosing crack–seal vein networks in limestones: Insight from an exhumed high-pressure cell, Jabal Shams, Oman Mountains. Journal of Structural Geology 32, 1279-1290.

Holland, M., van Gent, H., Bazalgette, L., Yassir, N., Strating, E.H.H., Urai, J.L., 2011. Evolution of dilatant fracture networks in a normal fault—Evidence from 4D model experiments. Earth and Planetary Science Letters 304, 399-406.

Holliday, D., 1970. The petrology of secondary gypsum rocks: a review. Journal of Sedimentary Research 40, 734-744.

Holloway, S., Chadwick, R., 1986. The Sticklepath-Lustleigh fault zone: Tertiary sinistral reactivation of a Variscan dextral strike-slip fault. Journal of the Geological Society, 143, 447-452.

Hood, S.D., Nelson, C.S., Kamp, P.J., 2003. Modification of fracture porosity by multiphase vein mineralization in an Oligocene nontropical carbonate reservoir, Taranaki Basin, New Zealand. AAPG Bulletin 87, 1575-1597.

Hooker, J., Laubach, S., Marrett, R., 2013. Fracture-aperture size—frequency, spatial distribution, and growth processes in strata-bounded and non-strata-bounded

fractures, Cambrian Mesón Group, NW Argentina. Journal of Structural Geology 54, 54-71.

House, M.R., 1989. Geology of the Dorset coast. Geologists' Association.

Howard, A., Warrington, G., Ambrose, K., Rees, J., 2008. A formational framework for the Mercia Mudstone Group (Triassic) of England and Wales. British Geological Survey.

Huang, Q., Angelier, J., 1989. Fracture spacing and its relation to bed thickness. Geological Magazine 126, 355-362.

Hudson, J., 1978. Concretions, isotopes, and the diagenetic history of the Oxford Clay (Jurassic) of central England. Sedimentology 25, 339-370.

Humphreys, F., 2004. Characterisation of fine-scale microstructures by electron backscatter diffraction (EBSD). Scripta materialia 51, 771-776.

Ingram, G.M., Urai, J.L., 1999. Top-seal leakage through faults and fractures: the role of mudrock properties. Geological Society, London, Special Publications 158, 125-135.

Instruments, O., 2005. Basics of EBSD. Instruments, Oxford.

Irwin, H., Curtis, C., Coleman, M., 1977. Isotopic evidence for source of diagenetic carbonates formed during burial of organic-rich sediments. Nature 269, 209-213.

Jackson, A., 2008. Bedrock geology UK South: an explanation of the bedrock geology map of England and Wales: 1: 625 000 fifth edition. British Geological Survey.

Jackson, J.A., 2005. Glossary of geology. Glossary of Geology, by JA Jackson. 2005 Approx. 900 p. 5th revised and enlarged ed. ISBN 3-540-27951-2. Berlin. Springer.

Jacoby, H.D., O'Sullivan, F.M., Paltsev, S., 2011. The influence of shale gas on US energy and environmental policy. MIT Joint Program on the Science and Policy of Global Change.

Jarvie, D.M., Hill, R.J., Ruble, T.E., Pollastro, R.M., 2007. Unconventional shale-gas systems: The Mississippian Barnett Shale of north-central Texas as one model for thermogenic shale-gas assessment. AAPG bulletin 91, 475-499.

Jeans, C., 1978. The origin of the Triassic clay assemblages of Europe with special reference to the Keuper Marl and Rhaetic of parts of England. Philosophical Transactions of the Royal Society of London. Series A, Mathematical and Physical Sciences 289, 549-636.

Jenkyns, H.C., Weedon, G.P., 2013. Chemostratigraphy (CaCO3, TOC, δ13Corg) of Sinemurian (Lower Jurassic) black shales from the Wessex Basin, Dorset and palaeoenvironmental implications. Newsletters on Stratigraphy 46, 1-21.

Jenkyns, H.C., Weedon, G.P., 2013. Chemostratigraphy (CaCO3, TOC, δ13Corg) of Sinemurian (Lower Jurassic) black shales from the Wessex Basin, Dorset and palaeoenvironmental implications. Newsletters on Stratigraphy 46, 1-21.

Ji, S., Saruwatari, K., 1998. A revised model for the relationship between joint spacing and layer thickness. Journal of Structural Geology 20, 1495-1508.

Jowett, E.C., Cathles III, L.M., Davis, B.W., 1993. Predicting depths of gypsum dehydration in evaporitic sedimentary basins. AAPG Bulletin 77, 402-413.

Kamb, W.B., 1959. Theory of preferred crystal orientation developed by crystallization under stress. The Journal of Geology, 153-170.

Kamerling, P., 1979. The geology and hydrocarbon habitat of the Bristol Channel Basin. Journal of Petroleum Geology 2, 75-93.

Karner, G.D., Lake, S.D., Dewey, J.F., 1987. The thermal and mechanical development of the Wessex Basin, southern England. Geological Society, London, Special Publications

28, 517-536.

Katahara, K., 2006. Overpressure and shale properties: Stress unloading or smectite-illite transformation?, 2006 SEG Annual Meeting. Society of Exploration Geophysicists.

Keary, P., Vine, F., 1990. Global Tectonics Blackwell. Oxford.

Kemp, S., McKervey, J., 2001. The mineralogy of mudrocks from the Lias Group of England. British Geological Survey

Kemp, S., Merriman, R., Bouch, J., 2005. Clay mineral reaction progress–the maturity and burial history of the Lias Group of England and Wales. Clay minerals 40, 43-61.

Kendall, A., 1975. Anhydrite replacements of gypsum (satin-spar) veins in the Mississippian caprocks of southeastern Saskatchewan. Canadian Journal of Earth Sciences 12, 1190-1195.

Keulen, N., Den Brok, S., Spiers, C., 2001. Force of crystallisation of gypsum during hydration of synthetic anhydrite rock, 13th DRT conference: Deformation Mechanisms, Rheology, and Tectonics.

Kiriakoulakis, K., Marshall, J., Wolff, G., 2000. Biomarkers in a Lower Jurassic concretion from Dorset (UK). Journal of the Geological Society 157, 207-220.

Kiriakoulakis, K., Marshall, J., Wolff, G., 2000. Biomarkers in a Lower Jurassic concretion from Dorset (UK). Journal of the Geological Society 157, 207-220.

Koehn, D., Bons, P.D., Passchier, C.W., 2003. Development of antitaxial strain fringes during non-coaxial deformation: an experimental study. Journal of Structural Geology 25, 263-275.

Koehn, D., Hilgers, C., Bons, P.D., Passchier, C.W., 2000. Numerical simulation of fibre growth in antitaxial strain fringes. Journal of Structural Geology 22, 1311-1324.

Kowal-Linka, M., 2010. Origin of cone-in-cone calcite veins during calcitization of dolomites and their subsequent diagenesis: A case study from the Gogolin Formation (Middle Triassic), SW Poland. Sedimentary Geology 224, 54-64.

Krylov, A., Khlystov, O., Zemskaya, T., Minami, H., Hachikubo, A., Nunokawa, Y., Kida, M., Shoji, H., Naudts, L., Poort, J., 2008. First discovery and formation process of authigenic siderite from gas hydrate–bearing mud volcanoes in fresh water: Lake Baikal, eastern Siberia. Geophysical Research Letters 35, 1-6.

Kulatilake, P., Wu, T., 1984. Estimation of mean trace length of discontinuities. Rock Mechanics and Rock Engineering, 17, 215-232.

La Iglesia, A., González, V., López-Acevedo, V., Viedma, C., 1997. Salt crystallization in porous construction materials I Estimation of crystallization pressure. Journal of Crystal Growth 177, 111-118.

Lacazette, A., Engelder, T., 1992. Fluid-driven cyclic propagation of a joint in the Ithaca siltstone, Appalachian Basin, New York. International Geophysics 51, 297-323.

Ladeira, F., Price, N., 1981. Relationship between fracture spacing and bed thickness. Journal of Structural Geology 3, 179-183.

Lake, S.D., Karner, G.D., 1987. The structure and evolution of the Wessex Basin, southern England: an example of inversion tectonics. Tectonophysics 137, 347-378.

Lamarche, J., Lavenu, A.P., Gauthier, B.D., Guglielmi, Y., Jayet, O., 2012. Relationships between fracture patterns, geodynamics and mechanical stratigraphy in Carbonates (South-East Basin, France). Tectonophysics 581, 231-245.

Lang, W.D., Spath, L.F., Richardson, W.A., 1923. Shales-with-‘beef,’a Sequence in the Lower Lias of the Dorset Coast. Quarterly Journal of the Geological Society 79, 47-66.

Larson, S.Å., Tullborg, E.-L., 1984. Stable isotopes of fissure-filling calcite from Finnsjön, Uppland, Sweden. Lithos 17, 117-125.

Lash, G.G., Engelder, T., 2005. An analysis of horizontal microcracking during catagenesis: Example from the Catskill delta complex. AAPG bulletin 89, 1433-1449.

Laubach, S., Reed, R., Olson, J., Lander, R., Bonnell, L., 2004. Coevolution of crack-seal texture and fracture porosity in sedimentary rocks: cathodoluminescence observations of regional fractures. Journal of Structural Geology 26, 967-982.

Laubach, S.E., 2003. Practical approaches to identifying sealed and open fractures. AAPG bulletin 87, 561-579.

Laubach, S.E., Eichhubl, P., Hilgers, C., Lander, R., 2010. Structural diagenesis. Journal of Structural Geology 32, 1866-1872.

Laubach, S.E., Lorenz, J., 1992. Preliminary assessment of natural fracture patterns in Frontier Formation sandstones, southwestern Wyoming. 43rd Annual Field Conference Guidebook, 87-96.

Laubach, S.E., Olson, J.E., Gross, M.R., 2009. Mechanical and fracture stratigraphy. AAPG bulletin 93, 1413-1426.

Lavenu, A.P., Lamarche, J., Gallois, A., Gauthier, B.D., 2013. Tectonic versus diagenetic origin of fractures in a naturally fractured carbonate reservoir analog (Nerthe anticline, southeastern France). AAPG Bulletin 97, 2207-2232.

Law, A., 1998. Regional uplift in the English Channel: quantification using sonic velocity. Geological Society, London, Special Publications 133, 187-197.

Leslie, A., Spiro, B., Tucker, M., 1993. Geochemical and mineralogical variations in the upper Mercia Mudstone Group (Late Triassic), southwest Britain: correlation of outcrop

sequences with borehole geophysical logs. Journal of the Geological Society 150, 67-75.

Limpert, E., Stahel, W.A., Abbt, M., 2001. Log-normal Distributions across the Sciences: Keys and Clues On the charms of statistics, and how mechanical models resembling gambling machines offer a link to a handy way to characterize log-normal distributions, which can provide deeper insight into variability and probability—normal or log-normal: That is the question. BioScience 51, 341-352.

Liu, X., Flemings, P.B., 2007. Dynamic multiphase flow model of hydrate formation in marine sediments. Journal of Geophysical Research: Solid Earth 112, 1-23.

Lloyd, G.E., 2000. Grain boundary contact effects during faulting of quartzite: an SEM/EBSD analysis. Journal of Structural Geology 22, 1675-1693.

Loganathan, P., Burau, R., 1973. Sorption of heavy metal ions by a hydrous manganese oxide. Geochimica et Cosmochimica Acta 37, 1277-1293.

Longstaffe, F.J., 1986. Oxygen isotope studies of diagenesis in the basal Belly River sandstone, Pembina I-Pool, Alberta. Journal of Sedimentary Research 56, 78-88.

Lorenz, J.C., Finley, S.J., 1991. Regional Fractures II: Fracturing of Mesaverde Reservoirs in the Piceance Basin, Colorado. AAPG Bulletin 75, 1738-1757.

Machel, H.G., 1985. Fibrous gypsum and fibrous anhydrite in veins. Sedimentology 32, 443-454.

MacKenzie, W., 1972. Fibrous calcite, a Middle Devonian geologic marker, with stratigraphic significance, District of Mackenzie, Northwest Territories. Canadian Journal of Earth Sciences 9, 1431-1440.

Maher Jr, H.D., Ogata, K., Braathen, A., 2016. Cone-in-cone and beef mineralization

associated with Triassic growth basin faulting and shallow shale diagenesis, Edgeøya, Svalbard. Geological Magazine, 1-16.

Maliva, R.G., Dickson, J., 1992. The mechanism of skeletal aragonite neomorphism: evidence from neomorphosed mollusks from the upper Purbeck Formation (Late Jurassic-Early Cretaceous), southern England. Sedimentary Geology 76, 221-232.

Maliva, R.G., Siever, R., 1988. Diagenetic replacement controlled by force of crystallization. Geology 16, 688-691.

Mandl, G., 2005. Rock joints. Springer.

Marrett, R., Laubach, S., 1997. Diagenetic controls on fracture permeability and sealing. International Journal of Rock Mechanics and Mining Sciences 34, 204.

Marrett, R., Ortega, O.J., Kelsey, C.M., 1999. Extent of power-law scaling for natural fractures in rock. Geology 27, 799-802.

Marshall, J.D., 1982. Isotopic composition of displacive fibrous calcite veins: reversals in pore-water composition trends during burial diagenesis. Journal of Sedimentary Research 52, 615-630.

Marshall, J.D., Pirrie, D., 2013. Carbonate concretions—explained. Geology Today 29, 53-62.

Matsumura, M., Hashimoto, Y., Kimura, G., Ohmori-Ikehara, K., Enjohji, M., Ikesawa, E., 2003. Depth of oceanic-crust underplating in a subduction zone: Inferences from fluid-inclusion analyses of crack-seal veins. Geology 31, 1005-1008.

Mauldon, M., Dunne, W., Rohrbaugh, M., 2001. Circular scanlines and circular windows: new tools for characterizing the geometry of fracture traces. Journal of Structural Geology 23, 247-258.

Mauldon, M., Rohrbaugh Jr, M., Dunne, W., Lawdermilk, W., 1999. Fracture intensity

estimates using circular scanlines, Proceedings of the 37th US Rock Mechanics Symposium: Rock Mechanics for Industry, Balkema, Rotterdam, 777-784.

Maxwell, S.C., Urbancic, T., Steinsberger, N., Zinno, R., 2002. Microseismic imaging of hydraulic fracture complexity in the Barnett shale, SPE annual technical conference and exhibition. Society of Petroleum Engineers.

Mazumder, S., Karnik, A.A., Wolf, K.-H.A., 2006. Swelling of coal in response to CO2 sequestration for ECBM and its effect on fracture permeability. SPE Journal 11, 390-398.

McBride, E.F., 1974. Significance of color in red, green, purple, olive, brown, and gray beds of Difunta Group, northeastern Mexico. Journal of Sedimentary Research 44, 760-773.

McCaffrey, K., Sleight, J., Pugliese, S., Holdsworth, R., 2003. Fracture formation and evolution in crystalline rocks: Insights from attribute analysis. Geological Society, London, Special Publications 214, 109-124.

Mclane, M., 1995. Sedimentology. New York. Oxford, Oxford Uni. Press.

Means, W., Li, T., 2001. A laboratory simulation of fibrous veins: some first observations. Journal of Structural Geology 23, 857-863.

Menpes, R.J., Hillis, R.R., 1995. Quantification of Tertiary exhumation from sonic velocity data, Celtic Sea/south-western approaches. Geological Society, London, Special Publications88, 191-207.

Milholland, P., Manghnani, M.H., Schlanger, S.O., Sutton, G.H., 1980. Geoacoustic modeling of deep-sea carbonate sediments. The Journal of the Acoustical Society of America 68, 1351-1360.

Miliorizos, M., Ruffell, A., 1998. Kinematics of the Watchet-Cothelstone-Hatch fault system: implications for the fault history of the Wessex basin and adjacent areas. Geological Society, London, Special Publications 133, 311-330.

Mohamed El Tabakh, B., Warren, J.K., 1998. Origin of fibrous gypsum in the Newark Rift Basin, eastern North America. Journal of Sedimentary Research 68, 88-99.

Monecke, T., Gemmell, J.B., Monecke, J., 2001. Fractal distributions of veins in drill core from the Hellyer VHMS deposit, Australia: constraints on the origin and evolution of the mineralising system. Mineralium Deposita 36, 406-415.

Montgomery, S.L., Jarvie, D.M., Bowker, K.A., Pollastro, R.M., 2005. Mississippian Barnett Shale, Fort Worth basin, north-central Texas: Gas-shale play with multi–trillion cubic foot potential. AAPG bulletin 89, 155-175.

Morad, S., De Ros, L., 1994. Geochemistry and diagenesis of stratabound calcite cement layers within the Rannoch Formation of the Brent Group, Murchison Field, North Viking Graben (northern North Sea)—comment. Sedimentary Geology 93, 135-141.

Mörk, M.B.E., Moen, K., 2007. Compaction microstructures in quartz grains and quartz cement in deeply buried reservoir sandstones using combined petrography and EBSD analysis. Journal of Structural Geology 29, 1843-1854.

Murray, R., 1964. Origin and diagenesis of gypsum and anhydrite. Journal of Sedimentary Research 34, 512-523.

Narr, W., Schechter, D.W., Thompson, L.B., 2006. Naturally fractured reservoir characterization. Richardson, TX: Society of Petroleum Engineers.

Narr, W., Suppe, J., 1991. Joint spacing in sedimentary rocks. Journal of Structural Geology 13, 1037-1048.

Nelson, R., 2001. Geologic analysis of naturally fractured reservoirs. Gulf Professional Publishing.

Nemčok, M., Gayer, R., Miliorizos, M., 1995. Structural analysis of the inverted Bristol Channel Basin: implications for the geometry and timing of fracture porosity. Geological Society, London, Special Publications 88, 355-392.

Nichols, G., 2009. Sedimentology and stratigraphy. John Wiley & Sons.

Noiriel, C., Renard, F., Doan, M.-L., Gratier, J.-P., 2010. Intense fracturing and fracture sealing induced by mineral growth in porous rocks. Chemical Geology 269, 197-209.

Nüchter, J.-A., Stöckhert, B., 2007. Vein quartz microfabrics indicating progressive evolution of fractures into cavities during postseismic creep in the middle crust. Journal of Structural Geology 29, 1445-1462.

O'Brien, D.K., Manghnani, M.H., Tribble, J.S., Wenk, H.-R., 1993. Preferred orientation and velocity anisotropy in marine clay-bearing calcareous sediments, Carbonate microfabrics. Springer, 149-161.

Odling, N., Gillespie, P., Bourgine, B., Castaing, C., Chiles, J., Christensen, N., Fillion, E., Genter, A., Olsen, C., Thrane, L., 1999. Variations in fracture system geometry and their implications for fluid flow in fractured hydrocarbon reservoirs. Petroleum Geoscience 5, 373-384.

Oliver, N.H., Bons, P.D., 2001. Mechanisms of fluid flow and fluid–rock interaction in fossil metamorphic hydrothermal systems inferred from vein–wallrock patterns, geometry and microstructure. Geofluids 1, 137-162.

Olson, J.E., Bahorich, B., Holder, J., 2012. Examining hydraulic fracture: natural fracture interaction in hydrostone block experiments, SPE Hydraulic Fracturing Technology

Conference. Society of Petroleum Engineers.

Olson, J.E., Laubach, S.E., Lander, R.H., 2007. Combining diagenesis and mechanics to quantify fracture aperture distributions and fracture pattern permeability. Geological Society, London, Special Publications 270, 101-116.

Olson, J.E., Laubach, S.E., Lander, R.H., 2009. Natural fracture characterization in tight gas sandstones: Integrating mechanics and diagenesis. AAPG Bulletin 93, 1535-1549.

Ortega, O.J., Marrett, R.A., Laubach, S.E., 2006. A scale-independent approach to fracture intensity and average spacing measurement. AAPG Bulletin 90, 193-208.

Ortí, F., Rosell, L., Anadón, P., 2010. Diagenetic gypsum related to sulfur deposits in evaporites (Libros Gypsum, Miocene, NE Spain). Sedimentary Geology 228, 304-318.

Osborne, M.J., Swarbrick, R.E., 1997. Mechanisms for generating overpressure in sedimentary basins: a reevaluation. AAPG bulletin 81, 1023-1041.

Paquette, J., Reeder, R.J., 1990. New type of compositional zoning in calcite: Insights into crystal-growth mechanisms. Geology 18, 1244-1247.

Parnell, J., Honghan, C., Middleton, D., Haggan, T., Carey, P., 2000. Significance of fibrous mineral veins in hydrocarbon migration: fluid inclusion studies. Journal of Geochemical Exploration 69, 623-627.

Passchier, C.W., Trouw, R.A., 1996. Microtectonics. Springer.

Passchier, C.W., Urai, J.L., 1988. Vorticity and strain analysis using Mohr diagrams. Journal of Structural Geology 10, 755-763.

Paterson, M., 1973. Nonhydrostatic thermodynamics and its geologic applications. Reviews of Geophysics 11, 355-389.

Peacock, D., Mann, A., 2005. Evaluation of the controls on fracturing in reservoir rocks. Journal of Petroleum Geology 28, 385-396.

Peacock, D., Sanderson, D., 1991. Displacements, segment linkage and relay ramps in normal fault zones. Journal of Structural Geology 13, 721-733.

Peacock, D., Sanderson, D., 1992. Effects of layering and anisotropy on fault geometry. Journal of the Geological Society 149, 793-802.

Peacock, D., Sanderson, D., 1994. Geometry and development of relay ramps in normal fault systems. AAPG bulletin 78, 147-165.

Peacock, D., Sanderson, D., 1999. Deformation history and basin-controlling faults in the Mesozoic sedimentary rocks of the Somerset coast. Proceedings of the Geologists' Association 110, 41-52.

Pearson, M., Hendry, J., Taylor, C., Russell, M., 2005. Fatty acids in sparry calcite fracture fills and microsparite cement of septarian diagenetic concretions. Geochimica et Cosmochimica Acta 69, 1773-1786.

Pérez-Huerta, A., Cuif, J.-P., Dauphin, Y., Cusack, M., 2014. Crystallography of calcite in pearls. European Journal of Mineralogy 26, 507-516.

Philipp, S.L., 2008. Geometry and formation of gypsum veins in mudstones at Watchet, Somerset, SW England. Geological Magazine 145, 831-844.

Philipp, S.L., 2012. Fluid overpressure estimates from the aspect ratios of mineral veins. Tectonophysics 581, 35-47.

Phillips, W.J., 1972. Hydraulic fracturing and mineralization. Journal of the Geological Society 128, 337-359.

Polak, A., Elsworth, D., Yasuhara, H., Grader, A., Halleck, P., 2003. Permeability reduction of

a natural fracture under net dissolution by hydrothermal fluids. Geophysical Research Letters 30, NO 20.

Pommer, L., 2013. Using structural diagenesis to infer the timing of natural fractures in the Marcellus Shale. Unconventional Resources Technology Conference (URTEC).

Porta, J., 1998. Methodologies for the analysis and characterization of gypsum in soils: a review. Geoderma 87, 31-46.

Prior, D.J., Boyle, A.P., Brenker, F., Cheadle, M.C., Day, A., Lopez, G., Peruzzo, L., Potts, G.J., Reddy, S., Spiess, R., 1999. The application of electron backscatter diffraction and orientation contrast imaging in the SEM to textural problems in rocks. American Mineralogist 84, 1741-1759.

Putnis, A., Prieto, M., Fernandez-Diaz, L., 1995. Fluid supersaturation and crystallization in porous media. Geological Magazine 132, 1-13.

Raiswell, R., 1987. Non-steady state microbiological diagenesis and the origin of concretions and nodular limestones. Geological Society, London, Special Publications 36, 41-54.

Raiswell, R., Fisher, Q., 2004. Rates of carbonate cementation associated with sulphate reduction in DSDP/ODP sediments: implications for the formation of concretions. Chemical Geology 211, 71-85.

Ramsay, J.G., 1980. The crack-seal mechanism of rock deformation. Nature 284, 135-139.

Ramsay, J.G., Huber, M.I., 1987. The techniques of modern structural geology: Folds and fractures. Academic press.

Rawnsley, K., Peacock, D., Rives, T., Petit, J.-P., 1998. Joints in the Mesozoic sediments around the Bristol Channel Basin. Journal of Structural Geology 20, 1641-1661.

Renshaw, C., Park, J., 1997. Effect of mechanical interactions on the scaling of fracture length

and aperture. Nature 386, 482-484.

Reyer, D., Bauer, J.F., Philipp, S.L., 2012. Fracture systems in normal fault zones crosscutting sedimentary rocks, Northwest German Basin. Journal of Structural Geology 45, 38-51.

Richards, I.J., Connelly, J.B., Gregory, R.T., Gray, D.R., 2002. The importance of diffusion, advection, and host-rock lithology on vein formation: a stable isotope study from the Paleozoic Ouachita orogenic belt, Arkansas and Oklahoma. Geological Society of America Bulletin 114, 1343-1355.

Rinaudo, C., Franchini-Angela, M., Boistelle, R., 1989. Curvature of gypsum crystals induced by growth in the presence of impurities. Mineralogical Magazine 53, 479-482.

Rives, T., Razack, M., Petit, J.-P., Rawnsley, K., 1992. Joint spacing: analogue and numerical simulations. Journal of Structural Geology 14, 925-937.

Roberts, D., 1989. Basin inversion in and around the British Isles. Geological Society, London, Special Publications 44, 131-150.

Rodrigues, N., Cobbold, P.R., Loseth, H., Ruffet, G., 2009. Widespread bedding-parallel veins of fibrous calcite (’beef') in a mature source rock (Vaca Muerta Fm, Neuquén Basin, Argentina): evidence for overpressure and horizontal compression. Journal of the Geological Society 166, 695-709.

Ruffell, A., Coward, M., 1992. Basement tectonics and their relationship to Mesozoic megasequences in the Celtic Seas and Bristol Channel area. Geological Society, London, Special Publications 62, 385-394.

Ruffell, A., Shelton, R., 1999. The control of sedimentary facies by climate during phases of crustal extension: examples from the Triassic of onshore and offshore England and

Northern Ireland. Journal of the Geological Society 156, 779-789.

Rukin, N., 1990. The diagenesis of the Shales-with-beef of the Lower Lias, West Dorset. University of Liverpool.

Rustichelli, A., Di Celma, C., Tondi, E., Baud, P., Vinciguerra, S., 2016. Fibrous gypsum veins as diffuse features and within fault zones: the case study of the Pisco Basin (Ica desert, southern Peru). Journal of the Geological Society 173, 405-418.

Rutledge, J.T., Phillips, W.S., 2003. Hydraulic stimulation of natural fractures as revealed by induced microearthquakes, Carthage Cotton Valley gas field, east Texas. Geophysics 68, 441-452.

Saidov, T.A., Pel, L., Kopinga, K., 2015. Crystallization Pressure of Sodium Sulfate Heptahydrate. Crystal Growth & Design 15, 2087-2093.

Samankassou, E., Tresch, J., Strasser, A., 2005. Origin of peloids in early Cretaceous deposits, Dorset, South England. Facies 51, 264-274.

Sanderson, D.J., Roberts, S., Gumiel, P., Greenfield, C., 2008. Quantitative analysis of tin-and tungsten-bearing sheeted vein systems. Economic Geology 103, 1043-1056.

Sass, E., Bein, A., Almogi-Labin, A., 1991. Oxygen-isotope composition of diagenetic calcite in organic-rich rocks: evidence for ^{18}O depletion in marine anaerobic pore water. Geology 19, 839-842.

Scherer, G.W., 2004. Stress from crystallization of salt. Cement and concrete research 34, 1613-1624.

Schmidt, N.-H., Olesen, N.O., 1989. Computer-aided determination of crystal-lattice orientation from electron-channeling patterns in the SEM. Canadian Mineralogist 27, 15-22.

Seedhouse, J., Racey, A., 1997. Sealing capacity of the Mercia Mudstone Group in the East Irish Sea Basin: implications for petroleum exploration. Journal of Petroleum Geology 20, 261-286.

Selles-Martinez, J., 1994. New insights in the origin of cone-in-cone structures. Carbonates and evaporites 9, 172-186.

Serafeimidis, K., Anagnostou, G., 2014. On the crystallisation pressure of gypsum. Environmental Earth Sciences 72, 4985-4994.

Shearman, D., Mossop, G., Dunsmore, H., Martin, M., 1972. Origin of gypsum veins by hydraulic fracture. J. Inst. Min. Met., 149-155.

Shemesh, A., Ron, H., Erel, Y., Kolodny, Y., Nur, A., 1992. Isotopic composition of vein calcite and its fluid inclusions: Implication to paleohydrological systems, tectonic events and vein formation processes. Chemical Geology 94, 307-314.

Sibson, R., 1992. Implications of fault-valve behaviour for rupture nucleation and recurrence. Tectonophysics 211, 283-293.

Sibson, R.H., 1996. Structural permeability of fluid-driven fault-fracture meshes. Journal of Structural Geology 18, 1031-1042.

Simms, M., 2004. The Wessex Basin (Dorset and central Somerset). Geological Conservation Series 30, 53-107.

Smart, K.J., Ferrill, D.A., Morris, A.P., 2009. Impact of interlayer slip on fracture prediction from geomechanical models of fault-related folds. AAPG bulletin 93, 1447-1458.

Sorby, H., 1859. On the origin of cone-in-cone, Report of the twenty-nineth meeting of the British Assoc. for the Advancement of Science, Notices and Abstracts1859.

Spencer, S., 1991. The use of syntectonic fibres to determine strain estimates and deformation

paths: an appraisal. Tectonophysics 194, 13-34.

Stakes, D.S., Orange, D., Paduan, J.B., Salamy, K.A., Maher, N., 1999. Cold-seeps and authigenic carbonate formation in Monterey Bay, California. Marine Geology 159, 93-109.

Sterte, J., 1986. Synthesis and properties of titanium oxide cross-linked montmorillonite. Clays and Clay Minerals 34, 658-664.

Stewart, D., 1986. Diagenesis of the shallow marine Fulmar Formation in the central North Sea. Clay Minerals 21, 537-564.

Stoneley, R., 1982. The structural development of the Wessex Basin. Journal of the Geological Society 139, 543-554.

Stoneley, R., 1983. Fibrous Calcite Veins, Overpressures, and Primary Oil Migration: Geologic note. AAPG Bulletin 67, 1427-1428.

Stoneley, R., 1992. Review of the habitat of petroleum in the Wessex Basin: implications for exploration. Proceedings-Ussher Society 8, 1-1.

Stow, D.A., 2005. Sedimentary rocks in the field. Manson publishing.

Strijker, G., Bertotti, G., Luthi, S.M., 2012. Multi-scale fracture network analysis from an outcrop analogue: A case study from the Cambro-Ordovician clastic succession in Petra, Jordan. Marine and Petroleum Geology 38, 104-116.

Suchy, V., Dobes, P., Filip, J., Stejskal, M., Zeman, A., 2002. Conditions for veining in the Barrandian Basin (Lower Palaeozoic), Czech Republic: evidence from fluid inclusion and apatite fission track analysis. Tectonophysics 348, 25-50.

Swann, G., Munns, J., 2003. The hydrocarbon prospectivity of Britain's onshore basins. DTI, London.

Talbot, M., Holm, K., Williams, M., 1994. Sedimentation in low-gradient desert margin systems: A comparison of the Late Triassic of northwest Somerset (England) and the late Quaternary of east-central Australia. Geological Society of America Special Papers, 289: 97-117.

Tappin, D., Chadwick, R., Jackson, A.A., Wingfield, R., Smith, N., 1995. Geology of Cardigan Bay and the Bristol Channel. United Kingdom offshore regional report. Oceanographic Literature Review 42, 963.

Tarr, W., 1933. Origin of the "Beef" in the Lias Shales of the Dorset Coast. Geological Magazine 70, 289-294.

Tarr, W.A., 1922. Cone-in-cone. American Journal of Science, 199-213.

Testa, G., Lugli, S., 2000. Gypsum–anhydrite transformations in Messinian evaporites of central Tuscany (Italy). Sedimentary Geology 130, 249-268.

Thomas, R., 2013. Practical guide to ICP-MS: a tutorial for beginners. CRC press.

Tissot, B., Durand, B., Espitalie, J., Combaz, A., 1974. Influence of nature and diagenesis of organic matter in formation of petroleum. AAPG Bulletin 58, 499-506.

Toriumi, M., Hara, E., 1995. Crack geometries and deformation by the crack-seal mechanism in the Sambagawa metamorphic belt. Tectonophysics 245, 249-261.

Tréhu, A.M., Flemings, P.B., Bangs, N.L., Chevallier, J., Gracia, E., Johnson, J.E., Liu, C.S., Liu, X., Riedel, M., Torres, M.E., 2004. Feeding methane vents and gas hydrate deposits at south Hydrate Ridge. Geophysical Research Letters 31, NO 23.

Tucker, M., 1977. The marginal Triassic deposits of South Wales: continental facies and palaeogeography. Geological Journal 12, 169-188.

Tucker, M.E., 2009. Sedimentary petrology: an introduction to the origin of sedimentary

rocks. John Wiley & Sons.

Twiss, R.J., Moores, E.M., 1992. Structural geology. Macmillan.

Tyson, R.V., 1995. Abundance of organic matter in sediments: TOC, hydrodynamic equivalence, dilution and flux effects. Springer.

Underhill, J.R., Stoneley, R., 1998. Introduction to the development, evolution and petroleum geology of the Wessex Basin. Geological Society, London, Special Publications 133, 1-18.

Urai, J., Williams, P., Van Roermund, H., 1991. Kinematics of crystal growth in syntectonic fibrous veins. Journal of Structural Geology 13, 823-836.

Van Hoorn, B., 1987. The south Celtic Sea/Bristol Channel Basin: origin, deformation and inversion history. Tectonophysics 137, 309-334.

Van Noten, K., Claes, H., Soete, J., Foubert, A., Özkul, M., Swennen, R., 2013. Fracture networks and strike–slip deformation along reactivated normal faults in Quaternary travertine deposits, Denizli Basin, western Turkey. Tectonophysics 588, 154-170.

Vengosh, A., Jackson, R.B., Warner, N., Darrah, T.H., Kondash, A., 2014. A critical review of the risks to water resources from unconventional shale gas development and hydraulic fracturing in the United States. Environmental science & technology 48, 8334-8348.

Volland, S., Kruhl, J.H., 2004. Anisotropy quantification: the application of fractal geometry methods on tectonic fracture patterns of a Hercynian fault zone in NW Sardinia. Journal of Structural Geology 26, 1499-1510.

Vrolijk, P., 1987. Tectonically driven fluid flow in the Kodiak accretionary complex, Alaska. Geology 15, 466-469.

Walker, R.J., Holdsworth, R.E., Imber, J., Ellis, D., 2011. The development of cavities and

clastic infills along fault-related fractures in Tertiary basalts on the NE Atlantic margin. Journal of Structural Geology 33, 92-106.

Warpinski, N., Kramm, R.C., Heinze, J.R., Waltman, C.K., 2005. Comparison of single-and dual-array microseismic mapping techniques in the Barnett shale, SPE Annual Technical Conference and Exhibition. Society of Petroleum Engineers.

Warrington, G., Cope, J., Ivimey-Cook, H., 1994. St Audrie's Bay, Somerset, England: a candidate global stratotype section and point for the base of the Jurassic system. Geological Magazine 131, 191-200.

Watts, N., 1978. Displacive calcite: evidence from recent and ancient calcretes. Geology 6, 699-703.

Weertman, J., 1980. The stopping of a rising, liquid-filled crack in the Earth's crust by a freely slipping horizontal joint. Journal of Geophysical Research: Solid Earth 85, 967-976.

Wennberg, O., Svånå, T., Azizzadeh, M., Aqrawi, A., Brockbank, P., Lyslo, K., Ogilvie, S., 2006. Fracture intensity vs. mechanical stratigraphy in platform top carbonates: the Aquitanian of the Asmari Formation, Khaviz Anticline, Zagros, SW Iran. Petroleum Geoscience 12, 235-246.

Weyl, P.K., 1959. Pressure solution and the force of crystallization: a phenomenological theory. Journal of Geophysical Research 64, 2001-2025.

Whiticar, M.J., 1999. Carbon and hydrogen isotope systematics of bacterial formation and oxidation of methane. Chemical Geology 161, 291-314.

Whittaker, A., 1972. The Watchet Fault—a post Liassic transcurrent reverse fault. Bulletin of the Geological Survey, 41: 75-80.

Whittaker, A., Green, G.W., 1983. Geology of the country around Weston-super-Mare, 279.

HM Stationery Office.

Williams, P., Urai, J., 1989. Curved vein fibres: an alternative explanation. Tectonophysics 158, 311-333.

Wiltschko, D.V., Morse, J.W., 2001. Crystallization pressure versus “crack seal” as the mechanism for banded veins. Geology 29, 79-82.

Winkler, E.M., Singer, P.C., 1972. Crystallization pressure of salts in stone and concrete. Geological society of America bulletin 83, 3509-3514.

Wolff, G.A., Rukin, N., Marshall, J.D., 1992. Geochemistry of an early diagenetic concretion from the Birchi Bed (L. Lias, W. Dorset, UK). Organic geochemistry 19, 431-444.

Woodland, B.G., 1964. The nature and origin of cone-in-cone structure. Chicago Natural History Museum.

Worden, R., Benshatwan, M., Potts, G., Elgarmadi, S., 2015. Basin-scale fluid movement patterns revealed by veins: Wessex Basin, UK. Geofluids 16, 149-174.

Wright, S.I., Nowell, M.M., 2006. EBSD image quality mapping. Microscopy and Microanalysis 12, 72-84.

Wu, H., Pollard, D.D., 1995. An experimental study of the relationship between joint spacing and layer thickness. Journal of Structural Geology 17, 887-905.

Yardley, B., 1986. Fluid migration and veining in the Connemara Schists, Ireland, Fluid—rock interactions during metamorphism. Springer, 109-131.

Zanella, A., Cobbold, P.R., Rojas, L., 2014. Beef veins and thrust detachments in Early Cretaceous source rocks, foothills of Magallanes-Austral Basin, southern Chile and Argentina: Structural evidence for fluid overpressure during hydrocarbon maturation. Marine and Petroleum Geology 55, 250-261.

Zheng, Y.-F., Hoefs, J., 1993. Carbon and oxygen isotopic covariations in hydrothermal calcites. Mineralium Deposita 28, 79-89.

Ziegler, P.A., 1982. Geological atlas of western and central Europe. Geological Society of London.